WP2 – Deliverable 2.12

Report and geological maps of West Macedonia

Release Status: Public
Authors: Pavlos Tyrologou (CERTH), Nikolaos Koukouzas (CERTH), Christos Stergiou (CERTH), Christina Karatrantou (CERTH), Ioanna Badouna (CERTH), Christos Karkalis (CERTH), Agni Vamvaka (CERTH), Dimitrios Ktenas (HEREMA), George Makrodimitras (HEREMA), Constantinos Tzimeas (HEREMA), Efthimios Tartaras (HEREMA)

Edited by Mark Wilkinson
Date: 17/12/2025
Filename and Version: PilotSTRATEGY_Deliverable 2.12_FINAL
Project ID Number: 101022664

PilotSTRATEGY (H2020- Topic LC-SC3-NZE-6-2020 - RIA)

The PilotSTRATEGY project has received funding from the European Union's Horizon 2020 research and innovation programme under grant agreement No. 101022664

Document History

Location

This document is stored in the following location:

Filename	PilotSTRATEGY_Deliverable 2.12_FINAL
Location	

Revision History

This document has been through the following revisions:

Version No.	Revision Date	Filename/Location stored:	Brief Summary of Changes

Authorisation

This document requires the following approvals:

AUTHORISATION	Name	Signature	Date
WP Leader	Mark Wilkinson	Mark Wilkinson	10/12/2025
Project Coordinator	Isaline Gravaud	Isaline Gravaud	17/12/2025

Distribution

This document has been distributed to:

Name	Title	Version Issued	Date of Issue
Public			17/12/2025

The PilotSTRATEGY project has received funding from the European Union's Horizon 2020 research and innovation programme under grant agreement No. 101022664

The raw data for this report is listed below and can be retrieved from zenodo using their registered doi:

1. Geodatabase doi:10.5281/zenodo.17588447
2. Report and Dataset on Water Absorption, Effervescence, and Rock Stability from the Second Phase of the PilotSTRATEGY Mapping and Sampling Project, Mesohellenic Trough (Grevena, Greece) doi: 10.5281/zenodo.17176303
3. X-ray diffraction laboratory investigation for the Eptachori, Pentalofos and Tsotyli formations in West Macedonia doi: 10.5281/zenodo.10891026
4. Factual Report on XRF Analysis Conducted on Bulk Sedimentary Rock Samples from the Mesohellenic Trough doi: 10.5281/zenodo.10891028
5. West Macedonia water sampling campaign with chemical analysis including isotopes, helium, methane and hydrogen as part of the Pilot Strategy Horizon2020 project doi: 10.5281/zenodo.15835158

Suggested citation:
Tyrologou, P., Koukouzas, N., Stergiou, C., Karatrantou, C., Badouna, I., Karkalis, C., Vamvaka, A., Ktenas, D., Makrodimitras, G., Tzimeas, C., Tartaras, E. (2025). Deliverable D2.12 – Report and geological maps of West Macedonia, (PilotSTRATEGY, Horizon 2020, GA 101022664), doi: 10.5281/zenodo.17878501

Disclaimer

The information and views set out in this report are those of the author(s) and do not necessarily reflect the official opinion of the European Union. Neither the European Union institutions and bodies nor any person acting on their behalf may be held responsible for the use which may be made of the information contained therein.

Executive summary

This deliverable includes the results of the geological characterisation of the Mesohellenic Trough (MHT) in Western Macedonia, Greece, conducted within the framework of the PilotSTRATEGY project. The suitability of the basin for CO_2 geological storage is assessed by integrating field, laboratory, and geophysical datasets. The objective was to advance the knowledge on the geological model of the MHT and to identify key risks and uncertainties.

The MHT is a late-orogenic molassic basin of the Hellenides, comprising thick Oligocene-Miocene sedimentary series. Alternating sandstones, conglomerates, and marls dominate the successions forming the primary reservoir-seal system and resting unconformably upon Mesozoic ophiolitic and carbonate basement rocks. The main stratigraphic formations, including the Eptachori, Pentalofos, and Tsotyli, were field surveyed (geological mapping) and documented across nine regions lacking sufficient structural data. Gently dipping beds and limited fault activity, characterise the basin providing a stable structural framework suitable for long-term storage.

Petrophysical, geomechanical, and geochemical investigations were undertaken to evaluate the porosimetry and sealing properties of the rocks. Pentalofos and Eptachori sandstones exhibit porosities up to 10.8% and very low permeabilities (<0.01 mD), while marly intercalations; especially in the Tsotyli Formation, demonstrate high sealing capacity. The thick sandstone-marl alternations define multiple reservoir-seal pairs throughout the stratigraphic column. The geochemical investigation confirmed a significant lithological variability from silica-rich to carbonate-rich units. These alternate across the basin, influencing both reactivity under CO_2 exposure and mechanical strength.

Legacy seismic data were re-processed, significantly improving the subsurface imaging by enabling refined mapping of key horizons and fault geometries. The integration of the interdisciplinary analytical data led to a preliminary conceptual geological model, which was developed outlining the spatial relationships between reservoirs, seals, and potential migration pathways.

Risk assessment identified semi-quantitatively the main geological uncertainties. These include: (i) heterogeneity in sealing units, (ii) variability in reservoir quality, (iii) possible migration or leakage pathways, (iv) injection-induced seismicity, (v) ground deformation and brine displacement, and (vi) long-term geochemical alteration. Although the overall geological framework in the MHT appears suitable for CO_2 storage, these risks need further assessment by detailed modelling and ongoing monitoring.

In conclusion, the results of this deliverable establish that the MHT could provide favorable CO_2 storage sites and suggest that subsequent modelling, pilot-scale testing, and risk mitigation strategies are needed. Monitoring of gas migration and long-term geochemical interactions should be prioritized in future work to ensure the safety and durability of CO_2 storage operations in Western Macedonia.

The PilotSTRATEGY project has received funding from the European Union's Horizon 2020 research and innovation programme under grant agreement No. 101022664

Table of Contents

Document History 2

Location 2

Revision History 2

Authorisation 2

Distribution 2

Executive summary 4

1. Introduction 8

1.1. General 8

1.2. Aim and objectives of the works and research study 8

1.3. Structure of the report 9

1.4. Sources of information 9

1.5. Limitations 9

2. Area Description and desk study 11

2.1. Site Location 11

2.2. Site description and history 12

2.3. Geomorphology 15

2.4. Land uses 16

2.5. Demographics 17

2.6. Vegetation 18

2.7. Climate conditions 20

2.8. Hydrology and Hydrographic Network 24

3. Geological setting 27

3.1. Geological Overview of the Hellenides 27

3.2. The Mesohellenic Trough 29

3.2.1. Krania Formation 31

3.2.2. Eptachori Formation 31

3.2.3. Pentalofos Formation 32

3.2.4. Tsotyli Formation 32

The PilotSTRATEGY project has received funding from the European Union's Horizon 2020 research and innovation programme under grant agreement No. 101022664

3.2.5. Ondria Formation 33
3.3. Structural Evolution 34
3.4. Hydrogeology 38
3.5. Seismicity 39
3.5.1. Seismicity and periodicity 40
3.5.2. Fault systems 42
3.6. Volcanicity 43
4. Natural Hazards 44
4.1. Earthquakes 44
4.2. Flooding 44
4.3. Landslides 48
5. Geological on site survey 49
5.1. Fieldwork Approach and Observations 50
5.2. Mapping Area Overview 50
5.3. Lithostratigraphic/Stratigraphic Observations 51
5.4. Structural Geology Observations and kinematic analysis 63
5.4.1. Sampling strategy & execution 79
5.5. Rock water absorption investigation 80
5.5.1. Regional & Comparative Assessment of Hydrogeological Properties 124
5.6. Remote sensing mapping based on field observation 128
5.7. Map & Cross sections 132
6. Geochemical analysis 135
6.1. Geochemical investigation 135
6.2. Sampling Strategy and Analytical Framework 138
6.3. Geochemical and Isotopic results 142
6.4. Interpretation of gas sources and migration mechanisms 150
7. Re-processing of Legacy seismic data and interpretation 154
8. Geological conceptual modelling 161
9. Key engineering geology risks and uncertainties 165

The PilotSTRATEGY project has received funding from the European Union's Horizon 2020 research and innovation programme under grant agreement No. 101022664

10. Discussion: Risk Source Assessment 170
10.1. Site selection and characterization 170
10.2. Risk identification 171
10.3. Vulnerability assessment 171
10.4. Movement of the ground 172
10.5. Fault reactivation 172
10.6. Induced seismicity 172
10.7. Contamination of drinking water by displaced brines 172
10.8. Damage to hydrocarbon or mineral resources 172
10.9. Integrated evaluation 172
11. Conclusion 175
Bibliography 178
Appendices 188
Appendix I Factual reports SEM-EDS Analysis Conducted on Bulk Sedimentary Rock Samples from the Mesohellenic Trough 188
Appendix II XRD Analysis Conducted on Bulk Sedimentary Rock Samples from the Mesohellenic Trough 202
Appendix III XRF Analysis Conducted on Bulk Sedimentary Rock Samples from the Mesohellenic Trough 208
Appendix IV Photographic material field survey 211
Appendix V Supplementary material of SEM-EDS Analysis Conducted on Bulk Sedimentary Rock Samples from the Mesohellenic Trough 246
Appendix VI Supplementary material of XRD-EDS Analysis Conducted on Bulk Sedimentary Rock Samples from the Mesohellenic Trough 259
Appendix VII Earthquake data record 262
Appendix VIII Flood data record 311
Appendix IX Landslides data record 312
Appendix X Absorption test result (Excel file) 314

The PilotSTRATEGY project has received funding from the European Union's Horizon 2020 research and innovation programme under grant agreement No. 101022664

1. Introduction

1.1. General

The PilotSTRATEGY project brings together research teams from across Europe to test the feasibility of carbon capture and storage (CCS) by building a detailed understanding of candidate storage sites in five regions, in France, Poland, Spain, Portugal and Greece. The Mesohellenic Trough near Grevena is the Greek focus in West Macedonia. This basin was chosen because of its particularly favourable geological setting. It preserves thick successions of molasse deposits, alternating sandstones, conglomerates, and marls, overlain by Miocene sand–marl sequences, all resting directly against ophiolitic basement rocks. The interposition of these reservoir-prone and sealing lithologies, and the juxtaposed basement units, makes the area a compelling target for assessing CO_2 storage potential. This geological framework provides both potential reservoir horizons and natural seal rocks, but also introduces structural complexity and heterogeneity that must be carefully assessed. Within the PilotSTRATEGY project, Work Package 2 (Geocharacterization) has the primary responsibility of acquiring, compiling, and interpreting geological, geophysical, geomechanical, geochemical, and hydrogeological datasets that can define the storage potential of these formations. The present deliverable forms part of this work, documenting the outcomes of mapping, sampling, and laboratory investigations carried out for the Greek case study. This report is supplementary on a geodatabase that includes all desktop, laboratory and field work executed during the project duration. The database is provided under Creative Commons Attribution 4.0 International and is available from zenodo at https://zenodo.org/records/17588448 with a doi: 10.5281/zenodo.17588447.

1.2. Aim and objectives of the works and research study

The aim of this work is to provide an advanced geocharacterisation of the Mesohellenic Trough to assess its suitability as a potential CO_2 storage system. This involves five objectives that sum up as identification of promising reservoir units and the evaluation of their sealing capacity, structural integrity, and long-term stability.

First, to document the lithological variability of the Eptachori, Pentalofos, and Tsotyli formations, which represent the main reservoir and seal candidates. This was achieved through detailed field surveys and the collection of over one hundred rock samples, complemented by thirty-eight water samples from the wider basin.

Second, to investigate petrophysical and geomechanical properties through laboratory testing. Analysis also included preliminary testing on water absorption, effervescence, porosity, permeability, and stability.

Third, to analyze the mineralogical and geochemical composition of representative rocks using methods such as XRF, XRD, and SEM imaging, which allow for the identification of carbonate, silica, and clay fractions critical to understanding reservoir performance.

Fourth, to integrate structural observations from the field, particularly bedding, jointing, and faulting, with laboratory data in order to build a coherent geological framework.

Fifth, to provide datasets and interpretations that will feed directly into the conceptual geological model, or if possible, to future geomechanical simulations, and risk assessments undertaken in subsequent work packages.

The PilotSTRATEGY project has received funding from the European Union's Horizon 2020 research and innovation programme under grant agreement No. 101022664

1.3. Structure of the report

The report has been arranged to mirror the actual steps of the work, moving gradually from the raw observations in the field to their interpretation within a wider framework. After the introductory material, Chapter 4 sets the stage with a summary of the regional geological and tectonic setting of the MHT, showing how the study area fits into the wider geological picture of Western Macedonia. In Chapter 5, the mapping strategy, the sampling methods, and the reasoning behind the selection of sites across Regions 1 to 9, are described, while the results of the field surveys are presented in Chapter 6, which combines stratigraphic logs, photographs, and records of structural discontinuities. Chapter 6 should be read by taking also into consideration the related Appendixes. Chapter 7 includes the laboratory investigations, where geochemical results are presented. Chapter 8, makes an effort to synthesize the presented results by integrating all datasets into a conceptual model of the basin. Particular attention to the interplay between reservoirs and seals is given, as well as to the identification of possible migration pathways, and the role of structural features. In Chapter 9, the re-evaluation of legacy geophysical data is included, further refining the geological model of the MHT and improving the interpretative confidence of the other datasets. The main engineering geology risks and uncertainties are presented in Chapter 10, while in Chapter 11 a broader discussion is held placing the findings within the overall objectives of the project. Finally, Chapters 12 and 13 conclude the deliverable, summarizing the key outcomes and providing recommendations for the next steps of PilotSTRATEGY.

1.4. Sources of information

The study draws on a broad range of information sources that combine legacy data with newly acquired results. Published literature of the MHT and Western Macedonia provides a base framework for stratigraphy, structure, and regional tectonic evolution. Previous studies on the sedimentology, mineralogy, and hydrogeology of the area have been systematically reviewed and incorporated in this deliverable. Complementing this, the PilotSTRATEGY field campaigns have generated new datasets through systematic sampling, stratigraphic logging, and structural measurements across the study (Figure Erreur ! ***Utilisez l'onglet Accueil pour appliquer Heading 1 au texte que vous souhaitez faire apparaître ici.***.*1*). Laboratory analyses undertaken specifically for this deliverable include SEM-EDS imaging, XRD and XRF geochemical characterisation, and petrophysical tests (porosity, permeability, and water absorption). These results are directly linked to their International Geo Sample Number (IGSN) through registration on the SESAR2 platform, ensuring long-term traceability. Finally, regional hydrogeological and geophysical information from national agencies, together with datasets shared by consortium partners, have been integrated to complete the investigation.

1.5. Limitations

The present work is subject to limitations, related to the availability of legacy borehole and seismic data for the Region of Western Macedonia, Greece (Figure Erreur ! ***Utilisez l'onglet Accueil pour appliquer Heading 1 au texte que vous souhaitez faire apparaître ici.***.*1*). This required greater reliance on surface outcrop analogues. While outcrop studies provide essential information, they do not usually fully capture subsurface variability at reservoir depths. Laboratory results are necessarily based on a restricted number of samples, 120 rock and 38 water samples, which, although carefully chosen, cannot represent the full heterogeneity of a basin over several thousand square kilometres. Seasonal and logistical constraints during field campaigns also restricted the number of sites visited, particularly in areas with limited accessibility.

The PilotSTRATEGY project has received funding from the European Union's Horizon 2020 research and innovation programme under grant agreement No. 101022664

Further uncertainty is introduced by scaling laboratory results, such as permeability or mechanical strength, to reservoir dimensions, which becomes even more pronounced in areas characterized by heterogeneous or mixed lithologies such as conglomerates. In addition, the structural interpretations remain partially constrained by the lack of dense subsurface imaging data, meaning that fault continuity and connectivity must be inferred from surface exposures. These limitations are acknowledged and form part of the risk assessment framework, which could be refined in subsequent research phases through modelling, sensitivity analyses, and targeted acquisition of additional datasets.

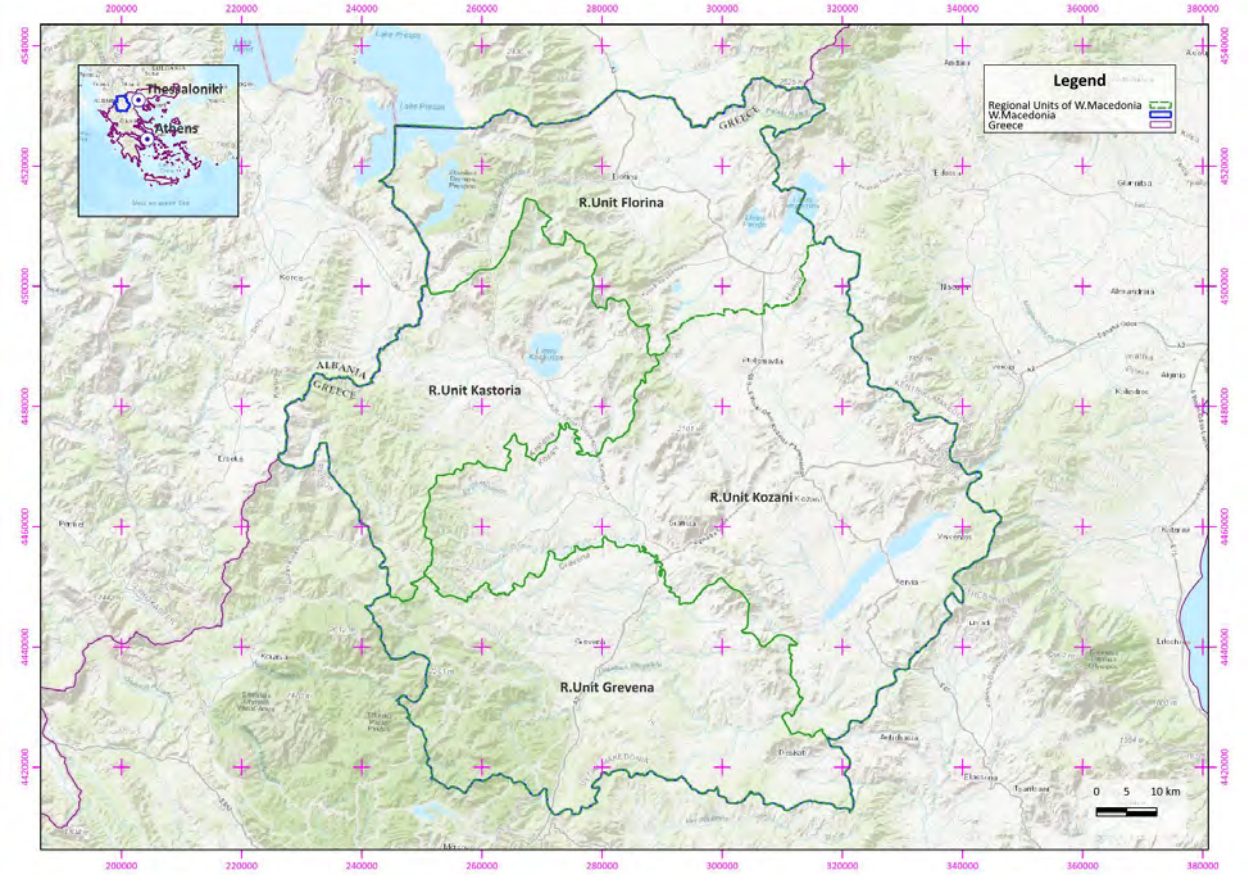

Figure **Erreur ! Utilisez l'onglet Accueil pour appliquer Heading 1 au texte que vous souhaitez faire apparaître ici.**.1: Regional Units of Western Macedonia (Florina, Kastoria, Grevena, and Kozani) and their administrative boundaries within Northern Greece.

The PilotSTRATEGY project has received funding from the European Union's Horizon 2020 research and innovation programme under grant agreement No. 101022664

2. Area Description and desk study

2.1. Site Location

The Mesohellenic Trough (hereafter MHT) is a late orogenic molassic-type basin of the Hellenides, located in northern Greece and southern Albania [1]. It is around 200km long and 30 to 40km wide. It extends with a NW-SE trend across the cities of Kastoria, Grevena and Kalambaka, and ending beneath the younger Neogene and Quaternary deposits of the Thessaly plain [2] (Figure 2.1). A significant part of the MHT is within the region of West Macedonia, where the West Macedonia Lignite Centre (WMLC) is also situated a bit further east (Ptolemais Basin).

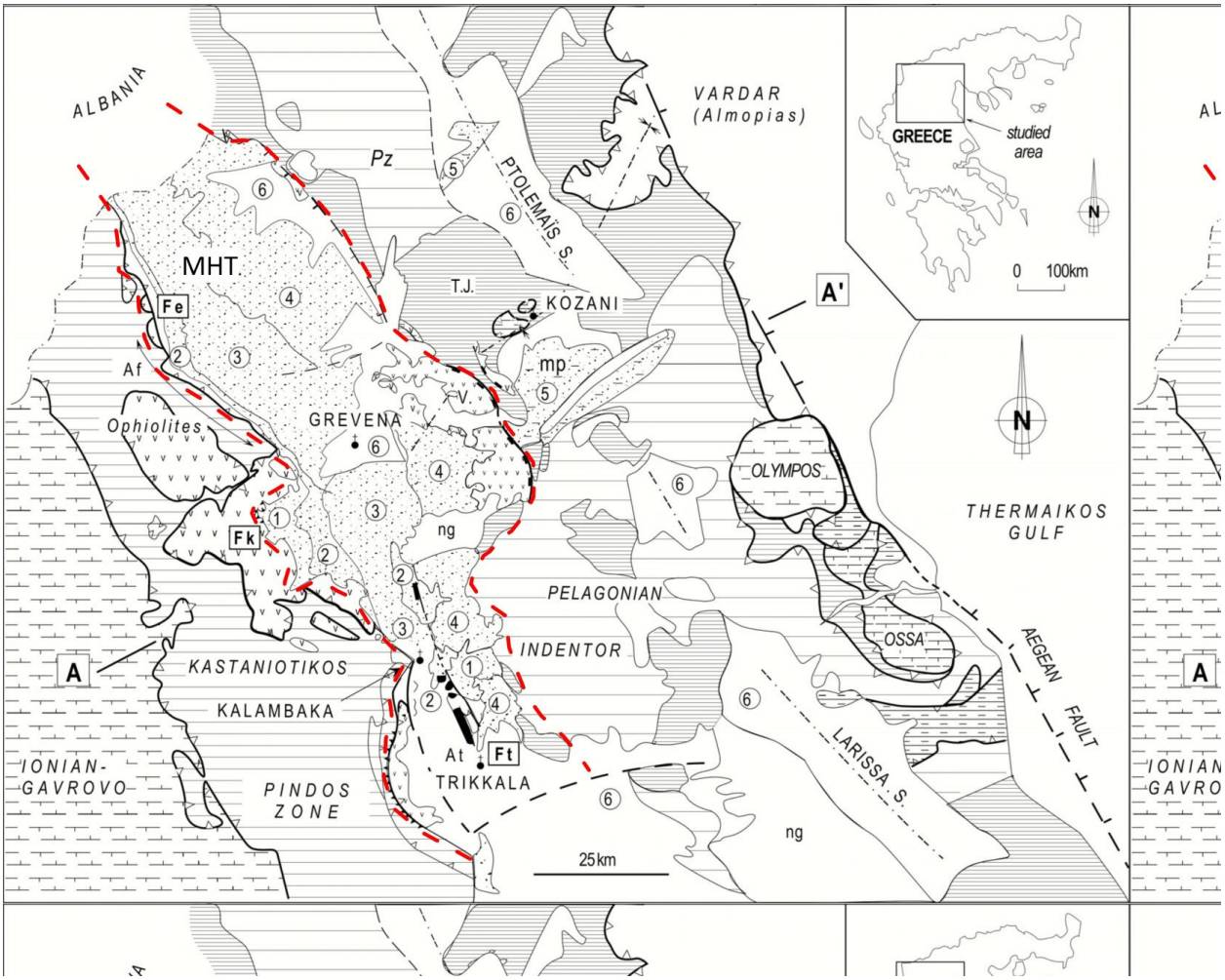

Figure 2.1: Simplified geological map of the Mesohellenic Trough (MHT), outlined with red dashed lines, and the broader geological framework[3]. 1 to 4: main formations (Fms) of the MHT, 1: Krania Fm (late Eocene), and 2: Eptachori Fm (Early Oligocene), 3: Pentalofos Fm (Late Oligocene-Ealry Miocene), 4: Tsotyli and Ondria Fms (Early-Middle Miocene), 5: Ptolemais basin (late Miocene-Pliocene, mp), 6: recent deposits. Abr. Ng : Neogene, Pz: Paleozoic, TJ: Triassic and Jurassic, V: Vourinos massif, S: synclines, A: anticlines (i.e., Af: Filippi anticline, At:

The PilotSTRATEGY project has received funding from the European Union's Horizon 2020 research and innovation programme under grant agreement No. 101022664

Theopetra-Theotokos anticline), Bold lines and Fe, Fk, Ft: major tectonic contacts and faults; lines with black triangles: Tertiary back-thrusts or main reverse series; Dashed lines: normal faults [4]

2.2. Site description and history

The MHT is considered the largest and most important basin of the last orogenic stage of the Hellenides where a significant amount of coal deposits [1]. Lignite has been found in more than 60 basins across Greece and it has been exploited mainly by the Power Public Corporation (P.P.C.) of Greece for electricity production. In northwestern Greece, covering the eastern part of the Region of Western Macedonia, the most significant lignite deposits occur in the Florina, Ptolemais-Amyntaio, Kozani-Servia, Sarandaporos basin system, and especially in the Ptolemais-Florina basin where the West Macedonia Lignite Centre (WMLC) is located [5]. In the MHT itself, coal occurrences have been identified mainly in the older Oligocene sedimentary formations, but without significant indications for mining potential, and the lignite occurrences are scattered, with variable petrographic and geochemical features [6].

Since the early 1950s, the lignite industry has shaped the development of West Macedonia. The intensive exploitation of domestic lignite deposits was a central political choice and contributed significantly to the electrification of Greece and consistently supported the security of the national energy supply. For decades, more than 25% of the regional GDP of West Macedonia and more than 22,000 direct and indirect jobs were based on the needs of local lignite activity. The region hosts the highest installed unit power compared to other regions regarding thermal power plant units. Out of 13,077.9 MW of installed net power, the region hosts 3,945 MW based on lignite units and another 375MW of hydroelectric power. Therefore, it covers 33% of Greece's total capacity, covering 39% of thermal unit power and 12% of hydroelectric plants. In addition, the downstream water potential of river Aliakmonas increases the hydroelectric power potential to 26.4%[7].

In the Region of Western Macedonia, CO_2 emissions are largely associated with the operation of lignite-fired power plants that historically supported the industrialisation of the region. This development was based on the extensive domestic lignite resources of the area. Today, almost all lignite units have been decommissioned, and Ptolemaida V is the only operational power plant. The Agios Dimitrios, Kardia, Meliti, and Amyntaio plants have all ceased operation, with Amyntaio closing in 2020 and Kardia and Agios Dimitrios following in the subsequent years[7]. Ptolemaida V (operation start in 2023) with an installed capacity of 660 MW, is the last lignite unit in Greece. According to national energy planning, the plant will continue to operate on lignite until 2028, after which it will be converted to natural gas with an expected unit capacity of around 1,000 MW. Until then, it remains the primary source of CO_2 emissions in Western Macedonia, while also being identified as a candidate facility for future integration with carbon capture and storage (CCS) technologies in line with the energy transition strategy in Greece[7].

Since May 2021, a new unit of electricity production from biomass operates in Grevena, which is based in the near area of the Mavranaioi village. Through the utilisation of wood waste, the new biomass plant contributes to meet the electrification needs of approximately 6,000 Greek households per year. It is expected that the production of electricity through biomass will achieve a reduction of CO_2 emissions per year of 12,000 tons, compared to crude oil[7]. In addition, the utilisation of the produced thermal energy and the heating of the industrial spaces, reduces the release of pollutants into the atmosphere.

In 2021, UNESCO formally inducted Geopark Grevena-Kozani into its Global Geoparks Network. The geopark covers an area of nearly 2,500 km^2 within West Macedonia. Approximately 1,100km^2 of the

The PilotSTRATEGY project has received funding from the European Union's Horizon 2020 research and innovation programme under grant agreement No. 101022664

Geopark spans across the Mesohellenic Trough. In Greece, UNESCO Global Geoparks are under the purview of the Natural Environment and Climate Change Agency (N.E.C.C.A.), supervised by the Ministry of Environment and Energy. The objectives of UNESCO Global Geopark Grevena-Kozani include the preservation and promotion of geoheritage, education and local, sustainable economic development including tourism[8].

Except for the network focused on geoparks, the network of protected areas in Greece is made up of several distinct categories that together safeguard the national natural heritage. These include biodiversity conservation zones, such as the Natura 2000 sites, which are part of a wider European ecological network. In addition, Greece has established national parks, wildlife refuges, and areas designated as protected landscapes or natural formations. Each category serves a specific role, from preserving habitats and species to maintaining the integrity of unique landforms and ecosystems.

According to Natural Environment & Climate Change Agency (N.E.C.C.A.), there are two Management Units in the wider area of the Region of Western Macedonia, the Management Unit of the Prespa National Park and Protected Areas and the Management Unit of the Northern Pindos National Park, which also cover parts of the Region of Epirus (Figure 2.2). In this context, several zones of important ecosystems are identified in the study area [9]. These are described in the following sub-chapters.

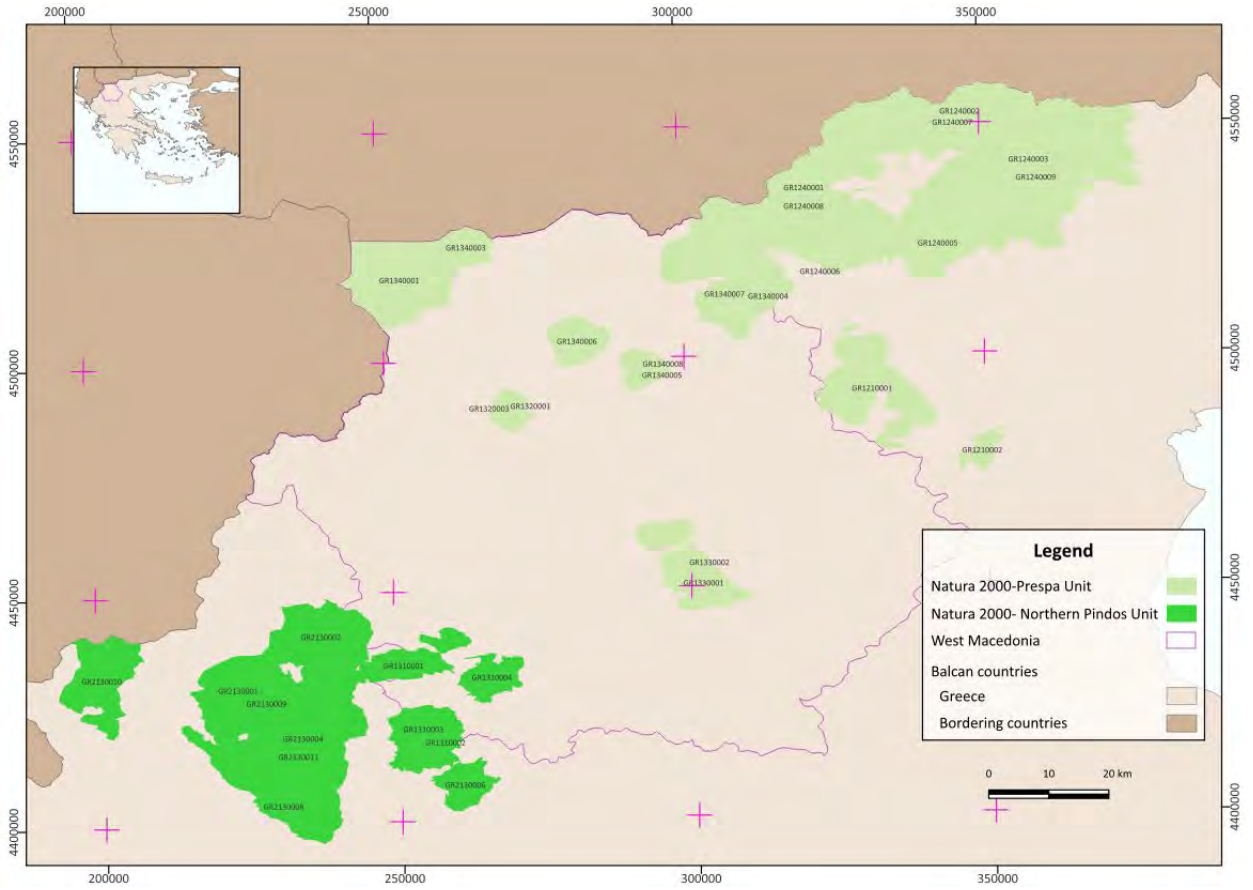

Figure 2.2: Natural protected areas in West Macedonia. The two Management Units that pertain in West Macedonia are the Prespa National Park and Northern Pindos National Park. Ref.system: EGSA 87.

The PilotSTRATEGY project has received funding from the European Union's Horizon 2020 research and innovation programme under grant agreement No. 101022664

This unit administrates the largest national park in Greece, covering a total area of 19,400 Ha. However, the zone under strict protection occupies only 20% of this area. The Prespa National Park is the natural habitat of more than 3,180 animal and plant species and it includes 23 Natura 2000 sites [10] (Table 2.1).

Table 2.1: Natura 2000 sites of Management Unit of the Prespa National Park and Protected Areas. Apart from the official latinized Greek names of the protected areas, the corresponding English names are provided in parentheses.

GR CODE	SITE
GR1210001	Oros Vermio (Vermio Mountain)
GR1210002	Stena Aliakmona (Straits of Aliakmonas)
GR1240001	Korufes Orous Vora (Voras mountain peaks)
GR1240002	Ori Tzena (Tzena Mountain)
GR1240003	Oros Paiko (Paiko Mountain)
GR1240004	Limni Agra (Agra Lake)
GR1240005	Stena Apsalou-Moglenitsas (Straits of Apsalou-Moglenitsas)
GR1240006	Limni & Fragma Agra (Lake and dam of Agra)
GR1240007	Ori Tzena & Pinovo (Tzena & Pinovo Mountains)
GR1240008	Oros Voras (Voras Mountain)
GR1240009	Oros Paiko-Stena Apsalou-Moglenitsas (Paiko Mountain-Straits of Apsalou-Moglenitsas)
GR1320001	Limni Kastorias (Kastoria Lake)
GR1320003	Limni Orestias (Kastorias) (Orestias Lake)
GR1330001	Oros Vourinos (Koryfi Apsrovouni) (Vourinos Mountain (Asprovouni peak)
GR1330002	Ori Voreiou Vourinou & Mellia (Northern Vourinos Mountain & Mellia)
GR1340001	Ethnikos Drymos Prespon (Prespa National Park)
GR1340003	Ori Varnounta (Varnountas Mountain)
GR1340004	Limnes Vegoritidas-Petron (Vegoritida-Petron Lakes)
GR1340005	Limnes Heimaditida-Zazari (Heimaditida-Zazari Lakes)
GR1340006	Oros Vernon-Koryfi Vitsi (Vernon Mountain-Vitsi peak)
GR1340007	Limni Petron (Petron Lake)
GR1340008	Limnes Heimaditida & Zazari (Heimaditida & Zazari Lakes)
GR1340009	Ori Varnounta-Evryteri Periochi (Varnountas Mountain-broader region)

Limestones and ophiolites are the most common rocks in the area. Small (Mikri in greek) and Great (Megali in Greek) Prespa Lakes are among the oldest lakes in Europe, as they were first formed between Late Miocene and Pleiocene. The Prespes hydrological basin is endorheic. Dolomites and metamorphic rocks build up the substrate of the basin. Vegoritida Lake is surrounded by Askio, Vermio and Voras Mountains, where limestones and metamorphic rocks prevail[10].

In earlier geological times, the Eordaia valley was covered by a vast lake, known as Lake Eordaia, covering an area of nearly 1,000 km² and reaching depths <250 meters. Over the course of subsequent geological periods, the geomorphology of the region shifted, and the original lake gradually gave way to a system of

The PilotSTRATEGY project has received funding from the European Union's Horizon 2020 research and innovation programme under grant agreement No. 101022664

five smaller lakes: Vegoritida, Petra, Heimaditida, Zazari, and the Sari-Gyol marsh. The Sari-Gyol marsh was eventually drained to make way for the development of the Ptolemais lignite mines. Today, Lake Vegoritida stands as the largest and deepest remnant of this ancient system, occupying the northern edge of the Eordaia valley and serving as a striking reminder of the palaeogeographic history of the valley. In the Northern Pindos National Park there are about 30 types of natural habitats where more than 2,300 species of flora and fauna exist. The park includes 13 Natura 2,000 sites [11] (Table 2.2).

Table 2.2: Natura 2000 sites of Management Unit of Northern Pindos National Park. Apart from the official latinized Greek names of the protected areas, the corresponding English names are provided in parentheses.

GR CODE	SITE
GR1310001	Vasilitsa
GR1310002	Valia Kalnta & Techniti Limni Aoou (Valia Calda & Artificial Aoos Lake)
GR1310003	Ethnikos Drymos Pindou (Valia Kalnta)-Evryteri Periochi (Pindos Nationa Park (Valia Calda)-broader region
GR1310004	Ori Orliakas & Tsourgiakas (Orliakas & Tsourgiakas Mountains)
GR1320002	Koryfes Orous Grammos (Grammos Mountain peaks)
GR2130001	Ethnikos Drymos Vikou-Aoou (Vikos-Aoos National Park)
GR2130002	Koryfes Orous Smolikas (Smolikas Mountain peaks)
GR2130004	Kentriko Tmima Zagoriou (Central part of the Zagori region)
GR2130006	Periochi Metsovou (Anilio-Katara) (Metsovo area (Anilio-Katara)
GR2130008	Oros Mitsikeli (Mitsikeli Mouuntain)
GR2130009	Oros Tymfi (Gkamila) (Tymfi Mountain (Gamila peak)
GR2130010	Oros Douskon, Oraiokastro, Dasos Meropis, Koilada Gormou, Limni Delvinakiou (Douskon Mountain, Oraiokastro, Meropi forest, Gormou valley, Delvinaki Lake)
GR2130011	Kentriko Zagori & Anatoliko Tmima Orous Mitsikeli (Central Zagori & eastern parts of Mitsikeli Mountain)

In the northern and eastern parts of the Management Unit, ophiolite rocks are dominant, while in the southern and western parts, limestones are the main rock type. Limestones are also located in numerous sites in central and north-northeastern areas of the Northern Pindos National Park. Basalts and peridotites are the main rocks found in the Valia Calda National Forest. The upper mantle peridotites occur near the Perivoli, Mikrolivado and Monachiti villages. The nearby area of the Aoos springs consists of sandstone and marl (flysch formation) and peridotite [11].

2.3. Geomorphology

The MHT is a 200 km length and 30 to 40 km in width elongated sedimentary basin that stretches from SE Albania to the Western Macedonia and Thessaly regions in NW Greece [12-14]. The basin is located on top of the Apulian and Pelagonian microcontinental tectonic plates [13] above the tectonic suture between the external and internal Hellenides [14]. The MHT is oriented by the Askio Mountain to the NE and the Pindos mountain range to the SW, corresponding to a topographic furrow [15]. Structurally, the MHT is characterised by complicated sedimentary structures and phases [16], which range highly in thickness and can reach up to 4 km [14, 17] vertically or parallel with the basin axis [17]. During Oligocene, the basin became

The PilotSTRATEGY project has received funding from the European Union's Horizon 2020 research and innovation programme under grant agreement No. 101022664

thinner at the edges and thicker in the center, resembling the shape of a canoe [15]. Due to different tectonic processes that took place during and after the formation of the basin, most strata tend to dip to the east [14]. Specifically, strata at the western margin of the MHT tend to show an ENE dip direction, which gradually decreases with the distance from the boundaries [13]. The strata on the eastern edge of MHT exhibit diverse dip direction compared to those of the western side characterized by low angle WSW dip [13]. The difference between dip of strata creates an asymmetrical syncline located in the northern MHT, in the Western Macedonia region. This region is typically mountainous, characterized by a variety of water sources, that do not communicate with the sea [18]. In Western Macedonia, approximately the 65% of the surface water in Greece is found, provided by Aliakmonas River, the largest river in the country, and numerous natural and artificial lakes [18]. The central area of the MHT in this region hosts the Grevenitis drainage basin [19], showing a "dendritic pattern" [20] which belongs to the broader Aliakmonas River drainage basin. Geomorphologic studies indicate that the drainage basin was subjected to extensive erosion [19, 21] and mature denudation [19, 22, 23]. In the eastern margin of the MHT, the Neogene-Quaternary Florina, Ptolemais-Amyntaio, Kozani-Servia, Sarandaporos basin system is found bounded by the Askio Mountains [24].

At the southern part of this basin system the Kozani basin [25] is found displaying an extreme topographic relief in its SE margin, which is assigned to intense neotectonic processes. This part of the basin differs from the NW margin, which shows smooth topographic relief with streams that flow straight, favouring the formation of a parallel drainage pattern [24]. Tectonics is the main geological feature that controls the morphology of the Kozani basin, represented by high morphological slopes, which mainly trend NE-SW and less frequently NW-SE, and an asymmetric local drainage systems [24]. Across the MHT several cross-sections have shown that the SW margin is more constant and has suffered a more restricted deformation compared to the NE margin [26]. The Grevena highland zone, which are located in the central parts of the northern Pindos mountain range, is a morphologically broad and uplifted area. It hosts high peaks with altitudes above 2000 m , comprising a succession of ridges, which are alternating with plateaus that were affected by deep erosion due to the occurrence of several rivers [27]. The central-west part of the MHT exhibits extended windows and resistant ridges that were formed in the ophiolitic rocks [26]. The relief changes and becomes relatively flat towards the SE parts of the MHT, until the area where the sediments of the MHT dip below the Late Miocene-Quaternary sediments of the Thessaly plain [15].

2.4. Land uses

Land use is an important factor in enabling and supporting the transition from coal in various contexts. Its negligence could be an important missed opportunity, both economically and as a contribution to environmental and social sustainability. Land uses can enable and contribute significantly to stimulating post-coal economic activities and growth. A well-planned re-purposing makes land available for a number of uses with benefits to climate change mitigation and improvements of environmental conditions. The main land uses in the Region of Western Macedonia are artificial surfaces (e.g. settlements, airports, lignite mines), agricultural areas, vegetation, wetlands and water bodies (Figure *2.3*Figure 2.3).

As the MHT extends across both the northwestern and southwestern sectors of West Macedonia, the overall pattern of land use remains broadly consistent throughout the area. The distribution of agricultural land, forest cover, and built-up zones shows only minor variations across the trough, suggesting that regional land use has been shaped more by uniform topographic and climatic conditions than by local geological differences (Figure *2.4*Figure 2.4).

The PilotSTRATEGY project has received funding from the European Union's Horizon 2020 research and innovation programme under grant agreement No. 101022664

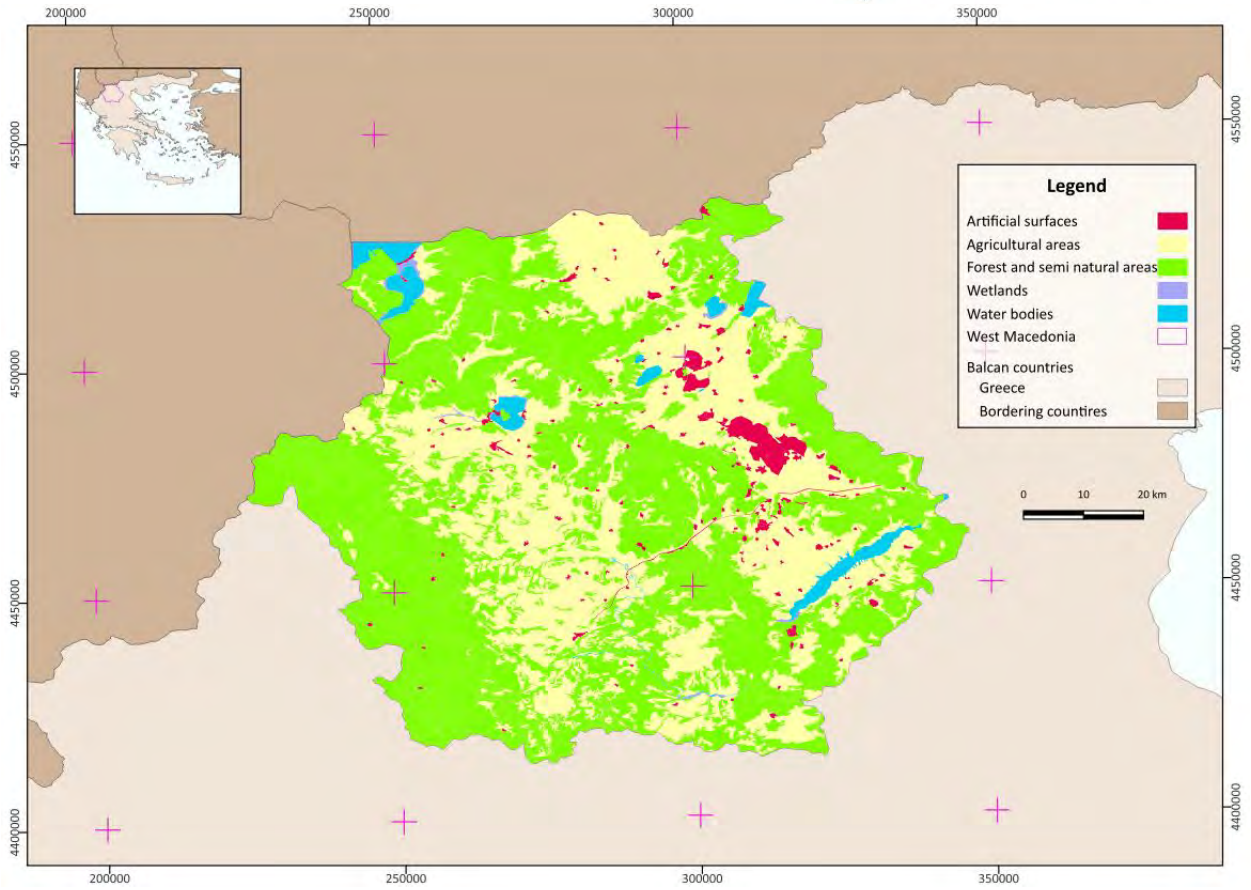

Figure 2.3: Land uses of the Region of West Macedonia. The large red areas highlight the lignite mines of the West Macedonia Lignite Centre. Ref.system: EGSA87.

2.5. Demographics

According to the 2021 Greek census, the total population of the Region of Western Macedonia region is 254,595 inhabitants (2.4% of the total population). It is classified as a low-density populated region (30 persons per km², as compared to the national average of 81.96 persons per km²). This is attributed to the mountainous nature of the region; 82% of the total surface area is mountainous and semi-mountainous, while most of the population (56%) lives in rural areas. The capital of the region is the city of Kozani, with 67,224 inhabitants. Other major towns are Ptolemaida with 35,334 inhabitants, Florina with 19,198 inhabitants, Kastoria with 16,393 inhabitants, and Grevena with 15,716 inhabitants.

According to European Employment Services [28], in Q4 2022, the Region of Western Macedonia recorder the second highest unemployment rate in Greece, namely 15.2%, accounting for 2.81% of all registered unemployed in Greece. Moreover, the region has the third highest long-term unemployment rate in Greece (57.25%). The major activity fields are the industrial generation of energy and the agriculture. In the Regional Units of Grevena, Florina and Kastoria the main vacancies are office worker, personal services, livestock farmer, market gardeners, nursery growers and forest workers.

The PilotSTRATEGY project has received funding from the European Union's Horizon 2020 research and innovation programme under grant agreement No. 101022664

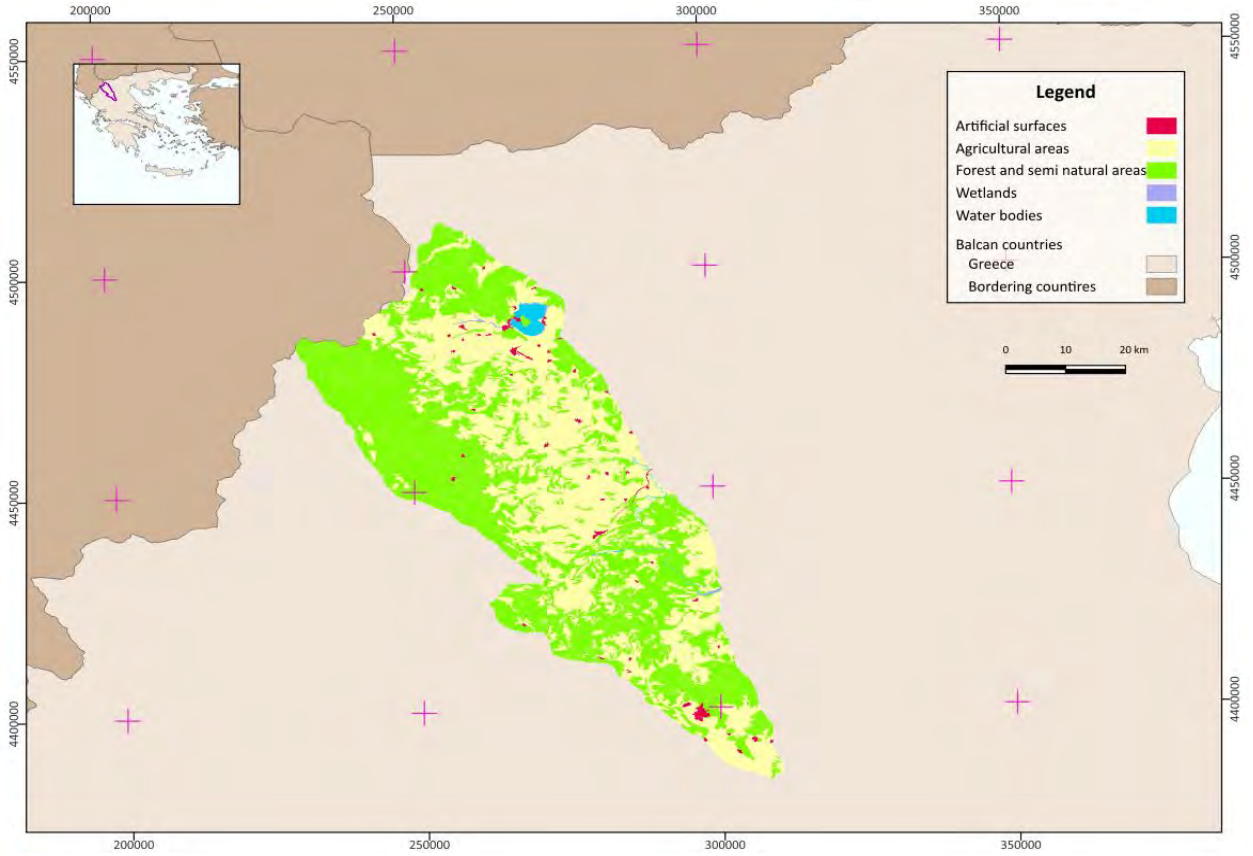

Figure 2.4: Land uses within the area of Mesohellenic Trough. The large water body appearing the northern part is the Orestias (Kastoria) Lake. Ref.system: EGSA 87.

A land re-purposing and spatial planning could provide potential contributions and benefit to climate change mitigation, post carbon economy, energy production and the environmental regeneration of mining lands.

In the Regional Unit of Kozani, shop assistants, drivers and mobile plant operators, unskilled workers, building erection and repair technicians and other technician workers in constructions are the most common vacancies. Lately, there has been a development in agriculture for organic products and super-foods. For every million tons of lignite produced, 185 jobs were maintained in the Mining-Energy Sector and a total of 725 jobs were created in the local labour market. This means that in 2028, with zero lignite production and the absence of solid interventions to halt the effects, jobs in Western Macedonia will marginally exceed 60 thousand, reduced by 33% compared to 2014. The gross domestic product (GDP) of the region was 4.0 billion € in 2018, accounting for 2.1% of Greek economic output. GDP per capita adjusted for purchasing power was 17,700 € or 59% of the EU27 average in the same year, while the GDP per employee was 79% of the EU average [29].

2.6. Vegetation

Information regarding the vegetation of the MHT were based on the environmental and spatial study provided by HEREMA [9]. The mountainous vegetation is mostly developed in the moderate and higher

The PilotSTRATEGY project has received funding from the European Union's Horizon 2020 research and innovation programme under grant agreement No. 101022664

altitudes comprising pure woodlands, shrubs, scattered vegetation and transition zones between fields and natural vegetation [9]. The regions with high altitudes, are mainly mountainous with alpine meadows, whereas beech, oak and pine forests, as well as firs, chestnuts, birches chasmophytic vegetation systems and riparian broadleaves have been also developed. At the middle altitudes, the dominant vegetation includes shrubs (i.e. low and high, deciduous, evergreen, and broad leaf species), including and transitional systems such as fields, which are currently in the recovery phase of natural vegetation. The whole region is usually covered with bushes. Plant species have been categorized by their family name (Figure 2.5).

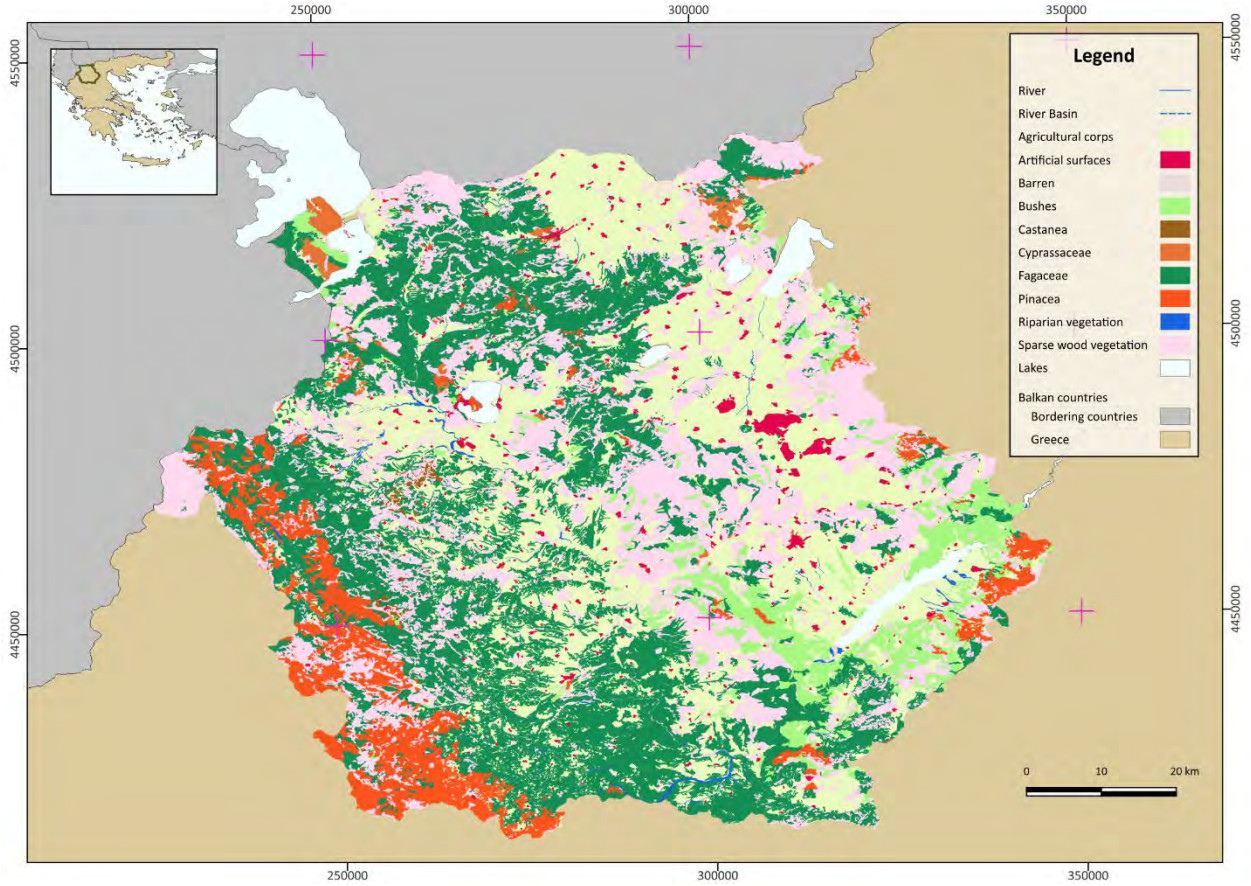

Figure 2.5: Vegetation map of Region of Western Macedonia. Ref.system: EGS87.

The soil, vegetation and fauna development are bio-climatically depended, whereas the vegetation is zonal-type, and it is associated with the occurrence of specific climatic zones. However, pockets of systems which are classified as soil dependent due to their influence from the morphological characteristics of the soil (e.g. points of concentration or water flow), are also observed.

The type of vegetation is an indicator of the basement geological formations and groundwater system. Plants like pines, beech, and oaks, have strong root systems that demand significant amount of water. They usually grow in sites where the substrate can sustain the growth of the roots. Limestones offer the appropriate support whereas their porosity permits water circulation.

The PilotSTRATEGY project has received funding from the European Union's Horizon 2020 research and innovation programme under grant agreement No. 101022664

2.7. Climate conditions

Greece is characterised by a predominantly Mediterranean climate, marked by long periods of sunshine throughout the year. Yet, notable variations occur across the country, largely shaped by its complex topography. The seasonal cycle can be broadly divided into two main periods: (i) a cold and rainy winter season, extending from mid-October to the end of March, and (ii) a warm and dry season, lasting from April through October[30].

According to Köppen–Geiger climate classification (Figure 2.6), Greece has mainly hot-summer Mediterranean climate (Csa), with different characteristics that vary depending on the exact location of each area (related to the morphology, altitude, distance from the sea), such as semi-arid climate (BS), including: a) cold semi-arid (BSk) in regions of Central Macedonia, Eastern Macedonia & Thrace, and Thessaly, and b) hot semi-arid (BSh) in coastal areas (e.g., Piraeus), as well as humid subtropical climate (Cfa) in both Central and Western Macedonia [9].

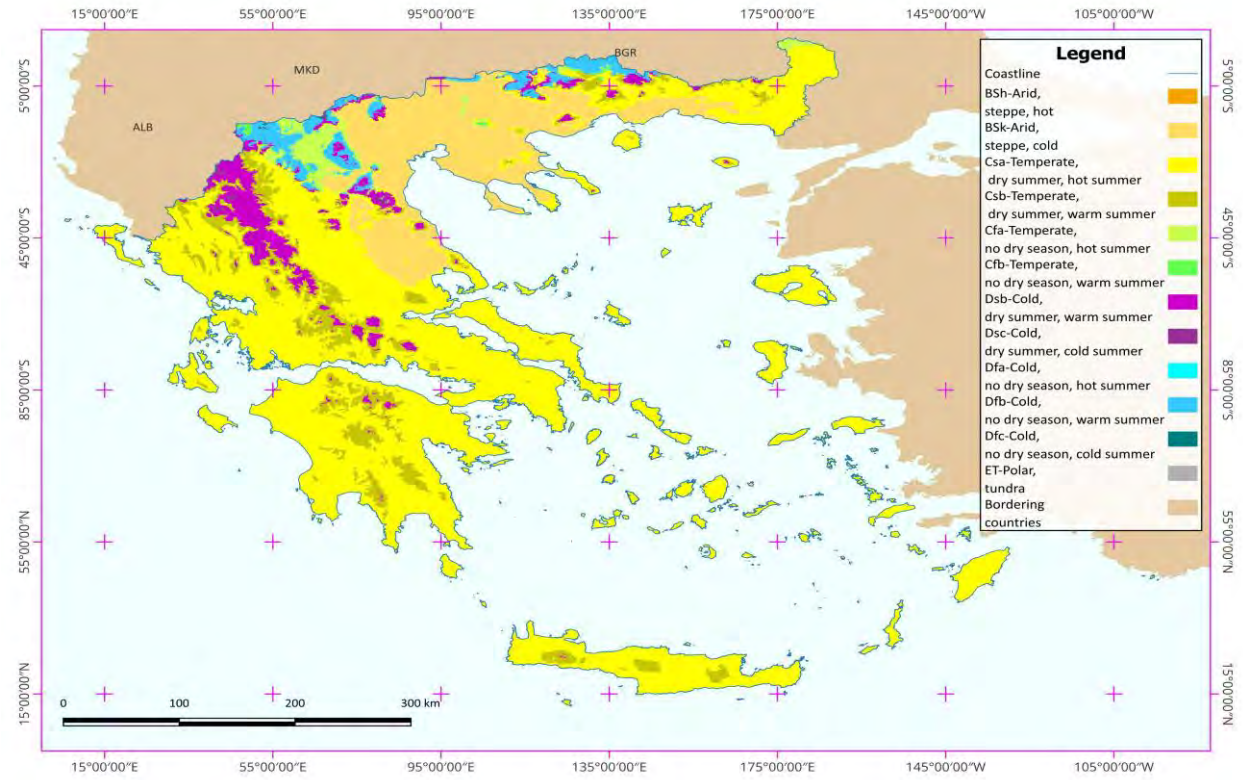

Figure 2.6: Climate distribution in Greece according to Köppen–Geiger climate classification[31]. Ref.system: WGS84

The Region of West Macedonia has a diverse climate as shown in Figure 2.7, with five major distinct climate zones, including [31]: 1. humid continental with warm and dry summer (Dsb), 2. hot-summer Mediterranean (Csa), 3. warm summer Mediterranean (Csa), 4. humid subtropical (Cfa), and 5) humid continental with warm summer and no dry season (Dfb).

The PilotSTRATEGY project has received funding from the European Union's Horizon 2020 research and innovation programme under grant agreement No. 101022664

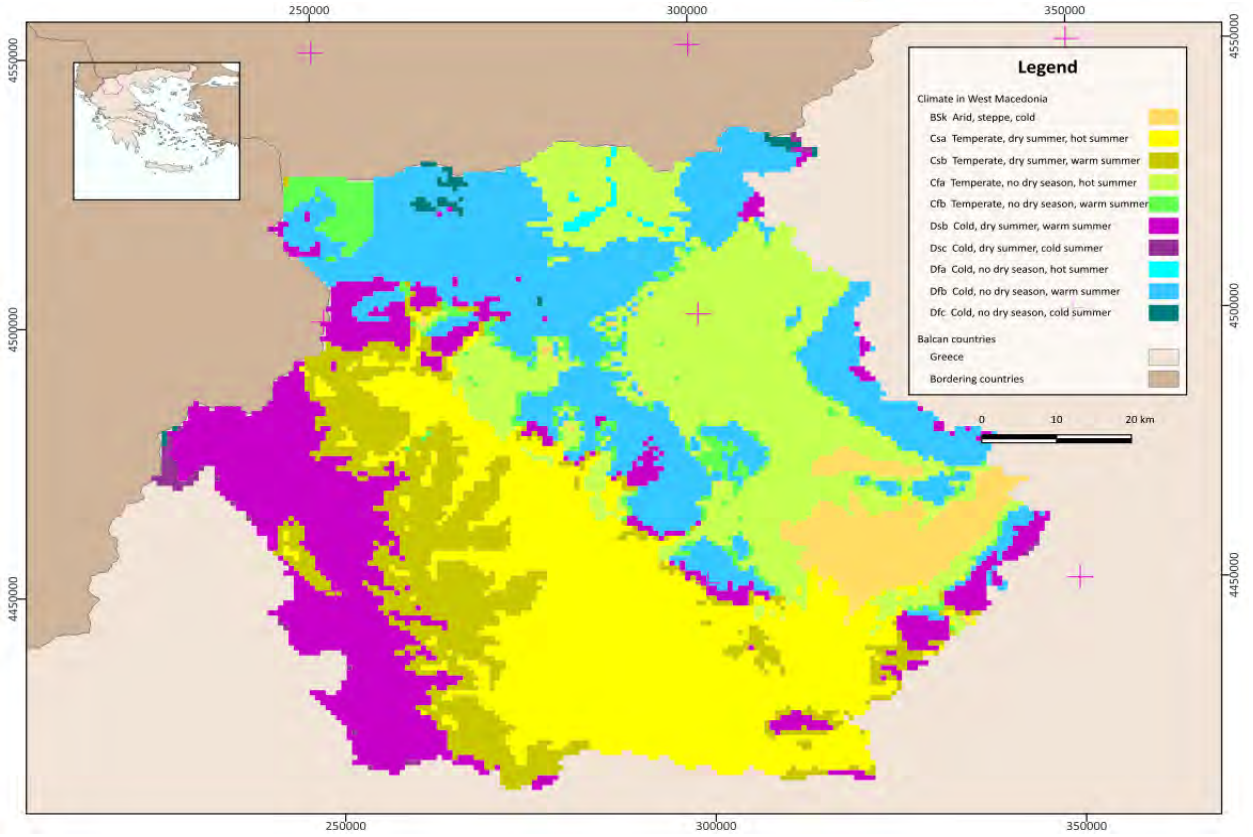

Figure 2.7: The climate distribution in the Region of Western Macedonia according to Köppen–Geiger climate classification [31]. Ref.system: EGSA87.

Mild winters and hot and dry summers are predominant, with average annual temperatures ranging between 14.5 and 17 °C[9, 30]. The average monthly temperatures are generally low from November until March, with January being the coldest month (1.2 °C). In contrast, moderate average monthly temperatures are observed from April until October (up to 17 °C) with July being the warmest month (~21.7 °C)[32]. The average rainfall shows a large spatial variation, typically ranging between 600 and 1,000 mm, with very high values being observed in the mountains (>1,200 mm) and significantly lower in the lowlands[32]. Throughout the typical seasonal cycle, high levels of rainfall are experienced from mid-October throughout March (cold and rainy winter season), while in the warm and dry season from April until October, lower levels of rainfall are recorded. Cold north winds of low intensity are typical responsible for both the low temperatures and a large number of frost days during winter, whereas the southwesterly, usually mild winds prevail in the summer[30]. Specifically, the climate of the Region of Western Macedonia is summarized below per regional unit.

At the Regional Unit of Grevena the climate is characterised as transitional from Mediterranean to Continental, maintaining the characteristics of the Mediterranean type in the lowlands and resembling more the continental type in the higher zones[9]. According to the Köppen–Geiger climate classification (Figure 2.6), hot summer (Csa) and warm summer (Csa) zones are predominant for the Mediterranean type, whereas in mountainous areas such as Pindos and Vourinos, humid continental climate with warm and dry summer (Dsb), and humid continental with warm summer and no dry season (Dfb) can be

The PilotSTRATEGY project has received funding from the European Union's Horizon 2020 research and innovation programme under grant agreement No. 101022664

characteristic for the continental type[31]. There are large thermometric differences between winter (minimum of about-12.6 ˚C based on years 2009-2022) and summer (maximum of about 38.2 ˚C based on years 2009-2022) (Figure 2.8a), while high rainfall typically appears in Northern Pindos (591 mm; data based on years 1991-1998) in the rest of the low altitude zones at Grevena (Figure 2.8b).

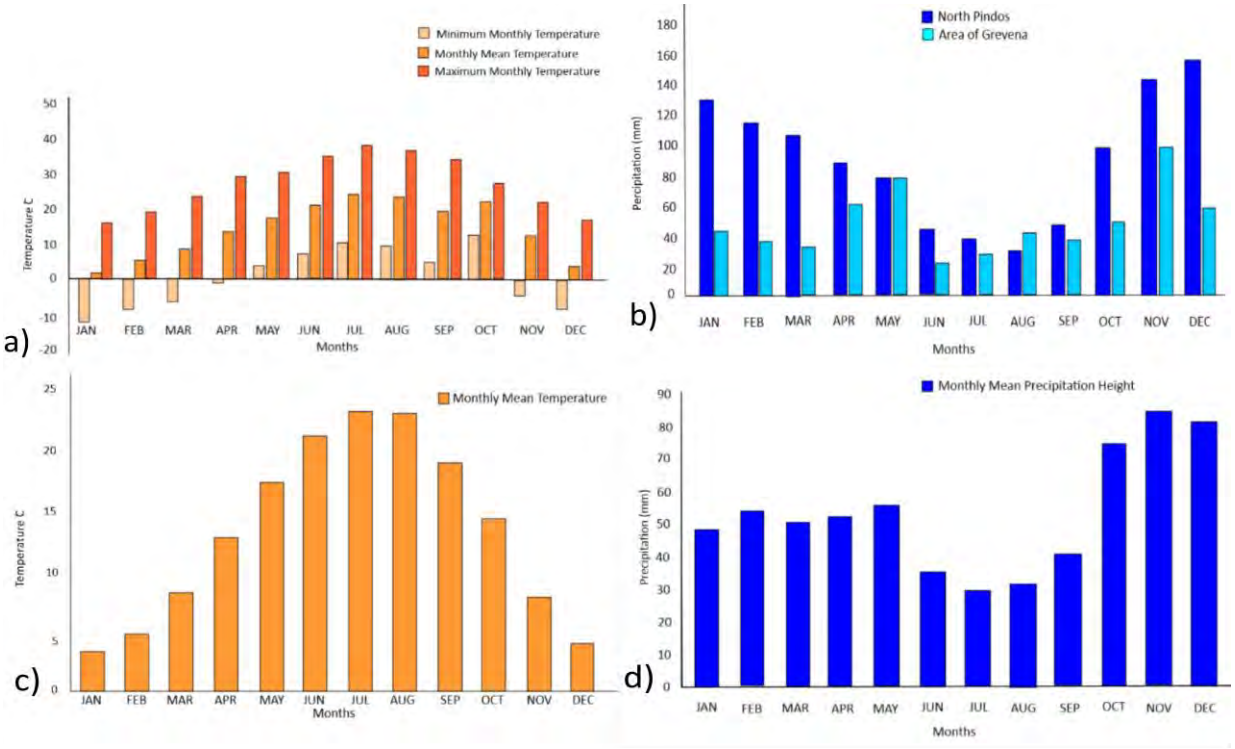

Figure 2.8: a. Temperature range for the Regional Unit of Grevena (2009-2022). b. Precipitation values for North Pindos and the lowland Regional Unit of Grevena (1981-2008, 1991-1998). c. Temperature range for the Regional Unit of Kastoria (1980-2001). d. Precipitation values for the Regional Unit of Kastoria (1980-2001).

At Kastoria the climate is identified as continental-Mediterranean[9]. According to the Köppen–Geiger climate classification (Figure 2.6), humid continental with warm and dry summer (Dsb) is characteristic for Grammos mountain, whereas humid subtropical (Cfa) and humid continental with warm summer and no dry season (Dfb) for areas with relatively low altitudes and the Kastoria Lake area[33]. There are significant variations in the annual average temperatures (Figure 2.8c), with the temperature dropping below 0 ˚C, in the cold winter months, whereas in the dry summer months maximum temperatures are about 30 ˚C[33, 34]. The area is characterized by high precipitation, snowfalls, dry seasons, frosts, hail and local winds [9]. The average annual precipitation height in the area, based upon the 1980-2001 period is about 641 mm and mainly occurs from autumn to spring[34, 35](Figure 2.8d).

The Kozani unit is characterised by a typical continental climate. According to Köppen–Geiger climate classification (Figure 2.6), humid subtropical (Cfa) and humid continental climate zones (Dfb) are predominant in Kozani and Ptolemaida areas[31]. Based on the Emberger diagram, the climate is sub-humid with severe winters. The cold and dry winters are followed by mild to warm summers, resulting to significant annual thermometric fluctuations. Minimum temperatures are typically detected in January (-1.2 ˚C) based on the data for the 1955-2010 period, whereas maximum temperatures (29.6 ˚C) are

The PilotSTRATEGY project has received funding from the European Union's Horizon 2020 research and innovation programme under grant agreement No. 101022664

recorded during the hot summer season, and particularly in July and August[9] (Figure 2.9a). Frost and snow are common features of the winter months, often persisting for extended periods in higher elevations and shaded valleys. In contrast, rainfall shows a more even distribution throughout the year, without a pronounced dry or wet season, which helps maintain relatively stable hydrological conditions across the region (Figure 2.9b).

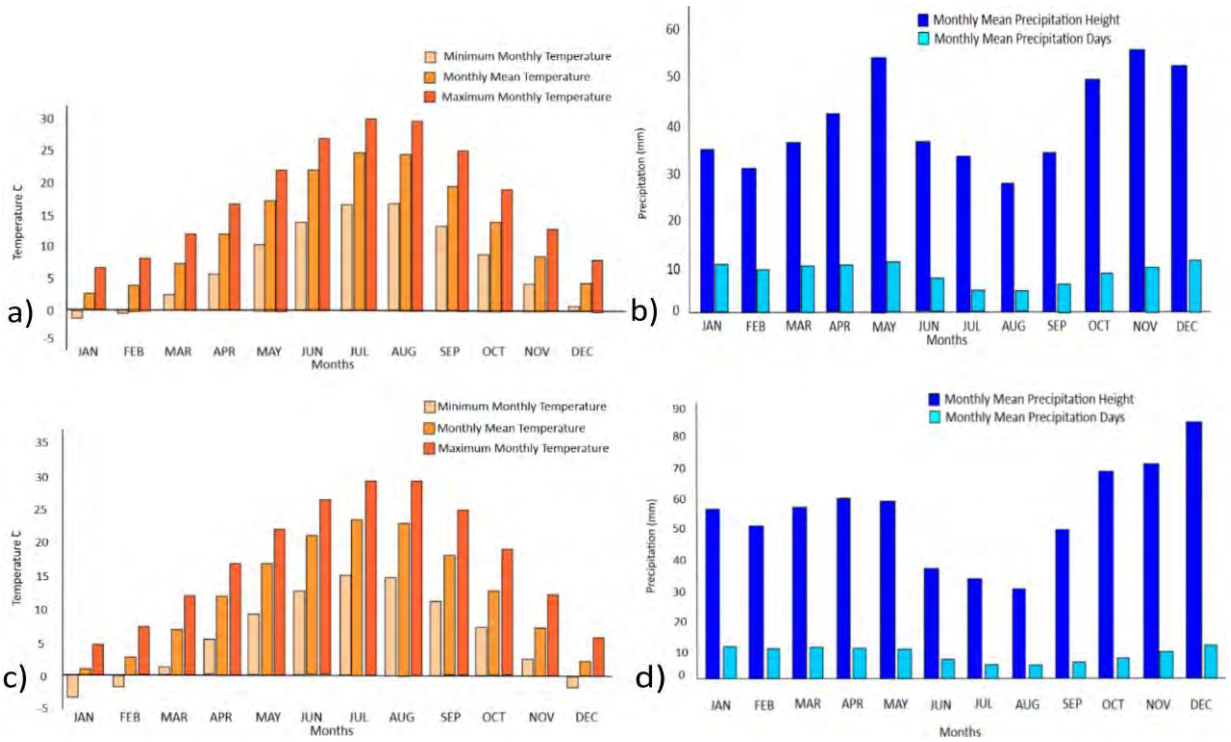

Figure 2.9: a. Temperature range for the Regional Unit of Kozani (1955-2010). b. Precipitation values for the Regional Unit of Kozani (1955-2010). c. Temperature range of Regional Unit of Florina (1960-2010). d. Precipitation values for the Regional Unit of Florina (1960-2010).

Florina is also characterized by a transitional climate from continental to Mediterranean[30]. According to the Köppen–Geiger climate classification (Figure 2.6), a humid subtropical climate (Cfa) along with a humid continental climate zone (Dfb) prevail in the Florina region[31]. Based on the Emberger diagram, the climate is humid with severely cold winters. During the wet winter season, phenomena of total frost are frequent with an average temperature of 3.9 ˚C (based on years 1960-2010), while even lower temperatures may be observed (minimum -3.1 ˚C in January) (Figure 2.9a). The annual rainfall is relatively high, averaging 663 mm over the period 1960-2010, and is distributed fairly evenly throughout the year. This pattern is characteristic of a transitional Mediterranean climate, where moderate precipitation is not concentrated in a single season but rather spread across the annual cycle, reducing the extremes of drought or heavy seasonal flooding [9] (Figure 2.9d).

The PilotSTRATEGY project has received funding from the European Union's Horizon 2020 research and innovation programme under grant agreement No. 101022664

2.8. Hydrology and Hydrographic Network

The Water District of West Macedonia (GR09) includes the Prespa River Basin (GR01) and Aliakmonas River Basin (GR02). The main hydrological basins of Water District GR09 [36] are presented in Figure 2.10 and summarized in Table 2.3. Figure 2.10 illustrates that the geographical boundaries of the GR09 water district extend beyond the administrative limits of the Region of Western Macedonia, following the water course of Aliakmonas River.

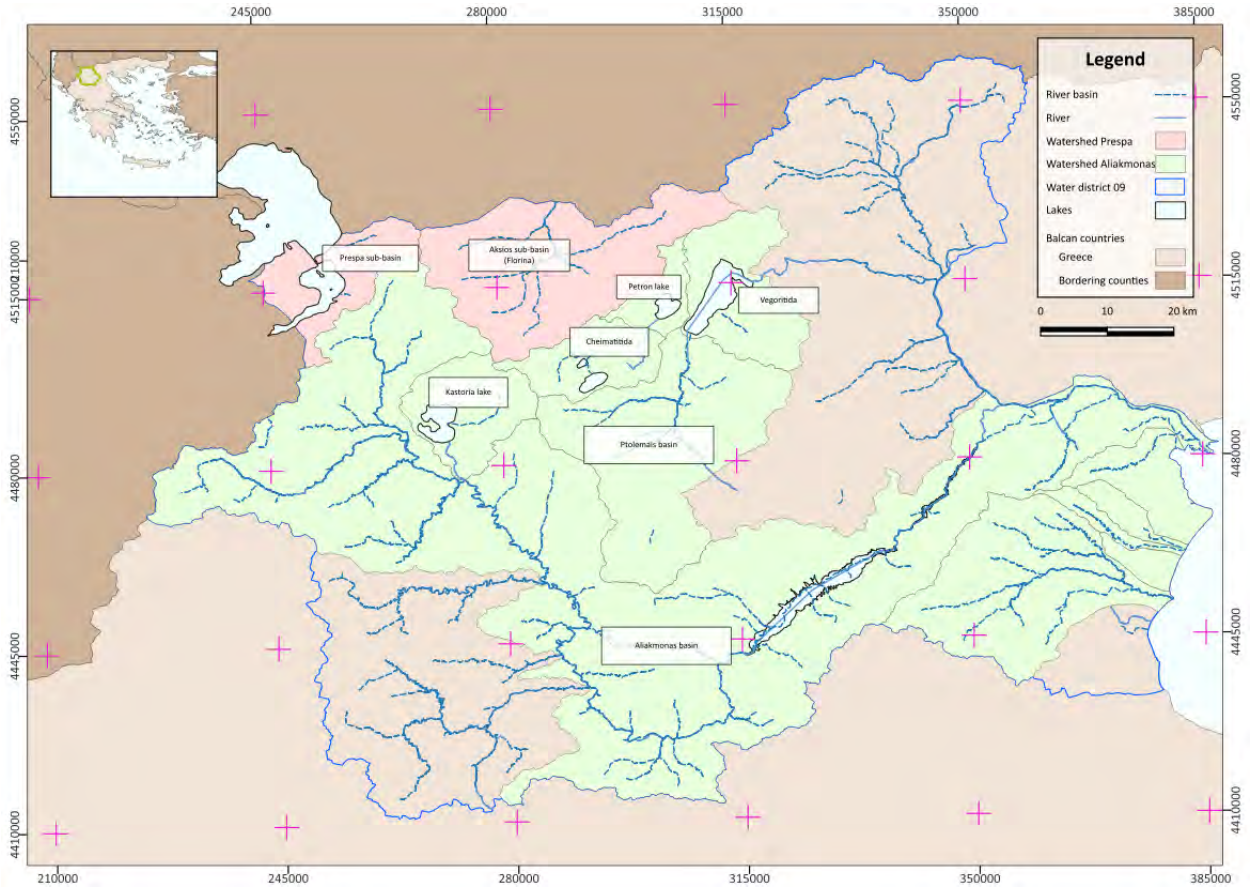

Figure 2.10: Hydrological basins of the Water District of West Macedonia (GR09). Ref.System: EGSA 87.

Table 2.3: Hydrological Basins of Water District of West Macedonia (GR09) and their area (km^2)

Hydrological Basin	Area (km^2)
Aliakmonas River	8,813
Ptolemaidas Basin	2,133
Axios River	863
Mavroneri River	815
Kastoria Lake (in Aliakmonas River Hydrological Basin)	353
Heimaditida, Vegoritida and Petron Lakes	-
Prespes Basin	-
Chelopotamos River	-

The PilotSTRATEGY project has received funding from the European Union's Horizon 2020 research and innovation programme under grant agreement No. 101022664

Within the geographic region under consideration, there are two distinct mountain complexes oriented along an almost north-south axis, effectively segmenting the terrain into three expansive flatland areas. The first mountain cluster comprises Verno (2,128 m), Askio (2,111 m), and Vourino (1,688 m), while the second cluster encompasses Vorras (2,524 m), Vermio (2,052 m), and Pieria (2,180 m) mountaints. To the west lie the plains of Kastoria and Grevena, centrally positioned are the plains of Ptolemaida, and to the east extend the plains of Edessa, Naoussa, Veria, and Pieria. Further to the north lies the plain of Florina, extending beyond the national borders of Greece[36].

The primary hydrological feature within the GR09 region is the Aliakmonas River, holding significant importance within the broader context of national water resources. Noteworthy for its intricate hydrographic system, the Aliakmonas River basin spans across the western and southern sectors of the Water District GR09. Its northern boundary is outlined by the Vernon and Vermio Mountains, while the western ridges of the Northern Pindos mountain range delineate its extent to the west. To the south, the limits of the district are marked by the Hasia and Kamvounia ranges, and to the east, by the Pieria Mountains. Following the implementation of initial flood mitigation infrastructure, the Aliakmonas River now channels the waters of the Regional Ditch (T66, covering an area of 1,443 km²) into its floodplain near the village of Kouloura. This Regional Ditch serves as a conduit for the drainage of waters originating from the Almopia and Edessa regions, including the waters of springs and tributaries of the eastern Vermio Mountain. Consequently, in conjunction with the Peripheral Ditch, the Aliakmonas River encompasses a total catchment area of 9,455 km², extending from the source of the river to its mouth at the Thermaikos Gulf. The flow dynamics of the Aliakmonas River are modulated by a series of artificial reservoirs, namely Hilarion, Polyfyto, Sfikia, Asomata, and Agia Varvara. These reservoirs have been strategically constructed to facilitate hydroelectric power generation and concurrently support irrigation activities in the Thessaloniki plain. Additionally, aside from the sub-basin related to the Regional Trench, prominent sub-basins include the Venetikos (871 km²), Promortsa (386 km²), the enclosed lake of Kastoria (353 km²), Edessa (292 km²), Tripotamos (252 km²), Arapitsa (178 km²), and Grevenitikos (117 km²)[36].

In the Water District GR09, a significant number of natural lakes are recorded, including those of Kastoria, Petron, Zazari, Heimaditida, Vegoritida, Small (Mikri) and Great (Megali) Prespa, and Agras (Table 2.4Table 2.4). The Ptolemaida basin is enclosed and situated at the center of the Water District, between the mountains of Vernon and Vermio, draining into the Lake Vegoritida. Primary sub-basins include those of Vegoritida (346 km²), Heimaditida (229 km²), and Petron (114 km²), as well as the closed Sari-Gyol basin (431 km²) [36]. The Axios basin forms part of the wider hydrological system of the Axios River, feeding its main course across Central Macedonia. The basin includes the plain of Florina and is surrounded by the Vernon and Vorras Mountains. The Aisonas (Mavroneri) basin lies in the eastern part of the district, encompassing the entire plain from the Pieria Mountains and Mount Olympus to the Aegean sea[36].

The PilotSTRATEGY project has received funding from the European Union's Horizon 2020 research and innovation programme under grant agreement No. 101022664

Table 2.4: Lakes of the Water District of West Macedonia (GR09) and their sizes (km^2)

Lake	Area (km^2)
Kastoria	28.84
Vegoritida	53.96
Petron	12.36
Zazari	1.7
Heimaditida	9.57
Small (Mikri) Prespa (the Greek part)	42.9 (47.37 total)
Great (Megali) Prespa (the Greek part)	38.64 (281.67 total)
Polyfytos	74
Sfikia	4.3
Asomaton	2.6
Aghia Varvara	0.9
Hilarion	21.9

The PilotSTRATEGY project has received funding from the European Union's Horizon 2020 research and innovation programme under grant agreement No. 101022664

3. Geological setting

3.1. Geological Overview of the Hellenides

The Hellenides are a part of the Alpine orogenic system, as a result of the collision between the Eurasian plate and the Apulian plate, which started in the end of the Cretaceous and outlasted the Paleogene-Neogene[37-39]. The MHT was formed during the latest stages of the Alpine orogeny on top of the obducted ophiolitic nappe (that resulted in the closure of Tethys Ocean) and palaeogeographically between the so-called "Internal" and "External" Hellenides, represented by the Pelagonian continental nappe and the Apulian plate, respectively[40-42]. The Pelagonian basement represents the western Eurasian continental part, and today, together with the overthrusted units, it borders the MHT to the east[41]. The western boundary of the trough is made of the Tethyan ophiolites (Pindos ophiolitic cover), which were thrust to the west onto the eastern Apulian margin during the last orogenic period (Figure 3.1). In more detail, the Pelagonian nappe consists of Palaeozoic or older crystalline basement (i.e., gneisses, schists and granitoids, with ages of 700 Ma as documented by[43]), a Permo-Triassic volcano-sedimentary sequence, and of a Triassic to Jurassic platform carbonate cover[43-46]. It had a long and complex geological evolution that had started already in the Palaeozoic[43], having experienced a Variscan ampibolitic-phase metamorphic event in the Carboniferous[44]. However, the older mineral assemblages and textures of the Pelagonian rocks were almost completely overprinted by the tectono-metamorphic events related to the closure of Tethys Ocean and the orogenic processes from the Late Jurassic onward[45], which were: an amphibolite-to greenschist-facies event in Late Jurassic-Early Cretaceous[46], an Aptian-Albian low-grade retrogressive event[47, 48], and a Paleocene to Eocene (60-45 Ma) high-pressure/low-temperature metamorphic event found only in basal sub units of the Pelagonian basement. The later was overprinted by very-low grade metamorphism between the Oligocene and Miocene[44, 46, 49, 50].

At the same time, the Apulian microplate to the west experienced continuous, mainly carbonate sedimentation throughout the Mesozoic times. Continental rifting at this carbonate platform during the Late Triassic resulted in the development of two basins, namely the Ionian and Pindos zones at the western and eastern part of the platform[46]. Shallow marine carbonates were deposited on the platform, while deep-sea carbonates and radiolarites were deposited in the basins[49, 50]. Therefore, the Pindos zone is considered to be a typical basin accommodating a succession of continuous Mesozoic deep-sea sediments, comprising cherts, clay- and siltstones, and deep-water carbonates, whereas the Maastrichtian–Palaeocene Pindos Flysch, deposited at the eastern margin of this basin, terminates the sequence[48]. The position of the Tethys Ocean, and therefore the origin of the ophiolitic assemblages obducted and thrusted (after the closure of the ocean) over the Pelagonian and the Apulian plate, remains under debate still today. It is either to the east of the Pelagonian (Axios or Vardar Ocean; e.g.,[51] or/and to the west, from within the Pindos basin that is in this case considered as oceanic[52]. Besides, the origin of the ophiolitic assemblages, the whole area was affected by Tertiary orogenic processes, which were associated with plate convergence between the Apulian and Pelagonian continental blocks, causing compression and crustal thickening. During the Paleogene-Neogene, thrusting and nappe-stacking advanced systematically toward the west-southwest[38]. This progression is also reflected in the development of successively younger flysch basins, which become progressively younger in age in the same direction, confirming the westward migration of deformation and basin formation[53, 54]. The mechanically heterogeneous Pindos zone was highly deformed during the Middle-Late Eocene, and created a series of imbricate thrust sheets that were emplaced over the Gavrovo-Tripoli zone of the External Hellenides zones. As a result of the Eocene compression, the Pindos zone can be characterised

The PilotSTRATEGY project has received funding from the European Union's Horizon 2020 research and innovation programme under grant agreement No. 101022664

as a large thrust system, extending with a NW-SE strike from Albanides to northern Greece, and continuing to the south, where it is curves at the Peloponnesse in an E-W orientation. The Pindos thrust system is considered to have been active until the late Oligocene[50, 55, 56]. Extension and normal faulting followed the Paleogene-Neogene compressive tectonics.

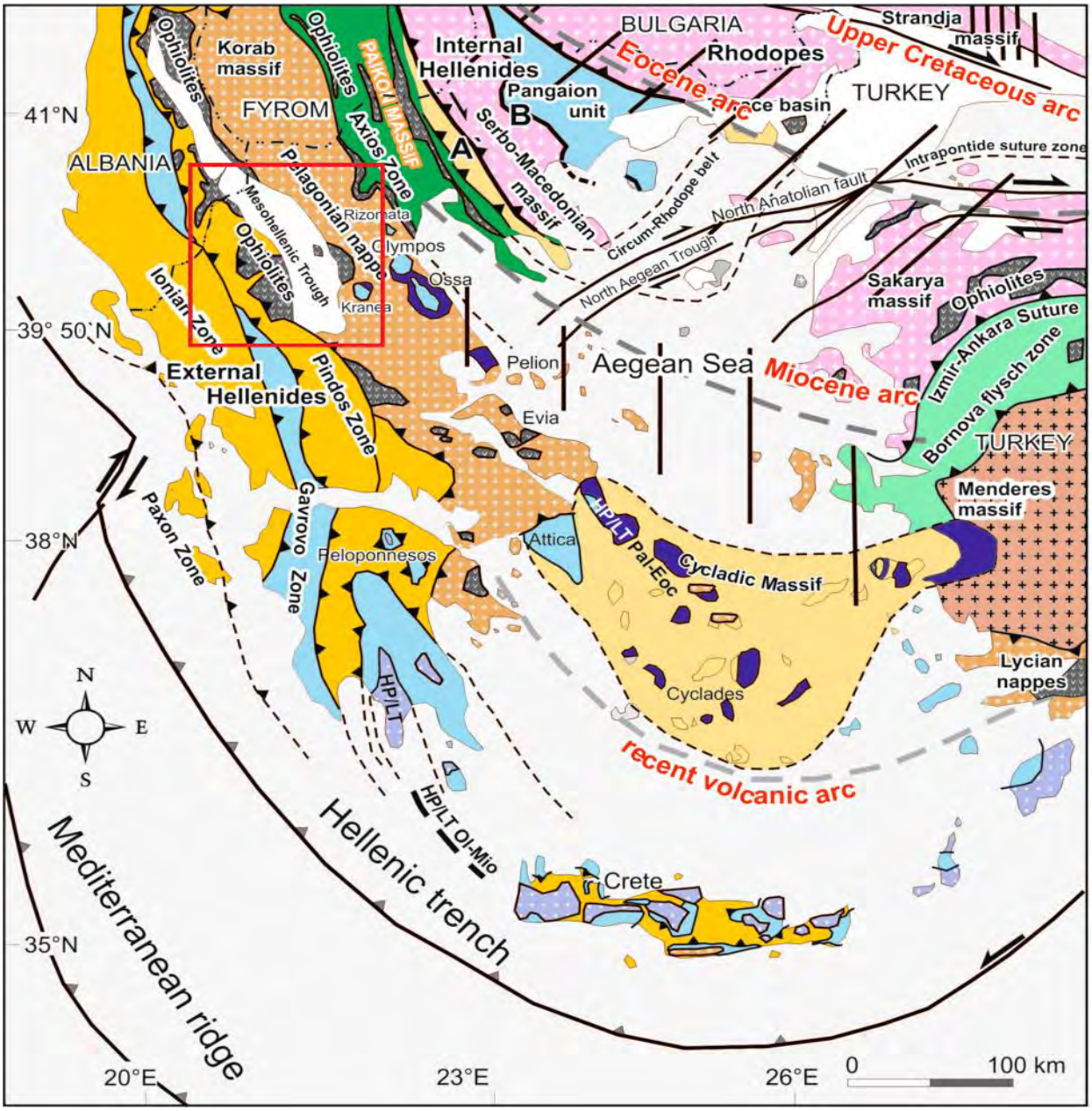

Figure 3.1: General geotectonic map of the Hellenides zones. The red square indicates the location of the Mesohellenic Trough in Greece (modified after Vamvaka et al., (2018)[41, 47, 57]).

The PilotSTRATEGY project has received funding from the European Union's Horizon 2020 research and innovation programme under grant agreement No. 101022664

3.2. The Mesohellenic Trough

The MHT was developed between Middle Eocene and Middle to Late Miocene in the suture area between the Apulian platform and the Pelagonian nappe[42] (Figure 3.2). The basin infill reaches a maximum thickness of 4 km in individual vertical sections[17, 58], while the cumulative thickness of the sediments is larger. It comprises five, mainly siliciclastic formations[40, 59] (Figure 3.2), which lie on the overthrusted Tythean ophiolitic rocks and the overlying Cretaceous limestones. The different formations show variations in thickness and facies across and along the axis of the basin[42], including fan-delta conglomerates, alluvial fans, turbiditic sandstones and shales, deltaic and flood-plain sandstone and siltstone, and sandy shelf sediments[17, 60].

Although more detailed studies have been carried out since the five MHT formations were first stratigraphically established, the initial division is still accepted today. Later studies involved facies identification, lateral stratigraphic relations and the description of internal unconformities in restricted parts of the basin[17, 26, 60-63]. The biostratigraphy of the basin is based mainly on planktic Foraminifera and nannoplankton, but also on bryozoa, gastropods and molluscs[1, 17, 58, 64-67]. The five formations, from lower (older) to the upper (younger) parts of the trough, are:

- The Krania Formation (Middle-Late Eocene)
- The Eptachori Formation (Late Eocene-Early Oligocene)
- The Pentalofos Formation (Late Oligocene-Early Miocene age: Chatian-Aquitanian)
- The Tsotyli Formation (Early-Middle Miocene age, late Aquitania-Burdigalia, up to Tortonian in places)
- The Ondria Formation (Middle Miocene, Burdigalian-Langian)

The subsidence and deposition seem to have started in two restricted areas in the Eocene, sited at the central westernmost part of the basin, named as the “Gulf of Krania”[40], and at the south-eastern part of the MHT (Figure 3.2). The other four formations were deposited along the basin and parallel to one another through time, from west to east (Figure 3.2). The spatial distribution and orientation of the formations, when viewed in relation to their age, clearly indicate an eastward migration of the depocentres through time[40, 64, 66] , with the Tsotyli Formation (Fm) resting directly on top of the Pelagonian nappe along the eastern margin of the trough[2].

Bedding appears fairly steep along the western edge of basin, dipping to the ENE, whereas the dipping angles progressively decrease to the east, as moving away from the margin. Although there are not any major changes or deformation of the strata observed across the basin, the homogeneity of its inclination breaks in the centre and along the eastern margin of the basin, where the strata dips with a low angle towards the WSW[42]. As a result, an asymmetrical syncline is formed across the western margin of the basin and eastward, as it is also confirmed by field observations[2, 42, 58, 68, 69] and the interpretation of seismic profiles[1, 17]. A second smaller syncline occurs at the eastern side of the basin, clearly observed in the southern domain, where it is separated from the western syncline by an uplifted structure along Theotokos and Vassiliki villages[2, 4, 42, 69].

The PilotSTRATEGY project has received funding from the European Union’s Horizon 2020 research and innovation programme under grant agreement No. 101022664

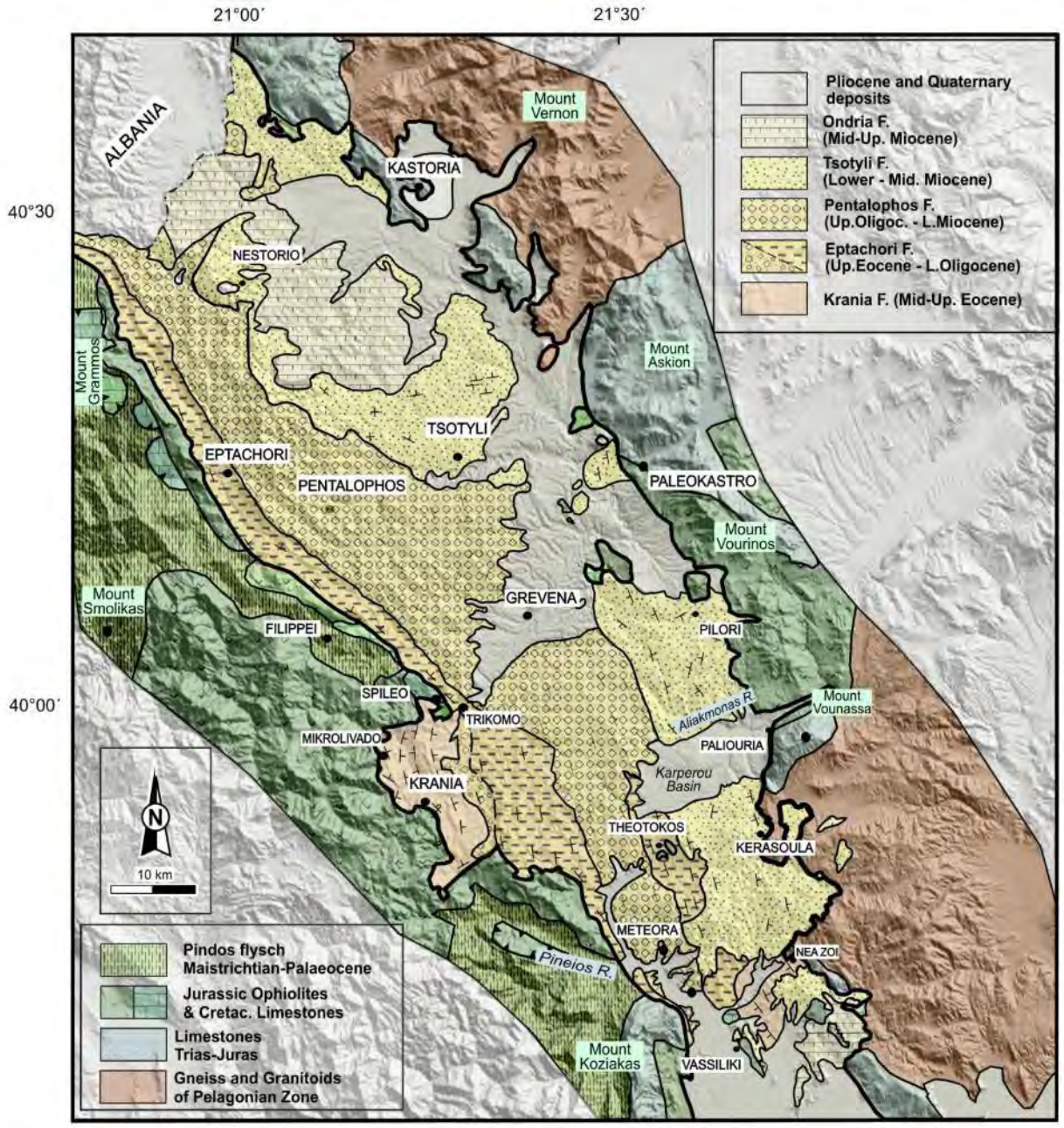

Figure 3.2: The Mesohellenic Trough formations and surrounding geological units [42].

The Mesohellenic Trough is built up from five main formations, each with its own distinct lithological and depositional features. Their principal characteristics are outlined in the following section.

The PilotSTRATEGY project has received funding from the European Union's Horizon 2020 research and innovation programme under grant agreement No. 101022664

3.2.1. Krania Formation

The Krania Fm was deposited between Middle and Late Eocene and incorporates the older fill of the MHT. It outcrops at the western margin of the MHT ("Gulf of Krania"[40]) and in the southeastern area near the Meteora region. The western occurrence of Krania Formation has attracted more attention, as shown by existing early studies [26, 40, 63], probably because of its good exposure and impressive tectonic structures that manifest important deformation [26, 42]. The strata is characterized by various facies including from base to top; coarse breccias, fan-delta with roughly bedded mainly ophiolitic conglomerates, shales, and turbitidic fine-grained sandstones and siltstones with nannofossils[17, 26], comprising *Nummulites*, *Discocyclina*, *Actinocyclina*, *Asterodiscus* and *Spiroclypeus* [65]. Large olistolithic blocks also occur in places, which together with the aforementioned Krania Fm facies witness a steep profile and unstable margin that fed the quickly subsiding basin area[42]. The shaly turbidites are an at least 1 km thick sequence, while the total thickness of the formation is estimated exceeding 1500 m[17, 26, 59] and even reaching 2000 to 3000 m[65].

For the southeastern Krania sub-basin strata, no clear thickness estimation exists, but studies provide the main sedimentological and structural features of its sequence[2, 14, 42, 58]. The first deposits consist of basal conglomerates and Lutetian benthic limestones with *Nummulites, Alveolines, Orbitolides* and *Fabiania*, and are overlain by a succession of marly turbiditic ("flysch-molasse type") sequences with *Globorotalia* which are interbedded with sandstone (Late Eocene[70, 71]).

In both Krania sub-basins, the tectonic structures that affected their strata reveal similar tectonic conditions and deformation for the two areas. The strata is asymmetrically folded along the NNW-SSE to NW-SE direction and cut by reverse faults that mainly strike along the NW-SE direction[2, 14, 26, 42, 70-72]. The contact of the formation with the basement rocks appears tectonized in both sub-basins, bearing strike-slip striations, mostly with a reverse dip-slip component. It is interpreted as related to the development and deformation of the Eocene sub-basins under a transpressional regime[42].

3.2.2. Eptachori Formation

The Eptachori Fm was deposited unconformably on the deformed strata of the Krania Fm, as well as on ophiolites and Cretaceous limestones during the latest Eocene and Early Oligocene. It occurs all along the western side of the MHT and outcrops as well in confined areas in the centre of the southern part of the basin (Theotokos and Kalambaka areas, Figure 3.2;[58, 59, 68]). Its thickness is estimated around 1000 m[58, 59]. The base of the formation has a conglomeratic to sandstone composition, which accumulated as alluvial fans or on fan deltas[17]. These are followed by marine turbiditic shales, gradually passing to sandstones. The gradual transition includes shale and minor lignite intercalations. For the turbiditic shales a Ruppelian age is inferred in the north by nannofossils , whereas a water depth of around 600 m is suggested by benthic foraminifera [64, 66]. The strata is characterised by steep dip angles right along the western margin (~60-70°), which shows a secondary inclination related to tectonic deformation, while no intense compressional structures, like the ones in the underlying Krania Formation, are observed [42]. Moving southwards, the basin thickness increases to ca 1200 m, based on seismic data interpretations [17]. In the southern part of the basin, the formation is smaller and coarser, consisting of marine sandstones and some pebbly conglomerates [42]. The deposition of the Eptachori Fm is interpreted to be controlled by strike-slip faulting, as indicated by the occurrence of dextral strike-slip faults of NW-SE to NNW-SSE orientation along the western part of the MHT and in the Theotokos and Vassiliki areas (central and southern part of MHT), where faulting forms positive flower structures. Such faults also affect the

The PilotSTRATEGY project has received funding from the European Union's Horizon 2020 research and innovation programme under grant agreement No. 101022664

Eptachori Fm itself, the older Krania Fm and the Pentalofos Fm strata, but not the younger Tsotyli deposits, and thus their development is chronologically placed during the Oligocene [42].

3.2.3. Pentalofos Formation

The Late Oligocene to Early Miocene Pentalofos Formation occupies all the central part of the basin, attaining a cumulative thickness of around 2500 m and comprising a remarkable volume of sediments [40, 59, 72-74]. South of the Nestorio village (in the North), the formation is estimated to reach a maximum thickness of 4000 m [58]. Its age is determined by numerous fossils traced in its strata (e.g., Bryozoa, Mollusques and Foraminifera, such as *Miogypsinoides, Lepidocyclina, Austrotrillina, Pararotalia, Globigerinoides, Operculina* fragments and others [58]) and comparison of seismic stratigraphy and stratigraphic observations with documented oxygen isotope curves and sea level changes [17, 75, 76].

The Pentalofos Formation is divided into the Tsarnos (or Taliaros at the northern part) and overlying Kalloni members [58, 60]. The lower part of Tsarnos Member thins quite abruptly toward the eastern part of the basin [58]. Near the western margin, the seismic stratigraphy shows a series of discontinuous reflections [17]. The base of the Pentalofos Formation (Tsarnos Member) is considered as an erosional surface that cuts Eptachori shales [17] and contains sandstones and minor channel-filling conglomerates, followed by alternating turbiditic sandstones and shales. The Kalloni member is exposed on the surface to a larger extent and mainly consists of sandy turbidites with more shaly intervals and rare channel-filling conglomerates [17, 58]. Near the centre of the southern part of the basin, a 350 m thick conglomerate member characterised by several unconformities forms the outstanding pinnacles of the Meteora region; these conglomerates correspond to remnants of deltaic bodies and Gilbert-type fan deltas [77]. The facies types of the Pentalofos Formation suggest water depths of 300–700 m [17].

3.2.4. Tsotyli Formation

The Early to Middle Miocene Tsotyli Formation extends along the eastern side of the basin and is characterised again by significant thickness, reaching more than 2000 m in places. Fauna and microfauna found include Lamellibranchia, Gastropods, Algae and Myogypsina. The base of the formation is characterized by conglomerates that are mainly ophiolite-derived in the northern part of the basin and polygenic, with gneissic conglomerates from the Pelagonian basement rocks, in the south, which shows the direct supply from the Pelagonian nappe to the east. The conglomerates pass upwards into alternating turbiditic conglomerates, sandstones and shales with several lateral facies changes [58, 78]. These are interpreted as shelf delta deposits, while the finest-grained deposits are related to prodeltaic domains [60]. In the north, the Tsotyli Fm seems to lie conformably on the underlying Pentalofos Fm. At the same time, in the southern part of the basin, an unconformity is observed between the two formations (i.e. between upper and lower Meteora conglomerates). In the wider area of the Theotokos village (Figure 3.2) the Tsotyli Fm directly overlies the Oligocene Eptachori Fm, whereas in the southernmost part of the MHT, east of Vassiliki village (Figure 3.2), it directly overlies the Eocene strata. Moreover, Tsotyli strata seem unaffected by the NNW-SSE trending strike-slip faults that cut the older Eptachori and Pentalofos Fm and form a positive flower structure in the Theotokos-Vassiliki areas [2], as also supported by seismic data interpretation [17]. Tectonic structures and stratigraphic relationships indicate that the strike-slip faults and the related flower structures were active until the end of Oligocene. This movement led to the uplift of both the basement and the overlying sediments, which were likely subjected to erosion before the deposition of the younger Tsotyli Fm. The latter was deposited during the Early to Middle Miocene in a newly formed basin that opened further to the east [42]. Before the Early Miocene, the MHT did not extend as far east as the area where the Tsotyli Fm was later deposited. This is supported by structural and

The PilotSTRATEGY project has received funding from the European Union's Horizon 2020 research and innovation programme under grant agreement No. 101022664

petrological indicators. Apart from the direct stratigraphic contact of the Tsotyli Fm with the underlying Pelagonian nappe units, the boundary is largely tectonic in nature. It is defined by low-angle normal faults striking NW–SE, with a southwestward sense of displacement. These faults were active during sedimentation, but their influence does not extend into the younger Pliocene deposits, which remain unaffected [2, 42]. Other evidence supporting the subsidence of the eastern-most part during the Early Miocene is the occurrence of laterites under the Tsotyli sandstones at a particular location (Taxiarches village area), which denotes surface exposure of the occurring ophiolites before the deposition of the Miocene strata [42].

3.2.5. Ondria Formation

The last deposited sediments of the MHT belong to the Middle Miocene (Burdigalian–Langian) Ondria Fm that designates the end of mollass e deposition. This formation is found only in the north-eastern and south-eastern parts of the trough and consists of sandy shelf deposits (i.e. sandstones, marls and limestones) that carry fossils that reveal a shallow-water setting (e.g., Lithothamnium, Ostrea, Pecten, Clypeaster [79]). The thickness of the deposits varies, but it is generally limited from between 100 to 600 m [79]. The patchy occurrence and relatively limited thickness of the formation are generally attributed to the erosional phase that followed. At the same time, it cannot be excluded that deposition was locally restricted rather than extending across the entire eastern part of the MHT above the Tsotyli Fm [63]. In the northern part, the base of the formation rests unconformably on top of the underlying Tsotyli Fm [80], which may denote a prior pause in sedimentation. In any case, the deposition of the Ondria Fm coincides with a general sea-level drop during the Tortonian [76] and may also be associated with a contemporaneous rather rapid uplift of the basin, which did not allow the basin to be completely filled with clastic material [63].

Regarding the source of the clastic material that filled the MHT, it seems that this has been mainly derived from the Pelagonian nappe in the east, as supported by the apatite fission track (AFT) data on sedimentary samples from all the MHT formations and gneissic samples from the Pelagonian nappe [14, 42]. Eptachori deposits exclusively originate from the weathering of the steep western boundary rocks (i.e., ophiolites and limestones), but the sediments of Pentalofos formation seem to have already been supplied by the eastern boundary of the basin [42]. This is the outcome of the analysis on Pentalofos sandstone samples, fairly close to the western margin of the basin. The same applies for the source of the clastic materials of the Pentalofos Fm , where the conglomeratic deposits clearly denote the compositional similarity to the Pelagonian rocks. This observation is consistent with earlier studies that identify the Pelagonian nappe as the principal sediment source from the Aquitanian onward, but it suggests that sediment supply may have started even earlier, during the Late Oligocene [61]. Fission-track analyses showing enhanced exhumation of the Pelagonian nappe in the Eocene [42] which point to high erosion rates at that time and continuing into the Oligocene–Miocene. Such processes could have delivered large volumes of detrital material to the eastern part of the basin.

All formations show coarser components towards the southern part of the basin, which is narrower and bears extensive delta fan deposits. This indicates that the source area of the sediments was in closer proximity than further north [42]. Paleo-depth contours based on geophysical data analysis [17] show a shallow deltaic environment near Meteora during the end of Oligocene [77] that deepened towards the central and the northern part of the basin [42]. This interpretation may not necessarily be valid [102] if the limited thickness of the southern deposits does not reflect the original palaeobathymetry of the basin.

The PilotSTRATEGY project has received funding from the European Union's Horizon 2020 research and innovation programme under grant agreement No. 101022664

Instead, it could be the result of later tectonic uplift and subsequent erosion that took place after the Middle to Late Miocene.

3.3. Structural Evolution

The MHT is traditionally known as a "molasse" basin, as initially called by Brunn (1956)[40], who was the first to study the area. The term "molasse" was in fact used in order to distinguish the type of sedimentation from the "flysch" that deposited in the front of the forming orogen, with the former lacking the intense compressional deformation that flysch is typically subjected to. However, the strata of MHT do not show the accepted horizontal and undisturbed bedding behind an orogenic range. The inclination of the strata, the sequence of the formations in space and time, internal facies changes and the structures characterising the broader region, show that the area experienced a rather complex history with different tectonic episodes, which also affected the development of the trough [42]. The modern term to characterise the Mesohellenic infill would be simply "turbidites", referring as a whole to the majority of the material deposited in this large elongated basin that opened and functioned from Early Oligocene to Late Miocene times.

The geodynamic association between the evolution of the basin and the subduction and underthrusting of the External Hellenides towards the E-NE [2, 4, 69] together with the relative movement of the Internal Hellenides towards the W-SW [39] during the Paleogene-Neogene is widely accepted. Nevertheless, different structural and geodynamic models have been proposed over the past years for the development of the MHT.

Different studies suggest that the basin was formed in a wide fore-arc position [63, 73] or as in a foreland depression [42, 72], while the type of the basin is more neutrally characterised as a piggy-back basin due to its development on top of the westward migrating ophiolitic and Pelagonian upper plate nappes [2, 4, 26, 42, 69, 72, 73]. Based on more detailed structural analysis the MHT could be refered as a "polyphased" strike-slip basin [81] in a foreland intermontane position [81].

Regarding the structural framework, documented interpretations include multiple types of faulting as the driving mechanism of the basin formation [2, 4, 14, 17, 26, 42, 63, 69, 72, 73]. Despite the discrepancy between the proposed interpretations, similarities also exist, which briefly include: 1) the (at least partly) tectonic control of the basin subsidence and evolution, 2) the western basin margin as faulted and uplifted (despite the interpretation on the type of faulting; [2, 4, 69, 82], and 3) the along-strike uplifted structures within the basin at the south-eastern part [2, 4, 17, 69].

Field observations and kinematic analysis allowed the recognition of the fault-zones related to the basin development and the definition of their type, as well as the timing of their activity, related to the stages of the basin evolution (Figure 3.3), excluding other relative movements that could be theoretically proposed [2, 14, 42, 69]. The development of the MHT initiated more or less contemporaneously with the last stages of the compressional deformation and thrusting of the Pelagonian upper plate [39, 83, 84] and Pindos units imbrication [38] in Middle Eocene. Its overall evolution occurred under an oblique plate convergence regime, while the main compression was migrating towards the west.

The Middle to Late Eocene Krania sub-basins developed by crustal flexure and subsidence due to loading of the overthickened Hellenides accretionary prism under a NE-SW transpressional regime (NE-SW main σ1 stress axis). During the late Eocene, the tectonic regime of the Krania basin shifted from passive

The PilotSTRATEGY project has received funding from the European Union's Horizon 2020 research and innovation programme under grant agreement No. 101022664

isostatic subsidence to active deformation. This change was driven by strike-slip faulting with a reverse component along the basin's western margin, ultimately causing the uplift and structural disturbance of the older Eocene sub-basins. At the same time, transverse ENE–WSW faults with a component of lateral slip developed along the northern margins of the Krania sub-basin. These structures are interpreted as part of the same tectonic episode, reflecting the reorganisation of stress fields and contributing to the overall structural evolution of the basin. Deformation intensity, however, was not uniform across the basin. In the eastern Krania sub-basin, the tectonic imprint is weaker, a contrast attributed to its palaeogeographic position further removed from the active compressional front that dominated the western margin.

The following stage in the evolution of the MHT is marked by renewed subsidence within an elongated and relatively narrow depression, where the Eptachori and Pentalofos formations accumulated successively from the Early Oligocene to the Early Miocene. The tectonic development of the trough during this interval was largely controlled by dextral strike-slip faults trending NW–SE to NNW–SSE. Their activity produced localized subsidence, positive flower structures along the western margin and in the southeastern sector, as well as sporadic compressional features, all under a transpressional stress regime. In addition to these structures, sinistral strike-slip faults with NE–SW to ENE–WSW orientation are found throughout the basin. Their kinematics and timing are compatible with the dextral system, and they are interpreted as antithetic Riedel faults, accommodating strain within the larger strike-slip framework.

The stress field reconstruction indicates that the maximum principal stress axis (σ_1) remained almost horizontal but shifted slightly from a NE–SW to a NNE–SSW orientation compared to the preceding Eocene stage. The extensional axis (σ_3) also lay nearly horizontal, oriented ESE–WNW. This configuration confirms that transpression persisted through the Oligocene, though with reduced intensity relative to the Eocene. The higher frequency of compressional structures, folds and reverse faults, together with uplift of the Eocene sub-basins, mark the paroxysmal close of the earlier tectonic episode. The strike-slip activity of this period helps explain variations in depocenter depth along the basin axis, with localized rapid subsidence driving the development of internal unconformities and pronounced facies changes.

Towards the end of the Oligocene and into the earliest Miocene, a more localized compressional pulse can be recognized. This event, associated with a WNW–ESE oriented σ_1 axis, is expressed by NW–SE sinistral strike-slip faults along the western basin margin and by rare NE–SW reverse faults cutting the Pentalofos strata. Although relatively minor, the imprint of this event points to a short-lived episode of stress reorganization.

In contrast, the Early Miocene saw a shift towards extensional tectonics, with the eastern part of the basin opening under the influence of low-angle normal faulting. Extension was directed sub-horizontally NE–SW, and marginal NW–SE trending faults with a minor strike-slip component facilitated further widening of the trough. It was within this structural context that the Tsotyli and Ondria formations were deposited. In the southeastern sector of the MHT, the Tsotyli Fm rests directly on Eocene strata, indicating that this area had remained outside the main depocenter during the Oligocene. Meanwhile, the Krania sub-basin, which had been deformed and uplifted at the close of the Eocene, functioned as a basement high until Early Miocene times, when renewed subsidence linked to low-angle normal faulting reactivated the area and re-incorporated it into the depositional system.

Apatite fission track (AFT) data from the MHT deposits records the extensional period of Early Miocene with the abruptly decreasing lag-times of AFT age groups of the samples with Early Miocene stratigraphic

The PilotSTRATEGY project has received funding from the European Union's Horizon 2020 research and innovation programme under grant agreement No. 101022664

age [i.e. lower stratigraphic levels of Tsotyli Fm of Aquitanian/Burdigalian age (~20Ma) [14]. This means shorter time between the exhumation of the source rocks from Pelagonian nappe and the deposition of the eroded material in the MHT (Tsotyli Fm). In contrast, increasing lag-times are shown for the following Middle Miocene period, which is consistent with the final filling of the MHT and the ending of its evolution [42] (Figure 3.3).

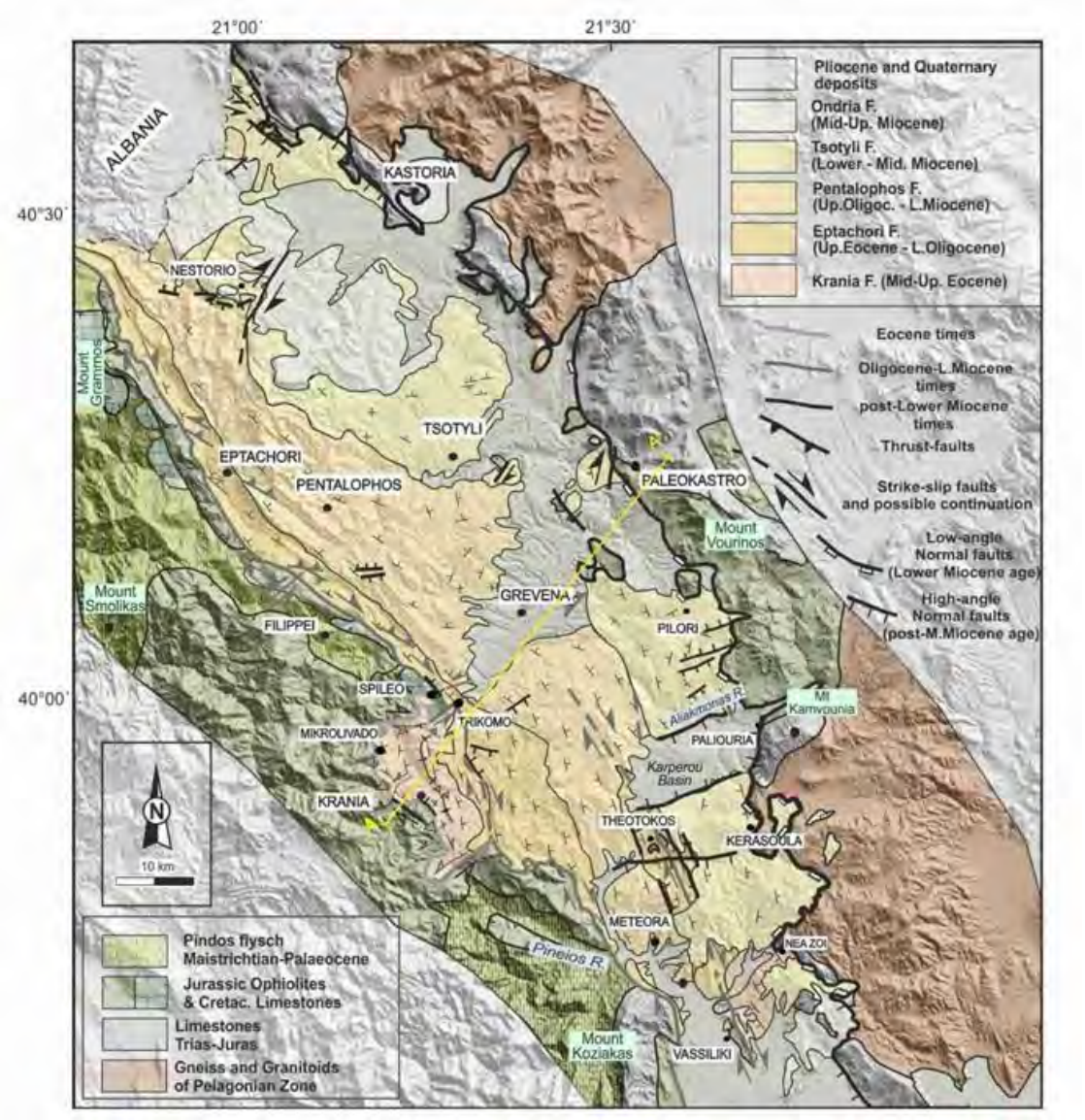

Figure 3.3: Geological map of the MHT with all faults relating to the evolution of the trough from the Middle Eocene onwards (modified after Vamvaka et al., (2020)[42]).

The extensional period that started at the beginning of the Miocene was interrupted by a compressional event during the Late Miocene, related to dextral NNE-SSW strike-slip faults and NW-SE-trending reverse

The PilotSTRATEGY project has received funding from the European Union's Horizon 2020 research and innovation programme under grant agreement No. 101022664

faults that cut the Miocene Tsotyli and Ondria formations, but not any Pliocene or younger deposits. Such faults are well observed in the northeastern part of the basin, near the villages of Nestorio, Tsotyli and Taxiarchis. In some places, overthrusting of the ophiolites onto Miocene sediments is also observed (i.e., east of Grevena city,[85] and further north in Albania,[86]). Paleo-stress analysis indicates that the regime was governed by horizontal σ1 and σ3 axes, with NE-SW and NW-SW trends, respectively.

The Late Miocene compressional event occurred in the middle of a generally extensional period, characterised by orogenic collapse and uplift of the Hellenides after Eocene crustal overthickening[14, 83, 84, 86, 87]. Finally, the post-Miocene times are characterised by continuous extension and high-angle normal faulting of variable orientations. NW-SE to NNE-SSW trending normal faults are observed in the MHT (near Trikomo and Theotokos villages) and between the Triassic carbonates of Pelagonian nappe and post-Miocene deposits along the eastern margin of the basin. NE-SW to ENE-WSW trending normal faults can be associated with the elongate topography today followed by several rivers in the area (e.g. Aliakmonas River). Both fault orientations can be related to pre-existing fracture zones, since they coincide with the direction of strike-slip faults in the Oligocene, reactivated under the younger extensional regime. During this post-Miocene period, the principal stress σ3 axis is orientated horizontally from NE-SW to almost N-S, while σ1 axis is vertical and σ2 usually also horizontal, striking NW-SE. The N-S orientation of σ3 is compatible with the present active tectonics of the area, as computed by the focal mechanisms[88, 89] and probably produces important seismic activity, as shown by the 1995, 2015 and 2021 Grevena-Kozani earthquakes, with the first being the greatest and causing extensive damage to many buildings[90-94].

Regarding the classification of the basin type, this was made based on the geodynamic position of the basin, its characteristics and the structural events that controlled its evolution. The term “piggyback”[95] is accepted for the MHT[2, 4, 26, 42, 73], as developed on the ophiolithic nappes during the eastward underthrusting of the External Hellenides (Gavrovo-Tripolitsa carbonate platform) under the Pelagonian nappe. However, this term does not provide further information for the exact geotectonic position of the basin or the stress regime and the events under which it was developed. The former description of the basin in a “forearc” position[63] is withdrawn due to the absence of a volcanic arc adjacent to the basin. In contrast, the term “foreland” is used to characterise the area behind the Pindos “thrust” zone, during continuous continental convergence. The further classification of the foreland setting as “intermontane” was chosen as used for low-angle subduction systems (and underthrusting) and also to specify the position of the basin on the upper plate of the colliding continental blocks, without necessarily related to compressional tectonics, but instead possibly associated to a series of different deformational patterns[81].

Looking into the tectonic mechanism that led to the formation of the basin, the Mesohellenic Trough can be certainly related to strike-slip faulting, which seems to have significantly controlled the evolution of the basin. The re-activation of the major strike-slip faults along the margins and within the MHT during alternating stress regimes is following Reading’s Cycle, which predicts that every strike-slip fault may undergo alternating periods of extension and compression, while the slip directions adjust along major crustal faults[96].

The diagnostic criteria for the classification of the basin using the pattern of polyphase strike-slip faulting are listed below[42, 81]:

- Asymmetry and the length-to-width ratios (4:1), typical of strike-slip basins.
- Axial infill, sub-parallel to the NW-SE principal displacement zone.
- Lateral migration of the depocenters from west to east, parallel to the principal bounding faults.

The PilotSTRATEGY project has received funding from the European Union’s Horizon 2020 research and innovation programme under grant agreement No. 101022664

- The presence of diverse depositional facies including landslide, alluvial-fan, fan-delta and turbidites.
- The presence of thick, but laterally restricted sedimentary sequences characterised by high sedimentation rates.
- Abrupt lateral and vertical facies variations in places.
- Localised rapid subsidence (e.g., Grevena and Pentalofos areas).

Strike-slip faulting is clearly expressed along the western margin and central sectors of the MHT. Its presence on the eastern side is also likely, although there the evidence is partly masked by overprinting from later episodes of normal faulting

3.4. Hydrogeology

The hydrogeological behavior of the geological formations is a function of lithological composition, geometry, connectivity and tectonic framework, as well as of textural features such as grain size and degree of consolidation[97]. The water behaviour within formations is determined by two main parameters: porosity and permeability (Figure 3.4). The permeability of granular formations is linked to primary porosity, which depends on grain size, shape, arrangement, and degree of consolidation. In non-granular and compact formations, permeability is controlled largely by fracture porosity [97].

Overall, the map highlights how the hydrogeological framework of West Macedonia is controlled by the interplay between lithology and structure. The contrast between low-permeability crystalline and molasse units and the highly permeable Quaternary deposits underlines the spatial variability of groundwater resources, while fault zones act as both barriers and conduits depending on their orientation and degree of activity (Figure 3.4). The karst aquifers dominate much of the region. These aquifers, developed in limestones and marbles, form the most important groundwater reservoirs, often capable of storing and transmitting large volumes of water. Their distribution is, however, interrupted by belts of impermeable flysch and bodies of igneous–volcanic rocks, which break up the continuity of the aquifers and create a patchwork of smaller, compartmentalised groundwater systems. Along the rims and floors of the basin , the limestone and marbles are associated with medium to high hydraulic conductivities, while for the younger alluvial sediments hydraulic conductivity is characterized as “Floating” (Figure 3.5). These formations are linked to medium to high permeability aquifers that are directly connected to surface processes, making them important for both recharge and local water supply.

What stands out from a hydrogeological perspective is the sharp contrast between the permeable karst and granular deposits on one side and the impermeable flysch (Pindos Zone; western rim of the MHT) and schistose and crystalline rocks (Pelagonian Zone; eastern rim of the MHT) on the other. The hydraulic conductivity classification shown on the map highlights this contrast: zones of high and medium permeability line up with the karst and alluvial formations, while large expanses of non-permeable terrain dominate the west. There are also small floating aquifers preserved in valley settings, adding yet another layer of complexity. Together, these features describe a highly varied groundwater landscape, where the main water resources are concentrated in karst and granular (molasse) systems but remain unevenly distributed and strongly shaped by the underlying geology.

The PilotSTRATEGY project has received funding from the European Union’s Horizon 2020 research and innovation programme under grant agreement No. 101022664

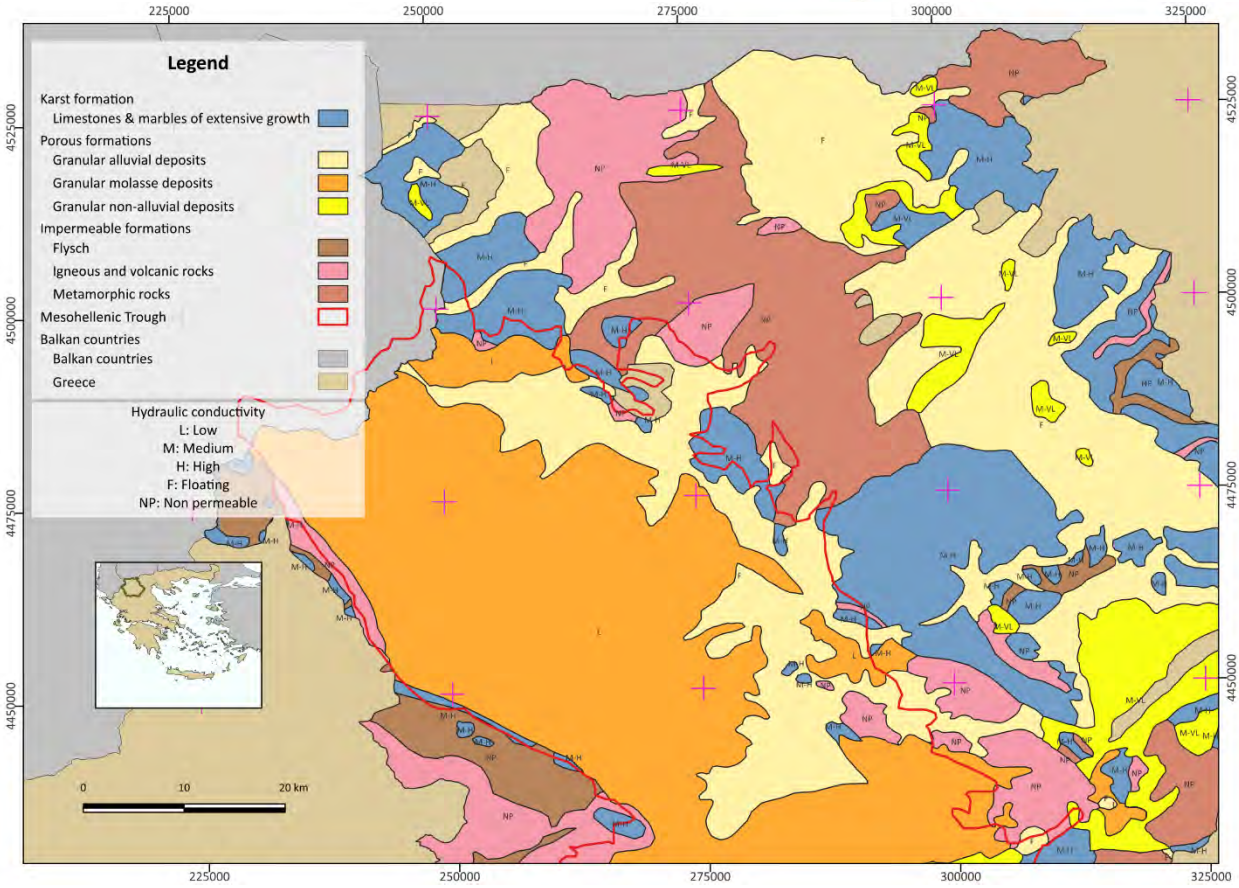

Figure 3.4: Hydrogeology map of West Macedonia. The Mesohellenic Trough is outlined in red. Ref. System: EGSA.87.

3.5. Seismicity

Greece and its surrounding areas constitute one of the most active regions across the eastern Mediterranean and Europe. The main geodynamic and geotectonic features include:

- Continental convergence, comprising the subduction of the oceanic part of the North African plate beneath the European plate, associated with intense crustal shortening and an uplift rate of a few mm/yr along the Hellenic Arc due to the sedimentary accretion of the African plate beneath the overriding Aegean microplate.
- Widespread, high-rate extension in the back-arc region due to the rollback of the subducting African slab.
- Significant right-lateral strike-slip motion along the North Aegean Trough (NAT) and the Cephalonia-Lefkada Transform Zone (CTFZ) due to the westward propagation of the Anatolian plate in the east and the offset between the oceanic-continental convergence in the west, respectively. Notably, the combination of all the above factors leads to significant left-lateral motion along the southeastern front of the Aegean–African interface [98].

According to the available seismological data, the Region of Western Macedonia is characterised as aseismic or of low seismic activity and is classified as a low seismicity zone [119]. In West Macedonia,

The PilotSTRATEGY project has received funding from the European Union's Horizon 2020 research and innovation programme under grant agreement No. 101022664

geological research and neotectonic mapping showed the existence of many important faults with recent activity. These faults could be characterised as active or potentially active faults (i.e., capable of producing earthquakes, mainly between 6 and 7 M in the Richter scale), with the Servia fault being distinguished as the most important one [9]. According to the latest Seismotectonic Atlas of Greece, the seismogenic faults in West Macedonia are characterized as normal (Figure 3.5) [98].

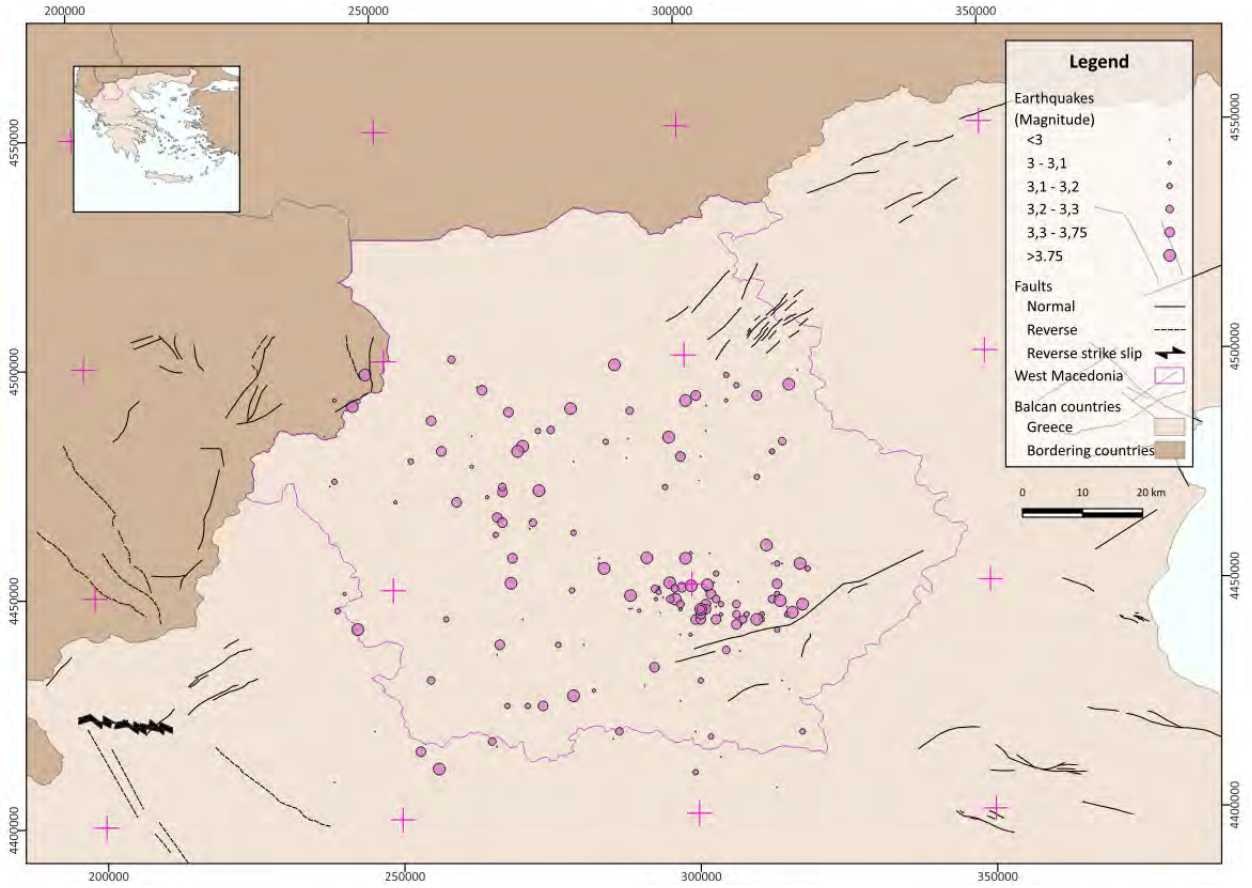

Figure 3.5: Seismotectonic map of West Macedonia (2003-2021). Ref. system: EGSA87.

3.5.1. Seismicity and periodicity

The law of the Gutenberg-Richter is expressed as the number λ of earthquakes of magnitude m ± Δm, with their epicentre in a certain space and occurrence over a certain period of time. Gutenberg-Richter law is expressed in the following mathematical equation (Equation 3.1):

Equation 3.1

$$log\lambda_m = \alpha - bm$$

where λm is the average annual rate of exceedance of the seismic magnitude m, 10α is the average earthquake number of a magnitude greater than or equal to 0 Richter, and b describes the relative probability of small and large earthquakes. As the b value increases, the number of larger magnitude earthquakes decreases compared to this of smaller magnitude events. The a and b parameters are

The PilotSTRATEGY project has received funding from the European Union's Horizon 2020 research and innovation programme under grant agreement No. 101022664

generally obtained by regression in a seismicity database from the source zones of interest (Figure 3.6Figure 3.6). Unless the source zone is extremely active, the database is likely to be relatively sparse.

Based on the Gutenberg-Richter law, the frequency of earthquakes in an area increases when their magnitude decreases. Using Equation 3.1 and data based on earthquake occurrence for the study area presented in appendix A, the following is inferred:

- earthquakes of magnitude M_s = 4.0 have a mean annual rate of exceedance λ_m = 1.488
- earthquakes of magnitude M_s = 5.0 have a mean annual rate of exceedance λ_m = 0.194
- earthquakes of magnitude M_s = 6.0 have a mean annual rate of exceedance λ_m = 0.023

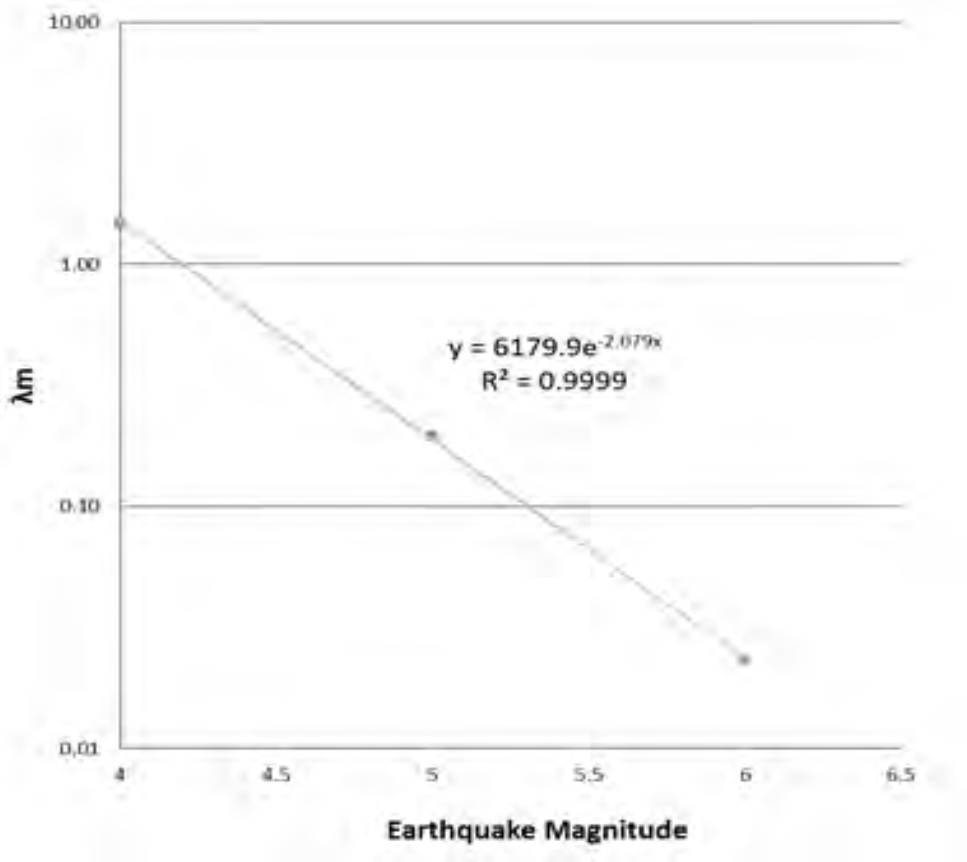

Figure 3.6: Application of Gutenberg–Richter law for West Macedonia.

These results underline that small- to moderate-magnitude earthquakes (around Ms 4.0-5.0) are relatively frequent and form part of the natural background activity of the region, while strong events exceeding Ms 6.0 are comparatively rare. Nevertheless, even with a much lower recurrence rate, such larger earthquakes remain significant in terms of seismic hazard, since they have the potential to cause widespread damage and trigger secondary effects such as landslides or ground deformation. The Gutenberg-Richter law therefore provides a useful statistical framework to quantify not only the likelihood of future seismic events, but also to highlight the importance of considering both frequent, low-magnitude activity and rarer, high-magnitude events in hazard and risk assessments for the area. Earthquake data

The PilotSTRATEGY project has received funding from the European Union's Horizon 2020 research and innovation programme under grant agreement No. 101022664

from the 1700-1900-time period have been omitted from the data analysis due to their qualitative nature. The return period for earthquake magnitude m is given by the following equation (Equation 3.2Equation 3.2):

Equation 3.2

$$TR = 1/\lambda m$$

Therefore, the corresponding return periods are:

- $T_R = \frac{1}{\lambda_4} = \frac{1}{\frac{1.488}{yr}} = 0.67\ years$ for earthquake magnitude 4,
- $T_R = \frac{1}{\lambda_5} = \frac{1}{\frac{0.194}{yr}} = 5.16\ years$ for earthquake magnitude 5,
- $T_R = \frac{1}{\lambda_6} = \frac{1}{\frac{0.023}{yr}} = 43\ years$ for earthquake magnitude 6.

Based on the above results, the general equation for calculating the seismicity return periods is provided, $T_R = 0.039M_S + 0.43628$, while Table 3.1 summarizes the maximum hypothetical potential magnitude of the earthquakes that are predicted to happen in a period of 1, 20, 50 and 100 years, respectively.

Table 3.1: Potential maximum earthquake magnitude over certain periods

Time period	1 year period	20 years period	50 years period	100 years period
Maximum Earthquake Magnitude (Richter)	4.4	5.2	6.3	8.3

Regarding the seismic hazard expressed as seismic acceleration (g) and based on the 1995 Kozani-Grevena earthquake, Kozani has a value of 0.22g and Grevena has a value of 0.24g. In addition, the 1812 earthquake indicates values of 0.25g and 0.09g for the areas of Kastoria and Florina, respectively. Overall, the Region of West Macedonia has an average seismic acceleration value of 0.16g[9]. The seismic data that the analysis is based can be found in the Appendix section (Table Appendix 10.9.11, Table Appendix 10.9.12).

3.5.2. Fault systems

The fault systems observed in West Macedonia are part of the “anti-Hellenides” fault system, which is characterised by the NW-SE trending Hellenic fold-and-thrust belt resulting in extended mountain chains and interposed valleys [99]. The region is characterized by the presence of several Composite Seismogenic Sources (CSSs), namely Amyntaio, Ptolemaida, Komanos, and Aliakmonas. In addition, the fault system of West Macedonia also comprises the Himatidis and Perdika Individual Seismogenic Sources (ISSs), although they do not belong to any of the *above* CSSs (Table Appendix 10.9.13).

The PilotSTRATEGY project has received funding from the European Union’s Horizon 2020 research and innovation programme under grant agreement No. 101022664

3.6. Volcanicity

The occurrence of magmatism in the MHT has not yet been proven, there are indications of volcanism in the basin attributed to different scenarios according to Papanikolaou et al. (1988)[63] and Ferrière et al. (2004)[4], where the MHT is the forearc basin of the Hellenic subduction zone[2]. Another theory by Kilias et al. (2015)[13], suggests that MHT is part of the piggy-back basin formed during the subduction of the African Plate and the westward shift of the Pelagonian units over the accretionary prism justifying the absence of magmatism. This scenario proposes that the development of the basin took place under the following three major tectonic phases: (a) the eastward back-thrusting during the Middle-Upper Eocene period, (b) the strike slip faulting during Oligocene-Miocene period, (c) the westwards detachment faulting, during the Lower-Middle Miocene period[2, 13, 14]. They are a result of a slow upwards migration of hydrothermal carbon dioxide through faults and fractures ordered from NE to SW, which is attributed to magmatic activity[100, 101]. Evidence of slow, upward migration of hydrothermal CO_2 along NE–SW-trending faults and fractures has been documented[121,122] in the neighboring Neogene-Quaternary Florina basin. These natural emissions may reflect the indirect influence of deeper magmatic processes.

The PilotSTRATEGY project has received funding from the European Union's Horizon 2020 research and innovation programme under grant agreement No. 101022664

4. Natural Hazards

4.1. Earthquakes

The Region of Western Macedonia has provided several indications for its seismic activity. In 1984, an earthquake of 5.6 M was recorded in the area of Kozani-Grevena[102, 103], causing restricted damage[104]. On May 13, 1995, however, an earthquake of Magnitude 6.6 struck the areas of Grevena and Kozani, causing extensive disasters. The damage was estimated at $450 million, while 20 human injuries were documented. An earthquake of 4.5 M preceded 4 minutes before the main shock, while an earthquake of 5.5 M struck the area on July 17, as part of the aftershock activity[105].

Despite the aforementioned events, in all studies on significant earthquakes before 1995, West Macedonia was considered an area without significant earthquakes and therefore as an area with little seismic danger. The Kozani earthquake in 1995 was the largest earthquake in Greece in that decade though[103, 106] and it raised some questions for the previously considered as tectonically inactive region of West Macedonia[105].

Systematic palaeoseismological and archaeological studies[107, 108], as well as results of historical studies of seismicity by other researchers[89, 109] provide further information for the seismicity of the area. For example, old manuscripts document an earthquake in 1695 that hit the small city of Serbia, while at least five strong earthquakes have occurred in the wider region in the last 2000 years and suggest that the seismic hazard is certainly not insignificant[110,128,129,130]. Historical records indicate that an earthquake strikingly similar in epicentral location to the 1995 event in Kozani and Grevena occurred in the year 1700, underscoring the long-term seismic activity of the area. Restoration of St. Nikolaos cathedral in Kozani and various other churches provide evidence of an earthquake of around 6.7-7.0 M magnitude[105].

In the broader region around Western Macedonia, historical data for the city of Veria show its destruction around AD 896[104] as well as the destruction of the fortress and a church of Veria in 1211[89], due to an earthquake of at least intensity VIII and magnitude 6.5 M. Also the city of Edessa is reported to have been significantly damaged due to an earthquake between September 1395 and August 1396 [109]. The area of Kastoria is reported to be hit in 1812 or 1813 by an earthquake of at least VIII intensity and 6.5 M according to two signs in a church wall[105, 110].

Archaeological excavations in ancient Pella, revealed the complete destruction of the city around 90 BCE. The presence of valuable ceramics and human skeletons in house ruins as well as the total destruction of low, well-built infrastructures indicate an earthquake of at least 6.5 M and X intensity[105, 111]. Archaeological excavations in the city of Aiani, 15 km south of Kozani, revealed abandoned houses buried under debris, indicating the occurrence of an earthquake around 200 BCE of at least IX intensity and at least 6.0 M. Tectonic uplifts of 60 cm along the fossil coastlines of Thessaly, indicate an earthquake of at least 7.0 M around 400 AD [112, 113].

4.2. Flooding

Flooding phenomena result from a combination of natural and anthropogenic factors. In Water District GR09 of Western Macedonia, which extends beyond the administrative boundaries of the region, intense rainfall events combined with restricted spatial conditions caused by human interventions can lead to flooding. Notable flood events include those that occurred in Kozani in 2012 and in Argos Orestiko in 2010,

The PilotSTRATEGY project has received funding from the European Union's Horizon 2020 research and innovation programme under grant agreement No. 101022664

both attributed to deficiencies in urban planning and inadequate maintenance of critical stream networks. Similarly, the 2010 floods in Kastoria were linked to the insufficient drainage capacity of the lake, resulting in the inundation of lakeside settlements and agricultural areas. In Florina in 2010, the Sakouleva river that passes through the city almost overflowed, while the floods of the same year of the Lower Kleines and Aetos cities of Florina, are attributed to the inability of the farmlands to drain adequately. The two major flooding episodes in West Macedonia though, are in 2003 in the village of Kefalari, Kastoria and in 2009 in the village of Poros, Grevena. These are also recorded in a European level database of significant flood episodes, that has been created to prevent and protect the population as well as the local activities[9].

The most important historical floods as emerged from the national preliminary flood risk assessment for the Water District (GR09) of West Macedonia are related to: a) the regional unit of Pieria, the plain of Katerini and the coastal area of Litochoro, and b) the regional unit of Pella, the lowland area of Mavropotamos (Almopeia area) and the lowland area of the Edessaios River. Also, flooding episodes are recorded in the delta of Aliakmonas River, along the Regional Trench T66, in the lakeside area of Kastoria Lake, in Aliakmonas river near the town of Siatista, in the riparian areas of the Grevenitis River and in the city of Florina[35].

In West Macedonia, a series of technical and summary reports were prepared as part of the consultation process to identify the Potentially High Flood Risk Zones, areas where serious flood risks have been recognized or where flooding is likely to occur. For each of these zones, Flood Hazard Maps (FHM) and Flood Risk Maps (FRM) were developed. Flood hazard refers to the occurrence of flooding in a defined area and is assessed for specific return periods, with magnitude expressed in terms of water depth, flow velocity, and other hydrogeological or hydraulic parameters. Flood risk, in turn, relates to the potential adverse consequences of such flooding for human health, the environment, cultural heritage, and economic activity Regarding the region of West Macedonia, the historical flood events that have been recorded are presented inFigure 4.1.

The PilotSTRATEGY project has received funding from the European Union's Horizon 2020 research and innovation programme under grant agreement No. 101022664

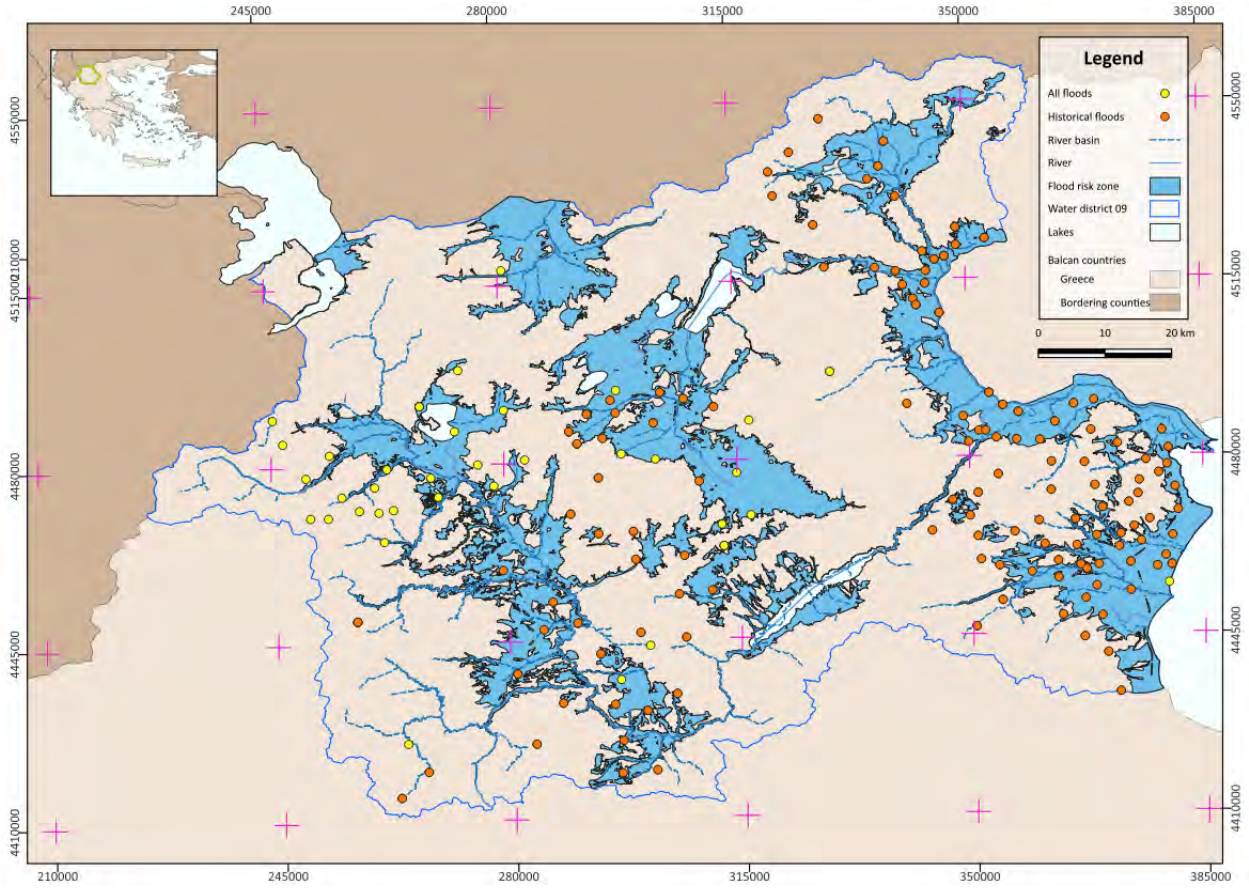

Figure 4.1: Flood risk map of West Macedonia. Ref.system: EGSA87.

The Potentially High Flood Risk Zones were delineated through a geographical cross-sectional analysis that combined two key factors: the likelihood of flooding and the potential for significant adverse consequences in the event of future flood events. The reports of the regional authorities and the significant historical floods were also taken into consideration. Flood risk maps show, for specific return periods (T=50, 100, 1000 years), the negative effects that floods have on these areas in terms of population, economic activity, the environment and cultural heritage. The flood risk maps refer to the Potentially High Flood Risk Zones and include the following scenarios of floods with[114]:

- A high probability of exceeding the 50-year return period,
- a moderate probability of exceeding a return period of 100 years,
- a low probability of exceeding a 1000-year return period,
- sea floods for a return period of 50 and 100 years.

The potential high flood risk zones of the Water District of West Macedonia (GR09) are the summarized in Table 4.1.

The PilotSTRATEGY project has received funding from the European Union's Horizon 2020 research and innovation programme under grant agreement No. 101022664

Table 4.1: Potential high flood risk zones of the Water District of West Macedonia (GR09).

RISK ZONE	LOCATION
GR09RAK0001	Low zone of regional ditch and associated rivers, plain of Katerini and Litochoro (880 km^2)
GR09RAK0002	Low zone through the Aliakmonas river (Sarakina district, Karpero) (102 km^2)
GR09RAK0003	Right shoreside area of artificial lake Polyphytos (63 km^2)
GR09RAK0004	Left shoreside area of artificial lake Polyphytos, low zone of Ftilia (51 km^2)
GR09RAK0005	Kozani Plain (70 km^2)
GR09RAK0006	Low Xirolimni zone (36 km^2)
GR09RAK0007	Low zone of the upper reaches of Aliakmonas and Lake Kastoria (637 km^2)
GR09RAK0008	Low zone of basin of Ptolemaida, lakeside areas of lakes Zazari, Heimaditita, Petron and south of lake Vegoritida (698 km^2)
GR09RAK0009	Arnissa area, Ag. Athanasios coastal areas north of Lake Vegoritida (34 km^2)
GR09RAK0010	Prespa basin low zone (26 km^2)
GR09RAK0011	Upper side of regional trench T66 (34 km^2)
GR09RAK0012	Low zone of the basin of Axios in the regional unit of Florina (Lygos) (290 km^2)
GR09RAK0013	Low zone of Mavropotamos (Almopeia area) and associated rivers (177 km^2)

The identification of Potentially High Flood Risk Zones in the Water District of West Macedonia was carried out using a structured methodology, which was developed by the Special Secretariat for Water as part of the Flood Risk Assessment framework of Greece[114]. The process followed three main steps, applied systematically to analysis cells with sizes at 500 × 500 meters. First, the maximum potential flood impacts across six key land-use categories (residential, industrial, agricultural, tourism, environmental, cultural areas) were evaluated. Then it was examined how flood intensity, defined by water depth and flow velocity, influences the severity of flood impacts. The third step combined the previous two factors into an overall flood impact assessment, by taking into account potential effects on population, economy, environment, and cultural heritage. Based on data and guidance from the Water Information System for Europe (WISE) and the European Environment Agency (EEA) each cell was assigned a vulnerability class, ranging in significance from very low (50) to very high (500)[114]. The results were further refined using the formula Risk = Vulnerability × Hazard, and the flood risks were classified into return periods of 50, 100 and 1,000 years. The assessment revealed that areas falling into the high or very high risk categories (high vulnerability and high flood hazard) are these with deeper and more rapid waters. In these zones, flood management, infrastructure protection, and emergency planning are of high priority to mitigate potential damage to communities, ecosystems, and heritage sites [114].(Table Appendix 10.9.14)

The PilotSTRATEGY project has received funding from the European Union's Horizon 2020 research and innovation programme under grant agreement No. 101022664

4.3. Landslides

In the Region of Western Macedonia, landslides are mostly observed in scattered localities along the mountainous national and provincional road, as well as in the lowland areas of Amyntaio and Ptolemaida, and are ascribed to (Table Appendix 10.9.15):

- anthropogenic activities,
- engineering structures, and
- built-up space (settlements) incidents [9].

In the some cases, landslides are assigned to alteration processes, which are caused by the human-intervention during the exploitation of natural resources, such as mining activities [9]. In other cases, landslides result from (anthropogenic or natural) faulting, cracks, slides or underground displacements [9]. Landslides do not influence the CO_2 storage sites, but they are mentioned for the completeness of the study.

The PilotSTRATEGY project has received funding from the European Union's Horizon 2020 research and innovation programme under grant agreement No. 101022664

5. Geological on site survey

For the PilotSTRATEGY project, geological field surveys in the southern MHT, Regional Unit of Grevena, was carried out in multiple campaigns between April and November 2024. The surveys targeted nine key regions (Regions 1–9), identified as lacking sufficient structural and lithological data (Figure 5.1). The overarching objective was to characterise the stratigraphy, structural framework, and sampling potential of formations relevant for CO_2 storage assessment under the PilotSTRATEGY project.

Data were collected through systematic mapping, discontinuity surveys, and rock sampling, following international standards (ISO 14689:2017; BS 5930:2015+A1:2020). Measurements of bedding, faults, and joints were conducted with a Brunton compass, while georeferencing was supported by handheld GPS. Photographic documentation and sample collection were complemented by detailed lithological descriptions. In total, over 80 survey sites were investigated, encompassing sandstones, marls, conglomerates, limestones, and ophiolitic rocks, all key to reconstructing the geological history of the basin and evaluating its potential as a CO_2 reservoir–seal system.

The survey confirmed the wide distribution of molasse formations (Krania, Kipourio, Pentalofos, Tsotyli), which are dominated by sandstones, marls, and conglomerates. These lithologies display variable textural and diagenetic characteristics that strongly influence their reservoir potential. Sandstones typically exhibit medium strength and limited weathering, making them suitable candidates for porosity–permeability testing, while marls and fine-grained limestones show tight discontinuities, underscoring their role as effective sealing horizons. In contrast, the conglomeratic units, though widespread, are heterogeneous in grain size and cementation, resulting in variable hydraulic behaviour.

Structurally, the fieldwork revealed a consistent NE-dipping bedding pattern, reflecting the asymmetric geometry of the basin. Bedding is commonly disrupted by steep fault zones and conjugate joint systems, particularly in areas such as the Felli Fault Zone, where strata are rotated to near-vertical dips. The ophiolitic rocks (serpentinites, peridotites, and associated ophiolitic conglomerates) form mechanically competent units with pervasive jointing. These discontinuities are significant both for understanding tectonic evolution and for evaluating their potential as fluid pathways.

The field observations therefore highlight the dual nature of the MHT for CO_2 storage:

- Reservoir potential is provided by medium - to thick-bedded sandstones and locally by conglomerates.
- Seal potential is offered by marls and fine-grained carbonate successions, as well as the tight bedding discontinuities observed in several molassic units.
- Structural control plays a key role, as faults and joint systems compartmentalise reservoirs and may act as preferential leakage pathways or barriers depending on mineralisation and infill.

This integrated dataset provides the foundation for the detailed stratigraphic, structural, and kinematic analyses that follow in Chapter 5.4. It also underpins the sampling campaign (Chapter 5.4.1), which targeted representative lithologies for laboratory analysis.

The PilotSTRATEGY project has received funding from the European Union's Horizon 2020 research and innovation programme under grant agreement No. 101022664

5.1. Fieldwork Approach and Observations

The field campaigns in the southern MHT (Grevena region) were undertaken between 2021 and 2025 to document the lithostratigraphy, structure, and sampling potential of formations relevant for CO_2 storage assessment. Nine regions were investigated through geological mapping, structural measurements, discontinuity surveys, and sampling.

The surveys confirmed the predominance of molasse formations (Eptachori, Pentalofos, and Tsotyli) interbedded with conglomerates and locally overlain by Pliocene deposits. These successions display repeated associations of sandstones and conglomerates with interbedded marls and marly limestones, forming natural reservoir-seal pairs. Ophiolitic rocks and their derived conglomerates occur along basin margins and fault zones, acting mainly as structural boundaries. The sampling campaign targeted representative lithologies, including sandstones, marls, conglomerates, limestones, and ophiolitic rocks, with the aim of assessing petrographic, geochemical, and petrophysical properties. These materials form the basis for evaluating the storage potential and sealing capacity of the formations infilling the basin. Overall, the integrated fieldwork highlights the coexistence of promising reservoir units and effective seals within a structurally complex framework. This duality underscores both the potential and the challenges of utilising the MHT for long-term CO_2 storage.

CERTH is committed to open data and metadata sharing sample information in an effort to promote a workplace of collaboration. Therefore, data from the samples collected are open and accessible from the SESAR2 database. They can be accessed here, https://www.geosamples.org/search-options/catalog-search.

5.2. Mapping Area Overview

Field surveys in the southern MHT, within the Regional Unit of Grevena, West Macedonia, focused on an area of maximum basin development where the sedimentary fill exceeds 4,000 m in thickness, with cumulative estimates surpassing 6–7 km (Figure 5.1). Bounded by the Pindos ophiolitic complex to the west and the Pelagonian carbonate massifs to the east, the region provides excellent exposures through road cuts and natural outcrops, making it an ideal natural laboratory for stratigraphic and structural studies relevant to CO_2 storage. Mapping and sampling concentrated on the three principal formations that record the main phases of basin infill from the Early Oligocene to the Early/Middle Miocene: the fine-grained turbidites of the Eptachori Fm, the coarse sandstones and conglomeratic channel fills of the Pentalofos Fm, and the marl–sandstone alternations and marly limestones of the Tsotyli Fm. The marginal Krania and Ondria formations are only locally preserved and were not systematically sampled.

The PilotSTRATEGY project has received funding from the European Union's Horizon 2020 research and innovation programme under grant agreement No. 101022664

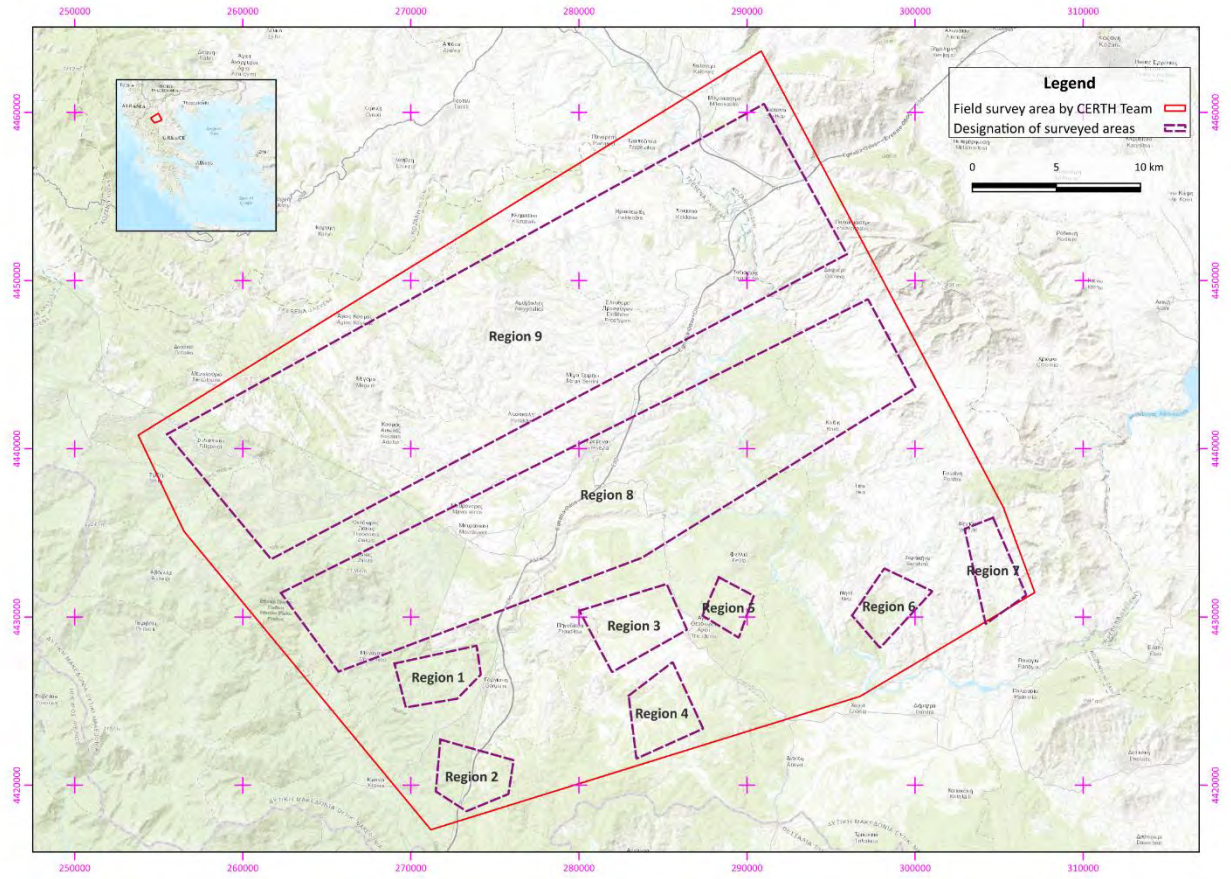

Figure 5.1: Map at 1:200,000 scale in the EGSA87 reference system showing the locations of surveyed Regions 1–9 outlining the broader study area at the Regional Unit of Grevena.

The surveyed regions (1–9) capture representative successions across the basin (Figure 5.1). Regions 1 and 2 encompass the sandstone–marl alternations of the Krania and Kipourio formations, Regions 3 to 5 the conglomerate- and sandstone-rich Pentalofos successions, and Regions 6 and 9 the marl–sandstone alternations of the Tsotyli Fm. Regions 7 and parts of 9 expose ophiolitic basement rocks and reworked ophiolitic detritus, as well as bedded limestones as analogues of marginal carbonate settings. Overall, bedding with gentle northeast dips is the dominant structural element in the sedimentary successions, offering laterally continuous marl seals and reservoir sandstones, while conglomerates display greater heterogeneity and ophiolites are pervasively fractured. Together, these mapping results outline the depositional and structural framework of the basin, underlining its suitability for evaluation as a potential CO_2 storage site

5.3. Lithostratigraphic/Stratigraphic Observations

The lithostratigraphic framework of the southern MHT, as revealed by the field campaigns, is dominated by thick molasse successions of Oligocene to Miocene age. These sequences record the progressive infill of the basin and provide the key lithologies for assessing CO_2 storage potential. The following stratigraphic

The PilotSTRATEGY project has received funding from the European Union's Horizon 2020 research and innovation programme under grant agreement No. 101022664

column illustrates the vertical arrangement, thickness, and lithological characteristics of the main formations of the MHT.

At the base, the Eptachori Fm (Early Oligocene) consists mainly of fine-grained turbidites, including marls, shales, and sandstones interbedded with conglomeratic horizons. Soft-sediment deformation features such as slumps and convolute laminations are common, reflecting unstable depositional conditions. The alternation of permeable sandstones and sealing marls forms small-scale reservoir–seal associations, although local deformation structures may disrupt continuity.

The overlying Pentalofos Fm (Late Oligocene–Early Miocene) is characterised by thick-bedded sandstones and polymictic conglomerates intercalated with sandy marls. Its lower members contain coarse channel-fill conglomerates ("Tsarnos"/"Taliaros"), while the overlying "Kalloni" Member is dominated by finer, shalier successions. Moderately cemented, laterally extensive sandstones form the basin's most significant reservoir lithologies, whereas the interbedded marls provide important local sealing intervals.

The Tsotyli Fm (Early-Middle Miocene) is composed predominantly of marls and marly limestones with thin interbedded sandstones and occasional conglomeratic lenses. Its fine-grained character and laterally continuous bedding make it the most effective regional seal in the stratigraphic succession. Basal conglomerates, where present, form transitional facies but possess only limited reservoir potential.

Pliocene conglomerates occur locally along the basin margins. Although generally uncemented and unbedded, and therefore of limited storage value, they remain important stratigraphic markers of late-stage basin evolution and post-Miocene tectonic tilting. In addition, ophiolitic rocks (serpentinites, harzburgites, gabbros) and ophiolitic-derived conglomerates are exposed along the margins. While mechanically competent, these units are heavily jointed and function less as reservoir or seal lithologies, instead forming tectonic boundaries that control basin architecture and fluid pathways.

The stratigraphic framework documented in Regions 1 to 7 captures the main depositional and tectonic elements of the MHT. From the Eocene-Oligocene molasse deposits of the Krania and Eptachori formations, through the Oligocene-Miocene coarse clastics of the Pentalofos Fm, and into the Miocene marl-sandstone alternations of the Tsotyli Fm, the sequence records the progressive infill of the basin. In places, this stratigraphy rests directly on the ophiolitic basement of the Vourinos complex, as clearly seen in Region 7, while younger Pliocene-Pleistocene fluvial and lacustrine sediments, together with Quaternary terraces, mark the more recent evolution of the landscape. The stratigraphic logs are the result of the field survey held in Regions 1 to 7 and represent the near surface stratigraphy (Figure 5.2-Figure 5.9). Approximate altitudes are given for each column. Taking this into consideration the columns highlight both the near surface vertical transitions between reservoir and seal units and the lateral heterogeneity that influences the potential of the basin for CO_2 storage. The presented stratigraphic logs provide a generalised field synthesis of the areas mapped and should not be confused with localised stratigraphic/sedimentary logs.

The PilotSTRATEGY project has received funding from the European Union's Horizon 2020 research and innovation programme under grant agreement No. 101022664

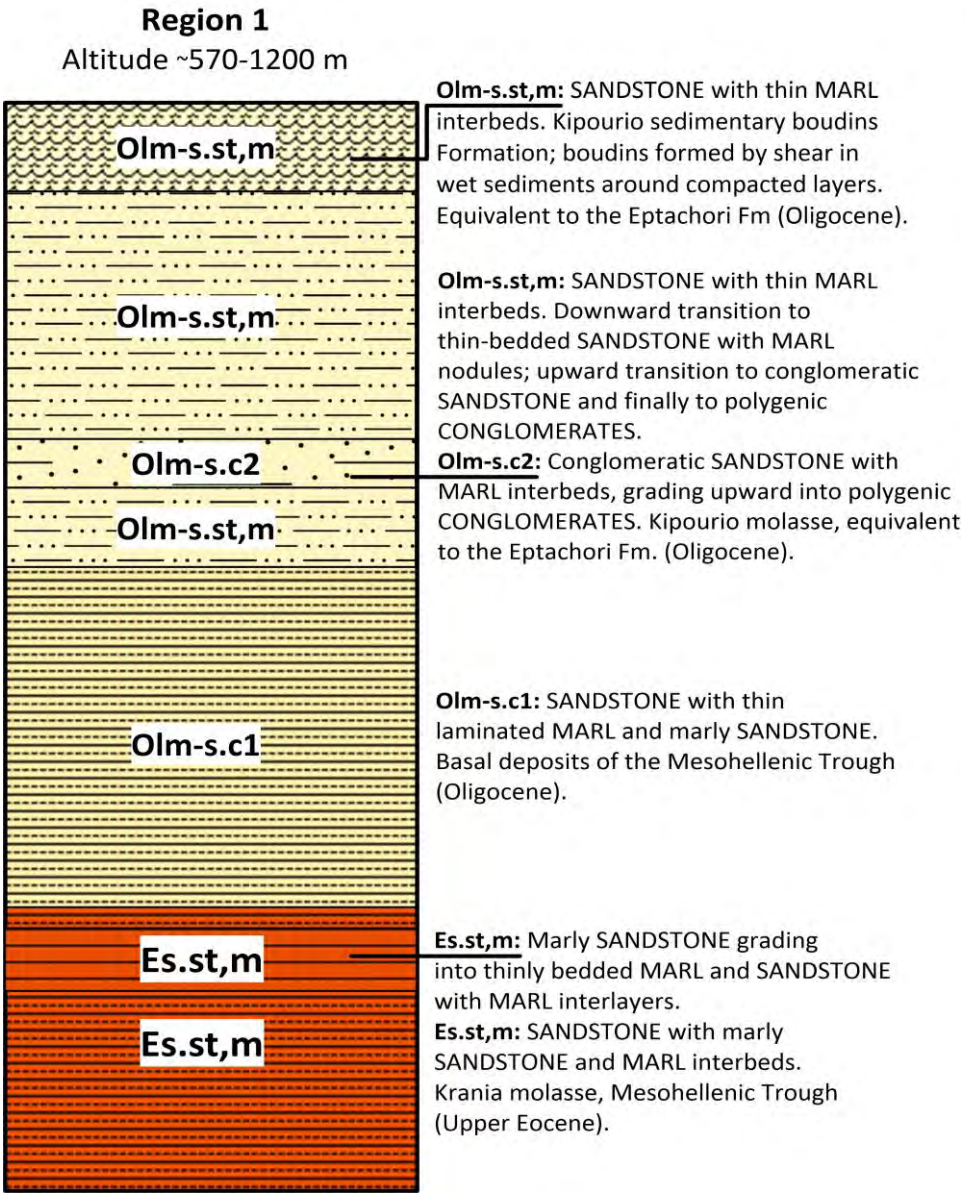

Figure 5.2: Synthetic stratigraphic column of Region 1 showing the near-surface geological succession observed in this area.

Region 1 spans altitudes of ~570 to 1200 m and exposes one of the thickest and most complete successions of the MHT among the survey regions 1 to 7, preserving both the Eocene and Oligocene molasse stages. At its base lie the Krania molasse deposits (Upper Eocene), consisting of alternating marly sandstone, marl, and thinly bedded sandstone (Figure 5.2). These units represent the initial syn-orogenic infill of the trough and provide the lithological foundation for the overlying sequences. Above, the Oligocene succession begins with thick intervals of sandstones interbedded with laminated marls and marly sandstones, which represent the basal layers of the main mollasic sedimentation. These are followed by alternating sandstones and marls that, in places, contain marl nodules forming discontinuous

The PilotSTRATEGY project has received funding from the European Union's Horizon 2020 research and innovation programme under grant agreement No. 101022664

horizons. The sandstone beds grade upward into conglomeratic sandstones and polygenic conglomerates, reflecting an increase in depositional energy.

A distinctive feature of this region is the development of the so-called “Kipourio sedimentary boudins”, where sandstone interbedded with thin marl was deformed into boudin-like structures due to shear flow in wet, unconsolidated sediments around more competent layers (Figure 5.2). These boudins are unique structural markers of synsedimentary deformation and provide insights into the dynamic depositional and tectonic environment of the Oligocene fill. Higher in the stratigraphy, conglomeratic sandstones interbedded with marls transition upward into thick polygenetic conglomerates, characteristic of proximal fan systems. Together, these coarse-grained deposits and their interbedded finer intervals record repeated alternations between high-energy fluvial or fan-delta activity and quieter, marl-dominated sedimentation. Overall, the succession in Region 1 documents the gradual shift from the early molasse deposition of the Krania Fm into the high-energy Kipourio molasse (Eptachori equivalent). The interplay of sandstones, marls, and conglomerates, together with features like the sedimentary boudins, highlight a strongly tectonically influenced depositional regime, where variations in sediment supply, subsidence, and synsedimentary deformation governed the stratigraphic architecture of the basin.

Figure 5.3: Representative field photograph of an outcrop related to the “Kipourio sedimentary boudins” as it appears in survey sites Region 1 and 2.

The PilotSTRATEGY project has received funding from the European Union’s Horizon 2020 research and innovation programme under grant agreement No. 101022664

Region 2 is situated between ~610 and 940 m elevation, and exposes a similar to Region 1 and more complete in comparison to Regions 3-6 succession of the MHT. At the base, the sequence begins with sandstones of the Krania molasse (Upper Eocene), consisting of alternating sandstone, marly sandstone, and marl (Figure 5.4). These units mark the first syn-orogenic infill and establish the transition into the younger molassic strata. Overlying these are the basal Oligocene deposits, which include thick packages of sandstones interbedded with marls and marly sandstones, occasionally containing sands and scattered cobbles. Above, the succession grades into unbedded to slightly bedded, well-cemented conglomerates, which locally alternate with sandy and marly intervals. These coarse-grained units reflect a phase of higher-energy deposition and mark the basal fill of the MHT. Higher in the succession, reddish to greenish marls appear which are interbedded with conglomerates that transition into conglomeratic sandstones. These colour variations and lithological alternations point to changing oxidation conditions and shifts between fluvial and shallow lacustrine environments. The upper part of the column is dominated by marly sandstones and sandstones intercalated with marl, equivalent to the Eptachori Fm, deposited during the Oligocene. Overall, the stratigraphy of Region 2 records the shift from the early molasse stage of the Krania deposits into the thick Oligocene fill of the basin. The alternation of conglomerates, sandstones, and marls reflects fluctuating depositional energy and sediment supply, linked to both tectonic activity and varying sediment provenance during the early evolution of the trough.

The PilotSTRATEGY project has received funding from the European Union's Horizon 2020 research and innovation programme under grant agreement No. 101022664

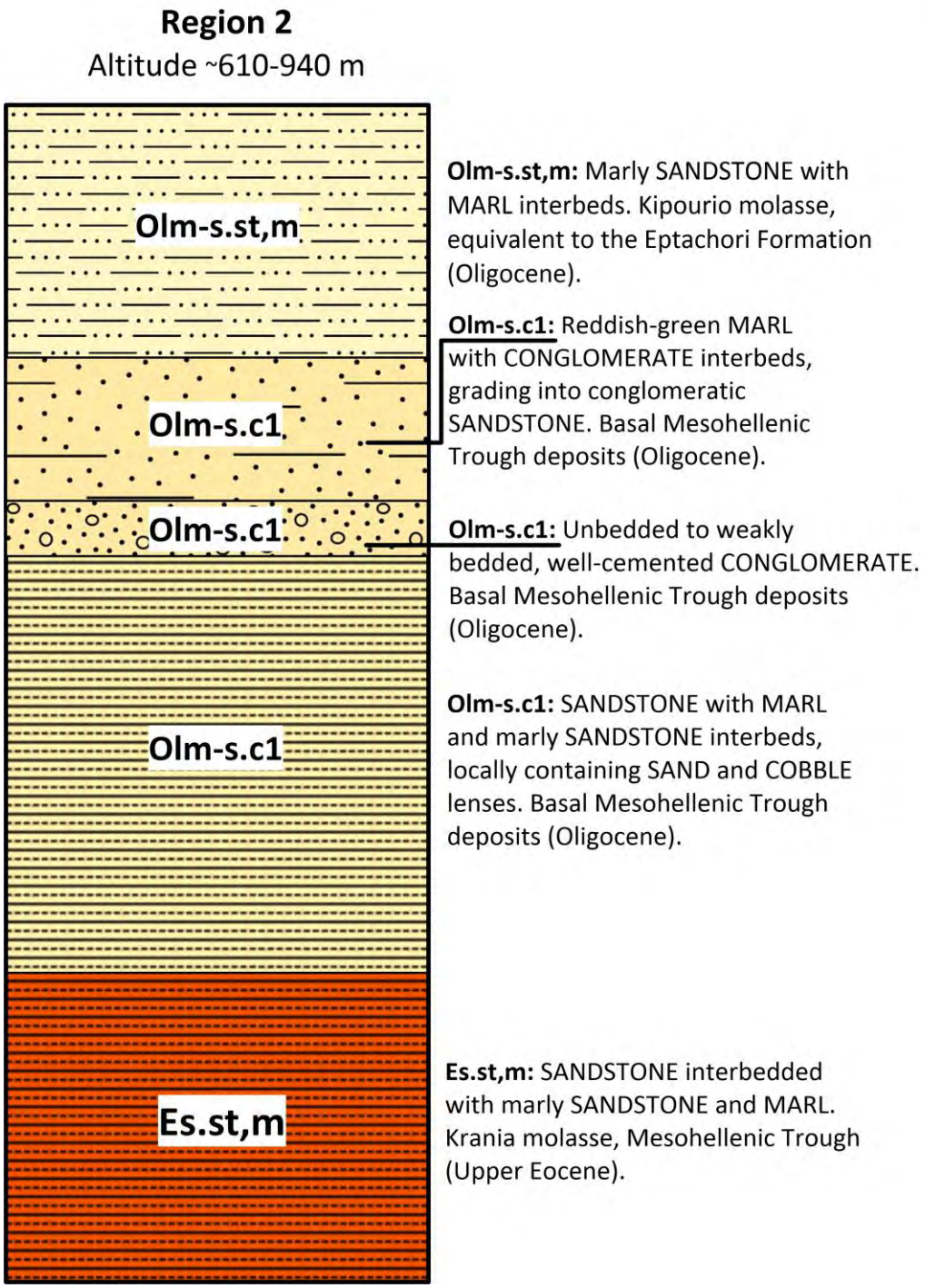

Figure 5.4: Synthetic stratigraphic column of Region 2 showing the near-surface geological succession observed in this area.

The succession exposed in Region 3 (altitude ~620-800 m) belongs to the Pentalofos Fm (Aquitanian, Lower Miocene) and records a complex alternation of conglomeratic and finer-grained deposits. At the

The PilotSTRATEGY project has received funding from the European Union's Horizon 2020 research and innovation programme under grant agreement No. 101022664

base, the sequence is dominated by unbedded to weakly bedded conglomerates, ranging from loose to well-cemented, and containing interbeds of sand and cobbles (Figure 5.5). These are overlain by thinly bedded marls alternating with fine sands, which gradually pass upward into more massive sandstones and conglomerates. Higher in the column, conglomerates interbedded with conglomeratic sandstones and sandy marls appear, reflecting repeated phases of channel activity alternating with quieter depositional intervals. This alternation continues with sandstone to conglomeratic sandstone units, again interlayered with conglomerates and marls, indicating lateral shifting of channels and bars within a high-energy fluvial setting. In the upper part of the sequence, conglomerates are interbedded with conglomeratic sandstones and sandy marls.

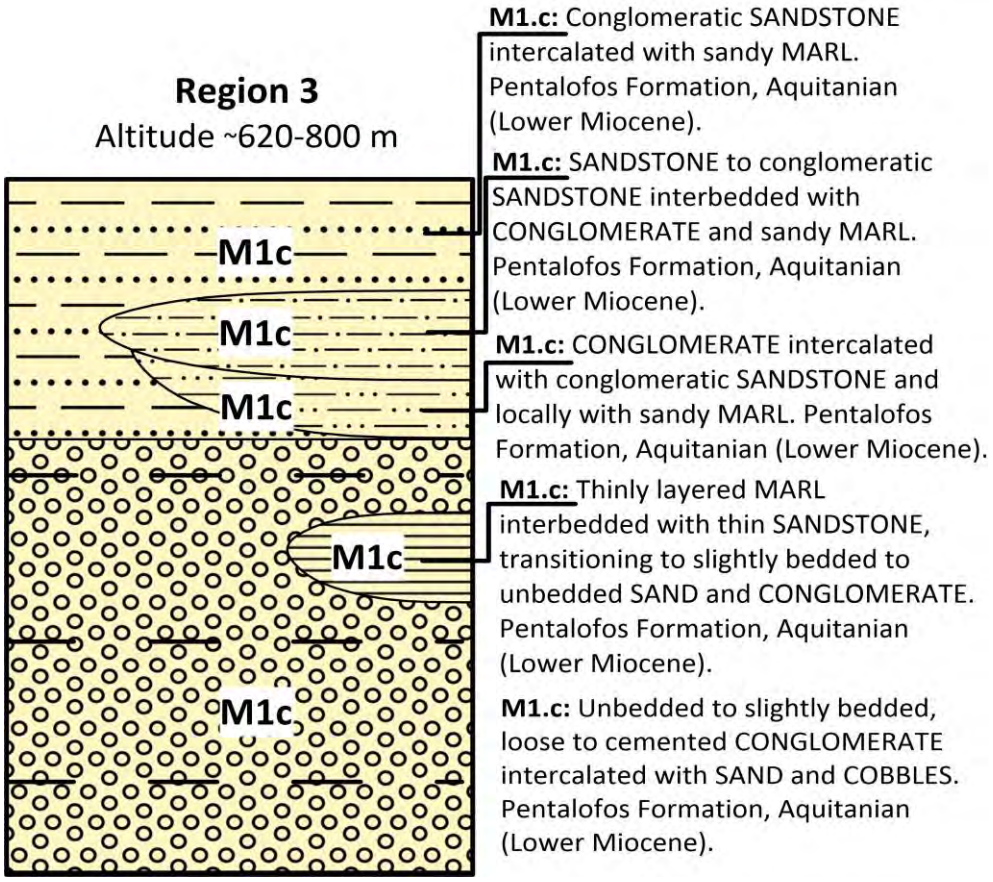

Figure 5.5: Synthetic stratigraphic column of Region 3 showing the near-surface geological succession observed in this area.

This arrangement reflects repeated shifts between phases of active channel deposition and intervals of lower energy. Above this, sandstones and conglomeratic sandstones appear together with further interbeds of conglomerates and marls, pointing to the lateral movement of channels and bar deposits within a high-energy fluvial environment. The succession is capped by conglomeratic sandstones with sandy marl layers, which preserve the continued input of coarse material but also record episodes of finer sedimentation. The succession in Region 3 therefore demonstrates the internal variability of the Pentalofos Fm. The alternation of conglomerates, sandstones, and marls records a fan system in which

The PilotSTRATEGY project has received funding from the European Union's Horizon 2020 research and innovation programme under grant agreement No. 101022664

sediment supply and flow energy changed repeatedly. Thick conglomerates mark episodes of high-energy deposition, while the finer horizons represent quieter conditions. Together, these cycles are consistent with tectonically driven sedimentation during the early Miocene infill of the MHT.

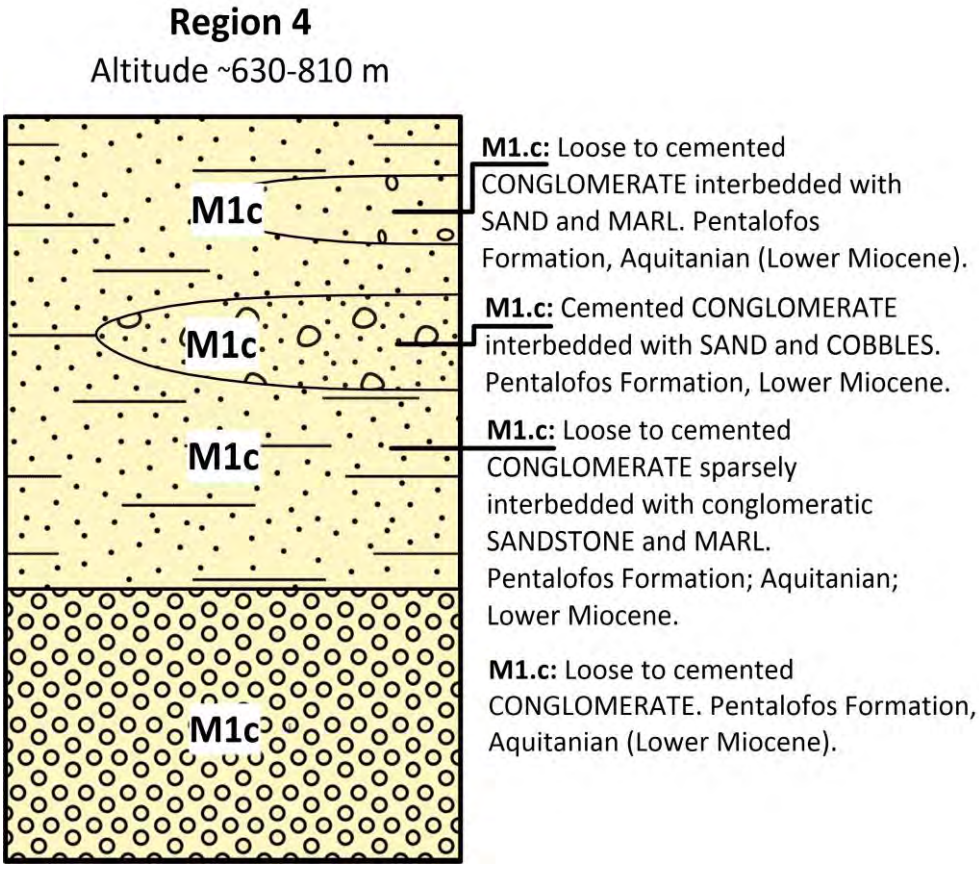

Figure 5.6: Synthetic stratigraphic column of Region 4 showing the near-surface geological succession observed in this area.

The stratigraphic succession of Region 4 (altitude ~630-810 m) is entirely assigned to the Pentalofos Fm (Aquitanian, Lower Miocene) and is dominated by thick accumulations of conglomeratic facies. At the base, the sequence consists of loose to cemented conglomerates, forming massive beds with variable clast support, which document high-energy depositional conditions (Figure 5.6). These are overlain by loosely to moderately cemented conglomerates interbedded with conglomeratic sandstone and marl, reflecting episodic shifts between coarse-grained channelized flows and finer overbank or low-energy intervals. Higher in the stratigraphy the deposits grade into well-cemented conglomerates intercalated with sands and cobbles. This could be evidence of more organized bar or channel deposits within a fluvial fan system. The upper part of the stratigraphy incorporates loose to cemented conglomerates interbedded with sand and marl, suggesting repetations between high-energy fluvial phases and low-energy depositional phases. The succession in Region 4 reflects a long-lived fluvial fan system developed close to the sediment source. The deposits are predominantly coarse, with conglomerates prevailing, but they are intermittently interrupted by thinner, finer-grained beds of sandstone and marl. This vertical alternation reflects shifts in depositional energy and sediment supply within a fan-related system during

The PilotSTRATEGY project has received funding from the European Union's Horizon 2020 research and innovation programme under grant agreement No. 101022664

the early Miocene evolution of the MHT. In addition to grain-size changes, the outcrops also show intervals that are better cemented alongside more weakly consolidated layers, this contrast is attributed to post-depositional diagenetic processes, like variable circulation of pore fluids and carbonate input, rather than to primary depositional energy alone.

Region 5 (altitude ~480–710 m) belongs entirely to the Pentalofos Fm (Aquitanian, Lower Miocene) and records a range of coarse clastic facies (Figure 5.7). The sequence begins with unbedded to bedded conglomerates, which contain intercalations of marl and sandy marl. These are overlain by marly sandstones interbedded with thin-bedded sandy marls, where minor jet lenses are also observed, indicating local variations in depositional energy. Higher the deposits grade into slightly bedded to unbedded conglomerates. The uppermost part of the column consists of slightly bedded sands and cobbles, reflecting a coarser-grained, higher-energy environment. Overall, Region 5 preserves a thick clastic succession that highlights the proximal to medial fan depositional character of the Pentalofos Fm, with alternating intervals of massive conglomerate and finer interbeds of sandstone and marl documenting lateral and vertical facies variability.

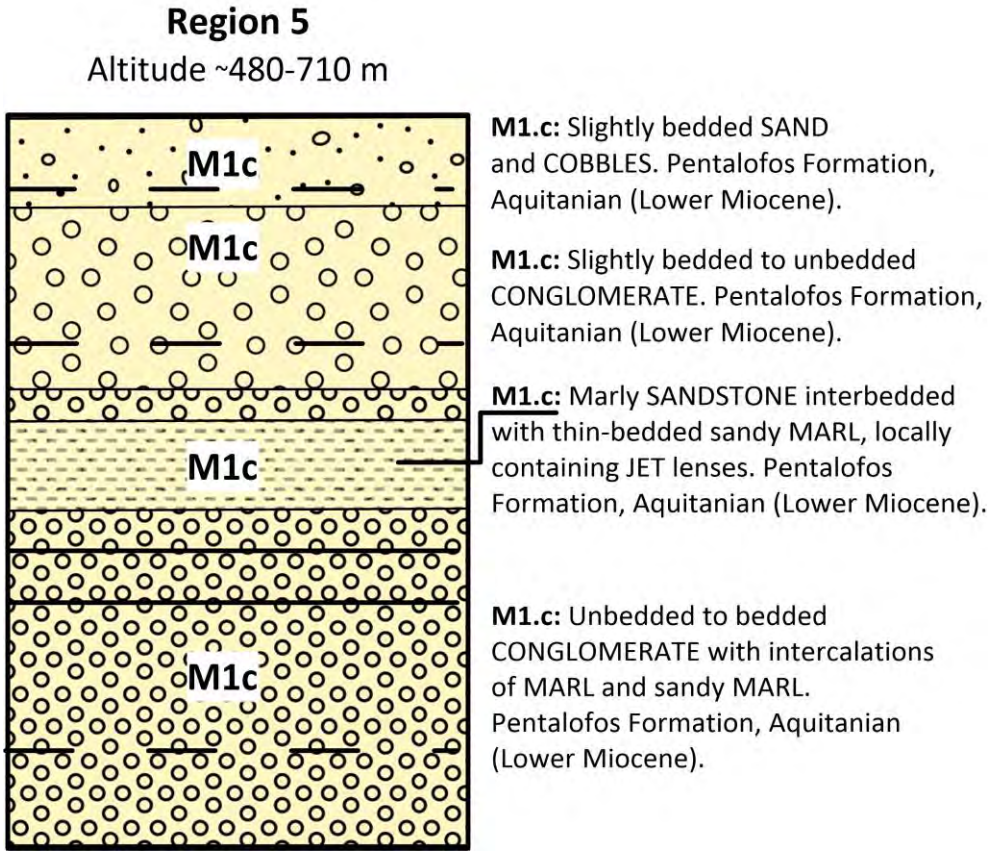

Figure 5.7: Synthetic stratigraphic column of Region 5 showing the near-surface geological succession observed in this area.

The PilotSTRATEGY project has received funding from the European Union's Horizon 2020 research and innovation programme under grant agreement No. 101022664

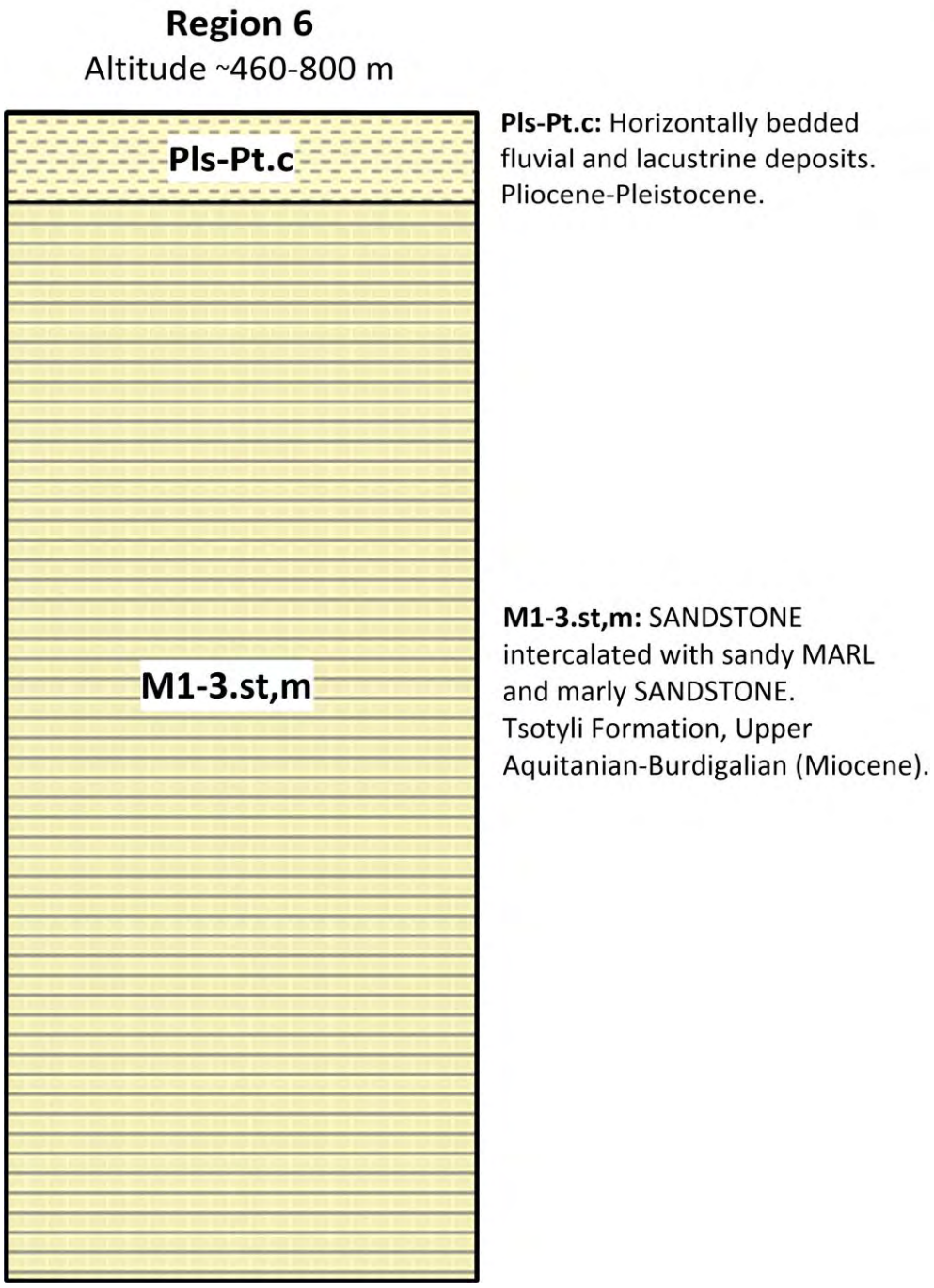

Figure 5.8: Synthetic stratigraphic column of Region 6 showing the near-surface geological succession observed in this area.

In Region 6 with elevations varying approximately between 460 and 800 m, the stratigraphy is dominated by the Miocene Tsotyli Fm, which forms a thick sequence of alternating sandstones, sandy marls, and marly sandstones, deposited between the Upper Aquitanian and Burdigalian (Figure 5.8). The stratigraphy

The PilotSTRATEGY project has received funding from the European Union's Horizon 2020 research and innovation programme under grant agreement No. 101022664

is capped by Pliocene-Pleistocene fluvial and lacustrine sediments, which occur as laterally continuous, horizontally bedded units. These younger deposits reflect the reorganisation of the basin into terrace and floodplain environments during the Quaternary.

The geological succession in Region 7, situated between 590 and 750 m elevation, begins with the ophiolitic basement of the Vourinos complex. At its base, the sequence is made up of peridotite, mostly harzburgite with some lherzolite, overlain by thick serpentinite bodies of the same origin and age (Upper Lias-Middle Malmian) (Figure 5.9). Above the basement, the ophiolitic conglomerates of the Tsotyli Formation are found, which locally include lateritic Fe-Ni lenses. These pass upward into alternating sandstones, sandy marls, and marly sandstones, representing the Miocene Tsotyli Fm (Upper Aquitanian-Burdigalian). The overlying part of the succession records younger sedimentary environments, fluvial deposits of Pliocene-Pleistocene age, followed by horizontally bedded fluvial and lacustrine successions, and later by terrace-related alluvial and lacustrine sediments of Upper Pliocene-Pleistocene age. The sequence is capped by red soils and limestone debris forming Quaternary terraces, and finally by a thin cover of recent deposits. This vertical succession documents tectonic uplift, fluvial reorganization, and lateritic weathering processes that shaped the current landscape. It shows a long-term transition from deep-seated ophiolitic basement through Miocene basin infill to Quaternary surface reworking.

The stratigraphic successions recorded in Regions 1 to 7 show in detail how the MHT was progressively filled, beginning with the first molasse deposits of the late Eocene and continuing into the Miocene and Quaternary. Regions 1 and 2 preserve the thickest near surface exposed successions, where the Krania molasse at the base (Upper Eocene) consists of alternating marly sandstones, marls, and thin sandstones. These deposits represent the earliest syn-orogenic infill and are overlain by the Oligocene Kipourio molasse (Eptachori equivalent). Sandstones interbedded with laminated marls and marly sandstones grade upward into conglomeratic sandstones and polygenic conglomerates, reflecting a steady increase in depositional energy. The development of the Kipourio sedimentary boudins in Region 1, formed by shear of wet sediments around more competent layers, provides rare structural evidence of synsedimentary deformation and speaks to the unstable conditions during early basin filling.

The overlying successions exposed in Regions 3, 4, and 5 belong to the Pentalofos Fm (Aquitanian–Lower Miocene). These are dominated by conglomerates, locally loose and poorly sorted, elsewhere well-cemented and interbedded with sandstones, marls, and sandy marls. The alternations reflect repeated shifts between high-energy fluvial channels and quieter phases of deposition, typical of proximal to medial fan environments. The variability in cementation and bedding style, as observed in Regions 4 and 5, suggests fluctuating hydrodynamic regimes and sediment supply, probably controlled by tectonic phases and local base-level changes. Minor marl or sandstone horizons record pauses in coarse clastic input, while the massive conglomerate packages reflect sustained phases of high-energy deposition.

In Regions 6 and 7, the Miocene Tsotyli Fm dominates the succession. Here, thick packages of sandstone, sandy marl, and marly sandstone (Upper Aquitanian–Burdigalian) show a more rhythmically bedded style compared to the coarse fan facies of the Pentalofos. These units provide both reservoir-quality sandstones and fine-grained intervals with sealing potential. Above, Pliocene–Pleistocene fluvial and lacustrine deposits occur as horizontally bedded successions, capped in Region 7 by terrace deposits with red soils and limestone debris. The base of Region 7 also exposes the Vourinos ophiolitic basement, with peridotite and serpentinite overlain by ophiolitic conglomerates containing lateritic Fe-Ni lenses, showing how inherited tectonic highs influenced both provenance and local stratigraphic architecture.

The PilotSTRATEGY project has received funding from the European Union's Horizon 2020 research and innovation programme under grant agreement No. 101022664

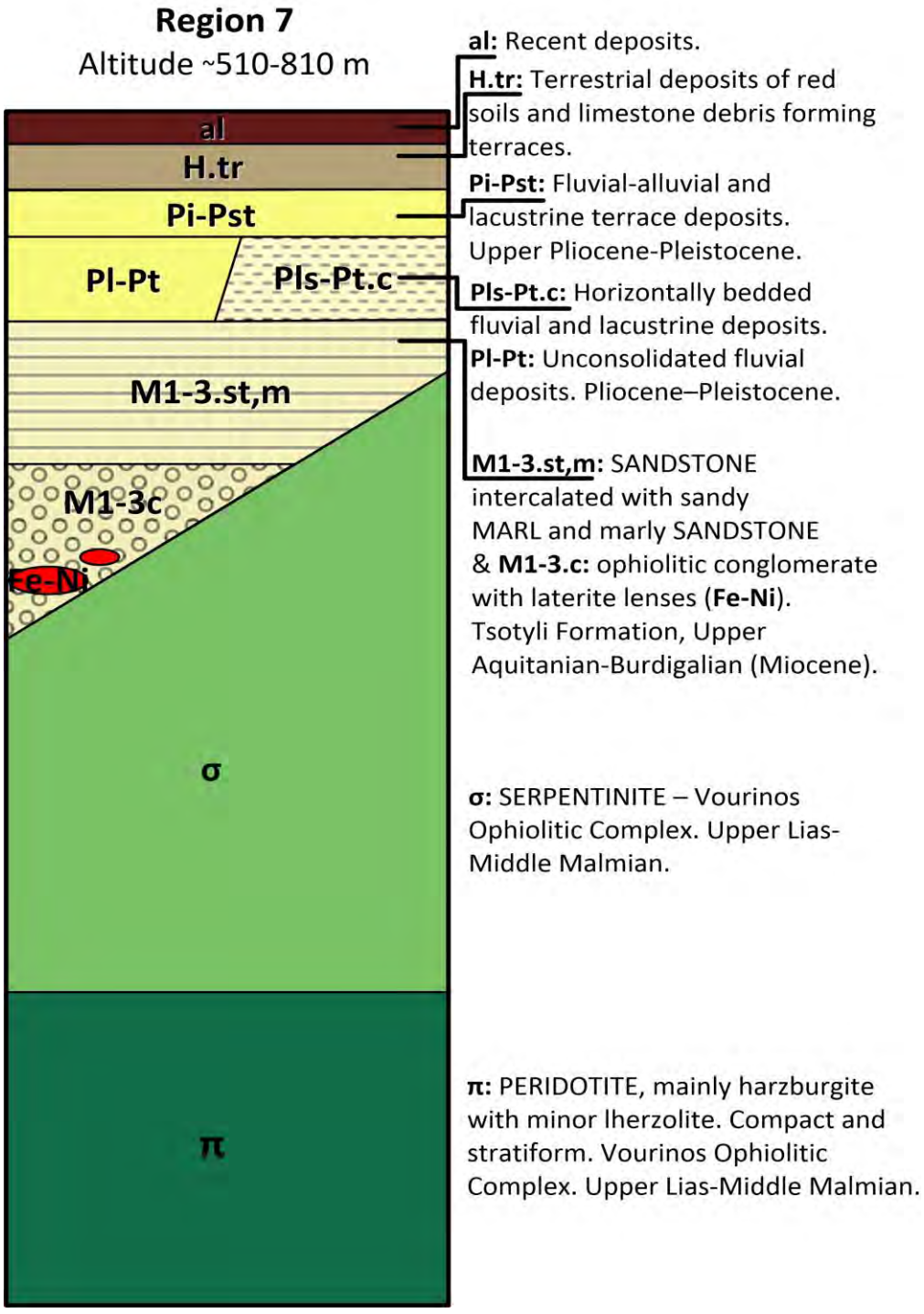

Figure 5.9: Synthetic stratigraphic column of Region 7 showing the near-surface geological succession observed in this area.

The PilotSTRATEGY project has received funding from the European Union's Horizon 2020 research and innovation programme under grant agreement No. 101022664

Altogether, the sequences in Regions 1 to 7 record the transition from early molasse deposition into thick Miocene fan systems, and finally into Quaternary reworking of the landscape. The recurring alternation of coarse and fine facies points to fluctuating sediment supply and hydrodynamic conditions. The presence of synsedimentary deformation structures, variable cementation, and local exposure of basement highlights the combined role of tectonics and sedimentary processes in shaping the basin fill.

In summary, the regional lithostratigraphic observations outline the progressive infill of the MHT, from the basal molasse deposits of the Krania and Kipourio successions, through the coarse conglomeratic bodies of the Pentalofos, and into the fine marl–sand alternations of the Tsotyli Fm. Across all regions, sandstones and conglomerates provide potential reservoirs, while marls and marly limestones form laterally continuous and regionally significant seals. Conglomeratic and ophiolitic domains add heterogeneity, with faults and joints acting as both risks and compartmentalising features. This region-by-region analysis, combined with the basin-wide synthesis, demonstrates that the MHT contains repeated reservoir–seal pairs, making it a suitable candidate for CO_2 storage evaluation.

5.4. Structural Geology Observations and kinematic analysis

The structural architecture of the southern MHT records the multiphase tectonic evolution of the Internal Hellenides. More than 2,600 structural measurements collected during the 2021–2025 campaigns, combined with detailed discontinuity surveys, confirm the coexistence of basin-wide trends and localised structural anomalies that directly influence reservoir–seal behaviour.

At the basin scale, bedding attitudes show a dominant northeastward dip, consistent with the asymmetric geometry of the trough. Average dips are gentle to moderate (15–35°), but local zones exhibit steep to vertical bedding, particularly near major fault systems. Faults are abundant and fall into three main orientation families: NW–SE trending steep planes compatible with dextral strike-slip kinematics, NE–SW trending steep planes associated with sinistral strike-slip kinematics, and ENE–WSW to E–W lower-angle faults corresponding to normal faulting. Joints are pervasive across all lithologies, forming steep conjugate sets with modal orientations toward the WNW, SSE and SSW; more than half of all joints dip steeper than 70°. Discontinuity characteristics show a marked contrast between bedding planes, which are generally tight and laterally limited (especially in marls), and joints/faults, which are more persistent and often open. This distinction is fundamental for evaluating reservoir compartmentalisation and seal integrity.

Although these structural patterns are consistent across the basin, field surveys revealed specific features of regional significance for CO_2 storage. In Regions 1 and 2, the molasse successions show consistent NE dips with limited deformation, while marl-rich intervals display tight intercalations, reinforcing their role as effective sealing horizons. In Regions 3 and 5, conglomeratic successions are widely exposed; their highly variable clast composition and discontinuous fracture networks suggest heterogeneous hydraulic behaviour, favouring lateral migration rather than vertical sealing. In Region 4, turbiditic sandstones and marls exhibit moderate dips and regular bedding, providing representative reservoir–seal pairs.

The most critical structural anomalies are observed in Regions 6 and 7, particularly along the Felli fault zone, where strata are rotated to near-vertical dips. Here, fault reactivation has strongly disrupted bedding continuity, generating potential leakage pathways. At the same time, these structures compartmentalise reservoirs into discrete fault-bounded blocks, which may trap CO_2 locally. Adjacent

The PilotSTRATEGY project has received funding from the European Union's Horizon 2020 research and innovation programme under grant agreement No. 101022664

ophiolitic rocks (serpentinites, harzburgites) are mechanically competent but pervasively jointed, acting more as compartmentalising boundaries than as reservoir or seal units.

In the Kivotos area, limestones and conglomerates are strongly tilted by faulting, producing bedding anomalies that highlight the intensity of late-stage deformation. These exposures provide a valuable analogue for understanding how reservoir–seal pairs respond to tectonic reactivation, especially under stress conditions similar to those expected during long-term CO_2 injection and storage.

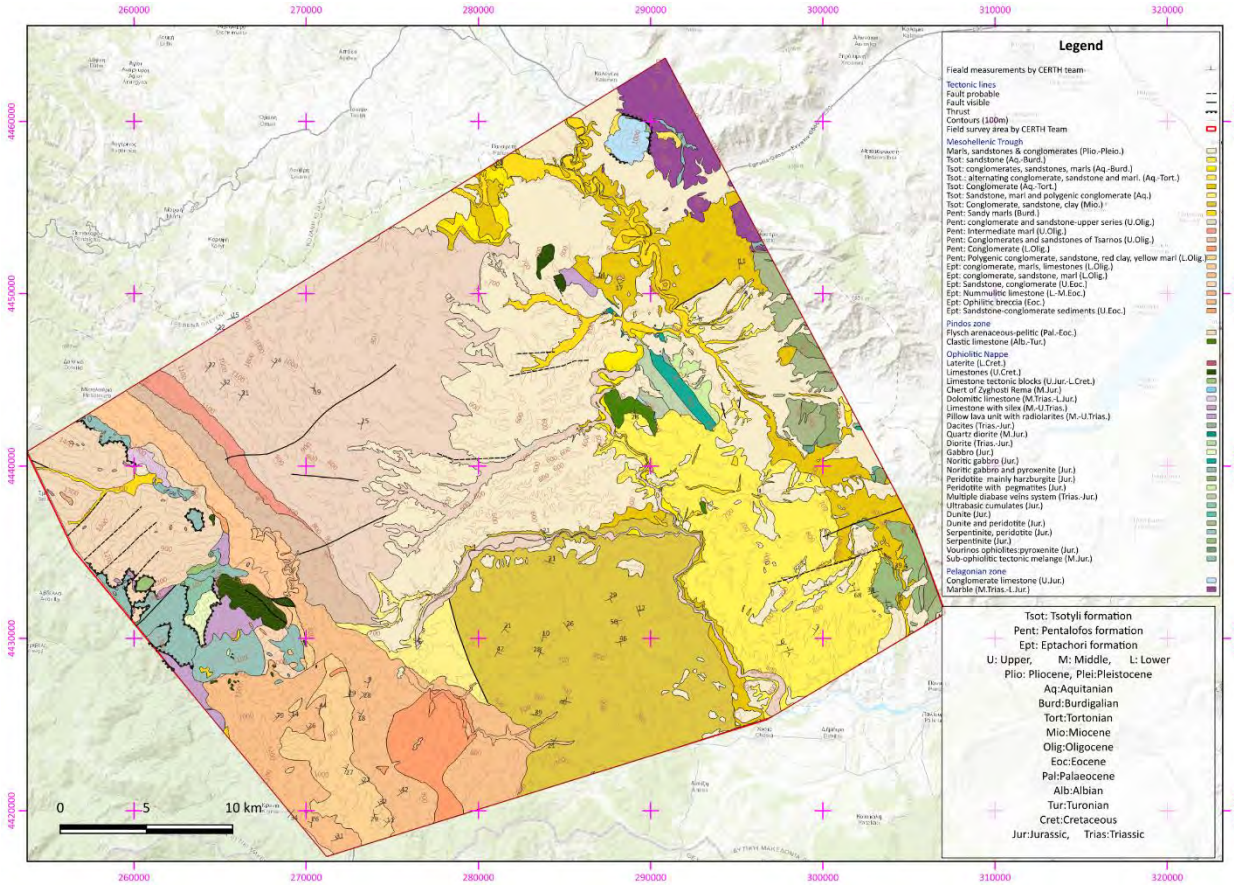

Figure 5.10: Geological map at 1:25,000 scale in the EGSA87 reference system showing the surveyed location. All the Holocene sediments have been removed. Regions 1 to 9 are outlined in red.

In summary, the structural dataset confirms that the MHT evolved through successive phases of compression, transpression, and extension, with post-orogenic exhumation producing steep unloading joints. The result is a structural mosaic where sandstones and conglomerates provide reservoir capacity, marls and marly limestones form laterally continuous seals, and faults and joints act as both potential migration pathways and compartment boundaries. For CO_2 storage assessment, particular attention must be given to zones of steep bedding and fault reactivation (notably at Felli and Kivotos), which represent the most critical structural risks to storage security.

The kinematic framework of the MHT has been evaluated through stereonet analysis of bedding, joint and fault measurements collected during the discontinuity surveys and field campaigns. All data were plotted

The PilotSTRATEGY project has received funding from the European Union's Horizon 2020 research and innovation programme under grant agreement No. 101022664

on Schmidt nets using Stereonet11 software [115, 116] which enabled the identification of principal structural sets and the reconstruction of the stress field responsible for their development.

Field campaigns across MHT Figure 5.10, together with additional data from Kivotos, provide a consistent picture of basin-wide tilting, strike-slip and normal faulting, and the development of joint networks that collectively determine reservoir connectivity and seal integrity relevant to CO_2 storage.

Bedding represents the dominant and most regionally continuous structural element. Measurements across sandstone–marl alternations in the area of the Krania, Kipourio and Basal formations consistently show gentle to moderate dips toward the northeast, with persistence frequently exceeding 20 meters. In Region 1 (Figure 5.11), bedding is the prevailing discontinuity, with only minor jointing observed, while soft-sediment deformation features, including slumps and boudinage structures, indicate syn-depositional instability later overprinted by brittle structures.

Figure 5.11: Explanatory field photograph at survey site 1_1. The bedding (red dashed lines) of the SANDSTONE and the MARL are highlighted. The average dip/dip direction structural data are also given. Coordinates (WGS84): N39.962814°, E21.349146°; Date of picture taken: 29.09.2024; Orientation: 58.86°.

Region 2 confirms this pattern, with additional evidence of widely spaced joints and occasional steep faults, such as site 2_1 (Figure 5.12) where sandstone and marl sequences are crosscut by a near-vertical

The PilotSTRATEGY project has received funding from the European Union's Horizon 2020 research and innovation programme under grant agreement No. 101022664

fault accompanied by three joint sets. These faults show calcite and clay infill, implying partial sealing and limited compartmentalisation of the rock mass.

Figure 5.12: Explanatory field photograph at survey site 2_1. The bedding (red dashed lines) of the SANDSTONE and the MARL are highlighted. The average dip/dip direction structural data are also given. Coordinates (WGS84): N39.91618667°, E21.35142667°; Date of picture taken: 03.11.2024; Orientation: 342.92°.

The stereonet from survey site 2_1 (Region 2) (Figure 5.13) illustrates the structural relationships between bedding, faults, and joint systems in the Pentalofos Fm. Bedding poles form a tight cluster dipping gently to the northeast (average orientation 22°/066°), confirming the regional tilting of strata toward the basin axis. Fault planes (five measurements) define a steep set striking NW–SE and dipping predominantly southwestward, compatible with dextral strike-slip kinematics under a NE–SW compressional regime. Three joint families are also identified: Joint set 29 dips steeply northeast, Joint set 30 dips steeply southwest, and Joint set 31 dips subhorizontal to gently southward. These steeply dipping conjugate joint sets cut across bedding, recording brittle deformation consistent with strike-slip tectonics. The stereonet documents a structural framework dominated by gently dipping bedding overlain by steep conjugate fault–joint systems, highlighting the overprint of transpressional stresses on an otherwise orderly basin stratigraphy.

The PilotSTRATEGY project has received funding from the European Union's Horizon 2020 research and innovation programme under grant agreement No. 101022664

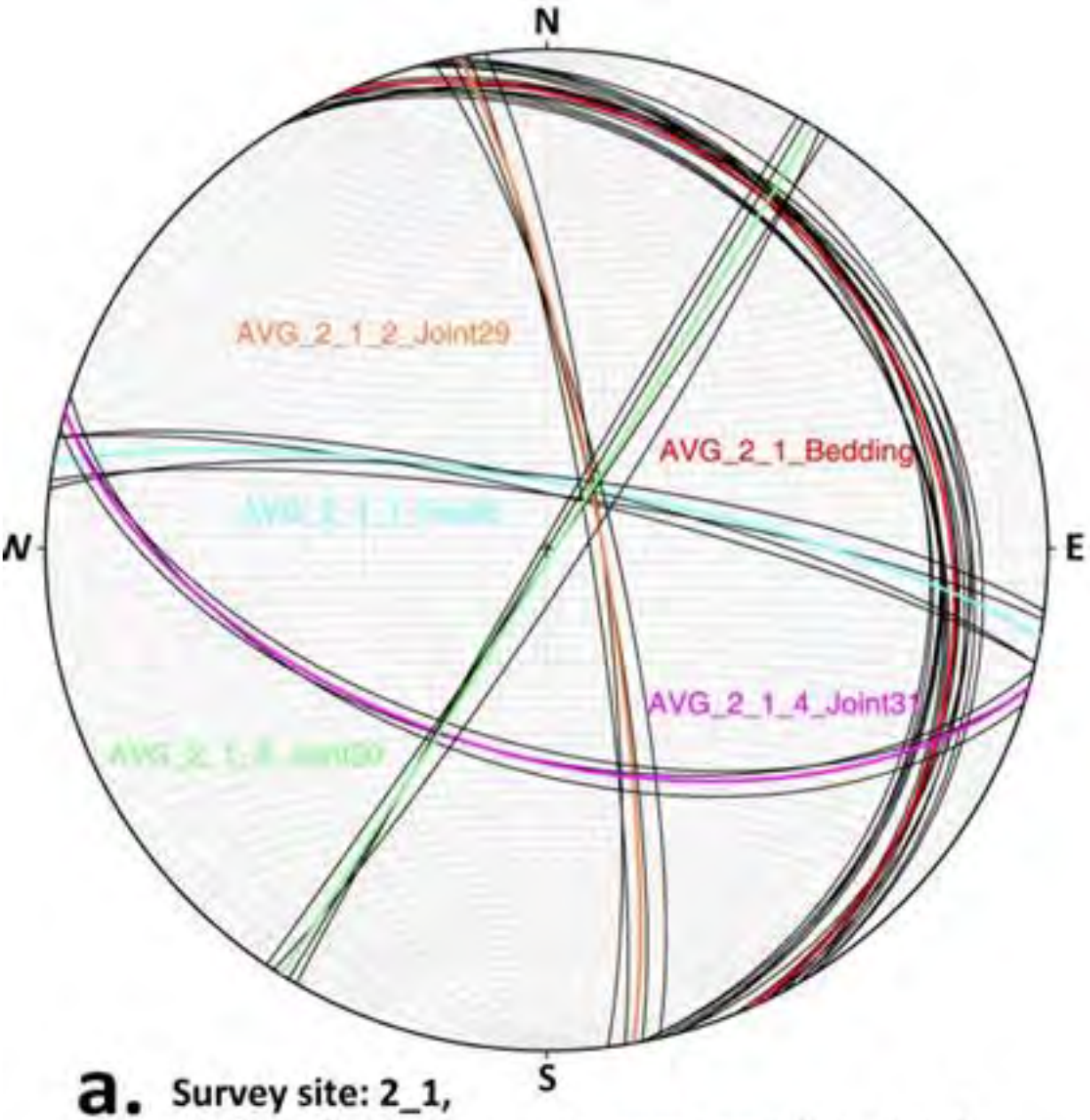

a. **Survey site: 2_1,**
Number of measurments, **bedding: 20, fault5: 5, joint29: 5, joint30: 5, joint31: 5.**

Figure 5.13: Structure attitude data for survey site 2_1 are plotted on Schmidt nets produced with the Stereonet11 software[115, 116]. Measurements refer dip/dip direction data for bedding, joint, and fault. Coordinates (WGS84) for site survey 2_1: N39.91618667°, E21.35142667°.

The PilotSTRATEGY project has received funding from the European Union's Horizon 2020 research and innovation programme under grant agreement No. 101022664

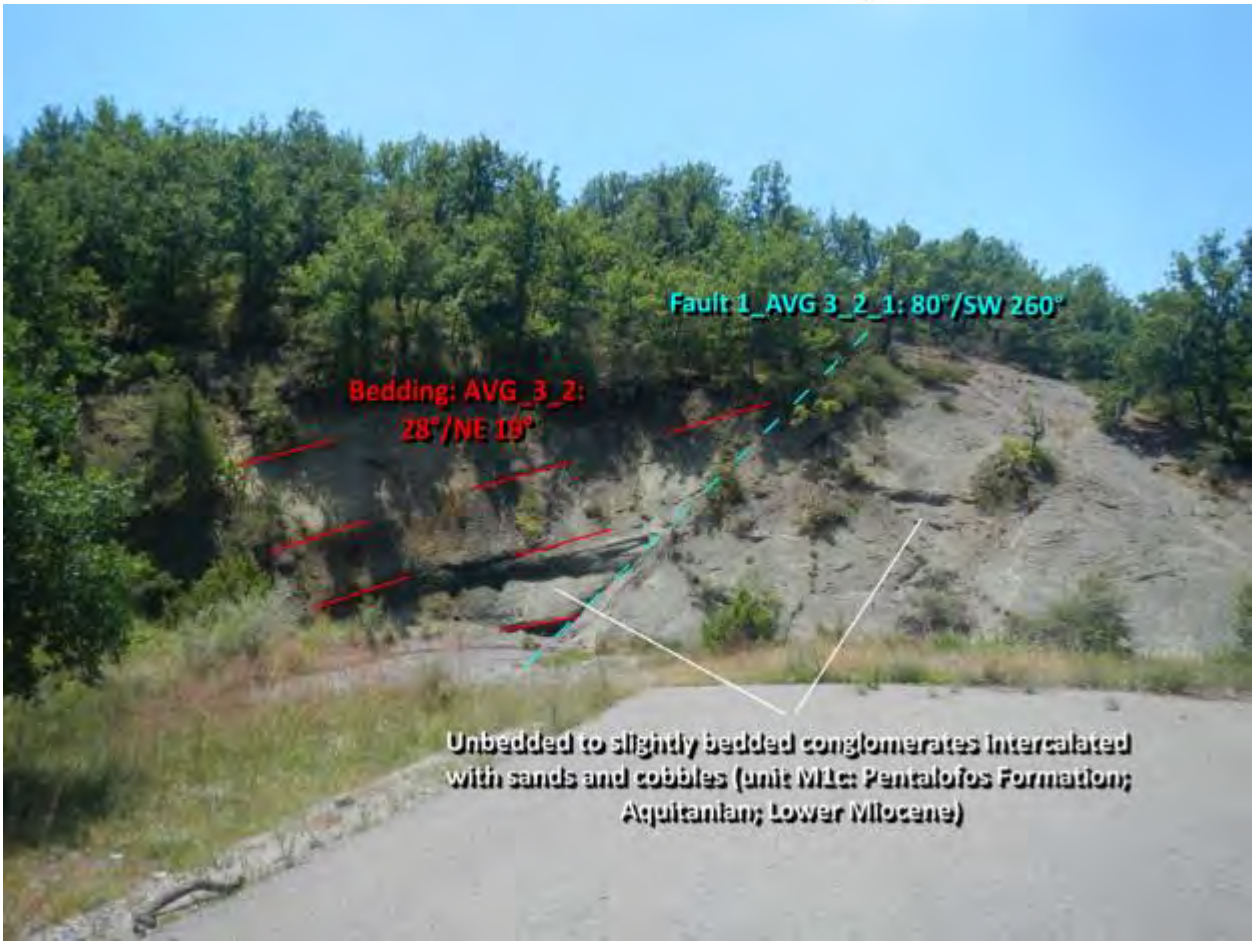

Figure 5.14: Explanatory field photograph at survey site 3_2. Outcrops of unbedded to slightly bedded conglomerates are shown and the bedding is highlighted (red dashed lines), as well as a fault (cyan dashed line) that cuts through the conglomerates. The average dip/dip direction structural data are also given. Coordinates (WGS84): N39.98797100°, E21.46691000°; Date of picture taken: 19.06.2024; Orientation: 199.30°.

Progressing upward into the Aquitanian Pentalofos Fm, Regions 3, 4 and 5 present a structural fabric dominated by conglomerates and conglomeratic sandstones. Bedding remains the primary control, but its role shifts due to the coarser lithologies. In Region 3, bedding dips are low to moderate, generally to the northeast, with faults documented in conglomeratic units such as at site 3_2 (Figure 5.14).

The stereonet from survey site 3_2 (Figure 5.15) displays the relationship between bedding and fault planes in conglomeratic facies of the Pentalofos Fm. Bedding poles form a consistent cluster dipping gently to the northeast (average orientation 26°/030°), confirming the regional tilting of the molasse succession. In contrast, the fault dataset (ten measurements) defines a steep southwest-dipping set striking NW–SE. This orientation is compatible with reactivated strike-slip kinematics under NE–SW compression, with later normal faulting components possible. The clear separation between the gentle bedding cluster and the steeply dipping fault plane demonstrates the superposition of brittle deformation on an otherwise orderly stratigraphy.

The PilotSTRATEGY project has received funding from the European Union's Horizon 2020 research and innovation programme under grant agreement No. 101022664

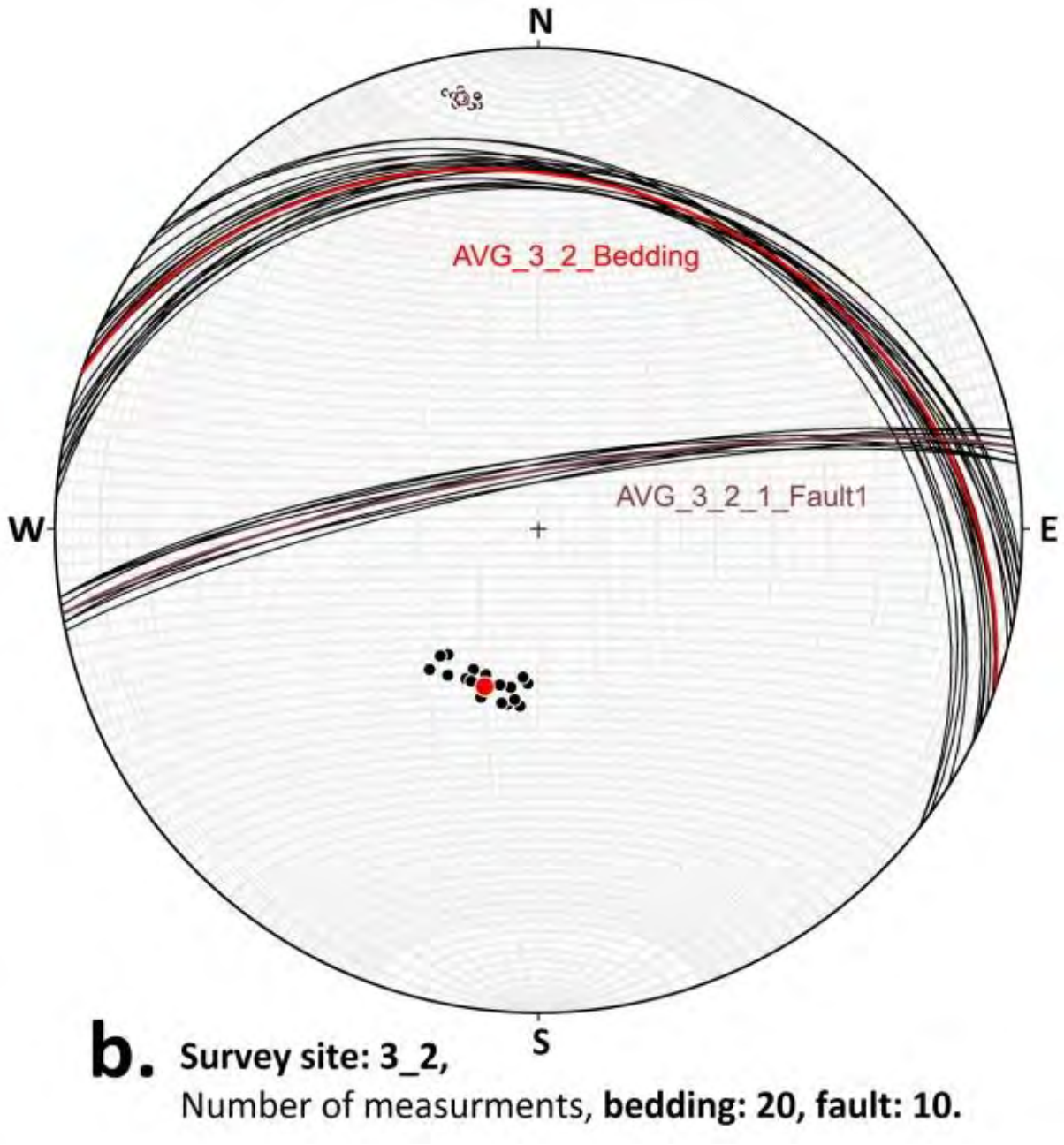

Figure 5.15: Structure attitude data for survey site 3_2 is plotted on Schmidt nets produced with the Stereonet11 software[115, 116]. Measurements refer dip/dip direction data for bedding and fault. Coordinates (WGS84) for site survey 3_2: N39.98797100°, E21.46691000°.

Field observations at this site noted clay-rich infill along fault planes, with localised seepage on conglomeratic surfaces, suggesting that while faults may act as potential vertical pathways for fluid migration, their partial mineralisation could reduce permeability and contribute to self-sealing. This fault showed clay-rich infill and minor seepage, highlighting the dual behaviour of faults as both transmissive

The PilotSTRATEGY project has received funding from the European Union's Horizon 2020 research and innovation programme under grant agreement No. 101022664

and sealing features. Jointing is present but often discontinuous. Region 4 represents a conglomerate-dominated end-member, where very thick beds with high persistence are present, and joints are limited to isolated sites such as 4_4 (Figure 5.16).

The stereonet from site 4_4 (Figure 5.17) illustrates the relationship between bedding and jointing within coarse conglomeratic deposits of the Pentalofos Fm. Bedding measurements (ten poles) define a moderately dipping set toward the northeast (average orientation 28°/045°), consistent with the general basin tilt documented elsewhere. A single dominant joint set (ten measurements) is also recorded, striking approximately N–S and dipping steeply to the west. The steep orientation of this joint set, combined with the limited number of families, indicates a relatively simple fracture framework compared with other conglomeratic sites where multiple sets occur. Importantly, field descriptions noted that bedding discontinuities at this site are very tight, with apertures below 0.1 mm, and that joints are laterally limited. This suggests a structurally stable block in which bedding continuity is preserved and fractures do not significantly compromise reservoir–seal behaviour.

Figure 5.16: Explanatory field photograph at survey site 4_4. Layers of cemented CONGLOMERATES exposed to erosion form a characteristic texture of accumulated COBBLES. Red dashed lines highlight bedding. the average dip/dip direction structural data are also given. Coordinates (WGS84): N39.96095667°, E21.48384667°; Date of picture taken: 22.08.2024; Orientation: 152.03°.

The PilotSTRATEGY project has received funding from the European Union's Horizon 2020 research and innovation programme under grant agreement No. 101022664

In the same location, surface exposed bedding discontinuities are very tight, with apertures below 0.1 mm, indicating low transmissivity and the potential for sealing capacity even in coarse clastic rocks. Region 5 extends this framework but also incorporates younger Pliocene–Pleistocene terrace deposits that mark neotectonic uplift and incision, demonstrating that recent vertical movements have reactivated older structural trends and influenced basin geomorphology (Figure 5.18).

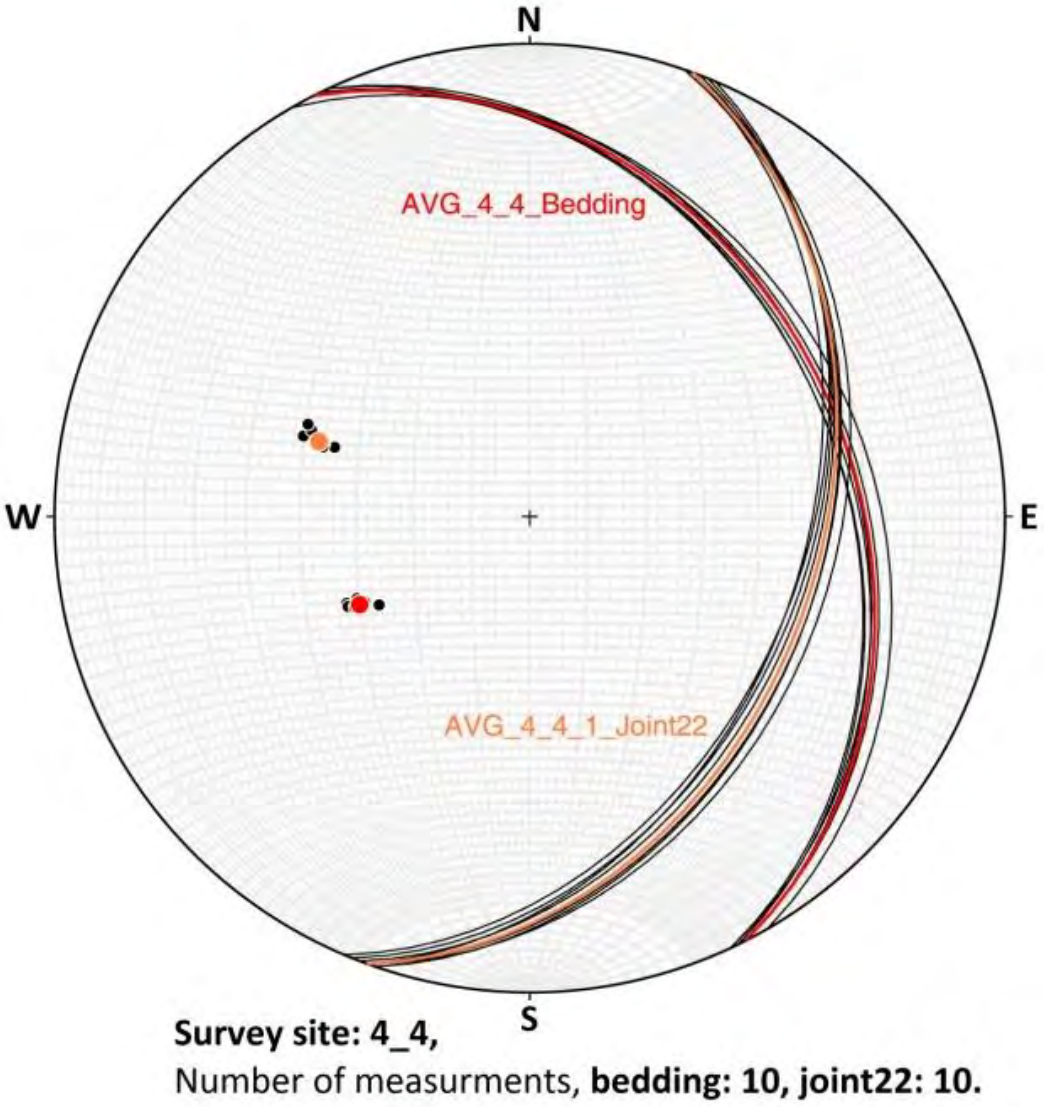

Figure 5.17: Structure attitude data for survey site 4_4 is plotted on Schmidt nets produced with the Stereonet11 software[115, 116]. Measurements refer dip/dip direction data for bedding and joint. Coordinates (WGS84) for site survey 4_4: N39.96095667°, E21.48384667°.

The PilotSTRATEGY project has received funding from the European Union's Horizon 2020 research and innovation programme under grant agreement No. 101022664

Figure 5.18: A panoramic photograph of survey sites 5_1, 5_1a and 5_1b from survey site 5_1c. Slightly bedded to unbedded conglomerates of the Pentalofos Formation, Mesohellenic Trough (Aquitanian; Lower Miocene) are found in contact with fluvial deposits of unconsolidated conglomerates, clays sands and loose sandstones of Pliocene to Pleistocene age. Coordinates (WGS84): N40.04928997°, E21.47977000°; Date of picture taken: 29.05.2024; Orientation: 0.00°.

The transition into the Miocene Tsotyli Fm, observed in Regions 6 and 9, introduces thinner-bedded sandstone–marl alternations, with consistently gentle dips and high bedding persistence. In Region 6, sandstone–marl alternations at sites such as 6_1 (Figure 5.19) and 6_2 (Figure 5.20) are fragmented by joint sets, but these remain subordinate to bedding and show evidence of steep dips typical of strike-slip related fractures.

The PilotSTRATEGY project has received funding from the European Union's Horizon 2020 research and innovation programme under grant agreement No. 101022664

Figure 5.19: Explanatory field photograph at survey site 6_1 showing sandstone bedding and the joint system 19. The average dip/dip direction structural data are also given. Coordinates (WGS84): N40.026338°, E21.659783°; Date of picture taken: 10.04.2024; Orientation: 10.32°.

The stereonets from Region 6 illustrate the structural character of the Tsotyli Formation, which is dominated by marl–sandstone alternations. At site 6_1 (Figure 5.21), bedding measurements (ten poles) define a gentle dip toward the northeast (average orientation 15°/040°), in line with the regional basin tilt. A single joint set (ten measurements) is also identified, dipping steeply to the southwest at approximately 69°. The combination of gently dipping bedding and a single steep joint set highlights the relative structural simplicity of this site compared to more fractured conglomeratic domains. Bedding continuity remains high, with lateral persistence across exposures, ensuring that marl-rich layers act as effective seals. The steep joint set represents a potential vertical pathway, but its limited lateral extent reduces the risk of compromising overall sealing integrity.

The PilotSTRATEGY project has received funding from the European Union's Horizon 2020 research and innovation programme under grant agreement No. 101022664

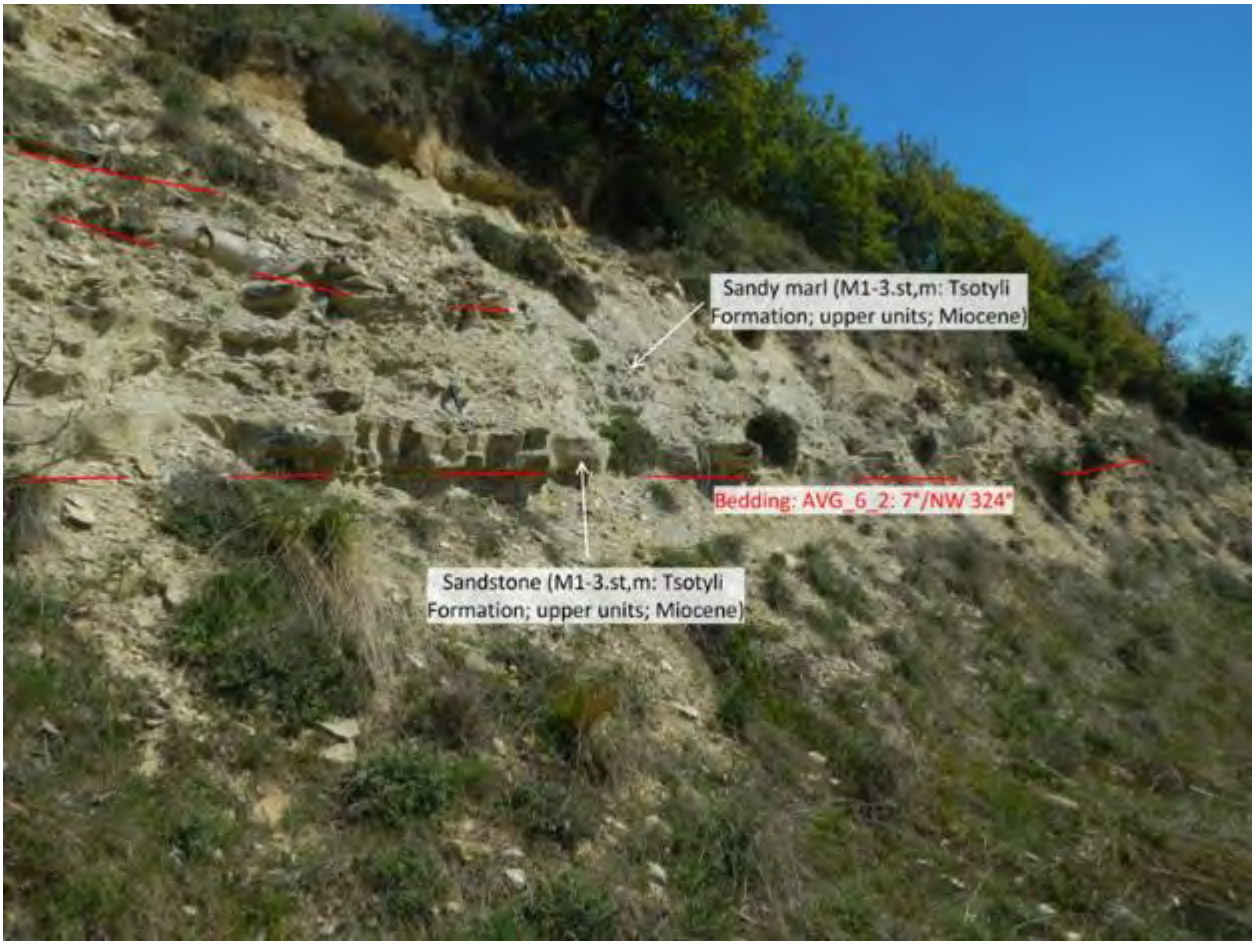

Figure 5.20: Explanatory field photograph at survey site 6_2 showing sandstone bedding and the average dip/dip direction structural data. Coordinates (WGS84): N40.003031°, E21.654256°; Date of picture taken: 10.04.2024; Orientation: 105.53°.

At site 6_2 (Figure 5.21), bedding poles (twenty measurements) form a tight cluster dipping very gently to the northeast (average orientation 10°/032°). Persistent jointing was not recorded at this site, reinforcing the dominance of bedding as the controlling structural feature. Such gentle, laterally continuous bedding planes in marl–sandstone alternations provide highly favourable conditions for caprock integrity and reservoir–seal coupling.

The PilotSTRATEGY project has received funding from the European Union's Horizon 2020 research and innovation programme under grant agreement No. 101022664

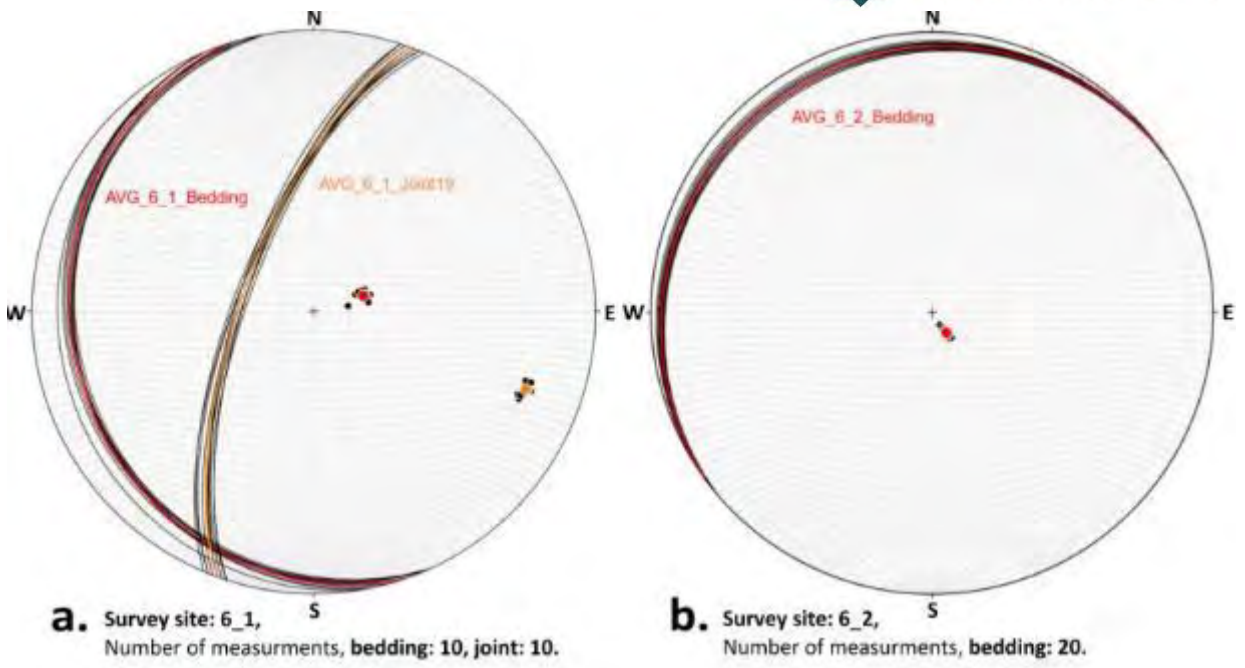

Figure 5.21: Structure attitude data for survey sites 6_1 and 6_2, are plotted on Schmidt nets produced with the Stereonet11 software[115, 116]. Measurements refer dip/dip direction data for bedding and joint. Coordinates (WGS84) for site survey 6_1 (N40.026338°, E21.659783°) and for 6_2 (N40.003031°, E21.654256°).

Region 9 (Figure 5.22) further confirms the regularity of this fabric, with numerous sandstone–marl successions of the Tsotyli and Pentalofos formations showing gently northeastward dipping bedding. However, within the same region, conglomerates and ophiolitic detritus display increased fracturing, and several steep joint sets were documented in serpentinites and peridotites of the Vourinos ophiolitic complex. These lithologies lack bedding as a structural control and instead are entirely dominated by joint networks, forming brittle frameworks that act more as compartmentalising boundaries than as reservoir or seal units (Figure 5.23).

The PilotSTRATEGY project has received funding from the European Union's Horizon 2020 research and innovation programme under grant agreement No. 101022664

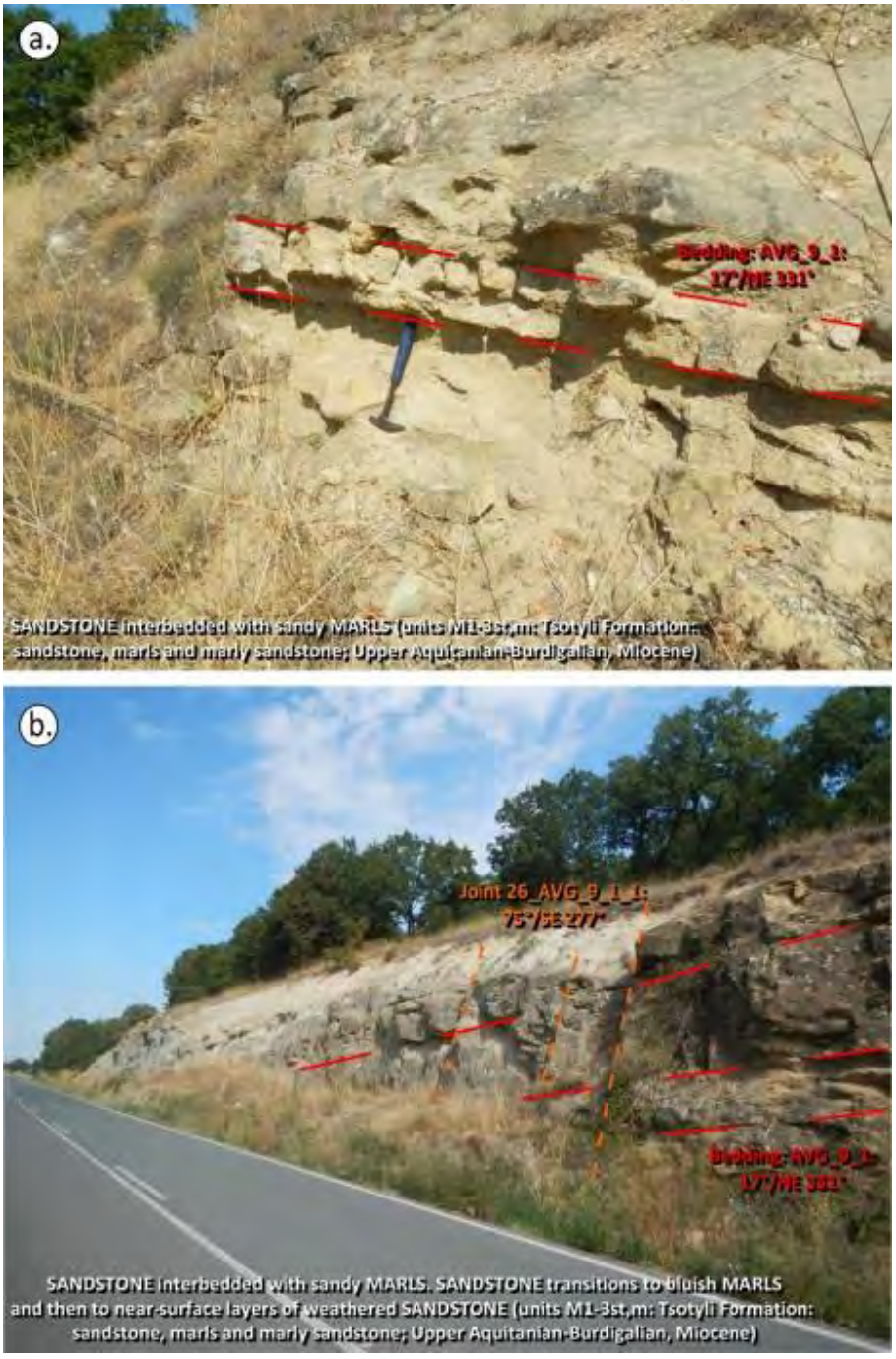

Figure 5.22: Explanatory field photographs at survey site 9_1. a. The bedding (red dashed lines) of the SANDSTONE interbedded with sandy MARLS is highlighted, Coordinates (WGS84): N40.18113333°, E21.51481500°; Date of picture taken: 07.09.2024; Orientation: 320.17°, b. The set of joints (Joint 26) fragmenting the sandstone beds are highlighted by orange dashed lines. The average dip/dip direction structural data for bedding and joints are also given. Coordinates (WGS84): N40.18170833°, E21.51289500°; Date of picture taken: 07.09.2024; Orientation: 330.21°.

The PilotSTRATEGY project has received funding from the European Union's Horizon 2020 research and innovation programme under grant agreement No. 101022664

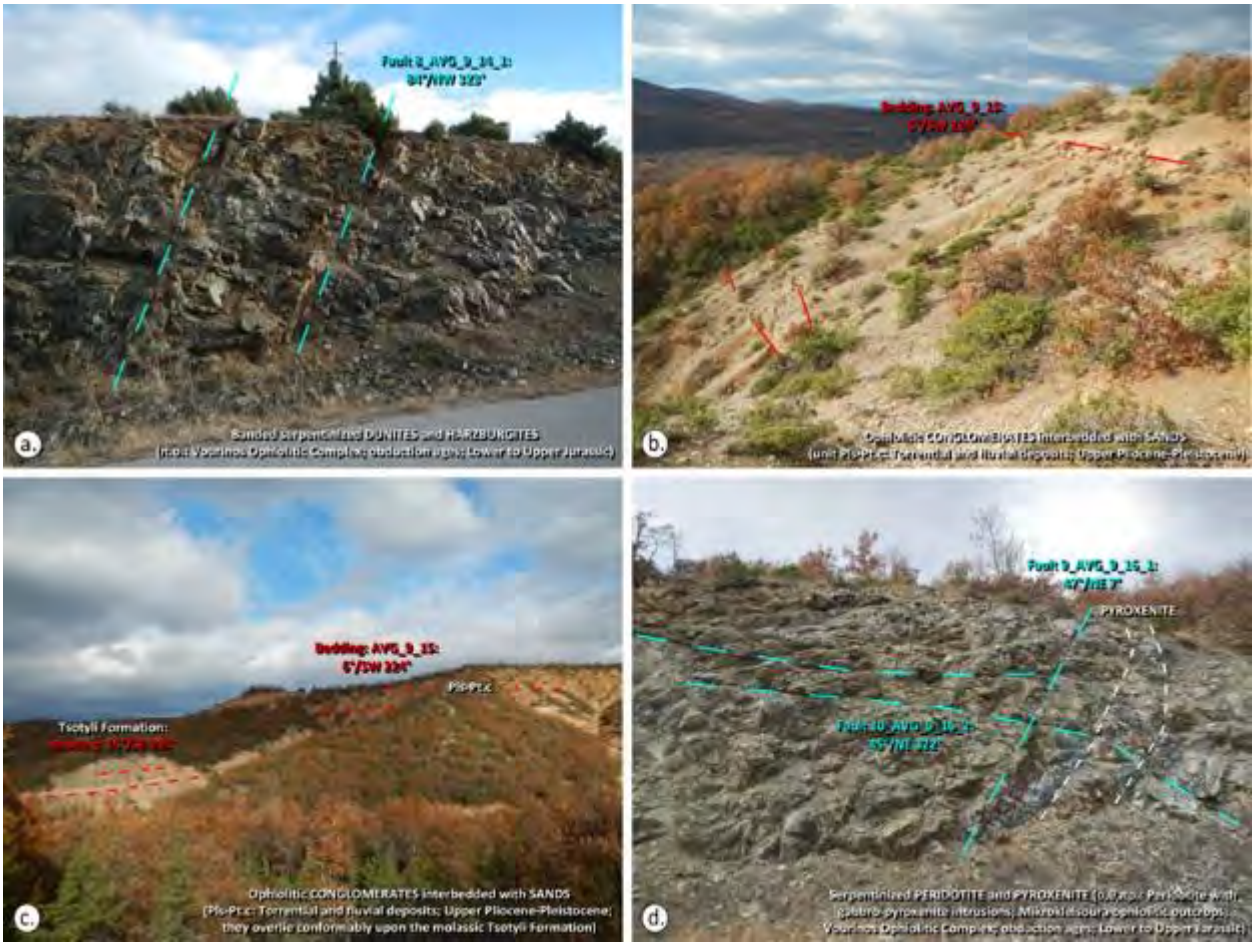

Figure 5.23: Explanatory field photographs at survey sites 9_14 to 9_16. a. Banded serpentinized DUNITE and HARZBURGITE and some minor faults (Fault 8) at survey site 9_14, b. Ophiolitic CONGLOMERATE interbedded with SAND at survey site 9_15, c. An overview at survey site 9_15 showing the contact between the molassic sediments of the Tsotyli Formation and the ophiolitic CONGLOMERATEES interbedded with SANDS which are part of the Pliocene-Pleistocene torrential and fluvial deposits, d. Serpentinized peridotite and pyroxenite cut by faults (Fault 9 & Fault 10) at survey site 9_16. Red dashed lines highlight bedding, and cyan dashed lines the faults. The average dip/dip direction structural data are also given. a. Coordinates (WGS84): N40.16018167°, E21.62336000°; Date of picture taken: 22.11.2024; Orientation: 72.33°, b. Coordinates (WGS84): N40.16453500°, E21.56930667°; Date of picture taken: 22.11.2024; Orientation: 200.94°, c. Coordinates (WGS84): N40.16462000°, E21.56935833°; Date of picture taken: 22.11.2024; Orientation: 14.54°, d. Coordinates (WGS84): N40.15390833°, E21.55621167°; Date of picture taken: 22.11.2024; Orientation: 14.51°.

Region 7, dominated by ophiolitic basement rocks, illustrates this point most strongly. Here, serpentinite and peridotite are dissected by three main SW-dipping joint sets, with high persistence and steep dips exceeding 70°(Figure 5.24). These joint-controlled fabrics contrast sharply with the sedimentary basin fill, highlighting the mechanical boundary conditions at the basin margins. The nearby Kivotos locality, represented by bedded limestones, shows that marginal carbonate units are also tilted and affected by faulting, offering an analogue for how tectonic reactivation influences reservoir–seal systems at depth.

The PilotSTRATEGY project has received funding from the European Union's Horizon 2020 research and innovation programme under grant agreement No. 101022664

Figure 5.24: Explanatory field photograph at survey site 7_1 showing joint system 1 fracturing the ophiolitic rocks. The average dip/dip direction structural data are also given.

Across all regions, faults fall into three dominant families. NW–SE steeply dipping planes are compatible with dextral strike-slip motion, NE–SW steep faults with sinistral kinematics, and ENE–WSW to E–W faults with normal displacement related to Miocene extension. Evidence from Region 2, with steep faults cutting molasse sandstones, and Region 3, where faults cut conglomerates, confirms the reactivation of these systems. Infill observations, including clay, calcite and locally oxidised surfaces, suggest variable transmissivity: some faults remain transmissive and seepage-prone, while others are effectively sealed. The widespread occurrence of steep conjugate joint sets across sandstones and conglomerates further reflects a brittle overprint related to strike-slip regimes, with post-Miocene exhumation introducing unloading joints, oxidation bands and weathering surfaces, as noted in conglomeratic outcrops.

The combined kinematic evidence supports a three-phase tectonic evolution of the MHT. During the Late Eocene to Oligocene, compression and transpression generated the northeastward tilting of strata, the development of asymmetric folds, and early strike-slip faults. In the Miocene, a shift to extensional tectonics reactivated parts of the strike-slip system with normal components, producing low-angle faults

The PilotSTRATEGY project has received funding from the European Union's Horizon 2020 research and innovation programme under grant agreement No. 101022664

and localised rotations of strata along basin margins. Post-Miocene exhumation and erosion resulted in the formation of steep unloading joints, surficial oxidation and Liesegang banding. These successive overprints explain the coexistence of regionally consistent bedding attitudes with localised structural anomalies, particularly along major fault zones such as the Felli fault.

For CO_2 storage, the implications of this kinematic framework are clear. Regionally continuous, tight bedding in marl-rich units such as the Krania and Tsotyli formations provides effective seals at basin scale, while the sandstones and conglomerates of the Kipourio and Pentalofos formations provide suitable reservoirs. However, steeply dipping faults and pervasive joint networks pose potential leakage risks, particularly where clay-free and open. Where these features are mineralised or clay-filled, they may instead function as barriers or self-sealing structures. Fault-bounded compartments offer opportunities for localised trapping, but their behaviour must be carefully constrained through detailed fault-seal analysis. The ophiolitic margins, while not suitable for storage, exert a mechanical control on basin deformation and influence the geometry of reservoir–seal pairs.

Overall, the kinematic dataset shows that the MHT is structurally complex but predictable, with repeated tectonic phases creating a structural mosaic of compartments, seals, and potential migration pathways. Effective CO_2 storage will depend on targeting areas where marl seals are intact, bedding dips are gentle, and faults and joints show evidence of sealing infills, while avoiding domains of steep fault reactivation and pervasively jointed ophiolitic rocks.

5.4.1. Sampling strategy & execution

The designated study area was systematically subdivided into nine sections to enable targeted sampling and precise acquisition of strike and dip measurements, with the overarching objective of identifying potential reservoir and cap rock formations suitable for CO_2 storage. This subdivision facilitated a detailed and methodical approach to fieldwork, ensuring that each sector was thoroughly examined for structural features relevant to reservoir integrity and sealing capacity. The additional structural measurements obtained within these subareas significantly improved the understanding of the spatial distribution and orientation of geological discontinuities, thereby strengthening the reliability of interpretations concerning storage security.

Structural measurements were acquired using a Brunton geological compass, while rock samples were collected following standard procedures as outlined in BS 5930:2015+A1:2020. Photographic documentation was carried out with a Nikon COOLPIX AW100 camera equipped with a GPS system, and georeferencing was performed using a Garmin Oregon 450 handheld GPS unit operating in WGS84. Lithological descriptions adhere to the criteria of “Geotechnical investigation and testing – Identification, description and classification of rock (ISO 14689:2017)”. A total of 117 samples were collected, with priority given to fresh, unweathered outcrops to ensure representative material for laboratory analysis. Where exposures were limited, as in the ophiolitic survey sites 7_1–3, 7_6, and 7_7, representative samples were obtained from adjacent survey areas. In all cases, the structural context of the samples, including bedding, jointing, and contacts, was carefully documented to allow integration of petrophysical results with the basin-scale structural framework.

This sampling strategy has generated a comprehensive dataset spanning both reservoirand seallithologies across the MHT. The inclusion of ultramafic and ophiolitic rocks provides insights into deformation fabrics

The PilotSTRATEGY project has received funding from the European Union’s Horizon 2020 research and innovation programme under grant agreement No. 101022664

and weathering processes that may affect reservoir connectivity. The samples collected underwent petrographic, geochemical, and petrophysical analyses, forming the basis for evaluating the storage potential of reservoir units and the sealing efficiency of cap rocks within the investigated formations.

All samples collected during the surveys have been registered in the System for Earth and Extraterrestrial Sample Registration (SESAR2). Each entry was given an International Geo Sample Number (IGSN), which provides a permanent identifier that ties the sample in the field to every laboratory analysis that follows. This way, petrophysical, geochemical, mineralogical, and imaging results can always be traced back to the original material. The dataset now includes 120 rock samples from Regions 1 to 9, together with 38 water samples from the areas of Grevena and Florina.

The registration of the material in SESAR2 guarantees that the data will remain accessible and reusable in the future. Alongside this, the project has committed to open science by making results available through Open Research Europe and depositing supporting datasets in Zenodo, where they are assigned permanent DOIs. Taken together, these steps make the MHT dataset both durable and open. The data can be checked, repeated, and built upon, offering a resource that goes beyond the scope of this report and will remain useful for future geological and geo-energy studies.

5.5. Rock water absorption investigation

The amount of water absorbed by a rock is directly related to its porosity, particularly its effective porosity. This refers to the interconnected pore spaces within the rock that can hold and transmit water, as opposed to total porosity, which includes all pores regardless of their connectivity. It is important to note that without vacuum saturation, the experimental method only measures a proportion of the effective porosity, as the results are influenced by factors such as pore throat size and trapped air.

In rocks, porosity can be classified broadly into two main types: a) Primary Porosity: This is the original porosity formed during the deposition of the rock. For instance, sedimentary rocks like sandstone have primary porosity from the spaces between grains, and b) Secondary Porosity: This arises after the rock has formed, often due to processes like fracturing, dissolution, or weathering, which create additional space in the rock matrix.

The capacity of a rock to absorb water under non-vacuum conditions reflects a proportion of its effective porosity. This is because factors like pore throat size can inhibit complete saturation, preventing water from entering every interconnected pore space. This measured proportion, however, is still a useful indicator in applications like hydrogeology, oil and gas exploration, and carbon capture and storage (CCS), where effective porosity determines the volume of fluids a rock can transmit and retain. The following stages were completed during each run of the experiment:

- Evaporation of water at room conditions (25 °C) after 24 hours was monitored – 975 ml of water remaining, 25 ml evaporated, corresponding to 60% room humidity.
- Samples were tested for effervescence using 10% HCl.
- Samples were photographed before testing.
- Samples were weighed before being dried in the oven.

The PilotSTRATEGY project has received funding from the European Union's Horizon 2020 research and innovation programme under grant agreement No. 101022664

- Samples were dried in an oven for 24 hours at 105°C.
- Samples were cooled for 40 minutes in a desiccator to prevent moisture absorption from the air.
- Samples were weighed after drying and before being submerged in water.
- The samples were submerged under ambient atmospheric pressure, not vacuum conditions.
- Samples were submerged in water for 24 hours.
- Samples were removed from water and placed on a grate above the tank for 15 minutes to drain as much of the surface water.
- The difference in water level in the tank was checked and compared to the initial volume.
- Samples were photographed after testing.

Descriptions of effervescence and the stability of the rock in water were made after the "Geotechnical investigation and testing - Identification, description and classification of rock (ISO 14689:2017)". ISO (2017). ISO 14689:2017 – Geotechnical investigation and testing – Identification, description and classification of rock. International Organization for Standardization. pp.21.

A total of 115 rock samples were subjected to the water absorption test. The experiment was designed to quantify the key physical and hydrogeological properties of a diverse suite of sedimentary, metamorphic and igneous lithologies. The acquisition of such information is a prerequisite for evaluating the suitability and long-term integrity of potential geological storage formations.

Although the samples were collected from surface exposures and have likely undergone natural wetting-drying cycles, the laboratory water absorption and stability tests remain relevant for assessing the petrophysical behaviour of these formations under near-surface conditions. If exposed samples retain low permeability and mechanical integrity despite repeated hydration and drying, it is reasonable to infer that their subsurface equivalents, preserved under burial and lithostatic confinement, would exhibit even lower permeability and higher sealing capacity. Therefore, these measurements provide a conservative estimate of the potential performance of the rock as cap layers in CO_2 storage settings. Moreover, evaluating the relationship between density, porosity, and water uptake offers valuable insight into lithological variability and diagenetic maturity, both of which are critical parameters for assessing reservoir-seal systems.

In the Appendix X each sample is identified by a code denoting the geographical origin (Regions 1 to 9), while the rock type is also given. For each sample, a series of measurements were recorded. These include physical properties such as weight (before and after oven drying, and after a 24-hour immersion period), volume, and calculated density. In addition to these, the experiment quantified several key performance indicators: the reactivity of the sample to hydrochloric acid (a proxy for carbonate content: a) non-calcareous, b) slightly calcareous, c) calcareous, d) highly calcareous), and its physical stability after 24 hours of water immersion based on a 1-5 Grade. According to ISO 14689:2017, grade 1 (Stable) indicates no visible changes in the specimen, grade 2 corresponds to cases where a few fissures are formed, or the specimen surface crumbles slightly, grade 3 (Fairly stable) display many fissures and break into small lumps, or their surfaces crumble extensively, grade 4 (Unstable) is given when the specimen largely disintegrates or nearly the entire surface crumbles, and grade 5 represents the most extreme form of instability, where the whole specimen becomes muddy or disintegrates completely into sand. Other

The PilotSTRATEGY project has received funding from the European Union's Horizon 2020 research and innovation programme under grant agreement No. 101022664

qualities that were tested include the total water absorption capacity, calculated both from the weight gain of each sample and from the change in water volume within the test tank.

The conduced water absorption test represents a relatively simple and fundamental laboratory procedure, but it provides an essential baseline for characterizing rock behavior. Thus, it serves as a first step towards more advanced, targeted, and high-precision analyses, establishing a foundation upon which future experimental work can be built.

CERTH is committed to open data and metadata sharing sample information in an effort to promote a workplace of collaboration. Therefore, data from the samples collected are open and accessible as follows:

- Water absorption, Effervescence, and Rock Stability testing is reported here, https://zenodo.org/records/17176304

Region 1 is exclusively composed of sandstone samples, which exhibit a moderate degree of variability. The densities are relatively consistent and cluster around 2.3 g/cm³ (Appendix X). Water absorption is present but generally low, with most samples absorbing between 10-50 g of water per 1000g of rock. All samples from this region demonstrated complete stability (Grade 1) after the 24-hour immersion period, indicating competent rock fabric despite their porosity.

The mass change and density comparison graphs reveal a high degree of uniformity among the samples (Figure 5.25). The densities are tightly clustered around 2.3 g/cm³, with minimal variation between samples (Appendix X) (Figure 5.26). The mass change plot clearly shows a slight decrease in weight after drying (indicating some initial moisture content) and a subsequent, more significant increase after the 24-hour test due to water absorption (Figure 5.25).

The water absorption capacity of these sandstones is generally low to moderate, with most samples absorbing between 10 and 50 ml of water per 1000g of rock (Figure 5.27). The sandstone sample 1_10 (sst) stands out as the most absorbent in this group. The density versus water absorption plot suggests a quite weak negative tendency, where slightly denser samples tend to absorb marginally less water, although the relationship is not statistically significant (Figure 5.28). This is a classic relationship indicating that porosity is the primary control on absorption. The reaction to acid and the stability analysis plot diagrams provide definitive classifications (Figure 5.29). All samples in region 1 are calcareous, indicating the presence of carbonate minerals, likely as cement or grains within the sandstone. Critically, the stability analysis shows that all 11 samples were fully stable (Grade 1) after 24 hours of immersion (Figure 5.30). Thus, despite being porous and calcareous, the rock fabric is robust enough to resist physical degradation from water saturation. The carbonate content versus water absorption box plot confirms that for this uniform rock type, the carbonate content does not introduce significant variability in absorption (Figure 5.31).

The PilotSTRATEGY project has received funding from the European Union's Horizon 2020 research and innovation programme under grant agreement No. 101022664

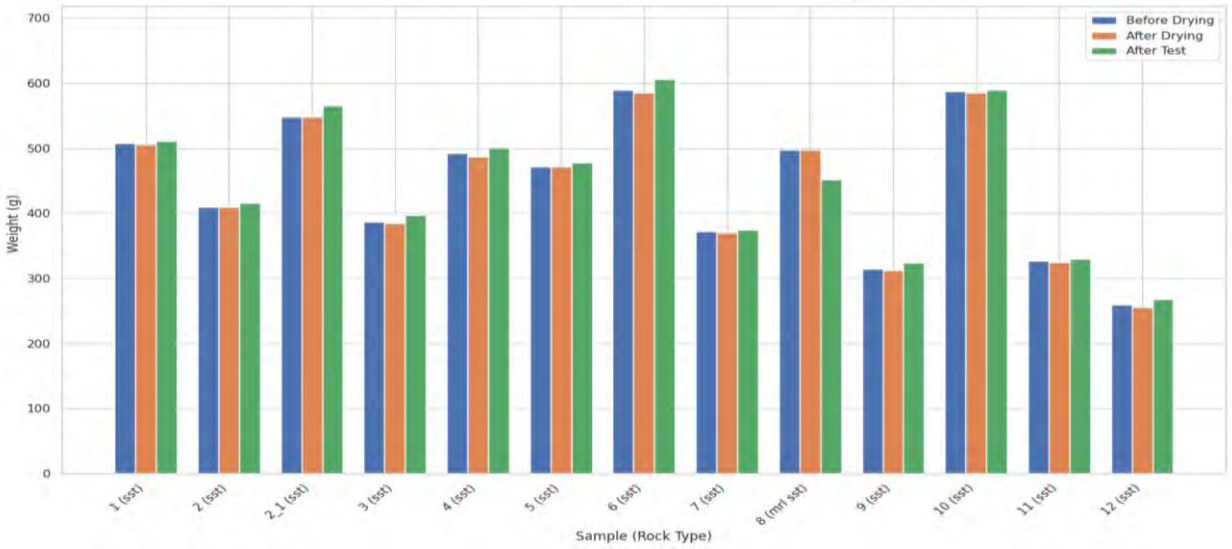

Figure 5.25: Bar chart of the mass change analysis for the examined samples from Region 1 (abbreviations: mrl sst = marly sandstone, sst = sandstone). Complete sample codes: 1_1, 1_2, 1_1, 1_2, 1_2_1, 1_3, 1_4, 1_5, 1_6, 1_7, 1_8, 1_9, 1_10, 1_11, 1_12.

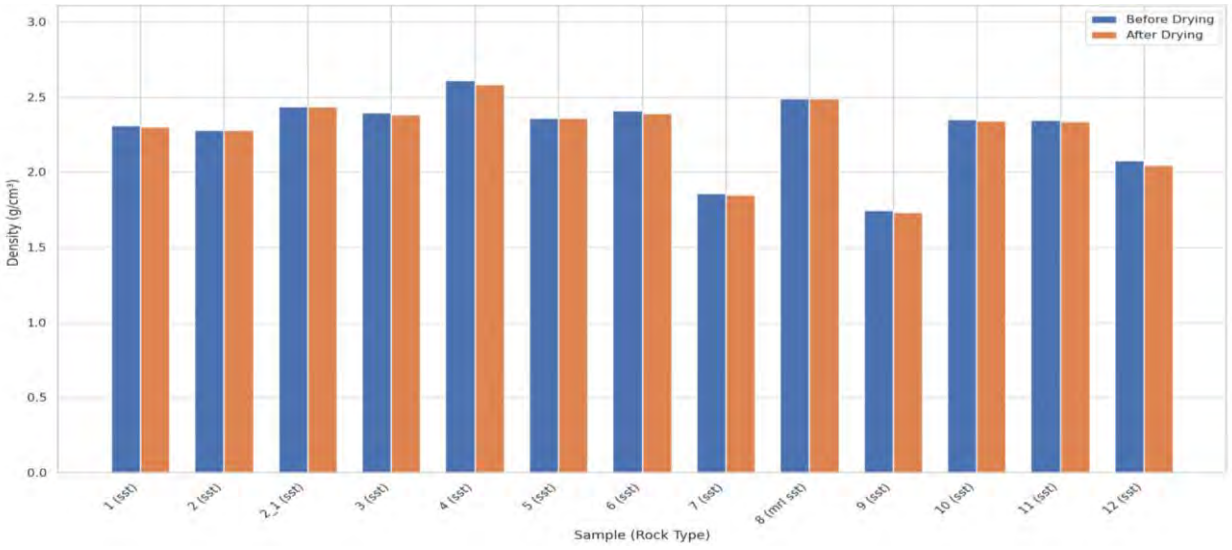

Figure 5.26: Bar chart of the density comparison analysis for the examined samples from Region 1. Complete sample codes: 1_1, 1_2, 1_2_1, 1_3, 1_4, 1_5, 1_6, 1_7, 1_8, 1_9, 1_10, 1_11, 1_12 (abbreviations: mrl sst = marly sandstone, sst = sandstone).

The PilotSTRATEGY project has received funding from the European Union's Horizon 2020 research and innovation programme under grant agreement No. 101022664

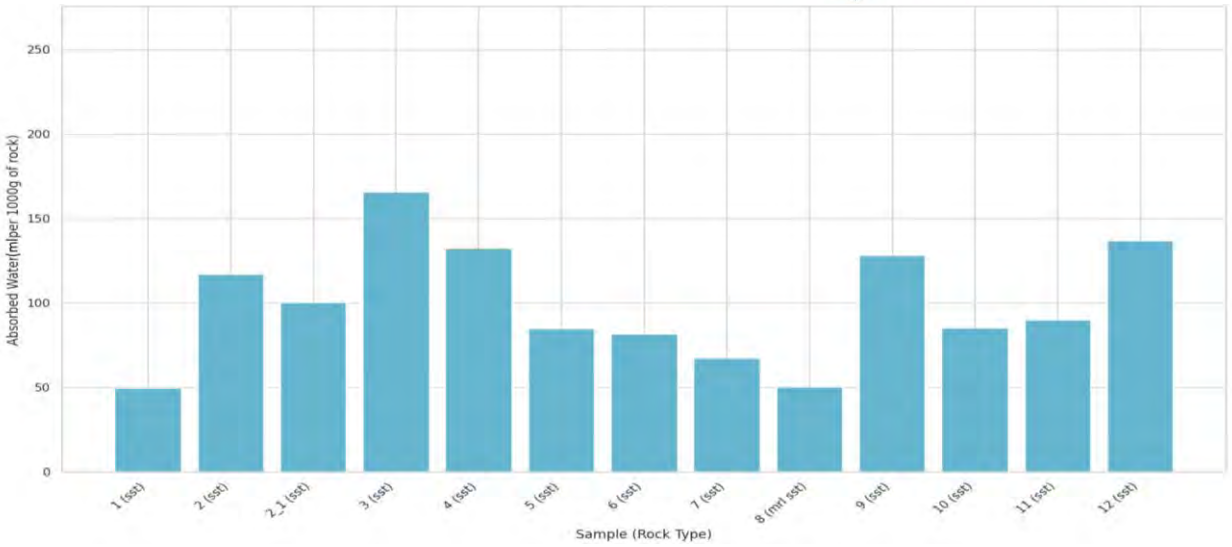

Figure 5.27: Bar chart of the absorbed water per 1000 g of rock for the examined samples from Region 1. Complete sample codes: 1_1, 1_2, 1_2_1, 1_3, 1_4, 1_5, 1_6, 1_7, 1_8, 1_9, 1_10, 1_11, 1_12 (abbreviations: mrl sst = marly sandstone, sst = sandstone).

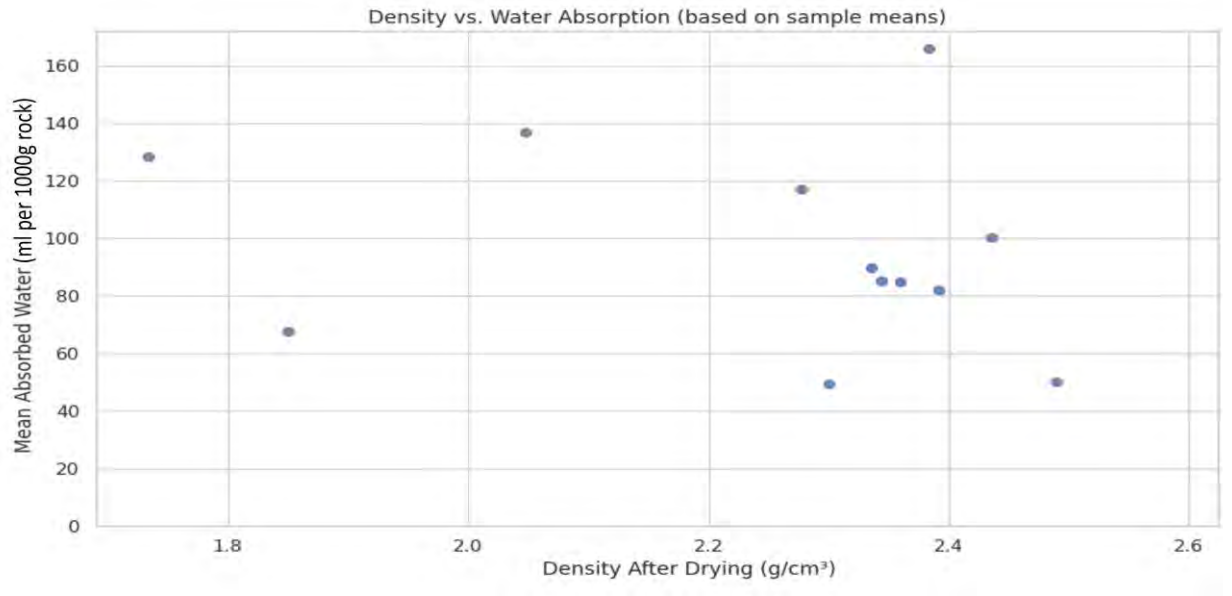

Figure 5.28: The absorbed water in ml per 1000 g of rock versus density after drying (g/cm3) for the examined samples from Region 1. The x-axis scale is intentionally limited to the observed range of measured densities to enhance visibility and resolution of the data distribution.

The PilotSTRATEGY project has received funding from the European Union's Horizon 2020 research and innovation programme under grant agreement No. 101022664

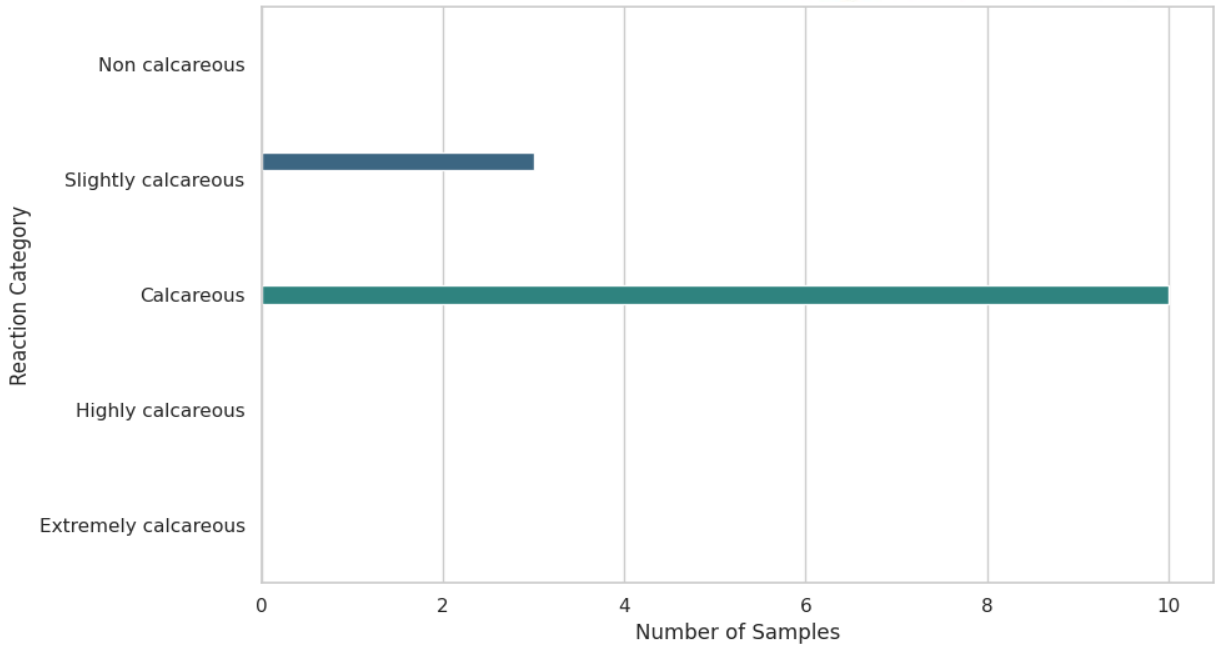

Figure 5.29: Distribution of samples from Region 1 after their reaction to hydrochloric acid (HCl). Reaction categorization is after ISO 14689:2017.

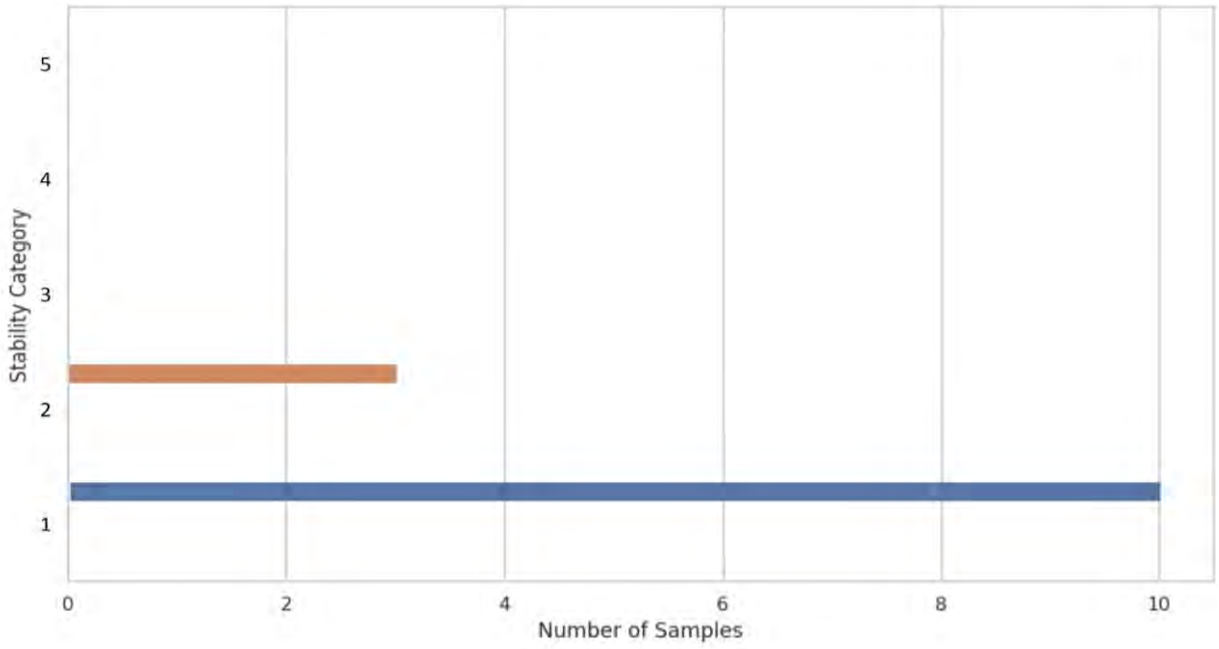

Figure 5.30: Bar chart showing the categorization of the samples from Region 1 after stability grade. Stability in water after 24 hours in ISO 14689:2017 includes the following grades: 1. Stable, 2. Fairly stable: a few fissures are formed, or specimen surface crumbles slightly, 3. Fairly stable: many fissures are formed and broken into small lumps, or specimen surface crumbles highly, 4. Unstable: specimen disintegrates, or nearly the whole specimen surface crumbles, and 5. Unstable: the whole specimen becomes muddy, or disintegrates completely into sand.

The PilotSTRATEGY project has received funding from the European Union's Horizon 2020 research and innovation programme under grant agreement No. 101022664

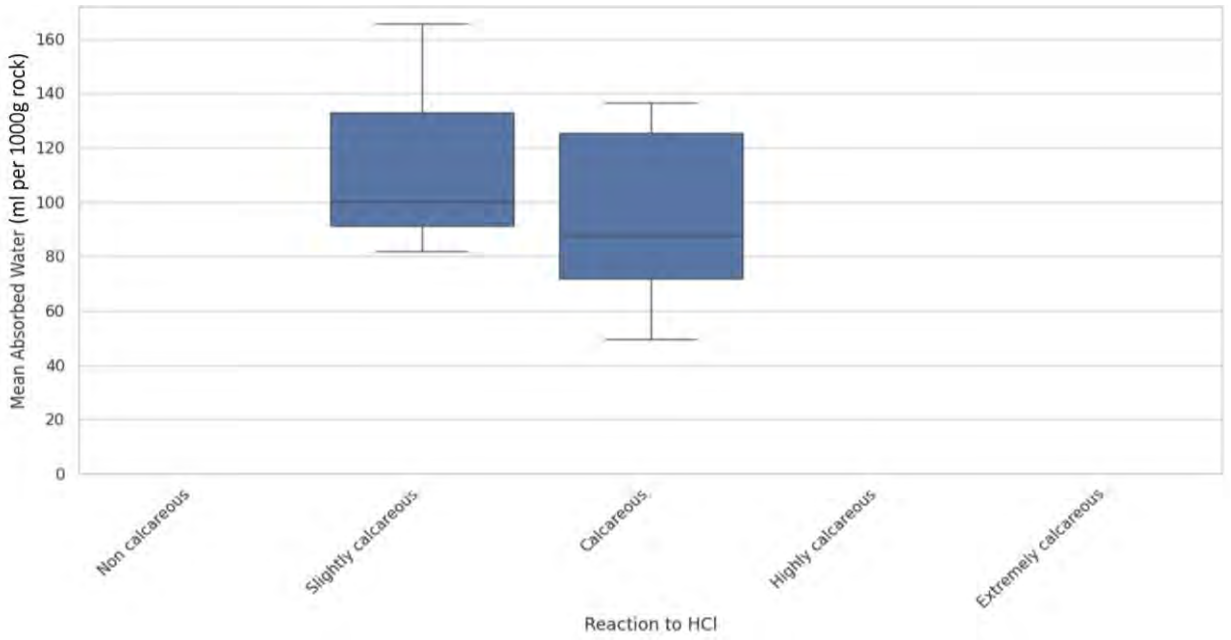

Figure 5.31: Box plot graph of the absorbed water of the samples from Region 1 versus the rock reaction to HCl categorization after ISO 14689:2017.

Region 2 is characterised by a mix of conglomerates and sandstones, including well-cemented and loose varieties. The lithological diversity is reflected in the wide range of physical properties documented during the water absorption testing (Figure 5.25, Figure 5.27). Densities vary significantly from approximately 1.56 to 2.63 g/cm³ (Appendix X). As a result, water absorption values are highly variable, containing some of the most absorbent samples in the entire dataset. Despite this high absorption capacity in some samples, all rocks from this region were observed to be stable (Grade 1).

The mass change and density graphs reveal the varied nature of the samples in Region 2 (Figure 5.32, Figure 5.33). The density comparison plot shows a wide distribution of densities between the samples, ranging from 1.56 g/cm³ for the marl sample 2_11 to 2.63 g/cm³ for the sandstone sample 2_20 (Appendix X) (Figure 5.33). This variability directly reflects the diverse lithologies, from conglomerate to sandstone and marl. Although the mass change plot further confirms this heterogeneity, the weight of the samples does not vary significantly before and after testing (Figure 5.32). Notable is the outlier sample 2_8a which before testing weighted 270 g and after testing weight shifted to 456 g (Appendix X).

The water absorption efficiency plot showcases a very wide range of absorption capacities (Figure 5.34). Sample 2_8a (marl), showing a significant mass change after testing and having a density after drying at 2.13 g/cm³, is by far the most absorbent (357 ml of water per 1000g of rock) (Appendix X, Figure 5.34). In contrary, most of the samples absorbed less than 150 ml of water per 1000 g of rock (Figure 5.34). The density versus water absorption plot shows a weak negative tendency, indicating that less dense, more

The PilotSTRATEGY project has received funding from the European Union's Horizon 2020 research and innovation programme under grant agreement No. 101022664

porous rocks may generally absorb more water, although the relationship is not statistically pronounced. (Figure 5.35).

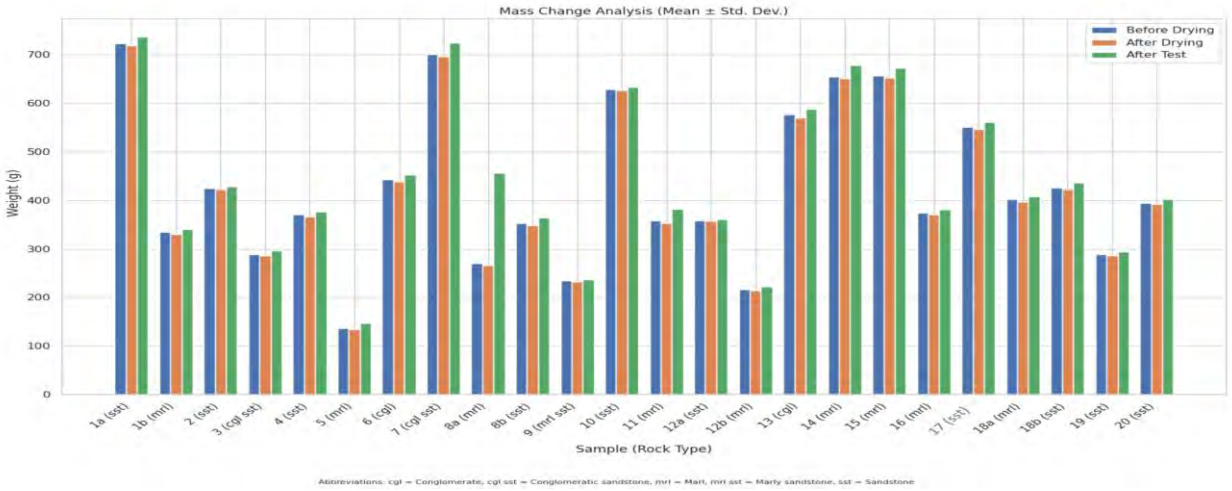

Figure 5.32: Bar chart of the mass change analysis for the examined samples from Region 2 (abbreviations: cgl = conglomerate, cgl sst = conglomeratic sandstone, mrl = marl, mrl sst = marly sandstone, sst = sandstone). Complete sample codes: 2_1a, 2_1b, 2_2, 2_3, 2_4, 2_5, 2_6, 2_7, 2_8a, 2_8b, 2_9, 2_10, 2_11, 2_12a, 2_12b, 2_13, 2_14, 2_15, 2_16, 2_17, 2_18a, 2_18b, 2_19, 2_20.

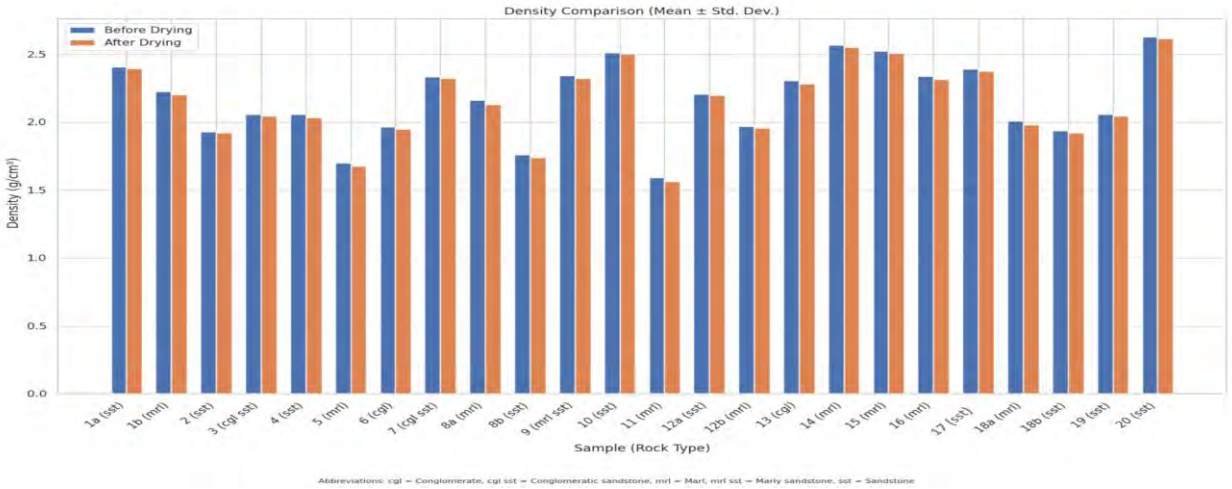

Figure 5.33: Bar chart of the density comparison analysis for the examined samples from Region 2 (abbreviations: cgl = conglomerate, cgl sst = conglomeratic sandstone, mrl = marl, mrl sst = marly sandstone, sst = sandstone). Complete sample codes: 2_1a, 2_1b, 2_2, 2_3, 2_4, 2_5, 2_6, 2_7, 2_8a, 2_8b, 2_9, 2_10, 2_11, 2_12a, 2_12b, 2_13, 2_14, 2_15, 2_16, 2_17, 2_18a, 2_18b, 2_19, 2_20.

The PilotSTRATEGY project has received funding from the European Union's Horizon 2020 research and innovation programme under grant agreement No. 101022664

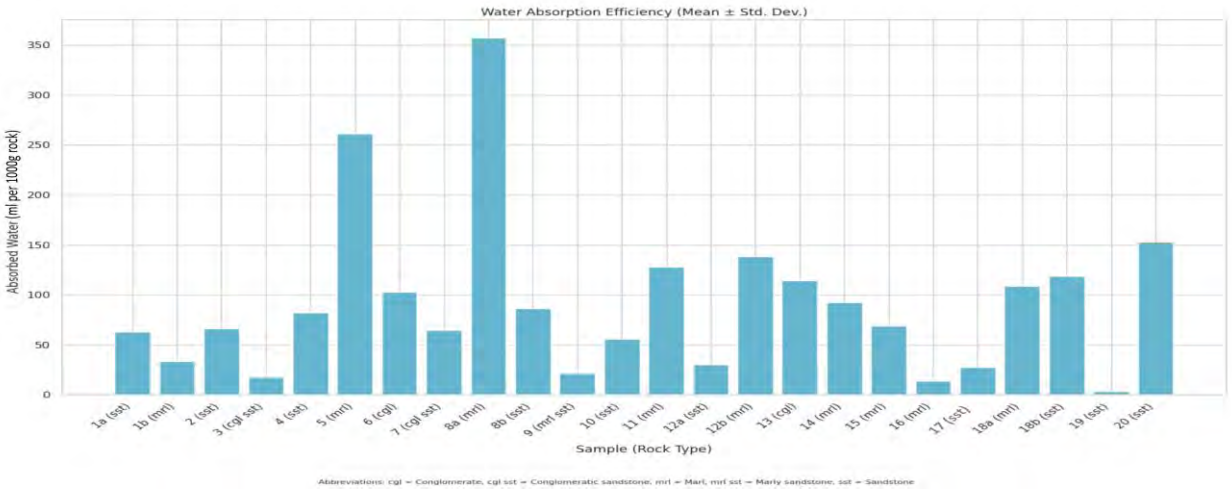

Figure 5.34: Bar chart of the absorbed water (ml) per 1000 g of rock for the examined samples from Region 2 (abbreviations: cgl = conglomerate, cgl sst = conglomeratic sandstone, mrl = marl, mrl sst = marly sandstone, sst = sandstone). Complete sample codes: 2_1a, 2_1b, 2_2, 2_3, 2_4, 2_5, 2_6, 2_7, 2_8a, 2_8b, 2_9, 2_10, 2_11, 2_12a, 2_12b, 2_13, 2_14, 2_15, 2_16, 2_17, 2_18a, 2_18b, 2_19, 2_20.

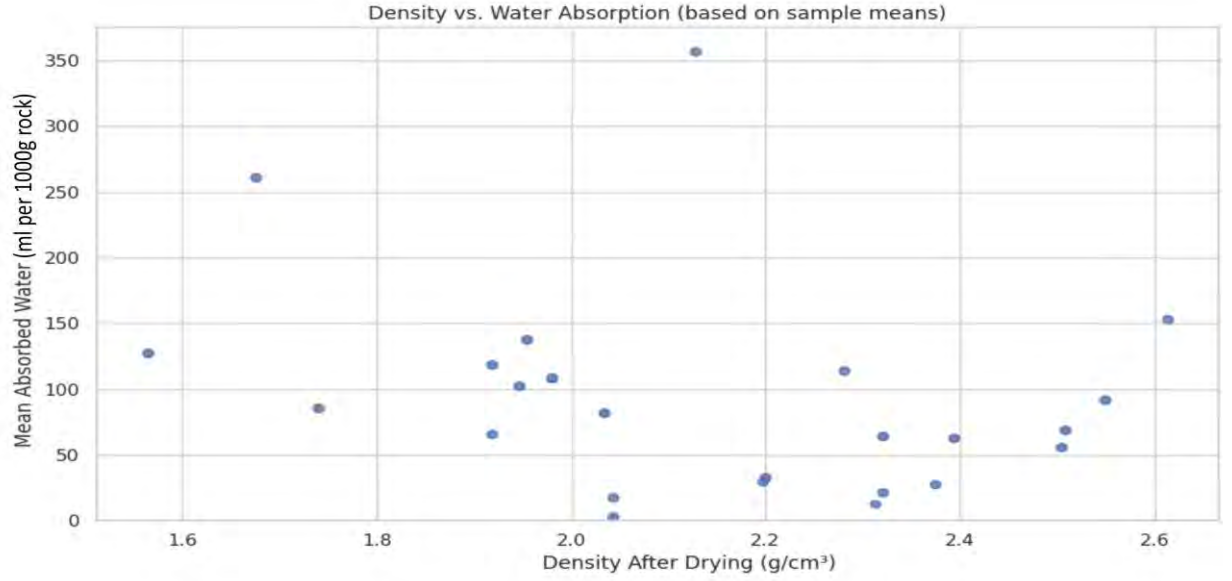

Figure 5.35: The absorbed water (ml) per 1000 g of rock versus density after drying (g/cm3) for the examined samples from Region 2. The x-axis scale is intentionally limited to the observed range of measured densities to enhance visibility and resolution of the data distribution.

The reaction to hydrochloric acid analysis shows that the majority of the samples are calcareous or highly calcareous, indicating a carbonate-rich composition either in the clasts or the cement (Figure 5.36). Exceptions are samples 2_10 (sandstone) and 2_17 (sandstone) which are described as non-calcareous (Figure 5.36). Most critically, the stability analysis suggests that despite the varying differences in density

The PilotSTRATEGY project has received funding from the European Union's Horizon 2020 research and innovation programme under grant agreement No. 101022664

and water absorption, most samples were fully stable (Grade 1) (Figure 5.37). Exceptions (Grade 2 and 5) are the marl and conglomerate samples 2_3, 2_5, 2_8a, 2_11, 2_13 and 2_15, which exhibit varying water absorptions (Figure 5.34, Figure 5.37). The water absorption capability for these samples may be less than that of some stable (Grade 1) sandstone samples. This finding indicates the importance of sufficient cementation to resist physical degradation upon saturation, and may reflect the occurrence of expanding clay minerals especially in sample 2_8a (Grade 5). The carbonate content versus water absorption box plot graph showcases that calcareous samples absorb the highest amounts of water. The slightly calcareous samples absorb less water, while the non-calcareous samples uptake restricted amounts around 50 ml of water per 1000g rock (Figure 5.38).

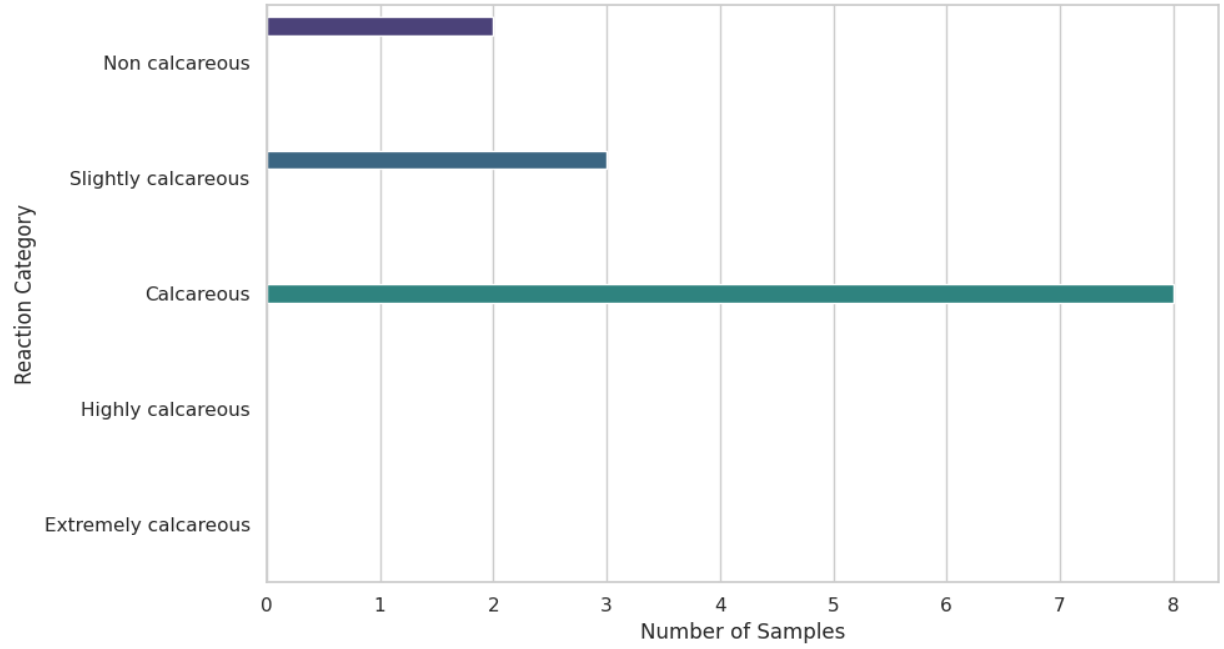

Figure 5.36: Distribution of samples from Region 2 after their reaction to hydrochloric acid (HCl). Reaction categorization is after ISO 14689:2017.

Ranging from conglomerates and sandstones to marls, is clearly expressed in the density and water absorption results. Densities span from 1.56 to 2.63 g/cm³, with marl sample 2_11 at the lowest end and sandstone sample 2_20 at the highest. This wide spread reflects differences in cementation and porosity, which in turn control the water absorption behavior. While most samples absorbed less than 150 ml of water per 1000 g of rock, sample 2_8a (marl) stood out as an extreme outlier, taking in 357 ml. The steep negative correlation between density and water absorption highlights the influence of porosity, where less dense rocks tend to retain more water.

The PilotSTRATEGY project has received funding from the European Union's Horizon 2020 research and innovation programme under grant agreement No. 101022664

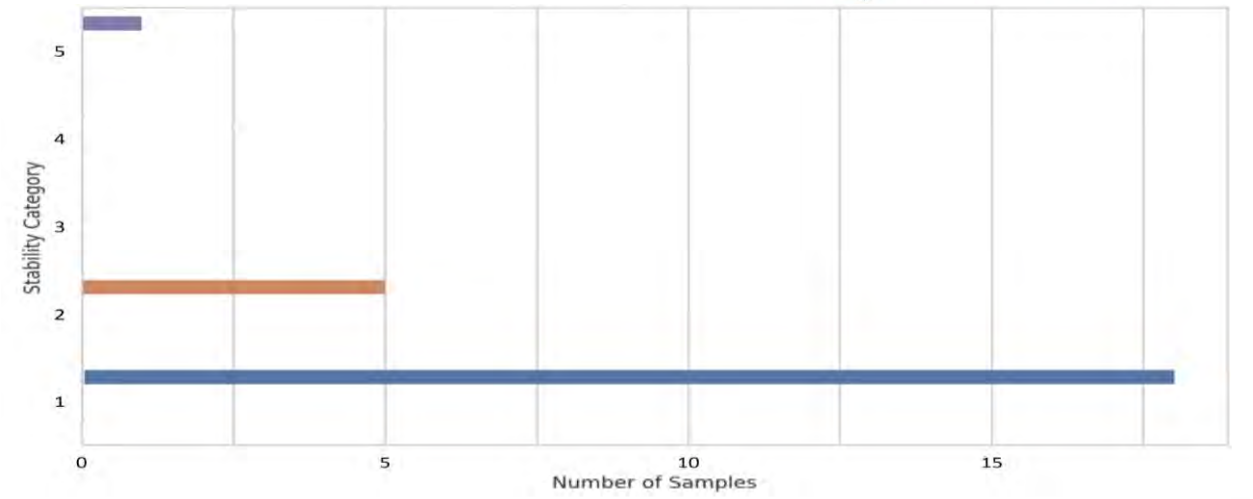

Figure 5.37: Bar chart showing the categorization of the samples from Region 2 after stability grade. Stability in water after 24 hours in ISO 14689:2017 includes the following grades: 1. Stable, 2. Fairly stable: a few fissures are formed, or specimen surface crumbles slightly, 3. Fairly stable: many fissures are formed and broken into small lumps, or specimen surface crumbles highly, 4. Unstable: specimen disintegrates, or nearly the whole specimen surface crumbles, and 5. Unstable: the whole specimen becomes muddy, or disintegrates completely into sand.

Despite these variations, the majority of rocks demonstrated stability (Grade 1), suggesting that cementation plays a critical role in resisting degradation upon saturation. Exceptions include several marl and conglomerate samples, notably 2_8a (Grade 5), which likely reflects the presence of expanding clay minerals. The carbonate-rich composition of most samples, confirmed by hydrochloric acid tests, further influences water absorption trends, with calcareous rocks generally showing higher uptake than non-calcareous ones. Overall, the results underline the importance of both mineralogical composition and textural properties in determining the durability of these lithologies under water interaction.

The samples from Region 3 consist of coarse-grained sedimentary rocks, specifically conglomeratic sandstones and conglomerates with only one sample being classified as marl (sample 3_5) (Appendix X, Figure 5.39, Figure 5.40). All samples were classified as stable or fairly stable (Grades 1 and 2), indicating that while they absorb water, their internal structure remains intact over the test period.

The mass change analysis shows that for most samples, the mass before drying, after drying, and after the test is very similar (Figure 5.39). The differences are minimal, especially when considering the standard deviation for sample 3_4. This suggests that the drying and testing process did not cause a significant permanent loss of mass for most samples. In addition, the density of the samples before and after drying is also very similar (Figure 5.40). Sample 3_1 (conglomeratic sandstone) is characterized by relatively low densities at 0.92 g/cm³ and 0.92 g/cm³ before and after drying, respectively (Appendix X). The densities of the rest of the samples (identified as conglomeratic sandstone, conglomerate, and marl) are clustered around 2.09 and 2.61 g/cm³ (Appendix X).

The water absorption graph shows a wide range of water absorption efficiency among the samples. The water absorbed by these samples totals 188 ml per 1000g rock, while samples 3_3a despite similar density

The PilotSTRATEGY project has received funding from the European Union's Horizon 2020 research and innovation programme under grant agreement No. 101022664

absorbed less than 25 ml of water (Figure 5.41). This suggests a significant microporosity associated with their clay and silt content.

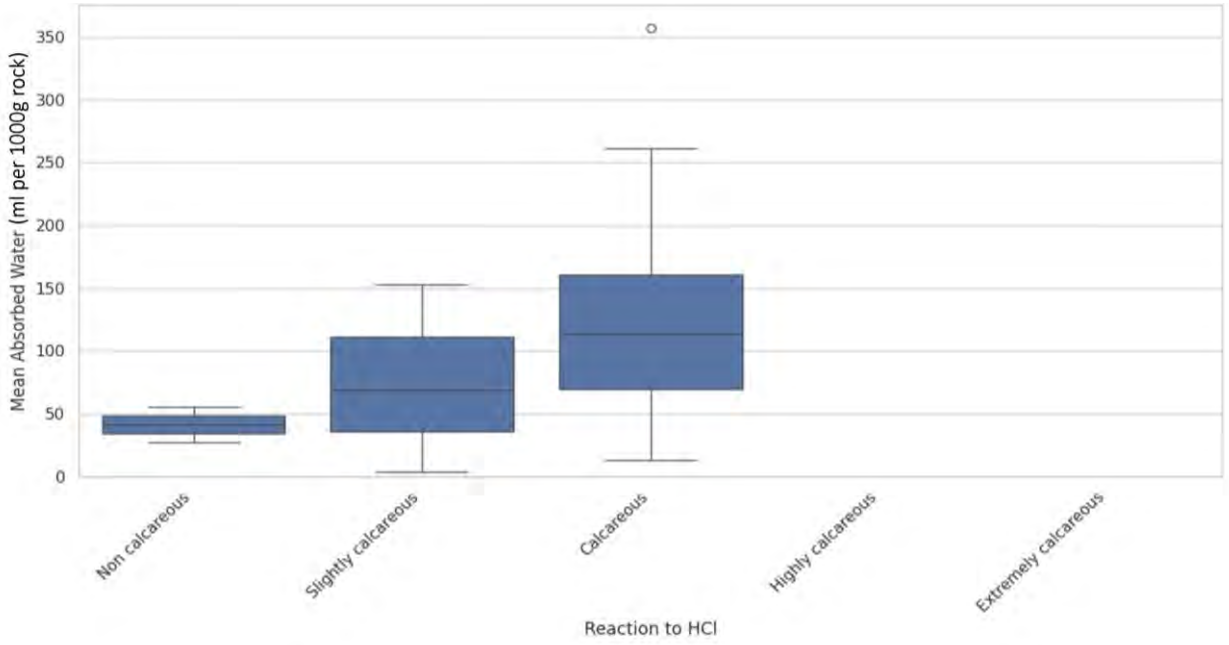

Figure 5.38: Box plot graph of the absorbed water (ml) per 1000g rock for the samples collected from Region 2 versus the rock reaction to HCl categorization after ISO 14689:2017.

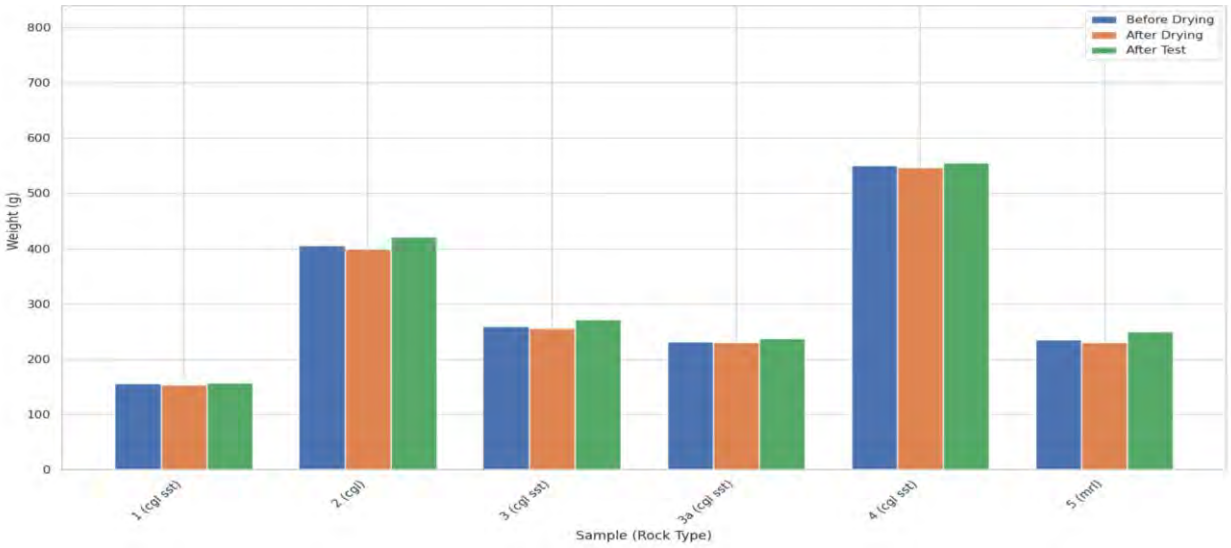

Figure 5.39: Bar chart of the mass change analysis for the examined samples from Region 3 (abbreviations: cgl sst = conglomeratic sandstone, cgl = conglomerate, mrl = marl). Complete sample codes: 3_1, 3_2, 3_3, 3_3a, 3_4, 3_5.

The PilotSTRATEGY project has received funding from the European Union's Horizon 2020 research and innovation programme under grant agreement No. 101022664

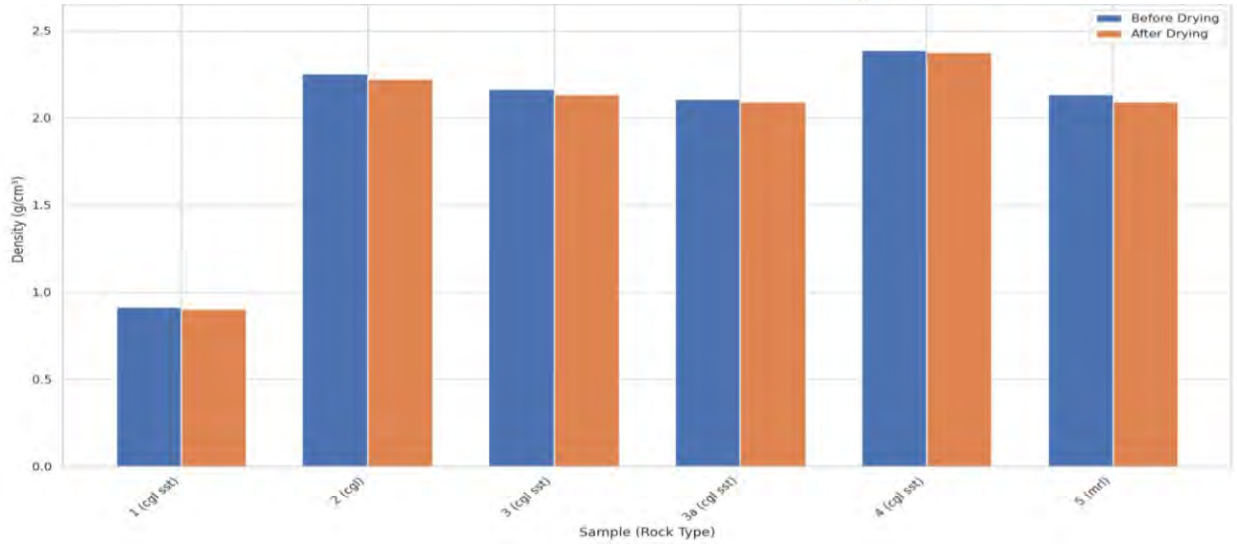

Figure 5.40: Bar chart of the density comparison analysis for the examined samples from Region 3 (abbreviations: cgl sst = conglomeratic sandstone, cgl = conglomerate, mrl = marl). Complete sample codes: 3_1, 3_2, 3_3, 3_3a, 3_4, 3_5.

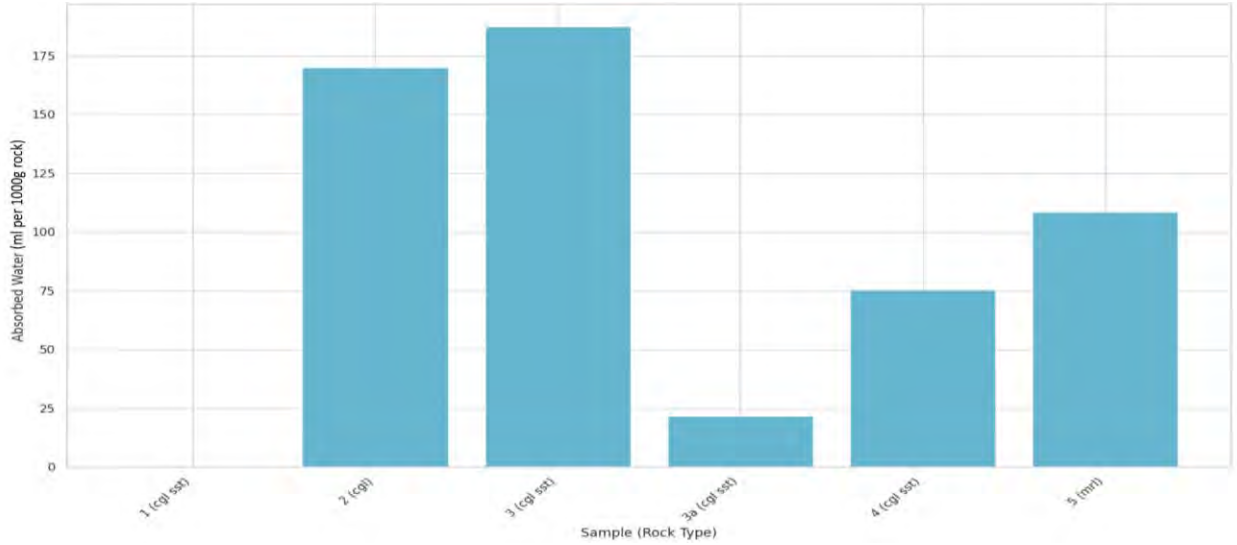

Figure 5.41: Bar chart of the absorbed water (ml) per 1000 g of rock for the examined samples from Region 3 (abbreviations: cgl sst = conglomeratic sandstone, cgl = conglomerate, mrl = marl). Complete sample codes: 3_1, 3_2, 3_3, 3_3a, 3_4, 3_5.

The density versus water absorption plot shows scatter, with no consistent relationship between sample density after drying and the mean absorbed water (Figure 5.42). As density increases, water absorption also tends to increase, though with significant variation. A significant number of samples tested as non-calcareous (3 samples), meaning they do not react with HCl (Figure 5.43). Two samples were slightly calcareous, and only one was calcareous. The stability analysis graph reveals that four of the six samples were classified as stable (Grade 1), indicating they are very stable in water over a 24-hour period, while

The PilotSTRATEGY project has received funding from the European Union's Horizon 2020 research and innovation programme under grant agreement No. 101022664

two samples 3_2 (conglomerate) and 3_5 (marl) graded as fairly stable. The relationship between carbonate content and water absorption suggests a link between carbonate content and the ability of the rock to absorb water (Figure 5.45). The non-calcareous samples show a wide range of water absorption (median around 75 ml per 1000g of rock), the slightly calcareous samples have a higher median absorption, around 100 ml per 1000g, and the calcareous sample has a median of about 110 ml (Figure 5.45).

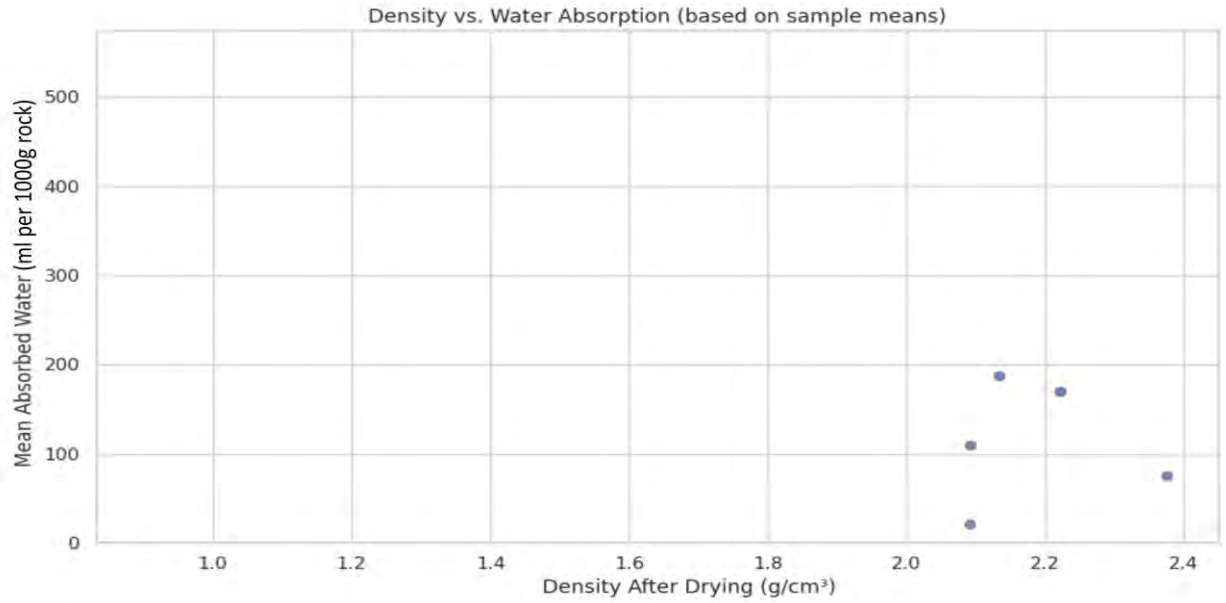

Figure 5.42: The absorbed water (ml) per 1000 g of rock versus density after drying (g/cm3) for the examined samples from Region 3. The x-axis scale is intentionally limited to the observed range of measured densities to enhance visibility and resolution of the data distribution.

The data for the samples tested from Region 3 may suggest that the type of rock and its carbonate content are key factors influencing its physical properties, particularly water absorption. The differences in water absorption, as seen in Figure 5.41, could be related to the mineral composition and pore structure of the samples. For example, while samples 3_3 and 3_3a are both conglomeratic sandstones, their water absorption is drastically different. This could be due to variations in their cementing material or porosity.

The stability data indicates that most of the tested samples are resistant to disintegration when exposed to water for 24 hours (Figure 5.44). The weak positive correlation between density and water absorption (Figure 5.42) is unexpected, as one might assume that a denser rock (with less porosity) would absorb less water. However, this may be due to the specific pore size and connectivity within the samples, where even a dense rock can have interconnected pores that allow for water absorption. The table data shows that some of the rocks with the highest water absorption (e.g. 3_2) are non-calcareous, while the single calcareous sample (3_5) has a lower absorption rate. This aligns with the trend seen in the box plot of Figure 5.45, which shows that non-calcareous rocks generally have a wider range of water absorption compared to the more consistently absorbent calcareous rocks.

The PilotSTRATEGY project has received funding from the European Union's Horizon 2020 research and innovation programme under grant agreement No. 101022664

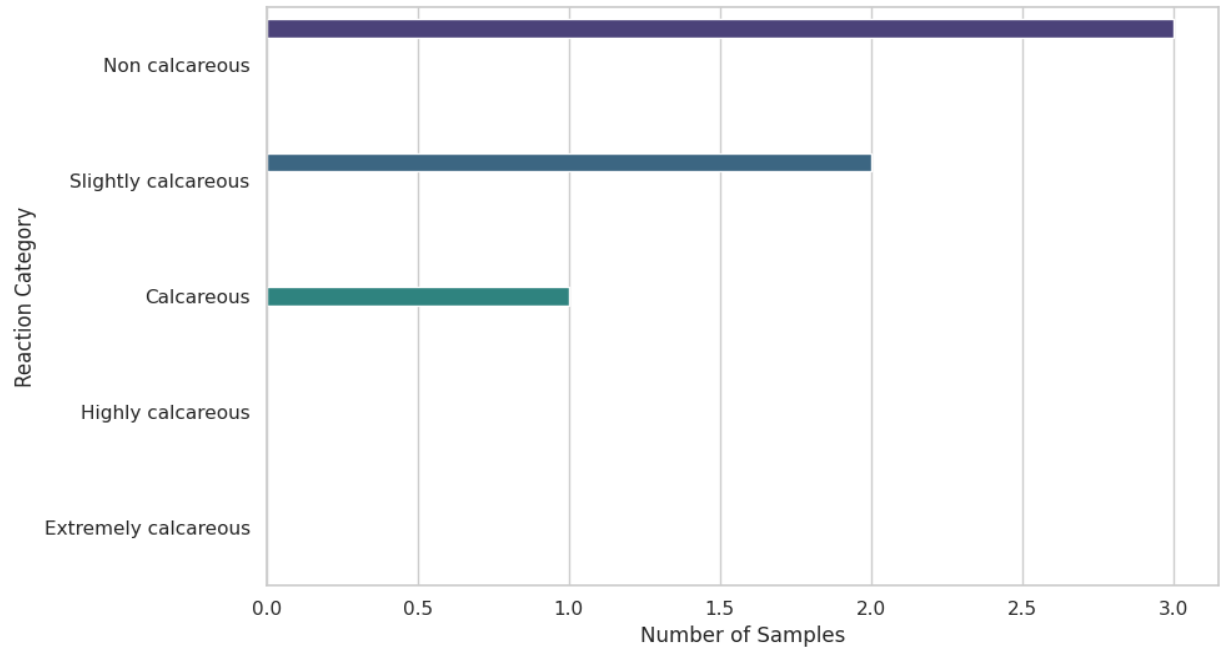

Figure 5.43: Distribution of samples from Region 3 after their reaction to hydrochloric acid (HCl). Reaction categorization is after ISO 14689:2017.

Region 4 is dominated by coarse-grained loose to well cemented conglomerates and conglomeratic sandstones. Samples 4_1 to 4_3 were not tested as they are loose not suitable for water absorption testing (Appendix X). In contrary, samples 4_4, 4_5, and 4_6, are well cemented and suitable for testing. Based on the mass change and density comparison analysis graphs, the samples from Region 4 show little change in mass and density after drying (Figure 5.46, Figure 5.47). The density comparison graph reveals that changes before and after drying among samples 4_4, 4_5 and 4_6 are not statistically significant (Figure 5.47). The water absorption efficiency graph shows that sample 4_4 (conglomeratic sandstone) has a mean absorbed water of just over 100 g per 1000g of rock, with a large standard deviation (Figure 5.48). Sample 4_6 (conglomerate) shows a similar value for absorption, while sample 4_5 absorbed around 50 ml of water per 1000g of rock (Figure 5.48). In addition, the water absorption versus density graph shows a generally negative trend (Figure 5.49). As the dry density of the rock decreases, its water absorption tends to increase. This is an expected relationship in rocks, as lower density often indicates a higher porosity. All the tested samples are from Region 4 are classified as "Slightly calcareous", meaning they show a slight reaction to an HCl test (Figure 5.50), whereas the stability analysis graph shows that samples are stable (4_5 and 4_6) and fairly stable (4_4). Stability indicates the well cementation of the “Slightly calcareous” conglomerates in Region 1, which are able to absorb in average around 90 ml of water per 1000 g of rock (Figure 5.52).

The PilotSTRATEGY project has received funding from the European Union’s Horizon 2020 research and innovation programme under grant agreement No. 101022664

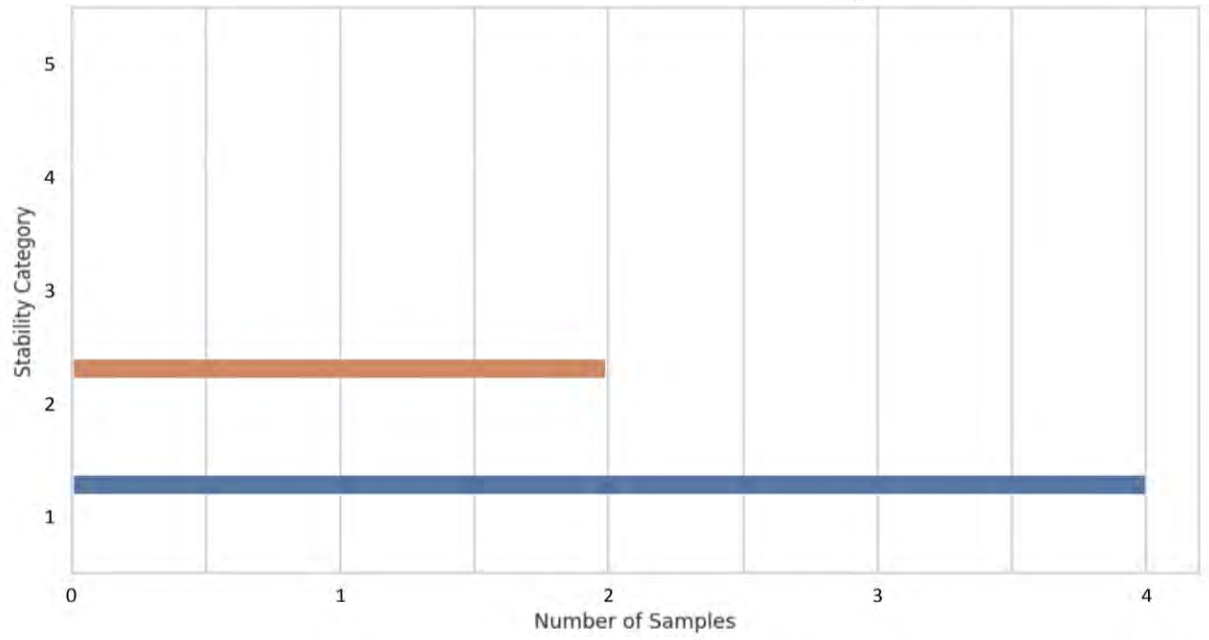

Figure 5.44: Bar chart showing the categorization of the samples from Region 3 after stability grade. Stability in water after 24 hours in ISO 14689:2017 includes the following grades: 1. Stable, 2. Fairly stable: a few fissures are formed, or specimen surface crumbles slightly, 3. Fairly stable: many fissures are formed and broken into small lumps, or specimen surface crumbles highly, 4. Unstable: specimen disintegrates, or nearly the whole specimen surface crumbles, and 5. Unstable: the whole specimen becomes muddy, or disintegrates completely into sand.

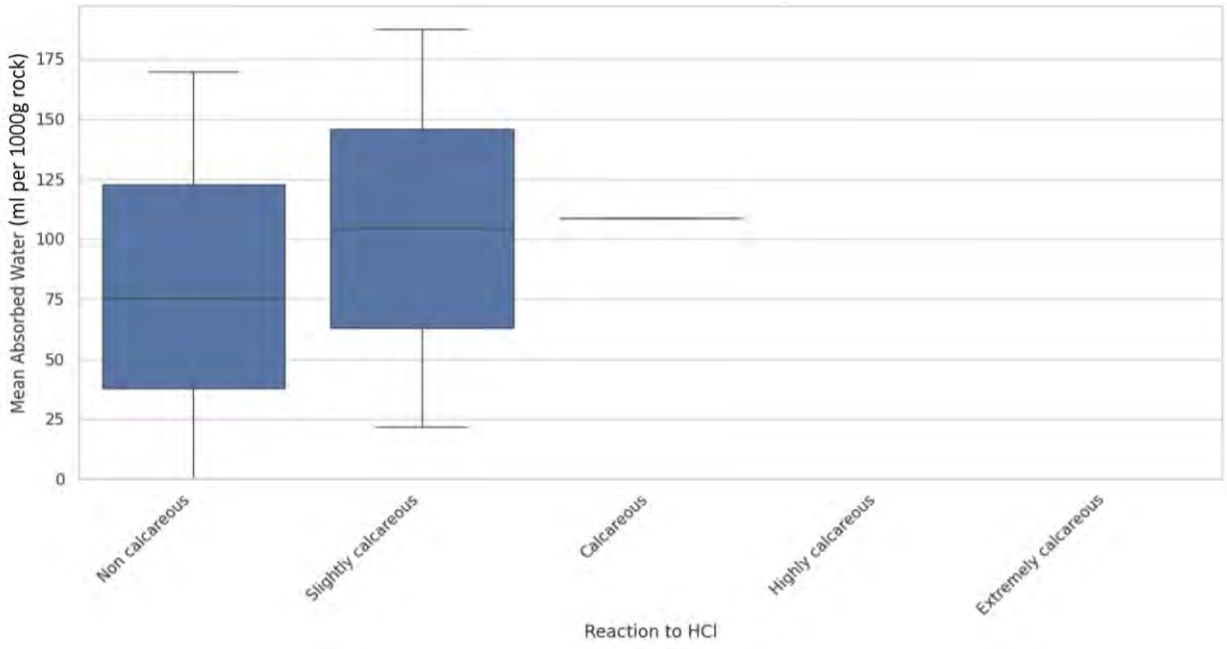

Figure 5.45: Box plot graph of the absorbed water (ml) per 1000g rock for the samples collected from Region 3 versus the rock reaction to HCl categorization after ISO 14689:2017.

The PilotSTRATEGY project has received funding from the European Union's Horizon 2020 research and innovation programme under grant agreement No. 101022664

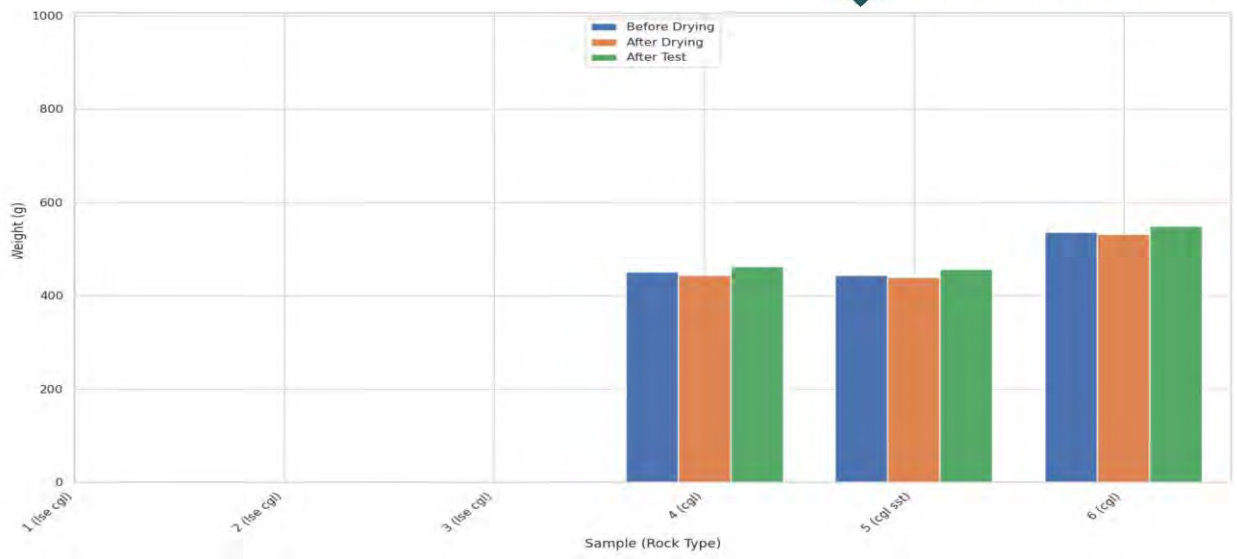

Figure 5.46: Bar chart of the mass change analysis for the examined samples from Region 4 (abbreviations: lse cgl = loose conglomerate, cgl = conglomerate, cgl sst = conglomeratic sandstone). Complete sample codes: 4_1, 4_2, 4_3, 4_4, 4_5, 4_6.

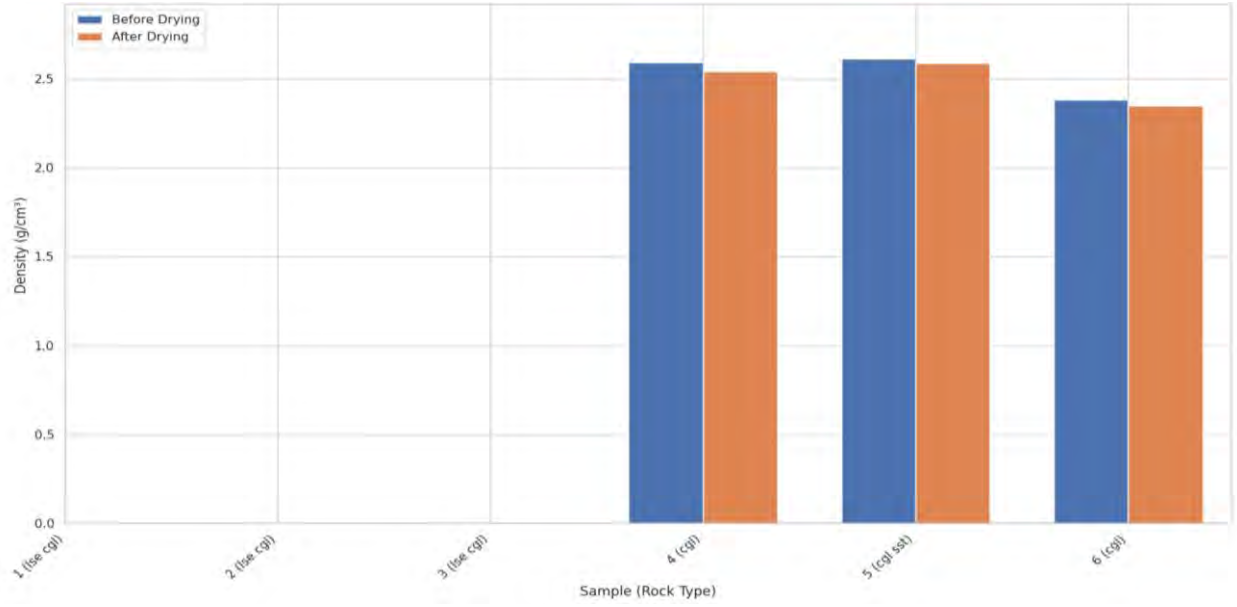

Figure 5.47: Bar chart of the density comparison analysis for the examined samples from Region 4 (abbreviations: lse cgl = loose conglomerate, cgl = conglomerate, cgl sst = conglomeratic sandstone). Complete sample codes: 4_1, 4_2, 4_3, 4_4, 4_5, 4_6.

The PilotSTRATEGY project has received funding from the European Union's Horizon 2020 research and innovation programme under grant agreement No. 101022664

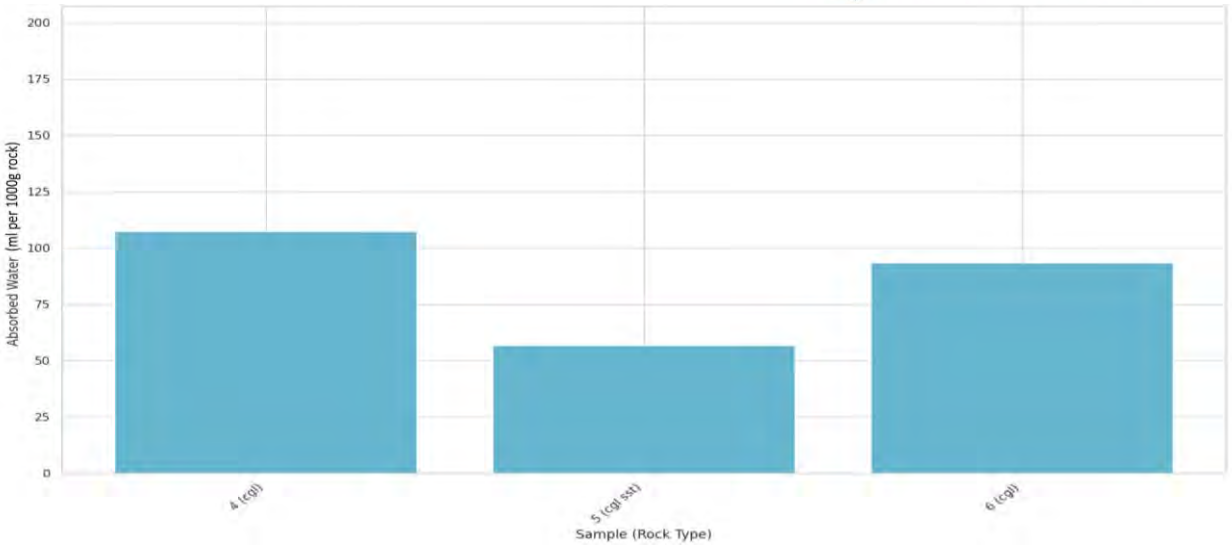

Figure 5.48: Bar chart of the absorbed water (ml) per 1000 g of rock for the examined samples from Region 4 (abbreviations: cgl = conglomerate, cgl sst = conglomeratic sandstone). Complete sample codes: 4_4, 4_5, 4_6.

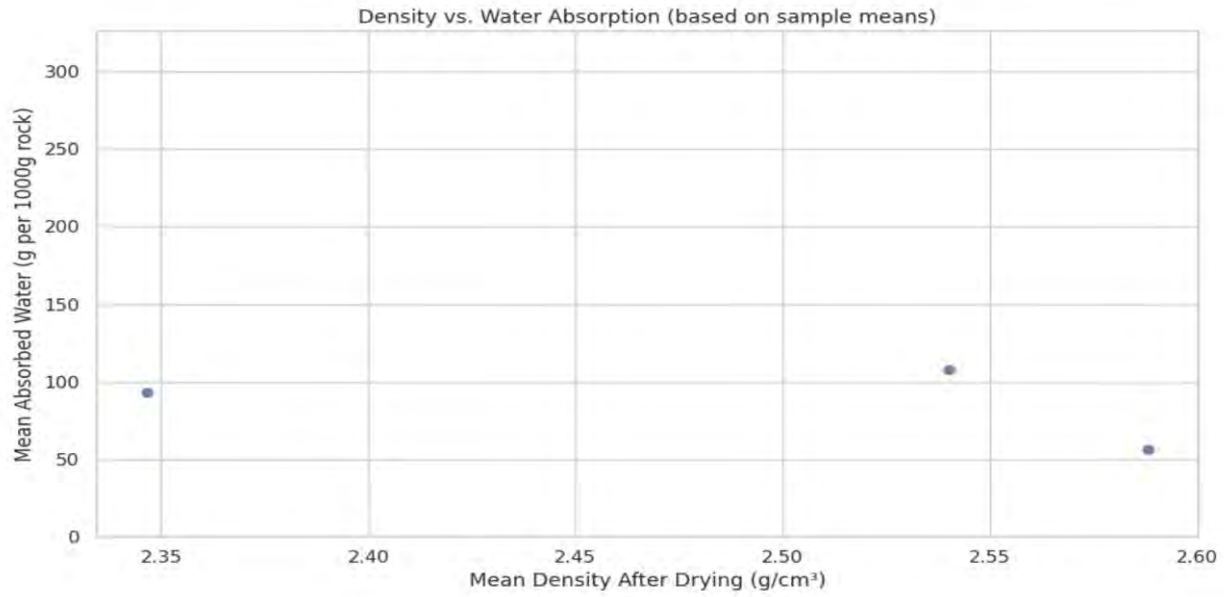

Figure 5.49: Water absorption (ml per 1000g of rock) versus dry density (g/cm³) for samples from Region 4. The x-axis scale is intentionally limited to the observed range of measured densities to enhance visibility and resolution of the data distribution.

The PilotSTRATEGY project has received funding from the European Union's Horizon 2020 research and innovation programme under grant agreement No. 101022664

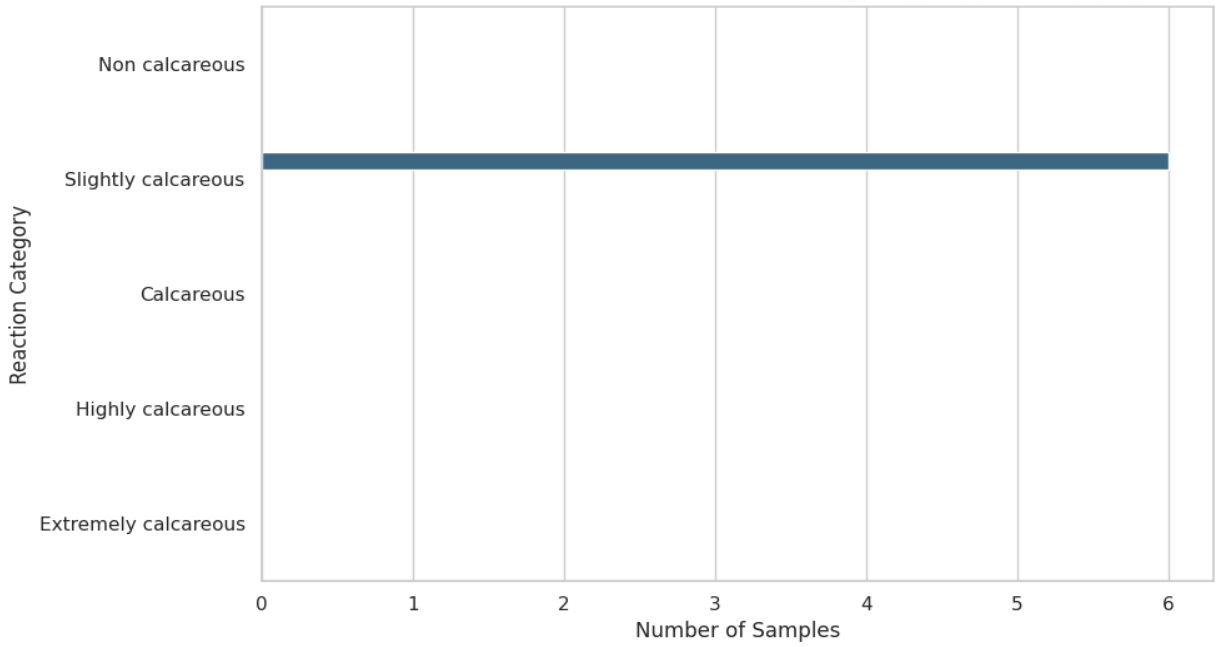

Figure 5.50: Distribution of Region 4 samples after their reaction to hydrochloric acid (HCl). Reaction categorization is after ISO 14689:2017.

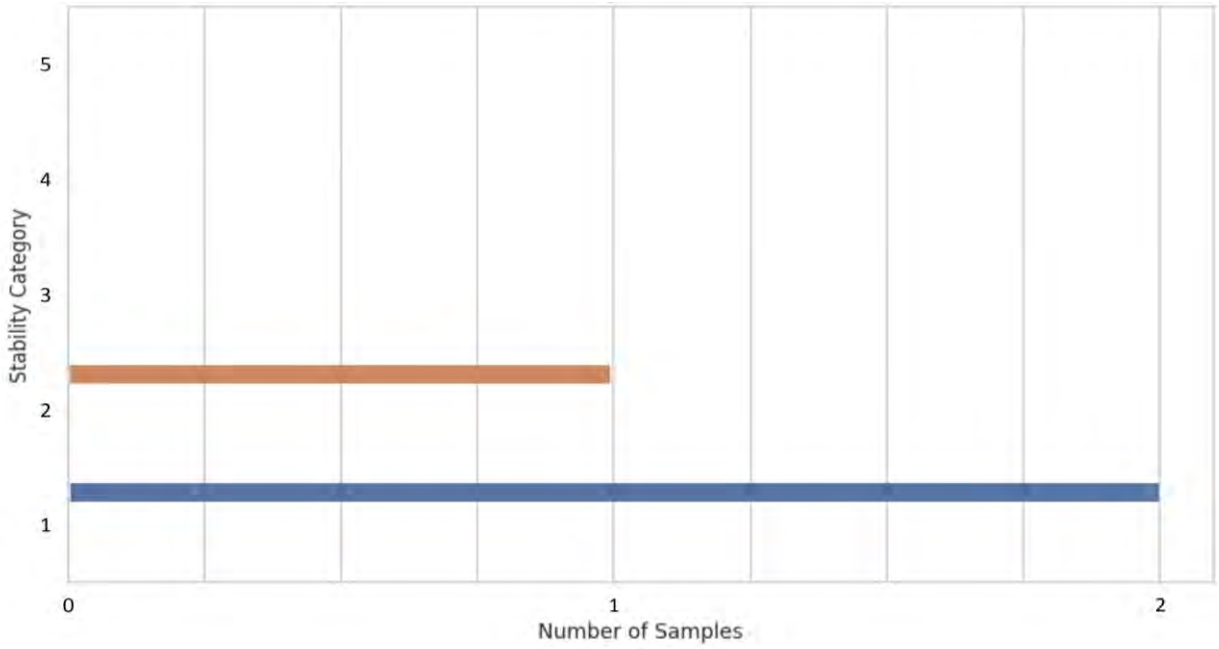

Figure 5.51: Bar chart showing the categorization of the samples from Region 4 after stability grade. Stability in water after 24 hours in ISO 14689:2017 includes the following grades: 1. Stable, 2. Fairly stable: a few fissures are formed, or specimen surface crumbles slightly, 3. Fairly stable: many fissures are formed and broken into small lumps, or

The PilotSTRATEGY project has received funding from the European Union's Horizon 2020 research and innovation programme under grant agreement No. 101022664

specimen surface crumbles highly, 4. Unstable: specimen disintegrates, or nearly the whole specimen surface crumbles, and 5. Unstable: the whole specimen becomes muddy, or disintegrates completely into sand.

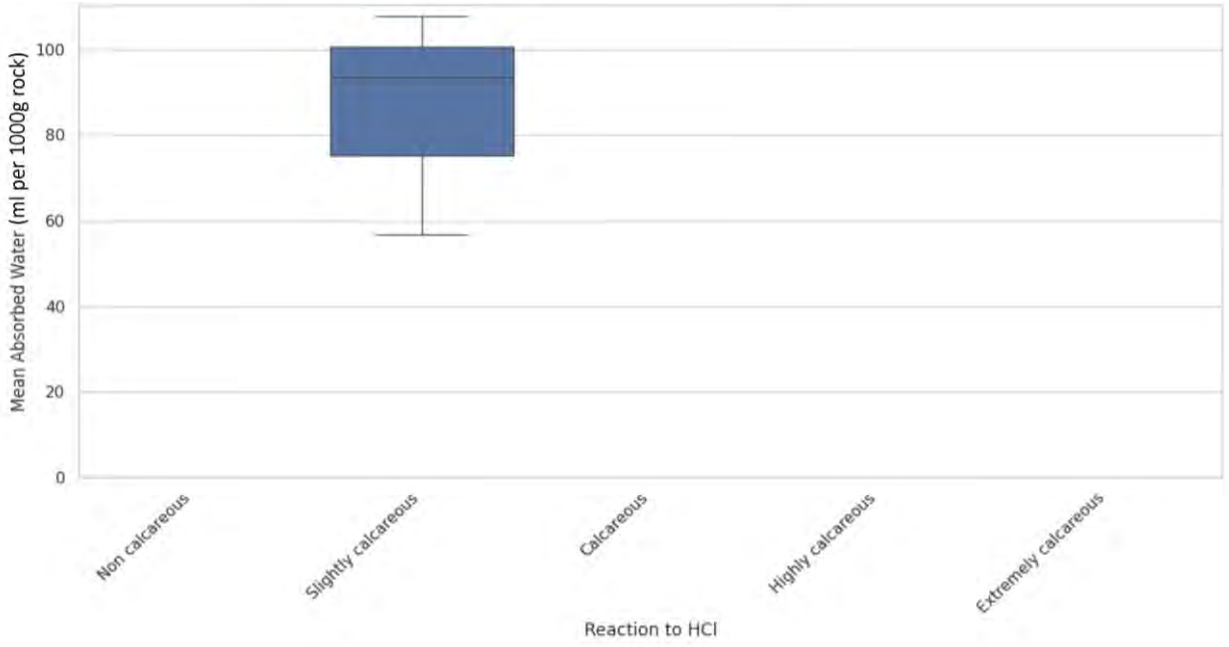

Figure 5.52: Box plot graph of the absorbed water (ml) per 1000g rock for the samples collected from Region 4 versus the rock reaction to HCl categorization after ISO 14689:2017.

The data suggests that for the samples from Region 4, there is no clear correlation between density and water absorption (Figure 5.49). While all samples are slightly calcareous, their water absorption and stability vary. This suggests that other factors, such as the specific pore structure or cementing material within the rock, are more influential on water absorption and stability of the sample, than just its carbonate content or overall density. For example, the higher absorption of sample 4_4 and its stability (Grade 2; Fairly stable) suggests that its porous structure allows for water uptake, which may lead to some disintegration over time (Figure 5.48). Conversely, sample 4_5, which is also slightly calcareous, absorbs much less water and is highly stable (Figure 5.48).

Region 5 is dominated by fine- to coarse-grained sedimentary rocks, including loose conglomerates, well-cemented conglomerates, sand and cobbles, marly sandstone, marl, sandy marl and marly sand (Appendix X). Samples 5_1 (loose conglomerate), as well as samples 5_2 and 5_3 (sand and cobbles) were not tested due to their physical characteristics. The mass change analysis graph shows that the mean weight of the samples remains very consistent before drying, after drying, and after the test (Figure 5.53). Similarly, the density comparison graphs indicate that the mean density of the samples is nearly identical before and after drying, with the values clustering around 2.2 to 2.6 g/cm^3 for most samples (Appendix X, Figure 5.54).

The water absorption efficiency graph reveals a wide range of values among the samples. The lowest value is 32 ml/1000g of rock for sample 5_1_1 and the highest is 477 ml/1000g for sample 5_6_1 (Appendix X, Figure 5.55). Most of the samples are characterized as “Slightly calcareous” (Figure 5.57), while stability

The PilotSTRATEGY project has received funding from the European Union’s Horizon 2020 research and innovation programme under grant agreement No. 101022664

varies significantly (Figure 5.57, Figure 5.58). Samples 5_1_1 (well cemented conglomerate) and 5_5 (marly sandstone) are stable (Grade 1), samples 5_4 (marly sandstone) and 5_6_2 (sandy marl) are fairly stable (Grade 2), samples 5_6_1 (marl) and 5_6_3b (marl) are unstable (Grade 4: specimen disintegrates, or nearly the whole specimen surface crumbles, and sample 5_6_3a (marly sand) is unstable (Grade 5: the whole specimen becomes muddy, or disintegrates completely into sand).

The density versus water absorption graph suggests a weak negative trend (Figure 5.56), while the carbonate content versus water absorption box plots graph shows that "Slightly calcareous" samples have a wide range of water absorption, with a median that is higher than this of the "Calcareous" sample 5_4 (Figure 5.59). The data for Region 5 suggests that the physical properties of the samples, particularly their water absorption and stability, are not determined by a single factor but by a complex interplay of their composition and structure. This is the result of their diverse lithology.

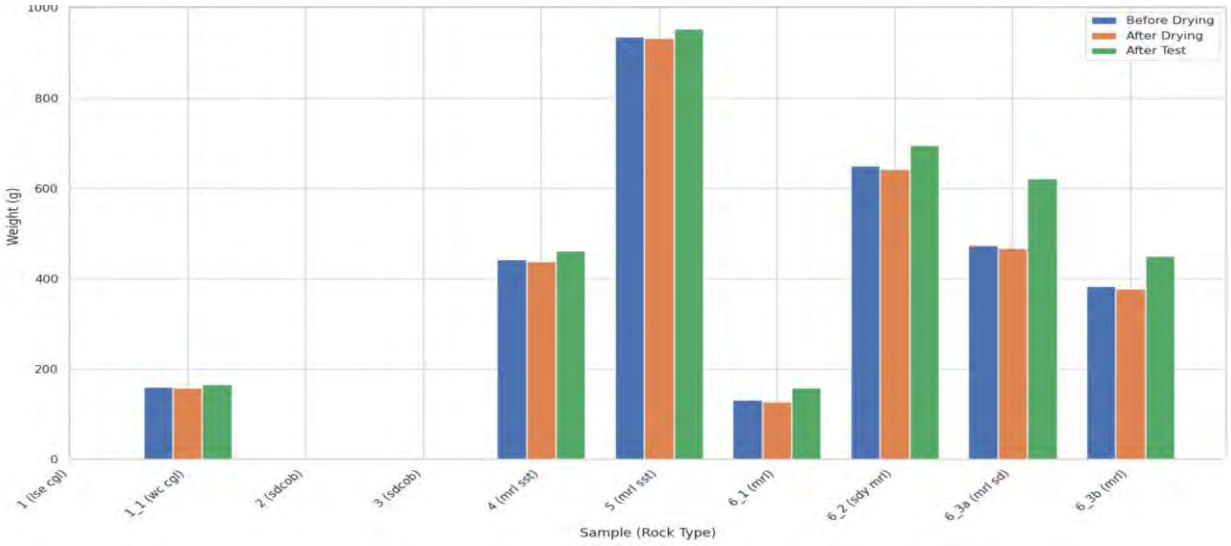

Figure 5.53: Bar chart of the mass change analysis for the examined samples from Region 5 (abbreviations: lse cgl = loose conglomerate, wc cgl = well-cemented conglomerate, sd cob = sand and cobbles, mrl sst = marl sandstone, mrl = marl, sdy mrl = sandy marl, mrl sd = marly sand). Complete sample codes: 5_1, 5_1_1, 5_2, 5_3, 5_4, 5_5, 5_6_1, 5_6_2, 5_6_3a, 5_6_3b.

The density versus water absorption plot may indicate a general tendency for lower-density samples to show higher water uptake, consistent with increased porosity, although the relationship is weak and should be interpreted cautiously (Figure 5.56). The wide interquartile range of the “Slightly calcareous” samples in Figure 5.59 is revealing of the way in which the specific mineral matrix and cementation of a rock, may affect the ability to absorb water. Furthermore, the stability data, in conjunction with the water absorption data, provides a valuable insight. The fact that samples with high water absorption (e.g. sample 5_4) can have a stability grade of 2 (fairly stable), while others with lower absorption (e.g. sample 5_1_1) are stable (Grade 1), highlights that the capacity to absorb water is a significant factor in the stability of the rock. Water penetration and excess absorption may weaken the internal structure of the rock, leading to disintegration like in the case of sample 5_6_1 (Figure 5.58). The samples with very low water

The PilotSTRATEGY project has received funding from the European Union’s Horizon 2020 research and innovation programme under grant agreement No. 101022664

absorption are, as expected, highly stable, as they are not subject to the same level of water-induced stress.

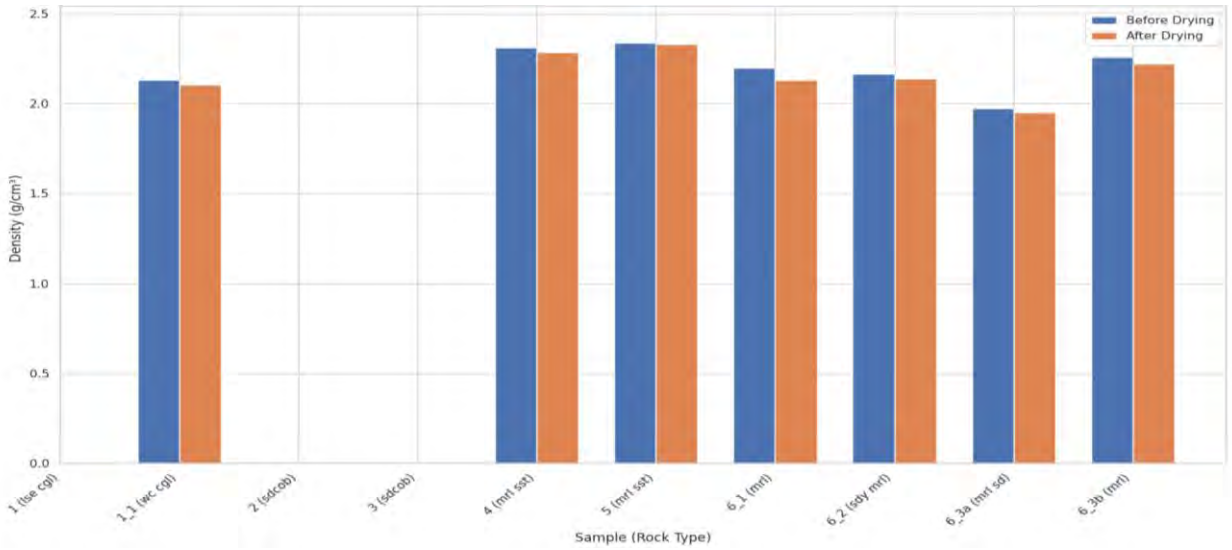

Figure 5.54: Bar chart of the density comparison analysis for the examined samples from Region 5 (abbreviations: lse cgl = loose conglomerate, wc cgl = well-cemented conglomerate, sd cob = sand and cobbles, mrl sst = marl sandstone, mrl = marl, sdy mrl = sandy marl, mrl sd = marly sand). Complete sample codes: 5_1, 5_1_1, 5_2, 5_3, 5_4, 5_5, 5_6_1, 5_6_2, 5_6_3a, 5_6_3b.

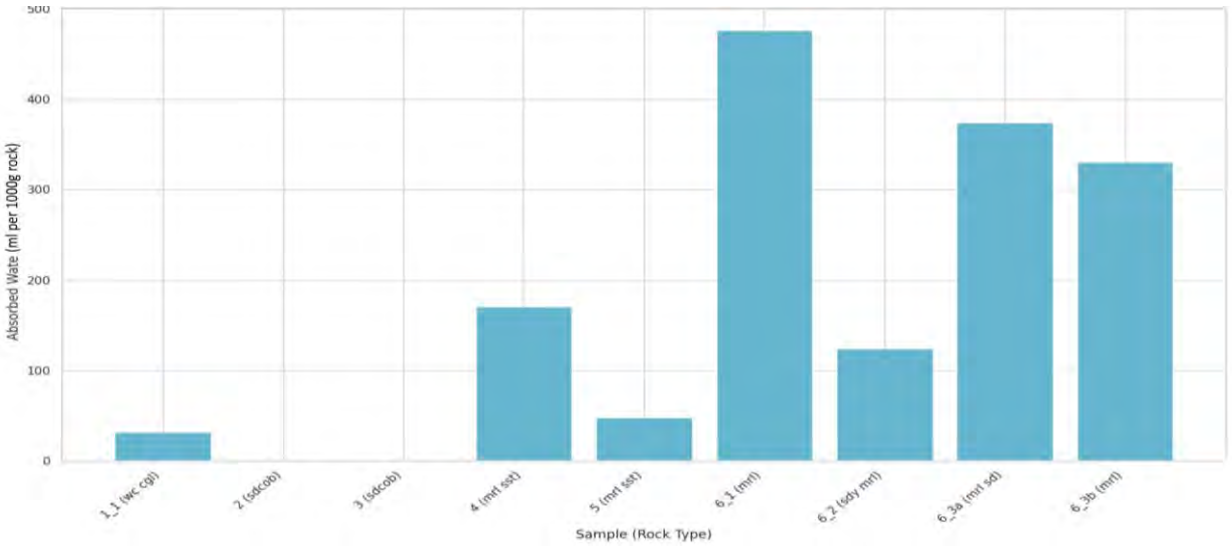

Figure 5.55: Bar chart of the absorbed water (ml) per 1000 g of rock for the examined samples from Region 5 (abbreviations: lse cgl = loose conglomerate, wc cgl = well-cemented conglomerate, sd cob = sand and cobbles, mrl sst = marl sandstone, mrl = marl, sdy mrl = sandy marl, mrl sd = marly sand). Complete sample codes: 5_1, 5_1_1, 5_2, 5_3, 5_4, 5_5, 5_6_1, 5_6_2, 5_6_3a, 5_6_3b.

The PilotSTRATEGY project has received funding from the European Union's Horizon 2020 research and innovation programme under grant agreement No. 101022664

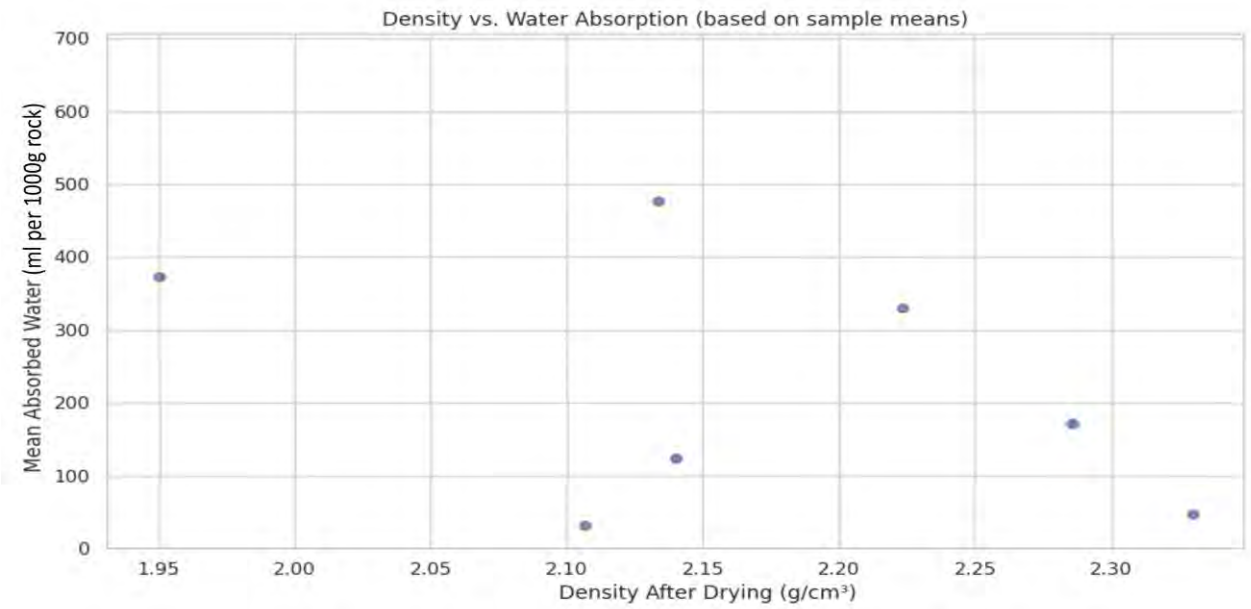

Figure 5.56: Water absorption (ml per 1000g of rock) versus dry density (g/cm³) for samples from Region 5. The x-axis scale is intentionally limited to the observed range of measured densities to enhance visibility and resolution of the data distribution.

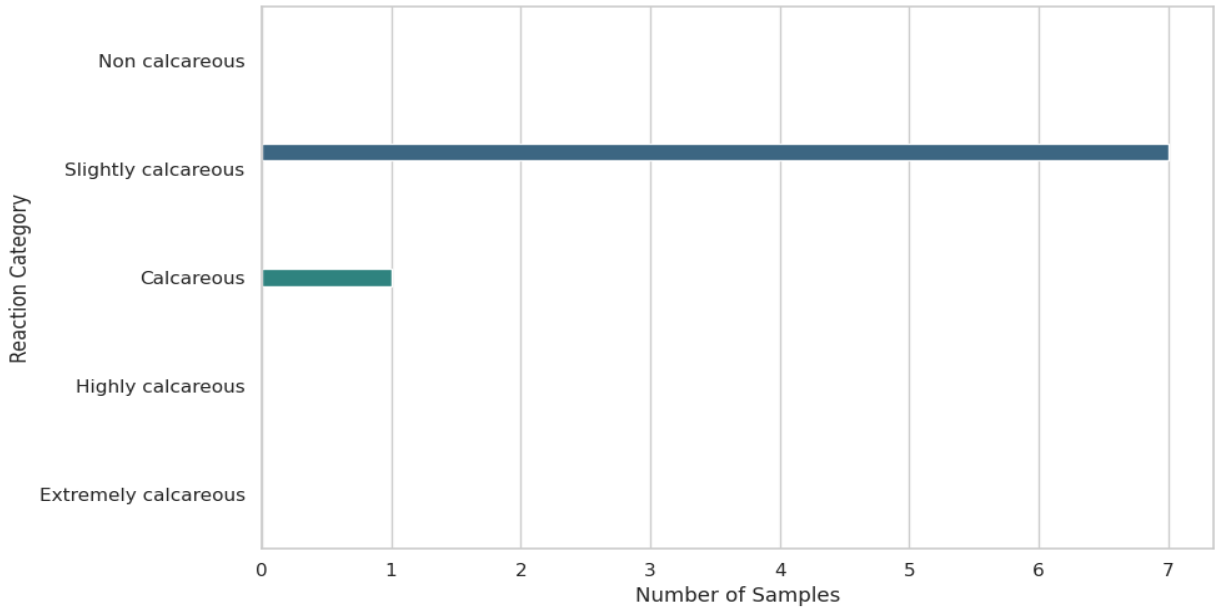

Figure 5.57: Distribution of Region 5 samples after their reaction to hydrochloric acid (HCl). Reaction categorization is after ISO 14689:2017.

The PilotSTRATEGY project has received funding from the European Union's Horizon 2020 research and innovation programme under grant agreement No. 101022664

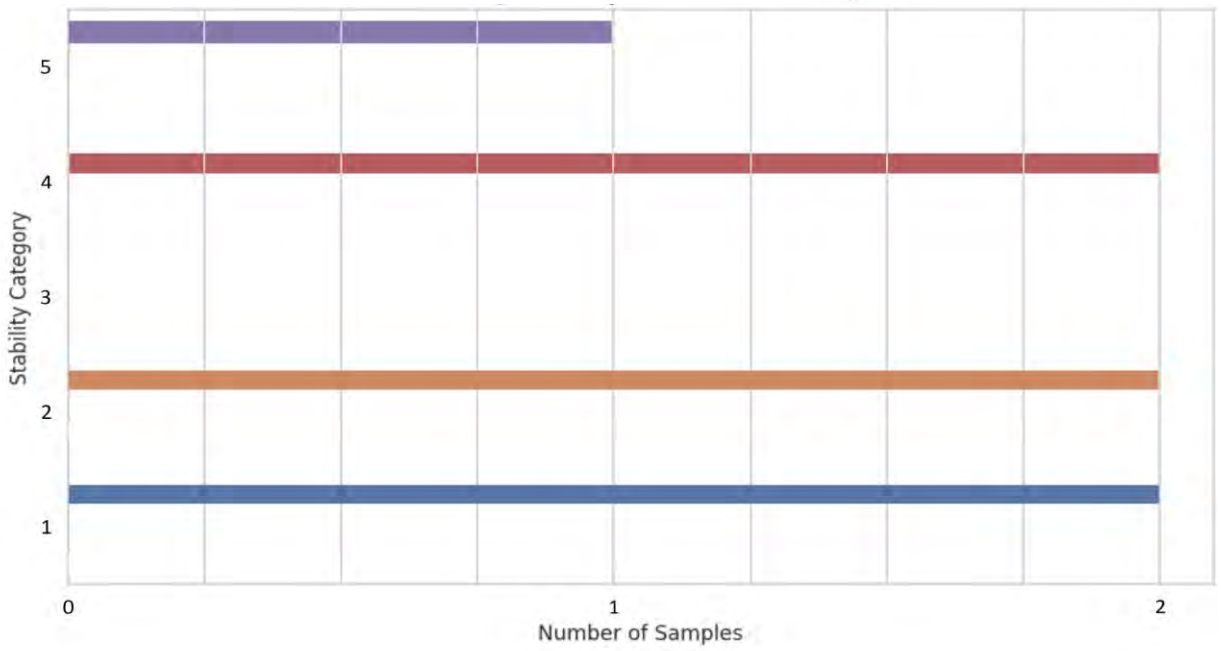

Figure 5.58: Bar chart showing the categorization of the samples from Region 5 after stability grade. Stability in water after 24 hours in ISO 14689:2017 includes the following grades: 1. Stable, 2. Fairly stable: a few fissures are formed, or specimen surface crumbles slightly, 3. Fairly stable: many fissures are formed and broken into small lumps, or specimen surface crumbles highly, 4. Unstable: specimen disintegrates, or nearly the whole specimen surface crumbles, and 5. Unstable: the whole specimen becomes muddy, or disintegrates completely into sand.

The samples from Region 6 are composed of two distinct sedimentary lithologies, sandstones and marly sandstones, which exhibit clearly different physical properties (Appendix X). The marly sandstones are less dense and significantly more absorbent than the sandstones. A critical finding for this region is the presence of both stable and unstable samples, with a direct correlation observed between the rock type and its physical integrity after water immersion.

Mass change analysis shows that the weight of the samples remains very consistent before, during, and after testing, indicating they are not significantly altered by the procedures (Figure 5.60). The density comparison plot shows that the sandstones (sst) are denser, clustering around 2.4-2.5 g/cm³, while the marly sandstones (mrl sst) are consistently less dense, with values around 2.2 g/cm³ (Appendix X, Figure 5.61). The mass change plot reflects this, showing a much greater weight gain after immersion for the marly sandstones compared to the sandstones (Figure 5.60).

The water absorption efficiency plot provides a clear quantitative distinction. The marly sandstones show restricted water absorption, while the sandstones are more absorbent, resulting to uptakes up to 541 ml/1000g of rock (Figure 5.62). The density versus water absorption correlation plot indicates a cluster representing a high-density/high-absorption group (sandstones) and another group of low-density/low-absorption group (marly sandstones) (Figure 5.63). The reaction to acid plot shows that all samples are “Slightly calcareous”, whereas all samples are classified as stable (Grade 1) (Figure 5.64, Figure 5.65).

The PilotSTRATEGY project has received funding from the European Union’s Horizon 2020 research and innovation programme under grant agreement No. 101022664

The general inverse relationship where lower density corresponds to higher water absorption is expected, as lower density often implies higher porosity. However, this trend is not always straightforward, as seen in the data for Region 6 samples. This implies that density alone is not a perfect predictor of water absorption, and the geometry of the pore spaces, whether they are interconnected or isolated, plays a more significant role.

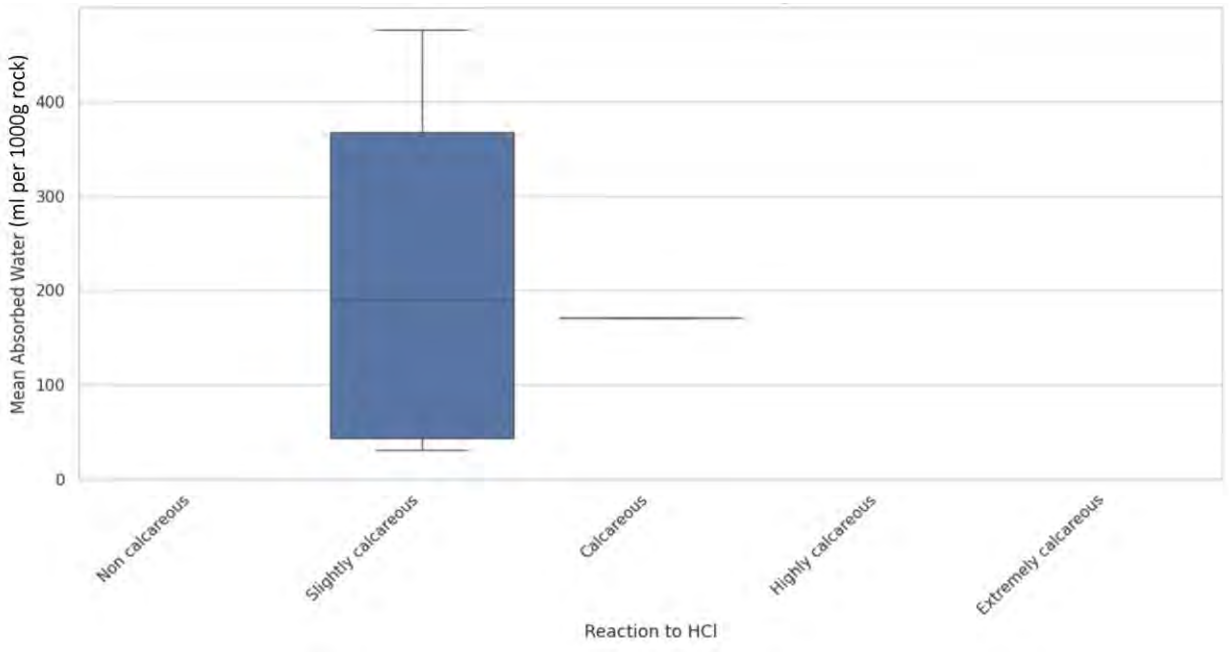

Figure 5.59: Box plot graph of the absorbed water (ml) per 1000g rock for the samples collected from Region 5 versus the rock reaction to HCl categorization after ISO 14689:2017.

The data for carbonate content vs. water absorption also shows a nuanced relationship (Figure 5.66). The varying water absorption among the slightly calcareous samples further supports that other factors like grain size are equally, if not more, influential on water absorption. A direct and critical relationship is observed between water absorption and stability. The majority of samples, particularly all those from Region 6, have low water absorption and are classified as very stable (Grade 1). This reinforces that the resistance of a rock to water uptake is a key factor in its durability and resistance to degradation.

Region 7 is dominated by ultramafic lithologies, mainly serpentinites and a serpentinized harzburgite, accompanied by sedimentary rocks including marly sandstone and different types of conglomerates (Appendix X). The serpentinites and the harzburgite are consistently non-calcareous and dense, while the sedimentary rocks show greater variability in density, porosity, and water absorption. All samples were observed to be completely stable (Grade 1).

In terms of physical properties, the serpentinized harzburgite (Sample 7_7) has a mean density of ~2.3 g/cm³ and a mean mass of ~365 g before drying. Both mass and density remain essentially unchanged after drying and water immersion, confirming its very low water content and lack of porosity. The

The PilotSTRATEGY project has received funding from the European Union's Horizon 2020 research and innovation programme under grant agreement No. 101022664

serpentinite samples (7_1–7_6) behave similarly, with densities between 1.85 and 2.33 g/cm³ and no measurable water absorption. The large standard deviation bars in the mass data reflect differences in sample size rather than inconsistencies in rock behavior, since density values are highly consistent (Figure 5.67, Figure 5.68).

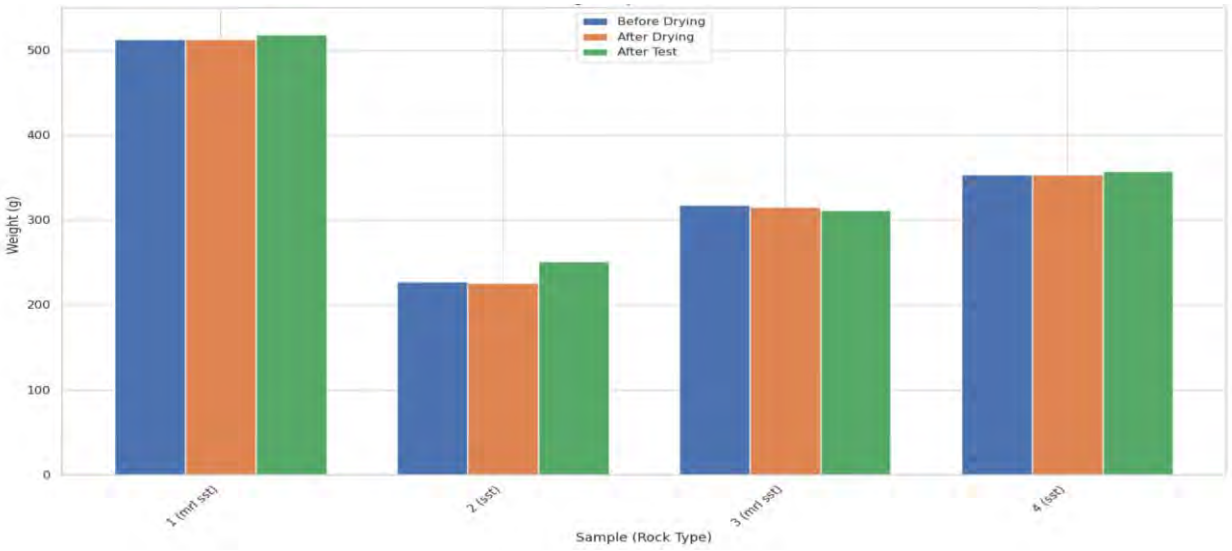

Figure 5.60: Bar chart of the mass change analysis for the examined samples from Region 6 (abbreviations: mrl sst = marl sandstone, sst = sandstone). Complete sample codes: 6_1, 6_2, 6_3, 6_4.

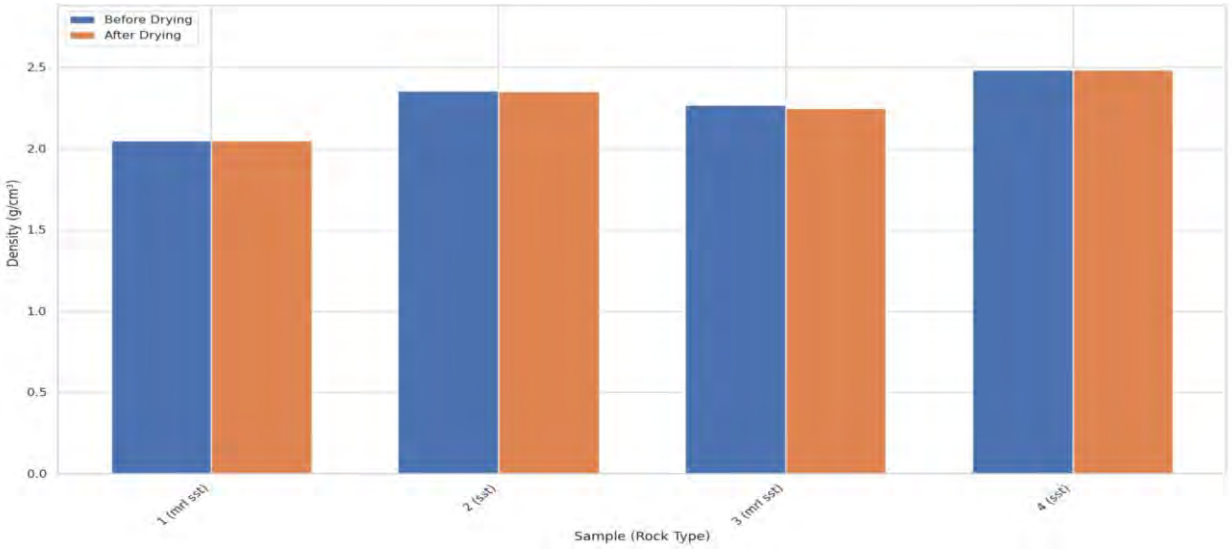

Figure 5.61: Bar chart of the density comparison analysis for the examined samples from Region 6 (abbreviations: mrl sst = marl sandstone, sst = sandstone). Complete sample codes: 6_1, 6_2, 6_3, 6_4.

The PilotSTRATEGY project has received funding from the European Union's Horizon 2020 research and innovation programme under grant agreement No. 101022664

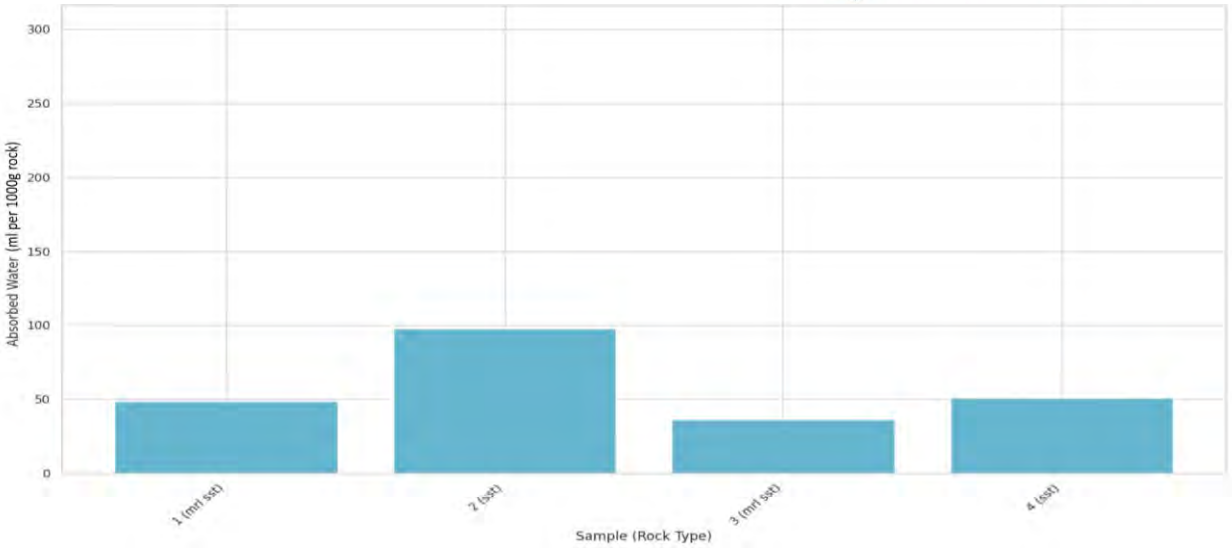

Figure 5.62: Bar chart of the absorbed water (ml) per 1000 g of rock for the examined samples from Region 6 (abbreviations: mrl sst = marl sandstone, sst = sandstone). Complete sample codes: 6_1, 6_2, 6_3, 6_4.

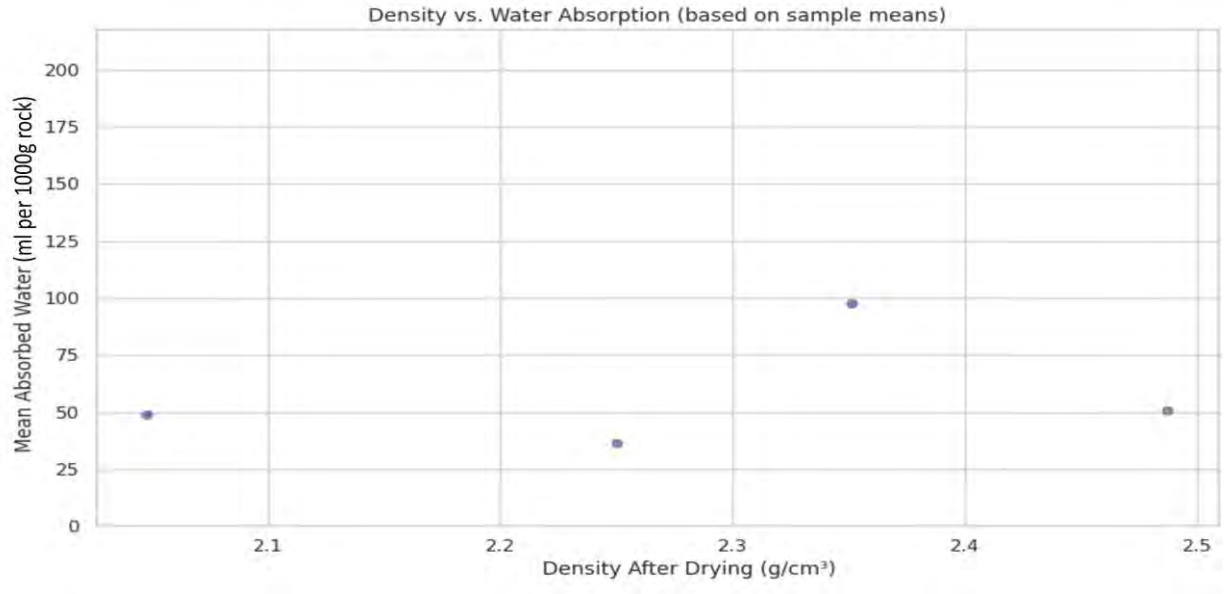

Figure 5.63: Water absorption (ml per 1000g of rock) versus dry density (g/cm³) for samples from Region 6. The x-axis scale is intentionally limited to the observed range of measured densities to enhance visibility and resolution of the data distribution.

The PilotSTRATEGY project has received funding from the European Union's Horizon 2020 research and innovation programme under grant agreement No. 101022664

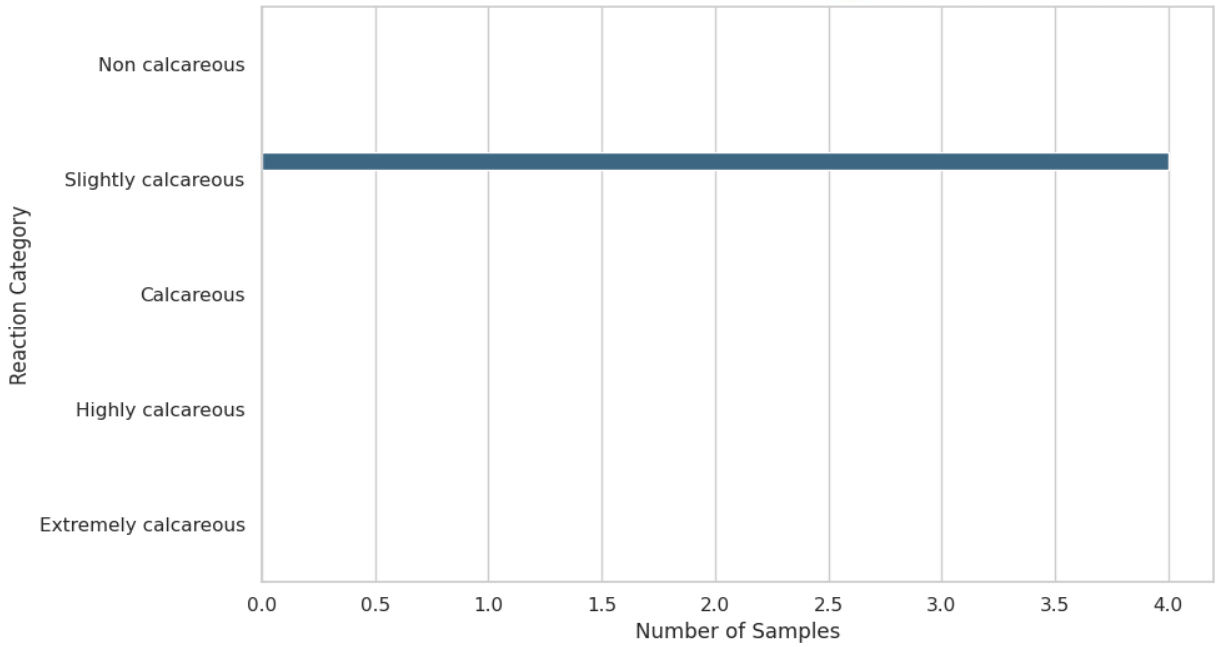

Figure 5.64: Distribution of Region 6 samples after their reaction to hydrochloric acid (HCl). Reaction categorization is after ISO 14689:2017.

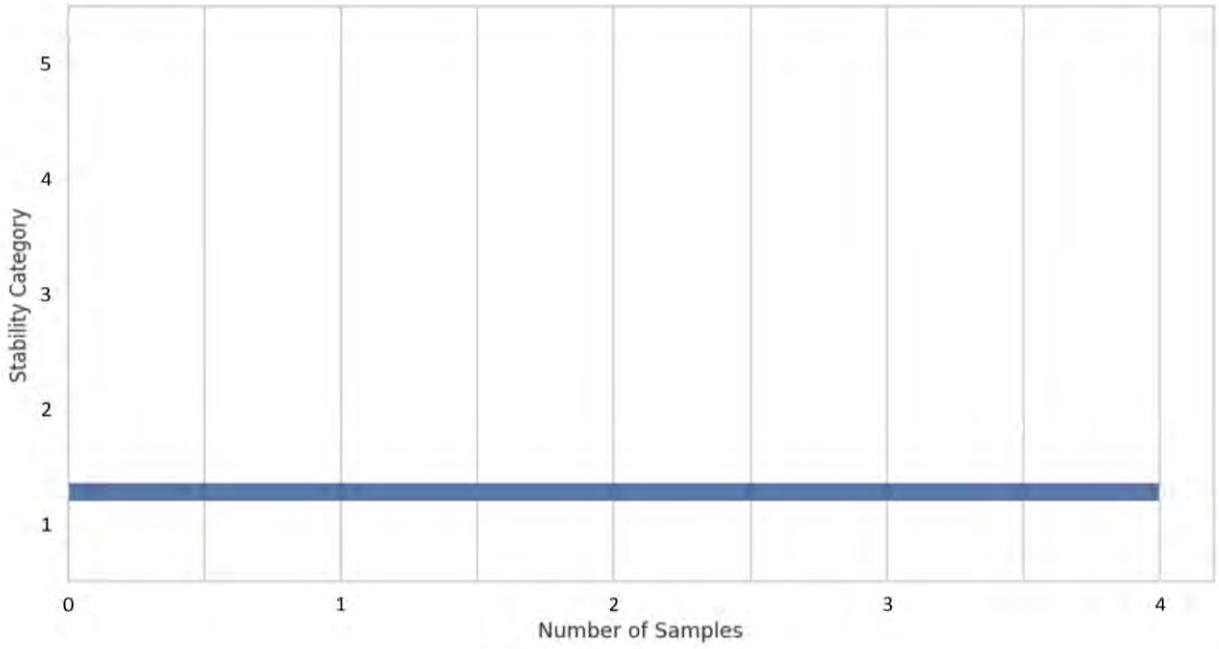

Figure 5.65: Bar chart showing the categorization of the samples from Region 6 after stability grade. Stability in water after 24 hours in ISO 14689:2017 includes the following grades: 1. Stable, 2. Fairly stable: a few fissures are formed, or specimen surface crumbles slightly, 3. Fairly stable: many fissures are formed and broken into small lumps, or

The PilotSTRATEGY project has received funding from the European Union's Horizon 2020 research and innovation programme under grant agreement No. 101022664

specimen surface crumbles highly, 4. Unstable: specimen disintegrates, or nearly the whole specimen surface crumbles, and 5. Unstable: the whole specimen becomes muddy, or disintegrates completely into sand.

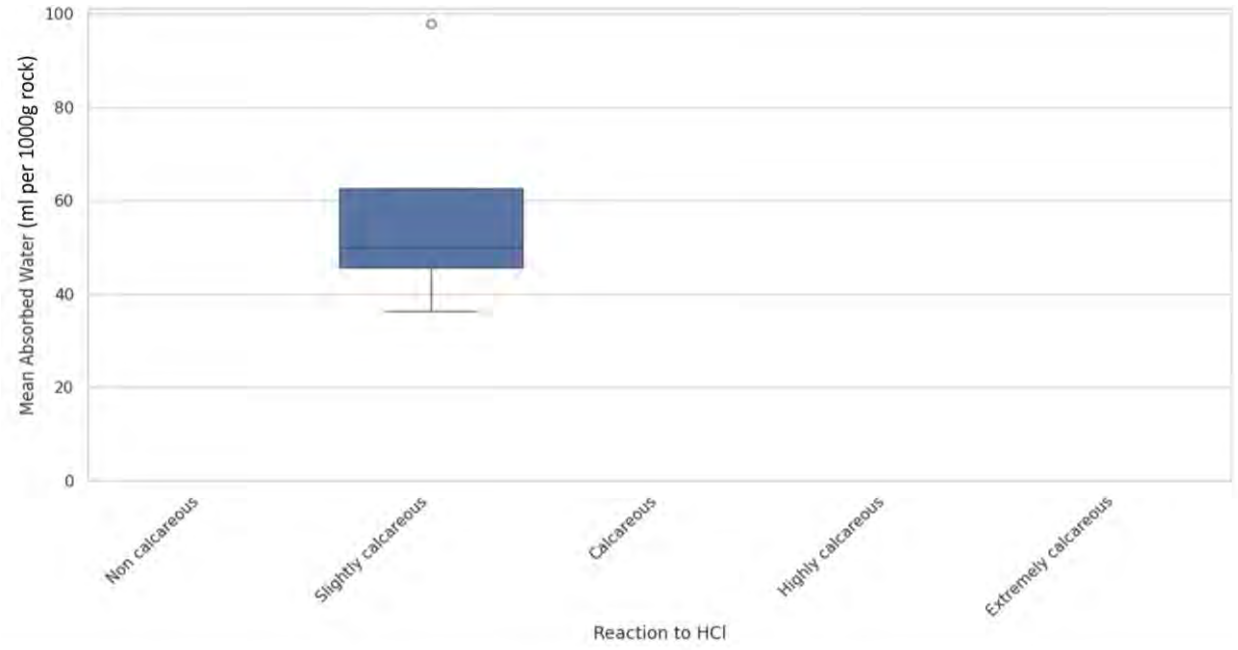

Figure 5.66: Box plot graph of the absorbed water (ml) per 1000g rock for the samples collected from Region 6 versus the rock reaction to HCl categorization after ISO 14689:2017.

The interaction with water is the key factor differentiating the lithologies. The ultramafic samples (serpentinites and harzburgite) absorbed negligible amounts of water, close to 0 g per 1000 g of rock, the lowest absorption values of all tested samples (Appendix X, Figure 5.69). In contrast, the sedimentary rocks show variable absorption: the marly sandstone (7_8) absorbed only minor amounts of water, while the conglomerates absorbed considerably more (Sample 7_8). Sample 7_8_1, a bedded conglomerate, absorbed 253 ml (348 ml per 1000 g of rock), making it the most porous and absorbent in the dataset, whereas sample 7_9 and the ophiolitic conglomerate (7_10) showed lower but still notable absorption values of 72 ml and 64 ml per 1000 g respectively (Appendix X).

The density versus water absorption correlation supports this distinction, with the serpentinized harzburgite plotting at the low end (dense and non-absorptive) and the conglomerates at higher absorption values (Figure 5.70). Taken together, the data underline the durability of the ultramafic rocks in this region, while highlighting the greater variability and porosity of the sedimentary lithologies. Chemically, most samples from Region 7 are non-calcareous, consistent with their ultramafic origins (Figure 5.71). Three sedimentary samples (marly sandstone and conglomerates) are slightly calcareous, which may contribute to their higher water absorption compared to the ultramafic rocks (Figure 5.71).

The PilotSTRATEGY project has received funding from the European Union's Horizon 2020 research and innovation programme under grant agreement No. 101022664

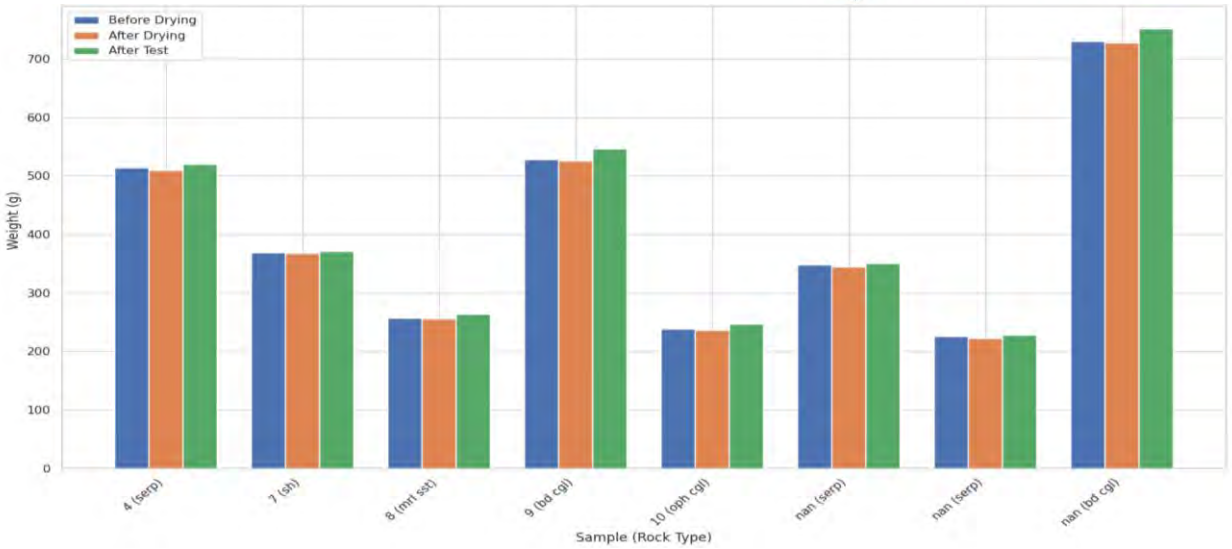

Figure 5.67: Bar chart of the mass change analysis for the examined samples from Region 7 (abbreviations: serp = serpentinite, sh = serpentinized hurzburgite, mrl sst = marl sandstone, bd cgl = bedded conglomerate, oph cgl = ophiolitic conglomerate). Complete sample codes: 7_1-3 (nan (serp), 7_4, 7_5-6 (nan (serp), 7_7, 7_8, 7_8_1 (nan (bd cgl), 7_9, 7_10.

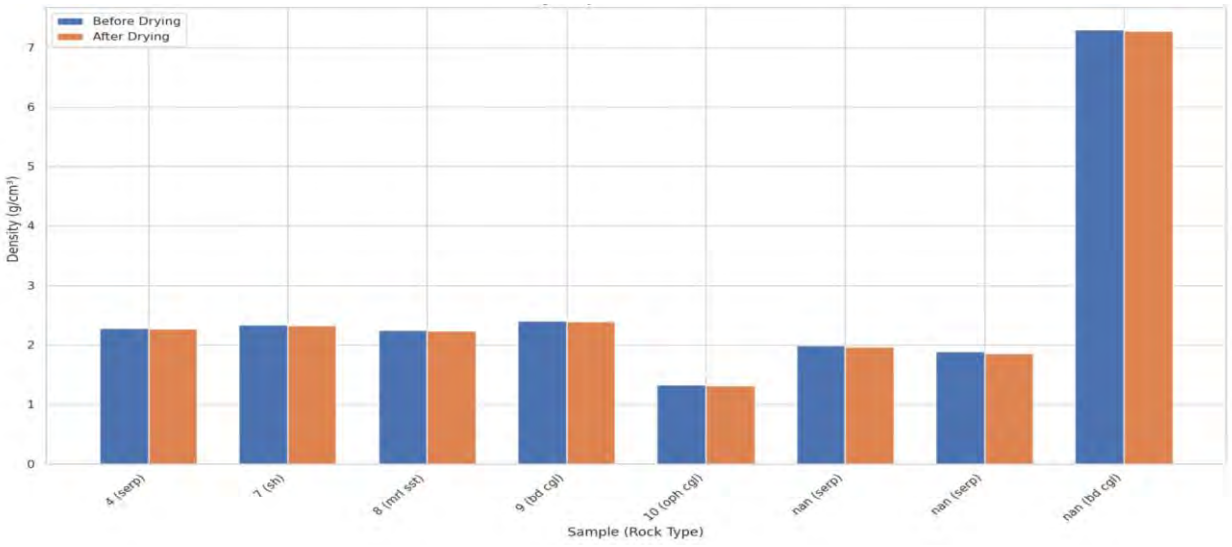

Figure 5.68: Bar chart of the density comparison analysis for the examined samples from Region 7 (abbreviations: serp = serpentinite, sh = serpentinized hurzburgite, mrl sst = marl sandstone, bd cgl = bedded conglomerate, oph cgl = ophiolitic conglomerate). Complete sample codes: 7_1-3 (nan (serp), 7_4, 7_5-6 (nan (serp), 7_7, 7_8, 7_8_1 (nan (bd cgl), 7_9, 7_10.

The PilotSTRATEGY project has received funding from the European Union's Horizon 2020 research and innovation programme under grant agreement No. 101022664

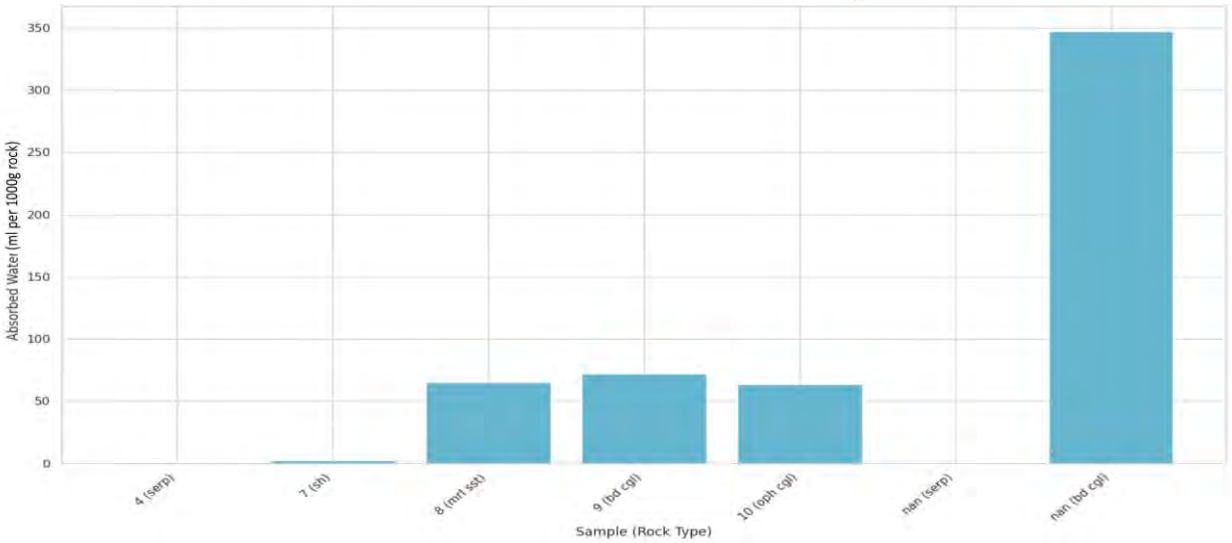

Figure 5.69: Bar chart of the absorbed water (ml) per 1000 g of rock for the examined samples from Region 7 (abbreviations: serp = serpentinite, sh = serpentinized hurzburgite, mrl sst = marl sandstone, bd cgl = bedded conglomerate, oph cgl = ophiolitic conglomerate). Complete sample codes: 7_1-3 (nan (serp), 7_4, 7_5-6 (nan (serp), 7_7, 7_8, 7_8_1 (nan (bd cgl), 7_9, 7_10.

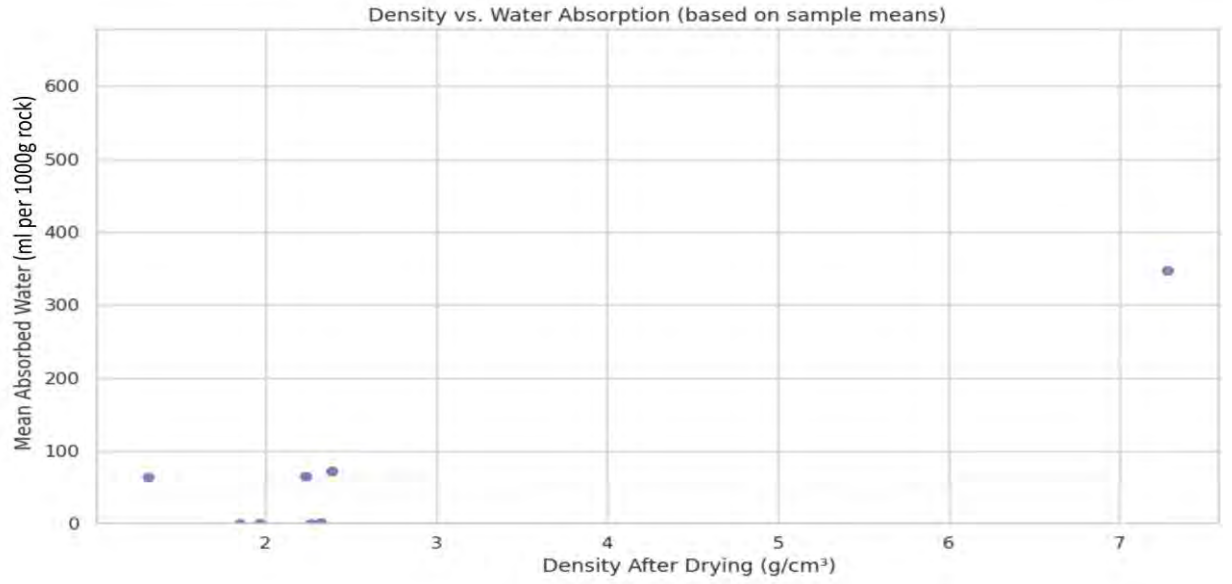

Figure 5.70: Water absorption (ml per 1000g of rock) versus dry density (g/cm³) for samples from Region 7. The x-axis scale is intentionally limited to the observed range of measured densities to enhance visibility and resolution of the data distribution.

The PilotSTRATEGY project has received funding from the European Union's Horizon 2020 research and innovation programme under grant agreement No. 101022664

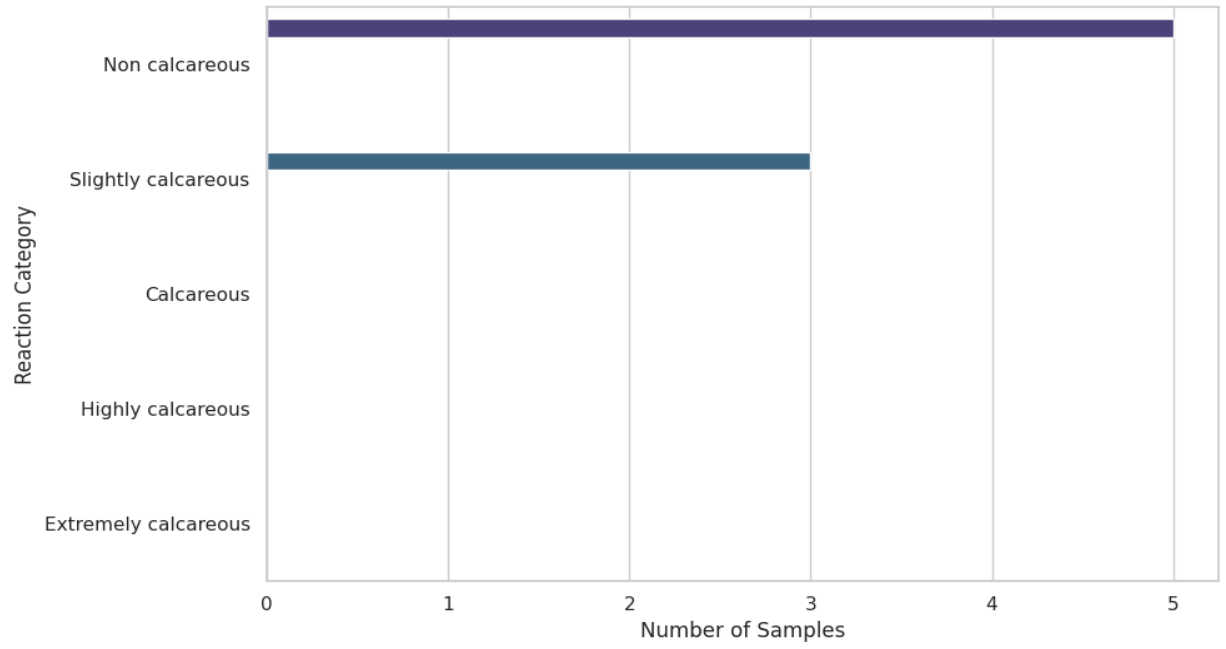

Figure 5.71: Distribution of Region 7 samples after their reaction to hydrochloric acid (HCl). Reaction categorization is after ISO 14689:2017.

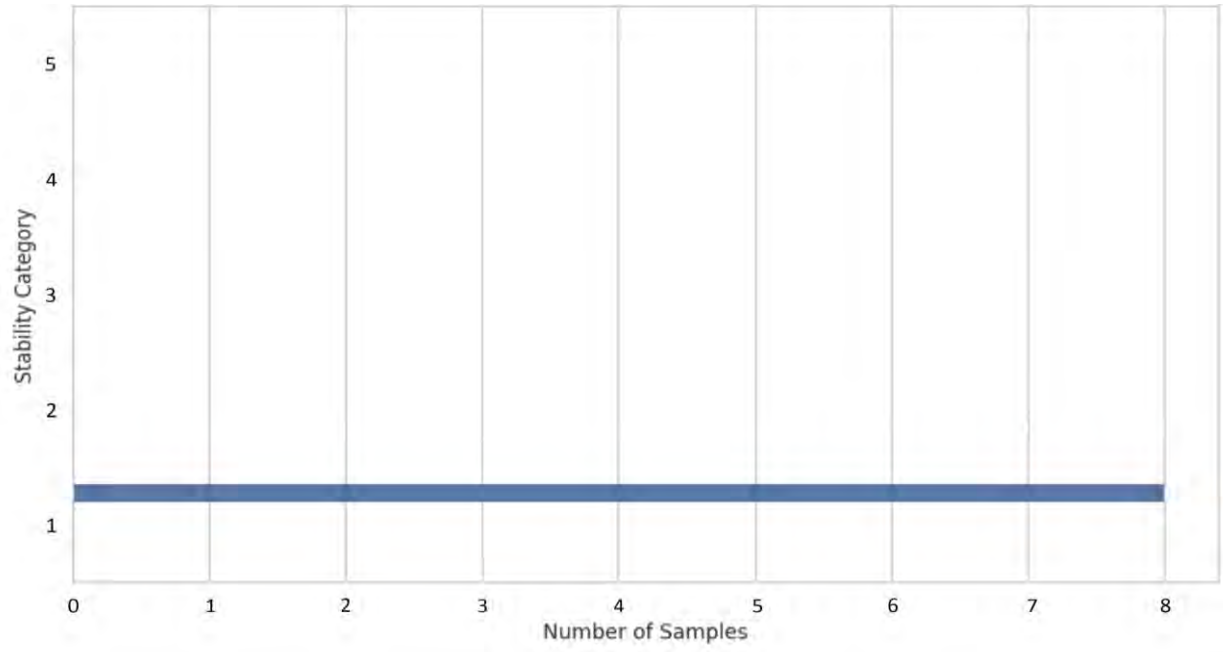

Figure 5.72: Bar chart showing the categorization of the samples from Region 7 after stability grade. Stability in water after 24 hours in ISO 14689:2017 includes the following grades: 1. Stable, 2. Fairly stable: a few fissures are formed, or specimen surface crumbles slightly, 3. Fairly stable: many fissures are formed and broken into small lumps, or

The PilotSTRATEGY project has received funding from the European Union's Horizon 2020 research and innovation programme under grant agreement No. 101022664

specimen surface crumbles highly, 4. Unstable: specimen disintegrates, or nearly the whole specimen surface crumbles, and 5. Unstable: the whole specimen becomes muddy, or disintegrates completely into sand.

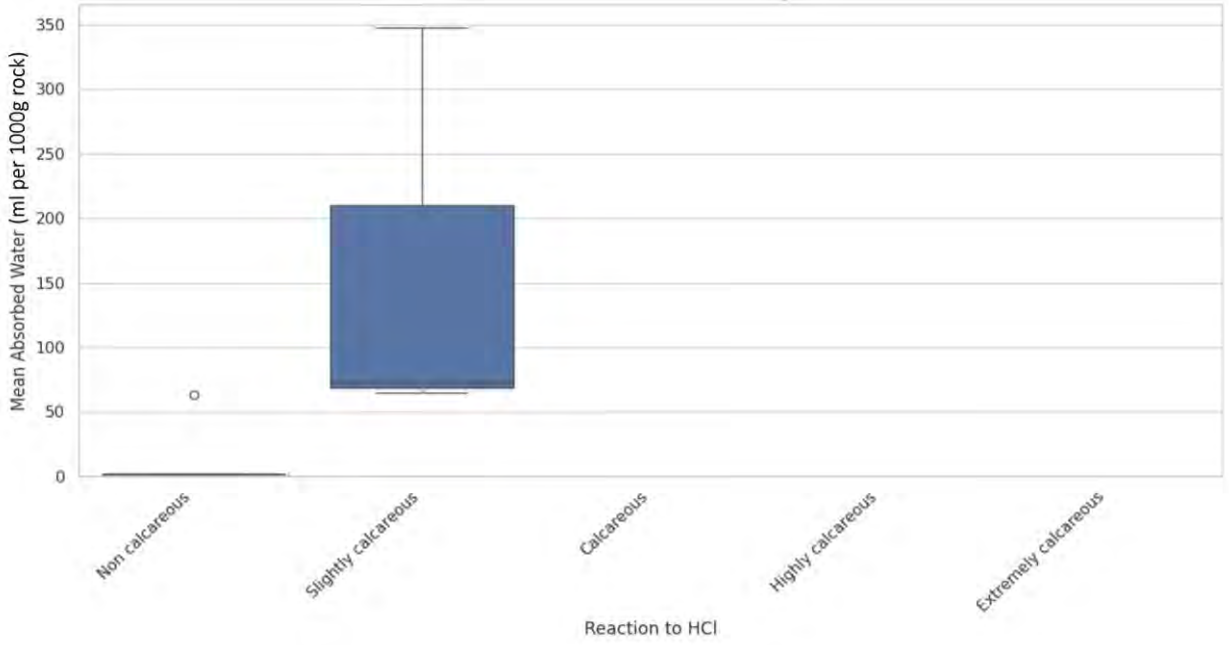

Figure 5.73: Box plot graph of the absorbed water (ml) per 1000g rock for the samples collected from Region 7 versus the rock reaction to HCl categorization after ISO 14689:2017.

Stability testing indicates that all Region 7 samples fall into stability Grade 1, meaning they remained intact and did not disintegrate during immersion (Figure 5.72). This stability, especially in the ultramafic rocks, is directly linked to their dense fabric and negligible water absorption. Even in the case of highly absorbent conglomerates, the cementation appears sufficient to prevent physical breakdown under saturation.

The box plot graph of the absorbed water (ml) per 1000g rock for the samples collected from Region 7 versus the rock reaction to HCl is indicative of varying amounts of absorbed water by the slightly calcareous sedimentary rocks and of the zero water absorption of the non-calcareous ultramafic lithologies (Figure 5.73).

Region 8 consists mostly of sandstones (both calcareous and slightly calcareous), with fewer conglomerates, conglomeratic sandstones, marly sandstones, marl, and sandy marl (Appendix X). Most specimens are carbonate-bearing, and their densities split into a lighter sand-dominated cluster (~1.8–2.6 g/cm³) and a denser marly/carbonate-rich group (~3.1–3.7 g/cm³) (Appendix X). Calcareous sandstones show low absorption and stay stable, while marly/clay-rich units take up far more water and may weaken. Overall, drying is repeatable, absorption tracks lithology, and only one sample shows strong degradation after 24 hours.

The mass-change analysis graph shows that “before drying” and “after drying” are almost indistinguishable for every sample, so the drying step was repeatable (Figure 5.74). The green “after test”

The PilotSTRATEGY project has received funding from the European Union’s Horizon 2020 research and innovation programme under grant agreement No. 101022664

bars rise by visibly different amounts among rocks: marl and clay-rich specimens elevate the most, while clean calcareous sandstones barely change (Figure 5.74). In the density comparison, blue and orange bars sit nearly on top of each other, confirming that drying had negligible effect on measured density (Figure 5.75). The plot separates into two visual clusters: lower-density sandier rocks (down near ~1.8–2.0 g/cm³, e.g., the sandy marl 8_17) and denser, carbonate- or fine-rich rocks (around ~3.1–3.7 g/cm³, the marl sandstone 8_14 is the upper extreme at ~3.7) (Appendix X, Figure 5.75). This compositional split foreshadows how they uptake water. The water-absorption plot makes the contrast explicit (Figure 5.76). Most sandstone absorb restricted amounts of water, while marly textures show more enrich profiles (Figure 5.76). Sample 8_4 (marly sandstone) absorbs roughly 500 g per 1000 g rock. A second group of elevated absorption scores includes the slightly calcareous sandstone 8_16 (~250 ml/1000g of rock) and the slightly calcareous conglomerate 8_5 (~240 ml/1000g of rock). At the opposite end, sample 8_10 (calcareous sandstone) absorbed ~30 ml/1000g of rock, illustrating how clean carbonate cement can suppress uptake (Figure 5.76).

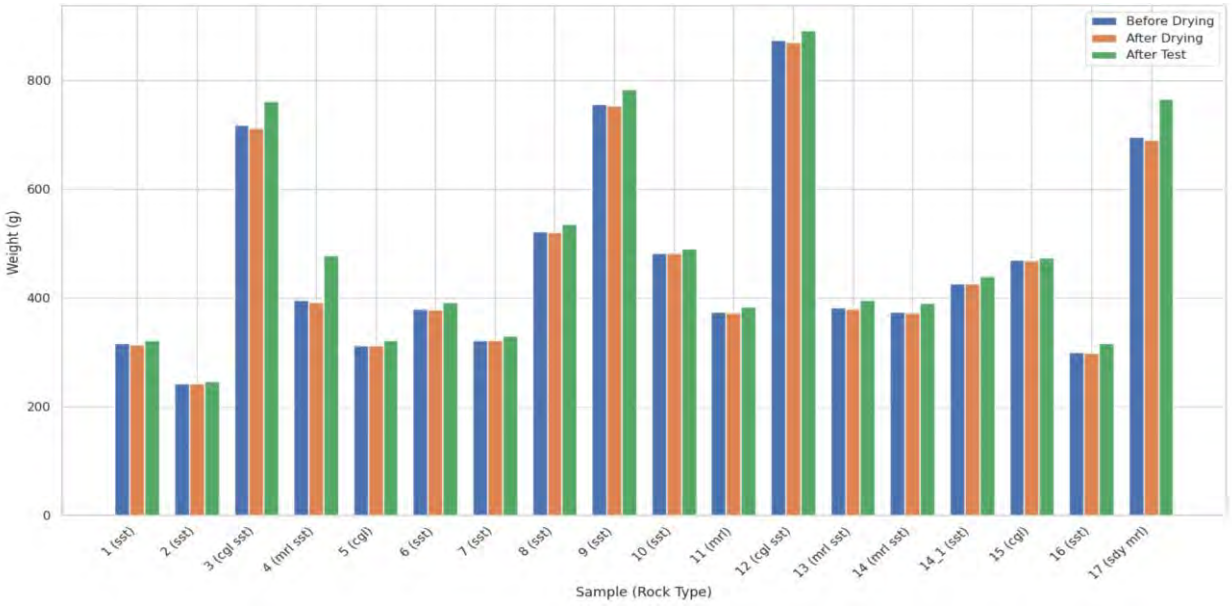

Figure 5.74: Bar chart of the mass change analysis for the examined samples from Region 8 (abbreviations: sst = sandstone, cgl sst = conglomeratic sandstone, mrl sst = marl sandstone, cgl = conglomerate, mrl = marl, sdy mrl = sandy marly). Complete sample codes: 8_1, 8_2, 8_3, 8_4, 8_5, 8_6, 8_7, 8_9, 8_10, 8_11, 8_12, 8_13, 8_14, 8_14_1, 8_15, 8_16, 8_17.

The density versus water absorption scatter plot indicates a weak positive trend, with samples that plot at higher density often also absorbing more water (Figure 5.77). That pattern is driven by the dense, marly group (e.g., 8_4, 8_14) perched high on both axes, while the clean calcareous sandstones cluster at mid-densities and low absorption rates (Figure 5.77). The acid-reaction plot shows that the set is overwhelmingly carbonate-bearing split mainly between “calcareous” and “slightly calcareous” varieties with only one non-calcareous sample (Figure 5.78). This indicates why many sandstones cluster at the low-absorption end, as carbonate cement tightens the pore network when the fabric is clean. The stability plot

The PilotSTRATEGY project has received funding from the European Union’s Horizon 2020 research and innovation programme under grant agreement No. 101022664

reveals that most samples are stable (Grade 1) (Figure 5.79). Exceptions are samples 8_3 (conglomeratic sandstone) and 8_11 (marl) which are classified as fairly stable (Grade 2). Sample 8_4 (marly sandstone), an absorption outlier linked to an absorption of 497 ml/1000g of rock, is categorized as Grade 4, meaning that high water uptake affects mechanical integrity (Appendix X, Figure 5.79). The carbonate-content based on the reaction to HCl versus the water absorption boxplot shows that the calcareous samples uptake consistently less water, compare to the slightly calcareous samples (Figure 5.80). The only non-calcareous sample falls in the mid-range (Figure 5.80). Based on Figure 5.71 it could be concluded that carbonate content alone does not control water uptake as lithology and matrix, especially marly/clayey content, govern both absorption and stability.

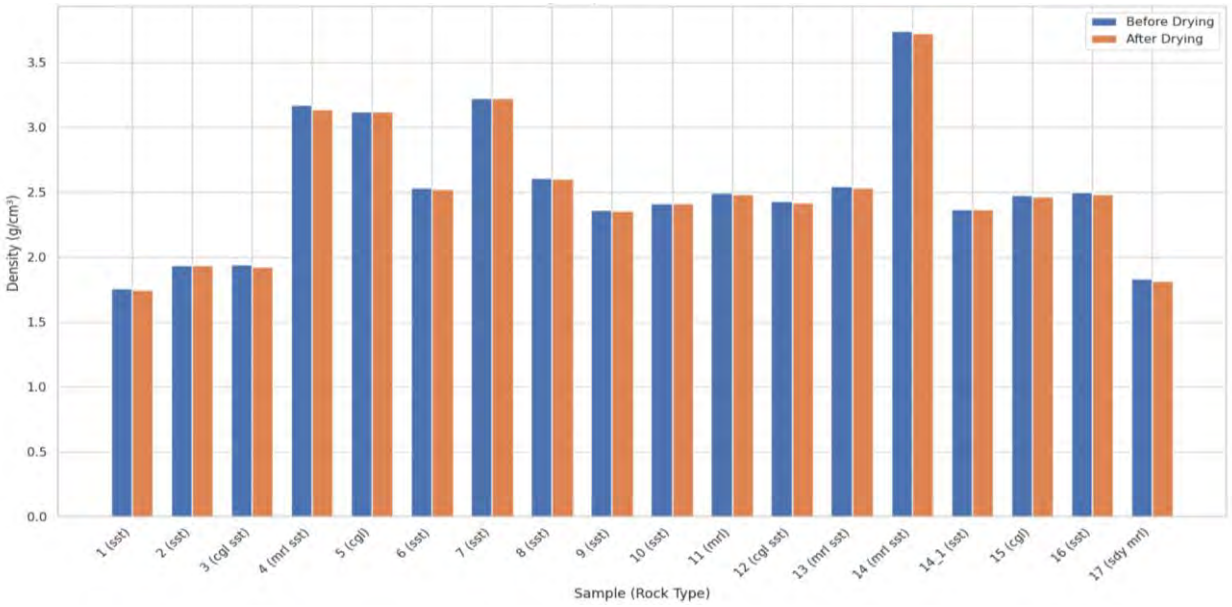

Figure 5.75: Bar chart of the density comparison analysis for the examined samples from Region 8 (abbreviations: sst = sandstone, cgl sst = conglomeratic sandstone, mrl sst = marl sandstone, cgl = conglomerate, mrl = marl, sdy mrl = sandy marly). Complete sample codes: 8_1, 8_2, 8_3, 8_4, 8_5, 8_6, 8_7, 8_9, 8_10, 8_11, 8_12, 8_13, 8_14, 8_14_1, 8_15, 8_16, 8_17.

The PilotSTRATEGY project has received funding from the European Union's Horizon 2020 research and innovation programme under grant agreement No. 101022664

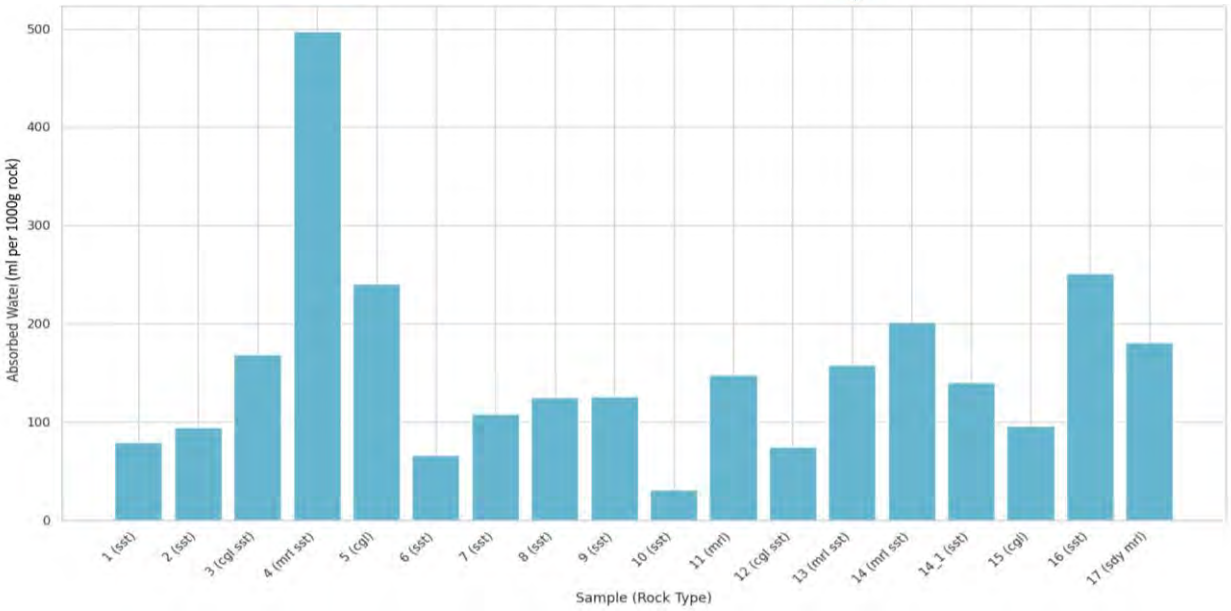

Figure 5.76: Bar chart of the absorbed water (ml) per 1000 g of rock for the examined samples from Region 8 (abbreviations: sst = sandstone, cgl sst = conglomeratic sandstone, mrl sst = marl sandstone, cgl = conglomerate, mrl = marl, sdy mrl = sandy marly). Complete sample codes: 8_1, 8_2, 8_3, 8_4, 8_5, 8_6, 8_7, 8_9, 8_10, 8_11, 8_12, 8_13, 8_14, 8_14_1, 8_15, 8_16, 8_17.

Region 9 is lithologically diverse, sandstones dominate, accompanied by marly sandstones, there are also found limestones and limestone conglomerate, ophiolitic breccia, conglomerate, and a wide suite of basic to ultrabasic igneous rocks (gabbro, norite, pyroxenite, peridotite) including serpentinized variants (Appendix XX). The graphs collectively show excellent repeatability in the drying step, generally low water uptake and high stability for crystalline igneous and highly calcareous rocks, and markedly higher uptake for marly/clay-rich textures. One compacted sand sample behaves as expected and collapses in water.

In the mass change analysis plot, the “before” and “after drying” bars are almost indistinguishable across the set, indicating a stable weighing protocol (Figure 5.81). The green “after test” bars rise modestly for most samples but climb noticeably where fine, marly matrices are present. The marly sandstone 9_12 and 9_27, and the ophiolitic breccia 9_13 and ophiolitic conglomerate 9_15, show the clearest mass gains after immersion—consistent with their higher absorptions (e.g., 9_12 ≈ 264 g/1000 g, 9_15 ≈ 207 ml/1000g) (Appendix XX, Figure 5.81). The density plot confirms that drying does not change measured density (Figure 5.82). Densities reflect lithology, with sandstones and marly sandstones clustering around ~2.1–2.9 g/cm³, serpentinites and peridotites around ~2.4–2.7, and most gabbros/diorites at ~2.6–3.1 (an exception is sample 9_18 (norite gabbro) at ~6.2 g/cm³). Limestone shows moderate densities at ~2.2–2.7 g/cm³ (Figure 5.82).

The PilotSTRATEGY project has received funding from the European Union’s Horizon 2020 research and innovation programme under grant agreement No. 101022664

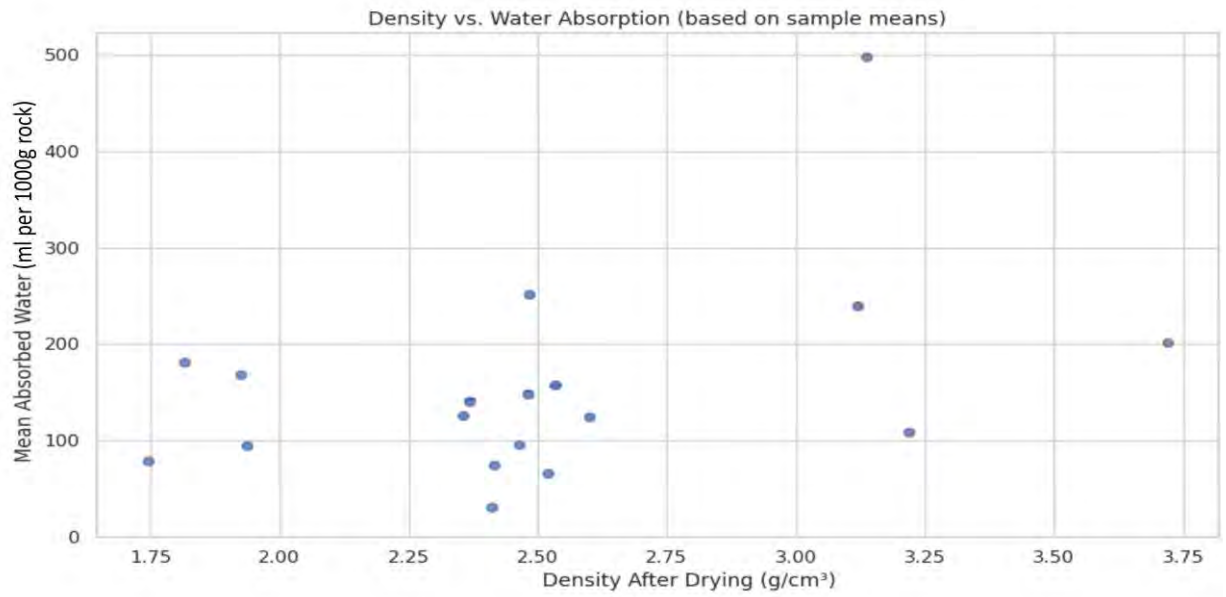

Figure 5.77: Water absorption (ml per 1000g of rock) versus dry density (g/cm³) for samples from Region 8. The x-axis scale is intentionally limited to the observed range of measured densities (1.75-3.75 g/cm³) to enhance visibility and resolution of the data distribution.

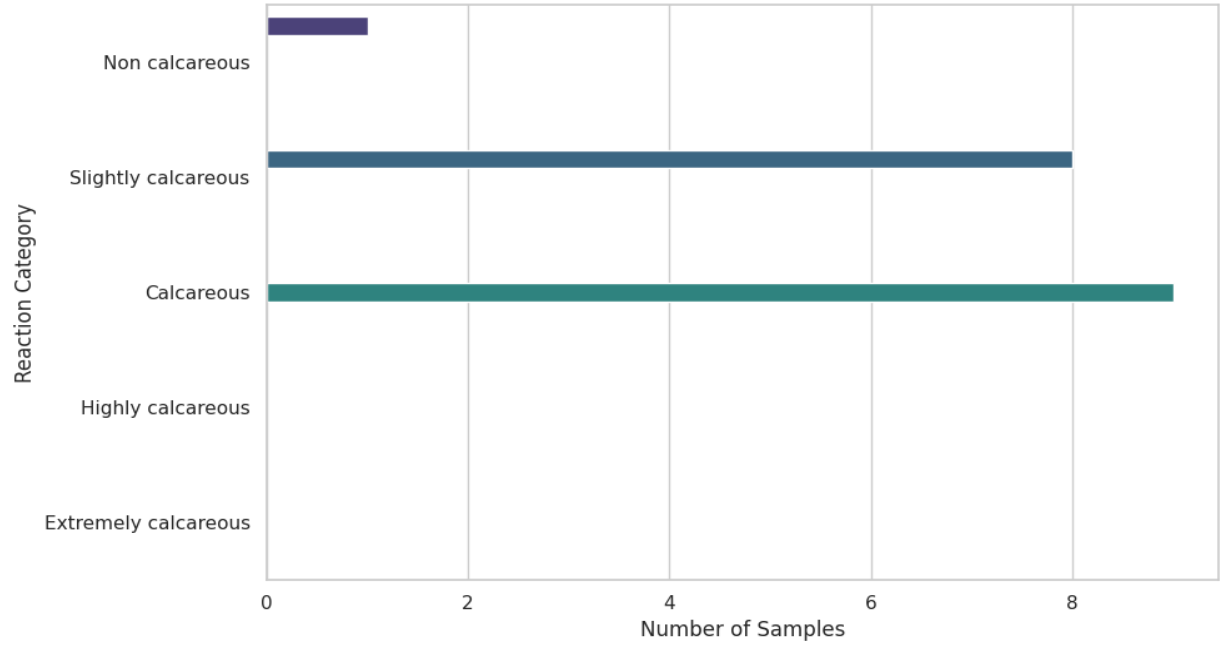

Figure 5.78: Distribution of Region 8 samples after their reaction to hydrochloric acid (HCl). Reaction categorization is after ISO 14689:2017.

The PilotSTRATEGY project has received funding from the European Union's Horizon 2020 research and innovation programme under grant agreement No. 101022664

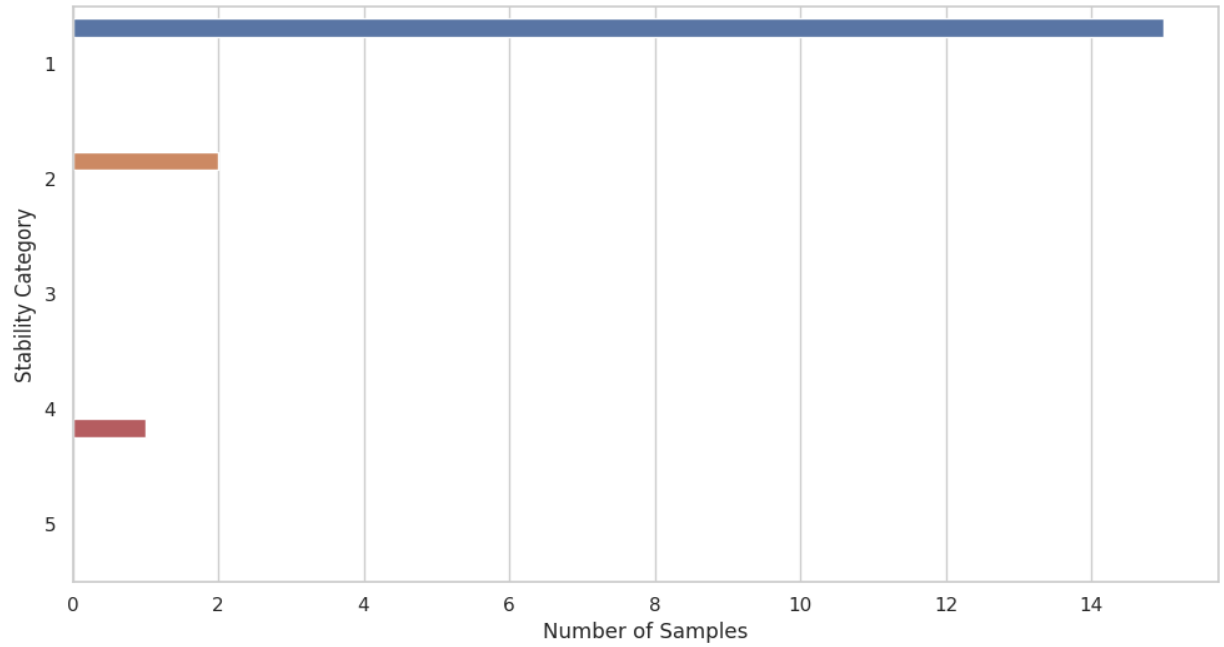

Figure 5.79: Bar chart showing the categorization of the samples from Region 8 after stability grade. Stability in water after 24 hours in ISO 14689:2017 includes the following grades: 1. Stable, 2. Fairly stable: a few fissures are formed, or specimen surface crumbles slightly, 3. Fairly stable: many fissures are formed and broken into small lumps, or specimen surface crumbles highly, 4. Unstable: specimen disintegrates, or nearly the whole specimen surface crumbles, and 5. Unstable: the whole specimen becomes muddy, or disintegrates completely into sand.

The water absorption efficiency graph shows that most crystalline and strongly calcareous rocks are near the base line and several absorbed no water (e.g. 9_16b, 9_19, 9_20i–ii, 9_22–23, KIV01, Figure 5.83). Highest absorption rates are confined to matrix-rich clastic rocks, such as 9_12 (marly sandstone, ~264 ml/1000g of rock) and 9_15 (ophiolitic conglomerate, ~207 ml/1000g of rock).

In the density versus water absorption graph, the regression line slopes gently downward, suggesting that as density increases, absorption tends to fall (Figure 5.84). The trend is anchored by dense, low-porosity lithologies (norite/gabbro, diorite, quartz diorite, highly calcareous limestones) that sit at high density with minimal absorption. Samples above this line are almost exclusively the marly and ophiolitic clastic rocks, illustrating that matrix and texture are important density when fine matter is present.

The PilotSTRATEGY project has received funding from the European Union's Horizon 2020 research and innovation programme under grant agreement No. 101022664

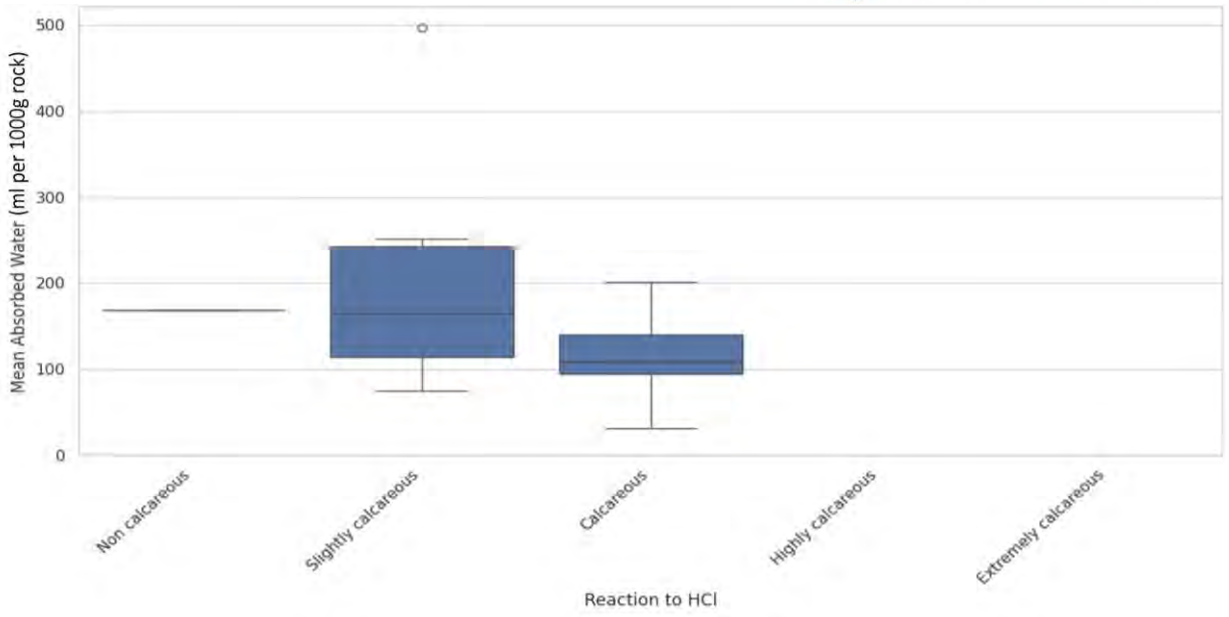

Figure 5.80: Box plot graph of the absorbed water (ml) per 1000g rock for the samples collected from Region 8 versus the rock reaction to HCl categorization after ISO 14689:2017.

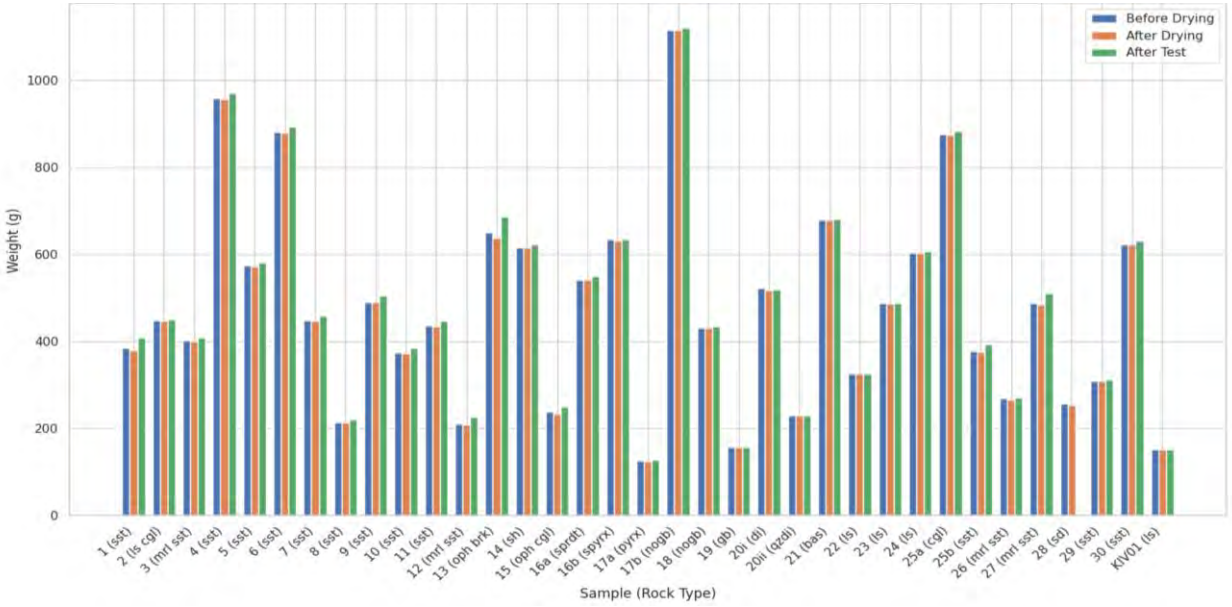

Figure 5.81: Bar chart of the mass change analysis for the examined samples from Region 9 (abbreviations: sst = sandstone, ls cgl = loose conglomerate, mrl sst = marl sandstone, oph brk = ophiolitic breccia, sh = serpentinized hurzburgite, oph cgl = ophiolite conglomerate, sprdt = serpentinized peridotite, spyrx = serpentinized pyroxenite, pyrx = pyroxenite, nogb = norite gabbro, gb = gabbro, di = diorite, qzdi = quartz diorite, bas = basalt, ls = limestone, cgl = conglomerate, sd = sand). Complete sample codes: 9_1, 9_2, 9_3, 9_4, 9_5, 9_6, 9_7, 9_8, 9_9, 9_10, 9_11, 9_12, 9_13, 9_14, 9_15, 9_16a, 9_16b, 9_17a, 9_17b, 9_18, 9_19, 9_20i, 9_20ii, 9_21, 9_22, 9_23, 9_24, 9_25a, 9_25b, 9_26, 9_27, 9_28, 9_29, 9_30, KIV01.

The PilotSTRATEGY project has received funding from the European Union's Horizon 2020 research and innovation programme under grant agreement No. 101022664

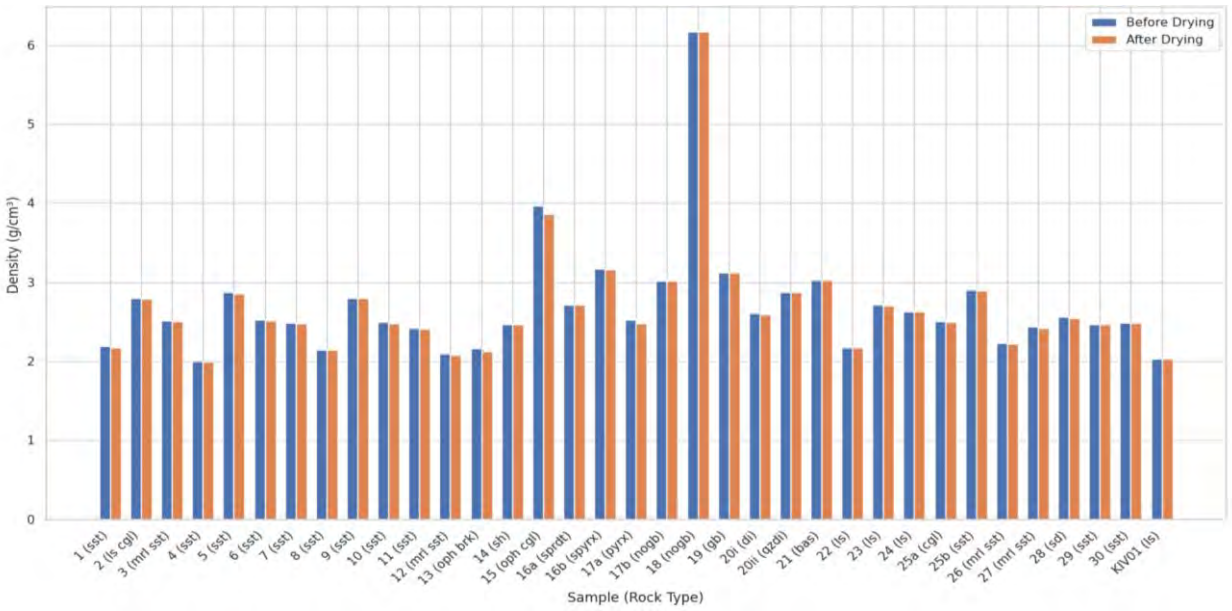

Figure 5.82: Bar chart of the density comparison analysis for the examined samples from Region 9 (abbreviations: sst = sandstone, ls cgl = loose conglomerate, mrl sst = marl sandstone, oph brk = ophiolitic breccia, sh = serpentinized hurzburgite, oph cgl = ophiolite conglomerate, sprdt = serpentinized peridotite, spyrx = serpentinized pyroxenite, pyrx = pyroxenite, nogb = norite gabbro, gb = gabbro, di = diorite, qzdi = quartz diorite, bas = basalt, ls = limestone, cgl = conglomerate, sd = sand). Complete sample codes: 9_1, 9_2, 9_3, 9_4, 9_5, 9_6, 9_7, 9_8, 9_9, 9_10, 9_11, 9_12, 9_13, 9_14, 9_15, 9_16a, 9_16b, 9_17a, 9_17b, 9_18, 9_19, 9_20i, 9_20ii, 9_21, 9_22, 9_23, 9_24, 9_25a, 9_25b, 9_26, 9_27, 9_28, 9_29, 9_30, KIV01.

The reaction to HCl histogram shows a broad variety between non-calcareous and highly calcareous samples (Figure 5.85). Additionally, the stability plot is consistent with most samples belonging to Grade 1 (stable, Figure 5.86). Two marly sandstone samples (9_12 and 9_27) are graded as fairly stable, and the sand sample 9_28, effectively disintegrated in water (Grade 5, Figure 5.86). The carbonate content versus water absorption box plot graph, suggests that the highly calcareous samples absorbed quite restricted amounts of water (several at or near 0 ml/1000g of rock, Figure 5.87). The calcareous class remains modest with a few mid-range values, and the slightly calcareous class exhibits the highest median and widest spread, due to the marly and ophiolitic clastic textures of the related samples (e.g. 9_12, 9_15). The non-calcareous class includes igneous rocks cluster near the axis, and the ophiolitic breccia (9_13) rising as an outlier, again pointing to matrix-controlled porosity (Figure 5.86).

The PilotSTRATEGY project has received funding from the European Union's Horizon 2020 research and innovation programme under grant agreement No. 101022664

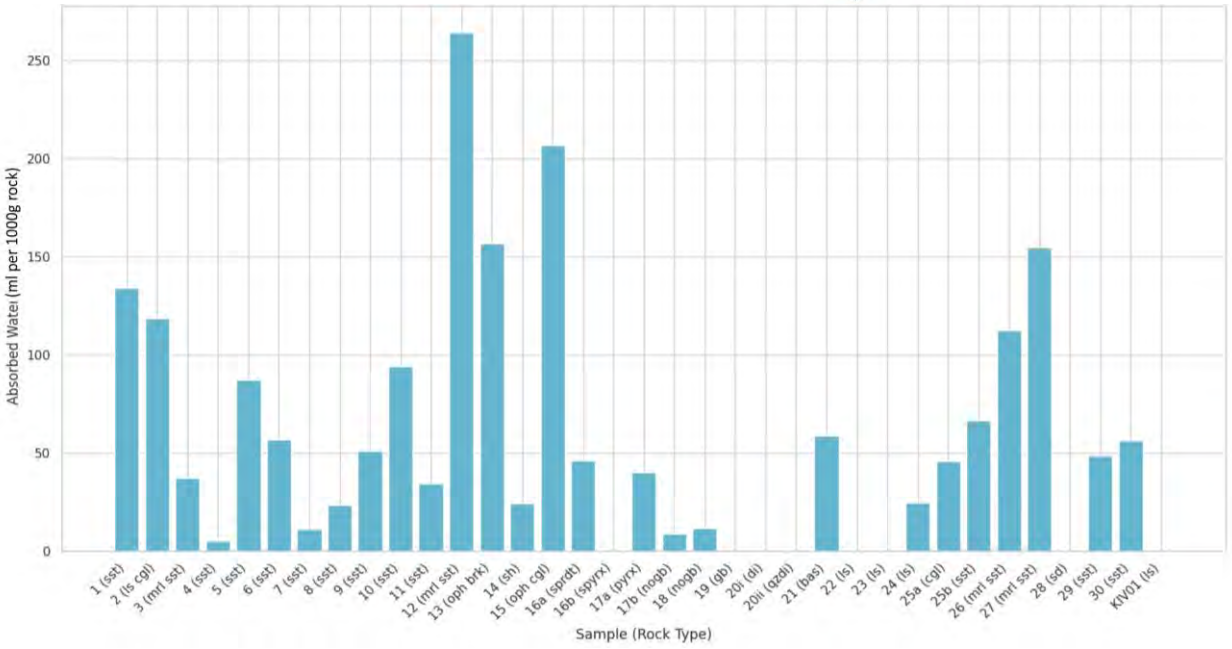

Figure 5.83: Bar chart of the absorbed water (ml) per 1000 g of rock for the examined samples from Region 9 (abbreviations: sst = sandstone, ls cgl = loose conglomerate, mrl sst = marl sandstone, oph brk = ophiolitic breccia, sh = serpentinized hurzburgite, oph cgl = ophiolite conglomerate, sprdt = serpentinized peridotite, spyrx = serpentinized pyroxenite, pyrx = pyroxenite, nogb = norite gabbro, gb = gabbro, di = diorite, qzdi = quartz diorite, bas = basalt, ls = limestone, cgl = conglomerate, sd = sand). Complete sample codes: 9_1, 9_2, 9_3, 9_4, 9_5, 9_6, 9_7, 9_8, 9_9, 9_10, 9_11, 9_12, 9_13, 9_14, 9_15, 9_16a, 9_16b, 9_17a, 9_17b, 9_18, 9_19, 9_20i, 9_20ii, 9_21, 9_22, 9_23, 9_24, 9_25a, 9_25b, 9_26, 9_27, 9_28, 9_29, 9_30, KIV01.

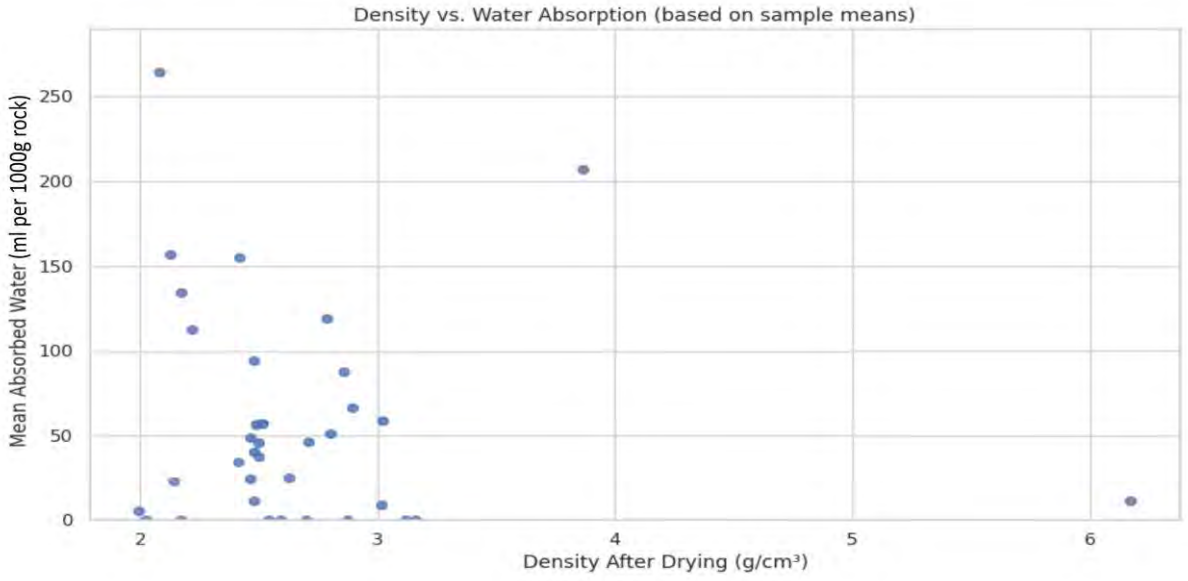

The PilotSTRATEGY project has received funding from the European Union's Horizon 2020 research and innovation programme under grant agreement No. 101022664

Figure 5.84: Water absorption (ml per 1000g of rock) versus dry density (g/cm³) for samples from Region 9. The x-axis scale is intentionally limited to the observed range of measured densities (2-6.17 g/cm³) to enhance visibility and resolution of the data distribution.

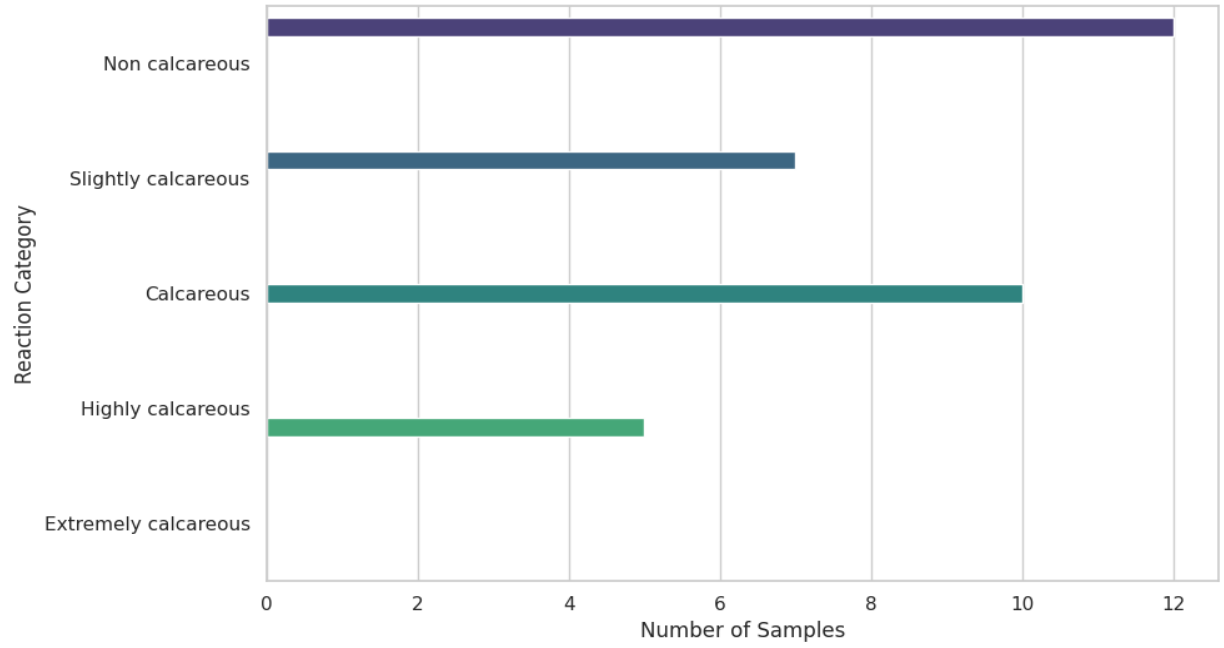

Figure 5.85: Distribution of Region 9 samples after their reaction to hydrochloric acid (HCl). Reaction categorization is after ISO 14689:2017.

Two clear patterns emerge from the sedimentary datasets. In Regions 1 and 6, well-cemented sandstones behave predictably: water uptake sits in the low, moderate band and stability is uniformly Grade 1. A useful contrast appears within Region 6, where denser sandstones stand apart from less-dense marly sandstones, the latter consistently more absorbent. Coarse clastics in Regions 2, 4 and 5 underline the decisive role of matrix and cement, with the well-cemented conglomerates in Region 4 being stable and showing modest water uptake. In Region 2, water absorption spans the full range from very low to very high, while Region 5 hosts the most fragile fabrics (marly/muddy units) that reach Grades 4–5.

At the other end of the spectrum, the ultramafic suite in Region 7 and the broader igneous set in Region 9 provide the durability baseline of the project, where dense, crystalline fabrics show near-zero absorption and unwavering Grade 1 stability. In contrary, the marly/clay-rich textures stand out. In Region 8, single marly sandstone drives both the highest absorption and the only stability Grade-4 outcome, while Region 9 includes several marly or ophiolitic clastic units with elevated water uptake and one compacted sand sample that collapses entirely. Yet both areas also confirm that clean calcareous sandstones and compact limestones remain dependable performers, with near zero uptake and great stability (Grade 1).

The PilotSTRATEGY project has received funding from the European Union's Horizon 2020 research and innovation programme under grant agreement No. 101022664

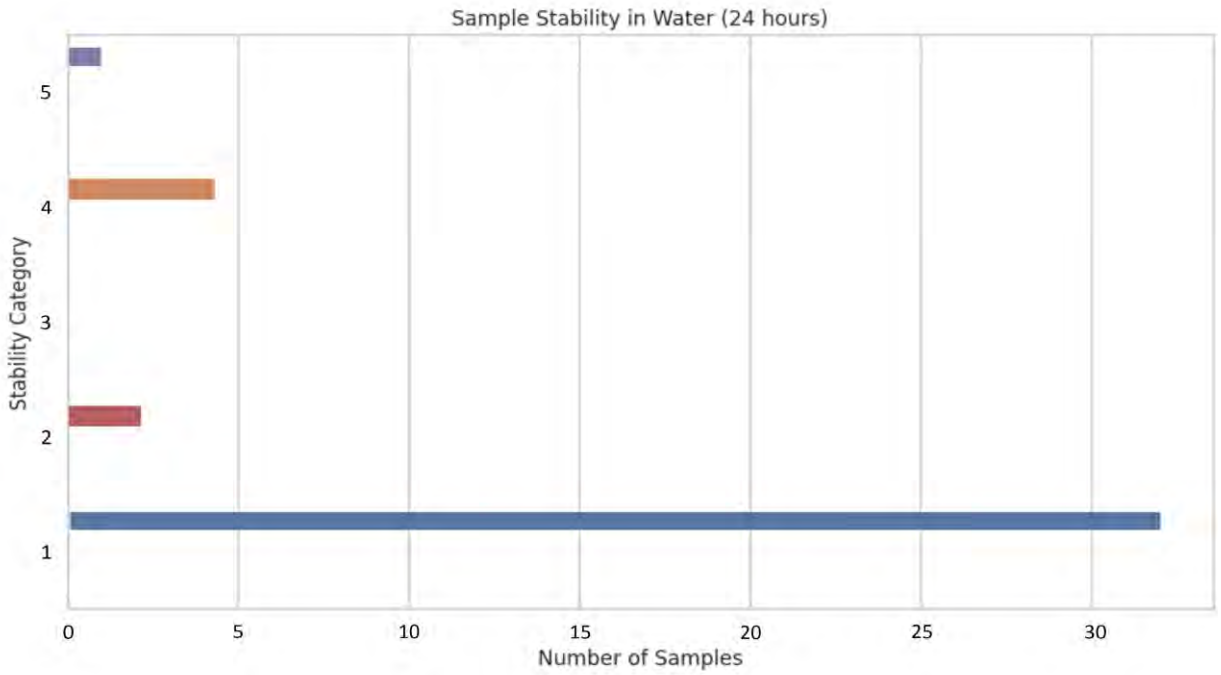

Figure 5.86: Bar chart showing the categorization of the samples from Region 9 after stability grade. Stability in water after 24 hours in ISO 14689:2017 includes the following grades: 1. Stable, 2. Fairly stable: a few fissures are formed, or specimen surface crumbles slightly, 3. Fairly stable: many fissures are formed and broken into small lumps, or specimen surface crumbles highly, 4. Unstable: specimen disintegrates, or nearly the whole specimen surface crumbles, and 5. Unstable: the whole specimen becomes muddy, or disintegrates completely into sand.

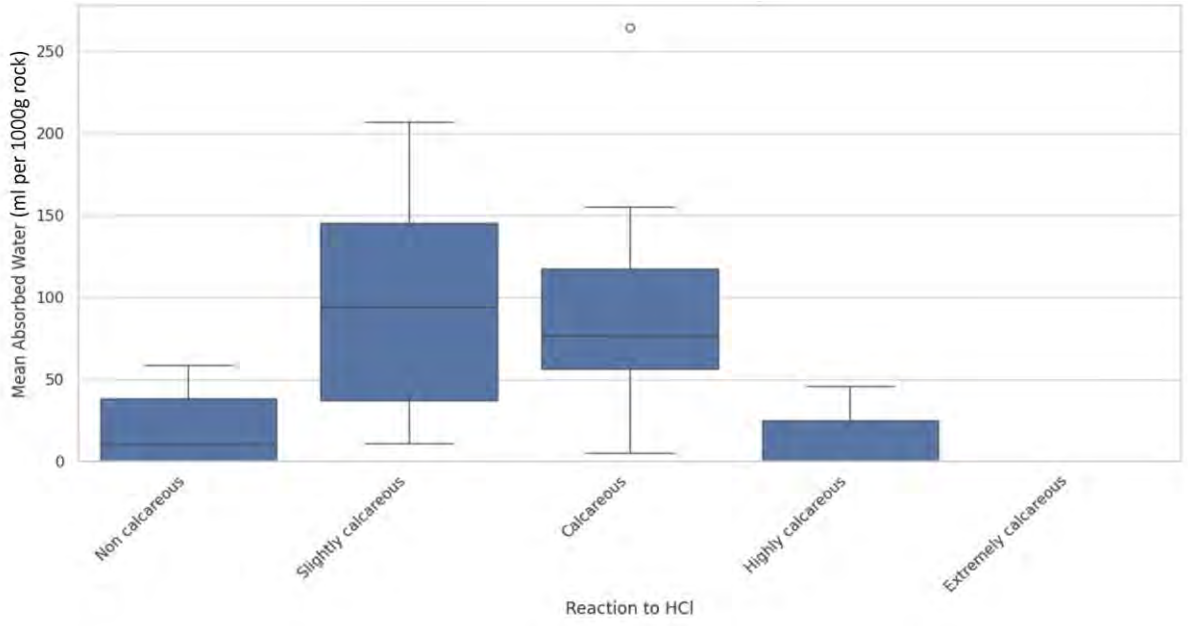

The PilotSTRATEGY project has received funding from the European Union's Horizon 2020 research and innovation programme under grant agreement No. 101022664

Figure 5.87: Box plot graph of the absorbed water (ml) per 1000g rock for the samples collected from Region 9 versus the rock reaction to HCl categorization after ISO 14689:2017.

Translating these findings to CCS engineering, reservoir and seal selection should reflect the same fabric controls. Clean from inclusions, well-cemented sandstones that show low to moderate water uptake and strong Grade-1 stability are promising storage reservoirs, provided that their porosity/permeability system supports injectivity and they lack swelling clays. Marly/clay-rich units, which in the presented tests are the most water-absorptive and occasionally unstable, can function as caprocks only after rigorous screening for their contents in swelling clays, capillary entry pressure, and chemical-mechanical sensitivity to CO_2-rich brines (swelling, softening, or carbonate dissolution). Compact limestones and dense crystalline rocks, while mechanically robust, are typically too tight for reservoirs; however, limestones demand geochemical assessment of CO_2-acidified brine reactivity (potential dissolution/porosity increase), and ultramafics, despite low permeability, may be targeted for in-situ mineral carbonation if permeability enhancement is engineered. Practically, CCS site appraisal should extend the basic durability tests with CO_2-specific protocols, core-flood experiments with CO_2-brine to track permeability/strength changes, triaxial testing pre- and post-exposure, mercury intrusion or NMR for pore connectivity, swelling tests on clay-bearing seals, and reactive-transport modelling for carbonate–CO_2 systems.

The results demonstrate that lithology exerts the strongest influence on water behaviour. Crystalline igneous rocks and well-cemented, highly calcareous limestones show no water uptake and remain entirely stable under water immersion. This confirms their compact, low-porosity nature. In contrast, marly, clay-rich, and poorly cemented sediments display the highest water absorption and are the only materials that show any measurable signs of instability.

The relationship between density and water absorption follows an inverse pattern, though the correlation is weak and not statistically significant. Most regions show a subtle trend of denser samples absorbing less water. Exceptions occur in Regions 3 and 8, where clay-rich or marly matrices preserve connected microporosity, allowing continued uptake even in samples of moderate density.

Sandstones exhibit a wide behavioural range. In Region 1, they are uniform, stable, and low to moderate in absorption. In Regions 6, 8, and 9, the clean calcareous varieties behave similarly, whereas marly or slightly calcareous sandstones absorb significanlty more water and display minor losses in stability. Conglomerates and conglomeratic sandstones show a strong dependence on their matrix composition. Well-cemented types, such as those from Region 4, are compact and stable with limited absorption. Where the matrix is clayey or ophiolitic, absorption rises sharply, as observed in the bedded conglomerates of Region 7, the slightly calcareous conglomerates of Region 8, and the ophiolitic varieties of Region 9.

Carbonate content is an important factor but not the sole determinant of absorption. Rocks classified as highly calcareous consistently occupy the lowest absorption range and remain entirely stable. Nevertheless, within the calcareous and slightly calcareous groups, the variability is considerable, reflecting the dominant influence of matrix composition and pore connectivity over simple chemical reactivity.

The PilotSTRATEGY project has received funding from the European Union's Horizon 2020 research and innovation programme under grant agreement No. 101022664

Instability is overall rare and limited to fine-grained or loosely consolidated materials. The vast majority of samples across all regions remain Grade 1 according to the ISO stability scale. Degradation is confined to specific lithologies: marls and marly sands from Region 5 (Grades 4 and 5), a single marly sandstone from Region 8 (Grade 4), and both marly sandstones (Grade 2) and loose sands (Grade 5) from Region 9.

The formations requiring particular caution include marly sandstones and marls from Regions 5, 8, and 9, which exhibit the highest absorption and the only non-Grade 1 results. Ophiolitic breccias and conglomerates also warrant attention, as their absorptive capacity varies widely with the nature of the matrix. Thus while most lithologies are compact and stable, clay-rich or weakly cemented rocks represent local vulnerabilities in the system.

5.5.1. Regional & Comparative Assessment of Hydrogeological Properties

Across Regions 1 to 9, the graphs highlight a consistent conclusion: fabric (marly/clayey matrices vs. clean, well-cemented frameworks) governs water uptake and, by extension, stability. Carbonate content helps but does not dominate the extent of the water uptake, while density is informative but can be misleading where clays create connected microporosity. The two independent uptake measurements (tank volume change and post-immersion weight gain) corroborate one another, reinforcing confidence in the dataset.

The reaction to HCl versus the water absorption indicates that carbonates content moderates, but does not dictate, uptake (Figure 5.87). “Highly calcareous” samples cluster at the bottom (generally 0 to 45 ml/1000g of rock in the plot), “calcareous” occupy a low to mid band (~10 to 95 ml/1000g of rock), and “slightly calcareous” show the widest spread (~10 to 255 ml/1000g of rock in the plot, extending to ~500 ml/1000g of rock in region-specific results). Non-calcareous crystalline rocks align with ~0–25 ml/1000g of rock, while non-calcareous clastics produce the outliers when their matrices are marly or muddy (e.g., Region 9, ophiolitic breccia, ~157 ml/1000g of rock).

The density versus water absorption graph showcases that denser rocks absorb less, but regional trendlines may diverge (Figure 5.89). High-density samples (e.g., gabbro/norite/diorite at ~2.7–3.1 g/cm³ with 0–25 ml/1000g of rock, one norite gabbro at ~6.2 g/cm³ with ~5–12 ml/1000g of rock) contrast with low-density, high-uptake marly sandstones (~2.1–2.4 g/cm³with ~150–500 ml/1000g of rock). This confirms density is helpful but insufficient where clayey matrices generate connected microporosity.

The water uptake versus the post-immersion weight gain shows a tightly consistent relation and approximately proportional across regions, indicating strong method concordance (Figure 5.87). Representative bands are visible: at ~50 ml/1000 g absorption, mass gains cluster around ~7–20 g, at ~150 ml/1000 g, gains lie roughly ~20–70 g, the largest absorptions (≥200 ml/1000g of rock) pair with mass increases in the tens of grams. The agreement between the two methods supports the reliability of the measurements.

The PilotSTRATEGY project has received funding from the European Union’s Horizon 2020 research and innovation programme under grant agreement No. 101022664

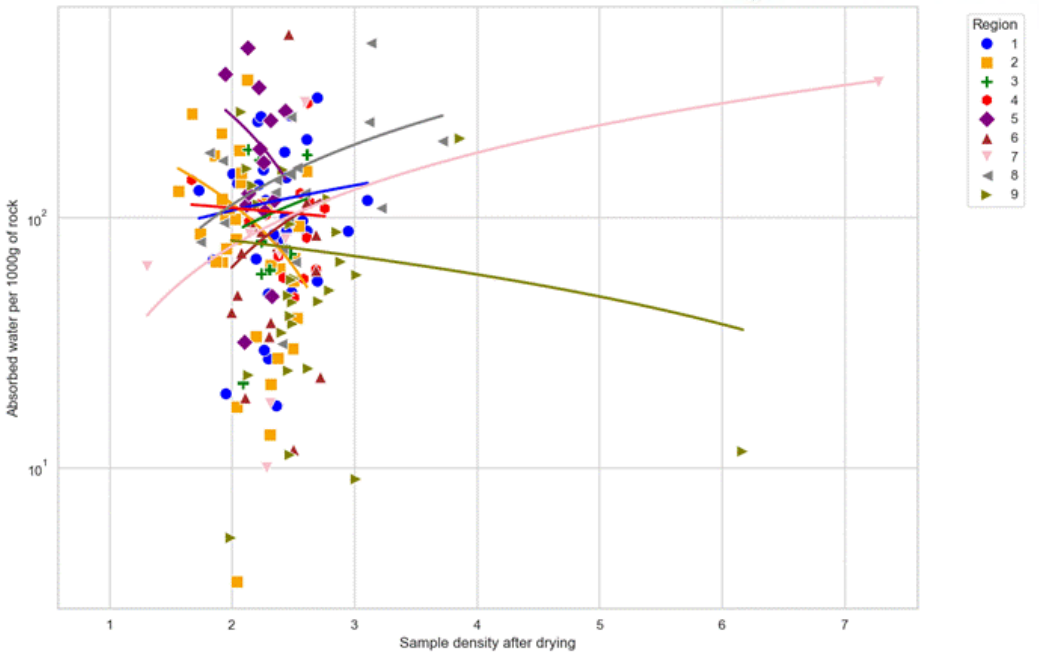

Figure 5.88: Density versus water absorption (log scale). Each point represents a sample (coloured/symbolled by Region 1 to 9), and curves indicate region-wise trends. Although some samples display a weak inverse relationship between density and absorption, the overall pattern is variable across regions. In several cases, clay-rich or marly matrices retain connected microporosity even at moderate densities, resulting in higher absorption values.

Finally, the water absorption versus stability graph suggests that most samples remain stable (Grade 1) even up to ~100–150 ml/1000 g, emphasizing the protective role of good cementation (Figure 5.87). Non-Grade-1 outcomes cluster at the high-absorption end: Grade 2 points appear between roughly ~40–130 ml/1000g of rock, Grade 4 occurs near ~200 ml/1000g of rock, and a Grade 5 failure is recorded for the compacted sand (Region 9, sample 9_28) despite near-zero retained absorption (disintegration) (Figure 5.87). These few cases align with marly/muddy textures or loose fabrics. Major conclusions after the comparative regional analysis, include:

1. Fabric dominates: Where matrices are marly/clayey, absorptions commonly exceed ~150 g/1000 g and can reach ~350–500, with occasional Grade 2–5 stability. Clean, well-cemented frameworks (igneous, compact limestones, calcareous sandstones) stay in 0–70 ml/1000g of rock and stable (Grade 1).
2. Carbonate helps, selectively: “Highly calcareous” samples consistently sit in 0–45 ml/1000g of rock, “calcareous” mostly at 10–95 ml/1000g of rock, “slightly calcareous” span ~10–255 ml/1000g of rock, and up to ~500 ml/1000g of rock (regional maxima), showing that reaction strength alone is not predictive without fabric context.
3. Density is necessary but insufficient: Although some rock types show an inverse relationship between density and water uptake, the overall trend across all samples is heterogeneous. In several regions, dense clay-bearing or still exhibit high absorption values (>100 ml/1000 g).

The PilotSTRATEGY project has received funding from the European Union’s Horizon 2020 research and innovation programme under grant agreement No. 101022664

Protocol is robust: Volumetric and gravimetric uptakes increase together across ~0–250+ ml/1000 g, supporting cross-regional comparability and modelling inputs.

4. Instability is rare and predictable. Failures occur only in loose or fine-grained materials (e.g., sand disintegration, marly/muddy clastics near ~175–200+ ml/1000g of rock). Most other lithologies remain Grade 1 even at ~100–150 ml/1000g of rock.
5. CCS engineering implications. Caprock candidates are compact limestones and crystalline igneous units occupying the 0–25 ml/1000 g group (often 0 ml/1000g of rock) with densities ≥2.6 g/cm³, they show minimal uptake and strong fabric integrity. For limestones, still evaluate CO_2–brine reactivity (possible dissolution/porosity change). Reservoir candidates could be clean, well-cemented sandstones with 30–120 ml/1000 g or rock absorption and verified Grade-1 stability (e.g., many in Regions 1, 6, 8, 9) are promising, provided permeability is adequate and swelling clays are limited. Conglomerates are matrix-controlled: well-cemented variants with ≤100 ml/1000g of rock may be local options, while marly/loose types (often ≥150–200 ml/1000g of rock) are poor choices.
6. Risk screening thresholds: Very low risk, could be ascribed to densities ≥2.6 g/cm³ and to absorption ≤25 ml/1000g of rock (igneous, compact carbonate). Manageable risk could be assigned to absorption ~30–120 ml/1000g of rock with Grade 1 (clean sandstones), if first confirm clay content and pore connectivity. Elevated risk could be related to absorption ≥150 ml/1000g of rock or any Grade ≥2 response (marly/muddy clastics, loose sands), these should be avoid as caprock and treat cautiously as reservoir host.

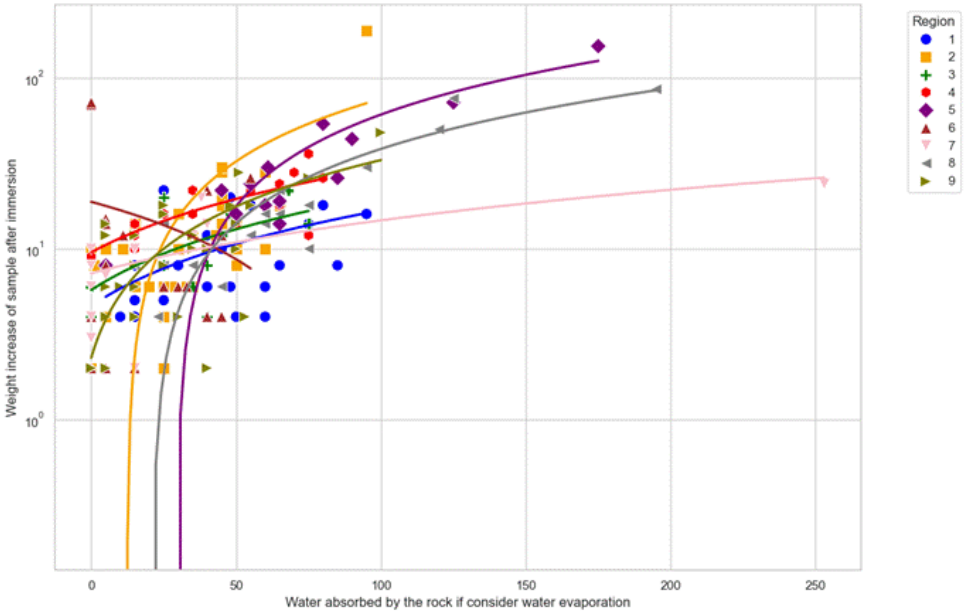

Figure 5.89: Water absorbed by the rock versus post-immersion weight gain (log scale). Volumetric uptake from the tank (x-axis) correlates strongly with gravimetric mass gain (y-axis) across all regions (Region 1 to 9), and smoothed lines illustrate consistent, near-proportional behaviour. This agreement validates the measurement protocol over the full uptake range (~0 to >250 ml).

The PilotSTRATEGY project has received funding from the European Union's Horizon 2020 research and innovation programme under grant agreement No. 101022664

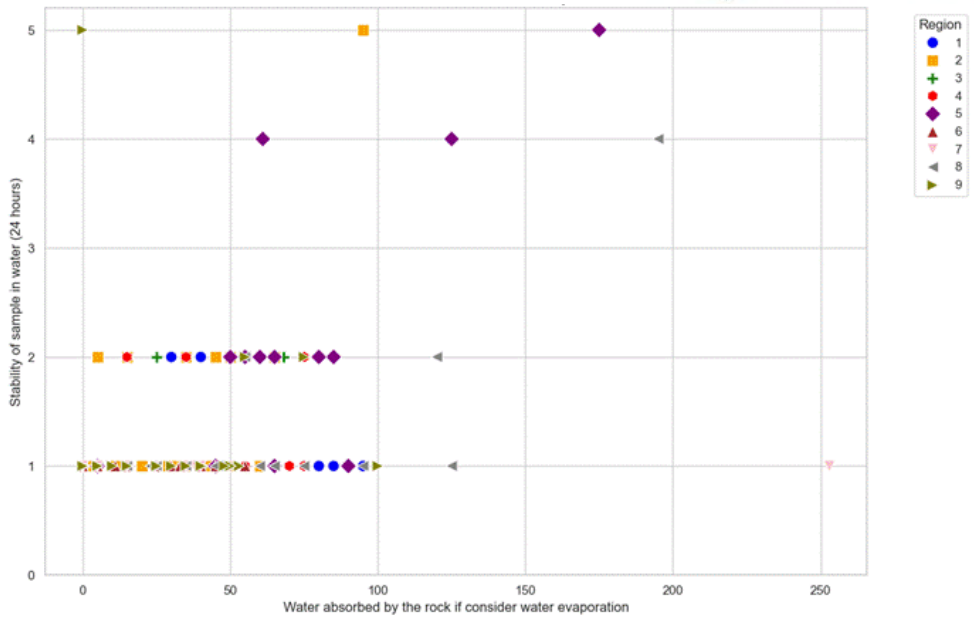

Figure 5.90: Absorbed water versus stability grade after 24 h immersion. Stability is overwhelmingly Grade 1, even up to ~100–150 ml/1000 g. Non-Grade-1 outcomes cluster at higher absorptions, with a few Grade 4–5 outliers linked to marly/muddy or loose materials. Stability grades: 1. Stable, 2. Fairly stable: a few fissures are formed, or specimen surface crumbles slightly, 3. Fairly stable: many fissures are formed and broken into small lumps, or specimen surface crumbles highly, 4. Unstable: specimen disintegrates, or nearly the whole specimen surface crumbles, and 5. Unstable: the whole specimen becomes muddy, or disintegrates completely into sand.

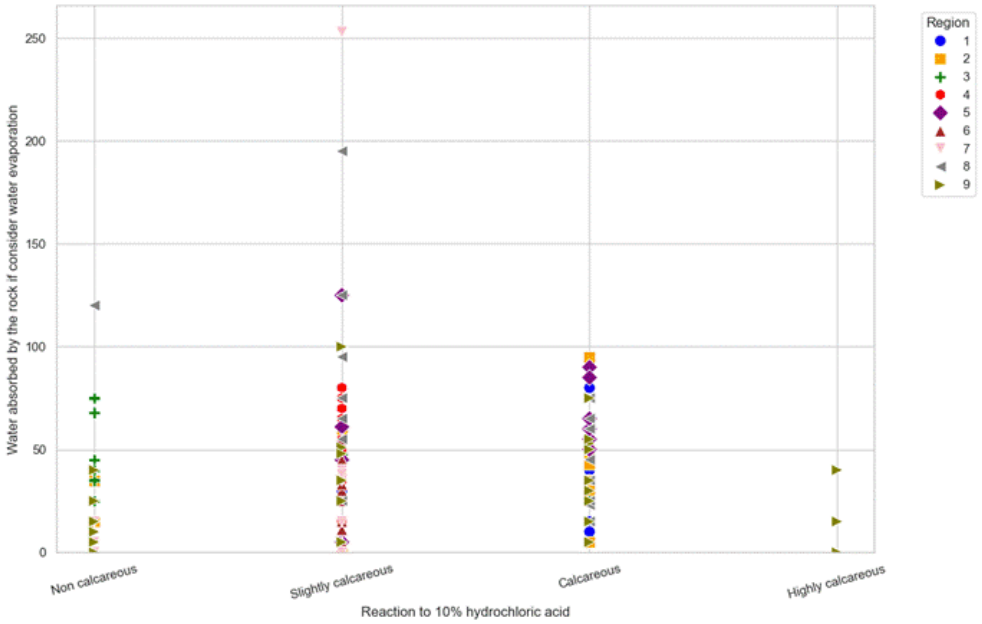

Figure 5.91: Reaction to 10% HCl versus water absorption. Samples are grouped by carbonate class. “Highly calcareous” rocks cluster at very low absorption (~0–40 ml/1000 g), “calcareous” sit mostly in the low–mid band,

The PilotSTRATEGY project has received funding from the European Union’s Horizon 2020 research and innovation programme under grant agreement No. 101022664

and “slightly calcareous” display the widest spread (extending beyond 200 ml/1000 g). Non-calcareous clastic rocks form occasional high-absorption outliers, highlighting that fabric and matrix, more than fizz strength, control uptake.

5.6. Remote sensing mapping based on field observation

The geological mapping procedure was designed to integrate detailed field observations with digital cartographic techniques and complementary remote sensing analysis, ensuring accurate lithological and structural representation at a scale of 1:25,000. The process began with the systematic digitisation of field measurements. Strike and dip values of bedding, faults, and other structural features were recorded in the field and georeferenced using handheld GPS devices. Photographic documentation was collected simultaneously, with each image assigned a geographic coordinate and information on orientation and angle, creating a geo-referenced photographic archive. These data points were imported into QGIS, where they provided the structural and lithological control for subsequent mapping.

In the next stage, polygons representing lithological units were digitised directly in QGIS on the basis of field observations. Lithological boundaries were delineated according to ground-truth data, including stratigraphic contacts, structural measurements, and field photographs. This step ensured that the map maintained consistency with observed geological features and that spatial relationships between lithologies were represented accurately at the target scale of 1:25,000.

Following the field-based digitisation, areas that remained inaccessible or insufficiently constrained were complemented using remote sensing products. Sentinel-2 MSI imagery was employed to support lithological discrimination, particularly in locations where field access was restricted. Level-2A products, atmospherically corrected to reduce residual atmospheric effects (>2%), were obtained from the Copernicus Open Access Hub (https://scihub.copernicus.eu/). Imagery from 11 August 2024, with near-zero cloud coverage, was selected to ensure optimal conditions for geological interpretation. Sentinel-2 Level-2A MSI imagery was processed in ESA SNAP software to generate natural (4-3-2) (Figure 5.92). and false-color (7-6-4) composites (Figure 5.93).

This configuration is recommended in the Sentinel-2 User Handbook [117] as a standard reference for visual inspection and for comparison with field observations. In addition, the 7-6-4 composite (B7–SWIR-2, B6–SWIR-1, B4–Red) was applied, as it enhances lithological contrasts and facilitates the discrimination of rocks, soils, and alteration zones due to the strong sensitivity of shortwave infrared bands to mineralogical and moisture variations. The effectiveness of SWIR-based composites for lithological mapping and mineral exploration has been highlighted extensively in the literature. The combined use of both composites ensured that the dataset supported reliable geological interpretation by integrating natural visual representation with enhanced mineralogical discrimination.

The PilotSTRATEGY project has received funding from the European Union’s Horizon 2020 research and innovation programme under grant agreement No. 101022664

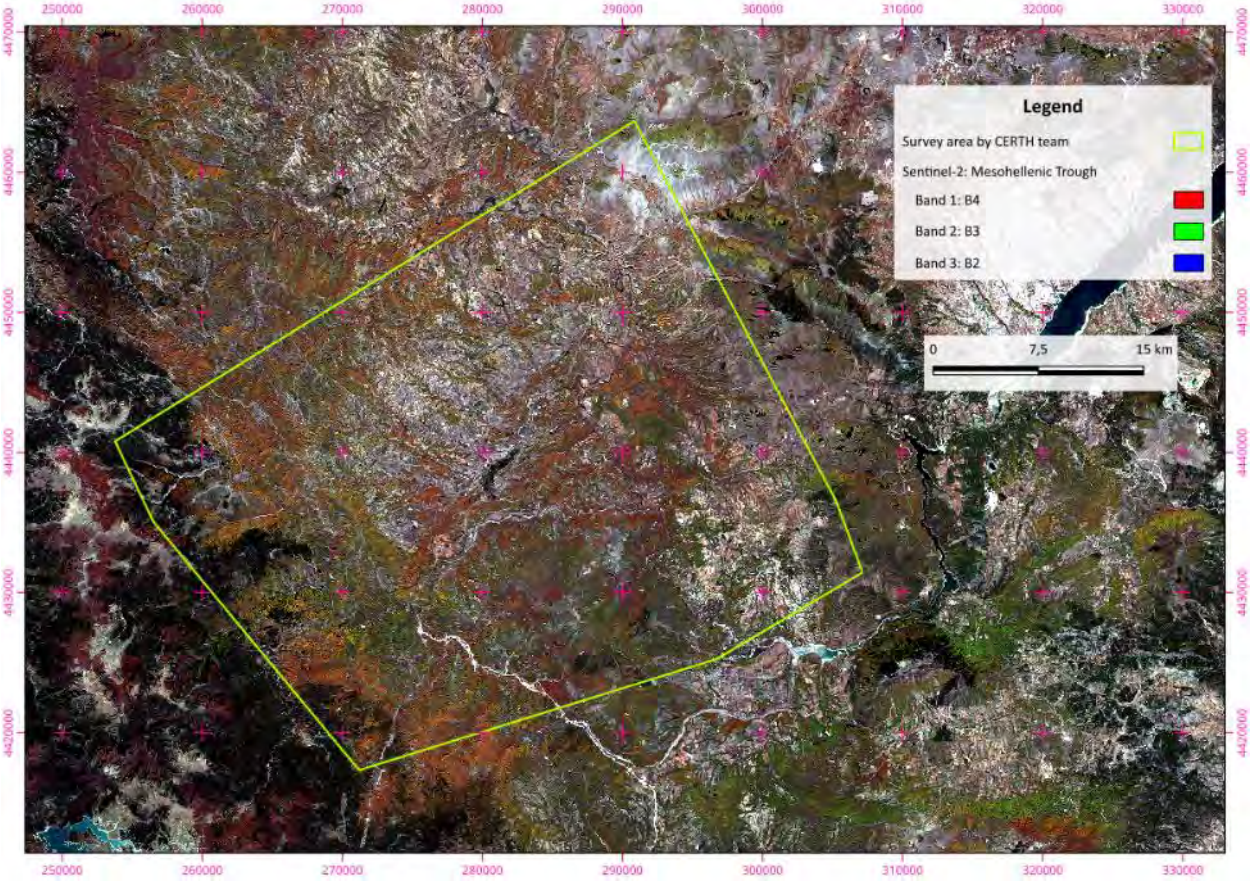

Figure 5.92: Sentinel-2 MSI natural color composite (bands 4–3–2) of the study area in West Macedonia, projected in the EGSA87 reference system. This combination approximates the spectral response of human vision, allowing a realistic depiction of surface features. Minor deviations in tone may occur due to atmospheric scattering and radiometric scaling of the blue channel (Band 2), which often enhances short-wavelength reflectance. The overlaid polygons delineate the study boundaries and newly mapped geological regions.

A supervised classification was performed to enhance lithological contrasts, with training areas defined for the dominant lithologies of the region. The classified raster was validated against available field evidence and subsequently integrated into QGIS as an additional dataset. This approach allowed lithological interpretation in remote or hazardous locations, without contradicting direct field observations. A supervised classification was conducted in ESA SNAP software to extract key lithological and land cover classes. Representative training areas (Regions of Interest) were defined for the dominant lithologies of the area, including conglomerates, sandstones, ophiolites, marls, limestones, and serpentinites, alongside vegetation and water bodies (Figure 5.94).

The PilotSTRATEGY project has received funding from the European Union's Horizon 2020 research and innovation programme under grant agreement No. 101022664

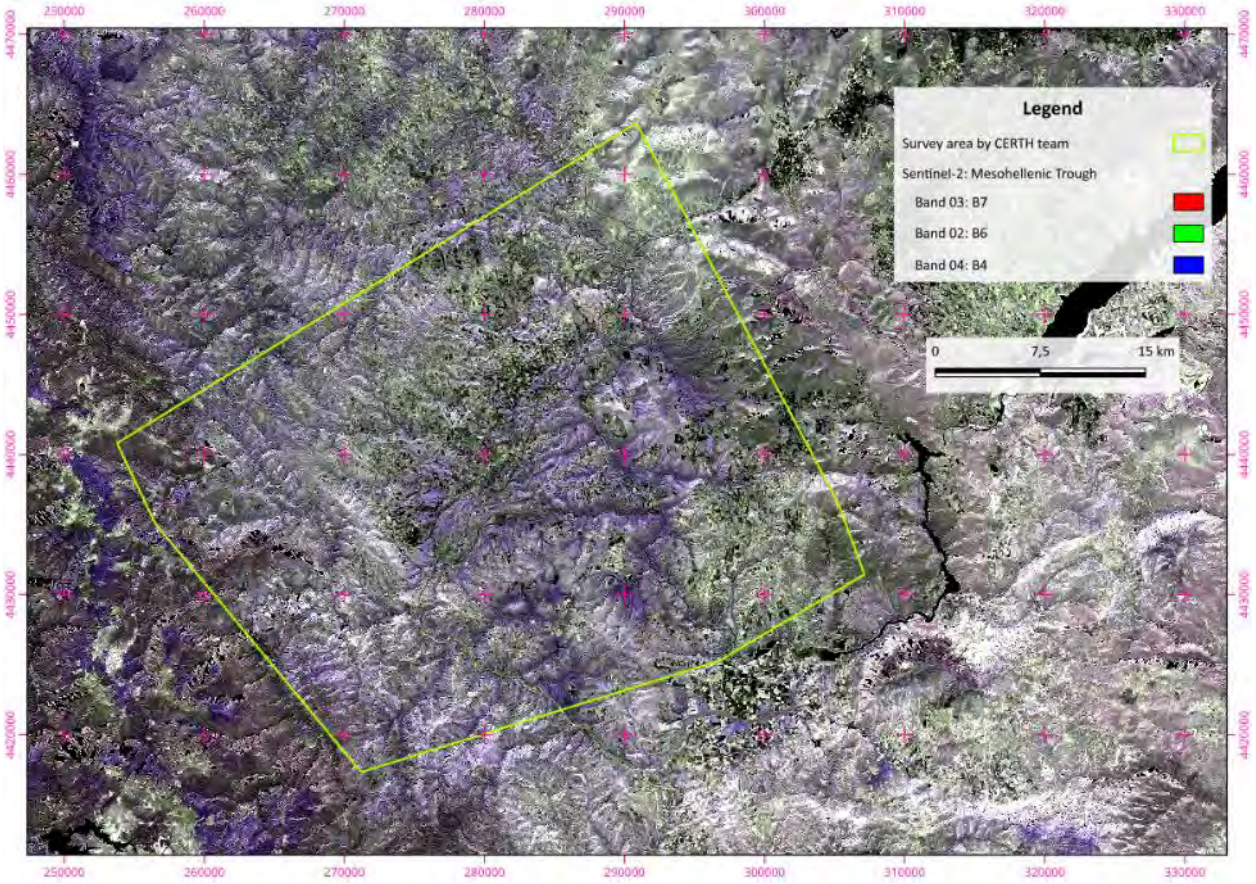

Figure 5.93: Sentinel-2 MSI false color composite of the study area in West Macedonia (bands 7–6–4), projected in the EGSA87 reference system. This band combination enhances lithological contrasts because shortwave infrared bands (B7 and B6) are highly sensitive to mineralogical composition and soil moisture. Vegetation is displayed in greenish tones, while soils and rock outcrops appear in varying hues of purple, brown, and grey, thereby facilitating geological interpretation and mapping of lithological units.

The Maximum Likelihood classifier was applied, and the resulting thematic raster was validated through comparison with available reference data. The output classified the spectral separability of lithological units. Conglomerates and sandstones appear in reddish-orange tones, limestones and marls in light green to yellow hues, serpentinites in purple shades, and ophiolites in purplish/greenish tones. These classes correspond well to the geological framework of the Mesohellenic Trough, where sedimentary successions coexist with ophiolitic fragments. The classified raster was exported as a GeoTIFF and imported into QGIS, where it was integrated with vector data derived from fieldwork.

The PilotSTRATEGY project has received funding from the European Union's Horizon 2020 research and innovation programme under grant agreement No. 101022664

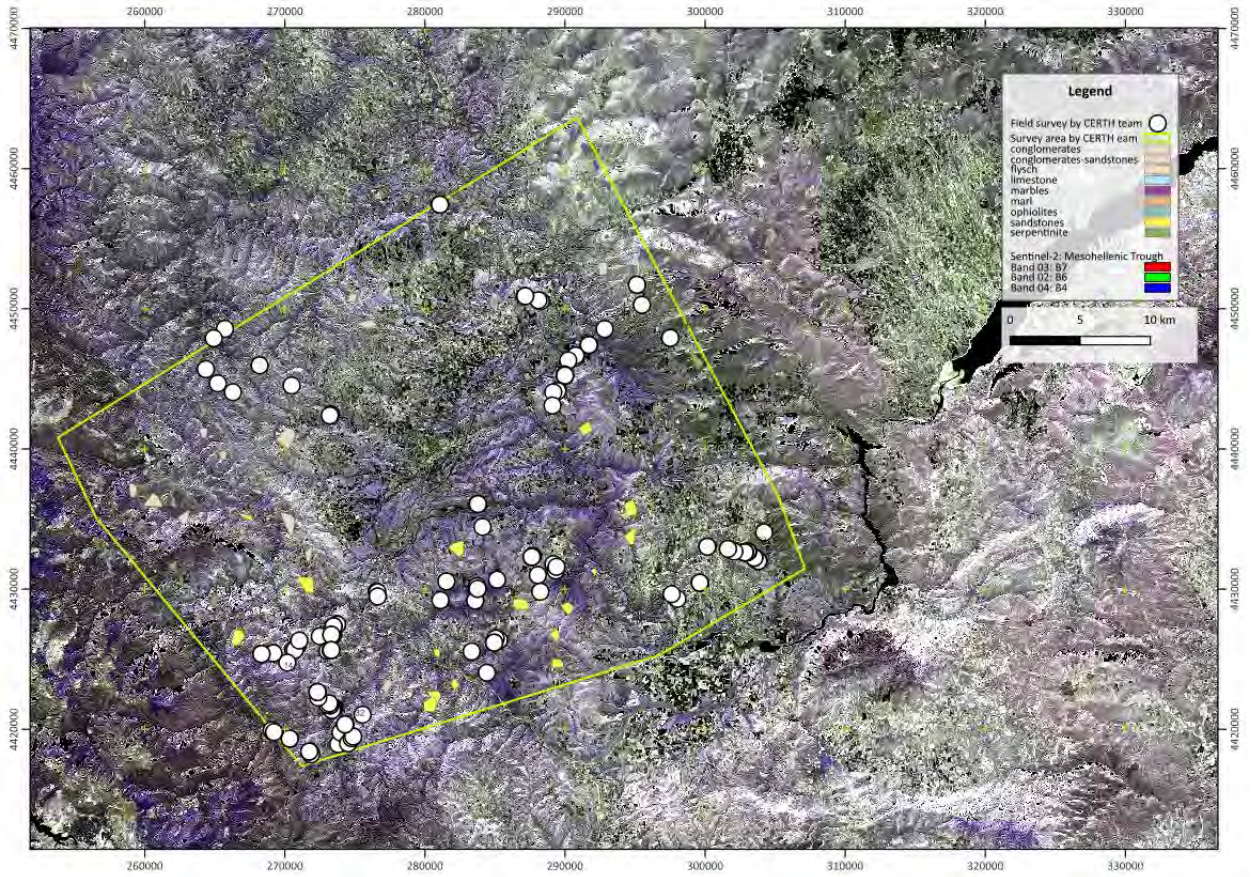

Figure 5.94: Supervised classification map of the study area (EGSA87 reference system) derived from Sentinel-2 imagery (7–6–4 composite). The classified units correspond to major lithologies, including conglomerates, sandstones, marls, limestones, serpentinites and ophiolites, highlighting their spatial distribution across the mapped region

The classified raster product obtained from SNAP was exported in GeoTIFF format. This file was imported into QGIS as a raster layer, where it was combined with geological vector data including points, lines, and polygons. The integration of these datasets allowed for the preparation of a final geological map that incorporates both remote sensing products and field observations. The distribution of these classes aligns with the geological framework of the MHT, where mixed sedimentary successions and ophiolitic fragments coexist. This approach demonstrates how optical remote sensing can support geological mapping by rapidly delineating lithological boundaries, complementing traditional field observations (Figure 5.95).

The PilotSTRATEGY project has received funding from the European Union's Horizon 2020 research and innovation programme under grant agreement No. 101022664

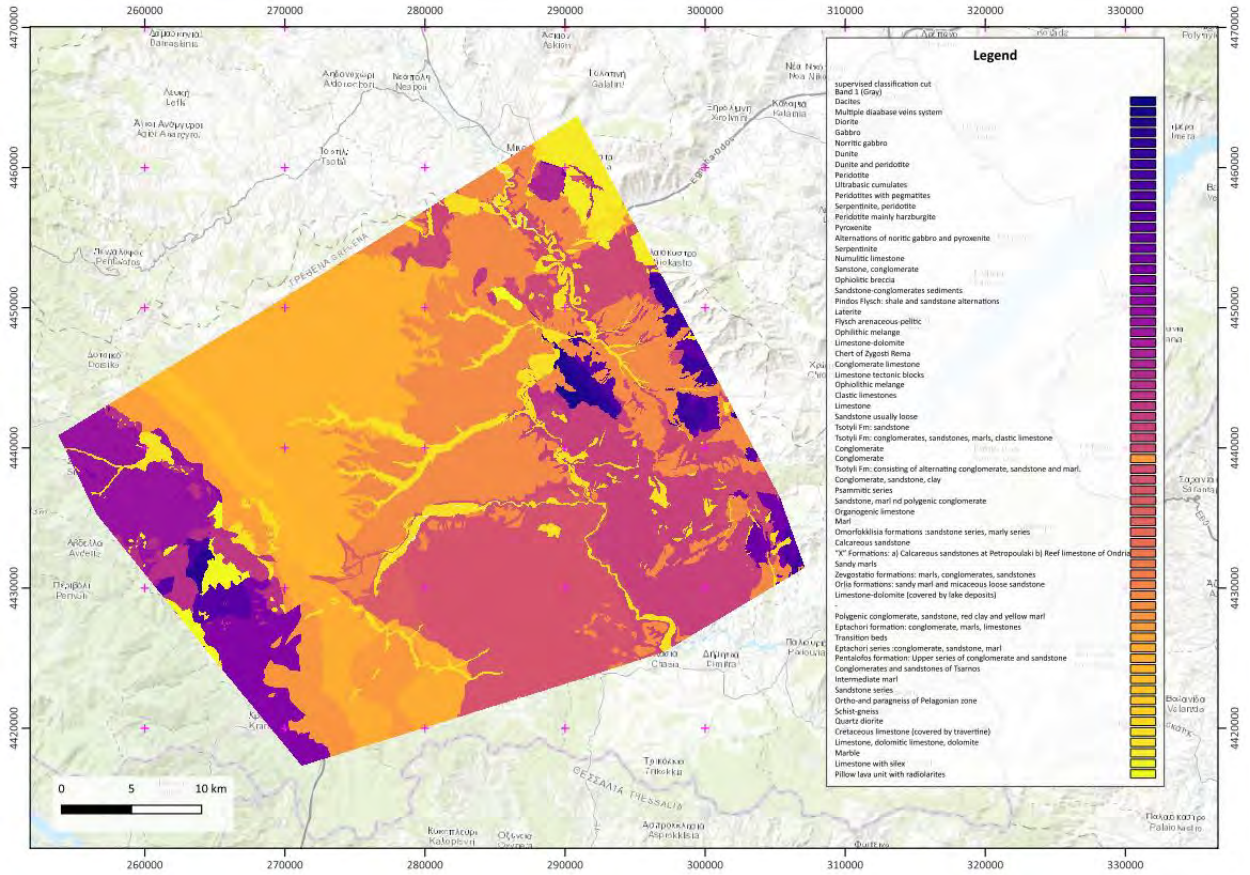

Figure 5.95: Supervised classification of Sentinel-2 MSI imagery (7-6-4 band combination) using the Maximum Likelihood algorithm. The classified raster, integrated with vector data in QGIS, delineates the distribution of lithological units within the MHT. The product complements field observations and supports the preparation of the 1:25,000 geological map.

Through the integration of field-based mapping, structural data, photographic documentation, and remote sensing analysis, a comprehensive geological map at 1:25,000 scale was produced. Remote sensing served as a complementary tool to strengthen interpretation in otherwise inaccessible areas, while the core mapping framework relied on direct field evidence and digitised structural measurements. This methodology ensured that the final geological map accurately reflects both lithological distribution and structural characteristics of the study area.

5.7. Map & Cross sections

The geological map of the study area (scale 1:25,000; reference system EGSA ’87) illustrates the structural and stratigraphic framework of the central and western part of the Mesohellenic Trough in Western Macedonia, Northern Greece (Figure 5.96). To the west, near the Prespa Lakes and along the boundary with Albania, the map displays the thick flysch successions of the Pindos Zone, consisting of sandstones, marls, and shales of Cretaceous–Paleogene age, which are locally overlain by Neogene continental deposits. Moving eastwards, the central part of the basin is dominated by the Mesohellenic succession,

The PilotSTRATEGY project has received funding from the European Union’s Horizon 2020 research and innovation programme under grant agreement No. 101022664

characterized by Oligocene to Miocene conglomerates, sandstones, marls, and intercalated limestones, which form the main sedimentary infill of the trough. The eastern margin, close to the Ptolemaida Basin and the Pelagonian crystalline massifs, is defined by tectonic contacts with ophiolitic units of Jurassic age, including peridotites, gabbros, basalts, and associated mélange. These ophiolitic rocks are interspersed with radiolarites and deep-marine carbonates, highlighting the remnants of oceanic crust emplaced during the Alpine orogeny. Fault systems and thrust contacts, mapped as continuous and inferred lines, delineate the structural architecture of the area, while Quaternary deposits locally cover the older formations in valley bottoms and plains. The cross-section traces (A–A' and B–B') Figure *5.97*Figure 5.98) provide key geological transects across the basin, allowing the reconstruction of subsurface geometry and the tectono-stratigraphic relationships between the major zones.

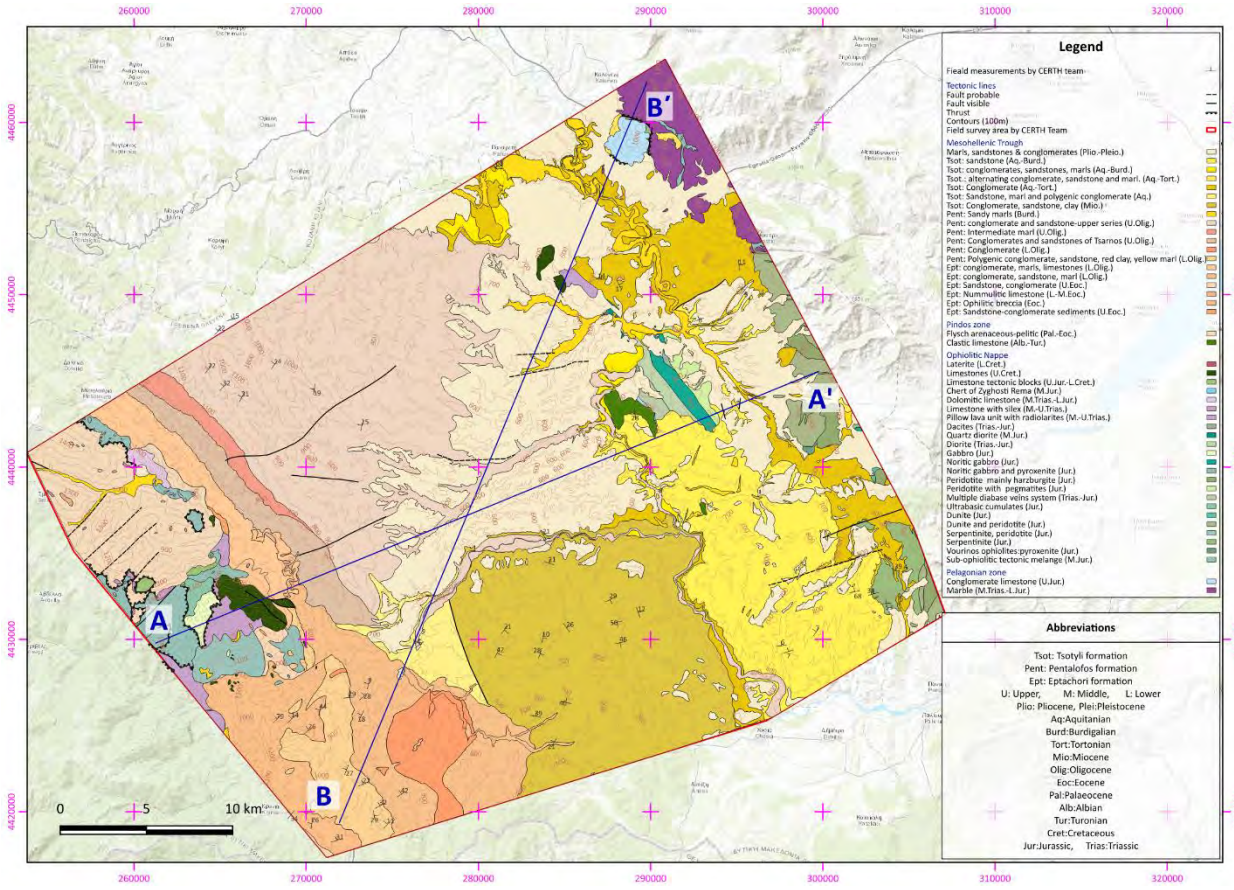

Figure 5.96: Geological map of the study area in Mesohellenic Trough, at a scale of 1:25,000, compiled in the Hellenic Geodetic Reference System 1987 (EGSA '87). The map illustrates the main lithostratigraphic units, tectonic structures, and cross-section lines (A–A', B–B')

Geological cross-section A–A' across the Mesohellenic Trough illustrates the main stratigraphic and structural configuration of the basin. The section shows a typical sedimentary succession unconformably overlying the Mesozoic basement composed of ophiolitic rocks and Cretaceous limestones. The sequence begins with the Oligocene Eptachori Formation, followed by the Tsotyli and Pentalofos Formations,

The PilotSTRATEGY project has received funding from the European Union's Horizon 2020 research and innovation programme under grant agreement No. 101022664

representing the progressive infilling of the basin from marine to continental environments. The ophiolitic complex was emplaced and deformed during the Late Jurassic to Cretaceous, later uplifted and eroded before the onset of Oligocene sedimentation. The cross-section highlights the regional unconformity that separates the deformed Mesozoic substratum from the overlying Plio-Pleistocene conglomerates, sands, and marls, as well as the fault-controlled architecture typical of the Mesohellenic Trough (Figure 5.97).

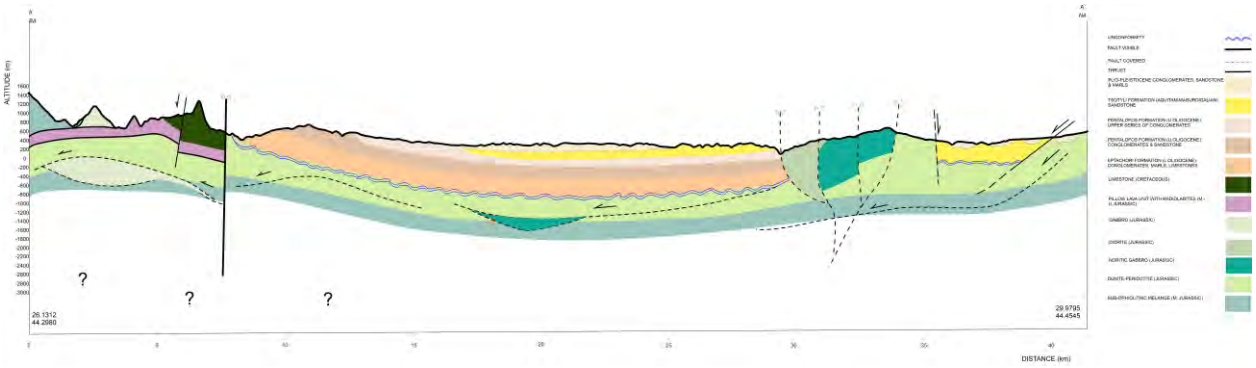

Figure 5.97: Geological cross-section of the Mesohellenic Trough showing the main lithostratigraphic units and structural features, from Jurassic ophiolites to Pliocene–Pleistocene conglomerates, sands and marls.

In the Grevena sub-basin, the corresponding sequence is absent, since this basin started opening during the Miocene and therefore postdates the sedimentation related to the Tsotyli Formation and all preceding units. However, the presence of an unconformity indicates a period of missing geological time, attributed to processes such as erosion or tectonic activity. The ophiolites were emplaced, deformed, and subsequently exposed above sea level, undergoing erosion. After the deposition of the Cretaceous limestones on top of the ophiolitic basement, the area emerged from the sea towards the end of the Cretaceous. A period of non-deposition followed, during which the Paleocene and Eocene are absent from the stratigraphic record of the Mesohellenic Trough. Sedimentation resumed in the Oligocene with the deposition of the Eptachori Formation, marking a continuous regional unconformity (Figure *5.98*Figure *5.98*).

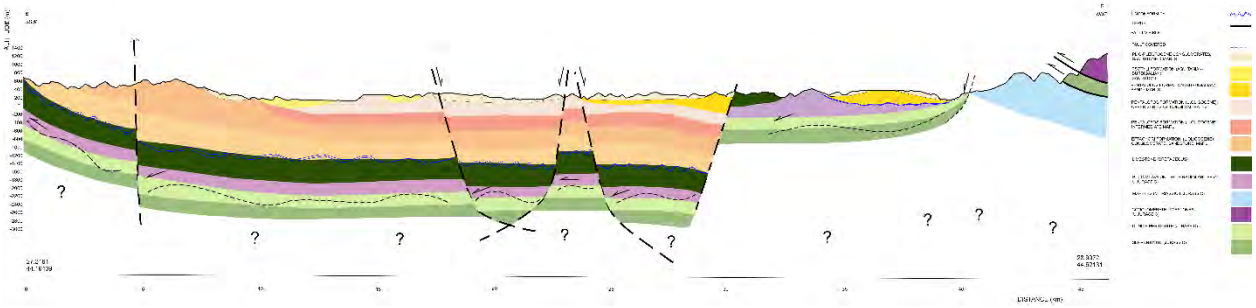

Figure 5.98: Geological cross-section across the Mesohellenic Trough illustrating basin geometry, major faults, and the contact between Plio-Pleistocene conglomerates, sands and marls, and Mesozoic formations.

The PilotSTRATEGY project has received funding from the European Union's Horizon 2020 research and innovation programme under grant agreement No. 101022664

6. Geochemical analysis

6.1. Geochemical investigation

Previous field investigations conducted as part of the PilotSTRATEGY Project on CO_2 storage led to the discovery of good low porosity low permeability seal rocks, but did not yield concrete evidence of an adequate reservoir rock[118]. To address this gap, water sampling campaigns were carried out in areas where natural gas emissions reveal existing permeable pathways. Although such zones are unsuitable for direct CO_2 storage due to their leakage behaviour, they serve as valuable natural analogues for understanding subsurface flow and reservoir performance. By examining these formations, the lithological and structural factors that control permeability and gas migration can be better restricted. This insight supports the identification of other parts of the basin with similar reservoir characteristics but stronger sealing capacity formations that, while not directly observable, are likely to retain fluids more effectively and therefore hold potential for secure CO_2 storage. The geochemical investigation is complemented by petrophysical and geomechanical investigation presented in D2.6 Petrophysics Report of all regions (doi: 10.5281/zenodo.12625689) and D2.8 Report on Geomechanical results for the 3 areas (doi: 10.5281/zenodo.12626692) respectively. The latter are publically accessible can be accessed in the Zenodo platform at the following link https://zenodo.org/communities/pilotstrategy.

Collecting data from: a) previous research conducted by Daskalopoulou et al, 2018[119], b) observations investigation in the field using anecdotal data, from publicly available media, and c) public indications of water springs with the elevated gas yield, the authors considered the local geology and concluded that the springs presented in Table 6.1 are promising places for an initial investigation.

The local geology of each water spring and sampling area is summarised based on published geological maps and field observations. Water springs at Katakali and Kivotos emerge through formations of the MHT, while spring emanations at Tropeouhos, Ammohori, Itea, Marina, Mesohori, Mesocampos and Neos Kafkasos are found at the Florina basin (Figure 6.1).

Table 6.1: Locations of water springs observed and suspected with a high possibility of gas content.

Name	N (WGS84)	E (WGS84)	X (Greek Grid, EGSA 87)	Y (Greek Grid, EGSA 87)	Z (m)
Katakali	39° 55' 31,15"	21° 40' 37,5"	30.1337	44.21760	404
Kivotos	40° 14' 35,55"	21° 25' 34,62"	28.0926	44.57643	547
Tropeouhos	40° 44' 25,45"	21° 26' 23,87"	28.3693	45.12806	695
Ammohori_1	40° 46' 39,93"	21° 28' 50,51"	28.7251	45.16854	633
Ammohori_2	40° 46' 54,80"	21° 28' 57,69"	28.7433	45.17308	631
Itea	40° 50' 1,64"	21° 30' 59,80"	29.0459	45.22988	613
Marina	40° 51' 44,29"	21° 29' 34,15"	28.8543	45.26211	595
Mesohori	40° 53' 12,92"	21° 29' 16,50"	28.8208	45.28956	589
Mesocampos	40° 53' 39,57"	21° 30' 41,36"	29.0218	45.29721	598
Neos Kafkasos	40° 54' 14,50"	21° 29' 37,49"	28.8754	45.30841	585

The PilotSTRATEGY project has received funding from the European Union's Horizon 2020 research and innovation programme under grant agreement No. 101022664

At Katakali, the near surface layers include Pliocene to Lower Pleistocene marls, sandstones, sandy marls, clays, and conglomerates of the Karperon basin [68]. A small lignite layer within the marls near the Sioutsa river indicates local marsh conditions, while fossil evidence (Planorbis, Neritina, and Radix ovate) suggests freshwater environments. Near basin margins, these sediments transition into unbedded fluvial-flash flood deposits. The lower stratigraphy includes:

1) the Miocene (Upper Aquitanian to Tortonian) Tsotyli Fm of the MHT (<2200 m in thickness). It is composed of ophiolitic conglomerates at the base, gradually transitioning into sandstones, marls, and sandy marls. The fossil content in the transition beds includes bryozoans (Retepora gigantea), corals (Siderastrea crenulata, Ceratotrochus duodecim sostatus), gastropods (Haustator magnasporulus, Turritella sp., Gypraea sp.), and bivalves (Chlamys multistriata, Panopea intermedia), indicating a marine depositional environment, and

2) the Middle to Upper Oligocene Eptachori Fm of the MHT, consisting of ophiolitic conglomerates with lateritic lenses at the base and interbedded sandstones and marls above. This formation lies unconformably over the metamorphic basement and contains a rich microfaunal assemblage (Milliolidae, Textulariidae, Cibicides sp., Almaena sp.), pointing to a shallow marine setting during its deposition[68].

The stratigraphy at Kivotos sampling site comprises Quaternary alluvial sediments, such as loose sands and clays, which are underlain by Pliocene to Pleistocene fluvial and lacustrine deposits forming terrace sequences composed of loose conglomerates, blue to greenish clays, sands, and friable sandstones [58]. The upper parts of this unit are characterised by red clays and conglomerates, suggesting alternating oxidising and reducing conditions in a dynamic depositional setting. Lower the Early Miocene (Aquitanian to Burdigalian) Tsotyli Fm of the MHT is found (<500 m in thickness), composed of conglomerates, and intercalated sandstones and clastic limestones, that exhibit rapid lateral facies changes and thinning. The fossil content (lamellibranchs, gastropods, algae and Miogypsina) suggests a shallow marine and marginal marine environment[58]. The lowermost unit in the area consists of brecciated Middle to Upper Cretaceous limestones with rudists and marly limestones, representing the tectonically deformed remnants of an older carbonate platform that forms the geological basement of the sequence.

The PilotSTRATEGY project has received funding from the European Union's Horizon 2020 research and innovation programme under grant agreement No. 101022664

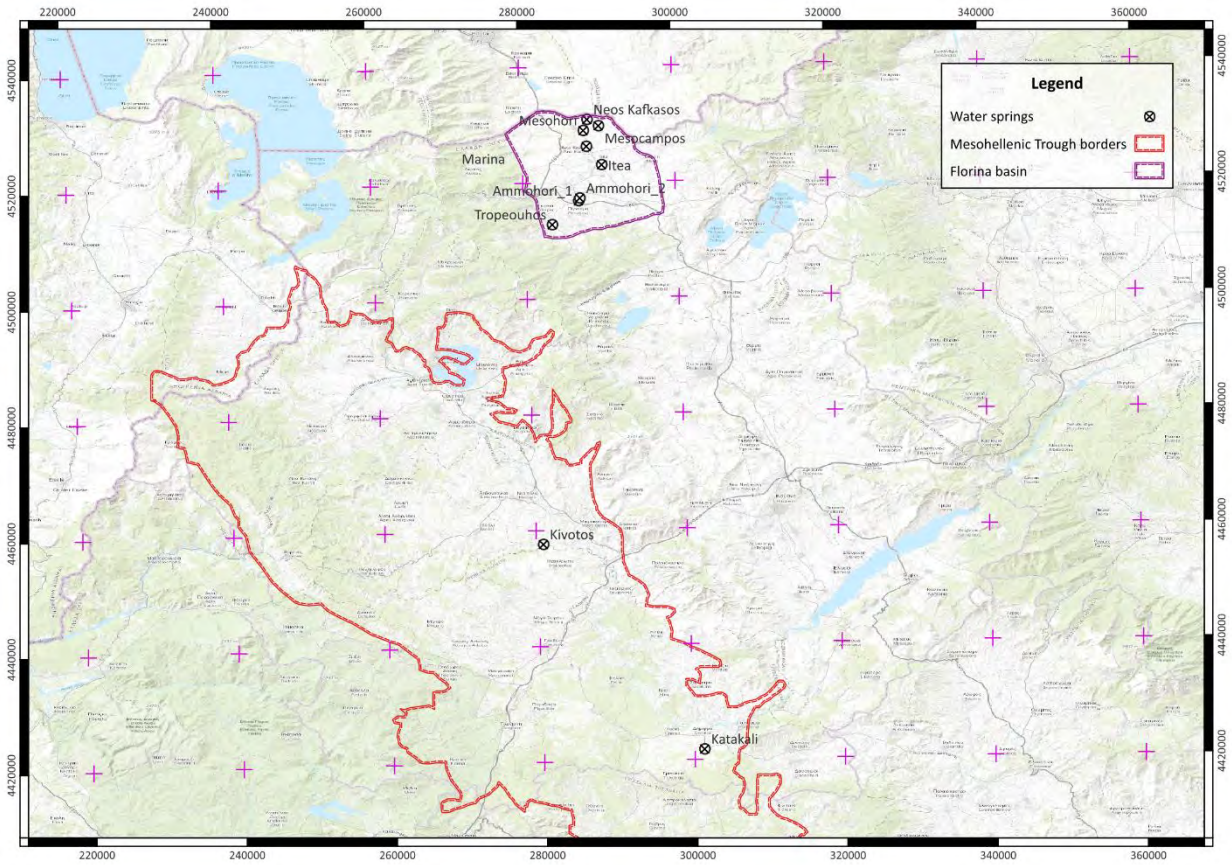

Figure 6.1: Map with the sample location in EGSA 87 grid system, scale 1:800.000, licence: CC-BY 4.0.

The stratigraphy at Tropeouhos, Ammohori, Itea, Marina, Mesohori, Mesocampos and Neos Kafkasos found at the Florina basin, comprises Neogene sands, clays, and conglomerates that grade downward into massive, whitish-brown to whitish-yellow fossiliferous marly limestones, marls, and clays (<100 meters in thickness)[120, 121]. The presence of lignite layers in the deeper parts indicates episodes of organic-rich deposition in marshy, low-energy environments. Fossil assemblages (*Neritina, Theodoxus macedonicus*) support a lacustrine to limnotelmatic depositional setting. Beneath these Neogene sediments lies the Pelagonian metamorphic basement of Palaeozoic age, composed predominantly of orthogneiss and paragneiss with intercalations of schists in the form of layers and lenses, and minor occurrences of amphibolites[120, 121].

Additionally, at Itea and Mesohori, the local stratigraphy includes Pleistocene conglomerates, sandstones, sands, and red clays, indicating deposition in fluvial to alluvial environments under oxidising conditions (<200 meters in thickness)[120]. These sediments represent a transitional phase between older Neogene units and more recent Quaternary deposits, reflecting intense weathering, erosion, sediment transport, and soil formation under subaerial conditions during the Pleistocene.

The PilotSTRATEGY project has received funding from the European Union's Horizon 2020 research and innovation programme under grant agreement No. 101022664

6.2.Sampling Strategy and Analytical Framework

Water samples for gas measurements were collected in accordance with the UK Environment Agency Methods for sampling and analysing methane in groundwater: a review of current research and practice [122], as well as Capasso and Inguaggiato, 1998[123] and Inguaggiato and Rizzo, 2004[124] . The sample collection method deployed is described below.

The sampling bottles were 100/125/250 ml vials crimped using a Teflon septum (Figure 6.2). Vial size was determined by the target analysis: 100 ml for carbon isotopes, ≥125 ml for noble gas isotopes. The future user/adopter is advised to pay particular attention to shipping and preservation of samples, as, despite the best efforts of the authors, the first two rounds of samples could not be measured reliably for gases in the laboratory due to the hot conditions of South Europe during spring and summer.

As prerequisite actions, before filling the vials with water sample, the vials were fully filled and rinsed with the same water to be sampled from the spring samples 2 or 3 times to reduce contamination.

Prior to the sampling, the spring water was measured for dissolved O_2 (mg/L), Conductivity (µS/cm), temperature (°C) and pH. The values of the latter were recorded in field books or digital devices. Physico-chemical conditions of the groundwater (pH, temperature, salinity) can contribute to CO_2 dissolution or release. Differences in He and CO_2 solubility and reactivity can determine the recorded variations in the He/CO_2 ratio [36]. The collection should be done as paired samples. In other words, two (2 nr) bottles of 100 ml, or 125 ml should be collected per location or sampling area. The first bottle is used for carbon, oxygen, hydrogen and helium isotopes, whereas the other bottle is used for gas chromatography (GC). Again, the exact size of the vials is dictated by the analysis to be performed. A balance between cost and volume collected should be established. Prior conduct with the laboratory to perform the analysis is highly recommended.

In bodies of water such as lakes, pools, seawater, or drainage galleries, as well as any location facilitating direct sample collection beneath the surface of the water, it is imperative to submerge and crimp the bottles. This entails placing the bottles underwater, allowing them to fill completely while ensuring that the caps remain submerged at all times to prevent any contact with the atmosphere to avoid any air contamination during the sampling phase. In addition, when the bottle is underwater, it is easier to tightly apply the rubber closure and the aluminium cap, and ensure that no atmospheric air is still trapped in the collected sample. A standard stainless-steel aftermarket crimper able to cap 8-32 mm aluminium plastic/full aluminium and stainless steel/tight caps was used for sealing the sampling bottles.

Both the rubber closure and aluminium cap (Figure 6.3) were applied and the vials were moved sideways to check if any air bubbles were visible to the naked eye. Crimping the bottle underwater might be a difficult task as the aluminium cap tends to float towards the surface.

The PilotSTRATEGY project has received funding from the European Union's Horizon 2020 research and innovation programme under grant agreement No. 101022664

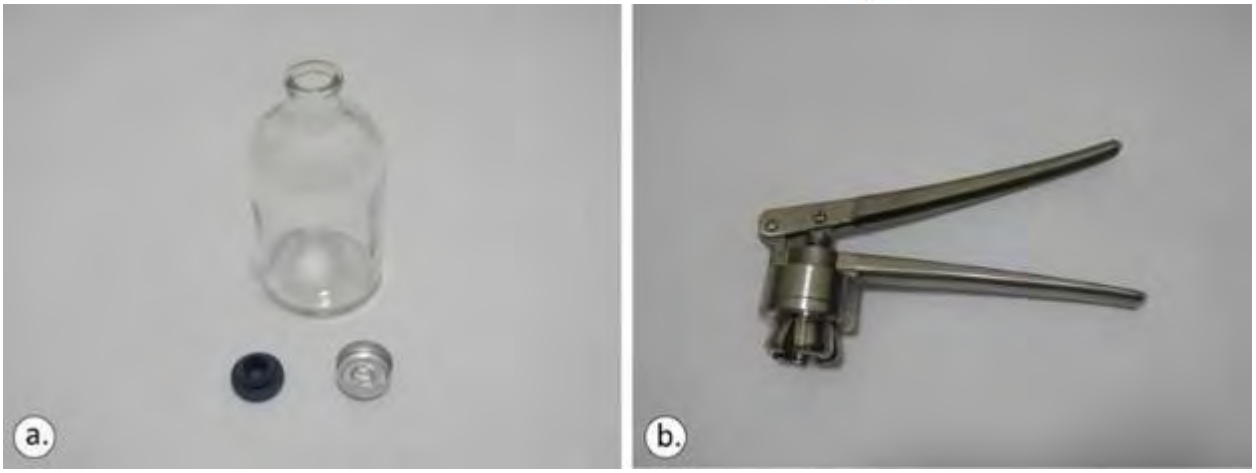

Figure 6.2: The 100ml crimp-top glass vial, the 20mm rubber closure (lower left) and aluminium cap (a) and the standard stainless-steel crimper (b), licence: CC-BY 4.0.

In any sampling action, it was ensured that the bottom of the bottle and the mouth of the crimper were levelled before applying force to the tongues (Figure 6.3). Otherwise, the aluminium cap will not be sealed perfectly. The sampling staff are advised to check the manual of the crimper and do considerable practice in sealing bottles before actually undertaking the sampling process. When bottles are sealed, it is advisable to check them again for bubbles under daylight and apply sealing tape around the neck of the bottle, covering also only the sides of the aluminium caps (Figure 6.3).

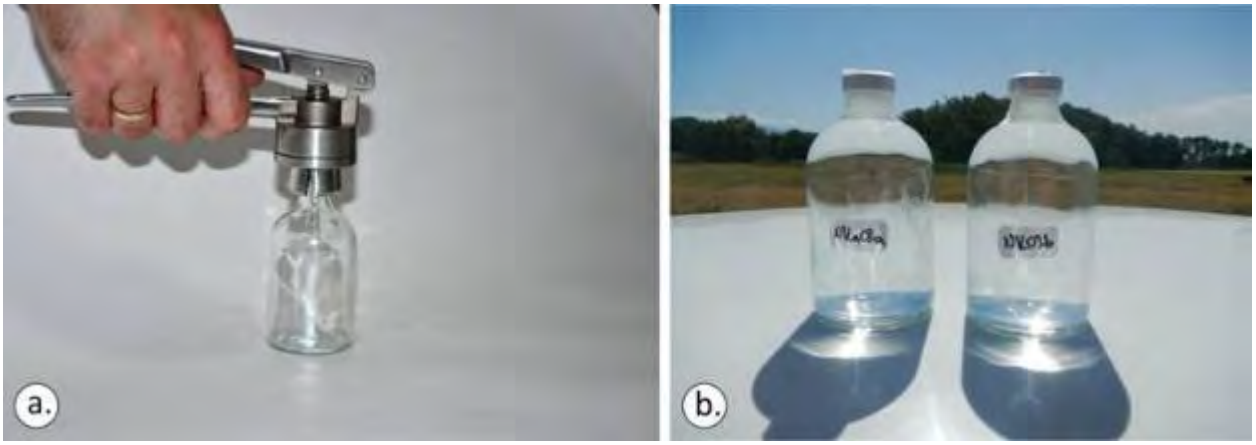

Figure 6.3: Ensuring that the bottom of the bottle and the mouth of the crimper are levelled before applying force to the tongues (a). Practice a lot after reading the manual and before commencing the sampling process (b), licence: CC-BY 4.0.

For water sampled from taps, a tube of suitable diameter, crafted from either silicone or Teflon, is required. This tube was inserted into the bottles until reaching the bottom, enabling the water to fill the container from bottom to top. Subsequently, the tube is slowly removed, ensuring the vial is entirely filled up to the upper portion of the bottle neck. Extreme care was taken to eliminate any air bubbles during this process, followed by sealing the vial securely to prevent air contamination.

The PilotSTRATEGY project has received funding from the European Union's Horizon 2020 research and innovation programme under grant agreement No. 101022664

It is recommended that the final procedure be conducted within a cylinder containing an identical sample of water extracted from the tap. This approach ensures the vial is fully submerged upon reaching its capacity, facilitating underwater sealing and crimping with water acting as a barrier to prevent air entrapment.

For inductively coupled plasma mass spectrometry (ICP-MS) analysis, employing plastic sterilised (Falcon) 50ml sampler filters (Figure 6.4), which have been appropriately acidified beforehand, is deemed sufficient.

Figure 6.4: Plastic (Falcon) 50 ml sample filters, license: CC-BY 4.0.

After the sampling took place, a visual observation of the existence or nonexistence of bubbles was noted. Samples were appropriately numbered on a pre-agreed sampling system and metadata such as location name, coordinates, time and data of sampling, related geological formation and any other observed data were properly recorded. Recording of sample numbers in each sample bottle is vital to minimise analytical problems during the laboratory investigation. All data collected, recorded and subsequently uploaded in SESAR, the System for Earth and Extraterrestrial Sample Registration. Each sample was allocated an International Geo Sample Number (IGSN) to ensure that they are Findable, Accessible, Interoperable, and Reusable (FAIR) [81]. The IGSN persistent identifier can link each sample with any analyses performed in any laboratory. Published data can be accessed via hyperlinked journals online. All data can be located via online geological data services or the Zenodo platform.

Four sampling campaigns were distributed across different seasons, with collections in summer 15-19 July 2023, spring 21–22 April 2024, late spring/early summer 5-6 June 2024, and late autumn/early winter 29 November–3 December 2024, enabling the assessment of potential seasonal effects such as temperature changes, precipitation patterns, organic matter input, and hydrological dynamics. In each case, the samples were shipped to an external accredited laboratory and specifically to the Laboratory for Stable Isotopes, Istituto Nazionale di Geofisica e Vulcanologia Sezione di Palermo in Italy for geochemical laboratory analysis that followed the below provided protocol.

Samples were analysed for He, H_2, O_2, N_2, CH_4 and CO_2 by gas chromatography (Perkin Elmer Clarus500 equipped with a double Carboxen 1000 column system, TCD-FID detectors) using Ar as the gas carrier. Ar was analysed with a Perkin Elmer XL gas chromatograph with MSieve 5A column, TCD detector having He

The PilotSTRATEGY project has received funding from the European Union's Horizon 2020 research and innovation programme under grant agreement No. 101022664

as carrier. Analytical uncertainties are ± 5%. Hydrocarbon analyses were performed with a Shimadzu 14a gas chromatograph equipped with a Flame Ionization Detector (FID) using He as the carrier gas. The analytical error is ≤5%.

Isotope determinations of $\delta^{18}O/^{16}O$ and δD in water samples were performed using the equilibration technique for oxygen and water reduction (hydrogen production using granular Zn) for hydrogen. Measurements were carried out using a FinniganDelta Plus mass spectrometer (Hydrogen) and an automatic preparation system coupled with an AP 2003 IRMS (Oxygen). Analytical precision for each measurement is better than 0.2‰ for δ18O and 1‰ for δD.

Carbon isotope composition of CO_2 was determined by using a Thermo Delta Plus XP, coupled with a Thermo TRACE Gas Chromatograph (GC) and a Thermo GC/C III interface. The TRACE GC is equipped with a Poraplot Q (25 m × 0.32 mm) column and uses Helium (5.6) as carrier gas at a constant flow of 0.9 cm^3 min^{-1}.

Undesired gas species, such as N_2, O_2, and CH_4, are vented to the atmosphere using back-flush of He and a Sige valve. The $^{13}C/^{12}C$ ratios are reported as $\delta^{13}C_{CO2}$ values relative to the V-PDB standard (Vienna Pee Dee Belemnite) [82]. Carbon isotope ratios were determined by comparing three in-house standards ($\delta^{13}C$ ranging from +0.3 ± 0.1‰ to −28.5 ± 0.3‰ vs V-PDB calibrated using a CO_2 standard (RM8564 [83]) with known isotopic composition ($\delta^{13}C$ = −10.45 ± 0.04‰ vs V-PDB) and two international standards (NBS 18 and NBS 19 [82]). External precision, computed as 1σ (standard deviation) on ten measurements of the same sample, is 0.1‰. The RM8564, NBS 18 and NBS 19 standards can be obtained from the Terrestrial Environment Radiochemistry Laboratory of the International Atomic Energy Agency (https://analytical-reference-materials.iaea.org/catalogs, web page accessed on 21/08/2025)

Carbon and Hydrogen isotopes of CH_4, both in free gases and in dissolved gases, were measured using a Thermo TRACE GC interfaced to a Delta Plus XP gas source mass spectrometer and equipped with a Thermo GC/C III (for Carbon) and with GC/TC peripherals (for Hydrogen). The gas chromatograph was equipped with an Rt-Q Plot column (Restek 30 m × 0.32 mm i.d.) and the oven was held at a constant temperature (50 °C for carbon and 40 °C for Hydrogen). The flow rate of carrier gas (He 5.6 grade) was held at a constant flux of 0.8 cm^3 min^{-1}. A split/splitless injector with a split ratio from 10:1 to 80:1 was used for sample introduction, except for diluted samples (CH_4 concentration lower than 10 mmol/mol) when direct on-column injection was performed.

The inlet system consists of a stainless steel loop with a known volume (50 µl), connected to a two-position six-port Valco® valve. Before the introduction of the sample, a vacuum of 10^{-2} mbar measured with an EBRO pressure gauge is ensured by a rotary vane pump. Once CH_4 was separated from the gas mixture, it was quantitatively converted to CO_2 by passing through a combustion oven (T = 940 °C) for $^{13}C/^{12}C$ ratios analysis or to H_2 by passing it through a reactor set at a temperature of 1440 °C for $^{2}H/^{1}H$ ratios analysis. Each sample analysis took about 500 s.

The PilotSTRATEGY project has received funding from the European Union's Horizon 2020 research and innovation programme under grant agreement No. 101022664

The $^{13}C/^{12}C$ ratios are reported as $\delta^{13}C\text{-}CH_4$ values for the V-P standard and $^{2}H/^{1}H$ ratios are reported here as $\delta^{2}H\text{-}CH_4$ values with respect to the V-SMOW standard. Carbon isotope ratios were determined by comparing an in-house standard ($\delta^{13}C = -49.5 \pm 0.2‰$) calibrated using four CH_4 standards (Isometric Instruments) with known isotopic composition ($\delta 1^{3}C$ ranging from $-23.9 \pm 0.3‰$ to $-66.5 \pm 0.3‰$ vs V-PDB).

Hydrogen isotope ratios were determined by comparing an in-house standard ($\delta^{13}C = -200 \pm 2.0‰$) with a CH_4 standard with known isotopic composition ($\delta^{2}H = -186.1 \pm 3.0‰$ vs V-SMOW). External reproducibility, estimated as 1σ (standard deviation) on ten measurements of the same sample, is 0.2‰ and 2.0‰ for carbon and hydrogen isotopes, respectively.

In CO_2-dominated gases having CH_4 concentrations lower than 1000 µmol/mol, the analyses of the isotope ratios of methane were carried out in the headspace gas samples collected using pre-evacuated 60 mL glass flasks filled with 20 mL of a 4 N NaOH solution.

The abundance and isotope composition of He, and the $^{4}He/^{20}Ne$ ratios, were determined by separately admitting He and Ne into a split flight tube mass spectrometer (Helix SFT). Helium isotope compositions are given as R/RA, where R is the ($^{3}He/^{4}He$) ratio of the sample and RA is the atmospheric ($^{3}He/^{4}He$) ratio ($RA = 1.386 \times 10^{-6}$). The analytical errors were generally < 1%. Location names, sampling date and coordinates of all new sampling sites together with raw chemical results can be found as supplementary material at https://doi.org/10.5281/zenodo.16914636 [84].

6.3. Geochemical and Isotopic results

Below are presented the results from all four sampling campaigns, starting with the isotope data analysis (Table 6.2-Table 6.5). As the samples are from groundwater, the Global Meteoric Water line was deployed as a universal baseline to analyse the data rather than the Local Meteoric Water line, which relies on precipitation samples only[125] (Figure 6.5). This is to identify deep fluid circulation, isotope shifts due to evaporation or water–rock interaction and in this case the GMWL provides a good universal baseline.

In the first sample campaign (Table 6.2, Summer 2023), most samples plot in close proximity to the Global Meteoric Water Line[126, 127], indicating a meteoric origin with little evaporation enrichment [128] (Figure 6.5). Katakali and Tropeouhos in the first round (Table 6.2) are the most depleted in both isotopes, indicating a colder recharge. Mesocampos and Kivotos are relatively enriched, possibly indicating partial evaporation[127]. Since the elevations of all sampling locations are relatively similar, altitude differences are unlikely to be the primary factor driving the observed isotopic variability. This original investigation did not provide any distinct chemical signature; however, during the Katakali sample collections (#10), there were clear observations of gas bubbles in the water sample. This is due to pressure decreases, causing these dissolved gases to come out of solution and form bubbles.

The PilotSTRATEGY project has received funding from the European Union's Horizon 2020 research and innovation programme under grant agreement No. 101022664

Table 6.2: Water samples collected between 15-19/07/2023, laboratory data analysis provided at 06/09/2023, first sample campaign, rounded to two significant figures.

N°	Spring location name	δD_{H20}	$\delta^{18}O_{H2O}$	Dissolved O_2 (mg L^{-1})	Conductivity (µS cm^{-1})	Temp (°C)	pH
1	Tropeouhos	-72	-10.0	7.9	-	17.5	6.04
2	Mesocampos	-50	-7.4	0.19	1686	16	6.06
3	Neos Kafkasos	-59	-8.5	0.76	575	14.1	6.08
4	Ammohori 1	-64	-9.0	8.3	920	17.5	6.07
5	Itea	-66	-9.6	2.73	1017	16.5	6.03
6	Mesohori	-62	-9.1	1.09	478	14	6.03
7	Ammohori 2	-70	-9.9	7.1	319	20.5	6.01
8	Marina	-68	-9.6	6.3	338	25.6	6.04
9	Kivotos	-57	-8.2	0.24	850	15.3	5.4
10	Katakali	-74	-10.5	0.25	1447	18	6.0

The second round of data (Table 6.3) indicated that Tropeouhos, Mesocampos and Neos Kafkasos had a shift towards depletion of isotopes, which indicates hydrologic change. This can be explained by seasonal input [129]. The first batch was collected in Summer (June 2023) during a low rainfall season, whereas the second batch was collected in Spring (April 2024) during a high rainfall season. This is consistent with a well-mixed aquifer or steady-state recharge conditions typical of early spring. This sample location above the GMWL (Figure 6.5) suggests that precipitation during the winter had enough time to infiltrate deeper into the ground and homogenise with groundwater before sampling [125, 126, 130, 131].

Table 6.3: Water samples collected between 21-22/04/2023, laboratory data analysis provided at 15/05/2024,second sample campaign.

N°	Spring location name	δD_{H20}	$\delta^{18}O_{H2O}$	Dissolved O2 (mg L^{-1})	Conductivity (µS cm^{-1})	Temp (°C)	pH
1	Tropeouhos	-75.0	-11.9	8.85	1803	14.4	7.5
2	Mesocampos	-59.0	-10.1	2.59	1984	13.5	5.67
3	Neos Kafkasos	-64.0	-11.0	1.60	468	14.5	5.42
4	Ammohori 1	-66.0	-10.7	7.06	971	12	6.49
5	Itea	-62.0	-10.0	2.91	972	13	5.61
6	Mesohori	-66.0	-10.8	2.50	450	13	6.5
7	Ammohori 2	-69.0	-11.2	7.78	318	14.8	5.7
8	Marina	-67.0	-11.2	8.15	347	14.1	6.29
9	Kivotos	-61.0	-10.3	1.75	803	14.9	7.25
10	Katakali	-76.0	-12.0	1.40	1440	16.1	7.5

The third round of samples collected were notably more depleted in δD and $\delta^{18}O$ and with higher deviation from GMWL related to rainfall patterns and evaporation, which is consistent with the June sampling period (Table 6.4). Still, most of the samples are in proximity to the GMWL, indicating that rainfall is still the prevailing factor (Figure 6.5).

The PilotSTRATEGY project has received funding from the European Union's Horizon 2020 research and innovation programme under grant agreement No. 101022664

Table 6.4: Water samples collected between 05-06/06/2024, laboratory data analysis provided at 24/07/2024,third round campaign.

N°	Spring location name	δD_{H2O}	$\delta^{18}O_{H2O}$	Dissolved O_2 (mg L^{-1})	Conductivity (µS cm^{-1})	Temp (°C)	pH
1	Tropeouhos	-80	-10.1	0.78	1694	20.0	7.04
2	Mesocampos	-58	-8.8	1.72	1809	20.3	6.01
3	Neos Kafkasos	-65	-9.7	1.05	477	17.0	5.83
4	Ammohori 1	-70	-8.9	4.87	968	21.0	6.76
5	Itea	-66	-9.3	2.63	712	16.1	5.83
6	Mesohori	-62	-9.2	2.27	485	16.0	6.22
7	Ammohori 2	-71	-9.6	7.33	301	21.4	6.20
8	Marina	-67	-9.2	7.00	329	22.9	6.56
9	Kivotos	-63	-8.2	1.05	781	18.8	7.65
10	Katakali	-73	-9.6	7.22	1468	18.0	8.48

The fourth batch of samples collected mostly in Winter (December) plots above the GMWL, suggesting winter recharge from isotopically lighter sources indicated by the isotope depletion (Table 6.5). The dispersion of the samples may reflect heterogeneity in recharge sources, mixing with deeper groundwater or longer water to rock contact time[125, 130] (Figure 6.5).

Table 6.5: Water samples collected between 29/11/2024 – 3/12/2024, laboratory data analysis provided at 06/03/2025, fourth campaign

N°	Spring location name	δD_{H2O}	$\delta^{18}O_{H2O}$	Dissolved O2 (mg L^{-1})	Conductivity (µS cm^{-1})	Temp (°C)	pH
1	**Katakali**	-11.1	-75	0.26	1505	15.1	8.04
2	**Kivotos**	-8.6	-58	0.25	855	14.3	7.75
3	**Tropeouhos**	-11.5	-78	0.41	1862	14.2	7.12
4	**Neos Kafkasos**	-9.8	-66	1..22	487	14.3	6.03
5	**Katakali-2**	-11	-75	0.26	1505	15.1	8.04
6	**Kivotos-2**	-8.8	-59	0.25	855	14.3	7.75
7	**Tropeouhos-2**	-11.4	-79	0.41	1862	14.2	7.12
8	**Plank (bottled water)**	-8.4	-49	-	-	-	-

In all sampling campaigns, the pH measured was either slightly alkaline, with values around 7.5 or slightly acidic and values around 5.4. There was only one exception in the third sample campaign, in the Katakali water sample, which registered an alkaline pH of 8.48.

The PilotSTRATEGY project has received funding from the European Union's Horizon 2020 research and innovation programme under grant agreement No. 101022664

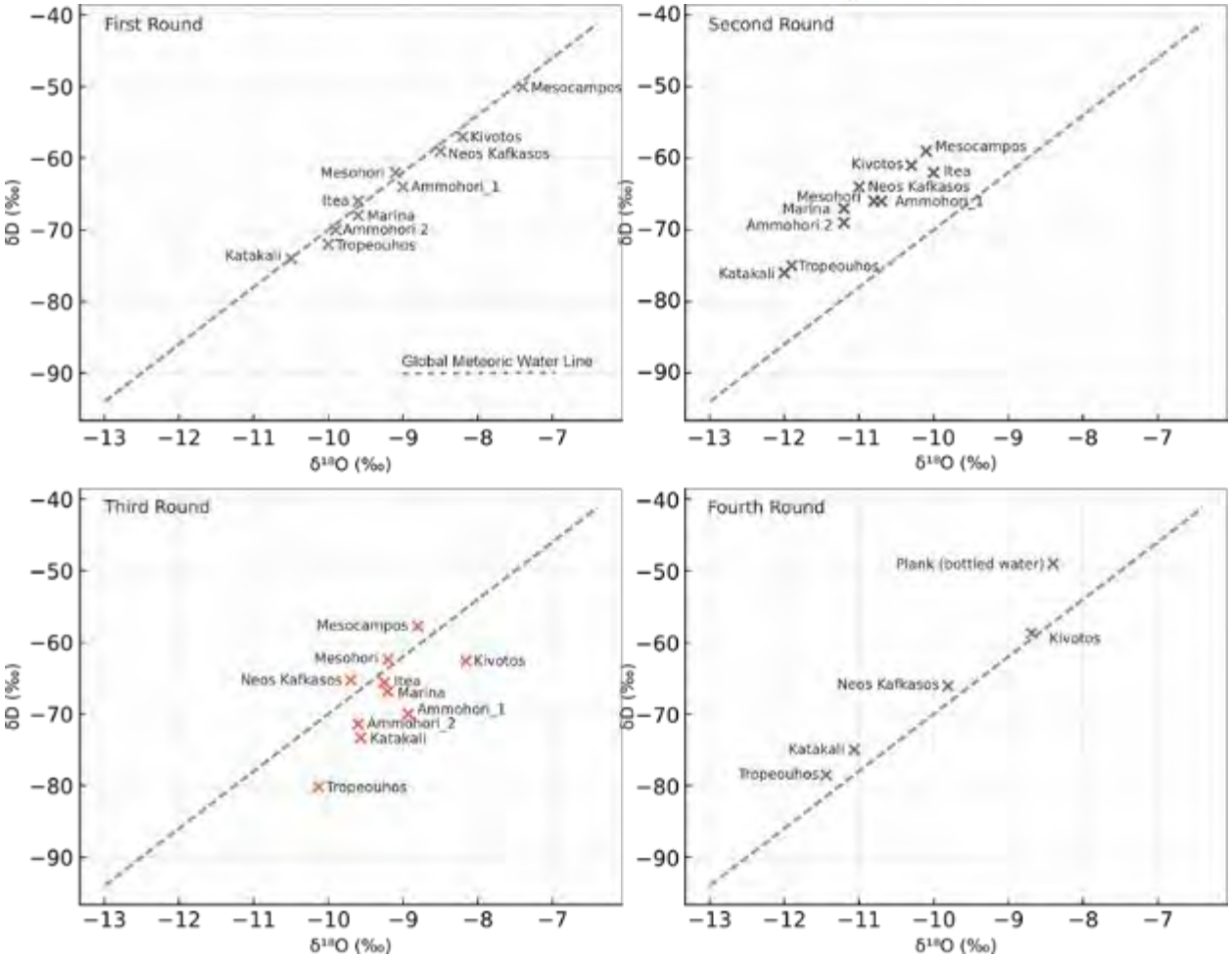

Figure 6.5: Stable Isotope composition of water samples collected in June 2023 with reference to the Global Meteoric Water Line (GMWL), licence: CC-BY 4.0.

The ICP chemical analysis of the second round presented in Table 6.6 revealed that all samples had high detectable levels of strontium (Sr) and barium (Ba) in the scale of μg L^{-1}. Concentrations remained well below drinking water guideline thresholds) which, according to the United States Environment Protection Agency, is 2 mg L^{-1} for Ba and 4 mg L^{-1} for Sr (National Primary Drinking Water Regulations | US EPA, web page accessed on 18/07/2025). The Si concentrations varied from 7.7 to 59.6 mg L^{-1}, indicating variable rock silicate interaction [132, 133].

The PilotSTRATEGY project has received funding from the European Union's Horizon 2020 research and innovation programme under grant agreement No. 101022664

Table 6.6: ICP chemical analysis of water samples from the surveyed sites at Mesohellenic Trough and Florina basin in ug L^{-1}.

Spring location / Elements	Kivotos	Ammohori 1	Ammohori 2	Itea	Marina	Mesohori	Neos Kafkasos	Katakali	Tropeou
Li	8	3	13	3	8	7	8	132	407
Be	<0.02	0.16	0.22	0.03	0.04	0.02	0.04	<0.02	1.03
B	269	41	15	37	15	90	60	933	716
Al	4	1455	7	40	25	146	30	5	92
Ti	0.10	87	0.20	0.15	0.63	11	0.12	0.41	1.8
V	0.05	5	0.75	0.92	2	0.71	0.79	0.19	0.25
Cr	0.19	5.01	0.86	0.63	2.64	0.58	0.12	0.61	0.23
Mn	5	37	10	18	0.29	682	436	8	444
Fe	7	2807	53	22	16	247	10	221	101
Co	0.01	1	0.03	0.12	0.03	2	2.03	0.40	0.30
Ni	<0.1	7.6	9.7	3.7	4.1	8.1	7.3	9.0	0.2
Cu	<0.1	6	47	9	1	15	1	<0.1	<0.1
Zn	<0.1	177	65	30	0.34	76	4.7	<0.1	0.9
As	0.02	0.44	0.05	0.31	0.66	0.15	0.44	0.13	1.5
Se	0.11	1.2	0.27	3.2	0.41	0.37	0.80	0.17	0.33
Br	466	128	88	47	41	58	44	185	303
Rb	0.97	4.4	0.31	0.57	0.39	0.99	0.94	1.1	39
Sr	591	660	281	260	208	214	260	544	902
Mo	0.14	0.24	0.12	1.09	0.19	0.18	0.31	0.10	6
Cd	<0.01	<0.01	<0.01	<0.01	<0.01	0.02	<0.01	<0.01	<0.0
Sn	0.01	0.23	0.02	0.04	<0.01	6.03	0.01	<0.01	<0.0
Sb	0.00	0.03	0.02	0.04	0.01	0.18	0.01	<0.01	0.01
Cs	0.01	0.25	0.00	0.00	0.00	0.02	<0.01	0.02	31.1
Ba	67	89	24	61	38	54	99	156	11
Tl	<0.01	0.03	<0.01	0.01	<0.01	0.01	0.01	<0.01	<0.0
Pb	0.01	4.77	1.22	0.23	0.01	7.89	0.09	<0.01	0.20
Bi	0.01	0.02	<0.01	<0.01	<0.01	0.05	<0.01	<0.01	<0.0
U	0.18	1.99	0.08	6.07	0.52	0.21	0.32	0.00	0.09
Si	15000	18000	27000	8000	26000	11000	14000	60000	1700

The PilotSTRATEGY project has received funding from the European Union's Horizon 2020 research and innovation programme under grant agreement No. 101022664

Regarding the rest of the chemical elements identified Tropeouhos and Ammohori_1 had high levels of Fe (1010 and 2807 μg L^{-1}), Mn (37 and 444 μg L^{-1}), and Al (92 and 1455 μg L^{-1}), respectively. Ammohori 1 also showed elevated Ti (86 μg L^{-1}) and Zn (176 μg L^{-1}), while Tropeouhos had significantly high concentrations of Li (406 μg L^{-1}), B (7160 μg L^{-1}), and Br (303 μg L^{-1}).

The Mesohori water sample had notable values of 132 μg L^{-1} of Al, 682 μg L^{-1} of Mn and 247 μg L^{-1} of Fe. The Neos Kafkasos water sample showed Mn values of 436 μg L^{-1}. The Katakali sample had prominent values of 132 μg L^{-1} of Li, 933 μg L^{-1} of B, 220 of Fe μg L^{-1}, 185 μg L^{-1} of Br. Mesokampos had 363 μg L^{-1} of Br. All other chemical elements detected from the second water sampling campaign were of considerably lower value.

The chemical composition of groundwater samples collected during the second campaign reflects a range of geochemical processes influenced by water–rock interaction and rock differences. The Tropeouhos and Ammohori_1 sample chemical results indicate active water and rock interaction involving iron-bearing minerals that undergo redox processes with Fe^{3+} (insoluble ferric) → Fe^{2+} (soluble ferrous) in anoxic environments[132, 134]. High concentration of Fe can be associated with dissolution of iron bearing minerals or the serpentinization process [135]. Both processes favour natural hydrogen production. The same applies to a lesser extent for the Mesohori and Katakali samples. Of particular interest are the Katakali and Tropeouhos samples that had high detectable levels of Li (131 and 406 μg L^{-1}, respectively), indicating deep circulation water interaction with igneous or silicate rocks. This deeper circulation, also supported by isotopic evidence provided in Figure 6.5, favours the generation and preservation of natural hydrogen conditions[136].

The geochemical analysis from the third sampling campaign presented in Table 6.7 revealed further information related to the gas component of the water samples. The Katakali water sample analysis provided values 4.4 ppm of H_2 coupled with 3,704 ppm of CH_4, suggesting active geochemical processes related to either organic degradation or serpentinisation. The Kivotos sample showed values of 29 ppm of He, 1.7 ppm of H_2, and 31,400 ppm of CH_4. The latter consists of anecdotal public observations suggesting strong methane generation potential and possible mantle-derived gas contribution to gas mix phase[137].

The Tropeouhos sample registered notable He levels (1,403 ppm), accompanied by low CH_4 concentrations at 89 ppm. This could be associated with deep-seated helium degassing coupled with some microbial or thermogenic methane input[138, 139].

Samples Ammohori_1 and Ammohori_2 registered elevated CO_2 concentrations of approximately 7–8%, while methane remained low at around 1 ppm. In addition, the Itea sample contained 60.7% CO_2 and 4 ppm of CH_4, suggesting a dominant CO_2 component in the gas phase. This is consistent with the accumulation of natural CO_2 in the Florina basin in the Tertiary formation and its leakage through fractures and permeable rocks[135]. The Mesohori sample registered 9 ppm of CH_4, while Mesokampos contained 34 ppm of CH_4 along with approximately 60% CO_2, pointing to variable organic or volcanic degassing influence [140]. Finally, the Neos Kafkasos sample exhibited 6 ppm of He, 2 ppm of H_2, and a substantial 40% CO_2, indicating multi-gas signatures possibly linked to deep fluid migration through faulted rocks [100, 140].

The PilotSTRATEGY project has received funding from the European Union's Horizon 2020 research and innovation programme under grant agreement No. 101022664

Table 6.7: Gas chemical analysis as a result of the third water sampling campaign, n.a denotes not enough sample quantity to perform the chemical analysis for that specific element.

Spring location	Katakali	Kivotos	Tropeouhos	Ammohori_1	Ammohori_2	Itea	Marina	Mesohori	Mesocampos	Neos Kafkasos
He (ppm)	n.a	29	1403	n.a	n.a	n.a	n.a	n.a	n.a	6
H2 (ppm)	4.4	1.7								1.9
O2 (%)	5.22 ×10⁻2	4.41 ×10⁻2	3.66 ×10⁻2	1.65	5.99	1.60 ×10⁻1	4.35	3.1 ×10⁻1	7.01 ×10⁻2	1.00 ×10⁻1
N2 (%)	18.14	19.87	24.81	19.02	19.88	2.19	16.34	16.42	2.02	9.48
CO (ppm)	n.a	n.a	n.a	0.2	0.2	n.a	0.2	n.a	n.a	2.2
CH4 (ppm)	3704	31400	89	1.2	1.1	4.1	0.8	9	34	n.a
CO2 (%)	0.79	1.58	2.16	7.08	7.87	60.68	4.13	3.3	60.22	40.01
Gas volume (cc per 120 cc of sample)	6.4	6.4	6.4	6.6	7.2	14.4	6.2	6.8	12.4	10
He (×10−4 cc L-1 STP)	0.0	16.4	794.6	0.0	0.0	0.0	0.0	0.0	0.0	5.3
H2 (cc L-1 STP)	0.00	0.00	0.00	0.00	0.00	0.00	0.00	0.00	0.00	0.00
O2 (cc L-1 STP)	0.04	0.02	0.02	0.96	3.82	0.20	2.39	0.19	0.08	0.09
N2 (cc L-1 STP)	17.0	11.3	14.0	11.1	12.7	2.8	9.0	10.0	2.20	8.40
CO (×10⁻⁶ cc L-1 STP)	<LOQ	<LOQ	0.0	12.5	13.9	0.0	7.3	0.0	0.0	779
CH4 (×10⁻⁶ cc L-1 STP)	362.5	1778.4	5.0	0.7	0.7	52.3	0.4	54.2	373.1	0.0
CO2 (cc L-1 STP)	8.90	0.90	1.20	4.10	5.00	77.30	2.30	2.00	66.10	35.40

Following the scientifically interesting results of the third campaign, a fourth one commenced with a focus on four promising locations of Katakali, Kivotos, Tropeouhos and Neos Kafkasos. To further elucidate the origin of the gas phase, the geochemical investigation considered the following analysis:

3) He
4) H_2
5) CH_4
6) CO_2
7) Helium isotopes (^3He, ^4He)
8) Deuterium of hydrogen (δ^2H-H_2)
9) Deuterium of methane (δ^2H-CH_4)
10) Deuterium of water (δ^2H-H_2O)

The PilotSTRATEGY project has received funding from the European Union's Horizon 2020 research and innovation programme under grant agreement No. 101022664

11) Oxygen-18 of carbon dioxide ($\delta^{18}O$-CO^2)
12) Oxygen-18 of water ($\delta^{18}O$ - H_2O)
13) Carbon-13 of methane ($\delta^{13}C$-CH_4)
14) Carbon-13 of carbon dioxide ($\delta 1^8O$-CO_2)
15) Carbon-13 of DIC ($\delta^{13}C$-DIC)
16) Carbon-14 of DIC (^{14}C-DIC)

This time, a blind sample system with duplicates was used during the laboratory analysis, together with a sample of water table as a blanket to increase the reliability of the chemical analysis results. Thus, the laboratory received codes only and not the actual locations of the samples. In all cases, the duplicate samples showed almost identical values. The results of the fourth campaign are presented in Table 6.8.
In this final fourth round, no hydrogen gas was registered. However, the Katakali samples showed a mean value of 306335 ppm CH_4 with $\delta^{13}CCH_4$ values around –70‰ and δDCH_4 near –230**‰**. On the same note, the Kivotos samples registered a mean of 43.5 ppm of He coupled with a mean 43550 ppm CH_4 with $\delta^{13}CCH_4$ at –75.5‰. The Tropeouhos samples showed a mean of 81 ppm of CH_4, in this case, the first sample showed no He values, whereas the second sample 1.4 ppm of He. The Neos Kafkasos, although sampled in duplicates, only one sample survived and was analysed. The sample that survived showed a value of 10 ppm of He and 7 ppm of CH_4. For the Neos Kafakasos sample, there was no $\delta^{13}CCH_4$ available. The δ^{13}CTDC was at –1.2‰) and δD was at –66‰).

Table 6.8: Targeted Gas chemical analysis as a result of the fourth water sampling campaign

Spring location	Katakali	Kivotos	Tropeouhos	Neos Kafkasos	Katakali-2	Kivotos-2	Tropeouhos-2	Plank (bottled water)
He (ppm)	-	43	-	10	-	44	1.4	-
H2 (ppm)	-	-	-	-	-	-	-	-
O2 (%)	0.12	0.19	0.21	0.58	0.1	0.24	0.21	3.3
N2 (%)	4.07	19.08	22.56	8.45	6.08	20.04	22.47	19.86
CH4 (ppm)	300370	43000	81	7	312300	44100	81	2.7
CO (ppm)								19.5
CO2 (%)	2.33	1.67	2.4	49.9	2.44	1.73	2.49	0.94
Gas volume (cc per 120 cc of sample)	7.4	6.2	6	10	7.6	5.8	5	5.6

The PilotSTRATEGY project has received funding from the European Union's Horizon 2020 research and innovation programme under grant agreement No. 101022664

He (×10–4 cc L-1 STP)	0.0	27.9	0.0	9.8	0.0	27.0	0.9	0.0
H2 (cc L-1 STP)	0.0	0.0	0.0	0.0	0.0	0.0	0.0	0.0
O2 (cc L-1 STP)	0.10	0.14	0.15	0.62	0.09	0.17	0.15	2.26
N2 (cc L-1 STP)	4.19	17.63	20.44	10.65	6.37	17.81	20.36	17.29
CH4 (×10⁻3 cc L-1 STP)	14558.3	1833	4.0	3.3	15440.5	1903.3	4.04	0.1
CO (×10⁻3 cc L-1 STP)	0.0	0.0	0.0	0.0	0.0	0.0	0.0	1.8
CO2 (cc L-1 STP)	26.90	19.10	27.40	587.10	28.20	19.70	28.40	10.70
total Alk	15.8	6.3	2.00	4.2	15.7	6.4	2.1	4.0
d13CTDC	13.9	-14.2	3.9	-1.2	14.4	-15.8	1.9	-11.2
d13CCH4	-69.5	-75.5	-	-	-69.8	-69.5	-	-
dDCH4	-251	-107	-	-	-230	-92	-	-

6.4. Interpretation of gas sources and migration mechanisms

Most samples were slightly acidic (around pH 5.4), suggesting interaction with silicate-rich lithologies, likely weathered ophiolites, or the influence of organic-rich soils. In contrast, the Katakali sample exhibited a distinctly alkaline pH (8.48), potentially indicating interaction with carbonate rocks (e.g. Triassic–Jurassic limestones) or serpentinized ultramafics undergoing low-temperature alteration, which commonly release hydroxide ions and elevate pH [136, 141, 142].

The sedimentary series of the MHT exhibits distinct geological and mineralogical characteristics that reflect its diverse depositional histories and diagenetic evolution. Sandstones from the Eptachori Fm, are fine-grained and well-bedded, siliceous in composition and display bioturbation features and fossils of plant fragments [143]. Quartz (<37 wt.%) is the dominant mineral, followed by calcite (<29 wt.%), albite (<13 wt.%), and muscovite (<13 wt.%). Minor mineralogy includes dolomite, chamosite, biotite, titanite, pyrite, crichtonite, actinolite and zircon [143]. Coupled with carbonate-rich microcrystalline cement, these features indicate deposition in a marine-influenced or lacustrine setting. Larger grain size, a mixed lithic content, and a calcareous composition characterise sandstones from the Pentalofos Fm. Calcite (<41 wt.%), dolomite (<18 wt.%), and quartz (<15 wt.%) with a notable feldspathic component (albite <12 wt.%) characterise mineralogy. Minor constituents include microcline, muscovite, aragonite, and traces of chlorite, titanite, chromite, pyrite, Fe-chromite, actinolite, apatite, andradite and enstatite[143]. These characteristics reflect depositional settings of higher-energy with significant detrital input, suggesting a mixed depositional environment influenced by the erosion of the ophiolitic rocks surrounding the MHT. Marly sandstones from the Tsotyli Fm show medium bedding, massive tabular structures, and a mixed siliceous-calcareous composition. Calcite (30 wt.%), quartz (29 wt.%), and albite (21 wt.%) are the main minerals, while the fine-grained, well-cemented matrix contains accessory muscovite, chlorite, dolomite

The PilotSTRATEGY project has received funding from the European Union's Horizon 2020 research and innovation programme under grant agreement No. 101022664

and aragonite, and traces of microcline, zircon and jacobsite[143]. Coupled with a moderate macro-porosity, these aspects suggest deposition in a high-energy environment with significant siliciclastic input.

The samples from Ammohori_1 and Tropeouhos displayed high levels of Fe (up to 2807 µg L^{-1}), Mn (up to 444 µg L^{-1}), and Al (up to 1455 µg L^{-1}), indicating reducing conditions that mobilise these elements from iron and manganese oxides and aluminosilicates. Such elevated concentrations are related to reductive dissolution of Fe/Mn oxides under anoxic conditions[135, 144] contribution from ophiolitic or volcanoclastic host rocks[145, 146], or possibly weathering of feldspars[147] or clay-rich layers typically found in flysch or schist rocks[135, 148, 149].

The exceptionally high concentrations of Li (up to 406 µg L^{-1}), B (up to 7160 µg L^{-1}), and Br (up to 363 µg L^{-1}) in Tropeouhos, Katakali, and Mesokampos samples suggest interaction with deeper, evolved fluids. These elements are typically enriched in hydrothermal systems[135], marine sedimentary or evaporite-hosted aquifers [150] or fluids with long residence times and extensive water–rock contact [146]. Boron and bromine enrichment may also indicate a marine or connate water signature, particularly in the Mesokampos sample, or mixing with residual basinal brines[150, 151].

To identify the actual source of the aforementioned discussed elements, an elaboration is provided. In the Florina Basin, the non-lignite intraseam sediments include both marl and sand lithologies, are primarily characterised by a dominance of illite and mica, alongside significant proportions of kaolinite, quartz, ferroan chlorite, and albite feldspar. Carbonate minerals are largely absent, with only traces of dolomite sporadically occurring, while the clay fraction includes smectite and disordered smectite/illite[152]. Sand samples contain slightly higher amounts of feldspar (<7.2 wt.% albite) and mica (<28.6 wt.%), whereas the marl samples show slightly higher proportions of clay minerals, including illite (37.8 wt.%), kaolinite (17.4 wt.%), and ferroan chlorite (9.3 wt.%)[152]. These characteristics indicate that deposition occurred in a fluvio-lacustrine environment with variable energy conditions. The dominance of illite, mica, and kaolinite, along with quartz and albite, suggests weathering and erosion of felsic or metamorphic source rocks under humid conditions. Marls being enriched in clay minerals and ferroan chlorite reflect lower-energy, possibly more stagnant depositional settings, while the sands, with higher quartz and feldspar content, point to intermittent higher-energy fluvial input. The scarcity of carbonates indicates limited diagenetic processes and supports deposition in a non-marine, siliciclastic-dominated basin with contributions from both soil-forming and fluvial processes. Furthermore, Gemeni et al. (2015)[135] have supported that the origin of Fe, Mn and Br is not related to hydrothermal systems but interaction with deeper igneous rocks[135].

While all samples had detectable Sr and Ba, their concentrations were below regulatory thresholds. Their presence is consistent with the dissolution of carbonate and feldspathic minerals. Sr points to contributions from marl, limestone, or plagioclase-rich rocks common in the Mesozoic sequences of West Macedonia, despite the variations suggesting diversified geological histories. Sandstone samples from the central parts of the MHT are classified mineralogically as feldspathic litharenites[143]. Similar mineralogical and geochemical characteristics are reported from the southeastern part of the MHT, where sandstone samples are classified geochemically as graywackes and litharenites[153].

The Katakali sample's combination of high pH, elevated Li and B, and relatively low transition metal concentrations points toward interaction with serpentinized ultramafic rocks. These lithologies commonly

The PilotSTRATEGY project has received funding from the European Union's Horizon 2020 research and innovation programme under grant agreement No. 101022664

generate hyperalkaline fluids through serpentinization reactions and are known potential sources of natural hydrogen[146, 154].

The third-round water samples from the West Macedonia region present a complex mixture of dissolved gases, reflecting interactions between geological formations, redox conditions, and possibly deep-seated fluid sources. Tropeouhos (1,403 ppm He) and Kivotos (29 ppm He) samples indicate significant helium enrichment, which is not produced in shallow processes. Such high He levels suggest input from a radiogenic source in crystalline basement rocks (U/Th decay)[155], or mantle-derived fluids migrating through deep-seated fault systems[155]. The Neos Kafkasos, even at the 6 ppm He complements this due to the proximity to Tropeouhos.

High CO_2 concentrations in Itea (60.7%), Mesokampos (~60%), and Neos Kafkasos (~40%), including Ammohori_1 and _2 (~7–8% CO_2) are related to the Florina basin, where natural CO_2 volcanic in origin have accumulated in the Miocene fluvial sandstones [140, 156]. The accumulations migrating via faults have been detected from depths of 296-338 m and 366-372 m below the surface and are well reported[156]. They also provide CO_2 analogues for CO_2 storage, which is also related to the PilotSTRATEGY Project[118].

Katakali (4.4 ppm H_2), Kivotos (1.7 ppm H_2), and Neos Kafkasos (2 ppm H_2) exhibit detectable hydrogen, a rare but significant indicator of water–rock reactions, that relates to: a) particularly serpentinization of ultramafic rocks (e.g., ophiolites), b) radiolysis of water in fractured rocks under the influence of natural radioactivity, and c) anaerobic corrosion of Fe-bearing minerals, particularly under reducing conditions. These processes are common in tectonically active zones, where fluid pathways are enhanced [136, 141, 142, 157-160].

In light of the data obtained from round 4 the Katakali samples, the high methane concentrations (>300,000 ppm) in both duplicates and slightly alkaline pH (~8) point toward a deep-seated methane source. The absence of helium and hydrogen, combined with $\delta^{13}CCH_4$ values around –70‰ and δDCH_4 near –230‰, strongly supports biogenic methane via microbial CO_2 reduction[137, 145], although further investigation may be needed to properly distinguish between bacterial imprint or diffusive fractionation[139]. The moderately enriched δD and $\delta^{18}O$ of water suggest some evaporation, but the dominant control appears to be long residence time and water–rock interaction with organic-rich strata (possibly lignites or deep-seated carbonates)[161]. The interpretation from the data received from the sample reflects a closed-system [161] microbially dominated environment with limited gas migration, depicted in Figure 6.6. Despite high CH_4, absence of He and H_2 implies limited serpentinization or mantle influence[137, 145, 162]. It is noted that Daskalopoulou et al. (2018)[119] report traces for helium and hydrogen which was not identified in the Katakali samples during this campaign. This is not necessarily contradictory and it can be for various reasons, including sampling method, sampling preservation and delayed time analysis, including analytical error. However, the high methane concentrations with biotic origin are confirmed by both studies.

The PilotSTRATEGY project has received funding from the European Union's Horizon 2020 research and innovation programme under grant agreement No. 101022664

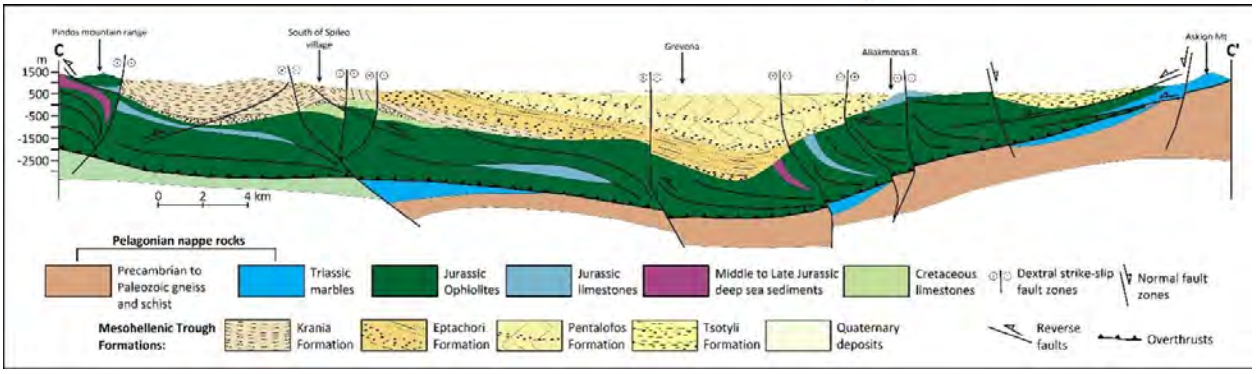

Figure 6.6: Geological cross section of Mesohellenic Trough with ınterpretative subsurface gas generation and migration mechanisms, licence: CC-BY 4.0.

On the contrary, in Kivotos samples, the presence of both He (43–44 ppm) and H_2 (1.7 ppm) with CH_4 (~43,000 ppm) suggests a hybrid gas system. Helium and hydrogen point to a possible serpentinization signature, typical for ultramafic lithologies (e.g. ophiolites) [145, 155]. CH_4 may derive from either microbial or abiotic processes, with low $\delta^{13}CCH_4$ (–75.5‰) still favouring a microbial pathway[137, 163]. This may indicate a mixed or transitional methane, either microbial with some thermogenic input or some hydrogen exchange during migration.

Slight enrichment in δD and $\delta^{18}O$ is consistent with moderate evaporation or prolonged water–rock interaction. A hybrid gas system dominated by microbial CH_4 with secondary abiotic inputs, possibly from ultramafic serpentinization or water–rock reactions, can potentially describe the main gas mechanism in this case.

In Tropeouhos, with its exceptionally high helium (up to 1403 ppm) and low CH_4 (81 ppm), it indicates a strong mantle-derived or radiogenic He component. The low CH_4 and absence of H_2 suggest minimal microbial or abiotic CH_4 production[138, 145, 162, 164] and possible degassing along deep fault pathways. Dominated by radiogenic/mantle degassing, possibly along deep fault structures. This site may represent a degassing zone rather than a storage environment.

The Neos Kafkasos with low but detectable He (10 ppm) and H_2 (2 ppm) combined with CO_2 at ~50% suggest mantle or deep carbonate reservoir interaction. Although $\delta^{13}CCH_4$ was not obtained due to the low concentration of CH_4, the data availability on $\delta^{13}C_{TDC}$ (–1.2‰) and δD (–66‰) suggests thermogenic gas mixing[165]. The reducing conditions and high CO_2 levels provide evidence for carbonate dissolution, blended together with the volcanic origin of trapped CO_2[140, 156]. Given the proximity of Mesokampos and Itea, which had elevated CO_2% levels, it suggests a CO_2-dominated system, possibly involving carbonate dissolution, or closed-system redox processes. The presence of He and H_2 supports some deep-origin fluid connectivity.

Kivotos and Kivotos-2 reported $\delta^{13}CCH_4$ ≈ -75.5 to -69.5‰, δDCH_4 ≈ -107 to -92‰. These samples have $\delta^{13}CCH_4$ within the biogenic range, but δDCH_4 values are much less depleted, potentially indicating mixed or transitional methane, either microbial with some thermogenic input or some hydrogen exchange during migration.

The PilotSTRATEGY project has received funding from the European Union's Horizon 2020 research and innovation programme under grant agreement No. 101022664

7. Re-processing of Legacy seismic data and interpretation

Seismic acquisition surveys have been carried out in the area of MHT during the period 1980-1984, where 623km of 2D seismic data were acquired with an explosive (dynamite) source. The early seismic campaigns include the GR-lines (1980), the L-lines (1982) and AO-lines (1983) as shown in Figure 7.1**.** Subsequently, between 1991-1994, an additional 662km of 2D seismic data were acquired using a Vibroseis source, comprising the so-called 'GRV' lines.

As part of the PilotSTRATEGY project the vintage ''GRV'' seismic data were reprocessed for the MHT[166]. Moreover, the 1980s (AO, GR and L lines) were also reprocessed substantially enhancing the subsurface image and improving the interpretation of the stratigraphic and structural framework of the basin. The seismic data were reprocessed using state-of-the-art seismic processing techniques to generate a high-quality pre-stack time-migrated (PSTM) dataset. The resulting profiles exhibit higher signal-to-noise ratios, clearer reflector continuity, and greater vertical resolution, providing a more reliable basis for identifying reservoir–seal pairs relevant to CO_2 storage. The geographic distribution of the reprocessed seismic grid is presented in Figure 7.1.

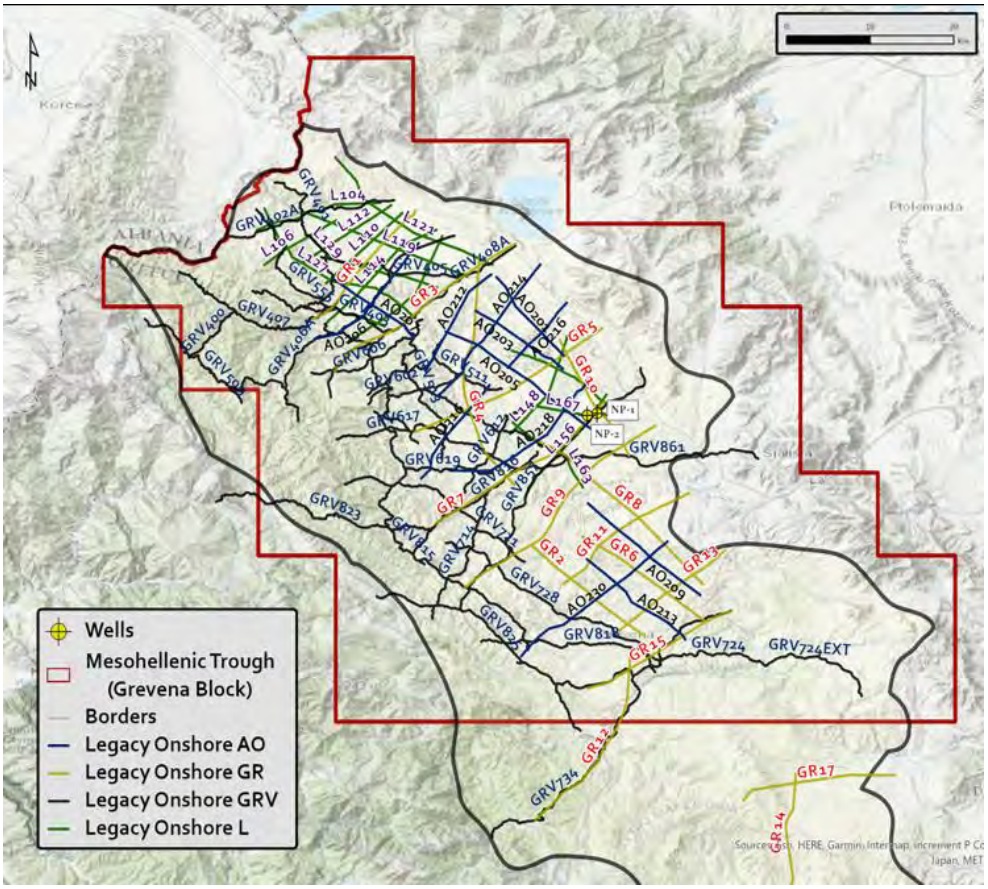

Figure 7.1 : Combined legacy seismic campaigns that have been re-processed in the area of MHT. Abbreviations: AO = Argos Orestiko, acquired using dynamite source, GR = Grevena, acquired using dynamite source, GRV = Grevena,

The PilotSTRATEGY project has received funding from the European Union's Horizon 2020 research and innovation programme under grant agreement No. 101022664

acquired using a vibroseis source, L = Legacy seismic lines acquired using a dynamite source from the Argos Orestiko and Neapolis provinces.

The application of modern processing workflows, including noise attenuation and spectral balancing, produced marked improvements in reflector definition. Examples of PreSTM section before and after post-stack processings are shown in Figure 7.2-Figure 7.4, demonstrating the gain in resolution and continuity. This improvement allows the consistent mapping of key stratigraphic horizons across the basin and the recognition of structures that were previously poorly imaged.

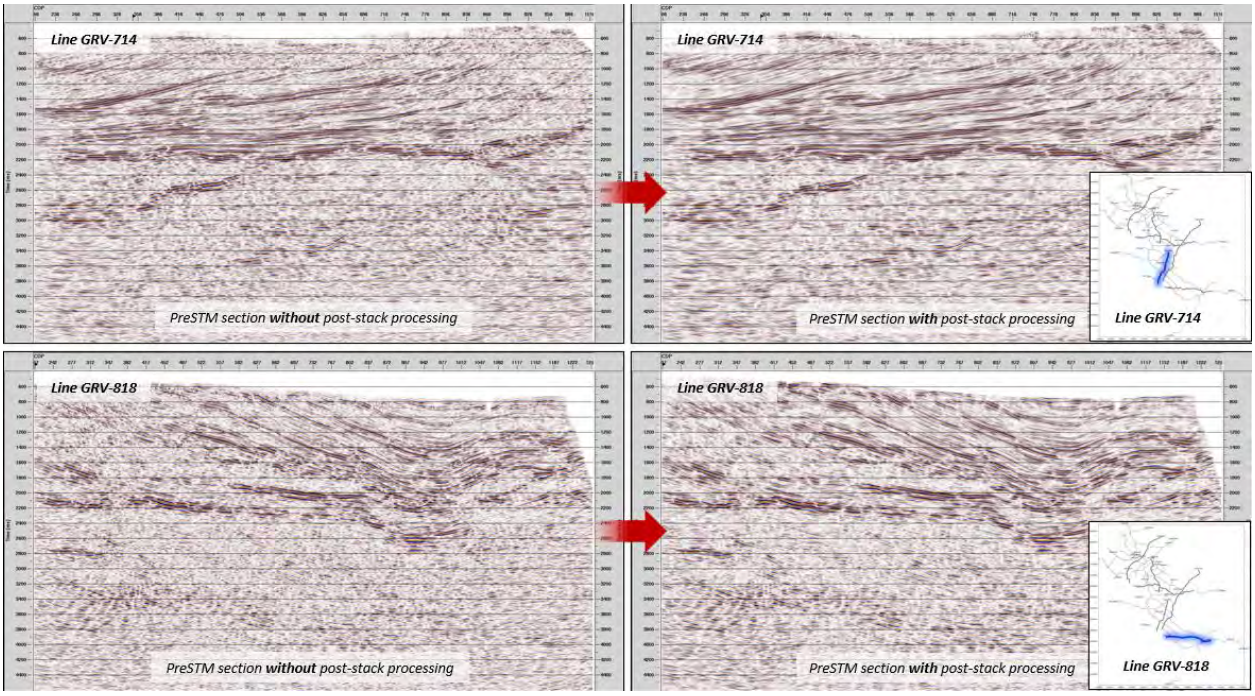

Figure 7.2: Examples of PreSTM sections before and after post-stack processing. Presented sections are generated with dynamic amplitude scaling (AGC).

Eight principal horizons (H1–H8) were mapped, ranging from the near-surface to the Alpine basement. Of particular importance are the tops of the Tsotyli, Pentalofos, and Eptachori formations, which represent the main potential storage–seal successions of the Mesohellenic Trough. The stratigraphic interpretation of these horizons along selected seismic lines is shown in Figure 7.5. To facilitate interpretation, the horizons have been correlated with known lithostratigraphic units and calibrated against borehole data from the Neapolis-1 and Neapolis-2 wells. A summary of the horizons, their depth ranges, lithologies, and relevance to CO_2 storage is presented in Table 7.1.

The PilotSTRATEGY project has received funding from the European Union's Horizon 2020 research and innovation programme under grant agreement No. 101022664

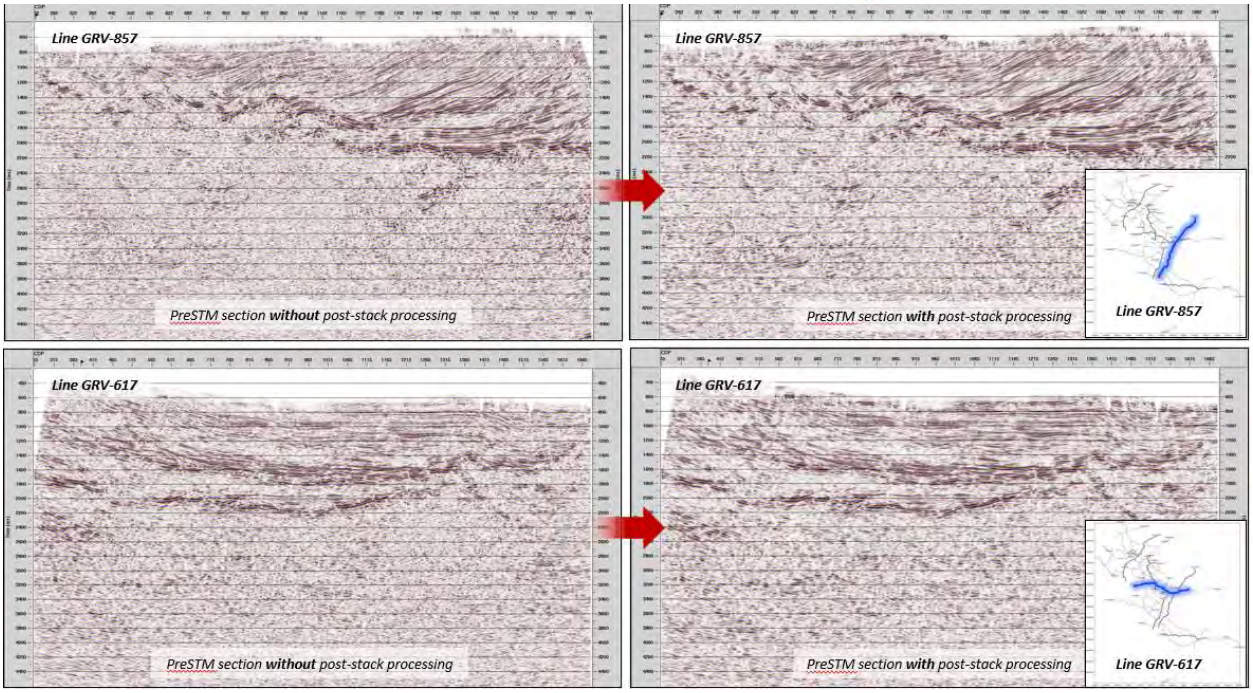

Figure 7.3: Examples of PreSTM sections before and after post-stack processing. Presented sections are generated with dynamic amplitude scaling (AGC).

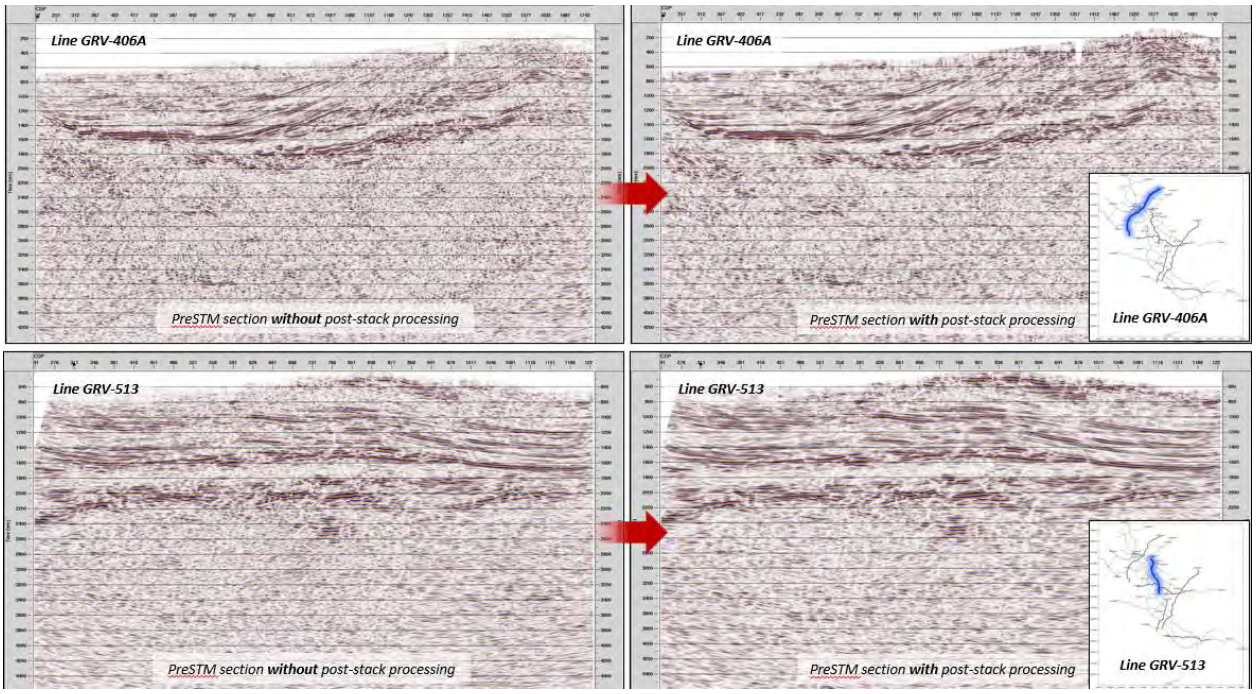

Figure 7.4: Examples of PreSTM sections before and after post-stack processing. Presented sections are generated with dynamic amplitude scaling (AGC).

The PilotSTRATEGY project has received funding from the European Union's Horizon 2020 research and innovation programme under grant agreement No. 101022664

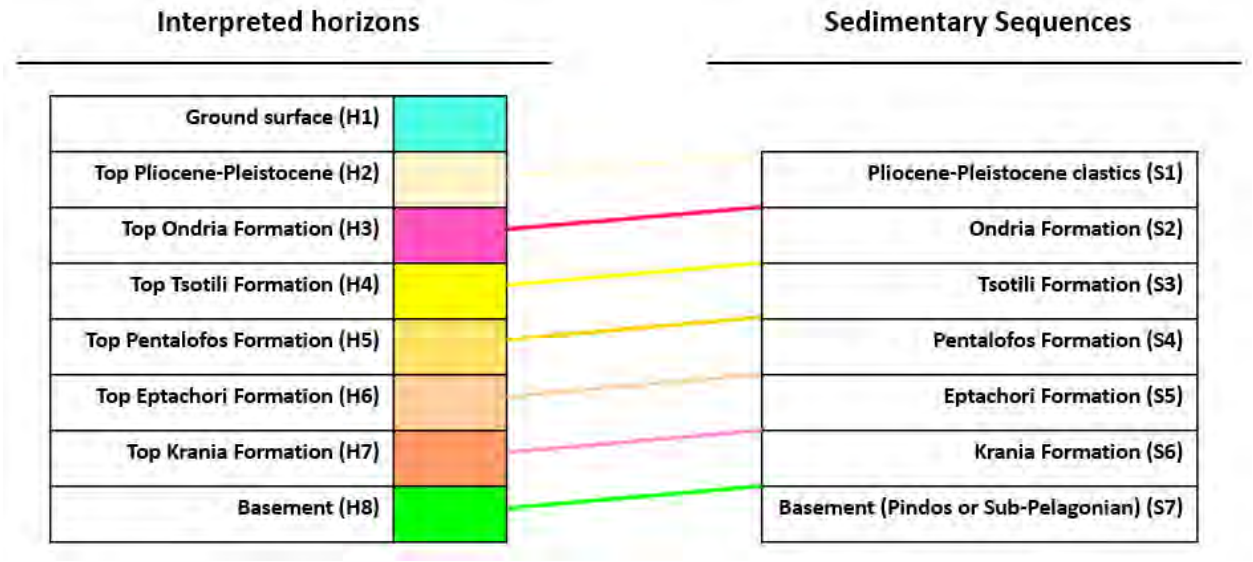

Figure 7.5: Interpreted Horizons (left panel) and sequences (right panel) indicated with colours.

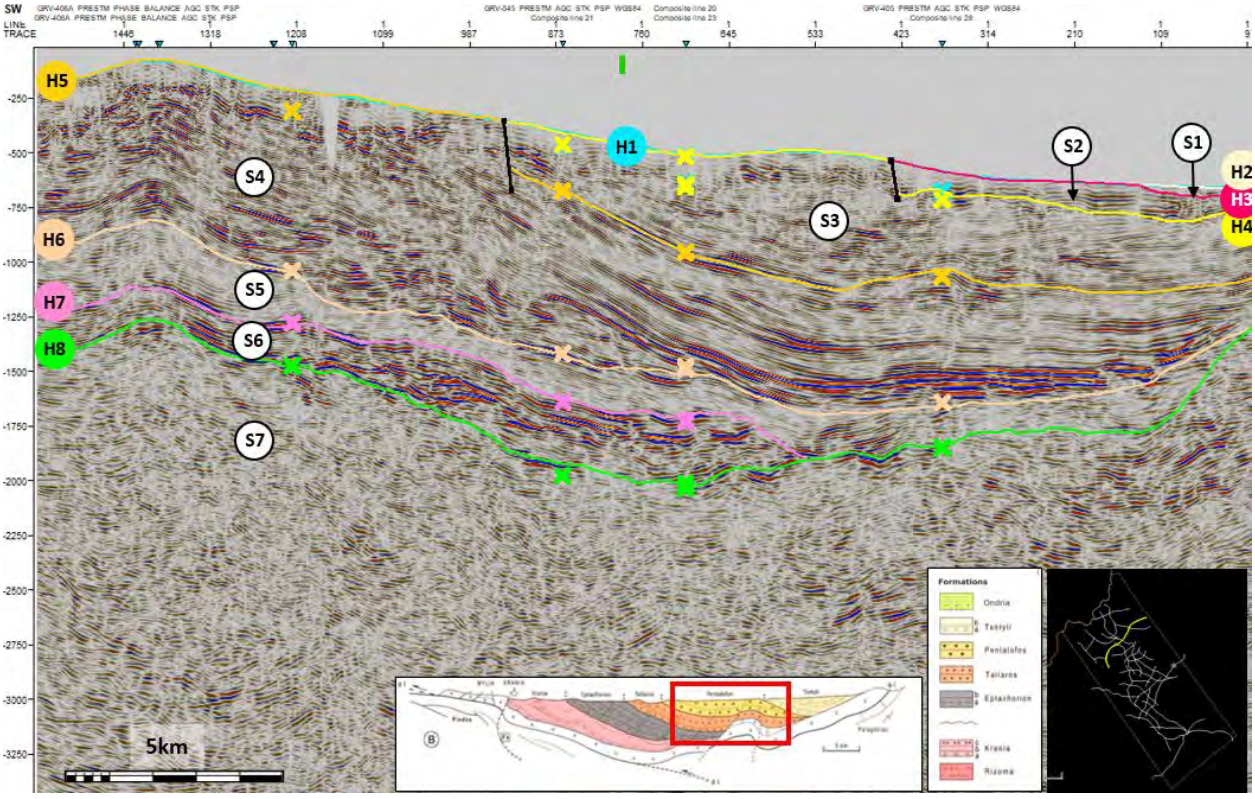

Figure 7.6: Regional interpreted seismic profile running from SW-NE. The profile's location is shown on the inset map, alongside the previously published geological model by Ferrière et al. (2013)[167], Zelilidis et al. (2002)[17] and Kontopoulos et al. (1999)[1].

The PilotSTRATEGY project has received funding from the European Union's Horizon 2020 research and innovation programme under grant agreement No. 101022664

Table 7.1: Overview of mapped horizons (H1–H8), their lithological interpretation, depth position, and relevance for CO_2 storage.

Horizon	Approximate Stratigraphic Position	Lithology / Formation	CO_2 Storage Relevance
H1	Near surface (0–500 m)	Quaternary–Pliocene clastics	Not relevant (unconsolidated deposits)
H2	Upper Miocene	Ondria Formation (sandstones, marls)	Local seal potential, limited reservoir quality
H3	Early–Middle Miocene	Tsotyli Formation (marls, marly limestones, thin sandstones)	Regional seal (laterally continuous)
H4	Late Oligocene–Early Miocene	Pentalofos Formation (sandstones, conglomerates, marls)	Reservoir units, interbedded marls as local seals
H5	Early Oligocene	Eptachori Formation (marls, shales, sandstones)	Reservoir–seal alternations
H6	Late Eocene	Krania Formation (molassic sandstones, marls)	Secondary reservoir–seal alternations
H7	Pre-Molasse	Pelagonian platform carbonates	Possible deep reservoir; sealing uncertain
H8	Basement (Alpine nappes, ophiolites)	Ophiolitic and metamorphic rocks	Probably not suitable (fractured, low storage potential)

Seismic facies analysis led to the identification of seven depositional sequences (S1–S7), spanning from Pliocene–Pleistocene clastics to the Alpine basement. These sequences reflect progressive subsidence and syn-tectonic deposition, consistent with a piggyback basin model. The classification of Horizon H8 as "not suitable for CO_2 storage" (Table 7.1) is based on the lithological and structural characteristics of the ophiolitic and metamorphic basement. These rocks exhibit extremely low primary porosity, pervasive fracturing, and no internal sealing capacity, as confirmed by seismic imaging and the lithological descriptions from the Neapolis wells and regional mapping. Their fabric prevents pressure containment and precludes the development of structural traps, making them unsuitable for CO_2 storage in accordance with established reservoir–seal criteria. Additionally, representative examples of seismic facies and depositional sequences are illustrated in Figure 7.7. The wedge-shaped stacking geometries visible in the reprocessed lines provide direct evidence of syn-depositional tectonic activity during Oligocene–Miocene times.

The reinterpreted seismic dataset revealed multiple trap configurations. Anticlinal traps, typically between 1 and 2.5 km wide, are developed within the Pentalofos and Eptachori formations. Fault-bounded traps are also abundant, reflecting the influence of normal faulting that compartmentalises the basin fill. In addition, stratigraphic traps such as pinch-outs and turbiditic lobes were recognised, although these are generally thinner and laterally discontinuous. Examples of anticlinal and fault-bounded traps are provided in Figure 7.8.

The PilotSTRATEGY project has received funding from the European Union's Horizon 2020 research and innovation programme under grant agreement No. 101022664

Sequence	Reflection Configuration	Amplitude	Frequency	Continuity	Interpretation	Example
S1	Parallel continuous to semi-continuous	High	High/Moderate	High	Pliocene-Pleistocene clastics	
S2	Parallel continuous	High	Moderate	High	Ondria Fm. Turbidites	
S3	Parallel semi-continuous with transparent reflections	Moderate	High/Moderate	Moderate	Tsotili Fm. Turbidites	
S4	Parallel continuous	High	Low	High	Pentalofos Fm. Turbidites	
S5	Parallel semi-continuous with transparent reflections	Low	Low	Moderate	Eptachori Fm. Turbidites	
S6	Parallel continuous to semi-continuous. Locally	High	Low	High	Krania Fm. Turbidites	
S7	Contorted to chaotic with transparent reflections	Low	Low	Low/Moderate	Carbonate basement	

Figure 7.7: Seismic facies overview of the MHT.

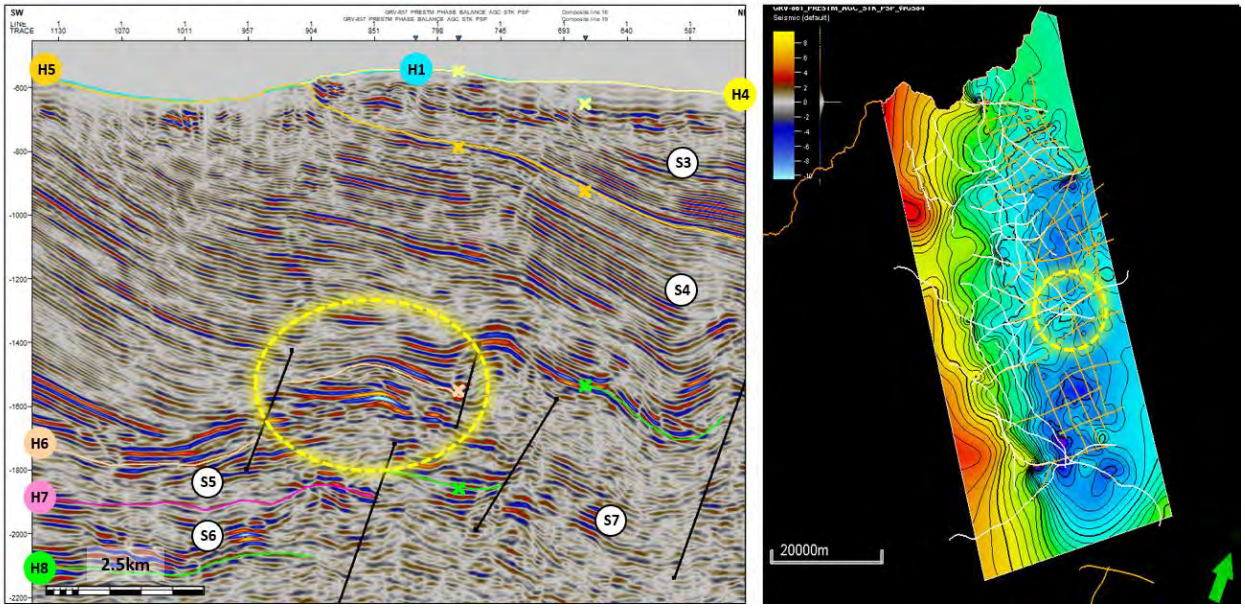

The PilotSTRATEGY project has received funding from the European Union's Horizon 2020 research and innovation programme under grant agreement No. 101022664

Figure 7.8: Possible anticline trap identified on the interpreted seismic profile (left) and the Top Eptachori Fm surface map (right) based on 2D regional interpreted seismic lines from both datasets, 1980s and 1990s, in the MHT region.

The integration of seismic interpretation with borehole data from Neapolis-1 and Neapolis-2 provides independent calibration of the stratigraphic model. Well data confirm that the Tsotyli Formation is dominated by deep-water turbiditic facies, where marls form laterally continuous seals and sand-prone lobes provide reservoir quality. Methane shows that they were recorded in both wells validate the migration potential of these units and suggest that they are suitable analogues for future CO_2 storage. The stratigraphic correlation between wells is illustrated in Figure 7.9.

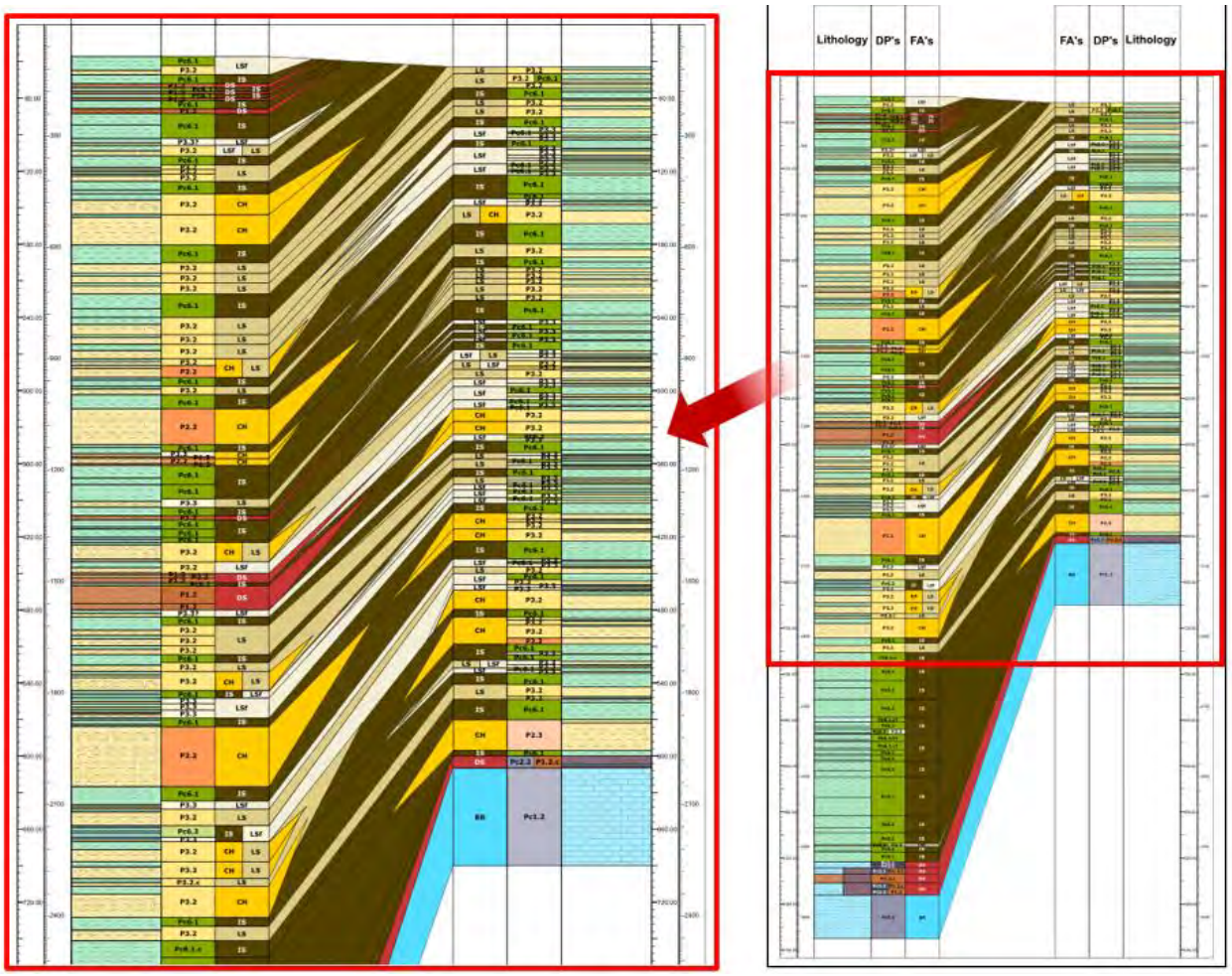

Figure 7.9: Correlated profiles of the Neapolis-1 and Neapolis-2 drill holes.

In conclusion, the re-evaluated geophysical dataset demonstrates the presence of robust reservoir–seal systems within the MHT. In particular, the laterally continuous marls of the Tsotyli Fm overlie sandstone and conglomeratic reservoirs of the Pentalofos and Eptachori formations. The improved imaging of stratigraphic horizons, depositional sequences, and trap geometries significantly enhances confidence in the basin's CO_2 storage potential.

The PilotSTRATEGY project has received funding from the European Union's Horizon 2020 research and innovation programme under grant agreement No. 101022664

8. Geological conceptual modelling

The geological conceptual model of the MHT brings together stratigraphic, structural, and geomechanical information to evaluate how CO_2 might behave once injected into deep saline formations. The cross-section (Figure 8.1) outlines the principal depositional units, beginning with the Eocene–Oligocene molasse (Krania and Eptachori Fm), followed by the Oligocene-Miocene coarse clastics of the Pentalofos Fm, and finally the Miocene sand-marl alternations of the Tsotyli Fm. These sequences rest upon locally exposed ophiolitic basement, which not only served as a source of detritus but also provides the structural framework that controls potential discontinuities.

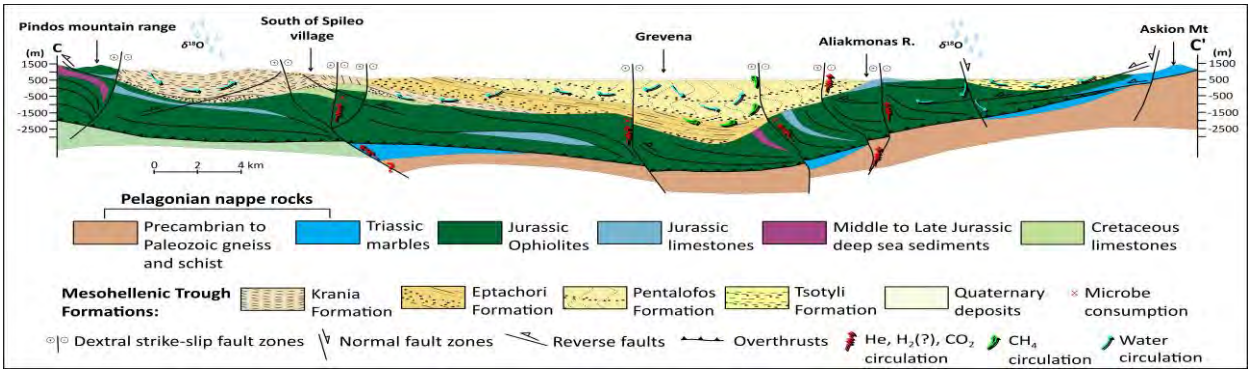

Figure 8.1: Geological cross-section of the MHT illustrating the interpreted mechanisms of subsurface gas generation and migration (modified after Tyrologou et al. (2023) [118]).

A central element of the conceptual model is the ability of the geological succession to act as a long-term seal for injected CO_2. The marl- and clay-rich intervals of the Tsotyli Formation provide the clearest evidence of this capacity. Laboratory results from sample TSO-1-3 show a porosity of 6.0% and an exceptionally low permeability of <0.01 mD, combined with an Nuclear Magnetic Resonnaince (NMR) formation factor of 273 and a clay-bound water fraction of 0.87[118] (i.e. formation factor (F) is a dimensionless property that expresses how electrically resistive a rock is relative to the resistivity of the pore fluid it contains. These NMR values are used to estimate the permeability of the sedimentary formations[168]. It links the rock's porosity and connectivity of pore spaces to its ability to transmit electrical current and, indirectly, fluids). These values point to very limited potential for fluid migration and strong resistive behaviour, both hallmarks of an effective caprock. Importantly, the petrophysical data also demonstrate that sealing potential is not confined to Tsotyli alone. In the Pentalofos Formation, sandstone samples (PENT-3-1 to PENT-3-3) yield porosities ranging from 4.9% to 10.8%, with uniformly low permeabilities (<0.01 mD)[118]. Their clay-bound water fractions (0.91–0.96) and formation factors (46–157) highlight internal variability: while some horizons are capable of serving as reservoir units, others contribute to sealing. The Eptachori Formation further strengthens this picture. Sample EPT-2-3, with a porosity of 7.4%, permeability <0.01 mD, and a clay-bound water fraction of 0.97, confirms that fine-grained intervals within its sequence can effectively hinder vertical CO_2 movement[118]. Taken together, these data suggest a layered system in which the Tsotyli marls provide the primary regional caprock, but

The PilotSTRATEGY project has received funding from the European Union's Horizon 2020 research and innovation programme under grant agreement No. 101022664

additional sealing capacity is distributed through the Pentalofos and Eptachori formations. This stratigraphic redundancy enhances the overall security of the storage complex.

Table 8.1: Comparative table summarising the seal capacity indicators (porosity, permeability, formation factor, and clay-bound water fraction) for samples from Tsotyli, Pentalofos, and Eptachori formation after Tyrologou et al. (2023) [118].

Formation/ Sample	Porosity (%)	Permeability (mD)	Formation Factor	Clay-Bound Water Fraction
Tsotyli (TSO-1-3)	6.0	<0.01	273	0.87
Pentalofos (PENT-3-1)	5.0	<0.01	112	0.96
Pentalofos (PENT-3-2)	10.8	<0.01	46	0.91
Pentalofos (PENT-3-3)	4.9	<0.01	157	0.94
Eptachori (EPT-2-3)	7.4	<0.01	123	0.97

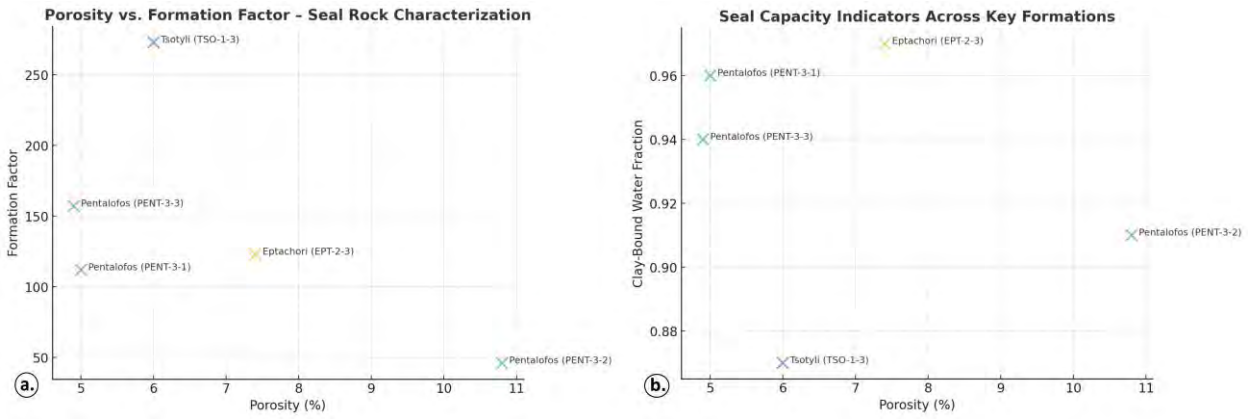

Figure 8.2: a. Seal capacity indicators for samples from the Tsotyli, Pentalofos, and Eptachori formations. The measurements show uniformly low porosity and negligible permeability (<0.01 mD), together with high clay-bound water fractions, confirming their effectiveness as caprocks. b. Cross-plot of porosity against formation factor for the same samples. The trend of low porosity combined with high formation factors highlights the limited transmissivity and strong sealing capacity of these lithologies. All data are from Tyrologou et al. (2023)[118].

Even with such favourable petrophysical characteristics, the risk of long-distance lateral or vertical CO_2 migration cannot be dismissed. Faults, joints, and coarse conglomeratic bodies may locally enhance transmissivity and create escape pathways. The potential for CO_2 to reach shallower aquifers, or in extreme cases the atmosphere, underscores the need for detailed structural analysis and continuous hydrogeological monitoring.

The PilotSTRATEGY project has received funding from the European Union's Horizon 2020 research and innovation programme under grant agreement No. 101022664

Another consideration is the potential for methane displacement, as emphasised by Tyrologou et al. (2025)[169]. CO_2 injection may drive CH_4 already stored in porous strata into overlying formations. Since isotopic surveys have confirmed the presence of biogenic methane in West Macedonia, incorporating this process into risk assessments is vital. The implications extend beyond greenhouse gas emissions to include possible impacts on freshwater aquifers.

The model must also consider the possibility of induced seismicity. Pressure increases from injection may reactivate existing discontinuities. Field observations indicate that bedding with gentle to moderate dips dominates the basin, while faults and joints are concentrated in ophiolitic and conglomeratic settings. This suggests general stability, but localised fault reactivation remains a possibility. Microseismic monitoring systems are therefore essential to detect early signs of stress redistribution.

Ground deformation in the form of uplift or subsidence is another potential outcome of injection. Reservoir pressure changes could cause measurable surface displacements, particularly where lithologies of contrasting compressibility overlap. In this respect, Quaternary terraces within the Pentalofos Formation (see Region 5 survey) provide valuable geomorphic benchmarks against which to monitor subtle changes in surface elevation.

The displacement of brine must be accounted for. Injection of supercritical CO_2 may force saline fluids laterally or vertically into overlying units. If these fluids enter freshwater aquifers, degradation of water quality could result. The marl–sand alternations of the Tsotyli Formation, with their consistently low porosity and negligible permeability, are expected to function as effective barriers. Nevertheless, local heterogeneities such as discontinuities or high-permeability channels could undermine containment, making site-specific evaluation and monitoring indispensable.

The reprocessed seismic data adds weight to the storage model by showing clear evidence for several types of traps. The most common are anticlines and fault-bounded traps, while smaller features such as stratigraphic pinch-outs and turbiditic lobes also occur and may provide extra capacity. The Neapolis boreholes help to tie these observations together: they confirm that sand-rich lobes within the Tsotyli Formation have good reservoir qualities, with thick marl units above them acting as seals. The fact thatboth wells recorded methane also proves that migration pathways are active and that the reservoir–seal system is capable of holding fluids.

When combined with the mineralogical and geochemical results, the seismic data shows that the basin has a strong potential for CO_2 storage but must be evaluated with careful attention to lithological heterogeneity, fluid–rock interactions, and the role of deep-seated gas inputs. Storage potential is real, but it depends heavily on how different rock types behave, how fluids interact with them, and how deep-seated gases influence the system. Altogether, these datasets refine the geological model of the MHT and place it into a wider geo-energy context, where CO_2 storage has to be considered alongside natural gas migration, serpentinization, and the hydrogeological setting.

The MHT system can be conceptualised in terms of sources, pathways, reservoirs, seals, and risks (Figure 8.3), as follows:

The PilotSTRATEGY project has received funding from the European Union's Horizon 2020 research and innovation programme under grant agreement No. 101022664

- Reservoirs. The Eptachori and Pentalofos formations represent the principal storage units. Their sandstones combine adequate thickness with interconnected pore systems, as confirmed by petrographic, geochemical, and imaging studies, making them suitable for accommodating injected CO_2.
- Seals. Above these reservoirs, the marl-rich intervals of the Tsotyli Formation serve as the primary caprock, reinforced by finer-grained horizons within the underlying molasse sequence. Together, these layers provide the low-permeability barriers needed to prevent upward migration of CO_2.
- Pathways. Potential migration routes include faults, joints, and coarse conglomeratic bodies. Where present, these features locally enhance permeability and could allow CO_2 to bypass the sealing units.
- Sources. The subsurface is known to host gases such as CH_4, He, and H_2. These may be mobilised during CO_2 injection, adding further complexity to the storage system and requiring careful monitoring.
- Risks. Four key risks must therefore be considered: (i) leakage of CO_2 beyond the designated storage horizon, (ii) displacement of CH_4 into overlying strata or the atmosphere, (iii) induced seismicity caused by reactivation of pre-existing faults, and (iv) displacement of brine into freshwater aquifers.

In this framework, the long-term security of CO_2 storage depends on striking the right balance between reservoir capacity, the effectiveness of the seals, and the control of potential migration pathways. Reducing uncertainty requires a continuous integration of geological, geochemical, and structural datasets, supported by targeted monitoring strategies that can ensure containment and system stability over time.

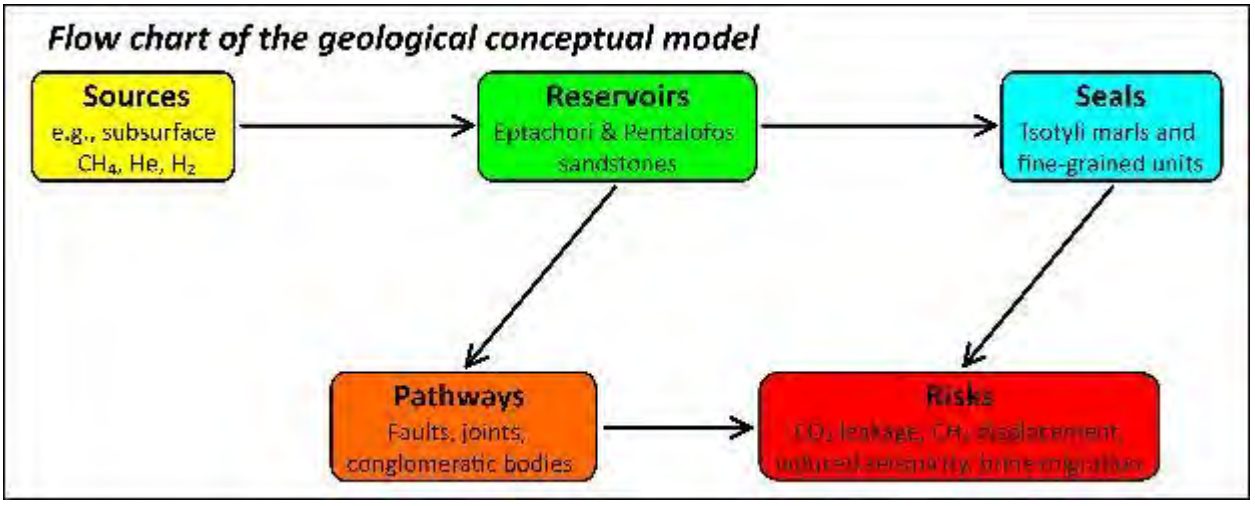

Figure 8.3: Flow chart summarising the geological conceptual model of the Mesohellenic Trough, showing how sources, reservoirs, seals, pathways, and risks interact to define CO_2 storage behaviour.

The PilotSTRATEGY project has received funding from the European Union's Horizon 2020 research and innovation programme under grant agreement No. 101022664

9. Key engineering geology risks and uncertainties

The long-term performance of CO_2 storage in the MHT will rely not only on the size and integrity of the stratigraphic framework, but also on how well a number of engineering geology risks are understood and managed. Such risks do not originate from a single factor, but from the overlap of lithological variations, structural discontinuities, fluid-rock reactions, and geomechanical changes linked to injection. This discussion reviews the main risks and uncertainties, using evidence drawn from field observations, laboratory tests, and recent hydrogeochemical investigations. Potential risks are summarized as follows: 1) Seal integrity and heterogeneity, 2) Reservoir quality and variability, 3) Gas migration and displacement, 4) Seismicity and structural reactivation, 5) Surface deformation and brine displacement, 6) Uncertainties in long-term behavior.

For seal integrity and heterogeneity, a major source of uncertainty lies in the sealing capacity of the marl- and clay-rich layers, especially those of the Tsotyli Fm. Laboratory tests suggest these rocks are highly effective barriers: for example, sample TSO-1-3 has a porosity of 6.0% and a permeability of less than 0.01 mD, together with a formation factor of 273 and a clay-bound water fraction of 0.87[118]. These values point to a very competent seal for the Tsotyli Formation. Comparable results come from the Pentalofos and Eptachori formations, where samples show porosities in the range of 4.9–10.8% and the same very low permeability (<0.01 mD), with clay-bound water fractions consistently high at 0.91–0.97[118]. This pattern indicates that several levels across the basin could serve as effective seals. Even so, the picture is not uniform. The presence of coarse conglomeratic beds in Pentalofos and local carbonate-rich intervals introduces heterogeneity, which may create bypass zones and reduce overall sealing efficiency.

For reservoir quality and variability, the presence of interconnected pore networks seen in SEM-EDS analysis and confirmed by automated image analysis, point to storage potential for the Eptachori and Pentalofos formations. However, these sandstones show porosity values up to 10.8% (sample PENT-3-2) and permeability <0.01 mD questioning the reservoir potential. Bulk composition varies markedly between units: XRF/XRD show a silica-rich Eptachori (~36 wt.% SiO_2) versus more carbonate-rich Pentalofos (~42 wt.% CaO), differences that bear directly on strength, reactivity, and fluid transmissivity and therefore add uncertainty to how the reservoir will behave under injection. Complementary water-absorption tests reinforce this contrast: Region 1 sandstones are uniformly stable (Grade 1) with modest uptake (~10-50 ml per 1000 g of rock), whereas Region 2 conglomerates span a much wider range in density (~1.56-2.63 g cm^{-3}) and absorb from ~50 ml to well over 300 ml per 1000 g, underscoring the heterogeneous response expected across the reservoir package (see also Appendix X). The new seismic interpretation highlights both opportunities and uncertainties for CO_2 storage in the MHT. While anticlinal and fault-bounded traps appear widespread, their effectiveness as long-term storage structures depend on the continuity and integrity of sealing units. Faults, in particular, present a dual role: they can create traps but also act as potential leakage pathways if reactivated. This makes fault-related uncertainty a central engineering risk that must be addressed with more detailed structural analysis and monitoring. The calibration with Neapolis boreholes confirms reservoir–seal pairs within the Tsotyli Formation, yet it also points to variability in sand body distribution and thickness. Such lateral heterogeneity increases uncertainty in predicting storage capacity and injectivity. Stratigraphic pinch-outs and turbiditic lobes, although adding capacity, are thinner and laterally discontinuous, which makes them more vulnerable to leakage or inefficient plume migration.

The PilotSTRATEGY project has received funding from the European Union's Horizon 2020 research and innovation programme under grant agreement No. 101022664

For gas migration and displacement, a further category of risk involves the behaviour of subsurface gases. The injection of CO_2 has the potential to mobilise gases already present in the system, including CH_4, He, and H_2, which have been reported from West Macedonia[118]. Of these, methane presents the greatest concern. Its migration upwards would constitute not only a greenhouse gas release but also a possible hazard for groundwater quality. Isotopic data indicate that much of the methane in the basin is of biogenic origin, suggesting relatively shallow accumulations that could respond to the pressure changes associated with injection. In addition, the presence of methane shows in the Neapoli-1 and Neapoli-2 boreholes validates the existence of active migration pathways. While this supports the geological model, it also raises concerns over interactions between stored CO_2 and pre-existing gas systems. Migration of methane or mixing with CO_2 could complicate both storage efficiency and monitoring strategies. Although most CO_2 storage studies place primary emphasis on containment integrity, the coexistence of multiple gases in the MHT adds a layer of uncertainty that must be incorporated into the design of monitoring programmes.

For seismicity and structural reactivation, structural observations from the field show that bedding remains the dominant discontinuity across most sedimentary units, with gentle northeast dips recorded in many locations. Faults and joint systems occur more sporadically, most often in conglomeratic intervals and in areas where ophiolitic basement is exposed. While the overall structural framework appears stable, increases in pore pressure linked to CO_2 injection could reactivate pre-existing discontinuities. Such reactivation would most likely generate low-magnitude seismic events, not necessarily damaging to infrastructure but with the potential to reduce seal effectiveness. This risk is especially relevant near fault zones, where transmissivity may be locally enhanced. For this reason, continuous seismic monitoring is important to detect any changes in stress within the reservoir–seal system. In addition, InSAR (Interferometric Synthetic Aperture Radar) can be used to monitor ground movement with millimetre to centimetre accuracy. Although the area is generally considered to have low seismic risk, such tools help ensure any deformation is noticed early.

For surface deformation and brine displacement, ground deformation represents another potential risk. This risk could be manifested either as localized subsidence or as uplift linked to changes in reservoir pressure. In the Pentalofos Formation, Quaternary terraces provide could constitute valuable geomorphic markers that can be used to track even subtle movements over time. Alongside this, the displacement of brine introduces additional hydrogeological concerns. The injection of supercritical CO_2 can force saline fluids upward or laterally, raising the possibility that they may enter overlying freshwater aquifers. Laboratory measurements confirm the strong sealing capacity of marl-rich intervals, yet variations in permeability and fracture density highlight that localised leakage pathways cannot be ruled out. For this reason, the risk of aquifer contamination must be addressed explicitly in the design of monitoring strategies and in the careful selection of injection zones.

For uncertainties in long-term behavior a final and critical source of risk lies in the long-term evolution of the storage system. Laboratory tests provide useful point-scale information, such as very low permeability (<0.01 mD) and rock fabrics that remain stable under water immersion. Nevertheless, these results only capture present-day conditions; over decades of CO_2 exposure, geochemical processes may alter these properties in ways that are difficult to predict. Reactions such as carbonate dissolution/precipitation and/or the precipitation of secondary minerals (e.g. clay minerals) could change porosity and permeability, either enhancing or reducing seal effectiveness. Evidence from XRF and SEM analyses already points to strong variability in carbonate content, clay proportions, and cement types among the

The PilotSTRATEGY project has received funding from the European Union's Horizon 2020 research and innovation programme under grant agreement No. 101022664

studied samples, emphasising that such heterogeneity must be considered. To address this uncertainty, reactive transport modelling is required to explore how reservoir and seal rocks may evolve under long-term storage conditions.

In summary, the principal engineering geology risks identified for the MHT include: (i) heterogeneity within sealing units, even though overall permeabilities remain very low; (ii) variability in reservoir quality between sandstones and conglomerates; (iii) the possible mobilisation of subsurface gases (e.g. CH_4); (iv) the chance of injection-induced seismicity; (v) ground deformation and brine displacement; and (vi) long-term geochemical changes affecting reservoir-seal pairs. Each of these carries uncertainties that cannot be fully resolved at present. Consequently, the safe implementation of CO_2 storage in the MHT will require an integrated strategy that brings together geological, geomechanical, and geochemical insights. Most definitely these should be supported by continuous monitoring, enabling adaptive risk management throughout the lifetime of the project.

Within the scope of this deliverable, the identified risks were ranked using a semi-quantitative risk matrix approach, a method widely employed in engineering geology and in the assessment of geological CO_2 storage. In this framework, each hazard is evaluated along two dimensions: its likelihood of occurrence and the severity of its potential impact (Table 9.1, Figure 9.1). Both factors are rated on a five-point scale, with likelihood ranging from rare to almost certain and impact from insignificant to catastrophic. The scores were derived from a combination of field observations, petrophysical and geochemical data, and analogues from other storage sites. This structured methodology, consistent with established guidelines[170-172], provides a transparent basis for prioritising risks. Using this system, containment-related issues such as CO_2 leakage and brine displacement emerge as the highest-priority concerns, whereas geomechanical effects, including induced seismicity and ground movement, are considered lower in both likelihood and impact (Table 9.1, Table 9.1).

Table 9.1: Risk hierarchy for CO_2 storage in the MHT, showing relative likelihood, impact, and priority of key geological and geomechanical hazards.

Risk	Likelihood (1-5)	Impact (1-5)	Priority level
CO_2 leakage	4	4	High
Brine displacement	3	4	High
CH_4 displacement	3	4	High
Long-term alteration	4	4	Moderate-High
Induced seismicity	2	3	Moderate
Ground movement	2	2	Low

The semi-quantitative methodology was used to perform the ranking of the risks, which was based on on-site observations, laboratory evaluations, and regional analogues. The risk of the leakage of CO_2 is at the apex of the hierarchy. Priority No. 1 was assigned to this (likelihood 4, impact 4) as any vent is the most serious scenario, resulting in the storage of integrity being violated. Although petrophysical tests show that the sampled formations have negligible permeability (<0.01 mD), the coexistence of faults or conglomeratic pathways stands for the continuation of the leakage possibly substantially. However, it is worth emphasizing that most of these observations come from near-surface observations and conditions, where the stress that rocks experience is limited. Deeper, at storage depths of around 800 meters, the situation could be quite different. Fractures are expected to be tightly closed under pressure, and the rock

The PilotSTRATEGY project has received funding from the European Union's Horizon 2020 research and innovation programme under grant agreement No. 101022664

layers are generally far less permeable, which greatly reduces the chance of any significant leakage. The higher gas concentrations found in some water samples probably point to small-scale, localized migration rather than a broader loss of containment. In fact, there are likely areas where the geological traps, especially those with strong sealing layers, can effectively hold gases such as methane or hydrogen. This suggests that, under the right structural and pressure conditions, the formations could still provide reliable containment.

Brine displacement has been classified in a category of similar high impact (likelihood 3, impact 5). Saline fluids if driven by reservoir pressures into overlying freshwater aquifers, the consequences on the environment may be very harsh and immediate. As for methane displacement, it has been rated with a slightly lower impact as compared with brine displacement (likelihood 3, impact 4), but it still is a major concern (Table 9.1, Figure 9.1). The presence of CH_4, He, and H_2 in the basin, has been recently confirmed[169]. The release of these gases could make the function of storage into a hard task and change the balances of greenhouse gases. At the same time, it could pose risks to shallow groundwater.

The possibility of long-term geochemical alteration was evaluated at likelihood 4, impact 4 (Table 9.1, Figure 9.1). This rating points to the uncertainties about the success of mineral–fluid interactions over the decades of CO_2 exposure. Differences in the content of carbonate and clay that had already been identified by XRF, XRD, and SEM analyses make it quite a challenge to fathom whether porosity and permeability will still be stable or significantly change.

Geomechanical risks were considered less dangerous (Figure 9.1). Seismic events caused by human activities were given a probability score of 2 and an impact score of 3 (Table 9.1, Figure 9.1). Ground-based investigations indicate that bedding with mild dips is the main structural characteristic, and the occurrence of active faulting is very scarce. However, it is still possible that a small portion of the fault could be reactivated, especially if high injection pressures are reached. The rating of ground movement was the lowest (likelihood 2, impact 2) (Table 9.1, Figure 9.1). In the case of any subsidence or uplift, they will be minimal, and more significantly, can be measured by using the Quaternary terraces and other geomorphic markers that are present in the basin.

Overall, such a hierarchy indicates that monitoring resources are better allocated first to containment integrity. The non-risks areas of CO_2 leakage and brine displacement should be of major focus, and then shift attention towards management of subsurface gas interactions and long-term alteration processes. Although geomechanical risks were assessed as having lower likelihood and impact, they still need to be closely monitored by regular checking to detect any unexpected behaviour at the earliest stage.

The PilotSTRATEGY project has received funding from the European Union's Horizon 2020 research and innovation programme under grant agreement No. 101022664

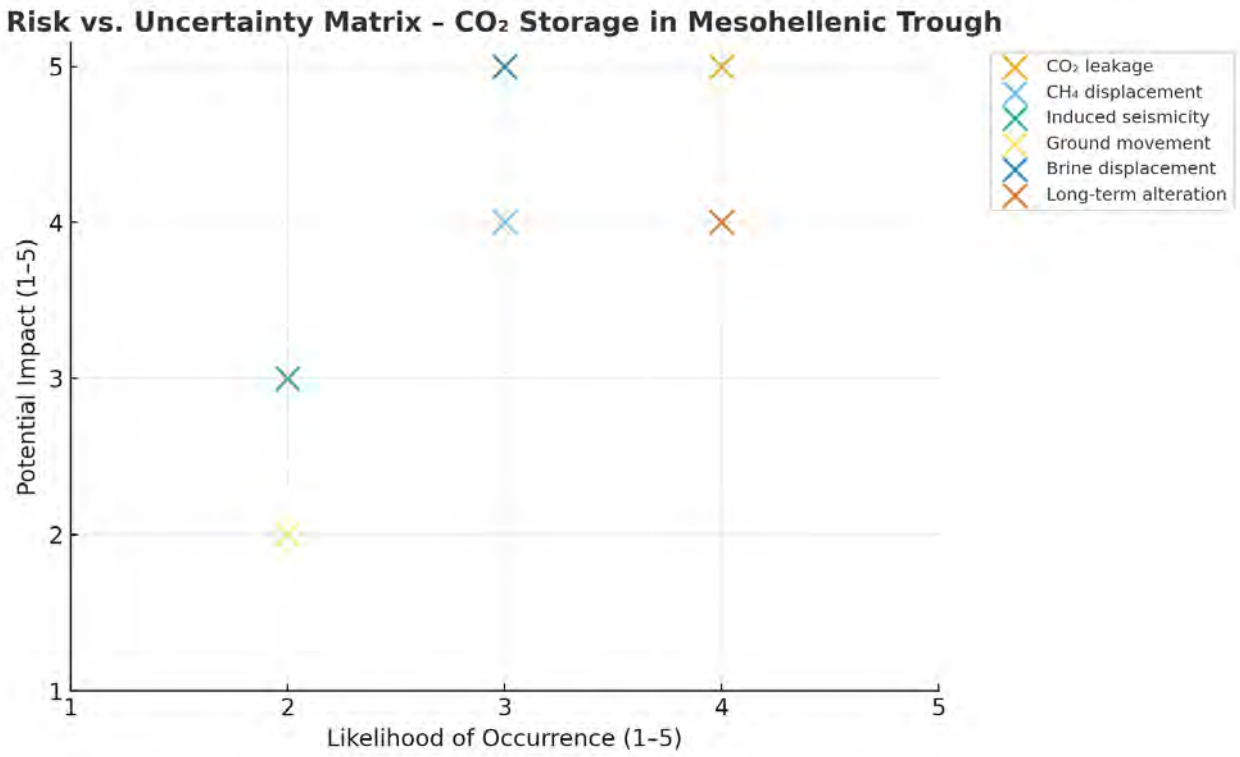

Figure 9.1: Risk-uncertainty matrix for CO_2 storage in the MHT. The position of each hazard reflects its estimated likelihood (x-axis) and potential impact (y-axis). Risks linked to containment, such as CO_2 leakage and brine displacement, fall into the high-impact field. Methane displacement and long-term geochemical change are ranked at intermediate levels, while induced seismicity and ground movement are placed in the lower-likelihood and lower-impact range, though they still warrant systematic monitoring.

The PilotSTRATEGY project has received funding from the European Union's Horizon 2020 research and innovation programme under grant agreement No. 101022664

10. Discussion: Risk Source Assessment

10.1. Site selection and characterization

Selecting an appropriate site is fundamental to the safe and efficient storage of CO_2. In the MHT, this process has relied on integrating evidence from stratigraphy, structure (mapping and geophysical analysis), and petrophysical testing. Sandstone units of the Eptachori and Pentalofos formations stand out as potential reservoirs, with porosities reaching 10.8% in places (sample PENT-3-2) and pore systems shown to be interconnected through SEM imaging and automated analysis. Marl-rich intervals of the Tsotyli Formation display porosities around 6.0%, extremely low permeabilities (<0.01 mD), and high clay-bound water fractions, indicating their effectiveness as caprocks. Bedding across much of the basin dips gently to the northeast, while faults and joints are mainly found in conglomeratic successions and near the ophiolitic basement.

The re-evaluation of geophysical data provides critical spatial and structural context to these observations. More than 1,200 km of legacy 2D seismic profiles (acquired between 1980 and 1994) were reprocessed during the PilotSTRATEGY project using state-of-the-art broadband pre-stack time migration workflows. This effort significantly enhanced reflector continuity and vertical resolution, allowing clearer imaging of the stratigraphic architecture and fault geometries across the Mesohellenic Trough. Eight major seismic horizons (H1 to H8) were mapped, from Quaternary cover to the Alpine basement, defining the principal reservoir and seal successions of the basin. Of particular interest are the tops of the Tsotyli, Pentalofos, and Eptachori formations, which form laterally continuous, alternating sandstone-marl packages suitable for reservoir–caprock coupling. These horizons were calibrated against the Neapolis-1 and Neapolis-2 wells, confirming the seismic-stratigraphic interpretation and providing direct lithological correlation for the conceptual storage model.

The assessment of the MHT as a potential site for long-term CO_2 storage highlights both its considerable geological advantages and the uncertainties that must be addressed before deployment. The size of the basin and the stratigraphic framework are favourable as sedimentary successions locally exceed 6-7 km in thickness, with cumulative molassic deposits forming repeated reservoir–seal pairs[18]. Field surveys (2024-2025) confirmed the predominance of the Eptachori, Pentalofos, and Tsotyli formations, defining the primary reservoir and sealing system of interest.

Seismic facies analysis further supports this interpretation, identifying seven depositional sequences (S1–S7) consistent with progressive syn-tectonic subsidence during Oligocene–Miocene time. The reprocessed profiles reveal anticlinal and fault-bounded traps typically 1–2.5 km wide, as well as local stratigraphic traps such as pinch-outs and turbiditic lobes. The distribution of these features confirms that structural and stratigraphic compartmentalisation play a major role in controlling potential storage zones.

Reservoir porosity reaches up to 10.8 % in the sandstones of the Pentalofos Fm (sample PENT-3-2) and 7.4 % in the Eptachori sandstones, although measured water permeabilities are consistently very low (<0.01 mD). This suggests that, while sandstones may possess moderate pore volumes, their connectivity is limited, likely behaving as tight or partially sealed intervals rather than effective fluid reservoirs under current conditions. SEM and automated image analyses confirm pore connectivity, while XRF and XRD data show compositional contrasts between formations: Eptachori samples are silica-rich (~36 wt.% SiO_2),

The PilotSTRATEGY project has received funding from the European Union's Horizon 2020 research and innovation programme under grant agreement No. 101022664

whereas Pentalofos sandstones are more calcareous (~42 wt.% CaO). These variations may influence both mechanical strength and geochemical reactivity under CO_2 exposure.

10.2. Risk identification

Risk identification defines the potential mechanisms through which containment might fail or storage performance could be compromised. In the MHT, the main concerns include CO_2 leakage through faulted or permeable zones, displacement of indigenous gases (CH_4, He, H_2), pressure-induced fault reactivation, brine migration into freshwater aquifers, and geochemical alteration affecting porosity and permeability. These risks are based on field observations, petrophysical and geochemical testing, and analogues from similar storage settings.

The new seismic interpretation directly adds to this risk assessment. Enhanced imaging of reflector geometries has allowed detailed mapping of faults, stratigraphic discontinuities, and potential migration pathways. While most faults are confined to conglomeratic successions and near the ophiolitic margins, the overall basin structure is gently dipping and stable. The presence of laterally extensive marly horizons (notably within the Tsotyli Fm) provides regional seals, reducing the likelihood of vertical CO_2 escape, whereas fault-bounded compartments may act as secondary containment structures.

Seal integrity appears robust, with marl- and clay-rich intervals of the Tsotyli Fm acting as the principal caprock (sample TSO-1-3: porosity 6.0%, permeability <0.01 mD, formation factor 273, clay-bound water fraction 0.87). Comparable properties in Pentalofos and Eptachori samples (porosity 4.9-10.8%, clay-bound water 0.91-0.97) confirm multiple sealing levels[142]. Nevertheless, conglomeratic bodies and carbonate-rich interbeds may create local bypass pathways, affecting seal certainty.

10.3. Vulnerability assessment

Vulnerability focuses on environmental or infrastructural elements potentially affected by storage decline. The main risk relates to freshwater aquifers that could be impacted by brine displacement or gas leakage. Surface infrastructure might also be sensitive to ground deformation. Lithological variability reinforces this vulnerability: sandstones in Region 1 are stable and absorb modest water volumes (10-50 ml/1000 g), whereas conglomerates in Region 2 vary widely (>300 ml/1000 g) with densities of 1.56-2.63 g/cm³. This heterogeneity implies spatially variable exposure risks.

Subsurface gas dynamics add complexity. The basin hosts CH_4, He, and H_2 accumulations of biogenic and thermogenic origin[197]. Methane poses dual risks as potential upward migration into aquifers and atmospheric release as a greenhouse gas. Isotopic data indicate biogenic CH_4 sources, suggesting shallow accumulations that could be disturbed by CO_2 injection, underscoring the importance of risk frameworks integrating both CO_2 and co-existing gases.

The integration of seismic interpretation with borehole data from Neapolis-1 and Neapolis-2 provides a robust calibration point for this vulnerability assessment. Both wells confirm the presence of methane shows within the Pentalofos and Tsotyli formations, validating the existence of active migration pathways. These observations demonstrate that the same structures capable of gas movement also define the potential storage geometry, reinforcing the need for careful pressure management and continuous geophysical monitoring.

The PilotSTRATEGY project has received funding from the European Union's Horizon 2020 research and innovation programme under grant agreement No. 101022664

10.4. Movement of the ground

In general changes in reservoir pressure may cause uplift or subsidence. In the MHT, such effects are expected to be modest but diagnostic of subsurface behaviour. Quaternary terraces in the Pentalofos Fm serve as benchmarks for detecting subtle vertical movements linked to injection. Continuous ground-motion monitoring therefore provides an early warning system and feedback for reservoir management.

10.5. Fault reactivation

In CO_2 storage sites, faults can act as either seals or conduits depending on their mechanical state. Mapping shows faults concentrated in conglomeratic successions and near the ophiolitic basement. Under elevated injection pressures, these structures could be reactivated, forming migration pathways for CO_2 or brine. Although the likelihood of large-scale reactivation is low, the consequences could be serious. Geomechanical modelling and site-scale monitoring are thus essential.

Geophysical data reinforce this understanding: seismic imaging reveals multiple trap types (anticlinal, fault-bounded, stratigraphic) that enhance storage security when combined with borehole calibration from the Neapolis wells. However, structural compartmentalisation introduces uncertainty in plume migration and pressure distribution, requiring dynamic modelling and microseismic surveillance.

10.6. Induced seismicity

Injection-induced seismicity is a related but distinct concern. Increasing pore pressures alters the stress field and may trigger small seismic events. Structural surveys indicate gently dipping strata, while seismological research suggests limited active faulting, pointing to a stable setting. Any induced seismicity is expected to be of low magnitude, yet microseismic events serve as early indicators of stress redistribution. Dense monitoring arrays will be necessary to detect and interpret such signals.

10.7. Contamination of drinking water by displaced brines

Saline formation water could be displaced upward during CO_2 injection, potentially affecting freshwater aquifers. Laboratory results show that marl-rich intervals such as the Tsotyli Fm have very low permeability (<0.01 mD) and act as effective barriers, but local heterogeneities, such as fractures or permeable interbeds, cannot be excluded. Given the regional reliance on groundwater, this risk must be integrated into site design and long-term hydrogeological monitoring.

10.8. Damage to hydrocarbon or mineral resources

Although the MHT is not a major hydrocarbon basin, it contains biogenic gas and mineral occurrences linked to the small lignite layers and the ophiolitic basement. CO_2 injection could interact with these systems, mobilising gases or altering mineral stability. Coordination with resource mapping and other subsurface uses should form part of the assessment framework.

10.9. Integrated evaluation

The MHT has the scale and stratigraphic architecture to accommodate large storage volumes, estimated at ~1.0 Gt for the Pentalofos Fm and 0.85 Gt for the Eptachori[142]. Its persistence of marl-rich seals with negligible permeability compares favourably with other European sites. Yet, uncertainties remain regarding lithological heterogeneity, gas migration, and geochemical alteration. Addressing these requires

The PilotSTRATEGY project has received funding from the European Union's Horizon 2020 research and innovation programme under grant agreement No. 101022664

pilot-scale injection, hydrogeochemical monitoring, and geomechanical modelling to bridge laboratory and field scales.

Overall, the viability of CO_2 storage in the MHT depends on continuous integration of geological, geochemical, and structural datasets as summarized in Table 10.1. Sustained monitoring, iterative modelling, and stakeholder engagement will be essential to manage risks such as CO_2 leakage, methane displacement, or aquifer contamination. The PilotSTRATEGY project provides a strong foundation for this effort and highlights that long-term storage security must be grounded in evidence-based risk assessment and adaptive management.

Table 10.1: Synthesis of the main strengths, weaknesses, opportunities, and risks (SWOT) for CO_2 storage in the MHT. The table integrates field observations, petrophysical and geochemical analyses, and regional assessments to provide an overview of the storage potential of the basin and associated uncertainties.

Strengths	Weaknesses	Opportunities	Risks
Thick sedimentary successions (>6 km) providing large storage volumes	Marked lithological heterogeneity, especially in conglomerates	Estimated storage capacity >1.8 Gt CO_2 across Pentalofos and Eptachori formations	Potential CO_2 leakage through faults or conglomeratic pathways
Multiple reservoir–seal pairs (Eptachori, Pentalofos, Tsotyli formations)	Variable reservoir quality with densities ranging 1.56–2.63 g/cm³	Integration of SEM, XRF, and XRD data provides robust mineralogical and petrophysical framework	Brine displacement into overlying freshwater aquifers
Marl-rich Tsotyli intervals with very low permeability (<0.01 mD) acting as effective caprocks	High compositional variability: silica-rich Eptachori vs. carbonate-rich Pentalofos	Use of reactive transport modelling to anticipate long-term mineral–fluid interactions	Mobilisation of indigenous gases (CH_4, He, H_2) during injection
Porosity values up to 10.8% in Pentalofos sandstones with interconnected pore systems	Laboratory tests provide only point-scale results, uncertain long-term extrapolation	Pilot-scale injection tests could refine capacity and risk assessments	Induced seismicity and local fault reactivation under elevated pressures
Presence of natural geomorphic benchmarks (Quaternary terraces) for monitoring ground movement	Potential bypass zones in conglomeratic and carbonate interbeds reducing seal performance	Strong alignment with EU decarbonisation and CCUS strategies	Long-term geochemical alteration affecting porosity and permeability
Seismic imaging confirms multiple trap styles (anticlinal, fault-bounded, stratigraphic)	Stratigraphic traps show lateral discontinuity and limited capacity	Borehole calibration (Neapolis-1 and -2 wells) improves confidence in reservoir–seal interpretation	Active migration pathways confirmed by methane shows may also guide CO_2 movement
Borehole–seismic integration	Structural compartmentalisation	Identification of stacked storage potential across	Compartmentalisation may limit

The PilotSTRATEGY project has received funding from the European Union's Horizon 2020 research and innovation programme under grant agreement No. 101022664

strengthens confidence in reservoir–seal architecture	due to faulting complicates plume migration	multiple reservoir–seal pairs	predictability and complicate pressure management

The PilotSTRATEGY project has received funding from the European Union's Horizon 2020 research and innovation programme under grant agreement No. 101022664

11. Conclusion

This deliverable cumulatively presents and cross examines a wide range of geological, geophysical, structural, petrophysical, and geochemical investigations to evaluate the MHT as a potential CO_2 storage site. The work combines field-based observations, laboratory measurements, and regional synthesis, creating one of the most complete assessments of this basin to date. The results underline both the potential of the system and the uncertainties that still need to be addressed before storage can proceed.

The stratigraphic framework of the basin is well constrained under the scope of the PilotSTRATEGY project. Successions from the Upper Eocene through the Miocene exceed several kilometres in thickness, and they record a natural alternation of coarse-grained molassic sediments with finer marl- and shale-rich intervals. This arrangement provides multiple reservoir–seal pairs. The sandstones of the Eptachori and Pentalofos formations offer storage potential, as porosity values reach 10.8% (sample PENT-3-2). In contrast, the marl-rich units of the Tsotyli Fm show restricted permeability (<0.01 mD) and high clay-bound water fractions, making them effective regional caprocks. This alternation in term of formations define a stratigraphy that is voluminous and suitable for long-term CO_2 containment.

Petrophysical and geomechanical data support this interpretation but also highlight the heterogeneity of the system. Sandstones and conglomerates vary in density, porosity, and absorption behaviour, with some conglomerates in Region 2 absorbing more than 300 ml per 1000 g of rock. Laboratory tests of mechanical properties, including elastic modulus and uniaxial compressive strength, indicate that most formations are competent under stress and can withstand injection-related pressure changes. One of the main challenges comes from the strong contrast between carbonate-rich and silica-rich facies, as revealed by XRF and XRD analyses. This means that the rocks of the basin will not all respond in the same way, either mechanically or geochemically, when subjected to CO_2 injection. In particular, samples from the Eptachori Fm are dominated by silica, with values around 36 wt.% SiO_2, whereas Pentalofos sandstones are much richer in calcium carbonate, with CaO contents reaching ~42 wt.%. These compositional differences are expected to shape fluid–rock interactions: silica-rich facies may remain relatively stable, while carbonate-rich layers are more prone to dissolution or secondary mineral precipitation. Both processes could gradually alter porosity and permeability, modifying reservoir behaviour over time. Because the long-term outcome of such reactions remains uncertain, the application of reactive transport modelling is essential to anticipate possible changes and reduce risk in future storage scenarios.

The reinterpretation of the seismic dataset provides a more detailed view of the storage architecture in the MHT and adds weight to the overall assessment of storage feasibility. The confirmation of multiple trap types, combined with borehole calibration, underlines that the basin hosts a diverse set of storage options, from fault-bounded compartments to broad anticlinal closures. These features improve the robustness of the conceptual model and demonstrate that storage is not restricted to a single structural style but can be distributed across several stratigraphic and structural domains.

At the same time, the geophysical evidence reinforces the importance of considering heterogeneity and compartmentalisation as central risks. Methane shows in the Neapolis wells highlight the existence of active migration pathways, which could equally affect injected CO_2. Thus, while the storage potential remains substantial, long-term safety will depend on careful site-specific appraisal, supported by monitoring strategies that are sensitive to both structural complexity and gas migration behaviour.

The PilotSTRATEGY project has received funding from the European Union's Horizon 2020 research and innovation programme under grant agreement No. 101022664

The geochemical investigation supports the interpretation of multiple water sources or flow paths, including both shallow, oxygenated meteoric water and deeper, more evolved fluids enriched in light elements. The results also show that gas compositions vary along their migration routes, reflecting interactions with different lithologies and fluid regimes. Where He and H_2 are present (e.g., Kivotos), the system involves both deeper lithological interaction (ultramafics/fracture pathways) and microbial methane generation in overlying sediments or mixed reservoirs.

In such cases, isotopes still point to dominantly biogenic CH_4 even if the gas migration system involves ophiolitic or deep rocks. Specifically, biogenic methane dominates in confined organic-rich environments (Katakali), while He and H_2 signals at Kivotos and Tropeouhos suggest deep crustal or mantle-derived fluids, potentially linked to serpentinization or radiogenic decay. Sites like Kivotos are most promising for mixed hydrogen generation, with some abiotic gas potential. Tropeouhos may serve more as a gas migration indicator, while Neos Kafkasos indicates natural CO_2 degassing rather than accumulation.

Where He and H_2 are also present (e.g., Kivotos), the system may involve both deeper lithological interaction (ultramafics/fracture pathways) and microbial methane generation in overlying sediments or mixed reservoirs. In such cases, isotopes still indicate biogenic CH_4 even if the gas migration mechanism involves ophiolitic or deep rocks. On the same note H_2 is difficult to find in the surface springs due to easy microbial consumption in the water .

Overall, the integration of geophysical, geochemical, and petrophysical datasets demonstrates that the MHT could host secure CO_2 storage at scale. However, success will rely on treating heterogeneity and fault-related migration not as minor complications but as central factors in site design, risk assessment, and adaptive management.

In summary, the MHT shows strong potential for geological CO_2 storage, with estimated capacities at 1.8 Gt in the Eptachori and Pentalofos formations. Its stratigraphy offers both thick reservoirs and competent caprocks. At the same time, the basin is heterogeneous, both laterally and vertically, and this heterogeneity introduces uncertainty in predicting reservoir behaviour, seal performance, and long-term stability. Addressing these challenges will require pilot-scale injection testing, coupled with hydrogeochemical and geomechanical monitoring. The results of this deliverable demonstrate that the MHT is a serious candidate for CO_2 storage in Greece. It provides the necessary geological framework, but safe and effective deployment will depend on integrating the datasets presented here with ongoing monitoring and modelling. This work therefore represents both a foundation for site development and a roadmap for future research.

A key priority is the long-term monitoring of gas seepage at selected sites, particularly Katakali, Kivotos, Tropeouhos, and Neos Kafkasos. It is well known that surface hydrogen emissions are not constant, and both the location and intensity of seepage may fluctuate over time. Similarly, gas sampling in groundwater, although useful, has limitations that may obscure short-term variability. Therefore, future work should emphasize systematic, long-term data collection rather than isolated measurements.

To close the existing knowledge gaps, it's important to set up a long-term monitoring program at the key sites of Katakali, Kivotos, Tropeouhos, and Neos Kafkasos. Each location should be checked regularly, ideally once a week, over a period of at least six months to a year. A handheld gas analyzer (such as the GA5000) can be used to take several readings during each visit, about six per day, focusing on hydrogen and helium levels. Whenever hydrogen is detected, water samples should also be collected for a full set

The PilotSTRATEGY project has received funding from the European Union's Horizon 2020 research and innovation programme under grant agreement No. 101022664

of laboratory analyses. The planned analyses should cover the major and trace elements of water, the concentrations of key gases (e.g., He, H_2, CH_4, CO_2), and a range of isotopes, including helium, hydrogen, oxygen, carbon, sulfur, and clumped isotopes, to trace where the gases come from and how they evolve over time.

To get a complete picture of the system, it is also important to sample not just groundwater, but rainfall and surface water as well. This will show how different parts of the water cycle might influence gas movement. If repeated measurements confirm steady hydrogen or helium signals at certain sites, then permanent monitoring instruments could be installed, once the necessary permits are secured, so data can be collected continuously rather than only during visits.

In parallel, a focused exploration effort should take place, bringing together geological mapping, targeted soil and water sampling, and shallow subsurface investigations. These activities will help reveal the pathways the gases follow and the geological features that control their release.

By combining these approaches, we can build a clearer understanding of how hydrogen and other gases behave in the region, whether they seep steadily or fluctuate, and identify the most promising sites for continued study. The insights gained will directly support better risk assessments, monitoring plans, and site selection for future CO_2 and hydrogen storage projects, setting a strong foundation for the next stage of work within the PilotSTRATEGY program.

The PilotSTRATEGY project has received funding from the European Union's Horizon 2020 research and innovation programme under grant agreement No. 101022664

Bibliography

1. Kontopoulos, N.F., Teresa; Zelilidis, Abraham; Alexiadis, Christos; Rigakis, Nikolaos, *Hydrocarbon potential of the middle Eocene-middle Miocene Mesohellenic piggy-back basin (central Greece): A case study.* Marine and Petroleum Geology, 1999. **16**(8): p. 811-824.
2. Vamvaka, A.K., A.; Mountrakis, D.; Papaoikonomou, J., *Geometry and structural evolution of the Mesohellenic Trough (Greece): a new approach*, in *Geological Society, London, Special Publications*, A.H.F.M. Robertson, D., Editor. 2006. p. 521-538.
3. Bornovas, J.a.R.-T.T., *Geological Map of Greece, scale 1:500.000*, I.G.M.E.I.o.G.a.M. Explorations), Editor. 1983.
4. Ferrière, J.R., J.Y.; Pavlopoulos, A.; Bonneau, M.; Migios, G.; Chanier, F.; Proust, J.N.; Gardin, S., *Geologic evolution and geodynamic controls of the Tertiary intramontane piggyback Meso-Hellenic basin, Greece.* Bulletin de la Société Géologique de France, 2004. **175**(4): p. 361-381.
5. Koukouzas, N., Kalaitzidis, S., Ward, C., *Organic petrographical, mineralogical and geochemical features of the Achlada and Mavropigi lignite deposits, NW Macedonia, Greece.* International Journal of Coal Greece, 2010. **83**: p. 387-395.
6. Koukouzas, C.K., N., *Coals of Greece: distribution, quality and reserves.* Geological Society, London, Special Publications, 1995. **82**(1): p. 171-180.
7. PPC Group. *The National Energy and Climate Plan (NECP, NOG 4893/B/2019), fully in tune with the ambitious objective of the EU to enhance Europe as the first climate-neutral continent by 2050, stipulates the complete lignite phase-out nation-wide by 2028.* 2024; Available from: https://www.ppcgroup.com/en/environment/lignite-phase-out/.
8. Natural Environment and Climate Change Agency. *Protected Areas In Greece*. Available from: https://necca.gov.gr/en/areas-of-action/protected-areas/.
9. Spinos, S., et al., *Environmental and spatial study of the Mesohellenic Trough and development prospects of the wider region of West Macedonia*, H.H.a.E.R.M.C.H. SA), Editor. 2020.
10. Natural Environment and Climate Change Agency. *Management Unit of Prespa National Park and Protected Areas of Western Macedonia*. Available from: https://necca.gov.gr/en/mdpp/the-management-unit-of-prespes-national-park-and-protected-areas-of-western-macedonia/.
11. Natural Environment and Climate Change Agency. *Management Unit of Northern Pindos National Park*. Available from: https://necca.gov.gr/en/mdpp/management-unit-of-northern-pindos-national-park/.
12. Christopoulou, M.A.K., Petros; Kostoglou, Nikolaos, Paraskevopoulou, Chrysothemis; Sideridis, Alkiviadis; Petrounias, Petros; Rogkala, Aikaterini; Stock, Sebastian; Koukouzas, Nikolaos, *Evaluation of the CO2 Storage Capacity in Sandstone Formations from the Southeast Mesohellenic trough (Greece).* Energies, 2022. **15**(10).
13. Kilias, A.V., A.; Falalakis, G.; Sfeikos, A.; Papadimitriou, E.; Gkarlaouni, C.H. and Karakostas, B., *The Mesohellenic Trough and the Paleogene Thrace Basin on the Rhodope Massif, their Structural Evolution and Geotectonic Significance in the Hellenides.* Journal of Geology & Geosciences, 2015. **04**(02).
14. Vamvaka, A.S., Cornelia; Frisch, Wolfgang; Danišík, Martin; Kilias, Adamantios, *Fission track data from the Mesohellenic Trough and the Pelagonian zone in NW Greece: Cenozoic tectonics and exhumation of source areas.* International Geology Review, 2010. **52**(2-3): p. 223-248.

The PilotSTRATEGY project has received funding from the European Union's Horizon 2020 research and innovation programme under grant agreement No. 101022664

15. Wilson, J.W., *The origin and tectonostratigraphic evolution of the Meso-Hellenic Trough, Northern Greece and Albania* 1993a, University of Edinburgh: Edinburgh, UK.
16. Tasianas, A.K., Nikolaos, *CO2 Storage Capacity Estimate in the Lithology of the Mesohellenic Trough, Greece.* Energy Procedia, 2016. **86**: p. 334-341.
17. Zelilidis, A.P., D.J.W.; Kontopoulos, N., *Sedimentation and basin evolution of the Oligocene-Miocene Mesohellenic basin, Greece.* AAPG Bulletin, 2002. **86**(1): p. 161-182.
18. Yiannakou, A.E., Dimosthenis; Zeka, Dimitra, *Spatial Interactions between the Settlement Network, Natural Landscape and Zones of Economic Activities: A Case Study in a Greek Region.* Sustainability, 2017. **9**(10).
19. Mouratidis, I.D., G.; Astaras, T.; Savvidis, S., *Sustainable water resources management through the use of GIS technology.* Global NEST Journal, 2013. **12**(2): p. 140-151.
20. Howard, D.A., *Drainage Analysis in Geologic Interpretation: A Summation.* AAPG Bulletin, 1967. **51**(11): p. 2246-2259.
21. Strahler, A., *Quantitative geomorphology of drainage basins and channel networks*, in *Handbook of Applied Hydrology*, M. Hill, Editor. 1964: New York. p. 54.
22. Asraras, T., *Quantitative geomorphological study of West part of Vertiskon mountain (Central Macedonia)*. 1980, Aristotle University of Thessaloniki. p. 1-214.
23. Strahler, A.N., *Hypsometric (Area-Altitude) Analysis of Erosional Topography.* Geological Society of America Bulletin, 1952. **63**(11).
24. Simou, E.K., V.; Papantoniou, G.; Papanikolaou, D.; Nomikou, P., *Morphotectonic analysis of Kozani Basin (Western Macedonia, Greece).* Bulletin of the Geological Society of Greece, 2017. **47**(2).
25. Parcharidis, I.N., Konstantinos; Serelis, Konstantinos; Baskoutas, Ioannis, *Integrated Use of Optical and Radar Satellite Data for Active Faults and Corresponding Displaced Landforms in Kozani Basin (Greece).* Geocarto International, 2001. **16**(3): p. 17-23.
26. Wilson, J., *The anatomy of Krania basin, northwest Greece.* Bulletin of the Geological Society of Greece, 1993. **28**(1): p. 361-368.
27. Efstratiou, N.B., Paolo; Elefanti, Paraskevi; Karkanas, Panagiotis; Ntinou, Maria, *Prehistoric exploitation of Grevena highland zones: hunters and herders along the Pindus chain of western Macedonia (Greece).* World Archaeology, 2006. **38**(3): p. 415-435.
28. European Employment Services. *Labour market indormation: Greece*. 2023; Available from: https://eures.europa.eu/living-and-working/labour-market-information/labour-market-information-greece_en#western-macedonia.
29. Eurostat;. *GDP per capita in purchasing power standards (PPS) at regional, national and European level (EU-27)* 2024; Available from: https://ec.europa.eu/eurostat/databrowser/view/tec00114/default/table?lang=en.
30. Energy, M.o.t.E.a., *Strategic Environmental Impact Study of the National Hazardous Waste Management Plan*. 2016.
31. Beck, H.E.Z., N. E.; McVicar, T. R.; Vergopolan, N.; Berg, A.; Wood, E. F., *Present and future Koppen-Geiger climate classification maps at 1-km resolution.* Sci Data, 2018. **5**(1): p. 180214.
32. Energy, M.o.t.E.a., *Strategic Environmental Impact Study, Flood Risk Management Plan of the River Basins of the Water Division of Western Macedonia*. 2020.
33. *GISWM*. Available from: https://www.geodm.gr.
34. Voulanas, D.T., N.; Hatzigiannakis, E., *Assessment of potential hydrological climate change impacts in Kastoria basin (Western Macedonia, Greece) using EUROCORDEX regional climate models.* Global NEST Journal, 2021. **23**(1): p. 43-54.

The PilotSTRATEGY project has received funding from the European Union's Horizon 2020 research and innovation programme under grant agreement No. 101022664

35. Ministry of the Environment, E.a.C.C.M., Special Secretariat for Water, *Adaptation Measures to Climate Change within the European Floods Directive (2007/60/EC).* 2012.
36. Ministry of the Environment and Energy, *Implementation of Directive 2007/60/EC-Preliminary Flood Risk Assessment*. 2012. p. 75-83.
37. Dewey, J.F., et al., *Plate Tectonics and the Evolution of the Alpine System.* Geological Society of America Bulletin, 1973. **84**(10).
38. Jones, G.R., Alastair H. F., *Tectono-stratigraphy and evolution of the Mesozoic Pindos ophiolite and related units, northwestern Greece.* Journal of the Geological Society, 1991. **148**(2): p. 267-288.
39. Mountrakis, D., *The Pelagonian microcontinent in Greece: a polyphase deformed fragment of the Cimmerian continent and its role in the geotectonic evolution of the Eastern Mediterranean.* Journal of Geology, 1986. **94**(335-347).
40. Brunn, J.H., *Contribution à l'étude géologique du Pinde septentrional et d' une partie de la Macédoine occidnetale.* Ann Géologique Pays Hel, 1956. **7**: p. 1-358.
41. Kilias, A.T., E.; Katrivanos, E.; Vamvaka, A.; Fasoulas, Ch.; Pipera, K.; Falalakis, G.; Avgerinas, St.; Sfeikos, A., *A geological cross-section through northern Greece from Pindos to Rhodope Mountain Ranges: a field guide across the External and Internal Hellenides.* Journal of the Virtual Explorer, In: (Eds.) Adamantios Kilias, and Stylianos Lozios, Geological field trips in the Hellenides, 2016. **50**(1).
42. Vamvaka, A., *Geometry of deformation and kinematic analysis in mesohellenic trough*. 2010, Aristotle University of Thessaloniki: National Documentation Centre of Greece. p. 215.
43. Anders, B., et al., *The oldest rocks of Greece: first evidence for a Precambrian terrane within the Pelagonian Zone.* Geological Magazine, 2005. **143**(1): p. 41-58.
44. Jacobshagen, V., *Geologie von Griechenland*, in *Geological Magazine*. 1986, Gebr. Borntraeger, Berlin. p. 558-559.
45. Kilias, A., *The Hellenides: A Multiphase Deformed Orogenic Belt, its Structural Architecture, Kinematics and Geotectonic Setting during the Alpine Orogeny: Compression vs Extension the Dynamic Peer for the Orogen Making. A Synthesis.* J. Geolo. Geosci., 2021. **5**(1): p. 56.
46. Yarwood, G.a.D., J., *Lower Cretaceous and younger thrusting in the Pelagonian rocks of the high Pieria, Greece*, in *6th Coll. Geology Aegean region*. 1997: Athens. p. 269-280.
47. Kilias, A., *The Alpine Geological History of the Hellenides from the Triassic to the Present—Compression vs. Extension, a Dynamic Pair for Orogen Structural Configuration: A Synthesis.* Geosciences, 2023. **14**(1): p. 10.
48. Robertson, A.H.F., et al., *Alternative tectonic models for the Late Palaeozoic-Early Tertiary development of Tethys in the Eastern Mediterranean region.* Geological Society, London, Special Publications, 1996. **105**(1): p. 239-263.
49. Karakitsios, V., *The Influence of Preexisting Structure and Halokinesis on Organic Matter Preservation and Thrust System Evolution in the Ionian Basin, Northwest Greece.* AAPG Bulletin, 1995. **79**(7): p. 960-980.
50. Sotiropoulos, S., et al., *Thrust sequences in the central part of the External Hellenides.* Geological Magazine, 2003. **140**(6): p. 661-668.
51. Avgerinas, A.K.A.K., A.; Mountrakis A., Frisch, W.; Dunkl, I.; Most, T., *Cretaceous structural evolution of the Pelagonian crystalline in western Voras Mt (Macedonia, Northern Greece).* Bulletin of the Geological Society of Greece, 2001. **34**(1).

The PilotSTRATEGY project has received funding from the European Union's Horizon 2020 research and innovation programme under grant agreement No. 101022664

52. Jacobshagen, V.D., S.; Kockel, F.; Kopp, K.O.; Kowalczyk, G.; Berckhemer, H.Y.; Buttner, D., *Structure and geodynamic evolution of the Aegean region*, in *IUG Scientific Report*, H. In: Closs, Roeder D., Schmidt, y K. (eds.), Editor. 1978. p. 537-564.
53. Faupl, P.P., A.; Migiros, G., *On the provenance of flysch deposits in the External Hellenides of mainland Greece: results from heavy mineral studies.* Geological Magazine, 1998. **135**(3): p. 421-442.
54. Richter, D., *The Flysch Stage in the Hellenides.* Zeitschrift der Deutschen Geologischen Gesellschaft, 1976. **127**(2): p. 467-483.
55. Fleury, J., *Les zones de Gavrovo – Tripolitsa et du Pinde – Olonos (Grèce continentale et Pèloponnèse du Nord).* , in *Évolution d'une plateforme et d'un bassin dans leur carde alpin. Sociètè Gèologique du Nord*. 1980. p. 1-651.
56. Schermer, E.R., *Geometry and kinematics of continental basement deformation during the Alpine orogeny, Mt. Olympos region, Greece.* Journal of Structural Geology, 1993. **15**(3-5): p. 571-591.
57. Vamvaka, A.S., C. and A., Kilias,, *Tertiary erosion history of the Pelagonian nappe (Hellenides, Greece), revealed by apatite low-temperature thermochronology*, in *Thermo 2018*. 2018: Quedlinburg.
58. Savoyat, E., Monopolis, D., and Bizon, G.,, *Geological Map of Greece, scale 1:50 000, Grevena Sheet*. 1972a, Institute of Geology & Mineral Exploration: Athens.
59. Brunn, J.H., *Geological Map of Greece, Pentalophos Sheet, scale 1:50 000*. 1960, IGEY, Athens.
60. Zelilidis, A., et al., *Late Eocene to Early Miocene depositional environments of the Mesohellenic Basin, North-Central Greece: Implications for hydrocarbon potential.* Geologica Balcanica, 1997. **27**(1-2): p. 45-55.
61. Desprairies, A.a.V., P., *Le sillon mesohellenique et la zone pelagonienne.* Bull. de la Soc. Geol. De France, 1976. **7**(XIX/1): p. 28-34.
62. Papanikolaou, D., Lekkas, E., Mariolakos, E. and Mirkou, R., *Contribution to the Geology of Ikaria Island, Aegean Sea.* Ann. Geol. Pays Hell., 1977. **29**(1): p. 1-28.
63. Papanikolaou, D.L., E.; Mariolakos, E. and Mirkou, R., *Contribution on the geodynamic evolution of the Mesohellenic trough.* Bulletin of the Geological Society of Greece, 1988. **20**: p. 17-36.
64. Barbieri, R., *Foraminifera of the Eptahorion Formation (early Oligocene) of the Mesohellenic Basin, northern Greece.* Journal of Micropalaeontology, 1992. **11**(1): p. 73-84.
65. Koumantakis J.; Matarangas, D.T.-M., S.; Georgiadou, E. and Economou, K., *Geological Map of Greece, scale 1:50 000. Panagia Sheet*. 1980, Institute of Geology and Mineral Exploration: Athens.
66. Zygojannis, N. and C. Müller, *Nannoplankton Biostratigraphy of the Tertiary Mesohellenic Molasse (Northwest Greece).* Zeitschrift der Deutschen Geologischen Gesellschaft, 1982. **133**(3): p. 445-455.
67. Zygojannis, N. and D. Sidiropoulos, *Heavy mineral distribution and paleogeographic framework of the Tertiary Molasse of the Mesohellenic basin, north-west Greece.* Neues Jahrbuch für Geologie und Paläontologie - Monatshefte, 1981. **1981**(2): p. 100-128.
68. Mavridis, A.M., D.; Tsaila-Monopolis, S.; Mostler, H.; Bornovas, J. & Apostolidis, N., *Geological Map of Greece, Ayiofillon Sheet, scale 1:50.000.* 1979, Institute of Geological and Mineral Explorations.
69. Vamvaka, A.K., A.; and Mountrakis, D. , *Geometry and structural evolution of the Mesohellenic Trough. A new approach (extended abstract).* , in *5th International Symposium on Eastern*

The PilotSTRATEGY project has received funding from the European Union's Horizon 2020 research and innovation programme under grant agreement No. 101022664

Mediterranean Geology, A. In: Chatzipetros, and Pavlides, S. (eds). , Editor. 2004: Thessaloniki, Greece. p. 209-212.

70. Savoyat, E.L., N. and Bizon, G., *Geological Map of Greece, scale 1:50 000, Trikala Sheet.* 1969, Institute of Geology and Mineral Exploration: Athens.
71. Savoyat, E.L., N.; and Bizon, G. , *Geological Map of Greece, scale 1:50 000, Kalambaka Sheet*. 1972b, Institute of Geology and Mineral Exploration: Athens.
72. Doutsos, T.K., J.; Zelilidas, A.; Kontopoulos, N., *Intracontinental wedging and post-orogenic collapse in the mesohellenic trough.* Geologische Rundschau, 1994. **83**(2): p. 257-275.
73. Ferrière, J.R., Jean-Yves; Migiros, Georges; Proust, Jean-Noël; Bonneau, Michel; Pavlopoulos, Andreas; Houze, Alexandre, *Initiation d'un bassin transporté: l'exemple du ≪sillon méso-hellénique ≫ au Tertiaire (Grèce).* Comptes Rendus de l'Académie des Sciences - Series IIA - Earth and Planetary Science, 1998. **326**(8): p. 567-574.
74. Zelilidis, A.a.K., N., *Depositional environment of the Pentalofos Formation in the Mesohellenic basin: application to the concept of hydrocarbon habitat.* Mineral Wealth, 1997. **102**: p. 45-52.
75. Abreu, V., A.; haddad, geoffrey, A., *Glacioeustatic Fluctuations: The Mechanism Linking Stable Isotope Events and Sequence Stratigraphy from the Early Oligocene to Middle Miocene</subtitle&gt*, in *Mesozoic and Cenozoic Sequence Stratigraphy of European Basins*, P.-C.H. de Graciansky, Jan; Jacquin, Thierry; Vail, Peter R., Editor. 1999. p. 245-269.
76. Haq, B.U.H., J.; Vail, P. R., *Chronology of fluctuating sea levels since the triassic.* Science, 1987. **235**(4793): p. 1156-67.
77. Ori, G.G.R., M., *Geometries of Gilbert-type deltas and large channels in the Meteora conglomerate, meso-Hellenic basin (Oligo-Miocene), central Greece.* Sentimentology, 1987. **34**: p. 845-859.
78. Savoyat, E.V., A.; Monopolis, D.; and Bizon, G. , *Geological Map of Greece, scale 1:50 000, Argos Orestikon Sheet*. 1971b, Institute of Geology and Mineral Exploration: Athens.
79. Savoyat, E.M., D.; and Bizon, G., *Geological Map of Greece, scale 1:50 000, Nestorion Sheet.* . 1971a, Institute of Geology and Mineral Exploration: Athens. .
80. Lekkas, E.L.P., D.; Kranis, ch.; Lozios, S. G.; Fountoulis, I. G.; Skourtsos, E.; and Nomikou, B., *Neotectonic Map of Greece, scale 1:100.000, explanatory issue*. 1999.
81. Busby, C.J., and Ingersoll, R.V., *Tectonics of sedimentary basins*. 1995, Blackwell Science, Cambridge (Mass.). p. 579.
82. Kostakioti, A., Xypolias, P., Kokkalas, S., Doutsos, T. *Quantitative analysis of deformation along the fault damage zone of the Klimatia Thrust (NW Greece, Ionian Zone)*. in *Bulletin of the Geological Society of Greece* 2004. Proceedings of the 10th International Congress, Thessaloniki.
83. Kilias, A.F., Charalampos; Priniotakis, Michalis; Sfeikos, Aris; Frisch, Wolfgang, *Deformation and HP/LT Metamorphic Conditions at the Tectonic Window of Kranea (W -- Thessaly, Northern Greece).* Zeitschrift der Deutschen Geologischen Gesellschaft, 1991. **142**(1): p. 87-96.
84. Kilias, A.F., W.; Ratschbacher, L.; and Sfeikos, A., *Structural evolution and metamorphism of blueschists, Ampelakia nappe, eastern Thessaly, Greece.* Bulletin of the Geological Society of Greece, 1991b. **25**(1).
85. Mavridis, A., Kelepertzis, A., Tsaila-Monopolis, S., Skourtsi-Koroneou, V., Moores, H., *Geological Map of Greece, scale 1: 50 000, Knidi Sheet*. 1985, Institute of Geology and Mineral Exploration: Athens.

The PilotSTRATEGY project has received funding from the European Union's Horizon 2020 research and innovation programme under grant agreement No. 101022664

86. Kilias, A.T., Markos; Mountrakis, Demosthenis; Shallo, Minella; Marto, Antrea; Turku, Ismail, *Geometry and kinematics of deformation in the Albanian orogenic belt during the Tertiary.* Journal of Geodynamics, 2001. **31**(2): p. 169-187.
87. Lister, G.S.B., Greetje; Feenstra, Anne, *Metamorphic core complexes of Cordilleran type in the Cyclades, Aegean Sea, Greece.* Geology, 1984. **12**(4).
88. Mountrakis, D.P., S.; Zouros, N.; Astaras, Th; Chatzipetros, A., *Seismic fault geometry and kinematics of the 13 May 1995 Western Macedonia (Greece) earthquake.* Journal of Geodynamics, 1998. **26**(2-4): p. 175-196.
89. Papazachos, B.a.P., C., *The earthquakes of Greece*. 1997, Thessaloniki, Greece: Ziti, P. and Co.
90. Hatzfeld, D.K., V.; Ziazia, M.; Selvaggi, G.; Leborgne, S.; Berge, C.; Guiguet, R.; Paul, A.; Voidomatis, P.; Diagnourtas, D.; Kassaras, I.; Koutsikos, I.; Makropoulos, K.; Azzara, R.; Di Bona, M.; Baccheschi, S.; Bernard, P.; Papaioannou, C., *The Kozani-Grevena (Greece) earthquake of 13 May 1995 revisited from a detailed seismological study.* Bulletin of the Seismological Society of America, 1997. **87**(2): p. 463-473.
91. Mountrakis, D.T., M.; Papazachos, C.; Thomaidou, E.; Karagianni, E.; Vamvakaris, D., *Neotectonic and seismological data concerning major active faults, and the stress regimes of Northern Greece.* Geological Society, London, Special Publications, 2006. **260**(1): p. 649-670.
92. Papanastassiou, D.D., G.; Voulgaris, N.; Stavrakakis, G., *The May 13, 1995, Kozani-Grevena (NW Greece) earthquake: Source study and its tectonic implications.* Journal of Geodynamics, 1998. **26**(2-4): p. 233-244.
93. Papazachos, C.M., D.; Karagianni, E.; Tranos, M.; and Vamvakaris, D., *Stress-field and active tectonics in northern Greece using seismological and neotectonic information*, in *10th Gongress Geology Society Greece*. 2004: Thessaloniki.
94. Rondoyanni, T., et al., *Active Faults Affecting Linear Engineering Projects: Examples From Greece.* Geotechnical and Geological Engineering, 2013. **31**(4): p. 1151-1170.
95. Ori, G.G., Friend, P.F., *Sedimentary basins formed and carried piggyback on active thrust sheets.* Geology, 1984. **12**(8): p. 475-478.
96. Reijs, J., McClay, K., *Salar Grande pull-apart basin, Atacama Fault System, northern Chile.* Geological Society, London, Special Publications, 1998. **135**: p. 127-141.
97. Dimopoulos, G., *Applied Geology-Hydrogeology*. Vol. 1. 1983, Thessaloniki: Aristotle University of Thessaloniki.
98. Kassaras, I., et al., *The New Seismotectonic Atlas of Greece (v1.0) and Its Implementation.* Geosciences, 2020. **10**(11).
99. Caputo, R.C., A.; Pavlides, S.; Sboras, S., *The Greek Database of Seismogenic Sources (GreDaSS): state-of-the-art for northern Greece.* Annals of Geophysics, 2013. **55**(5).
100. Ziogou, F., et al., *Potential Environmental Impacts of CO2 Leakage from the Study of Natural Analogue Sites in Europe.* Energy Procedia, 2013. **37**: p. 3521-3528.
101. Koukouzas, N., et al., *Geological modelling for investigating CO2 emissions in FlorinaBasin, Greece.* Open Geosciences, 2015. **7**(1).
102. Pavlides, S.a.S., K., *Neotectonics and active tectonics in low seismicity areas of Greece: Vegoritis (NW Macedonia) and Melos Isl. complex (Cyclades)-Comparison. .* Annales Geologiques des Pays Helleniques 1987. **33**: p. 161-176.
103. Papazachos, B.C., et al., *The natural process of generation of the main shock of Kozani-Grevena of 13 May 1995 (MS= 6.6) and of its seismic sequence.* Publication no 4. 1995, Geophysics Laboratory, Aristotelian University of Thessaloniki.
104. Mouyiaris, N., *Seismic history of the Aegean Region, 2400BC-AD 1990*, in *I*. 1994, Univ. of Patras.

The PilotSTRATEGY project has received funding from the European Union's Horizon 2020 research and innovation programme under grant agreement No. 101022664

105. Valera, E., *Earthquake in Grevena-Kozani, 1995*, in *Department of Geography*. 2077, Harokopio University
106. Hatzfeld, D., et al., *The Kozani-Grevena (Greece) Earthquake of May 13, 1995, Ms = 6.6. Preliminary Results of a Field Multidisciplinary Survey.* Seismological Research Letters, 1995. **66**(6): p. 61-70.
107. Stiros, S.C. and P.A. Pirazzoli, *Palaeoseismic studies in Greece: A review.* Quaternary International, 1995. **25**: p. 57-63.
108. Stiros, S.a.J., R., *Archaeoseismology Fitch Laboratory Occasional Paper 7*. Geological Society, London, Special Publications, ed. S. Stiros, & R.E, Jones (eds.). 1996, Athens: IGME - Institute of Geology & Mineral Exploration & The British School at Athens.
109. Evangelatou-Notara, F., *Earthquakes in Byzantium (13th-15th century), historical investigation.* Parousia, 1993(24): p. 184.
110. Golombias, G., *Notes of religious books of kastoria.* Makedonika, 1986. **25**(1).
111. Siganidou, M., *Pella, section 1, block 2, Archaeological excavations report*, in *Archaeologikon Deltion* 1981.
112. Pirazzoli, P.A., J. Laborel, and S.C. Stiros, *Earthquake clustering in the eastern Mediterranean during historical times.* Journal of Geophysical Research: Solid Earth, 1996. **101**(B3): p. 6083-6097.
113. Stiros, S.P., P.; Pomoni-Papaioannou, F.; Laborel, J.; Laborel, F.; Arnold, M., *Late Quaternary uplift of the Olympus-Pelion Range (Macedonia-Thrace, Greece).* Bulletin of the Geological Society of Greece, 1992.
114. *Government Gazette 2698/B/06.07.2018, (in Greek)*. Available from: https://floods.ypeka.gr/egyFloods/sdkp/EL09/FEK_B_2689_06072018.pdf.
115. Allmendinger, R.W.C., N.;, *Structural geology algorithms: Vectors and tensors in structural geology*. 2012: Cambridge University Press.
116. Cardozo, N.A., R., W.; , *Spherical projections with OSXStereonet.* Computers & Geosciences, 2013. **51**: p. 193-205.
117. Suhet.;, *Sentinel-2 User Handbook*, in *ESA Standard Document*. 2015.
118. Tyrologou, P., Vamvaka A., Koukouzas, N., Pedro, J., Fleury, M., Carneiro, J., Ribeiro, Ghikas, D., Mpatsi, A., Barradas, J.P., Faria, P., Veloso, F.,, *Progress for carbon dioxide geological storage in West Macedonia: A field and laboratory-based survey.* Carbon Reduction, (Re)use, and Removal Technologies and Practices collection, 2023: p. 1-31.
119. Daskalopoulou, K., et al., *Origin of methane and light hydrocarbons in natural fluid emissions: A key study from Greece.* Chemical Geology, 2018. **479**: p. 286-301.
120. Plastiras, V.M., D.; , *Geological Map of Greece, Grevena Sheet, scale 1:50.000.* 1987, Institute of Geological and Mineral Explorations: Athens.
121. Plastiras, V.R., D.;, *Geological Map of Greece, Kastoria Sheet, scale 1:50.000.* 1978, Institute of Geological and Mineral Explorations: Athens.
122. Environment Agency, *Methods for sampling and analysing methane in groundwater: A review of current research and practice*. 2021: Bristol.
123. Capasso, G. and S. Inguaggiato, *A simple method for the determination of dissolved gases in natural waters. An application to thermal waters from Vulcano Island.* Applied Geochemistry, 1998. **13**(5): p. 631-642.
124. Inguaggiato, S. and A. Rizzo, *Dissolved helium isotope ratios in ground-waters: a new technique based on gas–water re-equilibration and its application to Stromboli volcanic system.* Applied Geochemistry, 2004. **19**(5): p. 665-673.

The PilotSTRATEGY project has received funding from the European Union's Horizon 2020 research and innovation programme under grant agreement No. 101022664

125. Diamond, R.E., *Stable Isotope Hydrology*. 2022, Guelph, Ontario, Canada: The Groundwater Project. 102.
126. Gat, J.R., *Oxygen and hydrogen isotopes in the hydrologic cycle.* Annual Review of Earth and Planetary Sciences, 1996. **24**(Volume 24, 1996): p. 225-262.
127. Craig, H., *Isotopic Variations in Meteoric Waters.* Science, 1961. **133**(3465): p. 1702-1703.
128. Pang, Z., et al., *An Isotopic Geoindicator in the Hydrological Cycle.* Procedia Earth and Planetary Science, 2017. **17**: p. 534-537.
129. Lee, J.E. and I. Fung, *"Amount effect" of water isotopes and quantitative analysis of post-condensation processes.* Hydrological Processes, 2008. **22**(1): p. 1-8.
130. Clark, I.D. and P. Fritz, *Environmental Isotopes in Hydrogeology*. 1st ed. 2013, USA: CRC Press.
131. Kendall, C. and D.H. Doctor, *5.11 - Stable Isotope Applications in Hydrologic Studies*, in *Treatise on Geochemistry*, H.D. Holland and K.K. Turekian, Editors. 2003, Pergamon: Oxford. p. 319-364.
132. Langmuir, D., *Aqueous environmental geochemistry*. 1997: Prentice Hall. 618.
133. Chapelle, F.H., *5.14 - Geochemistry of Groundwater*, in *Treatise on Geochemistry*, H.D. Holland and K.K. Turekian, Editors. 2003, Pergamon: Oxford. p. 425-449.
134. Wood, W.W., *Hydrogeochemistry – A journey of discovery. The Groundwater Project*. 2025, Guelph, Ontario, Canada: The Groundwater Project.
135. Gemeni, V., et al., *Geochemical consequences in shallow aquifers from the long-term presence of CO2 in a natural field: The case of Florina Basin, W. Macedonia, Greece.* Greenhouse Gases: Science and Technology, 2015. **6**(4): p. 450-469.
136. Zgonnik, V., *The occurrence and geoscience of natural hydrogen: A comprehensive review.* Earth-Science Reviews, 2020. **203**: p. 103140.
137. Etiope, G. and B. Sherwood Lollar, *Abiotic methane on earth.* Reviews of Geophysics, 2013. **51**(2): p. 276-299.
138. Etiope, G., *Natural emissions of methane from geological seepage in Europe.* Atmospheric Environment, 2009. **43**(7): p. 1430-1443.
139. Prinzhofer, A. and É. Pernaton, *Isotopically light methane in natural gas: bacterial imprint or diffusive fractionation?* Chemical Geology, 1997. **142**(3): p. 193-200.
140. West, J.M., et al., *Comparison of the impacts of elevated CO_2 soil gas concentrations on selected European terrestrial environments.* International Journal of Greenhouse Gas Control, 2015. **42**: p. 357-371.
141. Etiope, G., *Natural hydrogen extracted from ophiolitic rocks: A first dataset.* International Journal of Hydrogen Energy, 2024. **78**: p. 368-372.
142. Wang, L., et al., *The Origin and Occurrence of Natural Hydrogen.* Energies, 2023. **16**(5).
143. Koukouzas, N., Tyrologou, P., Stergiou, C.L., Carneiro, J., Cantel,i P., Karatrantou, C., Asimakopoulou, S., *Characterization of Sandstone Formations in the Mesohellenic Trough for CO2 Storage: Insights from the Integration of Optical Mineralogy, Geochemistry, and Automated Imaging Techniques*, in *17th International Congress of the Geological Society of Greece*. 2025, Bulletin of the Geological Society of Greece: Mytilene, Greece. p. 792-797.
144. Houben, G.J., *Iron oxide incustrations in wells. Part 2: chemical dissolution and modeling.* Applied Geochemistry, 2003. **18**: p. 941-954.
145. Etiope, G., *Abiotic Methane in Continental Serpentinization Sites: An Overview.* Procedia Earth and Planetary Science, 2017. **17**: p. 9-12.
146. Boschetti, T., et al., *Boron, lithium and methane isotope composition of hyperalkaline waters (Northern Apennines, Italy): Terrestrial serpentinization or mixing with brine?* Applied Geochemistry, 2013. **32**: p. 17-25.

The PilotSTRATEGY project has received funding from the European Union's Horizon 2020 research and innovation programme under grant agreement No. 101022664

147. Banks, D. and B. Frengstad, *Evolution of groundwater chemical composition by plagioclase hydrolysis in Norwegian anorthosites.* Geochimica et Cosmochimica Acta, 2006. **70**(6): p. 1337-1355.
148. Oikonomopoulos, I.K., et al., *Clays from Neogene Achlada lignite deposits in Florina basin (Western Macedonia, N. Greece): A prospective resource for the ceramics industry.* Applied Clay Science, 2015. **103**: p. 1-9.
149. Oikonomopoulos, I.K., et al., *Mineralogical characterization of the intraseam layers of Lofoi lignite deposits in Florina basin (western Makedonia, northwest Greece).* Energy Sources, Part A: Recovery, Utilization, and Environmental Effects, 2016. **38**(11): p. 1562-1568.
150. Hanor, J.S., *Origin of saline fluids in sedimentary basins.* Geological Society, London, Special Publications, 1994. **78**(1): p. 151-174.
151. Edmunds, W.M. and P.L. Smedley, *Residence time indicators in groundwater: the East Midlands Triassic sandstone aquifer.* Applied Geochemistry, 2000. **15**(6): p. 737-752.
152. Koukouzas, N., et al., *Quantitative Evaluation of Minerals in Lignites and Intraseam Sediments from the Achlada Basin, Northern Greece.* Energy & Fuels, 2009. **23**(4): p. 2169-2175.
153. Christopoulou, M.A., et al., *Evaluation of the CO2 Storage Capacity in Sandstone Formations from the Southeast Mesohellenic trough (Greece).* Energies, 2022. **15**(10): p. 3491.
154. Etiope, G., et al., *Methane and hydrogen in hyperalkaline groundwaters of the serpentinized Dinaride ophiolite belt, Bosnia and Herzegovina.* Applied Geochemistry, 2017. **84**: p. 286-296.
155. Danabalan, D., et al., *The principles of helium exploration.* Petroleum Geoscience, 2022. **28**(2).
156. Koukouzas, N., et al., *Geological modelling for investigating CO2 emissions in Florina Basin, Greece.* Open Geosciences, 2015. **7**(1).
157. Prinzhofer, A., C.S. Tahara Cissé, and A.B. Diallo, *Discovery of a large accumulation of natural hydrogen in Bourakebougou (Mali).* International Journal of Hydrogen Energy, 2018. **43**(42): p. 19315-19326.
158. Moretti, I., et al., *Natural hydrogen emanations in Namibia: Field acquisition and vegetation indexes from multispectral satellite image analysis.* International Journal of Hydrogen Energy, 2022. **47**(84): p. 35588-35607.
159. Frery, E., L. Langhi, and J. Markov, *Natural hydrogen exploration in Australia – state of knowledge and presentation of a case study.* The APPEA Journal, 2022. **62**(1): p. 223-234.
160. Gelman, S.E., J.S. Hearon, and G.S. Ellis, *Prospectivity mapping for geologic hydrogen*, in *Professional Paper*. 2025: Reston VA.
161. Koukouzas, N.K., Pavlos; Koutsovitis, Petros; Karkalis, Christos, *An integrated approach to the coal deposits in the Mesohellenic Trough, Greece.* Bulletin of the Geological Society of Greece, 2019. **54**(1).
162. Etiope, G., et al., *Abiotic methane seepage in the Ronda peridotite massif, southern Spain.* Applied Geochemistry, 2016. **66**: p. 101-113.
163. Schoell, M., *The hydrogen and carbon isotopic composition of methane from natural gases of various origins.* Geochimica et Cosmochimica Acta, 1980. **44**(5): p. 649-661.
164. Murray, J., et al., *Abiotic hydrogen generation from biotite-rich granite: A case study of the Soultz-sous-Forêts geothermal site, France.* Applied Geochemistry, 2020. **119**: p. 104631.
165. Valentine, D.L., et al., *Carbon and hydrogen isotope fractionation by moderately thermophilic methanogens.* Geochimica et Cosmochimica Acta, 2004. **68**(7): p. 1571-1590.
166. Ktenas D., Makrodimitras G., Tzimeas K., Tartaras E., *D2.4 - Report on Seismic Reprocessing, West Macedonia.* , in *EU H2020 PilotSTRATEGY project 101022664*. 2024. p. 44.

The PilotSTRATEGY project has received funding from the European Union's Horizon 2020 research and innovation programme under grant agreement No. 101022664

167. Ferrière, J., et al., *Evolution of the Mesohellenic Basin (Greece) : a synthesis.* Journal of the Virtual Explorer, 2013. **45**: p. 1-51.
168. Coates, G.R.X., Lizhi; Prammer, Manfred G.;, *NMR Logging Principles and Applications*. Halliburton Energy Services Publication H02308, ed. H.E. Services. 1999, United States of America.
169. Tyrologou, P., et al., *Investigative research for occurrences of hydrogen, helium, methane and carbon dioxide in West Macedonia: linking geological reservoirs to subsurface gas generation and migration*. 2025.
170. Metz, B., Davidson, O., de Coninck, H.C., Loos, M., and Meyer, L.A. (eds.), *IPCC Special Report on Carbon Dioxide Capture and Storage*, C.U. Press, Editor. 2005: Cambridge, UK, and New York, NY, USA. p. 442.
171. International Energy Agency, *Risk assessment guidelines for CO_2 storage (Report 2009/06)*, I.E.A.G.G.R.D. Programme, Editor. 2009: Cheltenham, UK.
172. ISO, *ISO 31000:2018 Risk Management – Guidelines.*, I.O.f. Standardization, Editor. 2018: Geneva, Switzerland.
173. Tyrologou, P.V., Agnes; Koukouzas, Nikolaos; Pedro, Jorge; Fleury, Marc; Carneiro, Julio; Ribeiro, Carlos; Ghikas, Dina; Mpatsi, Anna; Barradas, Pedro, João; Faria, Paula, Veloso, Fernanda M.L.;, *Progress for carbon dioxide geological storage in West Macedonia: A field and laboratory-based survey [version 1; peer review: 1 approved, 2 approved with reservations].* Open Research Europe, 2023. **3**(85).
174. Doebelin, N. and R. Kleeberg, *Profex: a graphical user for the Rietveld refinement program BGMN.* Journal of Applied Crystallography, 2015. **48**(5): p. 1573-1580.

The PilotSTRATEGY project has received funding from the European Union's Horizon 2020 research and innovation programme under grant agreement No. 101022664

Appendix I Factual reports SEM-EDS Analysis Conducted on Bulk Sedimentary Rock Samples from the Mesohellenic Trough

Three (3) samples from sedimentary rocks originating from the Tsotyli (sample Tsot-1; marly sandstone), Eptachori (sample Ept-2; fine greywacke) and Pentalofos (sample Pent-3; greywacke) Formations of the Mesohellenic Trough were studied with a JEOL JSM-IT500 scanning electron microscope (SEM) equipped with an OXFORD INCA X-ACT energy-dispersive system (EDS) (Oxford Instruments Ltd., Abingdon, UK) at the Analytical Services Unit (ASU), Chemical Process and Energy Resources Institute (CPERI), Centre for Research and Technology Hellas (CERTH) (Figure Appendix. 10.9.1). The operating conditions were a 20 kV accelerating voltage and 0.4 mA probe current, 20 s analysis time, and a beam diameter of approximately 1 μm, in the back-scattering electron (BSE) mode. Samples were investigated by SEM-EDS micro-analyses for the mineralogical identification. In addition, the analysis was focused on the porosity of the samples collecting measurements of pores and acquiring representative microphotographs. The samples were field collected by hummer and obtained as rock chips (Figure Appendix. 10.9.1). No mechanical processing was applied. The flatter surfaces of these random samples were carbon coated and studied under the electron microscope. Previous investigations on these samples implemented geomechanical and petrophysical methods to characterise the parent sedimentary formations for their potential to hold CO_2 underground[173].

Figure Appendix. 10.9.1: The analyzed samples from the Tsotyli (Tsot-1; marly sandstone), Eptachori (Ept-2; fine greywacke) and Pentalofos (Pent-3; greywacke) Formations of the Mesohellenic Trough.

Sample 1: SESAR sample name: Tsot-1, alternative name: TS.

SESAR sample description: Grey, yellowish, brownish marly sandstone (to sandstone), possibly with some finer beds in between, with bedding thickness of 8 to 50 cm. Grain size (mm): ~0.05-1mm, arkose to calcite minerals (arenaceous, probably medium). No fossils seen. Partially unweathered (slightly reduced strength, weather penetrating in from fractures and bedding; some brown oxidation). Very strong (100-500: requires many blows of geological hammer to fracture it). It fractures mainly along the bedding and otherwise along existing fractures or weak surfaces, perpendicular to the bedding (not often). Not many fractures, pretty solid. No discontinuities.

The PilotSTRATEGY project has received funding from the European Union's Horizon 2020 research and innovation programme under grant agreement No. 101022664

SEM-EDS analytical results: The examination was focused in five random areas. All the examined areas include well-cemented mineral grains (**Erreur ! Source du renvoi introuvable.**a). The average bulk c hemistry of the sample is summarized in **Erreur ! Source du renvoi introuvable.**. The chemical elements with the highest incorporation are Si (avg. 52 wt.%) and Ca (avg. 24 wt.%), other elements include Al, Fe, K, Mg and Na (**Erreur ! Source du renvoi introuvable.**). The identified mineral phases by spot analyses i nclude mainly calcite and quartz, as well as minor plagioclase and K-feldspar (**Erreur ! Source du renvoi introuvable.**, **Erreur ! Source du renvoi introuvable.**a-c). The mineral grains rarely exceed 300 µm in width. Minerals belonging to the mica group were not detected. The cement is mainly siliceous (Si <63 wt.%) in composition and locally is crystalline (**Erreur ! Source du renvoi introuvable.**). Iron contents up t o 9.9 wt.% are indicative of the cement composition (**Erreur ! Source du renvoi introuvable.**, **Erreur ! Source du renvoi introuvable.**)

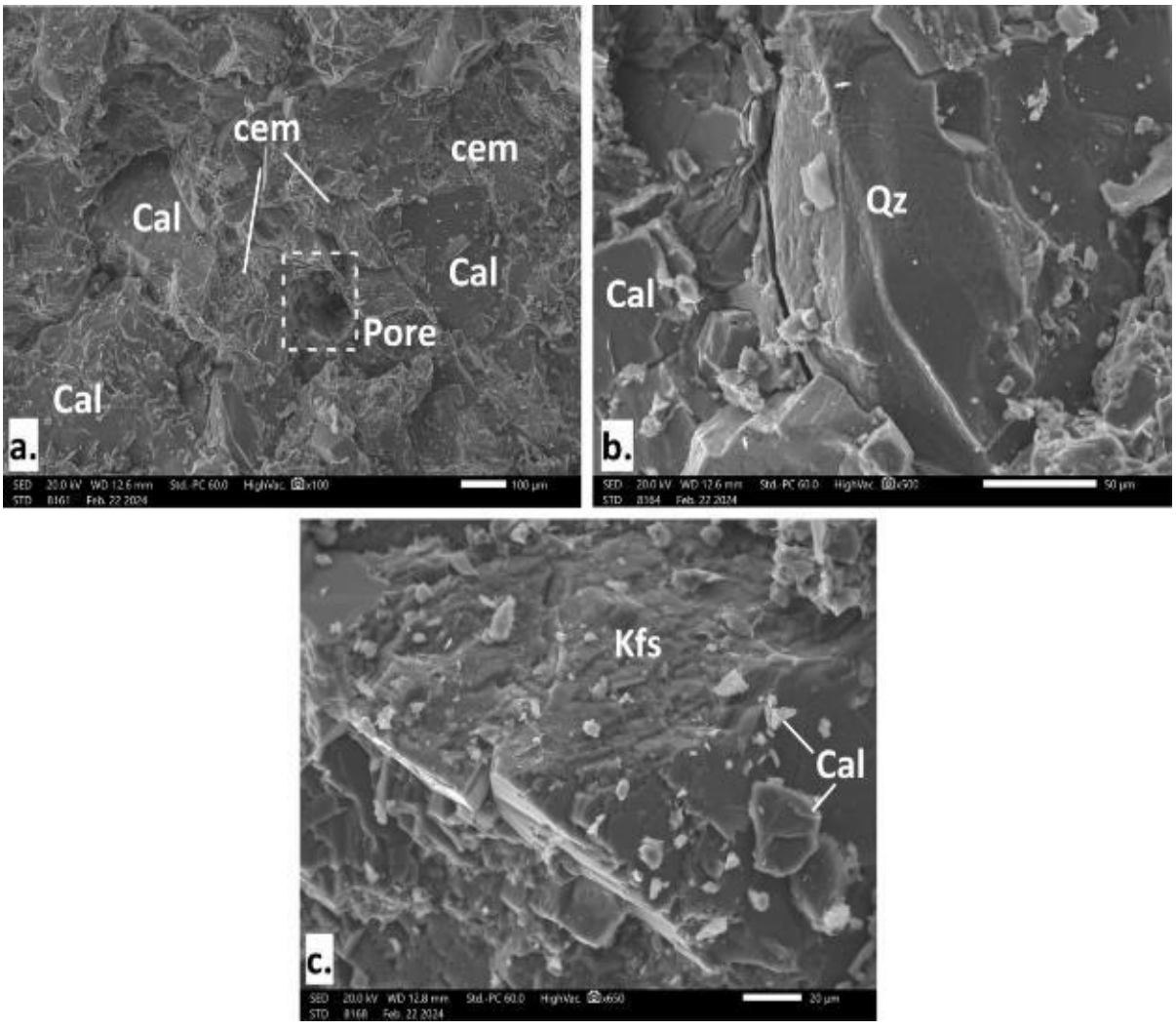

Figure Appendix. 10.9.2: SEM-EDS microphotographs of sample Tsot-1 showing: (**a**) Well-cemented (cem) calcite (Cal) grains, (**b**) Quartz (Qz) and calcite (Cal) grains, (**c**) K-feldspar (Kfs) crystals with calcite (Cal) grains on their surface.

The PilotSTRATEGY project has received funding from the European Union's Horizon 2020 research and innovation programme under grant agreement No. 101022664

The pores detected vary in shapes from rounded to irregular and elongated; their average size in width is 45 µm (**Erreur ! Source du renvoi introuvable.**, **Erreur ! Source du renvoi introuvable.**a-d). Please advise al so the Supplementary material section for a detail spectra presentation and additional SEM-EDS microphotographs of pores.

Table Appendix 10.9.1: Qualitative characteristics of spot analyses on representative mineral phases from sample Tsot-1 and Ept-2 (advice also the Appendix).

Sample Tsot-1	**Element (wt.%)**	**Al**	**Ca**	**Fe**	**K**	**Mg**	**Na**	**Si**	**Mineral phase**
Generic analyses	Spectrum 1	19	22	6.2	14	2.9	-	35	(?) Cal, Qz, Pl, Kfs
	Spectrum 2	6.9	19	4.6	-	-	4.1	63	cem
	Spectrum 3	-	2.0	-	-	-	-	96	Qz
	Spectrum 4	13	22	-	16	-	-	45	(?) Cal, Qz, Pl, Kfs
	Spectrum 9	7.5	36	9.9	-	6.0	-	37	Cem
Mapping	Map sum spectrum	8.3	41	6.4	3.2	3.1	2.3	36	(?) Cal, Qz, Pl, Kfs, cem
	Average chemical composition	11	24	7.0	11	4.0	3.0	52	
Spot analyses	Spectrum 5	4.8	73	-	3.8	-	-	15	Cal
	Spectrum 6	5.5	73	-	3.0	-	-	13	Cal
	Spectrum 7	17	-	-	17	-	-	66	Kfs
	Spectrum 8	-	94	-	-	-	-	-	Cal
	Spectrum 10	-	99	-	-	-	-	-	Cal
	Spectrum 11	-	96	-	-	-	-	-	Cal
	Spectrum 12	-	94	-	-	-	-	1.8	Cal
	Spectrum 13	4.0	-	-	-	-	-	89	Qz
	Overall average	10	56	7.0	10	4.0	3.0	45	
Sample Ept-2	**Element (wt.%)**	**Al**	**Ca**	**Fe**	**K**	**Mg**	**Na**	**Si**	**Mineral phase**
Generic analyses	Spectrum 22	3.7	53	8.3	-	8.8	-	26	(?) Cal, Qz, Pl, cem
Spot analyses	Spectrum 14	-	-	-	-	-	-	100	Qz
	Spectrum 15	-	-	-	-	-	-	100	Qz
	Spectrum 16	19	-	-	-	-	13	67	Ab
	Spectrum 17	-	97	-	-	-	-	-	cem
	Spectrum 18	15	-	-	26	2.0	-	52	Kfs
	Spectrum 19	14	13	-	21	-	-	48	Kfs
	Spectrum 20	-	-	-	-	2.8	-	93	Qz
	Spectrum 21	-	82	-	-	18	-	-	Cal
	Spectrum 23	-	99	-	-	-	-	-	Cal
	Spectrum 24	15	3.2	17.8	-	24	-	41	cem
	Spectrum 26	15	3.2	17.8	-	24	-	60	Chl
	Spectrum 27	-	93	-	-	-	-	-	Cal
	Overall average	13	55	15	24	13	13	65	

Abbreviations: Ab = albite, Cal = calcite, cem = cement, Chl = chlorite, Kfs = k-feldspar, Pl = plagioclase, Qz = quartz.

The PilotSTRATEGY project has received funding from the European Union's Horizon 2020 research and innovation programme under grant agreement No. 101022664

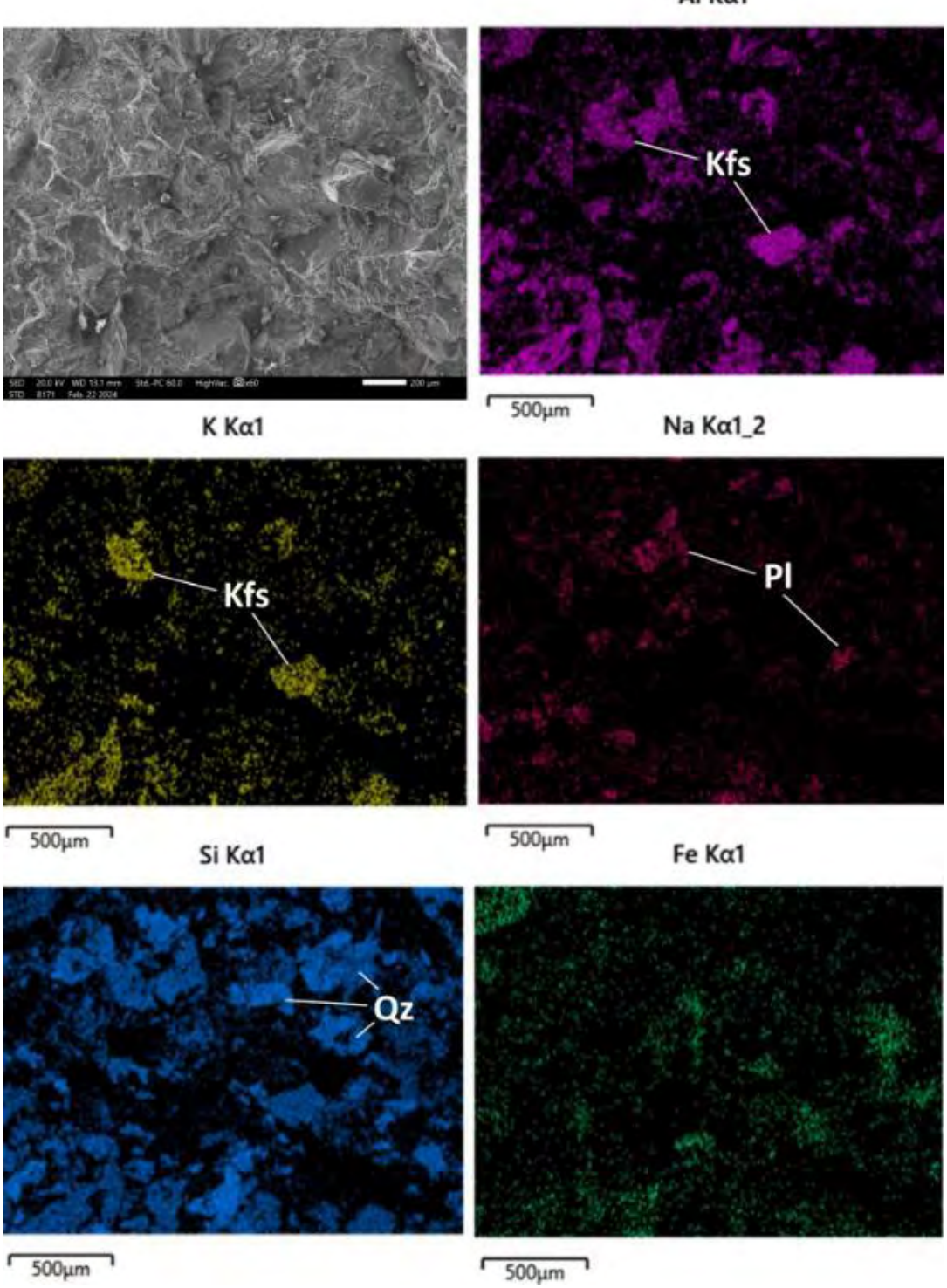

Figure Appendix. 10.9.3: SEM-EDS elemental mapping images for Al, K, Na, Si and Fe indicating the occurrence of K-feldspar (Kfs) and plagioclase (Pl) in sample Tsot-1. Iron contents highlight the cement distribution.

The PilotSTRATEGY project has received funding from the European Union's Horizon 2020 research and innovation programme under grant agreement No. 101022664

Table Appendix 10.9.2: Morphometric characteristics of the pores detected in samples Tsot-1, Ept-2 and Pent-3. Please advise also the images included in the Supplementary material section.

Micro-photograph	Number	Comment	Pore shape	Pore measurements in width (µm)
335578_TS_0003	No.1	P.b.g.	Rounded	123
335578_TS_0007	No.1	P.b.g.	Elongated	91
335578_TS_0007	No.2	P.b.g.	Elongated	42
335578_TS_0007	No.3	P.b.g.	Elongated	36
335578_TS_0010	No.1	P.b.g.	Irregular	55
335578_TS_0010	No.2	P.b.g.	Irregular	21
335578_TS_0010	No.3	P.b.g.	Irregular	82
335578_TS_0013	No.1	P.b.g.	Elongated	42
335578_TS_0018	No.1	P.b.g.	Irregular	7.0
335578_TS_0018	No.2	P.b.g.	Irregular	24
335578_TS_0018	No.3	P.b.g.	Rounded	5.7
335578_TS_0018	No.4	P.b.g.	Irregular	15
				Average width: 45 µm
335576_EP_0005	No.1	P.b.g.	Irregular	56
335576_EP_0005	No.2	P.b.g.	Elongated	135
335576_EP_0005	No.3	P.b.g.	Irregular	27
335576_EP_0009	No.1	P.b.g.	Irregular	37
335576_EP_0011	No.1	P.b.g.	Irregular	46
335576_EP_0013	No.1	P.b.g.	Rounded	46
335576_EP_0016	No.1	P.b.g.	Elongated	5.6
335576_EP_0018	No.1	P.b.g.	Rounded	175
				Average width: 66 µm
335576_EP_0007	No.1	P.c.	Rounded	17
335576_EP_0007	No.2	P.c.	Rounded	12
335576_EP_0007	No.3	P.c.	Rounded	11
335576_EP_0007	No.4	P.c.	Rounded	8.2
335576_EP_0007	No.5	P.c.	Rounded	5.9
				Average width: 11 µm
				Total average width: 38 µm
335577_PE_0003	No.1	P.b.g.	Irregular	93
335577_PE_0014	No.1	P.b.g.	Elongated	82
335577_PE_0014	No.2	P.b.g.	Elongated	51
335577_PE_0018	No.1	P.b.g.	Elongated	34
				Average width: 65.0 µm
335577_PE_0008	No.1	P.c.	Rounded	6.4
335577_PE_0008	No.2	P.c.	Rounded	4.9
335577_PE_0008	No.3	P.c.	Rounded	7.1
				Average width: 6.0 µm
				Total average width: 36.0 µm

Abbreviations: P.b.g.= pores between grains, P.c. = pores in cement.

The PilotSTRATEGY project has received funding from the European Union's Horizon 2020 research and innovation programme under grant agreement No. 101022664

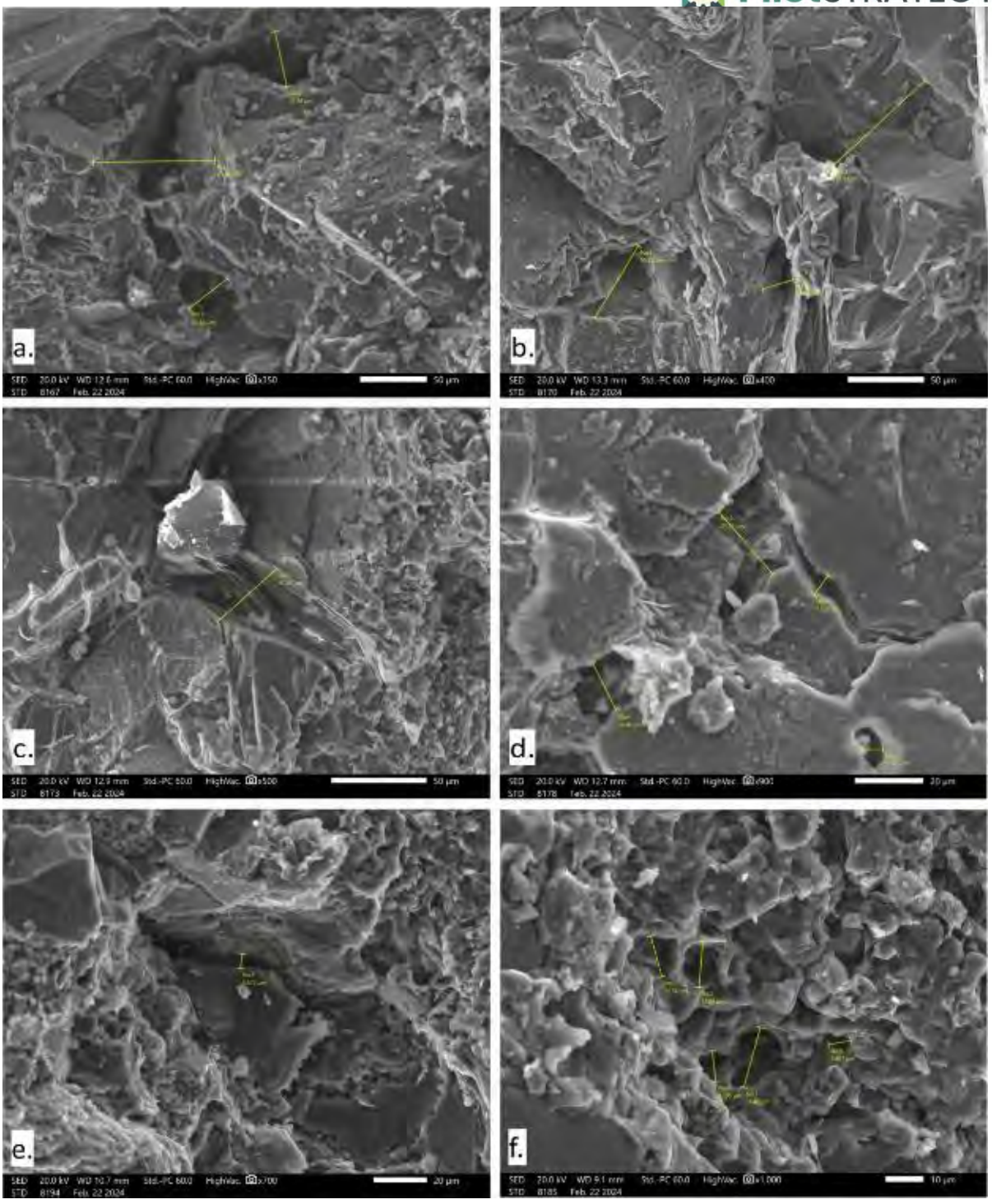

Figure Appendix. 10.9.4: Representative SEM-EDS microphotographs (a-d) of the detected pores in sample Tsot-1 and in sample Ept-2: (a-e) Pores detected in the intergranular space, (f) Pores detected in the calcareous cement.

Sample 3: SESAR sample name: Ept-2. Alternative name: EP.

The PilotSTRATEGY project has received funding from the European Union's Horizon 2020 research and innovation programme under grant agreement No. 101022664

SESAR sample description: Very strong, thickly bedded (20-30cm), partially weathered, medium gray-tan, fine greywacke. Joint fractures spaced 40-80cm apart, perpendicular to bedding. Trace fossils (invertebrate burrows) on bedding surfaces. Partially carbonized wood and leaf fragments. Water discoloration (Liesegang) penetrates 8-10 cm into bedding.

SEM-EDS analytical results: The examination was focused in seven random areas. All the examined areas include very well-cemented mineral grains (Figure Appendix. 10.9.5). Representative analysis of the bulk chemistry of the sample showed that it largely incorporates Ca (<53 wt.%) and Si (<26 wt.%), and in a minor extent Mg, Fe, Al (**Erreur ! Source du renvoi introuvable.**). Spot analyses indicate the occurrence o f calcite, quartz, plagioclase - mainly albite, K-feldspar (microcline or orthoclase), chlorite and titanite (Figure Appendix. 10.9.5a-c, Figure Appendix. 10.9.6). The mineral grains rarely exceed 200 µm in width. The cementing material includes up to 41 wt.% Si and up to 18 wt.% Fe (**Erreur ! Source du renvoi i ntrouvable.**). Locally, the cement is microcrystalline with dominant calcareous composition (Figure Appendix. 10.9.5c). Pores are rarely found in the intergranular space (**Erreur ! Source du renvoi introuvable.**, **Erreur ! Source du renvoi introuvable.**e). They vary in shape from rounded to irregular and elongated, while their sizes average 66 µm in width (**Erreur ! Source du renvoi introuvable.**). Pores (avg. 1 1 µm in width) were detected in the cement (**Erreur ! Source du renvoi introuvable.**, **Erreur ! Source du renvoi introuvable.**f). Please advise also the Supplementary material section for a detail spectra presentation and additional SEM-EDS microphotographs of pores.

The PilotSTRATEGY project has received funding from the European Union's Horizon 2020 research and innovation programme under grant agreement No. 101022664

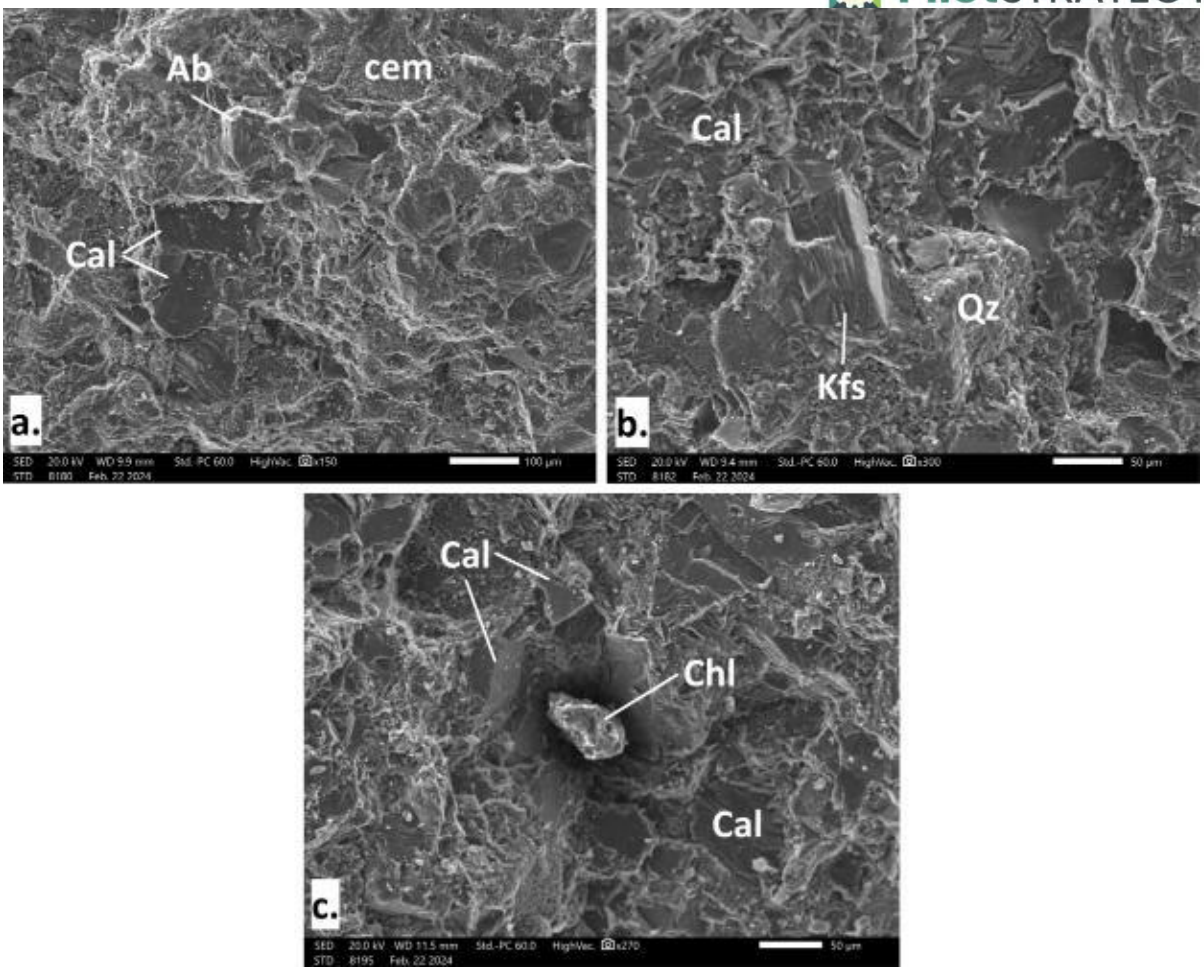

Figure Appendix. 10.9.5: SEM-EDS microphotographs (**a-c**) of sample Ept-2 showing: (**a**) Well-cemented (cem) calcite (Cal) and albite (Ab) grains, (**b**) Calcite (Cal) is the dominant mineral phase coexisting with quartz (Qz) and K-feldspar (Kfs), (**c**) Chlorite (Chl) grain in a pore found in a calcite (Cal) dominated mass.

The PilotSTRATEGY project has received funding from the European Union's Horizon 2020 research and innovation programme under grant agreement No. 101022664

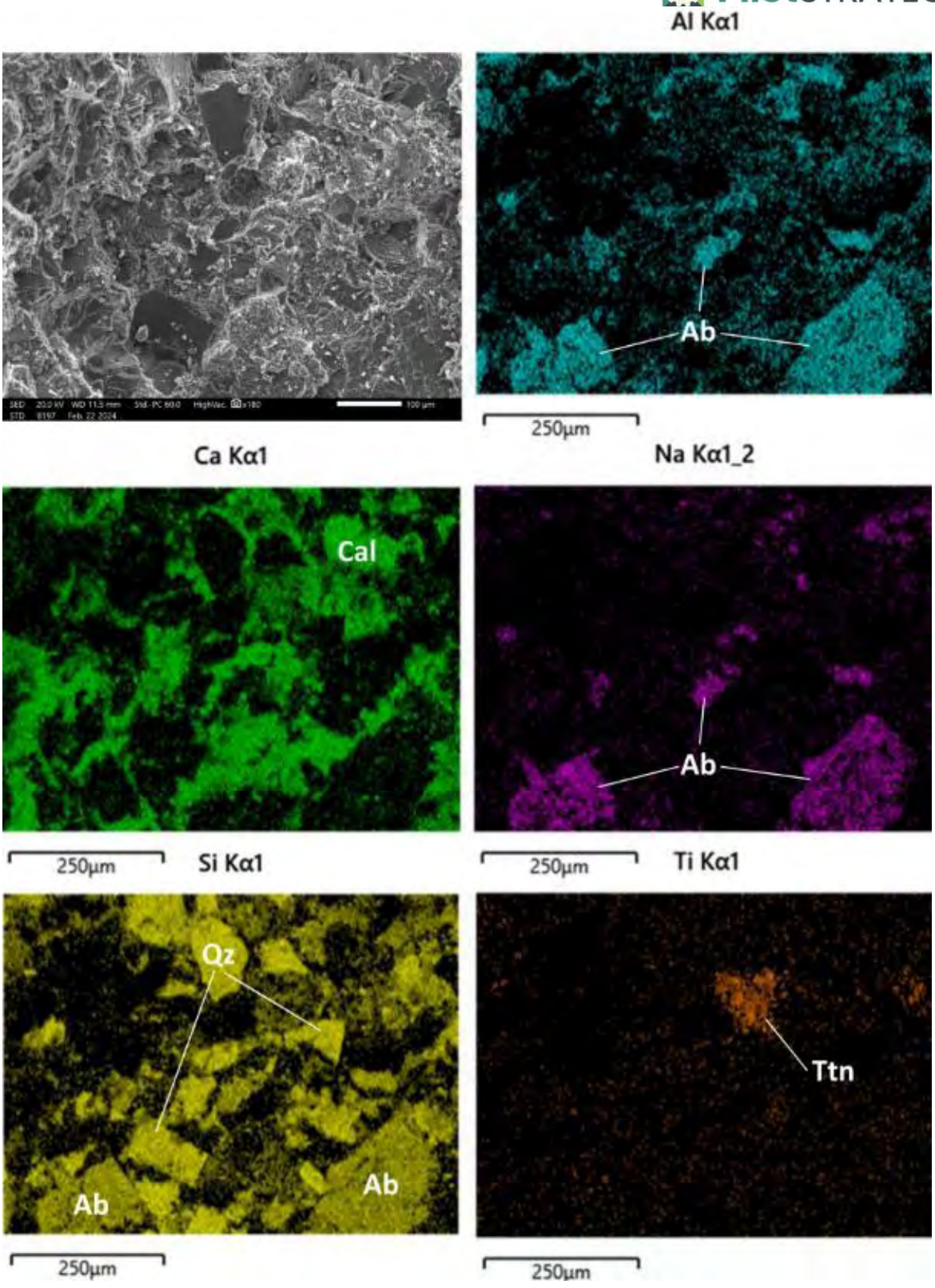

The PilotSTRATEGY project has received funding from the European Union's Horizon 2020 research and innovation programme under grant agreement No. 101022664

Figure Appendix. 10.9.6: SEM-EDS elemental mapping images for Al, Ca, Na, Si and Ti, suggesting the occurrence of albite (Ab), calcite (Cal), quartz (Qz) and titanite (Ttn) in sample Ept-2.

Sample 3: SESAR sample name: Pent-3. Alternative name: PE.

SESAR sample description: Medium weak to very strong, partially weathered, gray conglomerate. Alternation between units of varying grain size and strength: 1. 0.5-1.5m-thick beds of clasts are poorly sorted (0.5-10 mm with occasional larger clasts), sub-angular to sub-rounded, predominantly limestone with igneous/metamorphic clasts and fossil corals, grain-supported with clastic matrix. No interior bedding or structures. 2. 10cm-1m-thick beds of medium weak to very strong, partially weathered, gray greywacke. Grains are fine, angular, limestone-quartz-micas-various mafics. Interbedded with gray-tan mudstone. Some interior thin bedding, especially in mudstone layers. Some localized watersheds from outcrop face, no large faults, folds, or unconformities observed.

SEM-EDS analytical results: The examination was focused in four random areas. In all the examined areas the grains appear well-cemented (Figure Appendix. 10.9.7). The overall average chemical composition is dominantly calcareous (61 wt.%, Table Appendix 10.9.3)

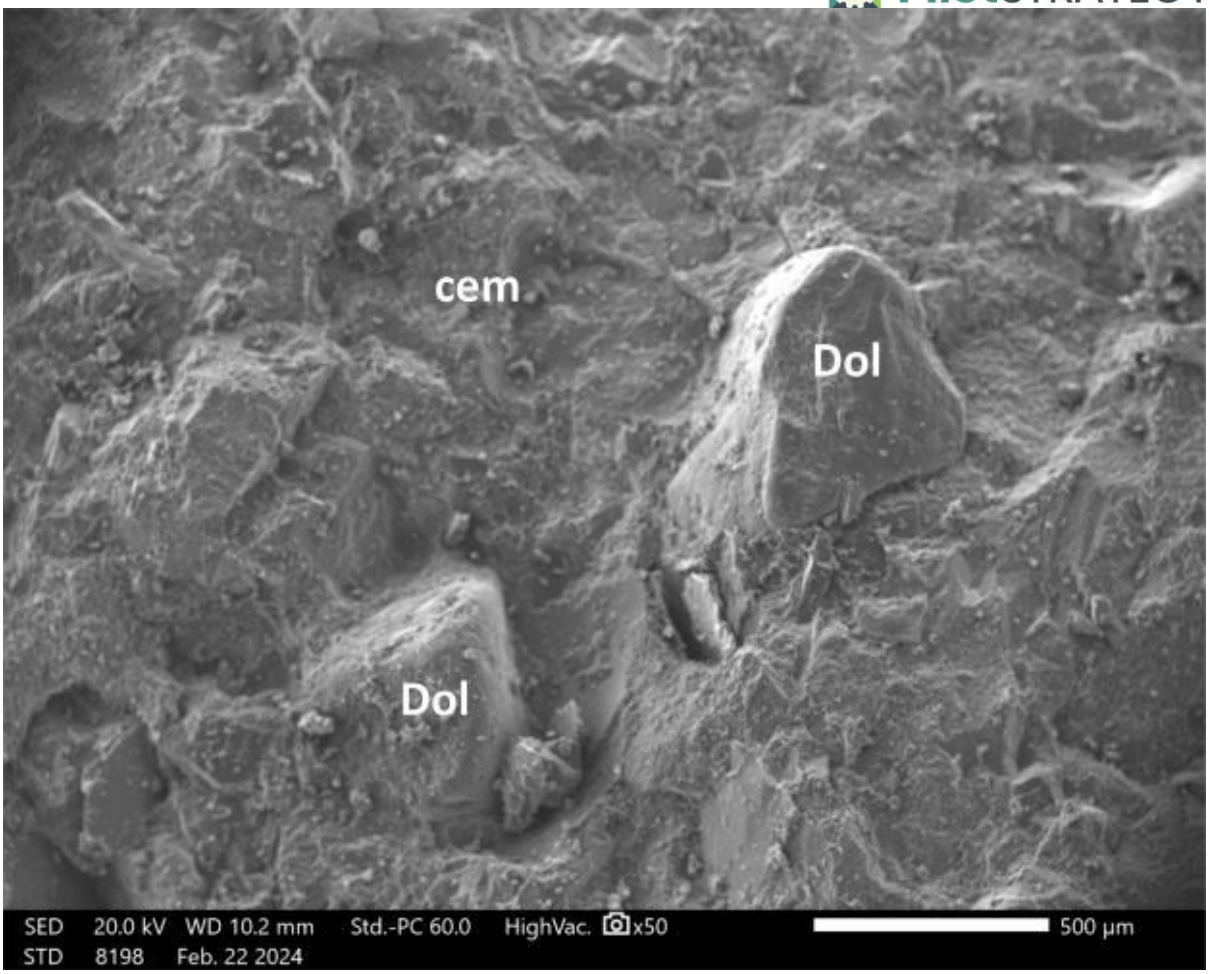

Figure Appendix. 10.9.7: SEM-EDS microphotograph of sample Pent-3 showing well-cemented (cem) dolomite (Dol) grains.

Spot analyses suggest the occurrence of calcite, quartz, dolomite, chlorite, plagioclase mainly albite and minor titanite Figure Appendix. 10.9.7, Figure Appendix. 10.9.8a-d, Figure Appendix. 10.9.9). The mineral grains may exceed 500 µm in width. The chemical composition of the cement is dominantly calcareous and may also include Mg and Si (Table Appendix 10.9.3). Pores (avg. 65 µm in width) are rare in the intergranular space and mainly have elongated shape (Figure Appendix. 10.9.10: Representative SEM-EDS microphotographs (a,b) of the pores detected in the intergranular space of sample Pent-3.a,b). In the calcareous cement pores have an average width of 6 µm (**Erreur ! Source du renvoi introuvable.**). Please a dvise also the Supplementary material section for a detail spectra presentation and additional SEM-EDS microphotographs of pores.

Table Appendix 10.9.3: Qualitative characteristics of spot analyses on representative mineral phases from sample Pent-3 (advise also the Supplementary material section).

	Element (wt.%)	Al	Ca	Fe	K	Mg	Na	Si	Ti	Mineral phase
	Spec 28	-	59	-	-	32	-	4.3	-	Dol
	Spec 29	4.6	53	-	-	29	-	11	-	Dol

The PilotSTRATEGY project has received funding from the European Union's Horizon 2020 research and innovation programme under grant agreement No. 101022664

Spot analyses	Spec 30	-	92	-	-	2.5	-	2.5	-	cem
	Spec 31	12	6.3	29	-	7.6	-	43	-	Chl
	Spec 32	-	96	-	-	-	-	-	-	Cal
	Spec 33	14	8.8	19	-	9.4	-	46	-	Chl
	Spec 34	-	100	-	-	-	-	-	-	Cal
	Spec 35	-	-	-	-	-	-	95	-	Qz
	Spec 36	-	99	-	-	-	-	-	-	Cal
	Spec 37	-	100	-	-	-	-	-	-	Cal
	Spec 38	-	63	-	-	29	-	4.4	-	Dol
	Spec 39	-	-	-	-	-	-	100	-	Qz
	Spec 40	-	63	-	-	32	-	-	-	Dol
	Spec41	26	-	8.0	19	3.8	-	47	-	Chl
	Spec 42	47	5.3	5.2	15	3.7	-	47	-	Chl
	Spec 43	-	100	-	-	-	-	-	-	cem
	Spec 44	-	30	-	-	-	-	11	43	Ttn
	Spec 45	22	6.8	7.9	20	5.3	-	39	-	Chl
	Spec 46	25	-	4.5	17	3.3	-	47	-	Chl
	Spec 47	-	91	-	-	-	-	5.7	-	Cal
	Spec 48	-	-	-	-	-	-	99	-	Qz
	Spec 51	19	-	-	-	-	13.4	68	-	Ab
	Over. avg	21	61	12	18	14	13	42	43	

Abbreviations: Ab = albite, Cal = calcite, cem = cement, Chl = chlorite, Dol = dolomite, over. avg = overall average, spec = spectrum, Qz = quartz.

Conclusions

The analyzed samples include rock chips obtained by hammering from marly sandstone (Tsot-1) and greywacke (Ept-2, Pent-3) originating from the Tsotyli, Eptachori and Pentalofos Formations of the Mesohellenic Trough (Figure Appendix. 10.9.1). SEM-EDS analysis of rock chips revealed indicative information on mineralogy and geochemistry of these samples.

The texture of all the examined samples includes well-cemented mineral grains. Sample Ept-2 exhibits a higher degree of cementation compared to the other two samples, while in sample Pent-3 grains are coarser exceeding 500 μm in width.

The PilotSTRATEGY project has received funding from the European Union's Horizon 2020 research and innovation programme under grant agreement No. 101022664

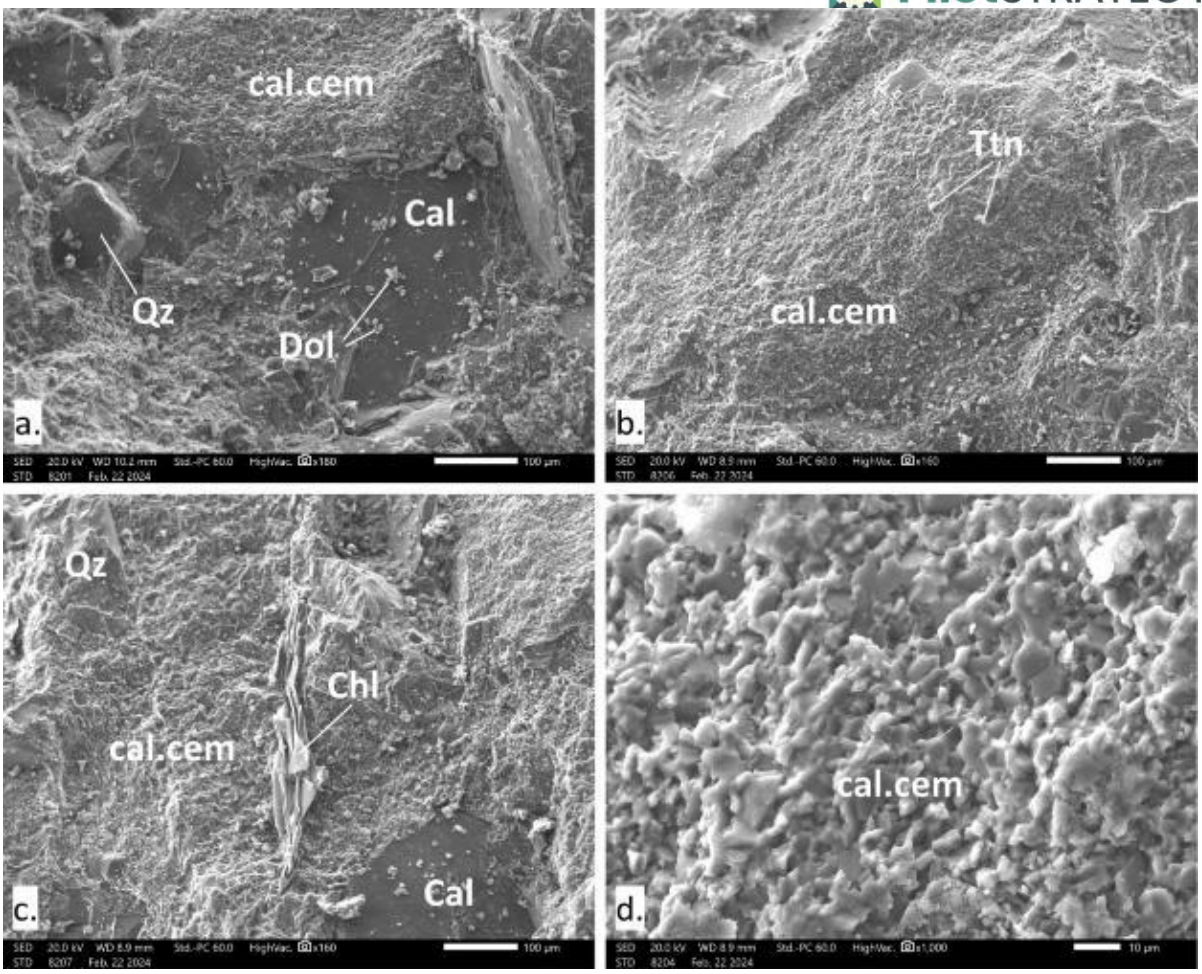

Figure Appendix. 10.9.8: SEM-EDS microphotographs of sample Pent-3. a) Calcite (Cal) and quartz (Qz) grains in calcareous cement (cal.cem). Tiny dolomite (Dol) grains are found on calcite. b) Titanite (Ttn) grains incorporated in calcareous cement (cal.cem). c) Calcite (Cal), chlorite (Ch) and quartz (Qz) in calcareous cement (cal.cem). d) The porous microcrystalline surface of the calcareous cement (cal.cem).

The average overall chemistry of sample Tsot-1 is dominantly siliceous (avg. 52 wt.%), while samples Ept-2 and Tsot-3 are calcareous incorporating up to 53 wt.% and 61 wt.% of Ca, respectively. Calcite and quartz are the dominant minerals in all the samples, while plagioclase, mainly as albite, is also present. K-feldspar is found in Tsot-1 and Ept-2. Chlorite and titanite occur only in the greywacke samples Ept-2 and Pent-3, whereas dolomite only in sample Pent-3. Cement in samples Tsot-1 and Ept-2 is siliceous in composition and bears varying Fe contents. In contrary, cement in sample Pent-3 is calcareous and incorporates Mg and Si contents. In samples, Ept-2 and Pent-3 the more calcareous areas of cement appear microcrystalline and exhibit porous surfaces. Pores (rounded to irregular and locally elongated) were detected in the intergranular space of the samples, as well as locally in the cement of samples Ept-2 and Pent-3. In average, the wider pores are found in sample Ept-2 (avg. 66 μm in width). Pores in the cement of samples Ept-2 and Pent-3 average 11 μm and 9 μm in width, respectively.

The PilotSTRATEGY project has received funding from the European Union's Horizon 2020 research and innovation programme under grant agreement No. 101022664

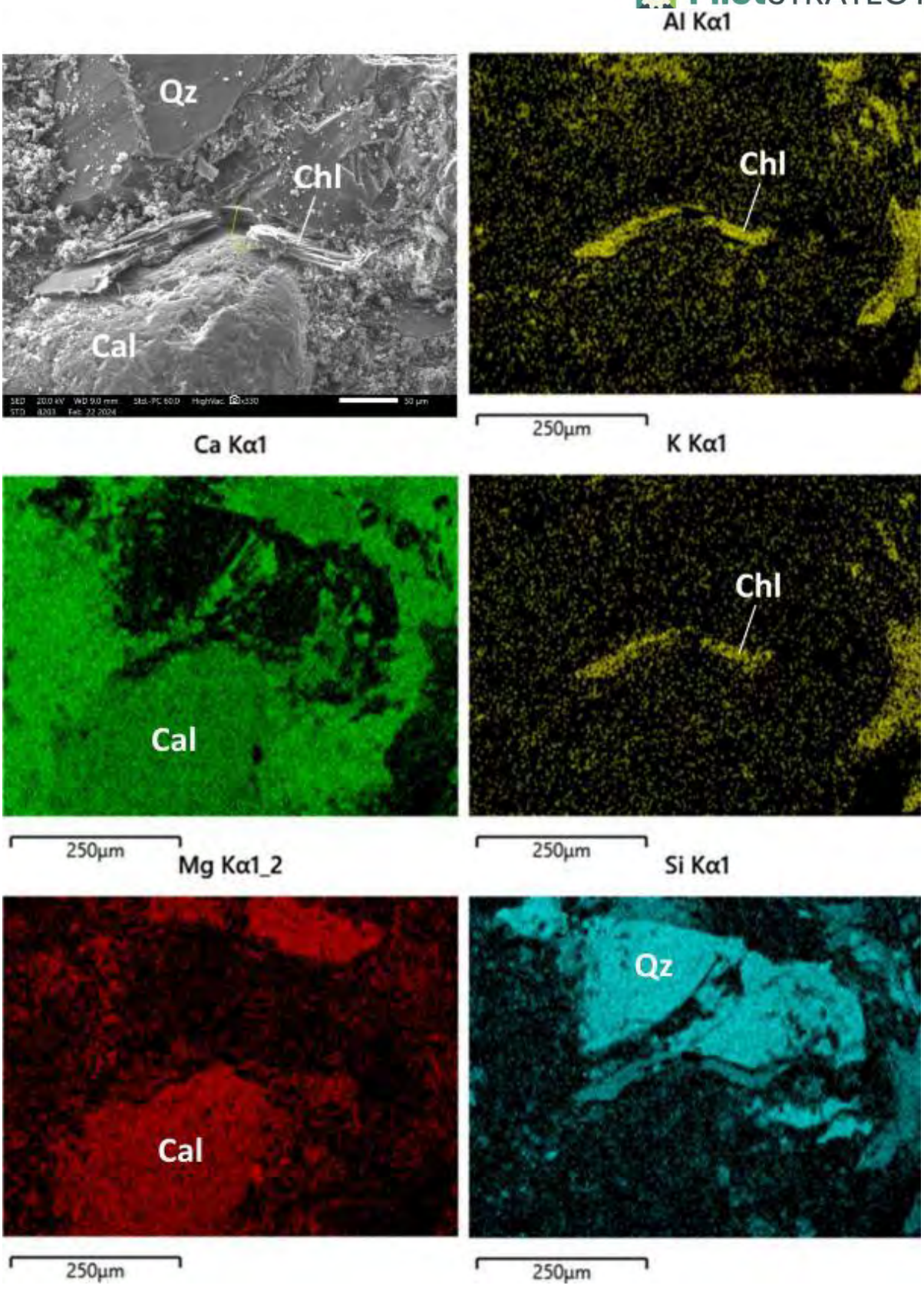

The PilotSTRATEGY project has received funding from the European Union's Horizon 2020 research and innovation programme under grant agreement No. 101022664

Figure Appendix. 10.9.9: SEM-EDS elemental mapping images for Al, Ca, K, Mg and Si, indicating the presence of quartz (Qz), chlorite (Chl) and calcite (Cal). Calcite is enriched in Mg in sample Pent-3.

Finally, several spot analyses acquired also background values as the unpolished mineral grains may be covered by debris. More accurate results on the mineralogy and geochemistry, as well as additional pore measurements will be obtained by future SEM-EDS analyses which is planned to be conducted on thin/polished sections.

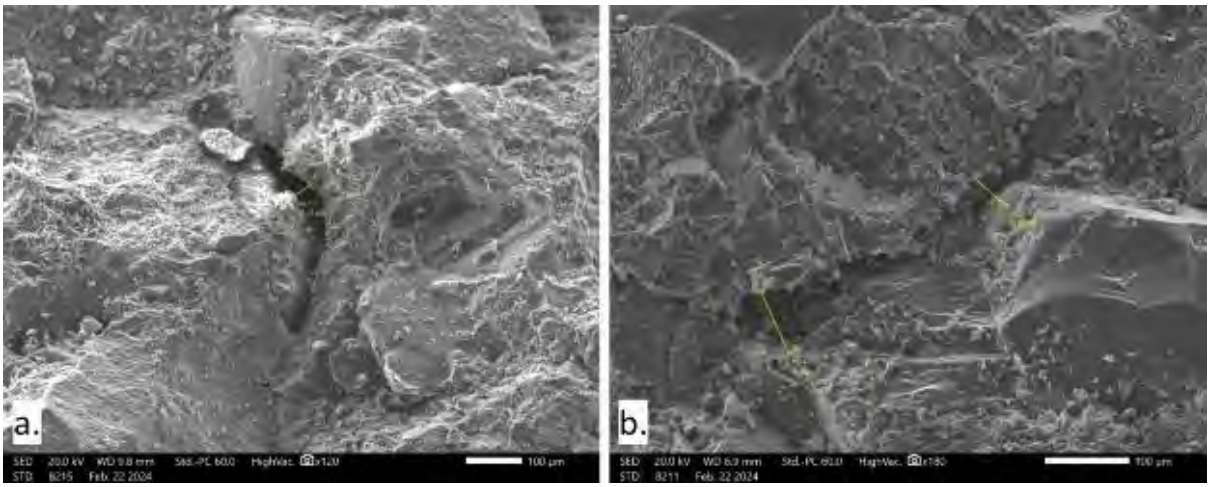

Figure Appendix. 10.9.10: Representative SEM-EDS microphotographs (a,b) of the pores detected in the intergranular space of sample Pent-3.

Appendix II XRD Analysis Conducted on Bulk Sedimentary Rock Samples from the Mesohellenic Trough

Three (3) sedimentary rock samples originating from the Tsotyli (sample Tsot-1; marly sandstone), Eptachori (sample Ept-2; fine greywacke) and Pentalofos (sample Pent-3; greywacke) Formations of the Mesohellenic Trough were powdered and analyzed by X-ray diffraction to determine their mineralogical composition. The samples were field collected by hummer and obtained as rock chips (Figure Appendix. 10.9.11). Previous investigations on these samples include geomechanical and petrophysical methods for the evaluation of the parent sedimentary formations to capture and store CO_2[118]. XRD analysis was performed using a Bruker D8 Advance diffractometer with a CuKα anode (λ = 0.1542 nm) operating at 40 kV and 30 mA at the Department of Mineralogy-Petrology-Economic Geology, School of Geology, Aristotle University of Thessaloniki (Figure Appendix. 10.9.11). The counting statistics of the XRD study were, step size: 0.019◦ 2θ, start angle: 3.000◦, end angle: 93.009◦ and scan speed: 0.19◦ 2θ/s. Rietveld refinement were implemented by using the Profex5 (v.5.2.7, [174]) software acquiring semi-quantitative estimates on the abundance of the mineral phases and on the chemical composition of the analyzed samples.

The PilotSTRATEGY project has received funding from the European Union's Horizon 2020 research and innovation programme under grant agreement No. 101022664

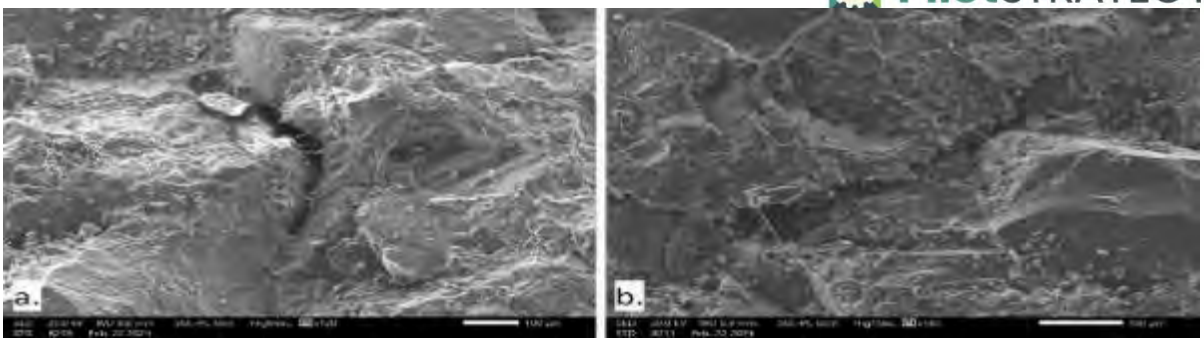

Figure Appendix. 10.9.11: The analyzed samples from the Tsotyli (Tsot-1; marly sandstone), Eptachori (Ept-2; fine greywacke) and Pentalofos (Pent-3; greywacke) Formations of the Mesohellenic Trough.

Sample 1: SESAR sample name: Tsot-1, alternative name: TS.

Table Appendix 10.9.4: Semi-quantitative mineralogical composition (wt.%) of sample Tsot-1 as measured by XRD.

	Mineral	Quantity	Refined composition
Major mineral phases	**Calcite**	30	$C_6\ Ca_6\ O_{18}$
	Quartz	29	$Si_3\ O_6$
	Albite	21	$Al_4\ Na_4\ Si_{12}\ O_{32}$
Minor mineral phases	**Muscovite**	7.2	$Al_{11.6800}\ Fe_{0.3200}\ K4\ Si_{12}\ O_{48}$
	Chlorite	7.1	$Al_{4.6820}\ Fe_{2.0490}\ H_{16}\ Mg_{7.9510}\ Si_{5.2480}\ O_{36}$
	Dolomite	4.5	$C_6\ Ca_3\ Mg_3\ O_{18}$
	Aragonite	1.4	$C_4\ Ca_4\ O_{12}$
	Rwp	28	
	Rexp	2.0	
	Quartz:Feldspar	1.4	

The PilotSTRATEGY project has received funding from the European Union's Horizon 2020 research and innovation programme under grant agreement No. 101022664

Table Appendix 10.9.5: Chemical compositions (wt.%) of the detected mineral phases in sample Tsot-1 (n.a.=not applicable).

Mineral	Quantity	H	C	O	Na	Mg	Al	Si	K	Ca	Fe	Ca:Si Total
Calcite	30	-	12	48	-	-	-	-	-	40	-	n.a.
Quartz	29	-	-	52	-	-	-	47	-	-	-	n.a.
Albite	21	-	-	49	8.8	-	10	32	-	-	-	n.a.
Muscovite	7.2	-	-	48	-	-	20	21	9.8	-	1.1	n.a.
Chlorite	7.1	1.4	-	49	-	17	11	13	-	-	9.6	n.a.
Dolomite	4.5	-	13	52	-	13	-	-	-	22	-	n.a.
Aragonite	1.4	-	12	48	-	-	-	-	-	40	-	n.a.
Weighted	100	0.10	4.4	48	1.8	1.8	4.3	23	0.70	14	0.77	0.60

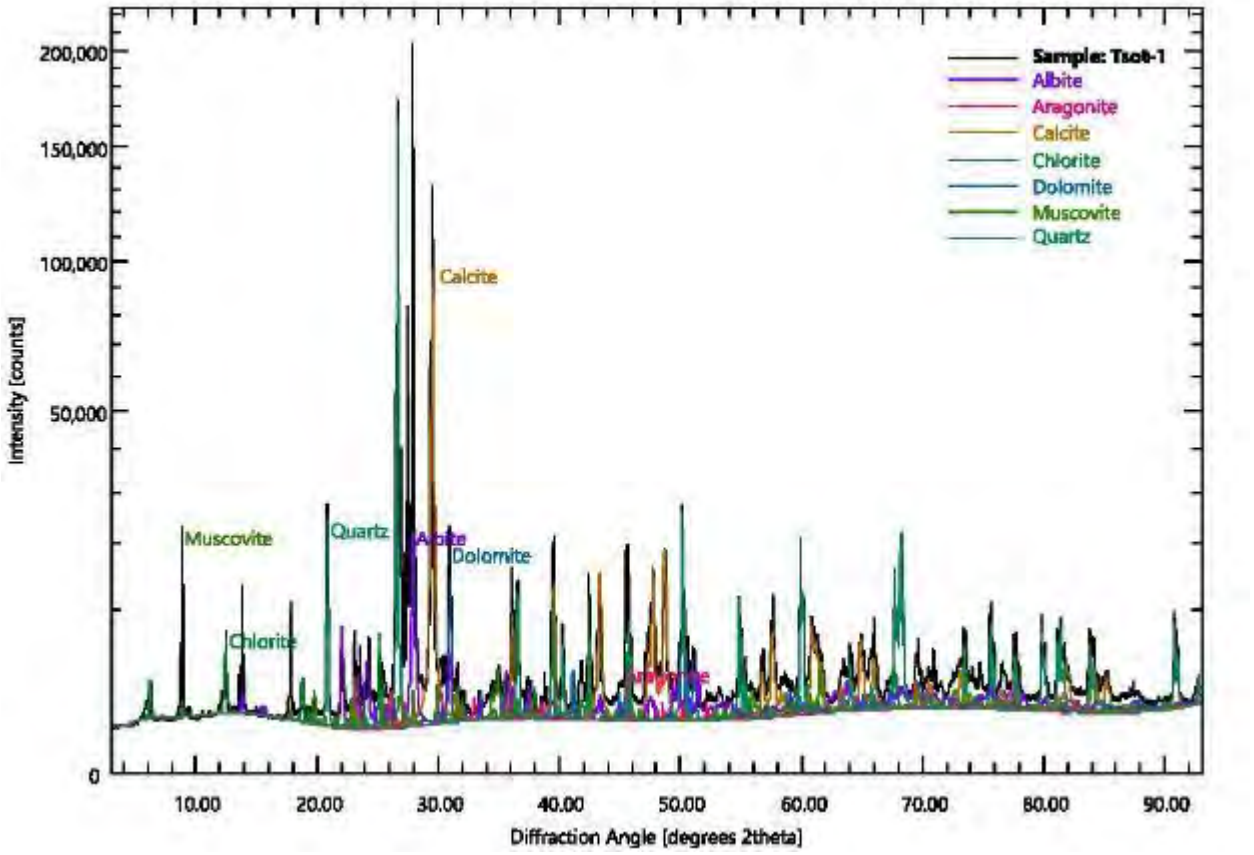

Figure Appendix. 10.9.12: XRD pattern and Rietveld refinement of sample Tsot-1. Major peaks for the detected minerals are highlighted.

Sample 3: SESAR sample name: Ept-2. Alternative name: EP.

Table Appendix 10.9.6: Semi-quantitative mineralogical composition (wt.%) of sample Ept-2 as determined by XRD.

	Mineral	Quantity	Refined composition
Major mineral phases	**Quartz**	37	C_6 Ca_6 O_{18}
	Calcite	29	Si_3 O_6
	Muscovite	13	$Al_{11.6800}$ $Fe_{0.3200}$ K4 Si_{12} O_{48}
	Albite	13	Al_4 Na_4 Si_{12} O_{32}
Minor mineral phases	**Dolomite**	4.6	C_6 Ca_3 Mg_3 O_{18}
	Chamosite	3.1	$Al_{5.2200}$ $Fe_{6.8400}$ $Mg_{2.5800}$ $Si_{5.3600}$ O_{36}
	Rwp	15	
	Rexp	2.0	
	Quartz:Feldspar	2.9	

The PilotSTRATEGY project has received funding from the European Union's Horizon 2020 research and innovation programme under grant agreement No. 101022664

Table Appendix 10.9.7: Chemical compositions (wt.%) of the identified mineral phases in sample Ept-2 (n.a.=not applicable).

Mineral	Quantity	C	O	Na	Mg	Al	Si	K	Ca	Fe	$Ca:Si_{Total}$
Quartz	37	-	53	-	-	-	47	-	-	-	n.a.
Calcite	29	12	48	-	-	-	-	-	40	-	n.a.
Muscovite	13	-	48	-	-	20	21	9.8	-	1.1	n.a.
Albite	13	-	49	8.7	-	10	32	-	-	-	n.a.
Dolomite	4.6	13	52	-	13	-	-	-	22	-	n.a.
Chamosite	3.1	-	44	-	4.8	10	12	-	-	29	n.a.
Weighted	100	4.1	50	1.1	0.76	4.2	25	0.81	13	1.1	0.52

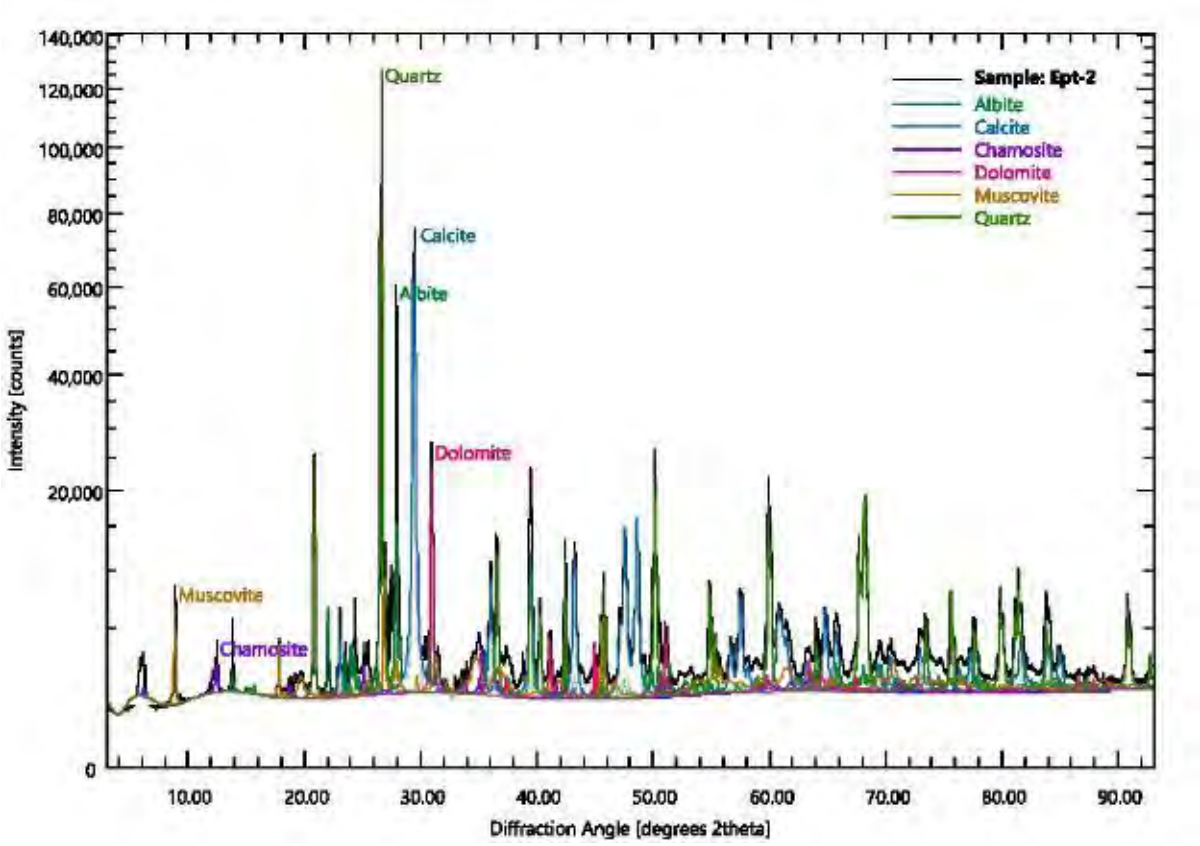

Figure Appendix. 10.9.13: XRD pattern and Rietveld refinement of sample Ept-2. Major peaks for the detected minerals are highlighted.

Sample 3: SESAR sample name: Pent-3. Alternative name: PE.

Table Appendix 10.9.8: Semi-quantitative mineralogical composition (wt.%) of sample Pent-3 after Rietveld refinement (n.a.=not applicable).

	Mineral	Quantity	Refined composition

The PilotSTRATEGY project has received funding from the European Union's Horizon 2020 research and innovation programme under grant agreement No. 101022664

Major mineral phases	**Calcite**	41	$C_6\ Ca_6\ O_{18}$
	Dolomite	18	$C_6\ Ca_3\ Mg_3\ O_{18}$
	Quartz	15	$Si_3\ O_6$
	Albite	12	$Al_4\ Na_4\ Si_{12}\ O_{32}$
Minor mineral phases	**Microcline**	8.0	$AL_4\ K_4\ Si_{12}\ O_{32}$
	Muscovite	4.3	$Al_{11.6800}\ Fe_{0.3200}\ K_{2.4000}\ Si_{12}\ O_{48}$
	Aragonite	2.6	$C_4\ Ca_4\ O_{12}$
	Rwp	21	
	Rexp	2.1	
	Quartz:Feldspar	1:1.3	

Table Appendix 10.9.9: Chemical compositions (wt.%) of the detected mineral phases in sample Ept-3.

Mineral	Quantity	C	O	Na	Mg	Al	Si	K	Ca	Fe	Ca:Si
Calcite	41	12	48	-	-	-	-	-	40	-	n.a.
Dolomite	18	13	52	-	13	-	-	-	22	-	n.a.
Quartz	15	-	53	-	-	-	47	-	-	-	n.a.
Albite	12	-	49	8.8	-	10	32	-	-	-	n.a.
Microcline	8.0	-	46	-	-	9.7	30	14	-	-	n.a.
Muscovite	4.3	-	50	-	-	21	22	6.1	-	1.2	n.a.
Aragonite	2.6	12	48	-	-	-	-	-	40	-	n.a.
Weighted	100	7.6	50	1.0	2.3	2.8	14	1.4	21	0.05	1.5

The PilotSTRATEGY project has received funding from the European Union's Horizon 2020 research and innovation programme under grant agreement No. 101022664

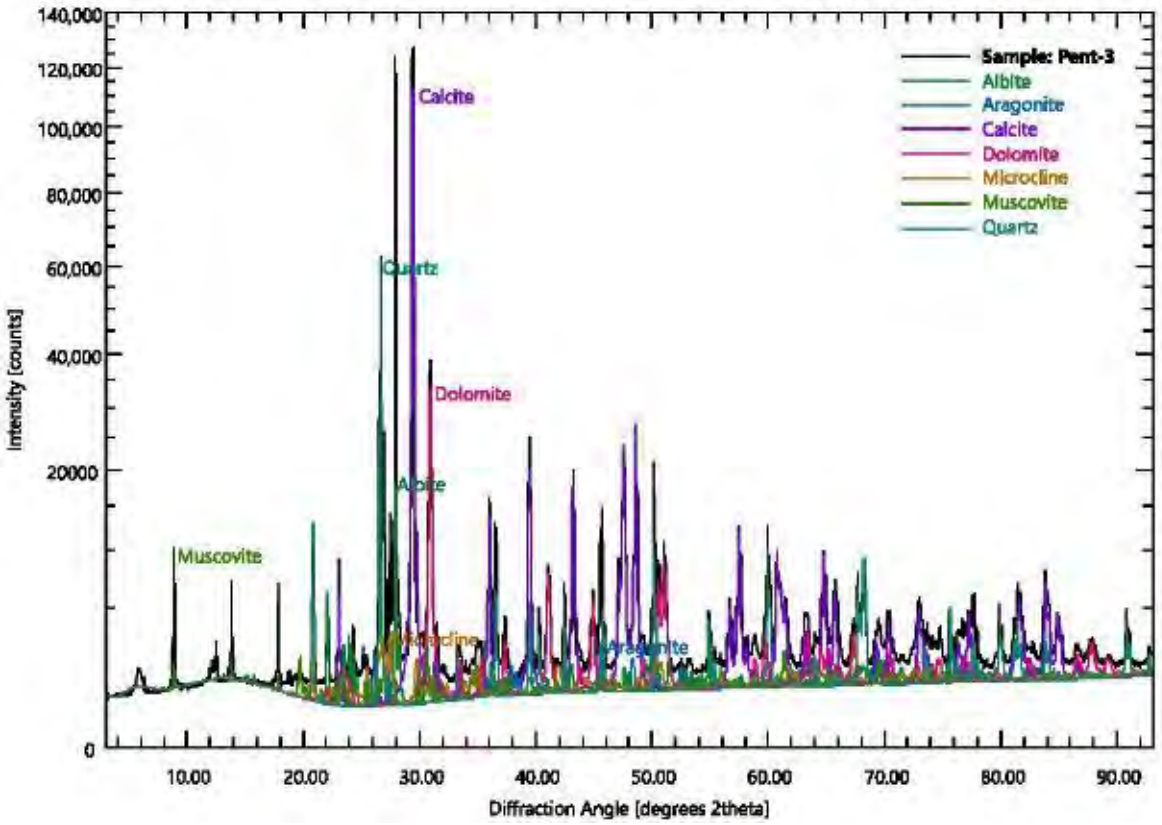

Figure Appendix. 10.9.14: XRD pattern and Rietveld refinement of sample Pent-3. Major peaks for the detected minerals are highlighted.

Appendix III XRF Analysis Conducted on Bulk Sedimentary Rock Samples from the Mesohellenic Trough

Three (3) sedimentary rock samples originating from the Tsotyli (sample Tsot-1; marly SANDSTONE), Eptachori (sample Ept-2; fine GREYWACKE) and Pentalofos (sample Pent-3; greywacke) Formations of the Mesohellenic Trough were powdered and analyzed by X-ray fluorescence (XRF) to determine their mineralogical composition. The samples were field collected by hummer and obtained as rock chips (**Erreur ! Source du renvoi introuvable.**). Pulps produced from the rock chip samples were formed into p ressed pellets by mixing 2.4 g of the binder CEREOX® with 9.6 g of rock pulp (i.e. sample-to-wax binder ratio of 4:1). The mixed material was homogenized in a mechanical mixer working at 24 rpm for 15 minutes and then pressed at 5 kbr (Figure Appendix. 10.9.15). The XRF analysis was performed using Bruker S4-PIONEER with a wavelength-dispersive X-ray fluorescence (WDXRF) analytical system at the Department of Mineralogy-Petrology-Economic Geology, School of Geology, Aristotle University of Thessaloniki. The spectrometer uses an Rh lamp and a system of 5 crystals: LIF200, LIF220, LIF420, XS-55, and PET. It also has two detectors: a gas proportional counter and a scintillation counter. The X-ray beam was used at its maximum energy of 50-60 kV. The element lines that were measured were the Ka and La lines, depending

The PilotSTRATEGY project has received funding from the European Union's Horizon 2020 research and innovation programme under grant agreement No. 101022664

on the element. The method includes corrections for overlaps and matrix effects. Analytical results are presented in Table 1, while major conclusions after XRF analysis are presented below by taking into consideration conclusions previously made after XRD and SEM-EDS analysis. Previous published investigations on these samples include geomechanical and petrophysical methods for the evaluation of the parent sedimentary formations to capture and store CO_2 [118].

Figure Appendix. 10.9.15: Representative photograph showing pulps and pressed pellets produced for the XRF analysis.

The PilotSTRATEGY project has received funding from the European Union's Horizon 2020 research and innovation programme under grant agreement No. 101022664

Table Appendix 10.9.10: Bulk geochemical analyses of major and minor elements for the analyzed samples Tsot-1, Ept-2 and Pent-3 from the Mesohellenic Trough

Element	Tsot-1	Ept-2	Pent-3
wt.%			
SiO_2	35	36	16
Al_2O_3	7.2	6.6	2.9
Fe_2O_3	2.7	3.3	1.2
CaO	30	26	42
MgO	4.2	7.2	6.0
Na_2O	1.0	0.74	0.39
K_2O	2.2	1.4	0.94
MnO	0.11	0.11	0.03
TiO_2	0.32	0.39	0.13
P_2O_5	0.08	0.10	0.06
LOI	17	18	30
Total	100	100	100
ppm			
Ba	189	149	66
Co	7.0	13	4.0
Cr	749	1,680	512
Cu	14	23	7.0
Ni	112	221	78
Rb	192	95	82
Sc	*bdl*	*bdl*	*bdl*
Sr	298	342	242
V	650	990	306
Zn	31	38	15
Zr	100	113	54

**LOI = Loss of ignition, bdl = below detection limit.*

Conclusions

The XRF analysis confirms suggestions and conclusions made on previously acquired SEM-EDS and XRD analytical results focusing on bulk samples obtained by hammering from marly SANDSTONE (Tsot-1) and greywacke (Ept-2, Pent-3) originating from the Tsotyli, Eptachori and Pentalofos Formations of the Mesohellenic Trough (**Erreur ! Source du renvoi introuvable.**).

Bulk geochemical analysis reveals that calcium and silica are the most enriched elements (Table Appendix 10.9.10). Sample Tsot-1 (24.85 wt.% SiO_2) is slightly siliceous in composition, sample Epth-2 (36 wt.% SiO_2) is dominantly siliceous, while sample Pent-3 is dominantly calcareous in composition (42 wt.% CaO, Table Appendix 10.9.10). These results are complementary to the semi-quantitative estimates obtained by XRD analysis (cf. Report_XRD_PilotStrategy03.04.2024.docx). In sample Tsot-1, calcite content is 30 wt.%, while quartz (29 wt.%) and albite (19 wt.%) percentages sum to 50 wt.%, supporting the siliceous profile acquired by XRF. In sample Ept-2, quartz (37 wt.%) is the dominant mineral phase followed by calcite (29 wt.%), while in sample Pent-3, calcite (41 wt.%) is the more enriched mineral phase, supporting the obtained geochemical results where SiO_2 is 36 wt.% in sample Ept-2 and CaO is 45 wt.% for sample Pent-3. In addition, the geochemical results support the suggested level of maturity of the analyzed samples with Etp-2 showing the highest and Pent-3 the lowest maturity.

The PilotSTRATEGY project has received funding from the European Union's Horizon 2020 research and innovation programme under grant agreement No. 101022664

Finally, sample Ept-2 shows the highest enrichment in minor elements, including 1,680 ppm of Cr and 990 ppm of V (Table Appendix 10.9.10). Relative enrichments in these trace elements, as well as in Co, Cu, Ni and Zn could be related to the highest incorporation of detrital material related to the ophiolitic basement rocks of the Mesohellenic Trough. Variations in trace elements may be associated with minor mineral phases not detected by the XRD analysis and the SEM-EDS examination of bulk samples. The study of thin-polished sections under a plane polarized and an electron scanning microscope shall clarify the mineral composition of the samples and conclude the mineralogical and geochemical investigation.

Appendix IV Photographic material field survey

For more information and referencing please advice the main part of this report.

Figure Appendix. 10.9.16: Survey site 3_1. Conglomeratic SANDSTONE beds (<30 cm in width) intercalated with beds consisting of sandy MARLS (<60 cm in width) that are related to Pentalofos Formation of the Mesohellenic Trough (Aquitanian; Lower Miocene). Coordinates (WGS84): N40.00146600°, E21.48474600°; Date of picture taken: 19.06.2024; Orientation: 321.33°.

The PilotSTRATEGY project has received funding from the European Union's Horizon 2020 research and innovation programme under grant agreement No. 101022664

Figure Appendix. 10.9.17: Survey site 3_1. Detail of the conglomeratic SANDSTONE (Pentalofos Formation; Mesohellenic Trough (Aquitanian; Lower Miocene). Coordinates (WGS84): N40.00146600°, E21.48474600°; Date of picture taken: 19.06.2024; Orientation: 4.38°.

Figure Appendix. 10.9.18: Survey site 3_3. Detail of the unbedded to slightly bedded, loose to cemented conglomerates that are intercalated with beds consisting of sand and cobbles (Pentalofos Formation; Mesohellenic Trough (Aquitanian; Lower Miocene). Coordinates (WGS84): N39.98762667°, E21.46712667°; Date of picture taken: 19.06.2024; Orientation: 296.79°.

The PilotSTRATEGY project has received funding from the European Union's Horizon 2020 research and innovation programme under grant agreement No. 101022664

Figure Appendix. 10.9.19: Survey site 3_2. Slightly bedded and loose sands and cobbles (Pentalofos Formation; Mesohellenic Trough (Aquitanian; Lower Miocene). Coordinates (WGS84): N39.98746500°, E21.46593333°; Date of picture taken: 10.04.2024; Orientation: 17.89°.

The PilotSTRATEGY project has received funding from the European Union's Horizon 2020 research and innovation programme under grant agreement No. 101022664

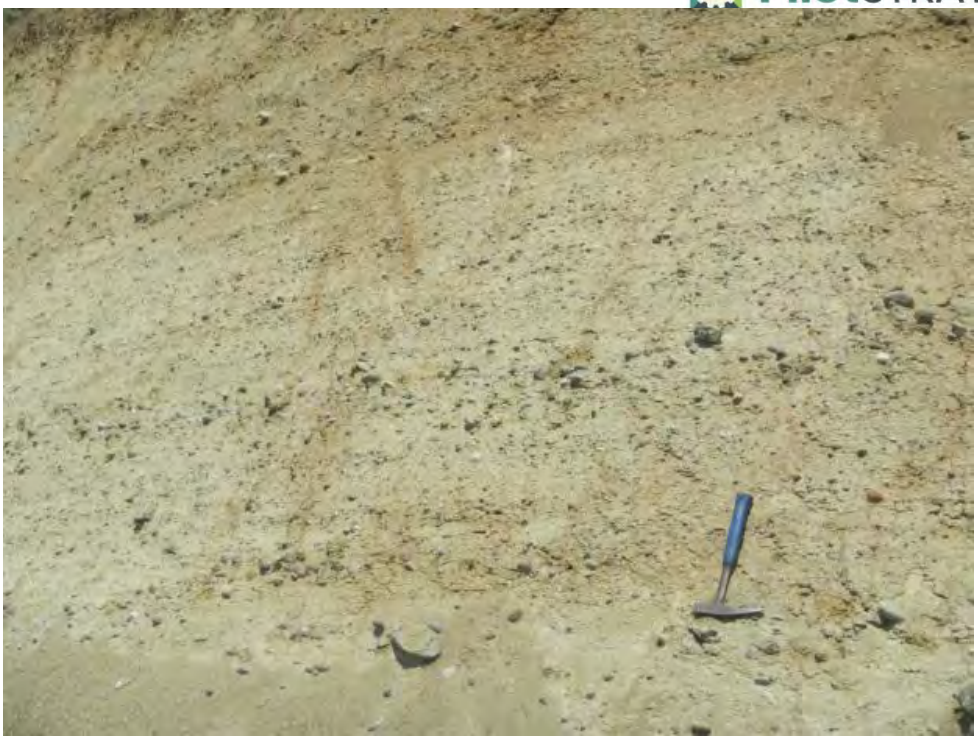

Figure Appendix. 10.9.20: Survey site 3_2. Detail of the slightly bedded and loose sands and cobbles (Pentalofos Formation; Mesohellenic Trough (Aquitanian; Lower Miocene). Coordinates (WGS84): N39.98778833°, E21.46639667°; Date of picture taken: 19.06.2024; Orientation: 15.96°.

Figure Appendix. 10.9.21: An overview of survey site 3_3. Sandstone to conglomeratic sandstone (<40 cm in width) intercalated with conglomerates and thin beds of sandy marls (<10 cm in width) (Pentalofos Formation; Mesohellenic Trough (Aquitanian; Lower Miocene). Coordinates (WGS84): N39.99600900°, E21.46842200°; Date of picture taken: 19.06.2024; Orientation: 105.71°.

The PilotSTRATEGY project has received funding from the European Union's Horizon 2020 research and innovation programme under grant agreement No. 101022664

Figure Appendix. 10.9.22: An overview of survey site 3_3a (Pentalofos Formation; Mesohellenic Trough (Aquitanian; Lower Miocene). Coordinates (WGS84): N39.99543000°, E21.46911500°; Date of picture taken: 19.06.2024; Orientation: 99.03°.

Figure Appendix. 10.9.23: Detail from the conglomerates that are intercalated with the conglomeratic SANDSTONES at survey site 3_3a (Pentalofos Formation; Mesohellenic Trough (Aquitanian; Lower Miocene). Coordinates (WGS84): N39.99525333°, E21.46924333°; Date of picture taken: 19.06.2024; Orientation: 92.61°.

The PilotSTRATEGY project has received funding from the European Union's Horizon 2020 research and innovation programme under grant agreement No. 101022664

Figure Appendix. 10.9.24: Detail from the conglomeratic SANDSTONE at survey site 3_3a (Pentalofos Formation; Mesohellenic Trough (Aquitanian; Lower Miocene). Coordinates (WGS84): N39.99536667°, E21.46927000°; Date of picture taken: 19.06.2024; Orientation: 23.50°.

Figure Appendix. 10.9.25: Detail of the conglomeratic SANDSTONE at survey site 3_3b (Pentalofos Formation; Mesohellenic Trough (Aquitanian; Lower Miocene). Coordinates (WGS84): N39.99687600°, E21.46801700°; Date of picture taken: 19.06.2024; Orientation: 108.98°.

seis

Figure Appendix. 10.9.26: Detail of the conglomeratic SANDSTONE beds (<20 cm in width) at survey site 3_4 (Pentalofos Formation; Mesohellenic Trough (Aquitanian; Lower Miocene). Coordinates (WGS84): N39.99951333°, E21.44267167°; Date of picture taken: 19.06.2024; Orientation: 343.78°.

Figure Appendix. 10.9.27: Detail of the bedded conglomerates that are interbedded with sands at survey site 3_4 (Pentalofos Formation; Mesohellenic Trough (Aquitanian; Lower Miocene). Coordinates (WGS84): N39.99964167°, E21.44267000°; Date of picture taken: 19.06.2024; Orientation: 314.15°.

Figure Appendix. 10.9.28: Overview of part of the survey area 3_5 where conglomerates are the dominant formation (Pentalofos Formation; Mesohellenic Trough (Aquitanian; Lower Miocene). Coordinates (WGS84): N39.98834333°, E21.43821167°; Date of picture taken: 19.06.2024; Orientation: 331.18°.

Figure Appendix. 10.9.29: Detail of interbedded thin (<20 cm in width) beds of marl and sand at survey site 3_5 (Pentalofos Formation; Mesohellenic Trough (Aquitanian; Lower Miocene). Coordinates (WGS84): N39.98723900°, E21.43789200°; Date of picture taken: 19.06.2024; Orientation: 297.32°.

The PilotSTRATEGY project has received funding from the European Union's Horizon 2020 research and innovation programme under grant agreement No. 101022664

Figure Appendix. 10.9.30: Detail of the conglomerates at survey site 5_1 (Pentalofos Formation; Mesohellenic Trough (Aquitanian; Lower Miocene). Coordinates (WGS84): N40.04976333°, E21.46659333°; Date of picture taken: 29.05.2024; Orientation: 258.00°.

Figure Appendix. 10.9.31: Detail of a joint (Joint21) filled by calcite at survey site 5_1(5) (Pentalofos Formation; Mesohellenic Trough (Aquitanian; Lower Miocene). Coordinates (WGS84): N40.04983000°, E21.46684667°; Date of picture taken: 29.05.2024; Orientation: 245.18°.

The PilotSTRATEGY project has received funding from the European Union's Horizon 2020 research and innovation programme under grant agreement No. 101022664

Figure Appendix. 10.9.32: Intercalated sands and cobbles at survey site 5_1b (Pentalofos Formation; Mesohellenic Trough (Aquitanian; Lower Miocene). Coordinates (WGS84): N40.0509000°, E21.47659167°; Date of picture taken: 29.05.2024; Orientation: 4.88°.

The PilotSTRATEGY project has received funding from the European Union's Horizon 2020 research and innovation programme under grant agreement No. 101022664

Figure Appendix. 10.9.33: Detail of the sands and cobbles from survey site 5_3. (Pentalofos Formation; Mesohellenic Trough (Aquitanian; Lower Miocene). Coordinates (WGS84): N40.01247833°, E21.53152667°; Date of picture taken: 29.05.2024; Orientation: 350.92°.

Figure Appendix. 10.9.34: Detail of the marly SANDSTONE at survey site 5_4 (Pentalofos Formation; Mesohellenic Trough (Aquitanian; Lower Miocene). Coordinates (WGS84): N40.00837333°, E21.53352667°; Date of picture taken: 29.05.2024; Orientation: 154.55°.

The PilotSTRATEGY project has received funding from the European Union's Horizon 2020 research and innovation programme under grant agreement No. 101022664

Figure Appendix. 10.9.35: Detail of the ophiolitic CONGLOMERATE at survey site 5_6_1. Calcite appears as the main cementing material (Pentalofos Formation; Mesohellenic Trough (Aquitanian; Lower Miocene). Coordinates (WGS84): N40.01762667°, E21.51365000°; Date of picture taken: 29.05.2024; Orientation: 340.21°.

The PilotSTRATEGY project has received funding from the European Union's Horizon 2020 research and innovation programme under grant agreement No. 101022664

Figure Appendix. 10.9.36: The beds of marl at survey site 5_6_3b near the contact with the conglomerate consisting of ophiolitic and limestone cobbles. A distinct red colored marl bed in found along the contact (Pentalofos Formation; Mesohellenic Trough (Aquitanian; Lower Miocene). Coordinates (WGS84): N40.01689000°, E21.51361500°; Date of picture taken: 29.05.2024; Orientation: 326.32°.

Figure Appendix. 10.9.37: A panoramic photograph of survey sites 5_1, 5_1a and 5_1b from survey site 5_1c. Slightly bedded to unbedded conglomerates of the Pentalofos Formation, Mesohellenic Trough (Aquitanian; Lower Miocene) are found in contact with fluvial deposits of unconsolidated conglomerates, clays sands and loose sandstones of Pliocene to Pleistocene age. Coordinates (WGS84): N40.04928997°, E21.47977000°; Date of picture taken: 29.05.2024; Orientation: 0.00°.

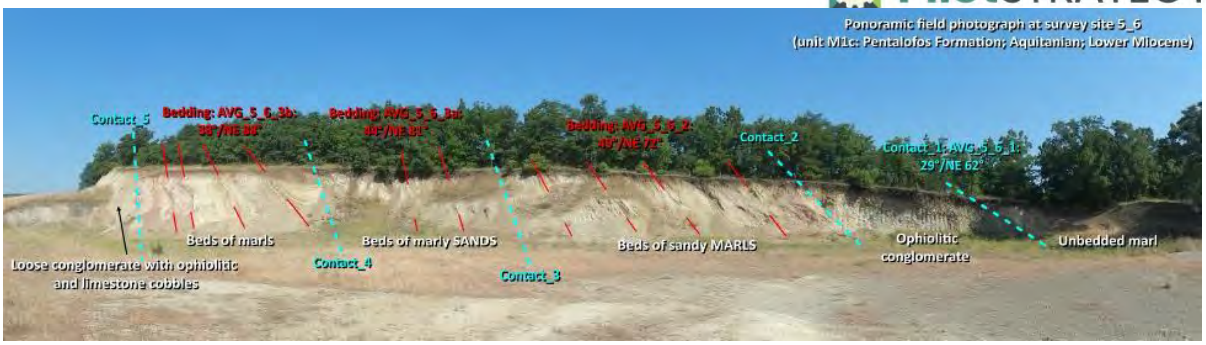

Figure Appendix. 10.9.38: A panoramic photograph at survey site 6_5. Along the scanline 6_5 (from right to left in this photograph), the stratigraphy transitions from unbedded marl to an ophiolitic conglomerate. This conglomerate is in contact with sandy marl, which then transitions into marly sand. Further along the line, the sequence transitions back to marl, which is in contact with a conglomerate composed of ophiolitic and limestone cobbles (Pentalofos Formation; Mesohellenic Trough (Aquitanian; Lower Miocene). Coordinates (WGS84): N40.01698167°, E21.51396500°; Date of picture taken: 19.06.2024; Orientation: 341.15°.

Figure Appendix. 10.9.39: Survey site 6_1. Sandstone beds (<30 cm in width, unit M1-3.st,m: Tsotyli Formation; sandstones, marls, sandy marls, upper units (Miocene). Coordinates (WGS84): N40°1'34.82", E21°39'35.22"; Date of picture taken: 10.04.2024; Orientation: 10.32°.

The PilotSTRATEGY project has received funding from the European Union's Horizon 2020 research and innovation programme under grant agreement No. 101022664

Figure Appendix. 10.9.40: Survey site 6_1. Detail of the fractured sandstone beds (<30 cm in width, unit M1-3.st,m: Tsotyli Formation; sandstones, marls, sandy marls, upper units (Miocene). Coordinates (WGS84): N40°1'34.75", E21°39'35.07"; Date of picture taken: 10.04.2024; Orientation: 17,66°.

The PilotSTRATEGY project has received funding from the European Union's Horizon 2020 research and innovation programme under grant agreement No. 101022664

Figure Appendix. 10.9.41: An overview of the survey site 6_1. Coordinates (WGS84): N40°1'28.84", E21°39'31.75"; Date of picture taken: 10.04.2024; Orientation: 354.54°.

Figure Appendix. 10.9.42: Survey site 6_2. Sandstone beds (<15 cm in width, unit M1-3.st,m: Tsotyli Formation; sandstones, marls, sandy marls, upper units (Miocene) intercalated with beds consisting of sandy marls (<60 cm in width). Coordinates (WGS84): N40°0'10.91", E21°39'15.32"; Date of picture taken: 10.04.2024; Orientation: 105.53°.

The PilotSTRATEGY project has received funding from the European Union's Horizon 2020 research and innovation programme under grant agreement No. 101022664

Figure Appendix. 10.9.43: Survey site 6_3. Sandstone beds (<30 cm in width) intercalated with sandy marls (<2 m in width, unit M1-3.st,m: Tsotyli Formation; sandstones, marls, sandy marls, upper units (Miocene). Coordinates (WGS84): N39°59'23.85", E21°38'12.53"; Date of picture taken: 10.04.2024; Orientation: 19.95°.

The PilotSTRATEGY project has received funding from the European Union's Horizon 2020 research and innovation programme under grant agreement No. 101022664

Figure Appendix. 10.9.44: Survey site 6_4. Sandstone beds (<10 cm in width) intercalated with thin-bedded marls (<5 cm in width, unit M1-3.st,m: Tsotyli Formation; sandstones, marls, sandy marls, upper units (Miocene). Coordinates (WGS84): N39°59'42.98", E21°37'51.38"; Date of picture taken: 10.04.2024; Orientation: 133.16°.

Figure Appendix. 10.9.45: Survey site 7_1. Joints in ophiolitic rocks (unit σ: serpentinite). Coordinates (WGS84): N40°1'12.98", E21°42'9.16"; Date of picture taken: 10.04.2024; Orientation: 19.46°.

Figure Appendix. 10.9.46: Survey site 7_2. Joints in ophiolitic rocks (unit σ: serpentinite). Coordinates (WGS84): N40°1'7.84", E21°42'9.80"; Date of picture taken: 10.04.2024; Orientation: 21.10°.

The PilotSTRATEGY project has received funding from the European Union's Horizon 2020 research and innovation programme under grant agreement No. 101022664

Figure Appendix. 10.9.47: Survey site 7_3. Joints in ophiolitic rocks (unit σ: serpentinite). Coordinates (WGS84): N40°1'3.97", E21°42'10.45"; Date of picture taken: 10.04.2024; Orientation: 28.01°.

Figure Appendix. 10.9.48: Survey site 7_4. Joints in ophiolitic rocks (unit σ: serpentinite). Coordinates (WGS84): N40°1'11.66", E21°41'57.45"; Date of picture taken: 10.04.2024; Orientation: 196.48°.

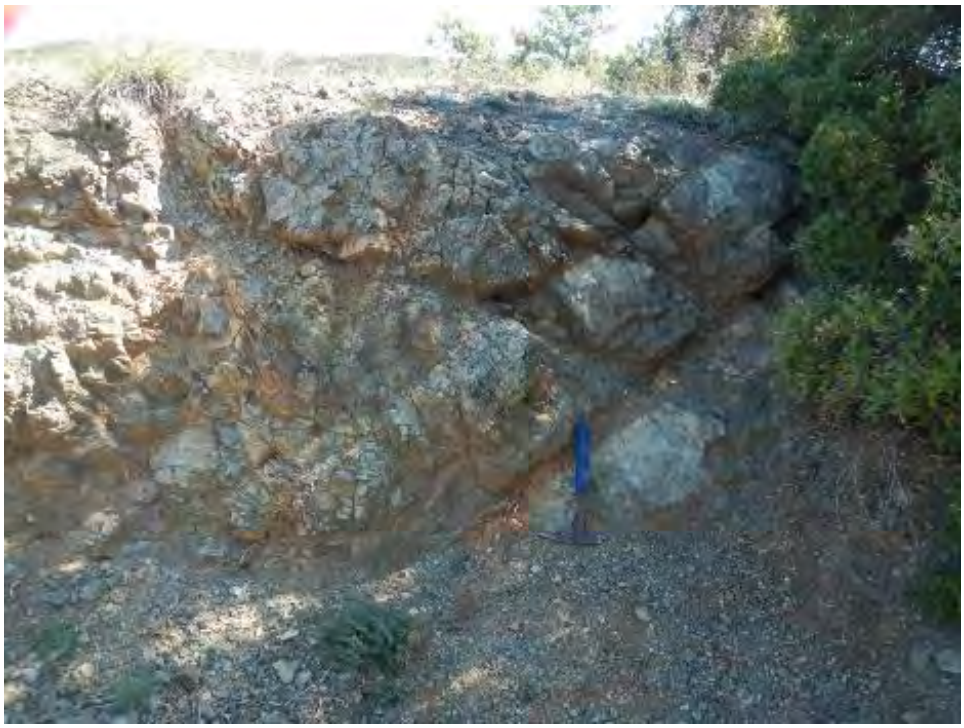

The PilotSTRATEGY project has received funding from the European Union's Horizon 2020 research and innovation programme under grant agreement No. 101022664

Figure Appendix. 10.9.49: Survey site 7_5. Joints in ophiolitic rocks (unit σ: serpentinite). Coordinates (WGS84): N40°1'25.52", E21°41'37.20"; Date of picture taken: 10.04.2024; Orientation: 45.50°.

Figure Appendix. 10.9.50: Survey site 7_6. Joints in ophiolitic rocks (unit σ: serpentinite). Coordinates (WGS84): N40°1'25.48", E21°41'36.89"; Date of picture taken: 10.04.2024; Orientation: 263.73°.

Figure Appendix. 10.9.51: Survey site 7_7. Joints in ophiolitic rocks (unit σ: serpentinite). Sample collected, hurzburgite. Coordinates (WGS84): N40°1'21.06", E21°41'28.05"; Date of picture taken: 10.04.2024; Orientation: 18.01°.

Figure Appendix. 10.9.52: Overview of the survey area 7_7 (unit σ: serpentinite). Coordinates (WGS84): N40°1'23.49", E21°41'29.56"; Date of picture taken: 10.04.2024; Orientation: 320.85°.

The PilotSTRATEGY project has received funding from the European Union's Horizon 2020 research and innovation programme under grant agreement No. 101022664

Figure Appendix. 10.9.53: Survey site 7_8. Overview of the survey site 7_8, unit M1-3.st,m: Tsotyli Formation; sandstones, marls, sandy marls, upper units (Miocene). Coordinates (WGS84): N40°1'24.99"", E21°40'56.23"; Date of picture taken: 10.04.2024; Orientation: 56.69°.

The PilotSTRATEGY project has received funding from the European Union's Horizon 2020 research and innovation programme under grant agreement No. 101022664

Figure Appendix. 10.9.54: Survey site 7_8. Beds of sandstone (<20 cm in width) and sandy marl (<1.5 in width, unit M1-3.st,m: Tsotyli Formation; sandstones, marls, sandy marls, upper units (Miocene). Coordinates (WGS84): N40°1'24.96", E21°40'56.32"; Date of picture taken: 10.04.2024; Orientation: 352.02°.

Figure Appendix. 10.9.55: Survey site 7_8. Beds of sandstone (<20 cm in width) and sandy marl (<1.5 in width, unit M1-3.st,m: Tsotyli Formation; sandstones, marls, sandy marls, upper units (Miocene) in contact with unit Pi-Pst: Fluvial-alluvial and lacustrine deposits in terraces, U.Pliocene-Pleistocene. Coordinates (WGS84): N40°1'24.92", E21°40'55.83"; Date of picture taken: 10.04.2024; Orientation: 39.13°.

The PilotSTRATEGY project has received funding from the European Union's Horizon 2020 research and innovation programme under grant agreement No. 101022664

Figure Appendix. 10.9.56: Survey site 7_8. The contact between sandy marls of unit M1-3.st,m (Tsotyli Formation; sandstones, marls, sandy marls, upper units (Miocene) and conglomerates of unit Pi-Pst (Fluvial-alluvial and lacustrine deposits in terraces, U. Pliocene-Pleistocene). Coordinates (WGS84): N40°1'24.87", E21°40'56.21"; Date of picture taken: 10.04.2024; Orientation: 7.92°.

The PilotSTRATEGY project has received funding from the European Union's Horizon 2020 research and innovation programme under grant agreement No. 101022664

Figure Appendix. 10.9.57: Survey site 7_8. Conglomerates of unit Pi-Pst (Fluvial-alluvial and lacustrine deposits in terraces, U.Pliocene-Pleistocene). Coordinates (WGS84): N40°1'25.86", E21°40'53.30"; Date of picture taken: 10.04.2024; Orientation: 123.89°.

The PilotSTRATEGY project has received funding from the European Union's Horizon 2020 research and innovation programme under grant agreement No. 101022664

Figure Appendix. 10.9.58: Survey site 7_9. Bedded conglomerates consisting mainly of limestone pebbles and rarely of ophiolitic pebbles (unit Pls-Pt.c: Horizontally bedded fluvial and lacustrine deposits (U.Pliocene-Pleistocene). Coordinates (WGS84): N40°1'31.44", E21°40'37.37"; Date of picture taken: 10.04.2024; Orientation: 187.45°.

Figure Appendix. 10.9.59: Survey site 7_9. Detail of the bedded conglomerates showing well-cemented and well rounded limestone pebbles (unit Pls-Pt.c: Horizontally bedded fluvial and lacustrine deposits (U.Pliocene-Pleistocene). Coordinates (WGS84): N40°1'31.62", E21°40'37.18"; Date of picture taken: 10.04.2024; Orientation: 207.56°.

The PilotSTRATEGY project has received funding from the European Union's Horizon 2020 research and innovation programme under grant agreement No. 101022664

Figure Appendix. 10.9.60: Survey site 7_9. Bedded conglomerates consisting mainly of limestone pebbles and rarely of ophiolitic pebbles (unit Pls-Pt.c: Horizontally bedded fluvial and lacustrine deposits (U.Pliocene-Pleistocene). Coordinates (WGS84): N40°1'31.18", E21°40'37.85"; Date of picture taken: 10.04.2024; Orientation: 214.60°.

The PilotSTRATEGY project has received funding from the European Union's Horizon 2020 research and innovation programme under grant agreement No. 101022664

Appendix V Supplementary material of SEM-EDS Analysis Conducted on Bulk Sedimentary Rock Samples from the Mesohellenic Trough

Sample Tsot-1: X-ray spectrums

Generic analysis

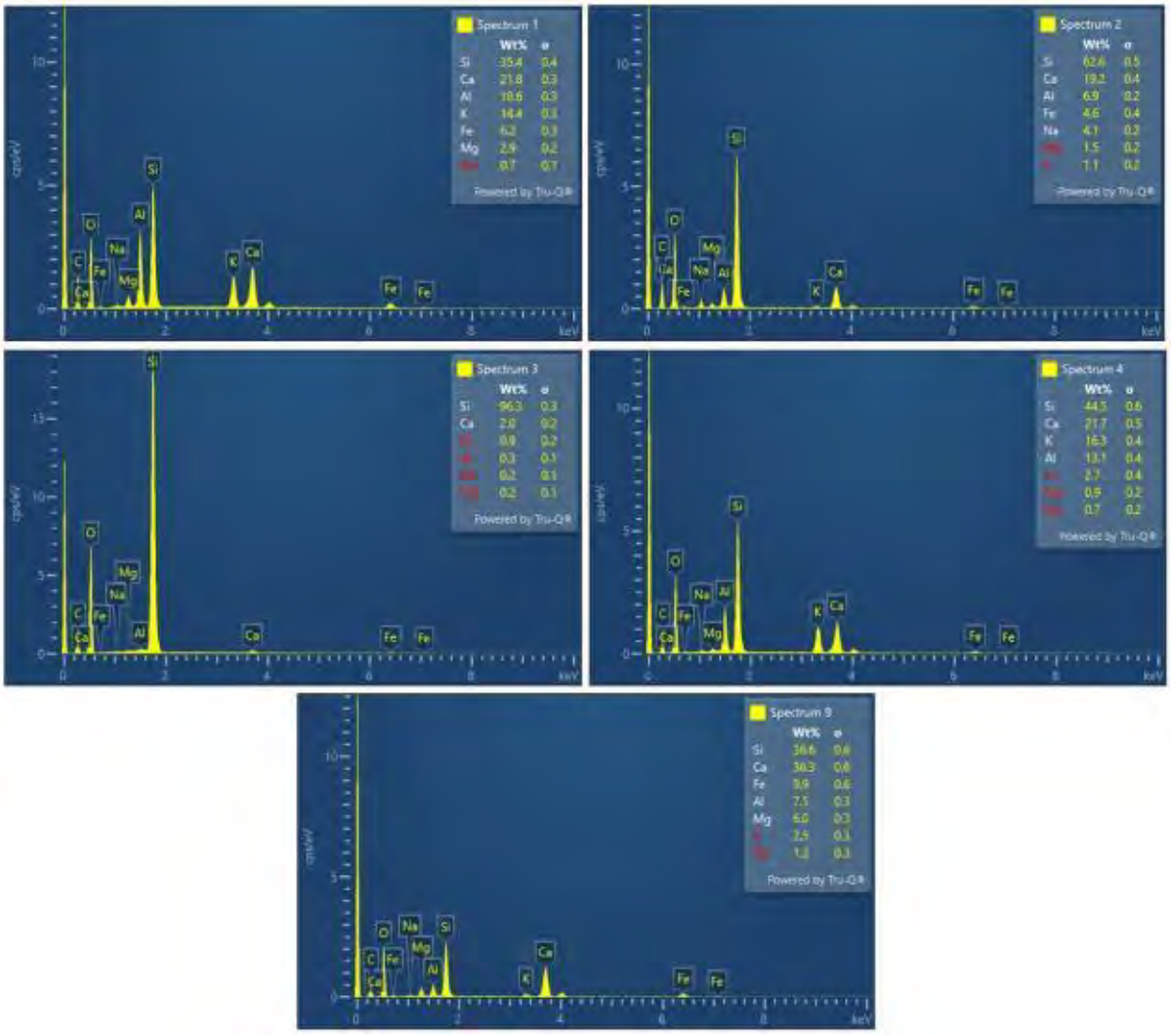

Figure Appendix. 10.9.61: SED-EDS spectra of generic analyses 1 to 9 from sample Tsot-1. Silicon, Ca, Al, K, Fe and Mg were the main detected elements. Carbon was not considered due to the carbon-coating of the polished section to facilitate the analysis.

Elemental mapping

The PilotSTRATEGY project has received funding from the European Union's Horizon 2020 research and innovation programme under grant agreement No. 101022664

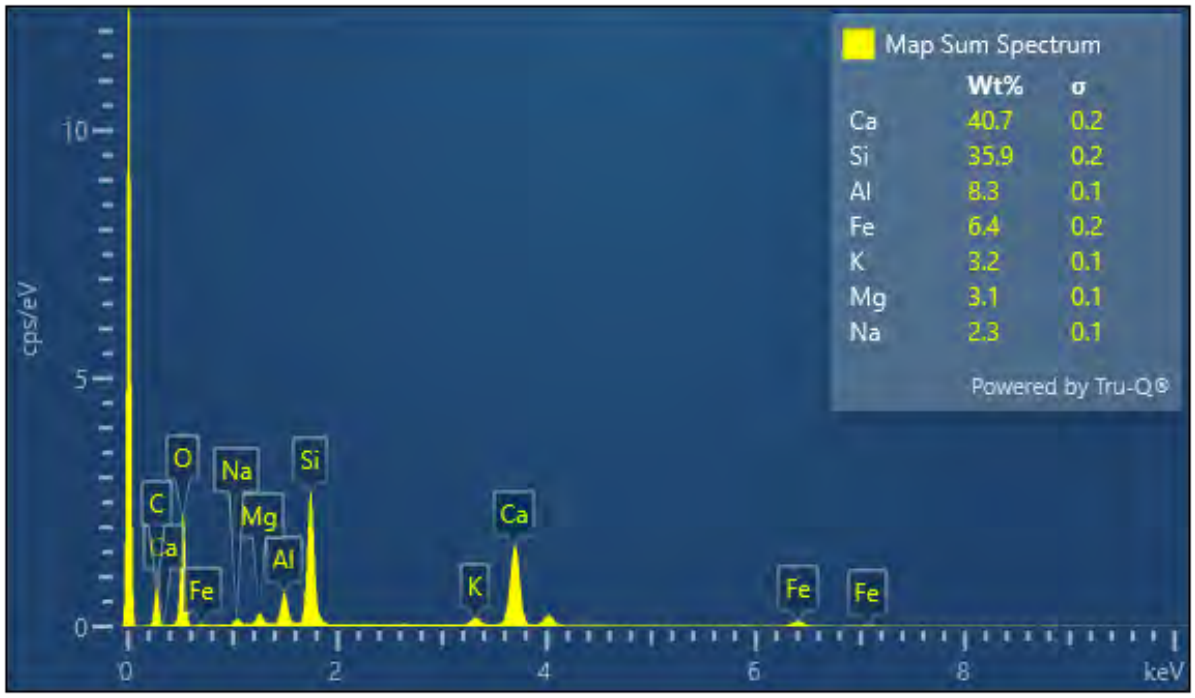

Figure Appendix. 10.9.62: SED-EDS spectra of elemental mapping from sample Tsot-1. Calcium, Si, Al, Fe, K, Mg and Na were the main detected elements. Carbon was not considered due to the carbon-coating of the polished section to facilitate the analysis.

Spot analyses

The PilotSTRATEGY project has received funding from the European Union's Horizon 2020 research and innovation programme under grant agreement No. 101022664

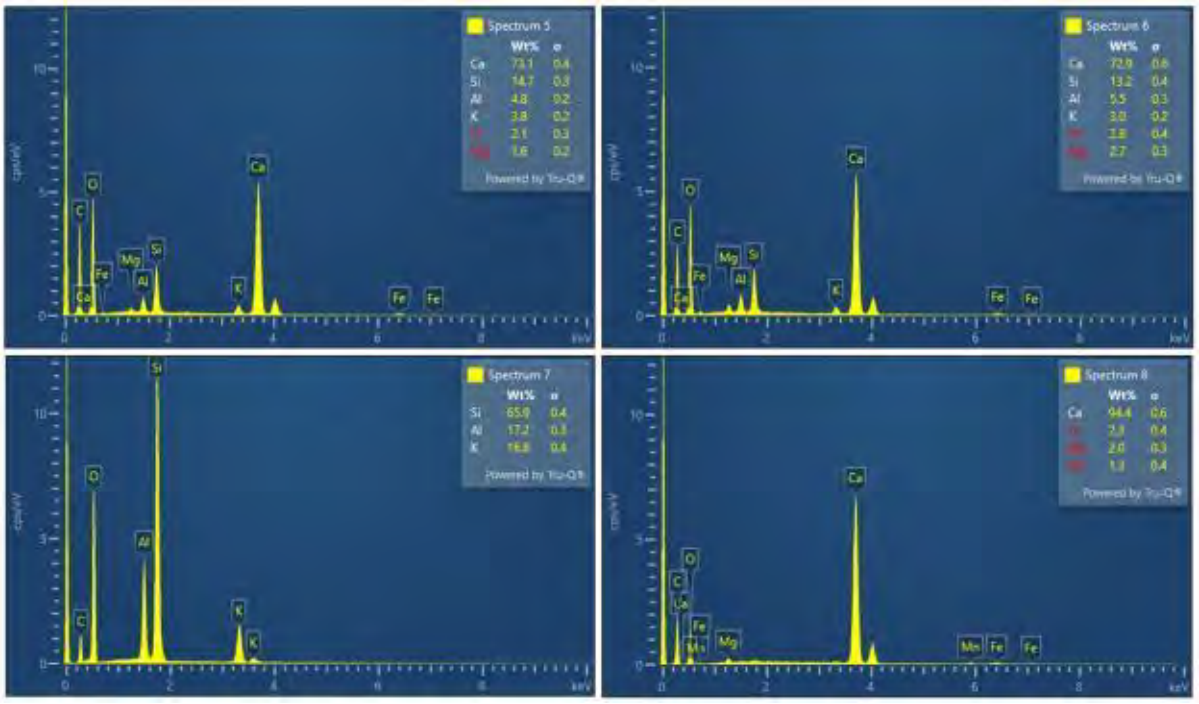

Figure Appendix. 10.9.63: SED-EDS spectra of spot analyses 5 to 8 from sample Tsot-1. For the detected mineral phases at sample Tsot-1 please advise Appendix I. Carbon was not considered due to the carbon-coating of the polished section to facilitate the analysis.

The PilotSTRATEGY project has received funding from the European Union's Horizon 2020 research and innovation programme under grant agreement No. 101022664

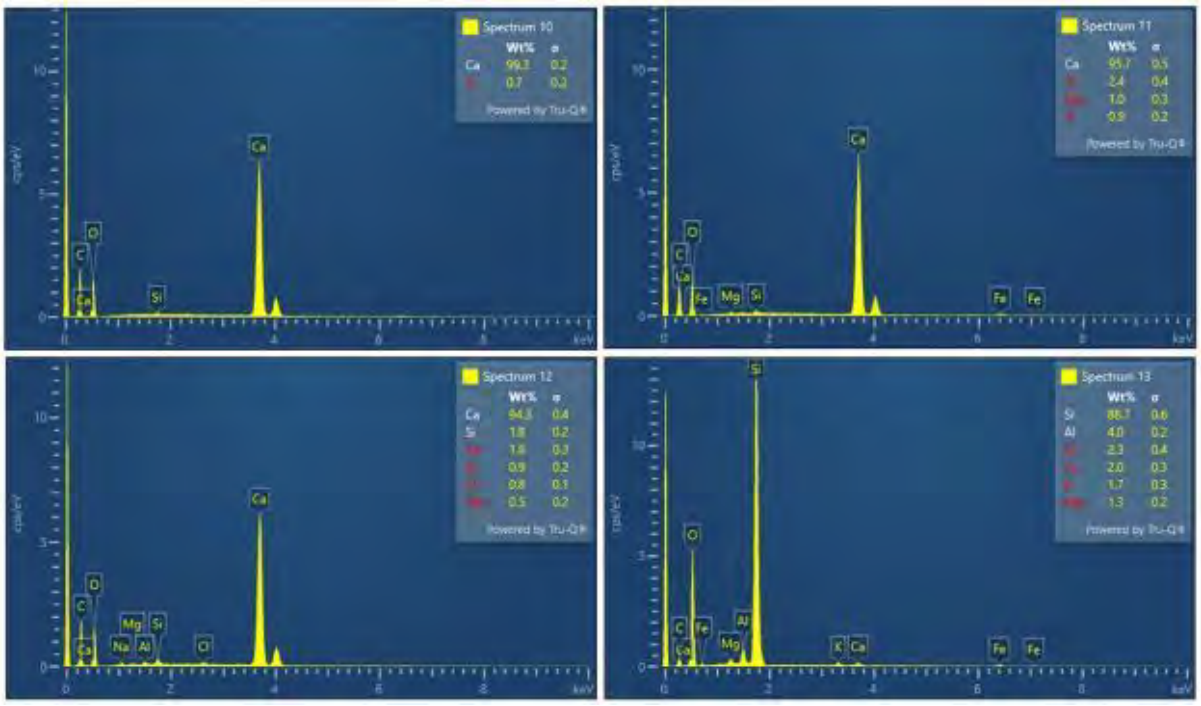

Figure Appendix. 10.9.64: SED-EDS spectra of spot analyses 10 to 13 from sample Tsot-1. For the detected mineral phases at sample Tsot-1 please advise Appendix I. Carbon was not considered due to the carbon-coating of the polished section to facilitate the analysis.

Sample Ept-2: X-ray spectrums

Generic analysis

The PilotSTRATEGY project has received funding from the European Union's Horizon 2020 research and innovation programme under grant agreement No. 101022664

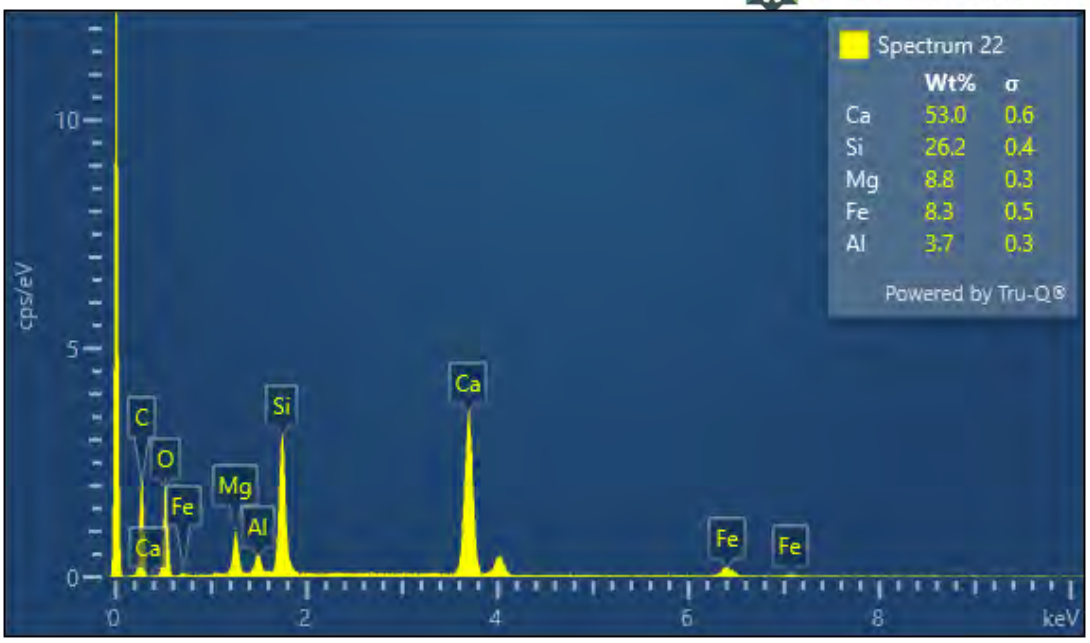

Figure Appendix. 10.9.65: SED-EDS spectra of generic analysis 22 from sample Ept-2. Calcium, Si, Mg, Fe and Al were the main detected elements. Carbon was not considered due to the carbon-coating of the polished section to facilitate the analysis.

Spot analyses

The PilotSTRATEGY project has received funding from the European Union's Horizon 2020 research and innovation programme under grant agreement No. 101022664

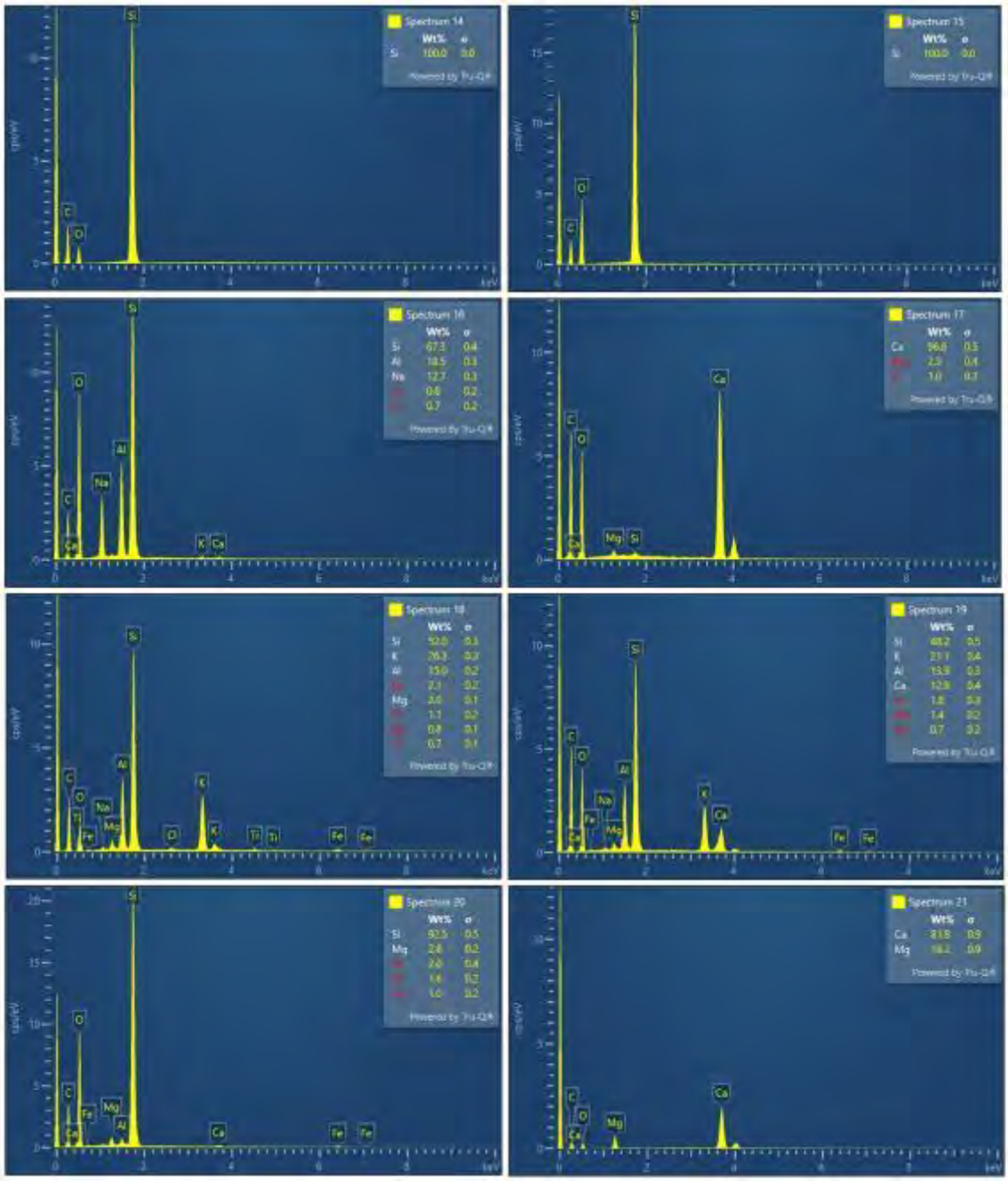

Figure Appendix. 10.9.66: SED-EDS spectra of spot analyses 14 to 21 from sample Ept-2. For the detected mineral phases at sample Ept-2 please advise Appendix I. Carbon was not considered due to the carbon-coating of the polished section to facilitate the analysis.

The PilotSTRATEGY project has received funding from the European Union's Horizon 2020 research and innovation programme under grant agreement No. 101022664

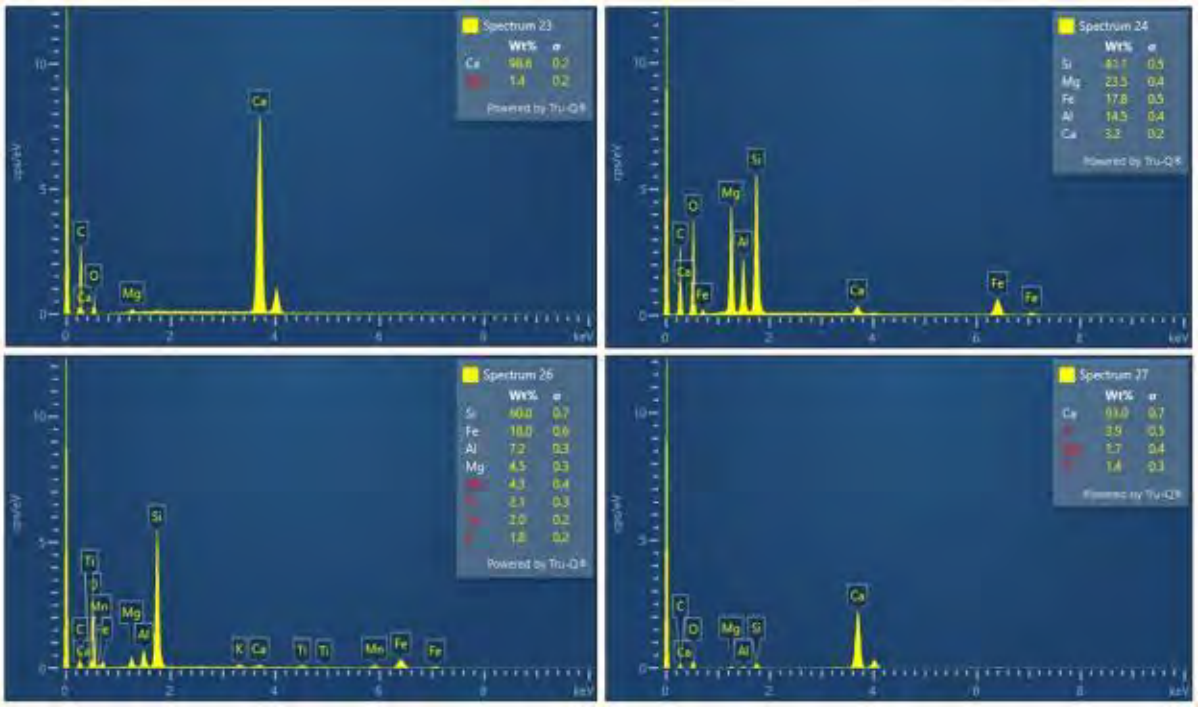

Figure Appendix. 10.9.67: SED-EDS spectra of spot analyses 23 to 27 from sample Ept-2. For the detected mineral phases at sample Ept-2 please advise Appendix I. Carbon was not considered due to the carbon-coating of the polished section to facilitate the analysis.

Sample Pent-3: X-ray spectrums

Spot analyses

The PilotSTRATEGY project has received funding from the European Union's Horizon 2020 research and innovation programme under grant agreement No. 101022664

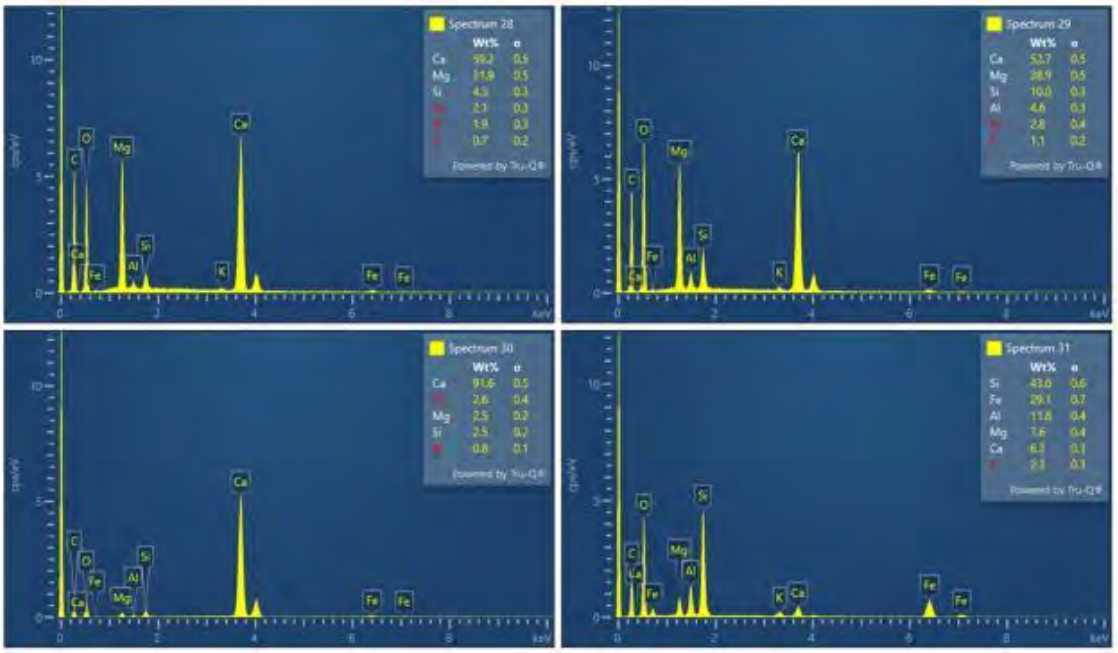

Figure Appendix. 10.9.68: SED-EDS spectra of spot analyses 23 to 27 from sample Pent-3. For the detected mineral phases at sample Pent-3 please advise Appendix I. Carbon was not considered due to the carbon-coating of the polished section to facilitate the analysis.

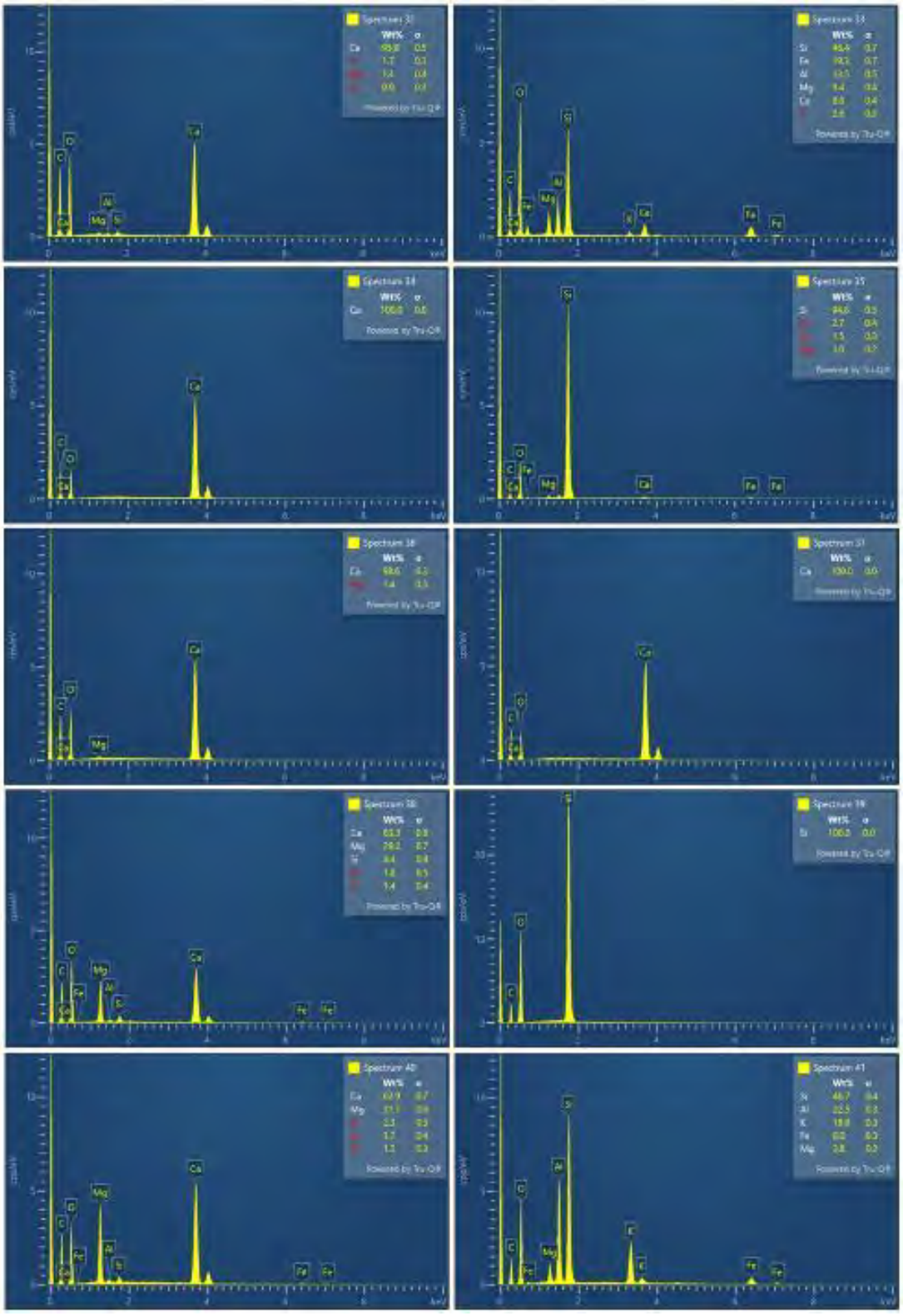

The PilotSTRATEGY project has received funding from the European Union's Horizon 2020 research and innovation programme under grant agreement No. 101022664

Figure Appendix. 10.9.69: SED-EDS spectra of spot analyses 32 to 39 from sample Pent-3. For the detected mineral phases at sample Pent-3 please advise Appendix I. Carbon was not considered due to the carbon-coating of the polished section to facilitate the analysis.

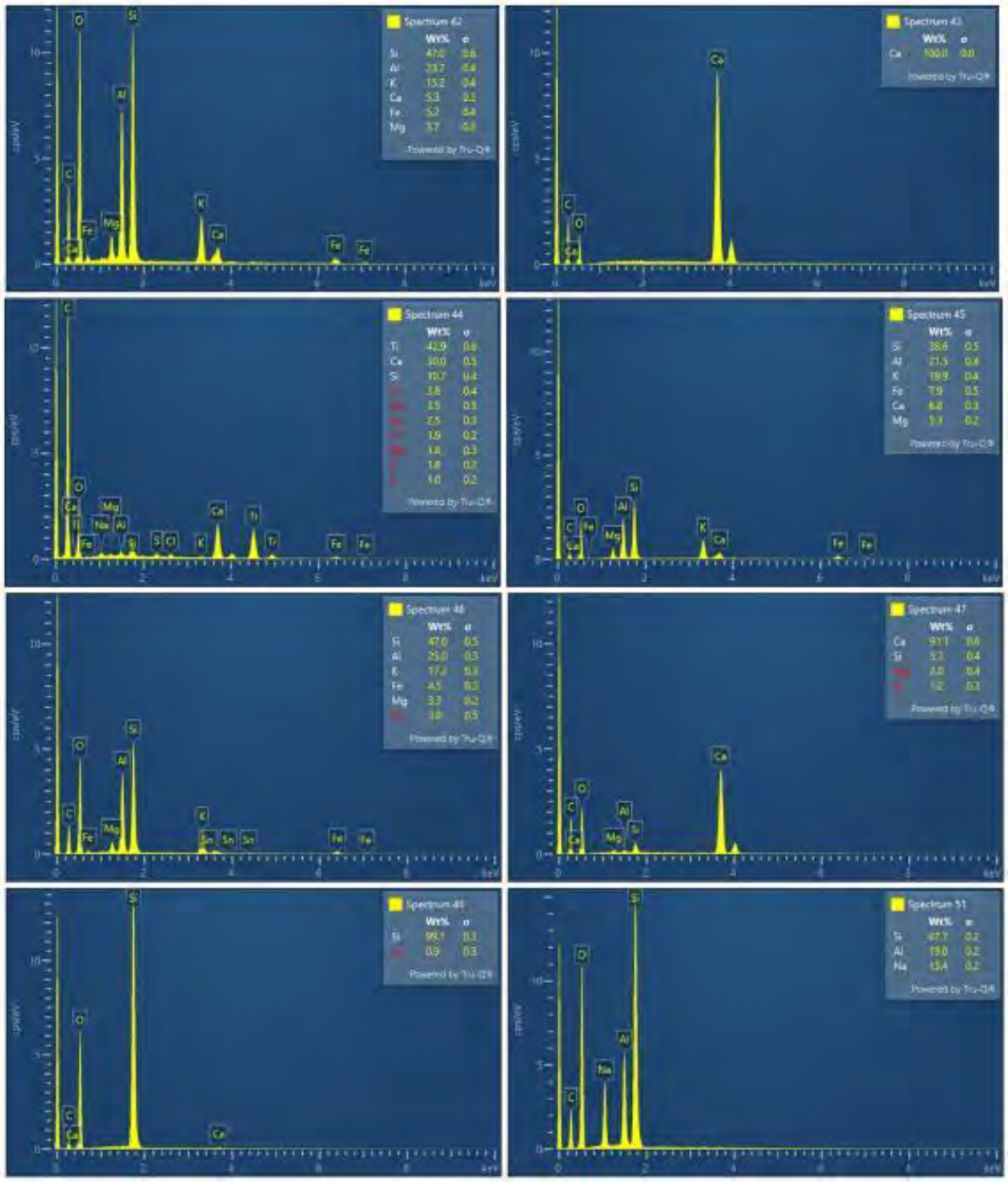

Figure Appendix. 10.9.70: SED-EDS spectra of spot analyses 42 to 51 from sample Pent-3. For the detected mineral phases at sample Pent-3 please advise Appendix I. Carbon was not considered due to the carbon-coating of the polished section to facilitate the analysis.

The PilotSTRATEGY project has received funding from the European Union's Horizon 2020 research and innovation programme under grant agreement No. 101022664

Pore measurements

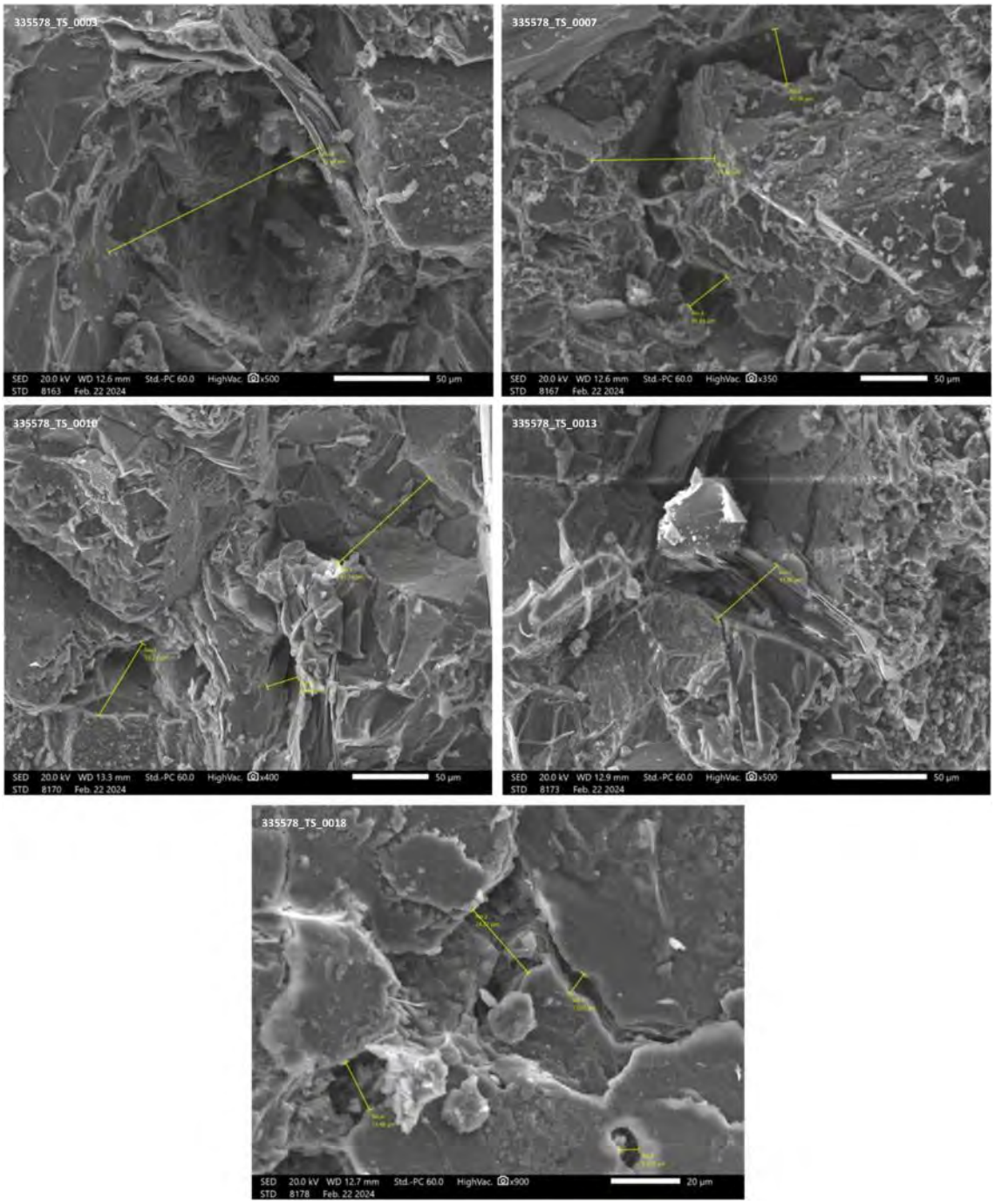

Figure Appendix. 10.9.71: SEM-EDS microphotographs showing the pores detected in sample Tsot-1.

The PilotSTRATEGY project has received funding from the European Union's Horizon 2020 research and innovation programme under grant agreement No. 101022664

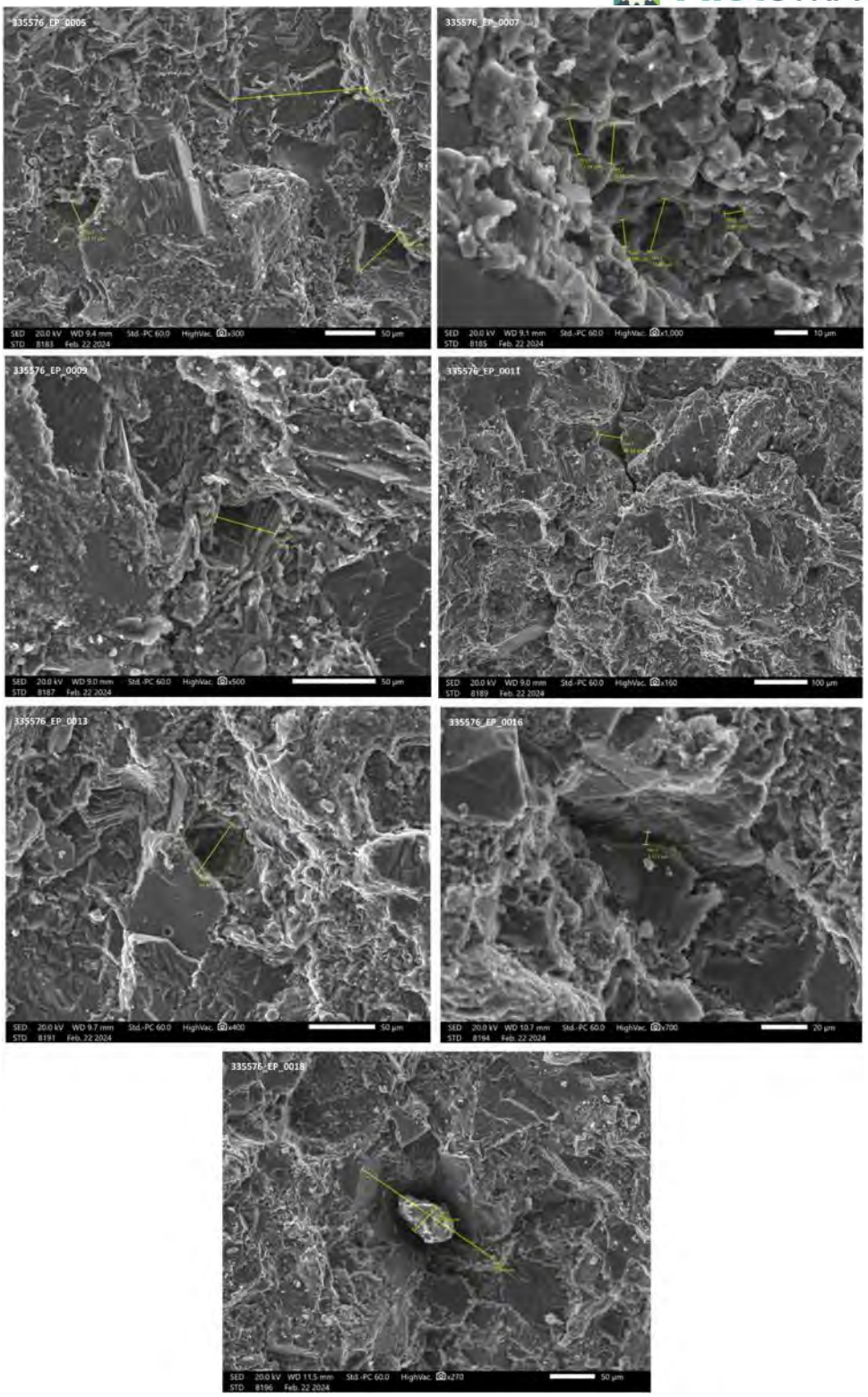

Figure Appendix. 10.9.72: SEM-EDS microphotographs showing the pores detected in sample Ept-2.

The PilotSTRATEGY project has received funding from the European Union's Horizon 2020 research and innovation programme under grant agreement No. 101022664

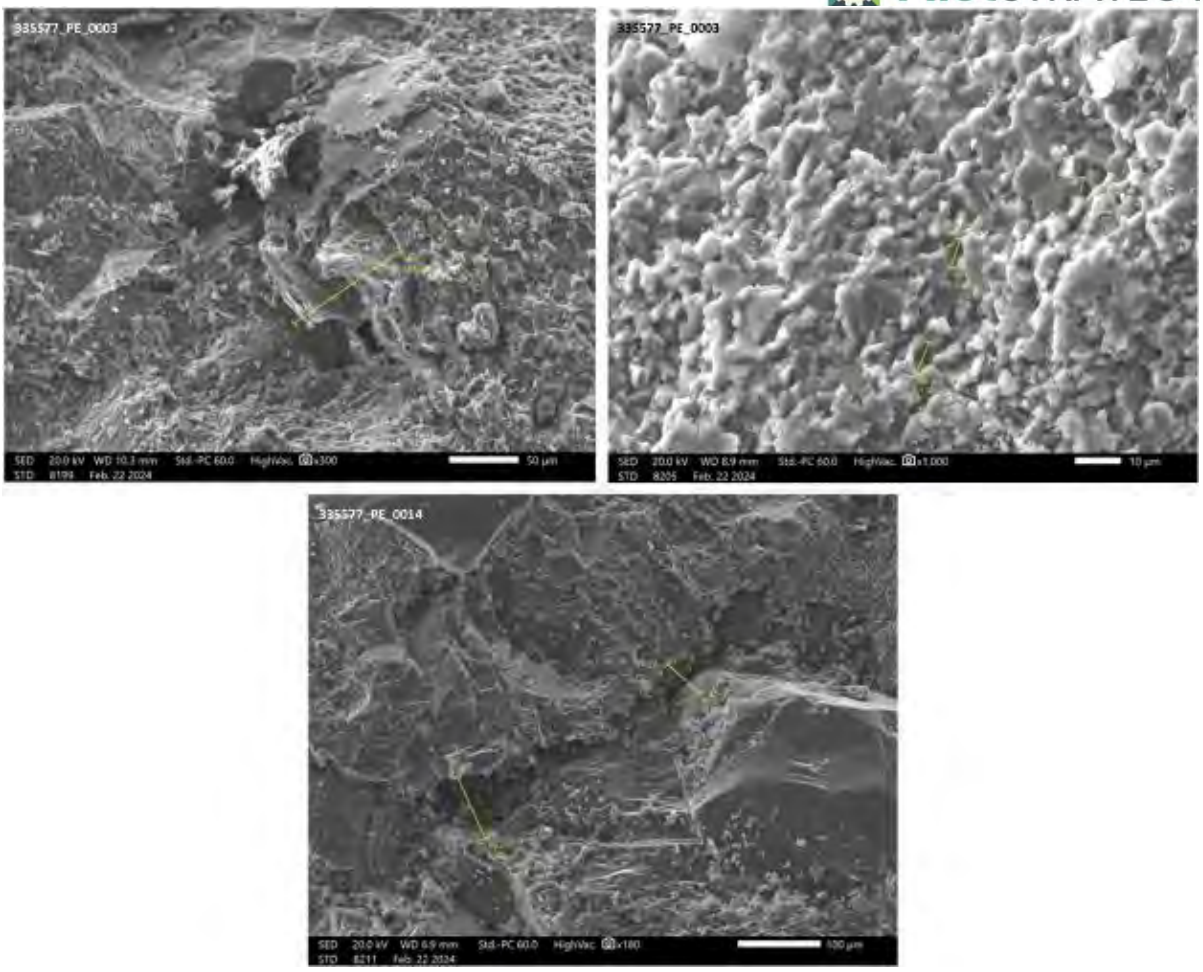

Figure Appendix. 10.9.73: SEM-EDS microphotographs showing the pores detected in sample Pent-3.

The PilotSTRATEGY project has received funding from the European Union's Horizon 2020 research and innovation programme under grant agreement No. 101022664

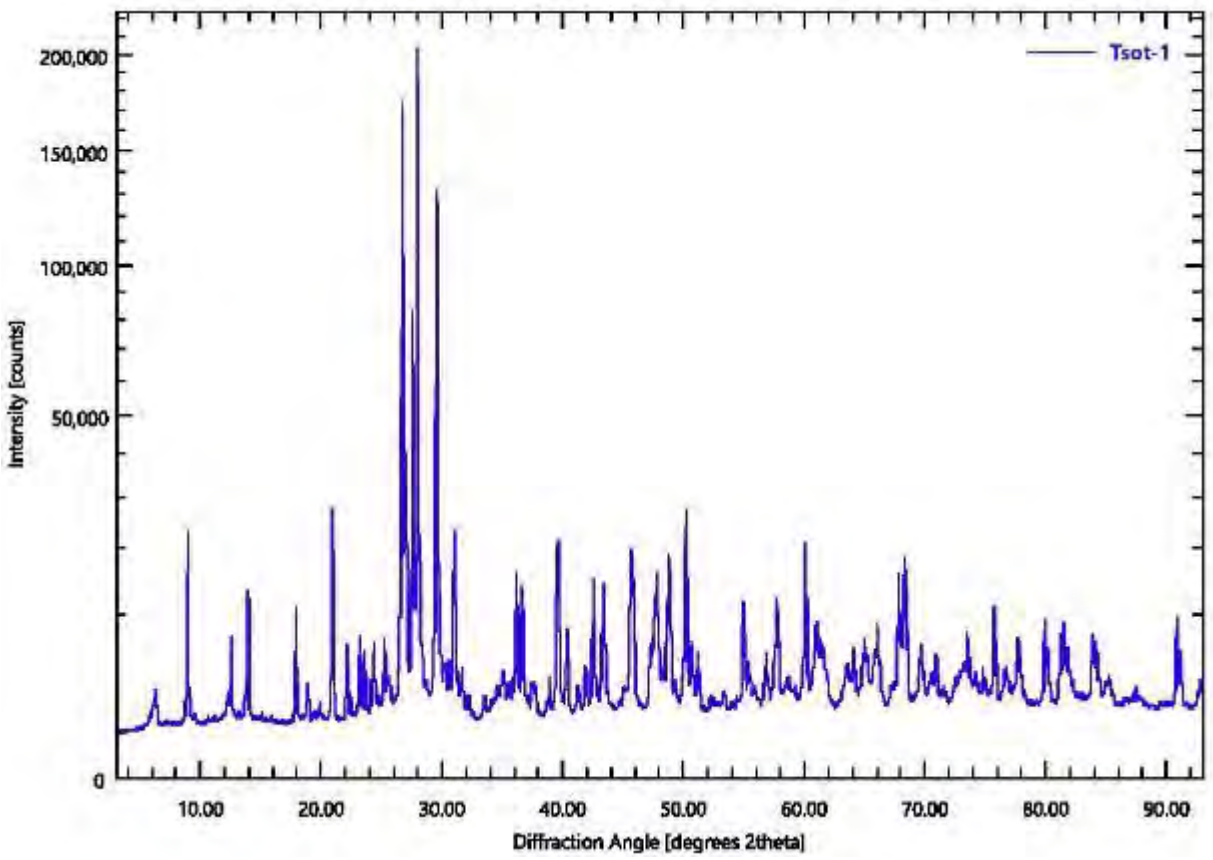

Figure Appendix. 10.9.74: Sample Tsot-1: Original X-Ray Diffraction (XRD) pattern - no Rietveld refinement

The PilotSTRATEGY project has received funding from the European Union's Horizon 2020 research and innovation programme under grant agreement No. 101022664

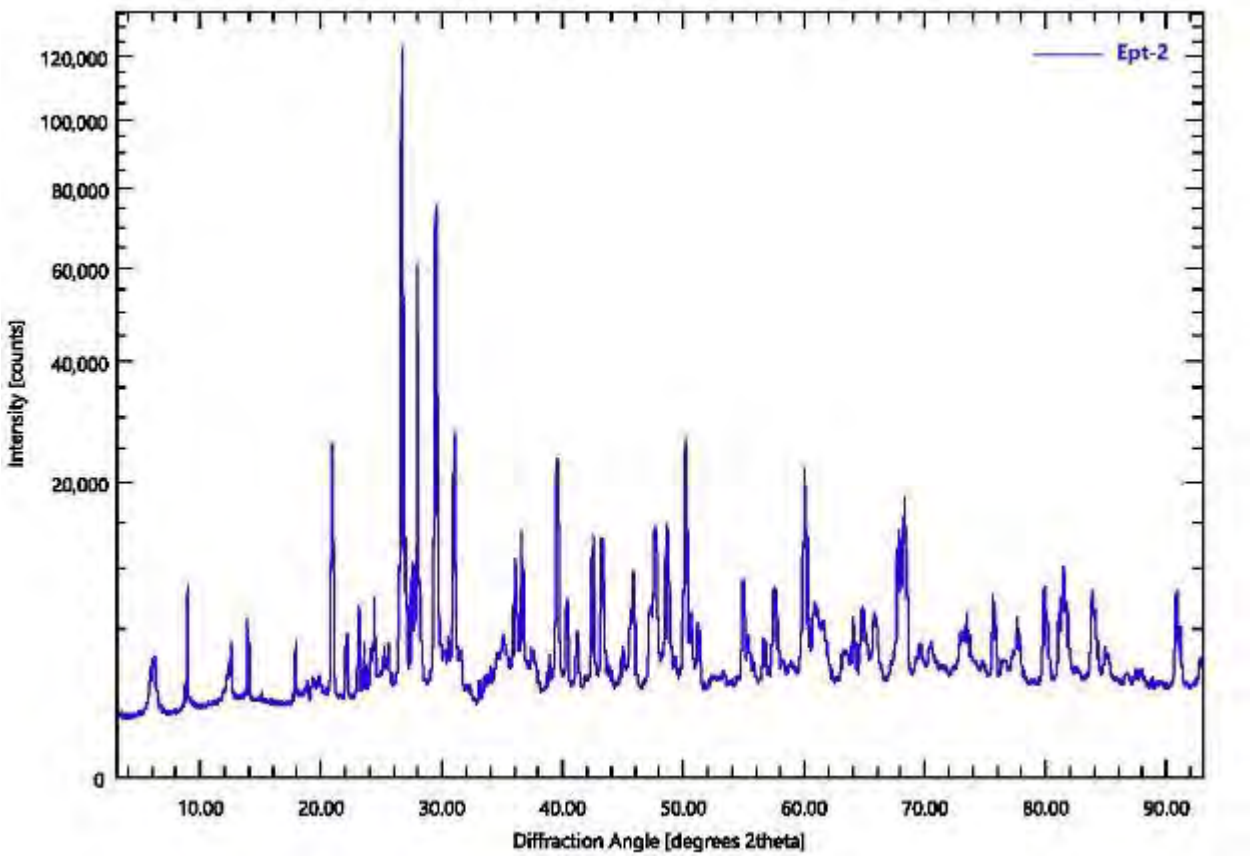

Figure Appendix. 10.9.75: Sample Ept-2: Original X-Ray Diffraction (XRD) pattern - no Rietveld refinement

The PilotSTRATEGY project has received funding from the European Union's Horizon 2020 research and innovation programme under grant agreement No. 101022664

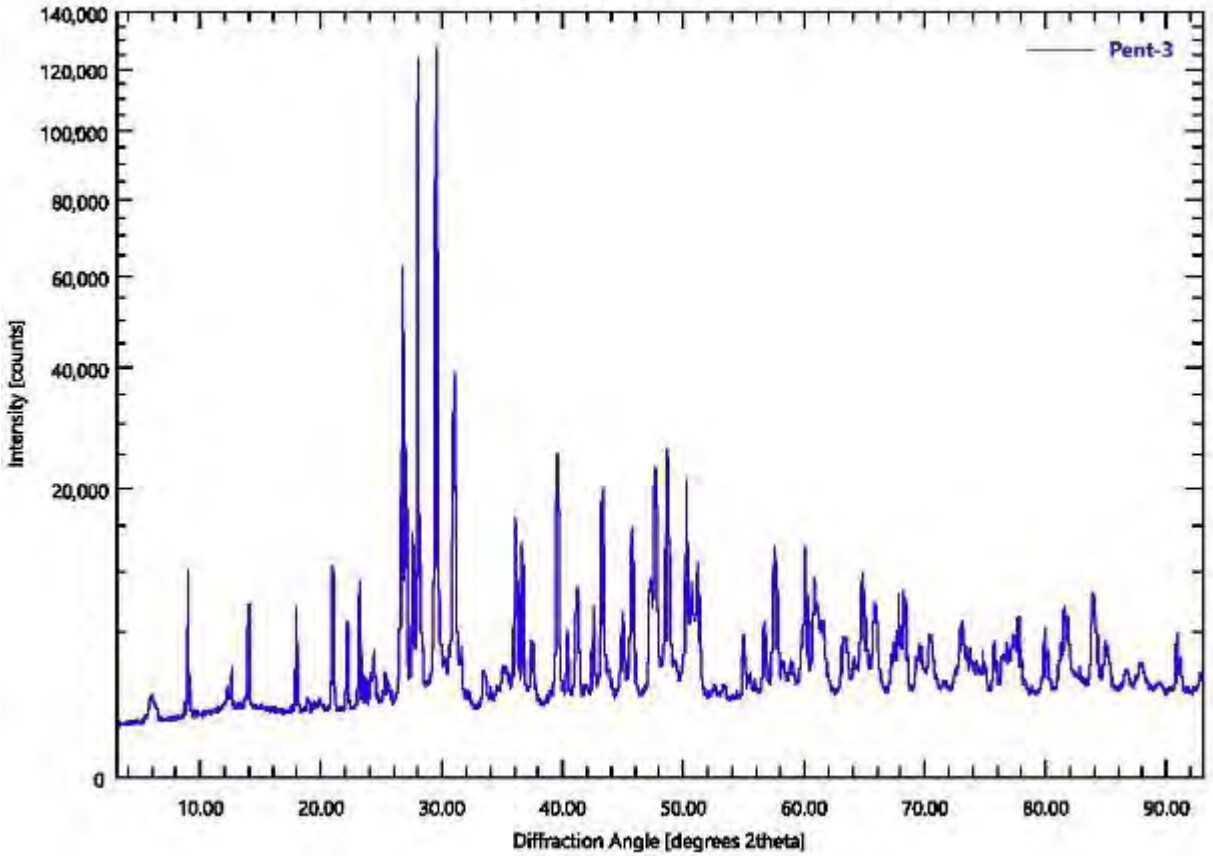

Figure Appendix. 10.9.76: Sample Pent-3: Original X-Ray Diffraction (XRD) pattern - no Rietveld refinement

The PilotSTRATEGY project has received funding from the European Union's Horizon 2020 research and innovation programme under grant agreement No. 101022664

Appendix VII Earthquake data record

Table Appendix 10.9.11: Number of earthquakes per time period for seismic periodicity calculations, West Macedonia.

Time Period 1900-1909								
Year	Month	Day	Time UTC	Magnitude	Latitude	Longitude	Depth km	Region
1906	9	28	2:30:00	5.7	40.900°N	20.700°E	20	
Time Period 1910-1919								
Year	Month	Day	Time UTC	Magnitude	Latitude	Longitude	Depth km	Region
1911	2	18	21:35:15	6.4	40.900°N	20.750°E	15	
1912	2	13	8:03:54	5.8	40.900°N	20.600°E	16	
1912	2	26	20:34:00	5.3	40.500°N	21.000°E	15	
1918	7	4	11:25:00	5.2	40.200°N	20.500°E	15	
1919	12	22	23:41:02	5.9	39.750°N	20.620°E	10	
Time Period 1920-1929								
Year	Month	Day	Time UTC	Magnitude	Latitude	Longitude	Depth km	Region
1920	9	14	2:08:45	5.3	40.880°N	21.600°E	15	
1920	11	29	15:48:06	5.2	40.560°N	21.290°E	12	
1922	12	7	16:37:01	5.5	40.010°N	21.510°E	25	
Time Period 1930-1939								
Year	Month	Day	Time UTC	Magnitude	Latitude	Longitude	Depth km	Region
1931	1	28	5:55:14	5.6	40.890°N	20.600°E	6	
Time Period 1940-1949								
Year	Month	Day	Time UTC	Magnitude	Latitude	Longitude	Depth km	Region
1941	6	24	15:15:58	5.0	40.500°N	21.000°E	15	
1943	3	25	2:51:06	5.5	40.410°N	21.890°E	59	
1948	3	26	3:02:09	5.0	40.600°N	21.470°E	39	
1949	6	26	5:42:34	5.1	39.800°N	20.470°E	52	
Time Period 1950-1959								
Year	Month	Day	Time UTC	Magnitude	Latitude	Longitude	Depth km	Region
1958	3	15	6:27:12	5.1	40.860°N	21.280°E	19	
Time Period 1960-1969								
Year	Month	Day	Time UTC	Magnitude	Latitude	Longitude	Depth km	Region
1960	5	26	5:10:17	6.4	40.560°N	20.630°E	20	
1960	5	26	5:37:58	4.5	40.600°N	20.700°E	10	
1960	7	9	22:42:57	4.7	40.740°N	20.710°E	32	
1962	2	16	13:46:29	4.6	40.500°N	20.500°E	15	
1962	6	28	6:51:08	5.0	40.760°N	20.690°E	40	
1964	2	27	1:37:51	4.2	40.540°N	21.400°E	44	

The PilotSTRATEGY project has received funding from the European Union's Horizon 2020 research and innovation programme under grant agreement No. 101022664

1964	12	15	8:20:44	4.2	40.500°N	20.900°E	33	
1966	1	17	8:39:43	4.7	40.090°N	20.570°E	46	
1966	2	14	13:45:34	4.2	40.100°N	21.000°E	0	
1966	8	8	11:43:41	4.2	40.700°N	21.600°E	47	
1967	5	1	8:15:47	4.7	39.750°N	21.420°E	38	
1967	5	4	17:11:03	4.3	39.800°N	21.100°E	0	
1967	5	4	13:13:36	4.4	39.780°N	21.520°E	60	
1967	12	2	14:18:57	4.4	40.700°N	21.400°E	33	
1967	12	30	21:27:20	4.6	40.660°N	21.470°E	34	
1968	2	21	1:00:42	4.0	40.600°N	21.000°E	1	
1969	10	12	13:34:20	5.1	39.760°N	20.550°E	46	
1969	10	13	1:02:31	5.7	39.780°N	20.590°E	27	
1969	11	16	9:33:41	4.2	40.090°N	20.970°E	5	
Time Period 1970-1979								
Year	Month	Day	Time UTC	Magnitude	Latitude	Longitude	Depth (km)	Region
1970	2	9	2:04:17	4.00	39.880°N	20.620°E	55	
1970	10	30	23:51:47	4.40	39.950°N	20.500°E	3	
1971	2	11	16:57:09	4.40	39.820°N	20.920°E	32	
1973	4	8	4:12:52	4.00	39.760°N	20.510°E	44	
1973	8	4	1:11:13	4.10	39.770°N	20.600°E	34	
1973	9	12	9:36:51	4.40	40.720°N	21.010°E	91	
1974	3	10	21:51:06	4.10	40.880°N	21.100°E	32	
1974	3	22	17:02:20	4.40	40.650°N	20.550°E	27	
1974	9	17	4:18:11	4.10	40.220°N	20.610°E	49	
1974	9	17	5:10:32	5.00	40.290°N	20.630°E	17	
1974	9	18	9:07:02	4.30	40.210°N	20.780°E	3	
1975	2	2	21:12:19	4.70	40.568°N	21.395°E	33	8 km WSW of Lechovo
1975	6	11	21:11:53	3.90	40.185°N	21.451°E	19	11 km N of Grevena
1975	9	20	21:48:36	3.60	40.588°N	21.499°E	14	0 km NE of Lechovo
1978	1	13	16:02:48	3.80	40.182°N	21.123°E	14	19 km WSW of Tsotili
1978	2	2	11:11:40	4.10	39.850°N	21.318°E	33	14 km NE of Metsovo
1979	3	29	2:19:04	3.30	39.990°N	21.113°E	10	25 km NNW of Metsovo
1979	10	14	15:00:05	4.30	40.200°N	21.441°E	54	11 km SW of Siatista
Time Period 1980-1989								
Year	Month	Day	Time UTC	Magnitude	Latitude	Longitude	Depth (km)	Region

The PilotSTRATEGY project has received funding from the European Union's Horizon 2020 research and innovation programme under grant agreement No. 101022664

1980	10	17	16:28:55	3.90	40.012°N	21.139°E	10	25 km WSW of Grevena
1981	1	31	15:33:14	3.70	40.641°N	21.636°E	10	5 km S of Xino Nero
1981	4	23	11:08:47	4.40	40.520°N	21.210°E	10	3 km NW of Maniakoi
1981	4	26	23:27:14	3.50	39.883°N	20.946°E	10	Greece-Albania border region
1981	5	17	7:47:44	3.30	40.596°N	21.546°E	10	4 km ENE of Lechovo
1981	7	3	22:06:28	3.60	39.829°N	21.282°E	11,2	10 km NE of Metsovo
1981	7	25	21:59:54	3.60	39.843°N	21.243°E	33	9 km NNE of Metsovo
1981	8	15	20:56:15	3.60	39.787°N	21.319°E	10	11 km E of Metsovo
1981	12	8	8:03:51	3.60	40.372°N	21.056°E	10	4 km S of Nestotio
1982	4	29	1:58:05	3.10	40.606°N	21.421°E	10	6 km WNW of Lechovo
1982	9	24	2:34:55	3.40	40.119°N	21.398°E	10	4 km NNW of Grevena
1982	10	25	23:41:11	4.40	40.598°N	21.625°E	33	7 km WSW of Filotas
1982	11	1	18:38:36	2.80	40.578°N	21.734°E	10	3 km WSW of Komnina
1982	12	10	17:22:17	3.00	40.130°N	21.341°E	10	8 km NW of Grevena
1983	6	5	23:51:34	3.50	40.464°N	21.707°E	9	6 km SSE of Ptolemaida
1984	2	7	18:28:18	3.90	40.513°N	21.656°E	10	1 km W of Ptolemaida
1984	2	9	1:51:06	4.30	40.477°N	21.623°E	10	4 km ESE of Anarachi
1984	4	4	16:42:45	3.10	39.955°N	21.573°E	10	Greece
1984	4	4	17:23:55	3.80	39.954°N	21.478°E	10	15 km SSE of Grevena
1984	8	27	0:00:24	3.00	40.429°N	21.217°E	16	4 km SW of Argos Orestiko
1984	10	24	9:05:30	3.80	40.063°N	21.624°E	10	16 km E of Grevena
1984	10	25	14:38:29	5.30	40.127°N	21.596°E	33	15 km ENE of Grevena
1984	10	25	14:49:14	4.00	40.073°N	21.541°E	10	9 km E of Grevena
1984	12	30	8:43:41	4.10	40.453°N	21.318°E	11,4	5 km E of Argos Orestiko
1985	2	16	5:50:56	4.00	39.790°N	21.731°E	10	12 km NE of Kastraki

The PilotSTRATEGY project has received funding from the European Union's Horizon 2020 research and innovation programme under grant agreement No. 101022664

1985	3	14	23:33:58	3.40	40.481°N	21.025°E	10	8 km NNW of Nestorio
1985	8	1	20:54:11	3.70	39.983°N	21.572°E	10	16 km SE of Grevena
1985	8	1	20:56:20	3.40	40.035°N	21.580°E	10	14 km ESE of Grevena
1986	4	15	22:10:11	2.70	40.608°N	21.385°E	10	9 km WNW of Lechovo
1986	8	2	5:03:13	2.70	40.434°N	21.597°E	9,8	6 km SSE of Anarachi
1986	12	27	22:40:28	3.00	40.448°N	20.933°E	10	11 km WNW of Nestorio
1987	1	22	10:22:18	3.10	40.560°N	21.658°E	10	5 km NNW of Ptolemaida
1987	2	19	22:41:25	4.10	40.200°N	21.560°E	35,4	7 km S of Siatista
1987	7	31	3:04:23	3.20	40.295°N	21.363°E	10	4 km NE of Tsotili
1987	11	13	5:11:49	3.80	40.423°N	20.937°E	10	10 km W of Nestorio
1987	12	22	21:57:42	3.30	39.894°N	21.614°E	10	17 km WSW of Deskati
1988	1	17	21:06:48	3.80	40.036°N	21.273°E	10	14 km WSW of Grevena
1988	3	12	16:43:35	3.40	40.258°N	21.111°E	6,8	17 km SSE of Nestorio
1988	4	27	11:06:03	3.30	40.418°N	21.267°E	10	4 km S of Argos Orestiko
1988	6	11	9:31:54	4.10	40.377°N	21.495°E	10	4 km NNW of Eratyra
1988	9	12	11:39:07	2.80	40.381°N	21.824°E	10	6 km NNE of Koila
1988	10	13	11:39:55	3.60	40.429°N	21.765°E	10	7 km W of Kleitos
1988	11	2	23:29:35	3.40	40.317°N	21.791°E	10	1 km S of Koila
1988	11	3	5:16:41	3.80	40.217°N	21.711°E	10	10 km W of Ano Komi
1989	1	20	18:31:34	3.60	40.392°N	21.402°E	10	10 km WNW of Eratyra
1989	2	10	14:17:24	3.20	40.430°N	21.254°E	9,3	2 km S of Argos Orestiko
1989	2	19	1:50:45	3.70	40.225°N	21.816°E	10	1 km W of Ano Komi
1989	2	19	8:52:31	3.70	40.244°N	21.877°E	10	4 km ENE of Ano Komi
1989	2	19	17:42:49	2.30	40.111°N	21.764°E	10	7 km SW of Aiani
1989	3	7	13:35:56	2.70	39.970°N	21.310°E	10	16 km SW of Grevena

The PilotSTRATEGY project has received funding from the European Union's Horizon 2020 research and innovation programme under grant agreement No. 101022664

1989	3	7	13:47:22	3.40	40.415°N	21.036°E	10	2 km W of Nestorio
1989	3	12	6:44:36	3.20	40.450°N	21.027°E	10	5 km NW of Nestorio
1989	4	12	18:22:05	3.20	40.342°N	21.842°E	10	4 km ENE of Koila
1989	5	4	5:33:19	2.90	40.585°N	21.398°E	10	7 km W of Lechovo
1989	5	4	5:56:48	2.50	40.577°N	21.410°E	10	7 km W of Lechovo
1989	5	25	1:48:47	3.30	40.640°N	21.623°E	10	5 km S of Xino Nero
1989	6	2	5:40:06	3.20	40.440°N	21.208°E	10	4 km WSW of Argos Orestiko
1989	6	17	15:36:08	3.10	39.850°N	21.050°E	19,4	14 km NW of Metsovo
1989	6	22	6:53:04	3.60	40.241°N	21.514°E	10	3 km SW of Siatista
1989	7	4	9:48:57	3.90	40.462°N	21.740°E	10	7 km SE of Ptolemaida
1989	7	23	8:30:10	3.60	40.381°N	21.683°E	10	10 km WNW of Koila
1989	7	29	10:38:08	3.90	40.373°N	21.499°E	16,9	3 km NNW of Eratyra
1989	8	2	9:47:43	3.80	40.332°N	21.780°E	10	0 km W of Koila
1989	8	28	9:44:45	3.40	40.417°N	21.681°E	10	10 km S of Ptolemaida
1989	8	28	10:40:33	3.60	40.405°N	21.850°E	10	3 km SSW of Kleitos
1989	11	18	7:19:16	3.10	40.033°N	21.875°E	10	5 km W of Livadero
1989	12	6	22:34:41	3.60	40.489°N	20.933°E	10	13 km NW of Nestorio
1989	12	7	16:00:05	3.10	40.276°N	21.313°E	10	1 km NNW of Tsotili
1989	12	15	12:47:00	3.50	40.490°N	21.820°E	10	7 km NNW of Kleitos
1989	12	18	3:52:29	2.00	40.375°N	21.358°E	10	12 km SE of Argos Orestiko
1989	12	20	12:33:34	3.70	40.449°N	21.836°E	10	2 km NW of Kleitos
1989	12	22	2:59:41	2.70	40.568°N	21.489°E	10	1 km S of Lechovo
1989	12	24	1:41:55	2.70	40.271°N	21.744°E	10	5 km of Kozani
Time Period 1990-1999								
Year	Month	Day	Time UTC	Magnitude	Latitude	Longitude	Depth (km)	Region
1990	1	9	12:23:28	2.90	40.517°N	21.877°E	10	9 km NNW of Akrini

The PilotSTRATEGY project has received funding from the European Union's Horizon 2020 research and innovation programme under grant agreement No. 101022664

1990	1	28	12:49:12	2.70	40.607°N	21.376°E	10	10 km WNW of Lechovo
1990	2	7	2:07:09	3.60	40.490°N	21.314°E	5	2 km SSW of Mavrochori
1990	2	7	20:14:05	3.30	40.465°N	21.278°E	10	2 km NE of Argos Orestiko
1990	2	8	1:43:16	3.30	40.556°N	21.375°E	5	6 km NE of Mavrochori
1990	2	17	20:16:33	3.10	40.491°N	21.546°E	10	1 km WNW of Emporio
1990	3	8	0:06:06	2.50	40.349°N	21.556°E	10	3 km N of GaLatitudeini
1990	3	14	17:40:55	3.10	39.927°N	21.748°E	5	5 km W of Deskati
1990	4	21	16:28:55	3.80	40.091°N	21.763°E	8,5	9 km SSW of Aiani
1990	5	16	11:49:03	2.60	39.899°N	21.448°E	5	20 km S of Grevena
1990	5	17	10:40:17	3.00	40.453°N	21.833°E	10	3 km NW of Kleitos
1990	6	22	3:24:03	2.50	40.127°N	21.201°E	10	Greece
1990	6	22	10:31:04	2.60	40.046°N	21.365°E	10	6 km SW of Grevena
1990	6	25	5:16:25	2.50	40.432°N	21.540°E	10	6 km SSW of Emporio
1990	7	2	0:46:20	2.30	40.103°N	21.604°E	10	15 km E of Grevena
1990	7	2	2:14:35	2.00	40.200°N	21.707°E	10	10 km WNW of Aiani
1990	7	16	9:02:59	3.30	40.046°N	21.161°E	5	23 km W of Grevena
1990	7	16	9:29:42	3.40	40.091°N	21.185°E	10	20 km W of Grevena
1990	8	17	14:26:27	2.30	40.588°N	21.590°E	10	8 km E of Lechovo
1990	8	19	1:36:30	2.50	40.440°N	21.447°E	33	10 km WSW of Emporio
1990	8	31	12:08:54	2.90	40.532°N	21.098°E	10	6 km WNWof Mesopotamia
1990	9	2	7:28:28	3.20	40.054°N	21.458°E	9,1	4 km SE of Grevena
1990	11	2	10:36:34	2.10	40.500°N	21.783°E	10	8 km E of Ptolemaida
1990	11	29	15:51:15	2.20	40.620°N	21.537°E	10	5 km NE of Lechovo
1991	2	7	1:32:58	3.10	40.578°N	21.476°E	10	1 km WSW of Lechovo
1991	2	20	9:18:31	2.70	40.427°N	21.837°E	10	1 km WSW of Kleitos

The PilotSTRATEGY project has received funding from the European Union's Horizon 2020 research and innovation programme under grant agreement No. 101022664

1991	2	21	10:05:19	3.50	40.419°N	21.791°E	10	5 km WSW of Kleitos
1991	5	20	14:34:14	2.70	40.134°N	21.295°E	10	Greece
1991	5	28	13:33:51	2.70	40.391°N	21.032°E	10	3 km SW of Nestorio
1991	7	31	14:12:25	2.50	40.541°N	21.368°E	10	5 km NE of Mavrochori
1991	8	5	23:00:55	2.40	40.597°N	21.246°E	10	6 km N of Chloi
1991	8	9	7:39:01	2.10	40.374°N	21.796°E	10	4 km N of Koila
1991	8	28	20:50:05	2.80	40.520°N	21.587°E	10	3 km NNE of Anarachi
1991	9	11	2:52:35	3.80	40.232°N	21.254°E	10,4	6 km WSW of Tsotili
1991	10	2	9:54:35	2.30	40.467°N	21.822°E	10	4 km NW of Kleitos
1991	10	19	4:57:40	3.90	40.641°N	21.363°E	10	12 km WNW of Lechovo
1991	10	19	17:22:15	3.80	40.642°N	21.359°E	11	12 km WNW of Lechovo
1991	11	17	2:18:47	2.20	40.152°N	21.494°E	5	9 km NE of Grevena
1991	11	24	0:39:37	2.10	40.268°N	21.758°E	5	4 km SW of Kozani
1991	12	26	10:10:08	3.00	40.451°N	21.086°E	5	4 km NNE of Nestorio
1992	2	21	12:19:33	3.10	39.894°N	21.582°E	10	19 km W of Deskati
1992	2	25	23:10:08	2.00	40.573°N	21.712°E	5	5 km S of Filotas
1992	2	27	10:33:58	3.00	40.454°N	21.868°E	5	2 km NNE of Kleitos
1992	2	27	10:46:26	2.70	40.435°N	21.735°E	10	10 km SSE of Ptolemaida
1992	3	23	1:41:15	3.10	40.131°N	21.241°E	5	16 km SSW of Tsostili
1992	4	10	15:11:30	2.60	39.918°N	21.796°E	10	1 km WSW of Deskati
1992	4	15	8:39:36	2.00	40.416°N	21.826°E	10	3 km WSW of Kleitos
1992	4	26	15:25:01	2.40	40.368°N	21.359°E	5	12 km NNE of Tsotili
1992	4	27	21:16:45	2.00	40.138°N	21.496°E	5	8 km NE of Grevena
1992	4	29	3:47:42	2.40	40.579°N	21.756°E	5	2 km SW of Komnina
1992	4	29	18:50:52	2.20	39.872°N	20.982°E	10	20 km WNW of Metsovo
1992	7	21	8:31:07	2.20	40.486°N	21.821°E	10	6 km NNW of Kleitos

The PilotSTRATEGY project has received funding from the European Union's Horizon 2020 research and innovation programme under grant agreement No. 101022664

1992	7	22	8:22:41	2.10	40.456°N	21.827°E	5	3 km NW of Kleitos
1992	7	27	8:23:47	2.00	40.449°N	21.822°E	10	3 km WNW of Kleitos
1992	9	22	13:32:35	3.70	40.363°N	21.280°E	11,7	10 km S of Argos Orestiko
1992	9	22	13:42:09	2.20	40.405°N	21.246°E	10	5 km SSW of Argos Orestiko
1992	10	6	14:52:37	2.10	39.790°N	21.026°E	10	Greece
1992	10	14	15:46:19	3.10	40.399°N	21.484°E	10	6 km NNW of Eratyra
1993	1	14	18:01:09	2.40	40.399°N	21.392°E	10	12 km WNW of Eratyra
1993	1	19	15:56:05	3.40	40.080°N	21.331°E	10	8 km W of Grevena
1993	2	14	9:43:31	2.00	40.495°N	21.845°E	10	7 km N of Kleitos
1993	2	17	9:16:09	2.10	40.492°N	21.859°E	10	6 km N of Kleitos
1993	2	18	9:04:16	2.00	40.478°N	21.880°E	10	5 km NNW of Akrini
1993	2	19	10:16:56	2.00	40.459°N	21.838°E	10	3 km NNW of Kleitos
1993	2	22	10:28:06	2.20	40.485°N	21.839°E	10	6 km NNW of Kleitos
1993	2	22	18:08:25	2.80	40.225°N	21.215°E	10	10 km WSW of Tsotili
1993	3	1	11:28:31	3.20	40.135°N	20.974°E	10	20 km ENE of Konitsa
1993	3	2	10:35:59	2.00	40.443°N	21.838°E	10	2 km NW of Kleitos
1993	3	4	7:36:39	2.60	40.025°N	21.580°E	10	14 km ESE of Grevena
1993	3	4	11:28:24	3.30	40.050°N	21.665°E	23,8	18 km SW of Aiani
1993	4	1	2:23:37	2.50	40.072°N	21.225°E	10	17 km W of Grevena
1993	4	1	14:40:58	3.20	40.457°N	21.579°E	10	3 km SSE of Emporio
1993	4	13	21:01:43	3.00	40.610°N	21.308°E	10	8 km NNE of Chloi
1993	4	22	7:51:33	2.10	40.454°N	21.681°E	10	6 km S of Ptolemaida
1993	4	25	5:10:01	2.50	40.051°N	21.723°E	10	14 km SSW of Aiani
1993	4	28	9:20:47	2.10	40.489°N	21.872°E	10	6 km N of Kleitos
1993	4	29	9:39:38	2.00	40.445°N	21.229°E	10	2 km WSW of Argos Orestiko
1993	4	30	9:30:52	2.00	40.469°N	21.747°E	10	7 km SE of Ptolemaida

The PilotSTRATEGY project has received funding from the European Union's Horizon 2020 research and innovation programme under grant agreement No. 101022664

1993	5	3	3:34:17	2.20	40.286°N	1.048°E	10	14 km S of Nestorio
1993	5	12	4:44:43	3.30	40.261°N	21.115°E	10	17 km SSE of Nestorio
1993	6	8	11:40:16	2.00	40.481°N	21.875°E	10	5 km NNE of Kleitos
1993	6	10	8:37:38	2.00	40.483°N	21.840°E	10	5 km NNE of Kleitos
1993	6	18	8:23:30	2.00	40.495°N	21.839°E	10	7 km NNW of Kleitos
1993	6	24	18:08:52	2.30	40.616°N	21.179°E	10	Greece
1993	6	25	6:49:58	2.90	40.416°N	21.206°E	10	Greece
1993	8	11	8:09:52	2.00	40.535°N	21.852°E	10	8 km SE of Komnina
1993	8	11	21:52:18	2.90	40.505°N	21.247°E	10	0 km NNE of Maniakoi
1993	8	12	8:41:29	2.40	40.517°N	21.866°E	10	9 km N of Kleitos
1993	8	22	8:38:35	2.40	40.489°N	21.831°E	5	6 km NNW of Kleitos
1993	8	27	16:11:28	2.30	40.447°N	21.253°E	5	Greece
1993	9	7	8:14:03	3.00	40.482°N	21.822°E	10	6 km NNW of Kleitos
1993	9	11	22:49:16	3.20	40.140°N	21.472°E	10	7 km NNE of Grevena
1993	9	23	11:09:52	2.30	40.488°N	21.848°E	10	6 km N of Kleitos
1993	9	24	13:03:29	2.50	40.363°N	21.328°E	5	11 km N of Tsotili
1993	9	25	3:37:47	2.40	40.572°N	21.059°E	10	8 km SE of Bilisht
1993	10	1	9:10:45	2.20	40.477°N	21.850°E	10	5 km N of Kleitos
1993	10	2	5:29:43	2.30	40.641°N	21.358°E	5	12 km WNW of Lechovo
1993	10	7	9:25:50	2.20	40.568°N	21.796°E	33	2 km SSE of Komnina
1993	10	7	11:00:30	2.30	40.481°N	21.294°E	5	4 km SSW of Mavrochori
1993	10	10	20:40:10	3.00	40.490°N	21.534°E	10	2 km W of Emporio
1993	10	12	9:35:37	3.10	40.440°N	21.833°E	5	2 km WNW of Kleitos
1993	10	13	9:21:41	3.00	40.455°N	21.869°E	10	2 km NNE of Kleitos
1993	10	13	9:44:11	3.10	40.467°N	21.771°E	10	8 km WNW of Kleitos
1993	10	15	9:21:20	3.00	40.425°N	21.864°E	10	0 km SE of Kleitos
1993	10	15	10:06:29	2.60	40.358°N	21.670°E	10	10 km WNW of Koila

The PilotSTRATEGY project has received funding from the European Union's Horizon 2020 research and innovation programme under grant agreement No. 101022664

1993	10	20	9:09:15	2.80	40.565°N	21.876°E	10	8 km ESE of Komnina
1993	10	24	8:40:59	2.00	40.417°N	21.805°E	10	4 km WSW of Kleitos
1993	10	31	1:47:57	2.10	40.624°N	21.482°E	10	4 km N of Lechovo
1993	11	1	8:23:36	2.40	39.857°N	21.597°E	10	15 km N of Kastraki
1993	11	23	10:59:55	2.10	40.454°N	21.882°E	5	2 km NW of Akrini
1993	12	4	16:53:51	3.20	40.167°N	21.473°E	10	9 km NNE of Grevena
1993	12	29	9:27:48	2.00	40.443°N	21.871°E	5	1 km NE of Kleitos
1994	1	4	9:46:30	2.10	40.487°N	21.872°E	10	6 km N of Kleitos
1994	1	4	11:34:41	2.20	40.460°N	21.778°E	10	7 km WNW of Kleitos
1994	1	18	9:10:45	2.00	40.367°N	21.818°E	33	4 km NNE of Koila
1994	1	28	8:19:06	2.00	40.093°N	21.847°E	5	8 km SSE of Aiani
1994	1	29	5:26:32	2.50	40.428°N	21.172°E	10	7 km WSW of Argos Orestiko
1994	1	29	5:30:44	3.50	40.361°N	21.221°E	5	10 km SSW of Argos Orestiko
1994	1	29	5:35:06	2.50	40.414°N	21.094°E	5	2 km E of Nestorio
1994	1	29	5:43:13	3.70	40.399°N	21.165°E	8,7	8 km E of Nestorio
1994	1	29	6:23:52	2.90	40.406°N	21.148°E	5	7 km E of Nestorio
1994	2	8	15:05:21	2.60	40.086°N	21.603°E	10	14 km E of Grevena
1994	2	11	9:28:26	2.10	40.488°N	21.858°E	5	6 km N of Kleitos
1994	2	20	4:42:30	3.20	40.290°N	21.424°E	5	8 km ENE of Tsotili
1994	2	29	0:20:07	3.30	40.612°N	21.699°E	10	1 km SSW of Filotas
1994	3	4	9:19:48	2.00	40.287°N	21.869°E	5	5 km ENE of Krokos
1994	3	15	9:58:44	2.20	40.394°N	21.801°E	10	6 km SW of Kleitos
1994	3	25	9:09:40	2.00	40.228°N	21.612°E	5	6 km ESE of Siatista
1994	3	29	11:26:12	2.00	40.440°N	21.825°E	10	2 km WNW of Kleitos
1994	3	30	15:15:48	2.30	40.030°N	21.424°E	10	6 km S of Grevena

The PilotSTRATEGY project has received funding from the European Union's Horizon 2020 research and innovation programme under grant agreement No. 101022664

1994	4	6	5:17:37	3.90	40.438°N	21.107°E	10	4 km NE of Nestorio
1994	4	14	8:23:45	2.10	40.126°N	21.707°E	5	10 km WSW of Aiani
1994	4	20	11:35:57	2.20	40.160°N	21.424°E	33	8 km N of Grevena
1994	4	21	11:30:29	2.10	40.474°N	21.873°E	2,1	4 km NNE of Kleitos
1994	5	1	8:20:17	2.40	39.903°N	21.438°E	10	?
1994	5	1	20:46:11	2.30	40.225°N	21.866°E	10	3 km E of Ano Komi
1994	5	18	7:58:14	2.30	40.408°N	21.868°E	10	2 km SSE of Kleitos
1994	5	20	0:08:45	2.80	40.554°N	21.663°E	10	4 km NNW of Ptolemaida
1994	6	8	11:26:38	2.10	40.381°N	21.739°E	5	7 km NW of Koila
1994	6	10	9:10:30	2.00	40.513°N	21.722°E	10	3 km E of Ptolemaida
1994	7	3	9:16:49	2.30	40.451°N	21.859°E	10	2 km N of Kleitos
1994	7	5	16:29:02	2.20	40.120°N	21.617°E	10	16 km ENE of Grevena
1994	7	12	17:35:25	2.90	40.635°N	21.528°E	10	6 km NNE of Lechovo
1994	7	12	13:02:54	2.10	40.588°N	21.435°E	10	4 km W of Lechovo
1994	9	7	2:10:45	3.70	40.209°N	21.762°E	14	5 km WSW of Ano Komi
1994	9	8	20:44:44	3.50	40.388°N	21.540°E	10	5 km NNE of Eratyra
1994	9	9	0:49:13	3.30	40.196°N	21.653°E	10	11 km SE of Siatista
1994	9	15	14:36:02	3.50	40.239°N	21.414°E	10	7 km ESE of Tsotili
1994	10	18	13:22:34	3.20	40.265°N	21.591°E	10	3 km E of Siatista
1994	10	18	13:33:26	3.20	40.221°N	21.594°E	10	6 km SE of Siatista
1994	10	27	21:32:48	3.10	40.332°N	20.990°E	10	10 km SW of Nestorio
1994	11	25	2:17:38	2.90	40.584°N	21.236°E	5	5 km NNW of Chloi
1994	11	27	12:01:07	2.10	40.049°N	21.634°E	10	18 km ESE of Grevena
1994	12	22	6:58:31	4.10	39.956°N	21.833°E	10	4 km NNE of Deskati
1994	12	22	20:42:13	2.60	39.981°N	21.713°E	5	10 km NW of Deskati
1995	1	30	8:08:50	2.30	40.273°N	21.808°E	10	1 km NW of Krokos

The PilotSTRATEGY project has received funding from the European Union's Horizon 2020 research and innovation programme under grant agreement No. 101022664

1995	2	5	13:13:40	2.00	40.333°N	21.088°E	5	9 km SSE of Nestorio
1995	2	5	13:46:13	3.20	40.373°N	21.171°E	10	10 km ESE of Nestorio
1995	2	5	14:12:40	2.10	40.383°N	21.064°E	10	3 km S of Nestorio
1995	2	7	13:46:46	2.50	39.876°N	21.757°E	10	Greece
1995	2	18	18:19:28	2.40	39.970°N	21.733°E	5	8 km NW of Deskati
1995	4	6	10:47:59	2.00	40.413°N	21.847°E	10	2 km SSW of Kleitos
1995	4	30	7:50:32	3.80	40.400°N	21.827°E	5	4 km SW of Kleitos
1995	5	1	22:47:21	2.90	39.818°N	21.064°E	10	11 km WNW of Metsovo
1995	5	13	8:42:11	4.10	40.070°N	21.739°E	10	12 km SSW of Aiani
1995	5	13	8:43:16	4.30	40.139°N	21.683°E	10	11 km WSW of Aiani
1995	5	13	8:47:12	6.60	40.149°N	21.695°E	14	10 km W of Aiani
1995	5	13	9:01:10	3.90	40.287°N	21.314°E	10	2 km NNW of Tsotili
1995	5	13	9:08:01	4.00	40.020°N	21.539°E	10	11 km SE of Grevena
1995	5	13	9:18:36	4.10	40.298°N	21.870°E	10	5 km NE of Krokos
1995	5	13	9:29:38	4.60	40.046°N	21.601°E	10	15 km ESE of Grevena
1995	5	13	9:32:48	3.90	40.279°N	21.421°E	10	8 km ENE of Tsotili
1995	5	13	9:37:06	3.70	40.413°N	21.705°E	10	11 km S of Ptolemaida
1995	5	13	9:55:26	2.60	40.142°N	21.773°E	10	4 km WSW of Aiani
1995	5	13	10:11:58	4.20	40.214°N	21.725°E	10	8 km W of Ano Komi
1995	5	13	10:26:14	3.90	40.135°N	21.474°E	10	6 km NE of Grevena
1995	5	13	10:29:46	3.40	40.214°N	21.605°E	10	7 km SE of Siatista
1995	5	13	10:33:04	4.30	40.181°N	21.745°E	10	6 km WNW of Aiani
1995	5	13	10:58:34	4.30	40.046°N	21.565°E	10	12 km ESE of Grevena
1995	5	13	11:06:02	3.60	40.212°N	21.417°E	10	9 km SE of Tsotili
1995	5	13	11:43:28	5.00	40.078°N	21.711°E	10	13 km SW of Aiani

The PilotSTRATEGY project has received funding from the European Union's Horizon 2020 research and innovation programme under grant agreement No. 101022664

1995	5	13	13:32:13	3.40	40.507°N	21.312°E	10	0 km SW of Mavrochori
1995	5	13	14:16:29	4.40	40.027°N	21.749°E	10	12 km NNW of Deskati
1995	5	13	15:04:56	3.40	40.364°N	21.421°E	10	8 km WNW of Eratyra
1995	5	13	15:25:40	4.10	39.981°N	21.247°E	10	19 km SW of Grevena
1995	5	13	16:14:31	3.10	40.310°N	21.640°E	10	7 km E of GaLatitudeini
1995	5	13	16:38:36	3.40	40.181°N	21.693°E	10	10 km W of Aiani
1995	5	13	17:10:57	3.90	40.244°N	21.581°E	10	3 km ESE of Siatista
1995	5	13	17:54:51	4.20	39.819°N	21.789°E	10	11 km S of Deskati
1995	5	13	18:05:58	4.80	40.041°N	21.594°E	10	15 km ESE of Grevena
1995	5	13	18:35:38	3.80	40.191°N	21.708°E	10	9 km WNW of Aiani
1995	5	13	18:54:55	3.80	39.882°N	21.445°E	10	22 km S of Grevena
1995	5	13	19:00:13	4.20	40.065°N	21.676°E	10	16 km SW of Aiani
1995	5	13	19:00:46	4.70	39.958°N	21.819°E	10	3 km N of Deskati
1995	5	13	19:29:38	3.20	40.244°N	21.729°E	10	7 km WSW of Krokos
1995	5	13	19:37:11	4.20	40.189°N	21.818°E	10	2 km N of Aiani
1995	5	13	21:02:18	3.90	40.124°N	21.498°E	10	7 km NE of Grevena
1995	5	13	21:40:50	3.70	40.220°N	21.718°E	10	9 km W of Ano Komi
1995	5	13	23:27:57	3.90	40.215°N	21.695°E	10	11 km W of Ano komi
1995	5	13	23:46:57	4.20	40.001°N	21.773°E	10	9 km NNW of Deskati
1995	5	13	23:53:42	4.60	40.069°N	21.564°E	10	11 km E of Grevena
1995	5	13	23:56:25	4.80	39.999°N	21.624°E	10	17 km WNW of Deskati
1995	5	14	1:02:57	4.30	40.087°N	21.545°E	10	10 km E of Grevena
1995	5	14	2:38:55	4.30	40.140°N	21.543°E	10	11 km ENE of Grevena
1995	5	14	2:46:58	4.80	40.079°N	21.589°E	10,5	13 km E of Grevena
1995	5	14	3:02:26	4.60	40.024°N	21.630°E	10	18 km ESE of Grevena

The PilotSTRATEGY project has received funding from the European Union's Horizon 2020 research and innovation programme under grant agreement No. 101022664

1995	5	14	3:09:35	4.60	40.073°N	21.583°E	10	13 km E of Grevena
1995	5	14	4:29:25	3.70	40.329°N	21.615°E	10	5 km E of GaLatitudeini
1995	5	14	5:09:30	3.30	40.295°N	21.882°E	10	6 km ENE of Krokos
1995	5	14	5:14:50	4.10	40.002°N	21.786°E	10	8 km NNW of Deskati
1995	5	14	5:59:15	4.80	40.017°N	21.567°E	10	14 km ESE of Grevena
1995	5	14	6:11:37	4.10	39.882°N	21.501°E	10	20 km NNW of Kastraki
1995	5	14	6:27:05	4.10	39.870°N	21.295°E	10	14 km NE of Metsovo
1995	5	14	7:30:08	4.20	40.054°N	21.516°E	10	8 km ESE of Grevena
1995	5	14	8:15:42	3.50	40.240°N	21.658°E	10	9 km ESE of Siatista
1995	5	14	8:35:09	4.50	40.150°N	21.688°E	10	11 km W of Aiani
1995	5	14	9:45:39	4.40	40.167°N	21.750°E	10	5 km W of Aiani
1995	5	14	10:21:13	3.80	40.416°N	21.413°E	10	11 km NW of Eratyra
1995	5	14	11:55:21	3.30	40.175°N	21.808°E	10	1 km NW of Aiani
1995	5	14	13:34:55	3.40	40.273°N	21.650°E	10	9 km E of Siatista
1995	5	14	14:46:56	4.40	40.181°N	21.706°E	10	9 km W of Aiani
1995	5	14	16:48:56	3.40	40.167°N	21.578°E	10	10 km SSE of Siatista
1995	5	14	17:27:26	3.50	40.378°N	21.679°E	10	10 km WNW of Koila
1995	5	14	18:32:04	3.80	40.246°N	21.708°E	10	9 km SW of Kozani
1995	5	14	21:31:12	4.30	40.118°N	21.617°E	10	16 km ENE of Grevena
1995	5	15	0:24:18	4.30	40.234°N	21.515°E	10	3 km SW of Siatista
1995	5	15	1:20:14	4.40	40.179°N	21.457°E	10	10 km NNE of Grevena
1995	5	15	2:13:43	3.60	39.964°N	21.555°E	10	17 kn SE of Grevena
1995	5	15	3:31:43	3.40	40.114°N	21.713°E	10	10 km WSW of Aiani
1995	5	15	4:13:55	5.20	40.034°N	21.655°E	13,9	18 km NW of Deskati
1995	5	15	5:54:47	3.90	40.055°N	21.491°E	10	6 km ESE of Grevena
1995	5	15	6:15:10	3.50	40.360°N	21.391°E	10	10 km W of Eratyra

The PilotSTRATEGY project has received funding from the European Union's Horizon 2020 research and innovation programme under grant agreement No. 101022664

1995	5	15	8:16:57	4.60	40.019°N	21.488°E	10	8 km SE of Grevena
1995	5	15	9:19:42	4.50	40.113°N	21.588°E	10	14 km ENE of Grevena
1995	5	15	11:42:54	4.10	39.910°N	21.806°E	10	1 km SSW of Deskati
1995	5	15	12:03:42	3.40	40.177°N	21.488°E	10	10 km SSW of Siatista
1995	5	15	13:02:30	3.60	40.335°N	21.413°E	10	8 km W of Eratyra
1995	5	15	13:50:51	3.60	40.171°N	21.660°E	10	13 km W of Aiani
1995	5	15	13:59:13	4.00	40.286°N	21.577°E	10	3 km NE of Siatista
1995	5	15	15:46:23	3.40	40.108°N	21.756°E	10	8 km SW of Aiani
1995	5	15	16:18:32	4.20	40.024°N	21.721°E	10	13 km NW of Deskati
1995	5	15	17:05:41	4.50	40.067°N	21.558°E	10	11 km E of Grevena
1995	5	15	20:00:04	4.10	40.098°N	21.717°E	10	11 km SW of Aiani
1995	5	15	22:47:32	4.40	40.193°N	21.661°E	10	12 km SE of Siatista
1995	5	16	4:37:27	4.70	40.001°N	21.529°E	10	12 km SE of Grevena
1995	5	16	5:04:09	4.10	39.778°N	21.631°E	10	6 km N of Kastraki
1995	5	16	7:17:23	4.10	39.946°N	21.503°E	10	16 km SSE of Grevena
1995	5	16	12:31:20	4.10	40.112°N	21.709°E	10	11 km WSW of Aiani
1995	5	16	17:57:50	4.50	40.005°N	21.676°E	10	14 km NW of Deskati
1995	5	16	21:54:16	4.50	39.953°N	21.616°E	10	16 km W of Deskati
1995	5	16	23:00:40	4.80	40.016°N	21.586°E	10	15 km ESE of Grevena
1995	5	16	23:57:27	4.80	40.061°N	21.678°E	16,3	16 km SW of Aiani
1995	5	17	1:55:19	3.40	40.178°N	21.599°E	10	10 km SSE of Siatista
1995	5	17	3:54:52	4.50	40.009°N	21.740°E	10	11 km NNW of Deskati
1995	5	17	4:14:25	5.20	40.101°N	21.632°E	18,6	17 km WSW of Aiani
1995	5	17	4:37:48	4.00	40.355°N	21.655°E	10	9 km ENE of GaLatitudeini
1995	5	17	4:48:33	4.50	40.017°N	21.639°E	10	17 km NW of Deskati

The PilotSTRATEGY project has received funding from the European Union's Horizon 2020 research and innovation programme under grant agreement No. 101022664

1995	5	17	7:19:26	4.20	39.990°N	21.740°E	10	9 km NW of Deskati
1995	5	17	9:45:07	5.10	39.992°N	21.557°E	10	15 km SE of Grevena
1995	5	17	10:07:39	4.00	39.949°N	21.469°E	10	15 km SSE of Grevena
1995	5	17	10:18:41	4.10	39.925°N	21.662°E	10	12 km W of Deskati
1995	5	17	10:21:38	3.30	40.463°N	21.629°E	10	5 km SE of Anarachi
1995	5	17	11:25:26	3.90	39.981°N	21.802°E	10	6 km N of Deskati
1995	5	17	11:28:37	4.30	39.976°N	21.667°E	10	13 km WNW of Deskati
1995	5	17	11:36:46	4.00	39.811°N	21.827°E	10	12 km S of Deskati
1995	5	17	15:37:57	4.30	39.901°N	21.762°E	10	4 km WSW of Deskati
1995	5	17	16:03:14	3.30	40.000°N	21.520°E	10	12 km SE of Grevena
1995	5	17	16:59:55	3.70	39.965°N	21.523°E	10	15 km SSE of Grevena
1995	5	17	23:51:46	3.80	40.001°N	21.684°E	10	13 km NW of Deskati
1995	5	18	3:48:58	3.80	40.080°N	21.853°E	10	9 km WNW of Livadero
1995	5	18	6:22:54	4.60	40.079°N	21.547°E	10	10 km E of Grevena
1995	5	18	7:21:05	3.80	40.002°N	21.651°E	10	16 km WNW of Deskati
1995	5	18	12:39:34	3.50	40.006°N	21.553°E	10	13 km SE of Grevena
1995	5	18	15:08:40	4.20	39.938°N	21.659°E	10	13 km W of Deskati
1995	5	19	1:03:40	4.20	39.947°N	21.697°E	10	Greece
1995	5	19	1:30:23	4.20	40.062°N	21.804°E	10	11 km S of Aiani
1995	5	19	1:33:54	4.20	39.986°N	21.803°E	10	6 km N of Deskati
1995	5	19	6:48:49	5.10	40.073°N	21.564°E	10	11 km E of Grevena
1995	5	19	7:36:47	4.10	40.031°N	21.563°E	10	13 km ESE of Grevena
1995	5	19	7:43:43	4.00	40.049°N	21.533°E	10	9 km ESE of Grevena
1995	5	19	12:29:51	4.10	39.987°N	21.835°E	10	7 km NNE of Deskati
1995	5	19	21:44:50	4.10	39.975°N	21.612°E	10	17 km WNW of Deskati

The PilotSTRATEGY project has received funding from the European Union's Horizon 2020 research and innovation programme under grant agreement No. 101022664

1995	5	19	23:15:52	4.00	39.927°N	21.646°E	10	14 km W of Deskati
1995	5	20	17:04:42	4.00	40.049°N	21.468°E	10	5 km SE of Grevena
1995	5	20	20:09:29	4.50	39.939°N	21.639°E	10	14 km W of Deskati
1995	5	20	20:35:46	4.00	40.014°N	21.619°E	10	18 km ESE of Grevena
1995	5	20	21:06:22	4.40	39.930°N	21.623°E	10	16 km W of Deskati
1995	5	20	21:19:32	3.90	40.010°N	21.876°E	10	6 km WSW of Livadero
1995	5	20	22:24:57	3.40	39.818°N	21.771°E	10	12 km SSW of Deskati
1995	5	21	2:06:05	3.10	39.969°N	21.531°E	5	15 km SE of Grevena
1995	5	21	4:04:23	4.60	40.033°N	21.620°E	10	17 km ESE of Grevena
1995	5	21	4:42:56	3.00	40.115°N	21.690°E	10	12 km WSW of Aiani
1995	5	21	5:05:44	3.00	40.037°N	21.573°E	10	13 km ESE of Grevena
1995	5	21	7:09:42	2.90	39.999°N	21.807°E	10	8 km N of Deskati
1995	5	21	7:21:30	3.20	40.130°N	21.843°E	5	4 km SSE of Aiani
1995	5	21	16:28:37	3.70	39.934°N	21.649°E	10	13 km W of Deskati
1995	5	21	20:38:28	4.10	40.115°N	21.479°E	10	5 km NE of Grevena
1995	5	21	21:10:09	3.70	39.975°N	21.738°E	5	8 km NW of Deskati
1995	5	22	3:45:58	3.50	40.144°N	21.813°E	10	2 km SSW of Aiani
1995	5	22	12:22:22	3.90	40.045°N	21.600°E	10	15 km ESE of Grevena
1995	5	22	17:46:51	4.10	40.221°N	21.530°E	10	4 km SSW of Siatista
1995	5	22	20:21:34	4.30	40.147°N	21.588°E	10	13 km SSE of Siatista
1995	5	22	21:10:32	4.10	39.913°N	21.653°E	10	13 km W of Deskati
1995	5	22	22:30:39	3.60	40.020°N	21.793°E	10	10 km N of Deskati
1995	5	23	4:37:38	4.40	40.110°N	21.704°E	10	11 lm WSW of Aiani
1995	5	23	5:51:57	4.30	40.105°N	21.857°E	10	7 km SSE of Aiani
1995	5	23	20:09:52	4.50	39.924°N	21.625°E	10	15 km W of Deskati

The PilotSTRATEGY project has received funding from the European Union's Horizon 2020 research and innovation programme under grant agreement No. 101022664

1995	5	23	20:59:48	4.20	39.834°N	21.664°E	10	13 km NNE of Kastraki
1995	5	24	1:00:37	4.00	40.027°N	21.596°E	10	15 km ESE of Grevena
1995	5	24	5:22:43	3.80	40.201°N	21.581°E	10	Greece
1995	5	24	5:43:24	3.90	40.168°N	21.518°E	5	10 km SSW of Siatista
1995	5	24	6:01:55	3.70	39.975°N	21.599°E	10	18 km WNW of Deskati
1995	5	24	6:18:00	2.80	39.957°N	21.668°E	5	12 km WNW of Deskati
1995	5	24	6:19:22	3.00	39.940°N	21.534°E	5	Greece
1995	5	24	6:24:08	4.20	39.997°N	21.564°E	5	15 km SE of Grevena
1995	5	24	6:30:18	3.40	40.027°N	21.615°E	10	Greece
1995	5	24	7:00:02	3.90	40.017°N	21.510°E	10	10 km SE of Grevena
1995	5	24	8:00:25	3.60	39.995°N	21.604°E	5	Greece
1995	5	24	8:20:10	3.00	40.091°N	21.620°E	5	16 km E of Grevena
1995	5	24	8:30:26	3.80	40.119°N	21.512°E	10	8 km ENE of Grevena
1995	5	24	8:57:26	2.90	40.158°N	21.600°E	5	12 km SSE of Siatista
1995	5	24	9:13:59	2.80	40.100°N	21.866°E	5	8 km SSE of Aiani
1995	5	24	9:21:49	3.10	40.107°N	21.797°E	10	6 km SSW of Aiani
1995	5	24	10:03:12	3.00	40.076°N	21.552°E	5	10 km E of Grevena
1995	5	24	10:25:07	3.00	40.121°N	21.469°E	5	5 km NE of Grevena
1995	5	24	10:45:37	3.50	40.129°N	21.514°E	5	Greece
1995	5	24	1:43:52	3.30	39.990°N	21.582°E	5	16 km SE of Grevena
1995	5	24	14:00:57	3.00	40.026°N	21.718°E	10	13 km NW of Deskati
1995	5	24	14:14:47	3.00	40.006°N	21.681°E	10	14 km NW of Deskati
1995	5	24	14:54:22	4.10	39.979°N	21.607°E	10	18 km WNW of Deskati
1995	5	24	15:07:38	2.80	40.001°N	21.548°E	5	13 km SE of Grevena
1995	5	24	15:58:58	3.10	39.979°N	21.635°E	10	16 km WNW of Deskati
1995	5	24	16:18:56	3.10	40.112°N	21.573°E	5	15 km ENE of Grevena
1995	5	24	17:34:26	4.00	40.055°N	21.614°E	5	16 km ESE of Gevena

The PilotSTRATEGY project has received funding from the European Union's Horizon 2020 research and innovation programme under grant agreement No. 101022664

1995	5	24	19:17:20	2.80	40.132°N	21.572°E	5	13 km ENE of Grevena
1995	5	24	19:29:07	3.20	40.131°N	21.707°E	5	10 km WSW of Aiani
1995	5	24	19:45:11	3.00	40.080°N	21.549°E	5	10 km E of Grevena
1995	5	24	20:07:59	2.90	40.116°N	21.619°E	10	16 km ENE of Grevena
1995	5	24	21:22:44	3.20	40.120°N	21.590°E	5	14 km ENE of Grevena
1995	5	24	21:35:23	2.80	40.062°N	21.613°E	10	16 km E of Grevena
1995	5	24	22:09:19	3.00	40.120°N	21.781°E	10	5 km SW of Aiani
1995	5	25	1:05:02	3.20	40.071°N	21.643°E	5	18 km SW of Aiani
1995	5	25	1:40:29	3.30	40.201°N	21.643°E	5	10 km SE of Siatista
1995	5	25	2:11:07	3.10	40.117°N	21.813°E	5	5 km S of Aiani
1995	5	25	4:05:45	3.90	40.096°N	21.578°E	10	12 km E of Grevena
1995	5	25	4:35:07	3.10	40.093°N	21.658°E	5	15 km WSW of Aiani
1995	5	25	8:30:22	3.70	40.027°N	21.655°E	5	17 km NW of Deskati
1995	5	25	8:48:53	3.70	40.097°N	21.722°E	5	11 km SW of Aiani
1995	5	25	9:05:10	2.90	40.064°N	21.451°E	5	3 km SE of Grevena
1995	5	25	14:08:05	3.00	40.098°N	21.789°E	10	7 km SSW of Aiani
1995	5	25	14:24:25	2.90	40.017°N	21.633°E	5	18 km NW of Deskati
1995	5	25	14:55:34	3.10	39.987°N	21.666°E	5	14 km WNW of Deskati
1995	5	25	16:09:39	2.30	40.067°N	21.622°E	5	16 km E of Grevena
1995	5	25	17:47:30	2.90	39.996°N	21.737°E	5	10 km NW of Deskati
1995	5	25	17:50:32	3.00	39.974°N	21.616°E	5	17 km WNW of Deskati
1995	5	25	18:15:08	3.00	40.079°N	21.699°E	5	13 km SW of Aiani
1995	5	25	18:24:43	3.10	40.040°N	21.797°E	5	12 km W of Livadero
1995	5	25	21:37:20	3.30	40.057°N	21.701°E	5	15 km SW of Aiani
1995	5	25	21:41:08	2.90	40.009°N	21.754°E	5	10 km NNW of Deskati

The PilotSTRATEGY project has received funding from the European Union's Horizon 2020 research and innovation programme under grant agreement No. 101022664

1995	5	25	22:42:18	3.00	40.112°N	21.721°E	5	10 km SW of Aiani
1995	5	25	23:12:16	3.50	40.173°N	21.808°E	5	1 km NW of Aiani
1995	5	26	1:38:33	2.90	40.060°N	21.645°E	5	18 km E of Grevena
1995	5	26	2:43:39	2.90	40.150°N	21.804°E	10	2 km SW of Aiani
1995	5	26	5:50:49	3.00	40.004°N	21.477°E	33	9 km SSE of Grevena
1995	5	26	6:46:22	3.00	40.042°N	21.666°E	5	17 km NW of Deskati
1995	5	26	11:31:16	3.10	40.267°N	21.706°E	10	7 km WSW of Kozani
1995	5	26	14:52:52	3.00	40.055°N	21.798°E	10	12 km S of Aiani
1995	5	26	15:54:54	3.90	40.153°N	21.471°E	10	8 km NNE of Grevena
1995	5	26	18:38:39	3.00	40.188°N	21.580°E	10	8 km SSE of Siatista
1995	5	26	21:34:10	3.10	40.293°N	21.699°E	5	7 km W of Kozani
1995	5	26	21:52:57	3.10	40.124°N	21.751°E	5	7 km SW of Aiani
1995	5	26	22:27:18	3.00	40.066°N	21.602°E	5	15 km E of Grevena
1995	5	26	22:58:52	2.90	40.082°N	21.648°E	5	Greece
1995	5	27	1:10:08	2.90	40.106°N	21.711°E	5	11 km SW of Aiani
1995	5	27	2:26:13	2.90	40.090°N	21.697°E	5	13 km SW of Aiani
1995	5	27	3:07:56	2.90	40.164°N	21.743°E	5	6 km W of Aiani
1995	5	27	4:09:59	2.90	40.149°N	21.621°E	5	14 km SSE of Siatista
1995	5	27	4:27:34	3.00	40.293°N	21.624°E	5	6 km ESE of GaLatitudeini
1995	5	27	4:29:17	3.10	40.076°N	21.837°E	5	9 km S of Aiani
1995	5	27	5:52:55	3.30	40.001°N	21.596°E	5	17 km ESE of Grevena
1995	5	27	9:06:10	3.00	40.148°N	21.763°E	5	5 km WSW of Aiani
1995	5	27	15:04:59	2.90	39.984°N	21.494°E	5	12 km SSE of Grevena
1995	5	27	16:17:28	3.00	40.159°N	21.774°E	10	3 km W of Aiani
1995	5	27	17:00:46	2.90	40.098°N	21.730°E	10	10 km SW of Aiani
1995	5	27	19:35:24	2.80	40.127°N	21.634°E	5	16 km WSW of Aiani
1995	5	27	23:53:15	2.90	40.116°N	21.649°E	5	15 km WSW of Aiani

The PilotSTRATEGY project has received funding from the European Union's Horizon 2020 research and innovation programme under grant agreement No. 101022664

1995	5	28	1:02:00	3.10	40.062°N	21.732°E	5	13 km SSW of Aiani
1995	5	28	1:12:07	3.10	40.087°N	21.718°E	5	12 km SW of Aiani
1995	5	28	4:18:15	3.10	39.959°N	21.744°E	5	6 km NW of Deskati
1995	5	28	5:14:44	3.20	40.152°N	21.721°E	5	8 km W of Aiani
1995	5	28	5:51:04	2.90	40.065°N	21.682°E	5	16 km SW of Aiani
1995	5	28	6:00:01	3.00	39.979°N	21.612°E	5	18 km WNW of Deskati
1995	5	28	6:08:05	3.00	40.002°N	21.569°E	5	15 km SE of Grevena
1995	5	28	20:32:11	3.10	40.294°N	21.732°E	10	4 km W of Kozani
1995	5	29	2:07:02	2.90	40.038°N	21.603°E	5	15 km ESE of Grevena
1995	5	29	2:55:56	2.90	40.033°N	21.663°E	5	17 km NW of Deskati
1995	5	29	3:16:22	2.80	40.141°N	21.491°E	5	8 km NE of Grevena
1995	5	29	3:47:05	2.90	40.004°N	21.517°E	5	11 km SE of Grevena
1995	5	29	8:21:50	3.10	40.100°N	21.551°E	10	10 km E of Grevena
1995	5	29	11:10:30	2.90	40.001°N	21.811°E	5	8 km N of Deskati
1995	5	29	16:51:07	3.00	40.145°N	21.600°E	5	Greece
1995	5	29	18:01:56	3.10	40.135°N	21.572°E	5	13 km ENE of Grevena
1995	5	29	18:58:22	3.10	40.028°N	21.540°E	5	11 km ESE of Grevena
1995	5	29	20:08:13	3.40	40.169°N	21.612°E	5	11 km SSE of Siatista
1995	5	30	0:55:57	2.90	40.158°N	21.505°E	10	10 km NE of Grevena
1995	5	30	2:01:37	3.00	40.126°N	21.559°E	5	12 km ENE of Grevena
1995	5	30	2:14:33	2.90	40.048°N	21.622°E	5	17 km ESE of Grevena
1995	5	30	4:07:02	3.30	40.019°N	21.670°E	5	15 km NW of Deskati
1995	5	30	4:27:33	3.00	39.977°N	21.490°E	5	13 km SSE of Grevena
1995	5	30	6:21:06	3.30	40.206°N	21.556°E	10	6 km S of Siatista
1995	5	30	6:45:59	4.10	40.108°N	21.351°E	5	7 km WNW of Grevena

The PilotSTRATEGY project has received funding from the European Union's Horizon 2020 research and innovation programme under grant agreement No. 101022664

1995	5	30	7:58:42	2.90	40.097°N	21.701°E	5	12 km SW of Aiani
1995	5	30	12:06:42	4.10	40.029°N	21.664°E	10	17 km NW of Deskati
1995	5	30	14:30:01	4.30	40.002°N	21.464°E	10	9 km SSE of Grevena
1995	5	30	17:50:51	2.90	39.989°N	21.627°E	5	17 km WNW of Deskati
1995	5	30	18:20:52	2.80	40.008°N	21.766°E	5	10 km NNW of Deskati
1995	5	30	19:18:06	2.90	40.153°N	21.526°E	10	11 km NW of Grevena
1995	5	30	19:56:42	2.80	40.039°N	21.627°E	10	17 km ESE of Grevena
1995	5	30	19:59:21	3.10	39.997°N	21.743°E	5	9 km NW of Deskati
1995	5	30	20:46:44	3.20	40.007°N	21.709°E	5	12 km NW of Deskati
1995	5	30	21:56:14	2.90	39.998°N	21.656°E	5	15 km WNW of Deskati
1995	5	30	22:28:16	2.90	40.109°N	21.583°E	10	13 km ENE of Grevena
1995	5	30	23:35:32	2.90	39.978°N	21.757°E	5	7 km NW of Deskati
1995	6	1	1:01:11	2.80	40.016°N	21.819°E	10	10 km N of Deskati
1995	6	1	5:09:58	3.00	40.103°N	21.861°E	10	7 km SSE of Aiani
1995	6	1	10:17:29	3.50	39.978°N	21.574°E	10	17 km SE of Grevena
1995	6	2	3:13:50	2.90	40.033°N	21.617°E	10	17 km ESE of Grevena
1995	6	2	4:59:28	3.00	40.075°N	21.697°E	5	14 km SW of Aiani
1995	6	2	7:47:16	3.30	40.088°N	21.655°E	14,3	16 WSW of Aiani
1995	6	2	16:08:59	3.10	40.095°N	21.876°E	5	Greece
1995	6	3	10:20:14	4.00	40.115°N	21.609°E	20	15 km ENE of Grevena
1995	6	3	22:27:36	3.10	39.999°N	21.687°E	5	13 km NW of Deskati
1995	6	4	20:15:42	3.70	40.192°N	21.576°E	10	8 km SSE of Siatista
1995	6	5	16:31:03	3.00	40.255°N	21.701°E	5	9 km SW of Kozani
1995	6	5	17:32:34	3.00	39.993°N	21.642°E	5	16 km WNW of Deskati
1995	6	5	18:20:46	3.10	40.064°N	21.486°E	10	5 km ESE of Grevena

The PilotSTRATEGY project has received funding from the European Union's Horizon 2020 research and innovation programme under grant agreement No. 101022664

1995	6	5	18:28:09	3.00	40.129°N	21.468°E	5	6 km NE of Grevena
1995	6	5	18:32:45	3.40	39.968°N	21.563°E	5	17 km SE of Grevena
1995	6	6	0:46:52	3.20	40.157°N	21.761°E	10	5 km W of Aiani
1995	6	6	4:35:59	4.20	40.175°N	21.634°E	20	12 km SE of Siatista
1995	6	6	9:02:05	3.10	40.129°N	21.814°E	5	3 km S of Aiani
1995	6	6	15:17:55	3.00	40.243°N	21.880°E	5	4 km ENE of Ano Komi
1995	6	7	8:37:37	4.10	40.167°N	21.699°E	58,1	10 km W of Aiani
1995	6	7	9:02:31	3.00	40.173°N	21.800°E	10	1 km WNW of Aiani
1995	6	7	20:23:44	3.20	40.129°N	21.768°E	5	5 km SW of Aiani
1995	6	8	0:41:11	3.00	39.945°N	21.766°E	5	4 km WNW of Deskati
1995	6	8	2:13:47	3.70	40.047°N	21.520°E	10	8 km ESE of Grevena
1995	6	8	6:14:15	3.30	40.127°N	21.821°E	5	4 km S of Aiani
1995	6	8	18:36:32	3.00	40.074°N	21.838°E	5	9 km WNW of Livadero
1995	6	8	19:39:38	3.00	40.116°N	21.825°E	5	5 km S of Aiani
1995	6	8	23:08:40	2.90	40.101°N	21.725°E	5	10 km SW of Aiani
1995	6	9	15:20:48	4.00	40.195°N	21.645°E	10	11 km SE of Siatista
1995	6	10	10:12:08	3.10	40.149°N	21.869°E	5	4 km ESE of Aiani
1995	6	11	17:20:11	3.70	40.143°N	21.682°E	10	11 km W of Aiani
1995	6	11	18:51:46	4.80	40.000°N	21.604°E	10	17 km ESE of Grevena
1995	6	11	20:38:22	4.00	40.094°N	21.584°E	10	13 km E of Grevena
1995	6	12	2:52:12	3.10	40.030°N	21.763°E	10	12 km NNW of Deskati
1995	6	12	3:19:51	3.30	39.972°N	21.732°E	10	8 km NW of Deskati
1995	6	12	5:27:54	3.40	39.984°N	21.665°E	10	14 km WNW of Deskati
1995	6	12	11:34:57	3.00	40.273°N	21.698°E	10	8 km WSW of Kozani
1995	6	12	12:49:11	3.40	40.002°N	21.758°E	10	Greece
1995	6	12	13:55:42	2.90	40.061°N	21.755°E	10	12 km SSW of Aiani
1995	6	12	16:28:49	2.90	40.213°N	21.731°E	10	Greece
1995	6	12	17:26:33	2.90	40.163°N	21.755°E	10	5 km W of Aiani
1995	6	14	2:35:22	3.00	40.001°N	21.819°E	10	8 km N of Deskati

The PilotSTRATEGY project has received funding from the European Union's Horizon 2020 research and innovation programme under grant agreement No. 101022664

1995	6	14	9:04:07	3.10	40.070°N	21.628°E	10	17 km E of Grevena
1995	6	14	9:42:29	3.70	39.989°N	21.785°E	10	7 km NNW of Deskati
1995	6	14	20:34:59	3.00	39.990°N	21.503°E	10	12 km SSE of Grevena
1995	6	15	1:14:35	3.30	40.116°N	21.776°E	10	6 km SW of Aiani
1995	6	16	0:52:08	3.00	40.061°N	21.815°E	10	11 km WNW of Livadero
1995	6	16	8:12:02	3.50	40.002°N	21.684°E	10	Greece
1995	6	17	6:14:53	4.30	40.009°N	21.594°E	10	16 km ESE of Gevena
1995	6	17	7:49:53	3.20	39.993°N	21.514°E	10	12 km SE of Grevena
1995	6	17	10:43:22	3.00	40.185°N	21.795°E	10	3 km NW of Aiani
1995	6	17	17:48:08	3.90	40.120°N	21.723°E	10	9 km WSW of Aiani
1995	6	17	21:51:16	2.90	40.179°N	21.709°E	10	9 km W of Aiani
1995	6	18	17:28:09	4.40	40.024°N	21.446°E	18,9	6 km SSE of Grevena
1995	6	18	23:02:30	3.80	40.118°N	21.518°E	10	8 km ENE of Grevena
1995	6	18	23:43:09	3.10	40.003°N	21.522°E	10	12 km SE of Grevena
1995	6	19	3:53:58	4.40	40.052°N	21.825°E	10	10 km W of Livadero
1995	6	19	4:41:31	4.30	40.203°N	21.673°E	10	12 km ESE of Siatista
1995	6	19	7:07:03	4.10	40.131°N	21.634°E	10	16 km WSW of Aiani
1995	6	19	15:00:20	4.60	40.011°N	21.868°E	10	6 km WSW of Livadero
1995	6	20	13:34:14	3.10	40.023°N	21.476°E	10	7 km SSE of Grevena
1995	6	20	14:00:13	3.10	39.931°N	21.517°E	10	18 km SSE of Grevena
1995	6	21	13:03:19	3.20	40.241°N	21.703°E	5	9 km SW of Kozani
1995	6	21	19:58:05	3.10	39.988°N	21.685°E	5	12 km WNW of Deskati
1995	6	21	5:36:48	3.00	40.115°N	21.578°E	5	13 km ENE of Grevena
1995	6	22	11:29:27	3.50	40.081°N	21.731°E	5	11 km SW of Aiani
1995	6	22	12:30:37	3.00	39.969°N	21.482°E	5	13 km SSE of Grevena

The PilotSTRATEGY project has received funding from the European Union's Horizon 2020 research and innovation programme under grant agreement No. 101022664

1995	6	24	20:17:46	3.90	40.202°N	21.685°E	5	12 km WNW of Aiani
1995	6	25	15:36:01	3.00	40.066°N	21.748°E	10	12 km SSW of Aiani
1995	6	26	19:01:26	2.90	40.161°N	21.810°E	10	0 km WSW of Aiani
1995	6	26	19:41:56	3.20	40.281°N	21.681°E	5	9 km WSW of Kozani
1995	6	27	4:05:46	3.80	40.044°N	21.581°E	5	13 km ESE of Grevena
1995	6	27	6:33:53	3.50	40.100°N	21.399°E	5	2 km NW of Grevena
1995	6	28	4:39:00	3.40	40.252°N	21.640°E	5	8 km E of Siatista
1995	6	28	18:18:59	3.10	40.081°N	21.856°E	5	9 km NW of Livadero
1995	6	28	23:16:29	3.00	40.211°N	21.702°E	5	10 km W of Ano Komi
1995	6	29	7:31:50	3.00	40.197°N	21.764°E	5	5 km NW of Aiani
1995	7	11	0:17:59	3.40	40.022°N	21.753°E	10	11 km NNW of Deskati
1995	7	14	21:19:39	3.80	40.034°N	21.700°E	10	15 km NW of Deskati
1995	7	14	23:18:15	5.20	40.192°N	21.532°E	21,9	7 km S of Siatista
1995	7	15	1:03:07	3.10	40.222°N	21.609°E	5	7 km SE of Siatista
1995	7	17	20:52:25	3.90	40.301°N	21.680°E	10	9 km W of Kozani
1995	7	18	3:09:06	4.50	40.070°N	21.560°E	10	11 km E of Grevena
1995	7	18	5:05:30	4.40	39.963°N	21.637°E	10	15 km WNW of Deskati
1995	7	18	5:13:30	4.10	40.334°N	21.687°E	10	8 km W of Koila
1995	7	18	7:42:52	4.60	39.988°N	21.722°E	10	10 km NW of Deskati
1995	7	18	20:19:07	4.50	40.047°N	21.647°E	10	19 km ESE of Grevena
1995	7	19	18:23:12	4.80	39.977°N	21.627°E	10	16 km WNW of Deskati
1995	7	21	13:27:48	4.00	40.061°N	21.555°E	62,7	11 km ESE of Grevena
1995	7	28	19:56:45	3.80	39.966°N	21.540°E	10	16 km SE of Grevena
1995	7	28	22:43:29	4.30	40.098°N	21.661°E	10	15 km WSW of Aiani
1995	7	30	9:28:12	4.00	39.995°N	21.810°E	33	7 km N of Deskati

The PilotSTRATEGY project has received funding from the European Union's Horizon 2020 research and innovation programme under grant agreement No. 101022664

1995	8	1	5:43:01	3.10	40.116°N	21.572°E	10	12 km ENE of Grevena
1995	8	1	23:38:50	2.90	40.015°N	21.628°E	10	18 km WNW of Deskati
1995	8	4	3:30:28	3.10	40.196°N	21.568°E	10	7 km SSE of Siatista
1995	8	5	18:14:43	4.20	40.293°N	21.594°E	10	4 km SE of GaLatitudeini
1995	8	8	18:18:25	2.90	40.151°N	21.636°E	10	14 km SSE of Siatista
1995	8	8	18:19:34	3.30	40.290°N	21.679°E	10	9 km W of Kozani
1995	8	8	19:02:56	3.30	40.090°N	21.649°E	10	16 km WSW of Aiani
1995	8	8	22:43:43	3.10	40.157°N	21.749°E	10	6 km W of Aiani
1995	8	9	0:39:04	3.20	40.150°N	21.760°E	10	5 km WSW of Aiani
1995	8	9	1:12:19	3.10	40.079°N	21.618°E	10	16 km E of Grevena
1995	8	9	4:12:47	2.90	40.126°N	21.584°E	10	14 km ENE of Grevena
1995	8	11	22:37:46	3.00	40.207°N	21.568°E	10	6 km SSE of Siatista
1995	8	13	18:28:00	3.00	40.282°N	21.655°E	10	9 km ENE of Siatista
1995	8	13	20:11:48	3.10	40.038°N	21.547°E	10	11 km ESE of Grevena
1995	8	13	20:22:10	3.70	40.115°N	21.474°E	10	5 km NE of Grevena
1995	8	14	17:57:03	4.10	40.175°N	21.686°E	10	11 km W of Aiani
1995	8	14	21:58:46	3.10	40.185°N	21.672°E	10	12 km W of Aiani
1995	8	20	18:53:11	3.70	40.287°N	21.757°E	10	3 km WSW of Kozani
1995	8	20	19:21:22	4.40	40.234°N	21.814°E	10	1 km NW of Ano Komi
1995	8	20	19:27:51	4.20	40.291°N	21.800°E	10	1 km SE of Kozani
1995	8	20	19:33:02	3.60	40.192°N	21.865°E	10	4 km SE of Ano Komi
1995	8	21	1:56:39	3.00	40.202°N	21.858°E	5	3 km SE of Ano Komi
1995	8	27	22:58:10	3.50	40.153°N	21.537°E	5	12 km NE of Grevena
1995	8	27	23:44:03	2.90	40.332°N	21.666°E	5	9 km E of GaLatitudeini
1995	8	28	6:47:12	3.00	40.148°N	21.749°E	5	6 km WSW of Aiani

The PilotSTRATEGY project has received funding from the European Union's Horizon 2020 research and innovation programme under grant agreement No. 101022664

1995	8	28	18:45:32	2.90	40.139°N	21.632°E	5	15 km SSE of Siatista
1995	8	28	22:30:29	2.90	40.055°N	21.599°E	5	14 km ESE of Grevena
1995	9	1	4:43:27	2.60	40.041°N	21.376°E	10	6 km SW of Grevena
1995	9	1	8:50:34	3.00	40.145°N	21.616°E	10	14 km SSE of Siatista
1995	9	1	17:25:02	2.90	40.103°N	21.592°E	10	14 km E of Grevena
1995	9	2	5:55:16	2.80	40.167°N	21.781°E	10	3 km W of Aiani
1995	9	2	16:23:32	3.10	40.118°N	21.617°E	10	16 km ENE of Grevena
1995	9	2	19:00:22	2.20	40.189°N	40.189°E	10	3 km NNW of Aiani
1995	9	2	21:57:16	2.10	40.133°N	21.607°E	10	15 km SSE of Siatista
1995	9	2	22:45:17	2.20	40.183°N	21.640°E	10	11 km SE of Siatista
1995	9	3	1:29:39	2.00	40.075°N	21.575°E	10	12 km E of Grevena
1995	9	3	3:59:26	3.00	40.009°N	21.550°E	10	13 km SE of Grevena
1995	9	3	10:07:27	2.30	40.160°N	21.615°E	10	12 km SSE of Siatista
1995	9	3	23:55:31	2.40	40.016°N	21.488°E	10	9 km SE of Grevena
1995	9	4	3:28:35	2.40	40.025°N	21.498°E	10	8 km SE of Grevena
1995	9	4	4:09:24	4.00	40.121°N	21.752°E	10	7 km SW of Aiani
1995	9	4	11:13:01	2.20	40.492°N	21.850°E	10	6 km N of Kleitos
1995	9	5	7:59:25	2.20	40.356°N	21.752°E	10	4 km NW of Koila
1995	9	5	13:23:41	2.80	39.913°N	21.870°E	10	5 km ESE of Deskati
1995	9	5	20:56:41	2.20	40.035°N	21.535°E	10	10 km ESE of Grevena
1995	9	6	2:29:23	2.90	40.043°N	21.550°E	5	11 km ESE of Grevena
1995	9	6	10:53:33	2.40	40.098°N	21.708°E	10	11 km SW of Aiani
1995	9	6	22:58:25	2.20	40.054°N	21.486°E	10	6 km SE of Grevena
1995	9	7	1:44:55	2.20	40.138°N	21.437°E	10	5 km N of Grevena
1995	9	7	7:58:29	2.50	40.275°N	21.639°E	20	8 km E of Siatista
1995	9	7	20:34:09	2.90	40.089°N	21.735°E	5	10 km SW of Aiani

The PilotSTRATEGY project has received funding from the European Union's Horizon 2020 research and innovation programme under grant agreement No. 101022664

1995	9	10	5:12:14	2.40	40.195°N	21.797°E	5	3 km NNW of Aiani
1995	9	11	2:58:34	3.10	40.174°N	21.830°E	10	1 km NE of Aiani
1995	9	11	18:33:15	2.90	40.025°N	21.606°E	10	16 km ESE of Gevena
1995	9	13	2:03:47	3.10	40.010°N	21.750°E	5	10 km NNW of Deskati
1995	9	13	6:44:46	3.00	40.111°N	21.597°E	5	14 km ENE of Grevena
1995	9	13	18:28:11	2.10	40.056°N	21.576°E	5	13 km ESE of Grevena
1995	9	13	20:37:00	2.20	40.032°N	21.449°E	10	6 km SSE of Grevena
1995	9	14	1:26:39	4.30	40.171°N	21.504°E	10	10 km SSW of Siatista
1995	9	14	1:30:28	3.10	40.169°N	21.602°E	5	11 km SSE of Siatista
1995	9	14	19:13:08	2.10	40.246°N	21.572°E	5	2 km SE of Siatista
1995	9	15	8:08:34	2.00	40.434°N	21.822°E	10	3 km W of Kleitos
1995	9	16	11:39:59	2.70	40.046°N	21.770°E	10	Greece
1995	9	17	9:33:13	2.80	40.059°N	21.631°E	10	17 km E of Grevena
1995	9	19	2:30:22	2.30	40.195°N	21.749°E	10	6 km WNW of Aiani
1995	9	19	4:03:44	2.20	40.198°N	21.734°E	5	8 km WNW of Aiani
1995	9	20	0:38:27	2.20	40.189°N	21.752°E	10	Greece
1995	9	20	8:47:47	2.60	40.156°N	21.542°E	5	11 km S of Siatista
1995	9	20	9:02:37	2.20	39.988°N	21.485°E	5	11 km SSEof Grevena
1995	9	20	14:31:50	2.50	40.087°N	21.767°E	5	9 km SSW of Aiani
1995	9	21	22:15:17	2.40	40.091°N	21.695°E	10	13 km SW of Aiani
1995	9	22	6:05:50	3.10	40.496°N	21.142°E	5	1 km WSW of Mesopotamia
1995	9	22	6:23:30	2.90	40.564°N	21.201°E	5	5 km WNW of Chloi
1995	9	24	3:07:49	2.40	40.466°N	21.168°E	10	4 km S of Mesopotamia
1995	9	24	23:57:44	2.60	40.076°N	21.801°E	10	9 km S of Aiani
1995	9	25	16:32:27	2.10	40.101°N	21.765°E	5	8 km SSW of Aiani
1995	9	26	1:55:33	2.20	40.149°N	21.629°E	5	14 km SSE of Siatista

The PilotSTRATEGY project has received funding from the European Union's Horizon 2020 research and innovation programme under grant agreement No. 101022664

1995	9	26	6:22:01	2.00	40.095°N	21.673°E	5	14 km WSW of Aiani
1995	9	26	15:41:44	2.10	40.141°N	21.718°E	5	9 km WSW of Aiani
1995	9	27	1:49:32	2.30	40.133°N	21.641°E	5	Greece
1995	9	28	8:58:47	2.20	40.484°N	21.832°E	5	6 km NNW of Kleitos
1995	9	28	12:13:59	3.20	40.118°N	21.598°E	10	15 km ENE of Grevena
1995	9	28	18:02:20	2.10	40.205°N	21.751°E	5	7 km WSW of Ano Komi
1995	10	5	18:52:30	2.10	40.039°N	21.451°E	10	5 km SSE of Grevena
1995	10	6	4:22:16	2.20	40.177°N	21.760°E	5	5 km WNW of Aiani
1995	10	6	5:41:59	2.50	40.162°N	21.782°E	5	3 km W of Aiani
1995	10	6	15:26:28	2.90	40.202°N	21.532°E	5	6 km S of Siatista
1995	10	8	11:21:47	2.20	40.420°N	21.733°E	10	10 km W of Kleitos
1995	10	9	9:06:29	2.20	39.892°N	21.431°E	33	21 km S of Grevena
1995	10	9	17:56:13	3.10	40.107°N	21.834°E	5	6 km S of Aiani
1995	10	10	3:04:35	2.90	40.165°N	21.638°E	5	13 km SE of Siatista
1995	10	10	23:00:58	2.00	40.243°N	21.844°E	5	2 km NE of Ano komi
1995	10	11	0:28:49	3.10	40.156°N	21.625°E	10	13 km SSE of Siatista
1995	10	13	13:50:16	3.00	40.134°N	21.590°E	5	14 km SSE of Siatista
1995	10	13	19:34:53	2.60	40.039°N	21.440°E	10	5 km SSE of Grevena
1995	10	15	13:55:22	2.30	40.553°N	21.570°E	10	6 km N of Anarachi
1995	10	15	14:18:13	2.50	40.080°N	21.484°E	5	4 km E of Grevena
1995	10	16	14:37:38	2.40	40.090°N	21.699°E	5	13 km SW of Aiani
1995	10	16	14:45:21	3.00	40.074°N	21.718°E	5	13 km SW of Aiani
1995	10	16	17:28:02	2.20	40.210°N	21.661°E	10	11 km ESE of Siatista
1995	10	17	0:11:24	3.00	40.076°N	21.750°E	5	11 km SSW of Aiani
1995	10	17	17:19:27	3.10	40.018°N	21.504°E	5	9 km SE of Grevena
1995	10	17	23:33:32	3.00	39.991°N	21.532°E	5	13 km SE of Grevena

The PilotSTRATEGY project has received funding from the European Union's Horizon 2020 research and innovation programme under grant agreement No. 101022664

1995	10	17	23:45:49	2.50	40.013°N	21.435°E	5	7 km S of Grevena
1995	10	18	5:15:40	2.70	40.123°N	21.769°E	5	6 km SW of Aiani
1995	10	18	8:01:01	2.00	40.175°N	21.657°E	5	13 km SE of Siatista
1995	10	18	9:33:54	3.30	40.118°N	21.657°E	5	14 km WSW of Aiani
1995	10	18	10:28:36	2.30	40.153°N	21.623°E	5	13 km SSE of Siatista
1995	10	19	9:15:16	2.20	40.160°N	21.458°E	5	8 km NNE of Grevena
1995	10	19	19:26:30	2.20	40.147°N	21.599°E	5	13 km SSE of Siatista
1995	10	23	9:28:44	3.00	40.119°N	21.522°E	10	8 km ENE of Grevena
1995	10	24	1:59:48	2.50	40.126°N	21.567°E	10	12 km ENE of Grevena
1995	10	25	2:50:32	2.60	40.051°N	21.432°E	10	3 km S of Grevena
1995	10	28	7:00:18	2.20	40.245°N	21.556°E	5	2 km SSE of Siatista
1995	10	29	17:05:28	2.30	40.155°N	21.652°E	5	Greece
1995	10	30	1:53:11	4.00	40.015°N	21.667°E	5	15 km NW of Deskati
1995	10	30	2:38:36	2.30	40.066°N	21.630°E	5	17 km E of Grevena
1995	10	30	2:41:46	2.00	40.055°N	21.602°E	5	15 km ESE of Grevena
1995	10	30	4:32:16	2.00	40.089°N	21.616°E	5	16 km E of Grevena
1995	10	30	12:06:45	2.10	40.203°N	21.638°E	5	10 km SE of Siatista
1995	10	30	15:04:01	2.30	40.164°N	21.787°E	5	2 km W of Aiani
1995	10	30	18:44:33	2.90	40.039°N	21.573°E	5	13 km ESE of Grevena
1995	11	1	9:42:13	2.20	40.089°N	21.753°E	5	10 km SW of Aiani
1995	11	1	14:08:31	3.00	40.378°N	21.670°E	10	11 km WNW of Koila
1995	11	1	17:15:55	3.00	40.153°N	21.680°E	10	11 km W of Aiani
1995	11	1	17:39:16	2.90	40.157°N	21.652°E	10	14 km W of Aiani
1995	11	2	10:49:22	2.10	40.572°N	21.473°E	5	2 km WS of Lechovo
1995	11	2	13:47:40	3.00	40.056°N	21.659°E	10	18 km SW of Aiani
1995	11	3	11:05:48	3.20	40.036°N	21.682°E	5	16 km NW of Deskati

The PilotSTRATEGY project has received funding from the European Union's Horizon 2020 research and innovation programme under grant agreement No. 101022664

1995	11	3	16:24:50	2.10	40.105°N	21.633°E	10	17 km WSW of Aiani
1995	11	3	191:44:35	3.00	40.034°N	21.633°E	10	18 km ESE of Grevena
1995	11	5	21:38:43	2.30	40.235°N	21.775°E	10	4 km WNW of Ano Komi
1995	11	6	18:04:30	2.30	40.171°N	21.670°E	5	12 km W of Aiani
1995	11	8	19:57:41	3.10	40.023°N	21.577°E	5	14 km ESE of Grevena
1995	11	9	2:32:28	2.20	40.197°N	21.711°E	5	9 km WNW of Aiani
1995	11	9	3:01:04	2.30	40.151°N	21.610°E	5	13 km SSE of Siatista
1995	11	9	4:15:02	2.70	40.299°N	21.305°E	10	4 km NNW of Tsotili
1995	11	9	19:38:02	2.20	40.153°N	21.735°E	10	7 km W of Aiani
1995	11	10	2:08:30	2.10	40.272°N	21.316°E	5	1 km NW of Tsotili
1995	11	10	2:24:34	2.20	40.070°N	21.563°E	5	11 km E of Grevena
1995	11	10	2:38:19	2.20	40.063°N	21.631°E	5	17 km E of Grevena
1995	11	10	3:23:04	2.30	40.165°N	21.682°E	5	11 km W of Aiani
1995	11	10	4:01:41	2.30	40.162°N	21.665°E	5	13 km W of Aiani
1995	11	10	14:21:49	2.30	40.186°N	21.734°E	10	Greece
1995	11	11	15:06:56	4.00	40.044°N	21.706°E	10	16 km NW of Deskati
1995	11	11	19:44:09	3.10	40.177°N	21.723°E	5	8 km W of Aiani
1995	11	12	5:17:50	2.90	40.055°N	21.539°E	5	10 km ESE of Grevena
1995	11	12	8:53:30	3.00	40.014°N	21.548°E	10	12 km SE of Grevena
1995	11	12	9:09:40	2.40	39.969°N	21.424°E	10	12 km S of Grevena
1995	11	12	9:22:37	2.30	40.009°N	21.485°E	10	9 km SSE of Grevena
1995	11	12	9:46:52	2.50	40.012°N	21.491°E	10	9 km SE of Grevena
1995	11	12	20:44:18	2.20	40.185°N	21.677°E	10	12 km W of Aiani
1995	11	12	22:22:46	3.00	40.120°N	21.583°E	5	13 km ENE of Grevena
1995	11	13	2:11:19	2.10	40.064°N	21.850°E	5	Greece
1995	11	13	2:21:04	2.90	40.010°N	21.819°E	10	9 km N of Deskati
1995	11	13	2:51:14	2.20	40.055°N	21.874°E	5	6 km WNW of Livadero

The PilotSTRATEGY project has received funding from the European Union's Horizon 2020 research and innovation programme under grant agreement No. 101022664

1995	11	13	2:57:07	2.40	40.048°N	21.880°E	5	5 km WNW of Livadero
1995	11	13	8:20:42	3.10	40.004°N	21.834°E	5	9 km NNE of Deskati
1995	11	13	13:40:32	4.20	40.047°N	21.716°E	10	15 km SW of Aiani
1995	11	13	15:22:44	2.10	40.116°N	21.727°E	5	9 km SW of Aiani
1995	11	13	15:52:53	2.30	40.089°N	21.697°E	5	13 km SW of Aiani
1995	11	13	16:30:06	2.10	40.142°N	21.764°E	5	5 km WSW of Aiani
1995	11	14	2:48:05	2.10	40.230°N	21.738°E	10	7 km W of Ano Komi
1995	11	15	12:41:27	3.10	39.931°N	21.267°E	5	19 km NNE of Metsovo
1995	11	15	15:21:18	4.00	40.134°N	21.737°E	10	7 km WSW of Aiani
1995	11	16	5:40:57	2.20	40.206°N	21.715°E	5	9 km WSW of Ano Komi
1995	11	17	6:02:08	2.50	40.166°N	21.679°E	5	11 km W of Aiani
1995	11	18	9:06:44	2.40	40.120°N	21.595°E	10	14 km ENE of Grevena
1995	11	18	14:01:40	3.00	40.118°N	21.871°E	5	6 km SE of Aiani
1995	11	19	12:37:25	2.40	40.085°N	21.578°E	5	12 km E of Grevena
1995	11	24	17:34:14	2.10	40.246°N	21.596°E	5	4 km ESE of Siatista
1995	11	25	2:30:03	2.00	40.498°N	21.627°E	10	4 km E of Anarachi
1995	11	28	4:34:47	2.80	40.134°N	21.642°E	10	15 km WSW of Aiani
1995	11	29	3:18:50	2.20	40.138°N	21.626°E	5	15 km SSE of Siatista
1995	11	30	19:44:51	2.80	40.097°N	21.757°E	5	9 km SW of Aiani
1995	12	1	0:22:12	3.20	39.939°N	21.613°E	5	16 km W of Deskati
1995	12	2	6:12:36	3.40	40.128°N	21.581°E	10	13 km ENE of Grevena
1995	12	3	9:02:07	3.00	40.030°N	21.608°E	10	16 km ESE of Gevena
1995	12	5	16:44:22	2.90	40.151°N	21.574°E	10	12 km SSE of Siatista
1995	12	5	16:59:16	2.00	40.167°N	21.521°E	5	10 km S of Siatista
1995	12	5	17:18:10	2.30	40.105°N	21.509°E	10	7 km ENE of Grevena
1995	12	5	17:22:38	2.60	40.180°N	21.557°E	10	9 km S of Siatista
1995	12	5	17:58:13	3.30	40.180°N	21.536°E	5	9 km S of Siatista

The PilotSTRATEGY project has received funding from the European Union's Horizon 2020 research and innovation programme under grant agreement No. 101022664

1995	12	5	22:15:36	2.90	40.125°N	21.558°E	10	12 km ENE of Grevena
1995	12	6	0:01:57	2.90	40.128°N	21.462°E	5	5 km NNE of Grevena
1995	12	6	10:02:25	2.20	40.132°N	21.448°E	5	5 km NNE of Grevena
1995	12	6	21:40:19	2.90	40.141°N	21.553°E	10	12 km ENE of Grevena
1995	12	6	21:56:30	3.10	40.137°N	21.433°E	10	5 km N of Grevena
1995	12	8	5:28:40	3.00	40.149°N	21.565°E	5	12 km S of Siatista
1995	12	8	5:46:47	2.60	40.112°N	21.513°E	10	7 km ENE of Grevena
1995	12	8	7:12:12	3.10	40.151°N	21.555°E	10	12 km S of Siatista
1995	12	8	11:48:36	2.30	40.032°N	21.467°E	10	6 km SSE of Grevena
1995	12	8	14:17:20	2.50	40.161°N	21.764°E	10	4 km W of Aiani
1995	12	9	15:23:51	2.10	40.168°N	21.662°E	10	13 km W of Aiani
1995	12	9	15:31:42	2.40	40.078°N	21.601°E	10	14 km E of Grevena
1995	12	11	11:44:32	2.90	40.131°N	21.694°E	10	11 km WSW of Aiani
1995	12	12	6:07:45	3.20	39.982°N	21.579°E	10	17 km SE of Grevena
1995	12	12	14:04:25	3.10	40.156°N	21.568°E	10	11 km S of Siatista
1995	12	12	23:23:04	2.20	40.113°N	21.771°E	10	6 km SW of Aiani
1995	12	12	23:55:45	2.50	40.067°N	21.834°E	10	9 km WNW of Livadero
1995	12	14	0:57:54	3.10	40.171°N	21.599°E	10	11 km SSE of Siatista
1995	12	14	16:57:18	2.00	39.976°N	21.470°E	10	15 km SSE of Grevena
1995	12	15	23:03:36	2.80	40.122°N	21.716°E	5	9 km WSW of Aiani
1995	12	19	12:30:30	2.00	40.463°N	21.871°E	10	3 km NNE of Kleitos
1995	12	19	15:55:08	2.20	40.042°N	21.407°E	10	5 km SSW of Grevena
1995	12	20	19:38:40	2.20	40.169°N	21.716°E	5	8 kn W of Aiani
1995	12	21	14:52:55	3.10	40.078°N	21.701°E	10	13 km SW of Aiani
1995	12	21	15:18:12	2.20	40.072°N	21.666°E	5	16 km SW of Aiani
1995	12	21	18:32:18	2.10	40.084°N	21.639°E	5	17 km WSW of Aiani

The PilotSTRATEGY project has received funding from the European Union's Horizon 2020 research and innovation programme under grant agreement No. 101022664

1995	12	23	0:58:27	3.10	39.996°N	21.555°E	5	14 km SE of Grevena
1995	12	23	3:44:07	3.00	40.085°N	21.659°E	5	16 km WSW of Aiani
1995	12	23	7:18:44	2.80	40.083°N	21.663°E	5	16 km SW of Aiani
1995	12	23	9:15:17	2.80	40.107°N	21.658°E	5	15 km WSW of Aiani
1995	12	23	15:10:38	2.90	40.169°N	21.593°E	5	11 km SSE of Siatista
1995	12	24	4:34:15	2.20	40.090°N	21.678°E	10	14 km SW of Aiani
1995	12	26	9:57:21	2.30	40.102°N	21.617°E	10	16 km E of Grevena
1995	12	31	0:22:36	3.10	40.465°N	21.231°E	5	2 km WNW of Argos Orestiko
1995	12	31	1:09:35	3.00	40.499°N	21.243°E	5	0 km SW of Maniakoi
1996	1	2	2:20:51	2.80	40.082°N	21.759°E	10	10 km SSW of Aianí, Greece
1996	1	5	16:37:12	2.60	40.002°N	21.470°E	10	9 km SSE of Grevená, Greece
1996	1	6	12:46:01	3.10	40.161°N	21.796°E	10	2 km W of Aianí, Greece
1996	1	11	5:14:12	2.40	40.094°N	21.566°E	10	11 km E of Grevená, Greece
1996	1	13	5:13:54	2.70	40.090°N	21.603°E	10	14 km E of Grevená, Greece
1996	1	20	23:29:43	2.20	40.060°N	21.742°E	10	13 km SSW of Aianí, Greece
1996	1	22	16:10:43	2.90	40.065°N	21.795°E	10	11 km S of Aianí, Greece
1996	1	22	11:58:22	3.00	40.001°N	21.546°E	5	13 km SE of Grevená, Greece
1996	1	22	7:52:29	2.20	40.085°N	21.764°E	5	9 km SSW of Aianí, Greece
1996	1	22	7:21:16	2.20	40.098°N	21.793°E	5	7 km SSW of Aianí, Greece
1996	1	22	4:00:59	3.10	40.031°N	21.811°E	10	11 km W of Livaderó, Greece
1996	1	24	9:07:15	2.10	40.458°N	21.837°E	5	3 km NNW of Kleítos, Greece
1996	1	25	23:12:46	2.10	39.843°N	21.489°E	5	17 km NW of Kastráki, Greece
1996	1	26	19:47:53	2.10	40.098°N	21.727°E	10	10 km SW of Aianí, Greece
1996	1	28	9:24:42	2.30	40.131°N	21.597°E	10	15 km SSE of Siátista, Greece

The PilotSTRATEGY project has received funding from the European Union's Horizon 2020 research and innovation programme under grant agreement No. 101022664

1996	1	29	11:54:42	2.30	40.018°N	21.782°E	5	10 km NNW of Deskáti, Greece
1996	1	31	3:44:22	3.10	40.056°N	21.701°E	10	15 km SW of Aianí, Greece
1996	2	1	18:39:42	2.20	40.087°N	21.711°E	10	12 km SW of Aianí, Greece
1996	2	3	19:35:41	2.20	40.203°N	21.774°E	10	5 km WSW of Áno Kómi, Greece
1996	2	5	5:42:23	3.50	40.136°N	21.667°E	10	13 km WSW of Aianí, Greece
1996	2	12	6:10:50	3.00	40.057°N	21.741°E	10	13 km SSW of Aianí, Greece
1996	2	13	17:52:30	2.10	40.150°N	21.804°E	10	2 km SW of Aianí, Greece
1996	2	15	22:49:04	2.30	40.083°N	21.639°E	10	17 km WSW of Aianí, Greece
1996	2	17	11:30:43	2.20	40.159°N	21.857°E	10	3 km E of Aianí, Greece
1996	2	17	5:37:53	2.40	40.207°N	21.644°E	5	10 km SE of Siátista, Greece
1996	2	18	18:30:15	2.50	40.605°N	21.580°E	10	7 km ENE of Léchovo, Greece
1996	2	18	17:52:10	2.60	40.633°N	21.594°E	10	6 km SSW of Xinó Neró, Greece
1996	2	18	11:12:57	2.10	40.595°N	21.516°E	10	2 km ENE of Léchovo, Greece
1996	2	19	20:14:57	2.40	40.633°N	21.383°E	10	10 km WNW of Léchovo, Greece
1996	2	19	0:40:30	2.00	40.601°N	21.553°E	10	5 km ENE of Léchovo, Greece
1996	2	19	0:28:20	2.20	40.567°N	21.543°E	10	4 km ESE of Léchovo, Greece
1996	2	22	19:31:39	2.10	40.550°N	21.489°E	10	3 km S of Léchovo, Greece
1996	2	22	19:14:39	2.00	40.596°N	21.524°E	10	2 km ENE of Léchovo, Greece
1996	2	22	15:23:07	2.40	40.571°N	21.521°E	10	2 km ENE of Léchovo, Greece
1996	2	22	11:20:54	2.00	40.613°N	21.552°E	10	5 km ENE of Léchovo, Greece
1996	2	22	7:51:47	2.20	40.593°N	21.529°E	10	3 km ENE of Léchovo, Greece
1996	2	22	7:49:34	2.50	40.602°N	21.549°E	10	5 km ENE of Léchovo, Greece
1996	2	22	7:47:25	4.00	40.638°N	21.627°E	10	5 km S of Xinó Neró, Greece

The PilotSTRATEGY project has received funding from the European Union's Horizon 2020 research and innovation programme under grant agreement No. 101022664

1996	2	22	3:08:03	2.50	40.557°N	21.463°E	10	3 km SW of Léchovo, Greece
1996	2	24	22:44:09	3.20	39.914°N	21.305°E	5	19 km NNE of Metsovo, Greece
1996	2	24	20:04:55	3.50	40.596°N	21.629°E	10	7 km WSW of Filótas, Greece
1996	2	24	16:36:23	2.20	40.592°N	21.576°E	10	7 km E of Léchovo, Greece
1996	2	24	10:29:29	2.90	40.611°N	21.577°E	5	7 km ENE of Léchovo, Greece
1996	2	24	5:53:29	2.00	40.588°N	21.501°E	10	0 km ENE of Léchovo, Greece
1996	2	24	3:38:36	2.10	40.166°N	21.558°E	5	10 km S of Siátista, Greece
1996	2	24	2:29:31	3.00	40.214°N	21.701°E	10	10 km W of Áno Kómi, Greece
1996	2	25	0:24:02	2.40	40.181°N	21.584°E	10	9 km SSE of Siátista, Greece
1996	2	26	23:59:03	2.80	40.637°N	21.572°E	5	7 km SW of Xinó Neró, Greece
1996	2	26	23:45:18	2.00	40.129°N	21.480°E	10	6 km NE of Grevená, Greece
1996	2	26	15:30:16	3.80	40.629°N	21.655°E	5	4 km W of Filótas, Greece
1996	2	27	22:51:57	2.40	40.114°N	21.514°E	5	8 km ENE of Grevená, Greece
1996	2	27	19:48:53	2.10	40.304°N	21.733°E	10	4 km W of Kozáni, Greece
1996	2	27	16:20:54	2.30	40.582°N	21.555°E	10	5 km E of Léchovo, Greece
1996	2	27	11:07:21	2.20	40.580°N	21.545°E	10	4 km E of Léchovo, Greece
1996	2	27	10:18:44	3.50	40.609°N	21.630°E	10,2	6 km WSW of Filótas, Greece
1996	2	27	8:52:27	2.40	40.631°N	21.558°E	10	7 km NE of Léchovo, Greece
1996	2	27	8:23:16	2.10	40.640°N	21.600°E	10	5 km SSW of Xinó Neró, Greece
1996	2	27	4:20:12	2.30	39.983°N	21.741°E	5	8 km NW of Deskáti, Greece
1996	2	27	0:50:46	2.40	40.632°N	21.554°E	10	7 km NE of Léchovo, Greece
1996	2	27	0:15:23	2.30	40.599°N	21.549°E	10	5 km ENE of Léchovo, Greece
1996	2	27	9:10:29	2.10	40.446°N	21.855°E	10	1 km N of Kleítos, Greece
1996	2	28	19:42:49	2.10	40.606°N	21.534°E	10	4 km NE of Léchovo, Greece

The PilotSTRATEGY project has received funding from the European Union's Horizon 2020 research and innovation programme under grant agreement No. 101022664

1996	2	28	19:25:45	2.00	40.599°N	21.556°E	5	5 km ENE of Léchovo, Greece
1996	2	28	15:14:08	2.50	40.572°N	21.525°E	10	3 km ESE of Léchovo, Greece
1996	2	29	23:01:42	2.00	40.538°N	21.469°E	10	5 km SSW of Léchovo, Greece
1996	2	29	18:07:22	2.10	40.590°N	21.533°E	10	3 km E of Léchovo, Greece
1996	2	29	3:51:08	2.90	40.642°N	21.594°E	10	5 km SSW of Xinó Neró, Greece
1996	3	24	23:11:22	3.40	40.159°N	21.261°E	33	12 km SSW of Tsotílli, Greece
1996	4	15	22:16:56	3.40	39.909°N	21.107°E	10	16 km NNW of Metsovo, Greece
1996	10	10	19:07:45	4.50	40.071°N	21.455°E	10	2 km ESE of Grevená, Greece
1997	2	13	20:10:24	4.00	40.198°N	21.635°E	51,6	10 km SE of Siátista, Greece
1997	3	26	12:35:18	3.60	40.083°N	21.644°E	5	17 km WSW of Aianí, Greece
1997	4	15	22:20:06	3.50	40.129°N	21.847°E	33	4 km SSE of Aianí, Greece
1997	6	19	15:01:30	3.40	40.199°N	21.403°E	57,6	9 km SE of Tsotílli, Greece
1997	8	19	19:03:49	3.70	40.058°N	21.397°E	33	3 km SW of Grevená, Greece
1997	8	22	3:17:47	4.20	40.189°N	21.570°E	33	8 km SSE of Siátista, Greece
1997	8	22	3:09:41	4.00	40.240°N	21.799°E	33	2 km WNW of Áno Kómi, Greece
1997	9	19	12:00:27	4.90	40.020°N	21.326°E	10	11 km SW of Grevená, Greece
1998	4	12	23:53:39	4.20	40.153°N	21.126°E	33	Greece
1998	6	20	11:40:23	4.00	40.078°N	21.709°E	10	13 km SW of Aianí, Greece
1998	11	12	22:10:36	3.00	40.440°N	21.420°E	12	11 km SE of Mavrochóri, Greece
1998	12	2	19:30:07	3.00	40.604°N	21.653°E	10	5 km WSW of Filótas, Greece
1998	12	11	7:28:10	3.20	40.140°N	21.400°E	10	6 km NNW of Grevená, Greece
1998	12	19	22:12:38	2.80	40.220°N	21.340°E	5	4 km SSE of Tsotílli, Greece
1998	12	28	16:54:34	2.90	40.110°N	21.790°E	25	6 km SSW of Aianí, Greece

The PilotSTRATEGY project has received funding from the European Union's Horizon 2020 research and innovation programme under grant agreement No. 101022664

1998	12	31	7:46:28	3.10	40.230°N	21.690°E	5	11 km WSW of Krókos, Greece
1999	1	17	8:57:28	3.10	40.060°N	21.600°E	5	14 km E of Grevená, Greece
1999	2	3	5:33:27	3.10	40.200°N	21.620°E	5	9 km SE of Siátista, Greece
1999	2	23	22:49:23	3.20	40.510°N	21.359°E	10	3 km E of Mavrochóri, Greece
1999	3	10	10:21:49	3.20	40.340°N	21.550°E	6	2 km N of GaLatitudeiní, Greece
1999	3	12	20:30:24	3.00	39.980°N	21.610°E	5	18 km WNW of Deskáti, Greece
1999	3	25	4:44:08	2.80	40.170°N	21.410°E	15	9 km N of Grevená, Greece
1999	4	1	21:50:31	3.10	39.770°N	21.130°E	5	4 km W of Metsovo, Greece
1999	4	12	17:16:27	4.10	40.465°N	21.481°E	10	7 km WSW of Empório, Greece
1999	4	22	10:39:08	3.00	40.070°N	21.595°E	10	14 km E of Grevená, Greece
1999	5	24	11:16:20	3.40	40.160°N	21.670°E	5	12 km W of Aianí, Greece
1999	5	27	5:43:50	3.00	39.790°N	21.020°E	5	14 km W of Metsovo, Greece
1999	6	5	22:51:34	3.00	40.220°N	21.850°E	10	1 km ESE of Áno Kómi, Greece
1999	6	12	2:58:00	3.70	40.490°N	21.570°E	11	0 km SW of Anaráchi, Greece
1999	6	20	17:41:59	3.30	40.180°N	21.070°E	5	23 km WSW of Tsotílli, Greece
1999	6	26	17:19:11	3.10	39.940°N	20.990°E	8	23 km ESE of Kónitsa, Greece
1999	7	3	5:04:01	3.30	40.330°N	21.330°E	10	7 km N of Tsotílli, Greece
1999	7	28	9:18:39	3.00	40.100°N	21.680°E	5	13 km WSW of Aianí, Greece
1999	7	31	22:31:31	3.00	40.160°N	21.710°E	10	9 km W of Aianí, Greece
Time Period 2000-2009								
Year	Month	Day	Time UTC	Magnitude	Latitude	Longitude	Depth (km)	Region
2000	1	14	9:08:23	4.00	40.042°N	21.861°E	10	7 km W of Livaderó, Greece
2000	1	29	12:58:29	2.90	40.170°N	21.570°E	5	10 km SSE of Siátista, Greece
2000	10	26	11:22:26	2.50	40.115°N	21.860°E	0	6 km SSE of Aianí, Greece

The PilotSTRATEGY project has received funding from the European Union's Horizon 2020 research and innovation programme under grant agreement No. 101022664

2000	12	2	14:07:59	2.40	40.172°N	21.655°E	10	13 km SE of Siátista, Greece
2000	12	2	14:02:34	3.50	40.410°N	21.670°E	5	11 km S of Ptolemaida, Greece
2000	12	2	13:58:58	3.10	40.190°N	21.860°E	5	4 km NE of Aianí, Greece
2001	1	7	3:27:15	2.30	40.087°N	21.842°E	0	8 km SSE of Aianí, Greece
2001	2	19	7:22:07	3.10	40.270°N	21.830°E	43	1 km NE of Krókos, Greece
2001	2	23	12:34:00	3.50	40.098°N	21.602°E	2	14 km E of Grevená, Greece
2001	3	30	22:27:17	3.20	40.187°N	21.515°E	0	8 km SSW of Siátista, Greece
2001	4	20	20:51:40	2.20	40.380°N	21.302°E	16	8 km SSE of Argos Orestiko, Greece
2001	5	17	2:01:07	2.80	40.550°N	21.280°E	5	2 km NE of Chlói, Greece
2001	5	25	14:12:52	3.00	40.170°N	21.310°E	5	10 km S of Tsotílli, Greece
2001	6	11	0:45:14	3.20	40.100°N	21.840°E	5	7 km SSE of Aianí, Greece
2001	6	15	17:34:49	3.30	40.140°N	21.210°E	5	16 km SW of Tsotílli, Greece
2001	7	16	10:49:28	3.10	40.450°N	21.840°E	13	2 km NW of Kleítos, Greece
2001	7	16	0:19:41	2.90	40.190°N	21.510°E	31	8 km SSW of Siátista, Greece
2001	9	25	3:55:39	3.20	40.390°N	21.190°E	4	9 km SW of Argos Orestiko, Greece
2001	9	25	0:10:26	3.20	40.500°N	21.665°E	10	2 km SW of Ptolemaida, Greece
2001	10	11	1:14:55	2.80	40.610°N	21.150°E	5	11 km N of Mesopotamía, Greece
2002	1	11	19:39:56	3.00	40.170°N	21.130°E	6	19 km WSW of Tsotílli, Greece
2002	1	11	18:44:35	3.10	39.970°N	21.390°E	5	13 km SSW of Grevená, Greece
2002	1	11	17:29:26	3.20	40.120°N	21.310°E	5	10 km WNW of Grevená, Greece
2002	1	14	11:16:29	2.80	39.930°N	21.440°E	9	17 km S of Grevená, Greece
2002	1	28	4:15:49	3.30	39.990°N	21.700°E	5	11 km NW of Deskáti, Greece

The PilotSTRATEGY project has received funding from the European Union's Horizon 2020 research and innovation programme under grant agreement No. 101022664

2002	4	8	4:40:28	3.00	40.330°N	20.970°E	5	12 km SW of Nestório, Greece
2002	5	28	4:47:10	3.00	40.210°N	21.560°E	22	5 km SSE of Siátista, Greece
2002	6	4	21:10:17	3.10	40.450°N	21.750°E	27	9 km SE of Ptolemaida, Greece
2002	6	13	18:39:44	3.30	40.170°N	21.800°E	13	1 km WNW of Aianí, Greece
2002	6	13	12:43:34	3.30	40.440°N	21.330°E	21	6 km ESE of Argos Orestiko, Greece
2002	8	20	0:15:39	3.40	40.348°N	21.063°E	10	7 km S of Nestório, Greece
2002	9	26	20:47:55	3.00	39.970°N	20.950°E	4	18 km ESE of Kónitsa, Greece
2002	11	3	19:44:57	3.00	40.160°N	21.180°E	29	16 km SW of Tsotílli, Greece
2002	12	23	22:35:25	3.20	39.910°N	21.330°E	5	20 km NE of Metsovo, Greece
2002	12	23	19:24:48	3.50	39.910°N	21.370°E	5	19 km SSW of Grevená, Greece
2002	12	23	17:12:20	3.20	39.890°N	21.360°E	4	20 km NE of Metsovo, Greece
2003	2	8	5:47:55	3.20	40.110°N	21.170°E	30	21 km SW of Tsotílli, Greece
2003	2	13	20:19:05	3.10	40.340°N	21.070°E	3	8 km S of Nestório, Greece
2003	2	15	19:49:27	2.70	40.060°N	21.440°E	4	2 km SSE of Grevená, Greece
2003	3	7	8:07:30	3.40	40.310°N	21.270°E	20	7 km NW of Tsotílli, Greece
2003	3	7	8:03:30	3.60	40.300°N	21.280°E	19	5 km NW of Tsotílli, Greece
2003	3	9	6:41:39	3.40	40.230°N	21.300°E	22	4 km SSW of Tsotílli, Greece
2003	3	10	22:47:24	3.20	39.810°N	21.660°E	5	10 km NNE of Kastráki, Greece
2003	3	13	21:37:27	3.00	40.470°N	21.220°E	13	3 km WNW of Argos Orestiko, Greece
2003	4	12	18:22:06	3.00	40.230°N	21.470°E	10	7 km WSW of Siátista, Greece
2003	6	6	10:05:25	2.40	40.166°N	21.679°E	10	11 km W of Aianí, Greece
2003	6	10	11:54:38	3.00	40.183°N	21.696°E	10	10 km WNW of Aianí, Greece
2003	6	11	17:13:02	3.60	40.173°N	21.633°E	10	12 km SE of Siátista, Greece

The PilotSTRATEGY project has received funding from the European Union's Horizon 2020 research and innovation programme under grant agreement No. 101022664

2003	6	12	9:20:23	2.70	40.131°N	21.529°E	4	10 km ENE of Grevená, Greece
2003	6	15	1:02:57	3.20	40.110°N	21.790°E	5	6 km SSW of Aianí, Greece
2003	6	15	14:27:19	2.60	40.184°N	21.744°E	10	6 km WNW of Aianí, Greece
2003	6	15	7:33:17	2.40	40.240°N	21.687°E	1	10 km SW of Kozáni, Greece
2003	8	8	13:16:10	2.60	40.383°N	21.666°E	2	12 km NE of GaLatitudeiní, Greece
2003	8	23	14:09:21	4.00	40.590°N	21.010°E	19	4 km SSE of Bilisht, Albania
2003	10	5	12:08:33	2.50	40.427°N	21.524°E	3	7 km SSW of Empório, Greece
2003	10	19	16:34:12	2.40	40.566°N	21.230°E	2	3 km NW of Chlói, Greece
2003	10	22	14:10:51	3.00	40.371°N	20.941°E	10	11 km WSW of Nestório, Greece
2004	4	28	20:14:43	3.00	40.080°N	21.630°E	10	17 km E of Grevená, Greece
2004	4	29	15:31:31	3.10	40.130°N	21.630°E	19	16 km SSE of Siátista, Greece
2004	6	17	23:03:30	3.00	39.890°N	21.030°E	33	18 km NW of Metsovo, Greece
2004	6	17	21:35:21	3.90	40.181°N	21.297°E	2,8	9 km SSW of Tsotílli, Greece
2004	6	19	7:43:20	3.00	40.288°N	21.334°E	12	3 km NNE of Tsotílli, Greece
2004	7	30	3:27:16	3.20	40.120°N	21.790°E	3	5 km SSW of Aianí, Greece
2004	8	14	11:29:50	2.50	39.973°N	21.844°E	4	6 km NNE of Deskáti, Greece
2004	8	14	5:33:25	3.30	40.140°N	21.740°E	7	7 km WSW of Aianí, Greece
2004	8	16	11:43:00	2.50	40.048°N	21.747°E	1	14 km SSW of Aianí, Greece
2004	8	19	12:42:41	2.80	40.465°N	21.527°E	13	3 km SW of Empório, Greece
2004	8	25	21:34:32	2.60	40.123°N	21.590°E	10	14 km ENE of Grevená, Greece
2004	8	28	10:00:17	3.20	40.167°N	21.417°E	10	9 km N of Grevená, Greece
2004	9	2	3:20:18	3.00	40.600°N	21.860°E	4	7 km E of Komniná, Greece
2004	10	28	0:46:34	3.70	40.180°N	21.820°E	12	1 km N of Aianí, Greece
2004	11	6	23:07:27	2.70	39.875°N	21.498°E	0	20 km NNW of Kastráki, Greece

The PilotSTRATEGY project has received funding from the European Union's Horizon 2020 research and innovation programme under grant agreement No. 101022664

2004	11	9	12:51:18	3.00	39.840°N	21.710°E	5	12 km SW of Deskáti, Greece
2004	11	23	16:01:02	3.60	40.360°N	21.280°E	22	10 km S of Argos Orestiko, Greece
2004	12	23	19:43:32	3.20	39.990°N	21.670°E	7	14 km WNW of Deskáti, Greece
2004	12	23	16:32:00	3.00	39.950°N	21.630°E	3	15 km W of Deskáti, Greece
2005	1	3	23:51:44	3.50	40.060°N	21.275°E	1,9	13 km WSW of Grevená, Greece
2005	2	27	20:10:40	3.00	39.790°N	20.950°E	41	13 km NE of Pérama, Greece
2005	3	14	5:07:44	3.10	40.540°N	20.950°E	19	10 km SSW of Bilisht, Albania
2005	6	1	5:34:22	3.20	40.380°N	20.950°E	5	10 km WSW of Nestório, Greece
2005	7	5	1:05:15	3.00	40.550°N	21.780°E	5	4 km S of Komniná, Greece
2005	7	10	20:00:48	3.20	40.390°N	21.780°E	10	6 km N of Koíla, Greece
2005	7	12	17:00:47	3.30	40.050°N	21.720°E	2	15 km SW of Aianí, Greece
2005	7	13	3:33:26	3.20	40.120°N	21.840°E	13	5 km SSE of Aianí, Greece
2005	7	19	22:36:15	3.20	40.420°N	21.100°E	19	3 km ENE of Nestório, Greece
2005	7	19	15:39:12	3.00	40.100°N	21.750°E	20	9 km SW of Aianí, Greece
2005	7	30	3:57:22	3.20	40.160°N	21.820°E	10	0 km S of Aianí, Greece
2005	8	3	12:54:21	3.20	40.480°N	21.350°E	17	4 km SE of Mavrochóri, Greece
2005	9	18	4:53:30	3.50	40.016°N	21.579°E	3	15 km ESE of Grevená, Greece
2005	9	22	8:23:19	3.20	40.090°N	21.820°E	5	8 km S of Aianí, Greece
2005	9	24	7:23:23	3.30	39.990°N	21.140°E	5	24 km N of Metsovo, Greece
2005	10	3	21:55:02	3.50	40.440°N	21.160°E	24	6 km S of Mesopotamía, Greece
2005	10	5	9:19:22	3.40	40.340°N	21.190°E	23	13 km SE of Nestório, Greece
2005	10	23	13:13:37	3.10	39.970°N	21.460°E	39	13 km SSE of Grevená, Greece
2005	11	2	9:09:32	3.10	40.410°N	21.220°E	23	5 km SW of Argos Orestiko, Greece

The PilotSTRATEGY project has received funding from the European Union's Horizon 2020 research and innovation programme under grant agreement No. 101022664

2005	11	2	6:28:47	3.70	40.500°N	21.140°E	21	1 km W of Mesopotamía, Greece
2005	11	9	23:18:53	3.00	40.530°N	21.680°E	19	1 km N of Ptolemaida, Greece
2005	11	9	22:45:41	3.10	40.440°N	21.810°E	20	4 km WNW of Kleítos, Greece
2005	11	9	22:05:21	3.10	40.540°N	21.720°E	13	4 km NE of Ptolemaida, Greece
2005	11	10	8:37:20	3.20	40.570°N	21.740°E	23	3 km SW of Komniná, Greece
2006	1	16	21:09:52	2.60	39.860°N	21.270°E	15	12 km NE of Metsovo, Greece
2006	1	25	21:01:22	2.80	40.135°N	21.700°E	0	10 km WSW of Aianí, Greece
2006	2	2	23:54:47	4.20	40.450°N	21.320°E	26	5 km E of Argos Orestiko, Greece
2006	2	2	21:42:58	3.40	40.560°N	21.240°E	20	2 km NW of Chlói, Greece
2006	2	2	0:00:27	3.70	40.517°N	21.292°E	18,4	2 km WNW of Mavrochóri, Greece
2006	2	3	0:00:27	4.00	40.440°N	21.310°E	25	4 km ESE of Argos Orestiko, Greece
2006	2	8	12:56:33	3.70	40.430°N	21.630°E	5	8 km SE of Anaráchi, Greece
2006	2	23	0:46:45	3.30	40.300°N	21.340°E	30	4 km NNE of Tsotílli, Greece
2006	3	5	7:06:44	3.20	40.126°N	20.956°E	2,2	19 km ENE of Kónitsa, Greece
2006	5	19	21:48:00	3.30	40.370°N	21.280°E	25	9 km S of Argos Orestiko, Greece
2006	6	3	14:07:04	3.00	40.480°N	21.680°E	15	3 km S of Ptolemaida, Greece
2006	6	11	5:08:57	3.10	40.080°N	21.650°E	8	17 km WSW of Aianí, Greece
2006	6	26	13:14:41	3.40	39.850°N	21.120°E	42	10 km NNW of Metsovo, Greece
2006	6	30	16:53:34	3.30	39.870°N	21.260°E	27	13 km NNE of Metsovo, Greece
2006	7	39	1:30:48	3.00	40.470°N	20.930°E	13	12 km WNW of Nestório, Greece
2006	8	3	21:09:03	2.90	39.780°N	21.820°E	4	Greece
2006	9	3	18:36:08	3.20	39.880°N	21.690°E	22	11 km WSW of Deskáti, Greece

The PilotSTRATEGY project has received funding from the European Union's Horizon 2020 research and innovation programme under grant agreement No. 101022664

2006	9	3	18:15:20	3.00	39.890°N	21.660°E	19	13 km WSW of Deskáti, Greece
2006	11	2	7:53:01	3.00	40.135°N	21.839°E	9,1	3 km SSE of Aianí, Greece
2006	11	13	1:30:55	3.20	40.280°N	21.420°E	24	8 km ENE of Tsotílli, Greece
2006	11	13	1:27:20	3.00	40.220°N	21.470°E	23	7 km SW of Siátista, Greece
2006	12	2	21:52:01	2.90	40.040°N	21.270°E	5	14 km WSW of Grevená, Greece
2007	1	6	1:27:44	3.20	40.370°N	21.600°E	23	6 km NE of GaLatitudeiní, Greece
2007	1	12	19:42:29	3.30	40.620°N	21.180°E	10	11 km NW of Chlói, Greece
2007	1	22	23:45:06	3.20	40.590°N	21.720°E	19	4 km SSE of Filótas, Greece
2007	2	1	13:56:22	3.10	40.240°N	21.650°E	11	9 km ESE of Siátista, Greece
2007	4	14	22:14:26	3.40	40.550°N	21.660°E	16	4 km NNW of Ptolemaida, Greece
2007	4	19	1:42:59	3.30	39.890°N	21.510°E	19	21 km NNW of Kastráki, Greece
2007	5	15	22:33:42	3.40	40.550°N	21.780°E	21	4 km S of Komniná, Greece
2007	7	17	23:47:04	3.50	40.110°N	21.660°E	10	14 km WSW of Aianí, Greece
2007	7	17	23:24:45	3.10	40.183°N	21.609°E	1,7	10 km SSE of Siátista, Greece
2007	7	17	22:31:17	3.10	40.172°N	21.587°E	8,2	10 km SSE of Siátista, Greece
2007	7	17	22:24:21	3.60	40.140°N	21.680°E	18	12 km WSW of Aianí, Greece
2007	7	17	22:14:55	2.50	40.153°N	21.596°E	1,6	12 km SSE of Siátista, Greece
2007	7	17	22:03:39	3.10	40.172°N	21.680°E	5,1	11 km W of Aianí, Greece
2007	7	17	21:56:22	3.50	40.160°N	21.690°E	20	11 km W of Aianí, Greece
2007	7	17	21:46:50	3.30	40.120°N	21.740°E	15	8 km SW of Aianí, Greece
2007	7	17	21:22:13	3.20	40.210°N	21.880°E	28	4 km ESE of Áno Kómi, Greece
2007	7	17	21:14:31	3.20	40.200°N	21.700°E	32	10 km WNW of Aianí, Greece
2007	7	17	21:09:25	4.00	40.150°N	21.620°E	19	14 km SSE of Siátista, Greece

The PilotSTRATEGY project has received funding from the European Union's Horizon 2020 research and innovation programme under grant agreement No. 101022664

2007	7	17	20:38:51	3.30	40.170°N	21.580°E	1,4	10 km SSE of Siátista, Greece
2007	7	17	20:11:22	3.00	40.110°N	21.320°E	4	9 km WNW of Grevená, Greece
2007	7	17	20:06:00	2.90	40.160°N	21.617°E	0	12 km SSE of Siátista, Greece
2007	7	17	20:00:49	3.80	40.182°N	21.609°E	9,9	10 km SSE of Siátista, Greece
2007	7	17	19:59:13	3.10	40.120°N	21.710°E	14	10 km WSW of Aianí, Greece
2007	7	17	19:06:03	3.30	40.171°N	21.619°E	0,2	11 km SSE of Siátista, Greece
2007	7	17	18:53:00	3.50	40.130°N	21.680°E	17	12 km WSW of Aianí, Greece
2007	7	17	18:28:48	3.20	40.140°N	21.710°E	19	9 km WSW of Aianí, Greece
2007	7	17	18:23:21	4.90	40.157°N	21.532°E	22,6	11 km S of Siátista, Greece
2007	7	17	13:47:09	3.40	40.100°N	21.740°E	2	9 km SW of Aianí, Greece
2007	7	18	22:19:56	3.00	40.220°N	21.810°E	28	1 km WSW of Áno Kómi, Greece
2007	7	18	11:40:59	3.20	40.220°N	21.820°E	32	1 km SW of Áno Kómi, Greece
2007	7	18	7:02:59	3.30	40.150°N	21.610°E	18	13 km SSE of Siátista, Greece
2007	7	18	5:02:58	3.40	40.110°N	21.670°E	7	14 km WSW of Aianí, Greece
2007	7	18	2:36:49	3.30	40.140°N	21.630°E	5	15 km SSE of Siátista, Greece
2007	7	18	2:23:48	3.60	40.120°N	21.670°E	12	13 km WSW of Aianí, Greece
2007	7	18	1:36:44	3.20	40.120°N	21.760°E	5	7 km SW of Aianí, Greece
2007	7	18	0:52:44	3.10	40.150°N	21.582°E	0	12 km SSE of Siátista, Greece
2007	7	19	17:22:38	3.30	40.150°N	21.700°E	17	10 km W of Aianí, Greece
2007	7	19	4:53:47	3.30	40.150°N	21.810°E	17	1 km SSW of Aianí, Greece
2007	7	19	4:25:26	4.60	40.130°N	21.670°E	18	13 km WSW of Aianí, Greece
2007	7	20	23:34:35	3.40	40.110°N	21.700°E	5	11 km WSW of Aianí, Greece
2007	7	31	3:33:05	4.20	40.610°N	21.500°E	17	2 km NNE of Léchovo, Greece
2007	8	5	21:43:46	3.20	40.164°N	21.587°E	3,8	11 km SSE of Siátista, Greece

The PilotSTRATEGY project has received funding from the European Union's Horizon 2020 research and innovation programme under grant agreement No. 101022664

2007	8	15	20:02:17	3.10	40.127°N	21.549°E	1,8	11 km ENE of Grevená, Greece
2007	8	16	3:51:44	2.60	40.131°N	21.534°E	3,1	10 km ENE of Grevená, Greece
2007	9	1	17:21:13	3.30	40.130°N	21.670°E	15	13 km WSW of Aianí, Greece
2007	9	1	17:19:57	3.00	40.120°N	21.790°E	10	5 km SSW of Aianí, Greece
2007	9	13	10:47:00	3.10	40.350°N	21.250°E	39	11 km S of Argos Orestiko, Greece
2007	9	13	0:50:14	2.90	40.304°N	21.336°E	8,2	4 km N of Tsotílli, Greece
2007	9	13	0:31:01	3.20	40.276°N	21.267°E	7,5	5 km WNW of Tsotílli, Greece
2007	9	19	22:50:50	3.00	40.220°N	21.830°E	41	0 km SSE of Áno Kómi, Greece
2007	10	26	16:54:16	3.10	40.160°N	20.970°E	20	21 km NE of Kónitsa, Greece
2007	11	25	6:44:07	3.30	40.482°N	21.375°E	1,2	5 km SE of Mavrochóri, Greece
2008	1	31	21:42:26	3.20	39.940°N	21.290°E	13	19 km SW of Grevená, Greece
2008	2	15	3:01:37	3.30	40.520°N	21.530°E	21	4 km NW of Empório, Greece
2008	2	25	9:11:37	3.30	40.110°N	21.753°E	0	8 km SW of Aianí, Greece
2008	2	29	10:01:37	3.30	40.110°N	40.110°N	10	14 km WSW of Aianí, Greece
2008	3	5	12:02:43	3.60	40.470°N	40.470°N	0	3 km S of Mesopotamía, Greece
2008	5	17	1:08:49	3.20	39.890°N	21.870°E	5	6 km SE of Deskáti, Greece
2008	6	2	10:24:12	2.80	39.980°N	21.560°E	31	16 km SE of Grevená, Greece
2008	6	26	22:36:18	3.20	39.940°N	21.330°E	7	18 km SSW of Grevená, Greece
2008	6	27	0:35:54	3.50	39.940°N	21.360°E	20	17 km SSW of Grevená, Greece
2008	6	28	21:59:58	2.80	40.420°N	21.420°E	25	11 km NW of Erátyra, Greece
2008	7	22	21:56:09	2.70	39.990°N	21.830°E	4	7 km NNE of Deskáti, Greece
2008	8	1	2:51:00	3.20	40.060°N	21.390°E	19	4 km SW of Grevená, Greece
2008	8	13	11:22:38	3.20	40.440°N	21.810°E	16	4 km WNW of Kleítos, Greece

The PilotSTRATEGY project has received funding from the European Union's Horizon 2020 research and innovation programme under grant agreement No. 101022664

2008	8	16	20:21:49	3.80	40.210°N	21.480°E	25	7 km SW of Siátista, Greece
2008	8	24	11:22:12	3.30	40.460°N	21.830°E	8	3 km NW of Kleítos, Greece
2008	9	21	18:00:01	2.50	40.430°N	21.670°E	5	9 km S of Ptolemaida, Greece
Time Period 2010-2019								
Year	Month	Day	Time UTC	Magnitude	Latitude	Longitude	Depth (km)	Region
2010	10	23	6:17:41	4.90	39.960°N	21.420°E	20	13 km S of Grevená, Greece
2011	5	7	1:35:45	4.10	40.363°N	21.352°E	13,6	11 km NNE of Tsotílli, Greece
2011	9	23	20:59:43	4.00	40.524°N	21.414°E	0	8 km E of Mavrochóri, Greece
2012	6	17	19:20:42	4.60	40.540°N	21.640°E	24	4 km NW of Ptolemaida, Greece
2013	1	6	23:22:30	3.90	40.110°N	21.780°E	8	6 km SSW of Aianí, Greece
2013	6	1	23:03:41	4.20	40.178°N	21.683°E	5,1	11 km W of Aianí, Greece
2013	7	2	10:45:21	4.80	40.124°N	21.850°E	22,2	5 km SSE of Aianí, Greece
2013	7	3	13:28:24	4.80	40.147°N	21.826°E	18,5	1 km SSE of Aianí, Greece
2013	7	27	4:38:33	4.30	40.140°N	21.870°E	10	5 km ESE of Aianí, Greece
2014	2	26	1:42:50	4.10	40.230°N	21.640°E	25	8 km ESE of Siátista, Greece
2015	5	26	17:53:05	4.40	40.231°N	21.564°E	17,1	3 km SSE of Siátista, Greece
2015	5	30	1:56:17	4.00	40.176°N	21.651°E	0,1	13 km SE of Siátista, Greece
2016	6	28	11:03:48	4.30	39.816°N	21.156°E	1	5 km NNW of Metsovo, Greece
2018	11	30	22:28:16	4.20	40.468°N	21.607°E	10	3 km SE of Anaráchi, Greece
2019	7	14	10:59:18	4.50	40.256°N	21.799°E	10	1 km WSW of Krókos, Greece
2019	7	14	10:50:13	4.90	40.220°N	21.865°E	10	3 km ESE of Áno Kómi, Greece
Time Period 2020-2022								
Year	Month	Day	Time UTC	Magnitude	Latitude	Longitude	Depth (km)	Region
2020	4	15	12:20:37	4.10	40.572°N	21.843°E	10	5 km ESE of Komniná, Greece

The PilotSTRATEGY project has received funding from the European Union's Horizon 2020 research and innovation programme under grant agreement No. 101022664

2020	6	1	23:15:01	3.20	40.459°N	21.483°E	10	7 km WSW of Empório, Greece
2021	3	23	0:08:03	4.40	40.090°N	20.996°E	10	20 km ENE of Kónitsa, Greece
2021	5	11	21:31:01	4.80	40.528°N	20.985°E	10	11 km S of Bilisht, Albania

Table Appendix 10.9.12: Number of earthquakes per time period, West Macedonia.

Time period	Number of earthquakes			
	4≤M<5	5≤M<6	6≤M<7	7≤M<8
900-1909	0	1	0	0
1910-1919	0	4	1	0
1920-1929	0	3	0	0
1930-1939	0	1	0	0
1940-1949	0	4	0	0
1950-1959	0	1	0	0
1960-1969	15	3	1	0
1970-1979	13	1	0	0
1980-1989	8	1	0	0
1990-1999	130	6	1	0
2000-2009	8	0	0	0
2010-2019	15	0	0	0
2020-2022	3	0	0	0
Sum	192	25	3	0

Table Appendix 10.9.13: Composite Seismogenis Sources and Individual Seismogenis Sources, West Macedonia

Faults	Composite Seismogenis Sources (CSSs)	Length	Faults direction	Faults description	Earthquakes (Magnitude)
Nymfeo ISS	Amyndeo CSS	13 km	NE-SW	trending structure showing angular segment boundary geometry	>6.0
Petron ISS	Amyndeo CSS	9 km		local depression where the Petron Lake is located	>6.0
Chimatidis ISS	-	12 km		joined with Nymfeo fault at a maximum depth of 7.5 km	<6.0
Vegoritida ISS	Ptolemaida CSS		NE		6,0
Vegora ISS	Ptolemaida CSS		SW	Vegora ISS overlaps the Vegoritida ISS, reaching a total length of more than 14 km	6,2
Perdika ISS		12 km		sub-parallel and synthetic with the Chimatidis Fault	<6.0
Mesovouni ISS	Komanos CSS		NE	borders the northwestern front of the Mount Vermion for at least 17 km	6,2
Proastio ISS	Komanos CSS		SW	northern borders of the lignite mines	6,0
Paleochori ISS	Aliakmonas CSS	21 km	SW	discontinuous escarpment that fades away towards SW	

The PilotSTRATEGY project has received funding from the European Union's Horizon 2020 research and innovation programme under grant agreement No. 101022664

Rymnio ISS	Aliakmonas CSS			Northeast of Palaeochori ISS, the Rymnio ISS is separated by an angular barrier	
Servia ISS	Aliakmonas CSS			Next to Rymnio fault and corresponds to the most prominent neotectonic structure of the Aliakmonas CSS	

Appendix VIII Flood data record

Table Appendix 10.9.14: Flood hazard risk zones, West Macedonia

RISK ZONE	LOCATION	FLOOD RISK	HAZARD CLASS	T=50 YEARS (%)	T=100 YEARS (%)	T=1000 YEARS (%)
GR09RAK0001	Low zone of regional ditch and associated rivers, plain of Katerini and Litochoro (880 km^2)	Low, except for limited areas (Katerini, Karditsa, Leptokarya and Korino) where the impacts are recorded to be from high to very high				
GR09RAK0002	Low zone through the Aliakmona river (Sarakina district, Karpero) (102 km^2)	Very low to low	Above 0.6		80	90
GR09RAK0003	Right shoreside area of artificial lake Polyphytos (63 km^2)	Low except for the area of Serbia and upstream of the Pierian Mountain	Above 0.6		45	80
GR09RAK0004	Left shoreside area of artificial lake Polyphytos, low zone of Ftilia (51 km^2)	Low except for the area of the upstream Bermian highlands.	Above 0.6	9	50	-
GR09RAK0005	Kozani Plain (70 km^2)	Low except for the upstream Bermian highlands	Above 0.6			
GR09RAK0006	Low Xirolimni zone (36 km^2)	Low to medium				
GR09RAK0007	Low zone of the upper reaches of Aliakmonas and Lake Kastoria (637 km^2)	Low, while it is observed to be higher along the entire length of the river on the upstream side of its bed and at Grevena region.	Above 0.6		49	68
GR09RAK0008	Low zone of basin of Ptolemaida, lakeside areas of lakes Zazari,	low to very low	Above 0.6		17	46

The PilotSTRATEGY project has received funding from the European Union's Horizon 2020 research and innovation programme under grant agreement No. 101022664

	Heimaditita, Petron and south of lake Vegoritida (698 km^2)					
GR09RAK0009	Arnissa area, Ag. Athanasios coastal areas north of Lake Vegoritida (34 km^2)	Low and it is increased only in limited areas such as in the low zone of Lake Vergotida and in the outlets of streams in the northern mountain zone				20
GR09RAK0010	Prespa basin low zone (26 km^2)					
GR09RAK0011	Upper side of regional trench T66 (34 km^2)	Low,high to very high in the upstream of the zone at the border with the zone GR09RAK00013 and at the limits of the zone towards Skydra	Under 0.4	80	80	80
GR09RAK0012	Low zone of the basin of Axios in the Prefecture of Florina (Lygos) (290 km^2)	Low, it rises gradually at the right bank of Lygos river towards W.Macedonia borders	Above 0.6		23	33
GR09RAK0013	Low zone of Mavropotamos (Almopeia area) and associated rivers (177 km^2)	Low	Above 0.6	8	15	28

Appendix IX Landslides data record

Table Appendix 10.9.15: List of recent landslides in West Macedonia

No	Region	Locality	Type
1	Grevena Regional Unit	Egnatia road from Grevena to Panagia village	Landslide on Engineering structures
2	Grevena Regional Unit	Grevena-M. Sirini provincial road	Landslide on Engineering structures
3	Grevena Regional Unit	On the road links Panorama-Perivoli, Samarina, Vasilitsa and Avdella	Landslide on Engineering structures
4		Access road of Kastoria city	Landslide on Engineering structures
5	Kozani Regional Unit	Velventos shelter	Landslide on Engineering structures
6	Kozani Regional Unit	Rymnio-Kamvounia provincial road	Landslide on Engineering structures
7	Kozani Regional Unit	Neapolis-Skalochori provincial road	Landslide on Engineering structures
8	Kozani Regional Unit	Palaiogratsano shelter	Landslide on Engineering structures

The PilotSTRATEGY project has received funding from the European Union's Horizon 2020 research and innovation programme under grant agreement No. 101022664

9	Kozani Regional Unit	Dilofos settlement (Kozani-Ioannina Old National Road)	Landslide on Engineering structures
10	Florina Regional Unit	Pyrgon junction at the Florina-Edessa national road	Landslide on Engineering structures
11	Florina Regional Unit-Kastoria Regional Unit	Along the National Road of Florina-Pisoderio-Kastoria	Landslide on Engineering structures
12	Florina Regional Unit	Florina-Alona provincial road	Landslide on Engineering structures
13	Grevena Regional Unit	Settlements of Philippaia, Polinerio and Panorama	Landslide in settlement region
14	Kastoria Regional Unit	Kefalari settlement	Landslide in settlement region
15	Kozani Regional Unit	Mavropigi settlement	Landslide in settlement region
16	Florina Regional Unit	Alona settlement	Landslide in settlement region
17	Kozani Regional Unit	Ptolemaida mine	Anthropogenic (mining activities of the Public Power Corporation-PPC)
18	Florina Regional Unit	Amynteo mine (west part)	Anthropogenic (mining activities of the Public Power Corporation-PPC)

The PilotSTRATEGY project has received funding from the European Union's Horizon 2020 research and innovation programme under grant agreement No. 101022664

Appendix X Absorption test result (Excel file)

Sample N.	Sample code	Rock type	Reaction to 10% hydrochloric acid	Weight (g) before drying	Weight (g) after drying	Sample volume	Sample density before drying	Sample density after drying	Weight after test (24 hours)	Water volume (ml) before test in the 2000 ml tank	Remaining water volume (ml) in the 2000 ml tank after test	Remaining water volume (ml) if consider water	Water absorbed by the rock if consider water evaporitization	Stability of sample in water (24 hours)	Calculation of the absorbed water per 1000g of rock	MIN	MAX	STDEV	AVG
1	**1_1**	Sandstone	Calcareous	508	506	220	2,31	2,3	511	1000	950	975	25	1	49	18	301	74	117
2	**1_2**	Sandstone	Calcareous	410	410	180	2,28	2,28	416	1000	927	952	48	1	117				
3	**1_2_1**	Sandstone	Slightly calcareous	548	548	225	2,44	2,44	566	1000	920	945	55	2	100				
4	**1_3**	Sandstone	Slightly calcareous	224	222	100	2,24	2,22	230	1000	945	970	30	2	135				
4	**1_3_1**	Sandstone	Slightly calcareous	920	920	400	2,30	2,30	942	1000	950	975	25	1	27				
4	**1_3_2**	Sandstone	Slightly calcareous	312	310	140	2,23	2,21	324	1000	900	925	75	1	242				
4	**1_3_3**	Sandstone	Slightly calcareous	220	220	100	2,2	2,2	228	1000	960	985	15	1	68				
4	**1_3_4**	Sandstone	Slightly calcareous	216	216	80	2,7	2,7	224	1000	910	935	65	1	301				
4	**1_3_5**	Sandstone	Slightly calcareous	444	438	180	2,47	2,43	456	1000	895	920	80	1	183				
4	**1_3_6**	Sandstone	Slightly calcareous	370	366	140	2,64	2,61	380	1000	900	925	75	1	205				
5	**1_4**	Sandstone	Calcareous	516	514	210	2,46	2,45	524	1000	930	955	45	1	88				
5	**1_4_1**	Sandstone	Calcareous	742	738	250	2,97	2,95	752	1000	910	935	65	1	88				
5	**1_4_2**	Sandstone	Calcareous	512	510	225	2,28	2,27	520	1000	960	985	15	1	29				
5	**1_4_3**	Sandstone	Calcareous	382	372	150	2,55	2,48	388	1000	880	905	95	1	255				
5	**1_4_4**	Sandstone	Calcareous	700	684	220	3,18	3,11	710	1000	895	920	80	1	117				

The PilotSTRATEGY project has received funding from the European Union's Horizon 2020 research and innovation programme under grant agreement No. 101022664

5	1_4_5	Sandstone	Calcareous	260	258	100	2,60	2,58	264	1000	950	975	25	1	97					
5	1_4_6	Sandstone	Calcareous	338	336	150	2,25	2,24	344	1000	890	915	85	1	253					
6	1_5	Sandstone	Calcareous	472	472	200	2,36	2,36	478	1000	935	960	40	2	85					
7	1_6	Sandstone	Slightly calcareous	590	586	245	2,41	2,39	606	1000	927	952	48	1	82					
8	1_7	Sandstone	Calcareous	372	370	200	1,86	1,85	374	1000	950	975	25	1	68					
9	1_8	Marly sandstone	Calcareous	498	498	200	2,49	2,49	452	1000	950	975	25	1	50					
10	1_9	Sandstone	Calcareous	314	312	180	1,74	1,73	324	1000	935	960	40	1	128					
11	1_10	Sandstone	Calcareous	588	586	250	2,35	2,34	590	1000	925	950	50	1	85					
12	1_11	Sandstone	Calcareous	228	226	100	2,28	2,26	232	1000	940	965	35	1	155					
12	1_11_1	Sandstone	Calcareous	286	284	120	2,38	2,37	288	1000	970	995	5	1	18					
12	1_11_2	Sandstone	Calcareous	402	402	200	2,01	2,01	408	1000	915	940	60	1	149					
12	1_11_3	Sandstone	Calcareous	418	416	170	2,46	2,45	420	1000	915	940	60	1	144					
12	1_11_4	Sandstone	Calcareous	272	270	100	2,72	2,7	274	1000	960	985	15	1	56					
12	1_11_5	Sandstone	Calcareous	170	170	65	2,62	2,62	175	1000	960	985	15	1	88					
12	1_11_6	Sandstone	Calcareous	510	508	260	1,96	1,95	512	1000	965	990	10	1	20					
13	1_12	Sandstone	Calcareous	260	256	125	2,08	2,05	268	1000	940	965	35	1	137					
14	2_1a	Sandstone	Sligthly calcareous	722	718	300	2,41	2,39	736	1000	930	955	45	1	63	MIN	MAX	STDEV	AVG	
15	2_1b	Marl	Sligthly calcareous	334	330	150	2,23	2,20	340	1000	964	989	11	1	33	0	357	79	89	
16	2_2	Sandstone	Sligthly calcareous	424	422	220	1,93	1,92	428	1000	947	972	28	1	66					
17	2_3	Conglomeratic sandstone	Sligthly calcareous	288	286	140	2,06	2,04	296	1000	970	995	5	2	17					
18	2_4	Sandstone	Sligthly calcareous	370	366	180	2,06	2,03	376	1000	945	970	30	1	82					
19	2_5	Marl	Calcareous	136	134	80	1,70	1,68	146	1000	940	965	35	2	261					
20	2_6	Conglomerate	Sligthly	442	438	225	1,96	1,95	452	1000	930	955	45	1	103					

The PilotSTRATEGY project has received funding from the European Union's Horizon 2020 research and innovation programme under grant agreement No. 101022664

			calcareous																
21	**2_7**	Conglomeratic sandstone	Sligthly calcareous	700	696	300	2,33	2,32	724	1000	930	955	45	1	65				
22	**2_8a**	Marl	Calcareous	270	266	125	2,16	2,13	456	1000	880	905	95	5	357				
23	**2_8b**	Sandstone	Calcareous	352	348	200	1,76	1,74	364	1000	945	970	30	1	86				
24	**2_9**	Marly sandstone	Calcareous	234	232	100	2,34	2,32	236	1000	970	995	5	1	22				
25	**2_10**	Sandstone	Non calcareous	628	626	250	2,51	2,50	632	1000	940	965	35	1	56				
26	**2_11**	Marl	Calcareous	358	352	225	1,59	1,56	382	1000	930	955	45	2	128				
27	**2_12a**	Sandstone	Sligthly calcareous	376	374	200	1,88	1,87	376	1000	950	975	25	1	67				
27	**2_12a_1**	Sandstone	Sligthly calcareous	334	332	170	1,96	1,95	338	1000	950	975	25	1	75				
27	**2_12a_2**	Sandstone	Sligthly calcareous	288	288	150	1,92	1,92	290	1000	975	1000	0	1	0				
27	**2_12a_3**	Sandstone	Sligthly calcareous	300	298	125	2,4	2,38	300	1000	975	1000	0	1	0				
27	**2_12a_4**	Sandstone	Sligthly calcareous	200	200	90	2,22	2,22	200	1000	975	1000	0	1	0				
27	**2_12a_5**	Sandstone	Sligthly calcareous	508	506	200	2,54	2,53	512	1000	955	980	20	1	40				
27	**2_12a_6**	Sandstone	Sligthly calcareous	502	500	200	2,51	2,50	506	1000	960	985	15	1	30				
28	**2_12b**	Marl	Sligthly calcareous	186	186	100	1,86	1,86	192	1000	942	967	33	1	177				
28	**2_12b_1**	Marl	Sligthly calcareous	152	152	75	2,03	2,03	158	1000	960	985	15	2	99				
28	**2_12b_2**	Marl	Sligthly calcareous	232	230	120	1,93	1,92	240	1000	925	950	50	2	217				
28	**2_12b_3**	Marl	Sligthly	220	218	105	2,10	2,08	228	1000	945	970	30	1	138				

The PilotSTRATEGY project has received funding from the European Union's Horizon 2020 research and innovation programme under grant agreement No. 101022664

			calcareous																
28	**2_12b_4**	Marl	Slighthly calcareous	254	250	150	1,69	1,67	260	1000	975	1000	0	1	0				
28	**2_12b_5**	Marl	Slighthly calcareous	134	134	65	2,06	2,06	138	1000	950	975	25	1	187				
28	**2_12b_6**	Marl	Slighthly calcareous	336	332	160	2,10	2,08	340	1000	925	950	50	2	151				
29	**2_13**	Conglomerate	Slighthly calcareous	576	570	250	2,30	2,28	588	1000	910	935	65	2	114				
30	**2_14**	Marl	Slighthly calcareous	654	650	255	2,56	2,55	678	1000	915	940	60	1	92				
31	**2_15**	Marl	Slightly calcareous	656	652	260	2,52	2,51	672	1000	930	955	45	2	69				
32	**2_16**	Marl	Calcareous	374	370	160	2,34	2,31	380	1000	970	995	5	1	14				
33	**2_17**	Sandstone	Non calcareous	550	546	230	2,39	2,37	560	1000	960	985	15	1	27				
34	**2_18a**	Marl	Calcareous	402	396	200	2,01	1,98	408	1000	932	957	43	1	109				
35	**2_18b**	Sandstone	Calcareous	426	422	220	1,94	1,92	436	1000	925	950	50	1	118				
36	**2_19**	Sandstone	Slightly calcareous	288	286	140	2,06	2,04	294	1000	974	999	1	1	3,5				
37	**2_20**	Sandstone	Slightly calcareous	394	392	150	2,63	2,61	402	1000	915	940	60	1	153				
38	**3_1**	Conglomeratic sandstone	Non calcareous	156	154	170	0,92	0,91	158	1000	975	1000	0	1	0	**MIN**	**MAX**	**STDEV**	**AVG**
39	**3_2**	Conglomerate	Non calcareous	406	400	180	2,26	2,22	422	1000	907	932	68	2	170	0	188	65	85
40	**3_3**	Conglomeratic sandstone	Slightly calcareous	260	256	120	2,17	2,13	272	1000	927	952	48	1	188				
41	**3_3a**	Conglomeratic sandstone	Slightly calcareous	232	230	110	2,11	2,09	238	1000	970	995	5	1	22				

The PilotSTRATEGY project has received funding from the European Union's Horizon 2020 research and innovation programme under grant agreement No. 101022664

42	**3_4**	Conglomeratic sandstone	Non calcareous	560	558	225	2,49	2,48	566	1000	935	960	40	1	72				
42	**3_4_1**	Conglomeratic sandstone	Non calcareous	564	560	250	2,26	2,24	572	1000	930	955	45	1	80				
42	**3_4_2**	Conglomeratic sandstone	Non calcareous	406	404	175	2,32	2,31	412	1000	950	975	25	1	62				
42	**3_4_3**	Conglomeratic sandstone	Non calcareous	196	196	75	2,61	2,61	202	1000	940	965	35	1	179				
42	**3_4_4**	Conglomeratic sandstone	Non calcareous	980	974	400	2,45	2,44	988	1000	900	925	75	1	77				
42	**3_4_5**	Conglomeratic sandstone	Non calcareous	676	672	300	2,25	2,24	676	1000	935	960	40	1	60				
42	**3_4_6**	Conglomeratic sandstone	Non calcareous	468	464	200	2,34	2,32	470	1000	975	1000	0	1	0				
43	**3_5**	Marl	Calcareous	235	230	110	2,14	2,09	250	1000	950	975	25	2	109				
44	**4_1**	Loose conglomerate	Slightly calcareous	N.A.	N.A.	N.A.	N.A.	N.A.	N.A.	N.A.	N.A.	N.A.	N.A.	N.A.	N.A.	**MIN**	**MAX**	**STDEV**	**AVG**
45	**4_2**	Loose conglomerate	Slightly calcareous	N.A.	N.A.	N.A.	N.A.	N.A.	N.A.	N.A.	N.A.	N.A.	N.A.	N.A.	N.A.	0	286	64	98
46	**4_3**	Loose conglomerate	Slightly calcareous	N.A.	N.A.	N.A.	N.A.	N.A.	N.A.	N.A.	N.A.	N.A.	N.A.	N.A.	N.A.				
47	**4_4**	Conglomerate	Slightly calcareous	650	640	250	2,60	2,56	666	1000	895	920	80	2	125				
47	**4_4_1**	Conglomerate	Slightly calcareous	140	135	50	2,80	2,70	144	1000	975	1000	0	1	0				
47	**4_4_2**	Conglomerate	Slightly calcareous	374	364	170	2,20	2,14	386	1000	940	965	35	1	96				

The PilotSTRATEGY project has received funding from the European Union's Horizon 2020 research and innovation programme under grant agreement No. 101022664

47	**4_4_3**	Conglomerate	Slightly calcareous	788	784	300	2,63	2,61	808	1000	910	935	65	1	83				
47	**4_4_4**	Conglomerate	Slightly calcareous	320	314	125	2,56	2,51	328	1000	960	985	15	2	48				
47	**4_4_5**	Conglomerate	Slightly calcareous	612	606	230	2,66	2,63	634	1000	905	930	70	1	116				
47	**4_4_6**	Conglomerate	Slightly calcareous	268	262	100	2,68	2,62	274	1000	900	925	75	2	286				
48	**4_5**	Conglomeratic sandstone	Slightly calcareous	444	440	170	2,61	2,59	456	1000	950	975	25	1	57				
49	**4_6**	Conglomerate	Slightly calcareous	1312	1308	540	2,43	2,42	1344	1000	900	925	75	1	57				
49	**4_6_1**	Conglomerate	Slightly calcareous	246	242	90	2,73	2,69	252	1000	960	985	15	1	62				
49	**4_6_2**	Conglomerate	Slightly calcareous	450	444	200	2,25	2,22	458	1000	925	950	50	1	113				
49	**4_6_3**	Conglomerate	Slightly calcareous	792	786	330	2,40	2,38	808	1000	920	945	55	1	70				
49	**4_6_4**	Conglomerate	Slightly calcareous	142	138	50	2,84	2,76	150	1000	960	985	15	2	109				
49	**4_6_5**	Conglomerate	Slightly calcareous	348	342	150	2,32	2,28	358	1000	940	965	35	2	102				
49	**4_6_6**	Conglomerate	Slightly calcareous	466	460	275	1,69	1,67	478	1000	910	935	65	1	141				
50	**5_1**	Loose conglomerate	Slightly calcareous	N.A.	N.A.	N.A.	N.A.	N.A.	N.A.	N.A.	N.A.	N.A.	N.A.	N.A.	N.A.	**MIN**	**MAX**	**STDEV**	**AVG**
51	**5_1_1**	Well cemented conglomerate	Slightly calcareous	160	158	75	2,13	2,11	166	1000	970	995	5	1	32	32	477	133	199
52	**5_2**	Sand and	Slightly	N.A.	N.A.	N.A.	N.A.	N.A.	N.A.	N.A.	N.A.	N.A.	N.A.	N.A.	N.A.				

The PilotSTRATEGY project has received funding from the European Union's Horizon 2020 research and innovation programme under grant agreement No. 101022664

		cobbles	calcareous																
53	**5_3**	Sand and cobbles	Slightly calcareous	N.A.	N.A.	N.A.	N.A.	N.A.	N.A.	N.A.	N.A.	N.A.	N.A.	N.A.	N.A.				
54	**5_4**	Marly sandstone	Calcareous	476	470	200	2,38	2,35	494	1000	920	945	55	2	117				
54	**5_4_1**	Marly sandstone	Calcareous	858	852	375	2,29	2,27	896	1000	885	910	90	1	106				
54	**5_4_2**	Marly sandstone	Calcareous	248	244	100	2,48	2,44	258	1000	910	935	65	1	266				
54	**5_4_3**	Marly sandstone	Calcareous	352	348	150	2,35	2,32	374	1000	890	915	85	2	244				
54	**5_4_4**	Marly sandstone	Calcareous	368	362	160	2,30	2,26	380	1000	915	940	60	2	166				
54	**5_4_5**	Marly sandstone	Calcareous	350	346	155	2,26	2,23	365	1000	910	935	65	2	188				
54	**5_4_6**	Marly sandstone	Calcareous	450	446	210	2,14	2,12	462	1000	925	950	50	2	112				
55	**5_5**	Marly sandstone	Slightly calcareous	936	932	400	2,34	2,33	954	1000	930	955	45	1	48				
56	**5_6_1**	Marl	Slightly calcareous	132	128	60	2,20	2,13	158	1000	914	939	61	4	477				
57	**5_6_2**	Sandy marl	Sligthly calcareous	650	642	300	2,17	2,14	696	1000	895	920	80	2	125				
58	**5_6_3a**	Marly sand	Sligthly calcareous	474	468	240	1,98	1,95	622	1000	800	825	175	5	374				
59	**5_6_3b**	Marl	Slightly calcareous	384	378	170	2,26	2,22	450	1000	850	875	125	4	331				
60	**6_1**	Marly sandstone	Slightly calcareous	512	512	250	2,05	2,05	518	1000	950	975	25	1	49	**MIN**	**MAX**	**STDEV**	**AVG**
61	**6_2**	Sandstone	Slightly calcareous	428	426	170	2,52	2,51	440	1000	970	995	5	1	12	0	541	113	61
61	**6_2_1**	Sandstone	Slightly calcareous	326	324	129	2,53	2,51	394	1000	975	1000	0	1	0				
61	**6_2_2**	Sandstone	Slightly	222	220	88	2,52	2,50	292	1000	975	1000	0	1	0				

The PilotSTRATEGY project has received funding from the European Union's Horizon 2020 research and innovation programme under grant agreement No. 101022664

			calcareous																
61	6_2_3	Sandstone	Slightly calcareous	326	326	150	2,17	2,17	332	1000	945	970	30	1	92				
61	6_2_4	Sandstone	Slightly calcareous	120	120	60	2,00	2,00	128	1000	970	995	5	1	42				
61	6_2_5	Sandstone	Slightly calcareous	92	92	40	2,30	2,30	92	1000	975	1000	0	1	0				
61	6_2_6	Sandstone	Slightly calcareous	74	74	30	2,47	2,47	78	1000	935	960	40	1	541				
62	6_3	Marly sandstone	Slightly calcareous	292	290	125	2,34	2,32	302	1000	964	989	11	1	38				
62	6_3_1	Marly sandstone	Slightly calcareous	152	150	65	2,34	2,31	165	1000	970	995	5	1	33				
62	6_3_2	Marly sandstone	Slightly calcareous	252	250	108	2,33	2,31	125	1000	975	1000	0	1	0				
62	6_3_3	Marly sandstone	Slightly calcareous	264	264	125	2,11	2,11	278	1000	970	995	5	1	19				
62	6_3_4	Marly sandstone	Slightly calcareous	632	628	280	2,26	2,24	654	1000	920	945	55	1	88				
62	6_3_5	Marly sandstone	Slightly calcareous	106	104	50	2,12	2,08	108	1000	975	1000	0	1	0				
62	6_3_6	Marly sandstone	Slightly calcareous	526	522	220	2,39	2,37	544	1000	935	960	40	1	77				
63	6_4	Sandstone	Slightly calcareous	538	538	200	2,69	2,69	544	1000	942	967	33	1	61				
63	6_4_1	Sandstone	Slightly calcareous	530	530	197	2,69	2,69	542	1000	930	955	45	1	85				
63	6_4_2	Sandstone	Slightly calcareous	208	208	100	2,08	2,08	210	1000	960	985	15	1	72				
63	6_4_3	Sandstone	Slightly calcareous	400	400	175	2,29	2,29	402	1000	975	1000	0	1	0				

The PilotSTRATEGY project has received funding from the European Union's Horizon 2020 research and innovation programme under grant agreement No. 101022664

63	**6_4_4**	Sandstone	Slightly calcareous	186	186	80	2,33	2,33	188	1000	975	1000	0	1	0				
63	**6_4_5**	Sandstone	Slightly calcareous	218	218	80	2,73	2,73	220	1000	970	995	5	1	23				
63	**6_4_6**	Sandstone	Slightly calcareous	392	392	150	2,61	2,61	396	1000	930	955	45	1	115				
64	**7_1-3**	Serpentinite	Non calcareous	348	344	175	1,99	1,97	350	1000	975	1000	0	1	0	**MIN**	**MAX**	**STDEV**	**AVG**
65	**7_4**	Serpentinite	Non calcareous	514	510	225	2,28	2,27	520	1000	975	1000	0	1	0	0	348	88	37
66	**7_5-6**	Serpentinite	Non calcareous	226	222	120	1,88	1,85	228	1000	975	1000	0	1	0				
67	**7_7**	Serpentinized Hurzburgite	Non calcareous	442	440	190	2,33	2,32	446	1000	975	1000	0	1	0				
67	**7_7_1**	Serpentinized Hurzburgite	Non calcareous	442	440	190	2,33	2,32	446	1000	975	1000	0	1	0				
67	**7_7_2**	Serpentinized Hurzburgite	Non calcareous	442	440	190	2,33	2,32	446	1000	975	1000	0	1	0				
67	**7_7_3**	Serpentinized Hurzburgite	Non calcareous	442	440	190	2,33	2,32	446	1000	975	1000	0	1	0				
67	**7_7_4**	Serpentinized Hurzburgite	Non calcareous	442	440	190	2,33	2,32	446	1000	975	1000	0	1	0				
67	**7_7_5**	Serpentinized Hurzburgite	Non calcareous	442	440	190	2,33	2,32	446	1000	975	1000	0	1	0				
67	**7_7_6**	Serpentinized Hurzburgite	Non calcareous	442	440	190	2,33	2,32	446	1000	975	1000	0	1	0				
67	**7_7_7**	Serpentinized Hurzburgite	Non calcareous	123	123	50	2,46	2,46	123	1000	975	1000	0	1	0				

The PilotSTRATEGY project has received funding from the European Union's Horizon 2020 research and innovation programme under grant agreement No. 101022664

67	**7_7_8**	Serpentinized Hurzburgite	Non calcareous	505	503	220	2,30	2,29	510	1000	970	995	5	1	10				
67	**7_7_9**	Serpentinized Hurzburgite	Non calcareous	233	233	100	2,33	2,33	236	1000	975	1000	0	1	0				
67	**7_7_10**	Serpentinized Hurzburgite	Non calcareous	460	460	200	2,30	2,30	460	1000	975	1000	0	1	0				
67	**7_7_11**	Serpentinized Hurzburgite	Non calcareous	280	278	120	2,33	2,32	274	1000	970	995	5	1	18				
67	**7_7_12**	Serpentinized Hurzburgite	Non calcareous	105	105	45	2,33	2,33	105	1000	975	1000	0	1	0				
68	**7_8**	Marly sandstone	Slightly calcareous	264	262	125	2,11	2,10	270	1000	975	1000	0	1	0				
68	**7_8_1**	Marly sandstone	Slightly calcareous	254	252	120	2,12	2,10	262	1000	975	1000	0	1	0				
68	**7_8_2**	Marly sandstone	Slightly calcareous	164	162	77	2,13	2,10	172	1000	975	1000	0	1	0				
68	**7_8_3**	Marly sandstone	Slightly calcareous	490	488	200	2,45	2,44	502	1000	935	960	40	1	82				
68	**7_8_4**	Marly sandstone	Slightly calcareous	162	162	75	2,16	2,16	166	1000	975	1000	0	1	0				
68	**7_8_5**	Marly sandstone	Slightly calcareous	408	408	190	2,15	2,15	420	1000	940	965	35	1	86				
68	**7_8_6**	Marly sandstone	Slightly calcareous	52	52	20	2,60	2,60	54	1000	960	985	15	1	288				
69	**7_8_1**	Bedded conglomerate	Slightly calcareous	730	728	100	7,30	7,28	752	1000	722	747	253	1	348				
70	**7_9**	Bedded congl	Slightly calcareous	528	526	220	2,40	2,39	546	1000	937	962	38	1	72				

The PilotSTRATEGY project has received funding from the European Union's Horizon 2020 research and innovation programme under grant agreement No. 101022664

		omerate																	
71	7_10	Ophiolitic conglomerate	Non calcareous	238	236	180	1,32	1,31	246	1000	960	985	15	1	64				
72	8_1	Sandstone	Slightly calcareous	316	314	180	1,76	1,74	322	1000	950	975	25	1	80	MIN	MAX	STDEV	AVG
73	8_2	Sandstone	Calcareous	242	242	125	1,94	1,94	246	1000	952	977	23	1	95	31	497	104	155
74	8_3	Conglomeratic sandstone	Non calcareous	718	712	370	1,94	1,92	762	1000	855	880	120	2	169				
75	8_4	Marly sandstone	Slightly calcareous	396	392	125	3,17	3,14	478	1000	780	805	195	4	497				
76	8_5	Conglomerate	Slightly calcareous	312	312	100	3,12	3,12	322	1000	900	925	75	1	240				
77	8_6	Sandstone	Calcareous	380	378	150	2,53	2,52	392	1000	950	975	25	1	66				
78	8_7	Sandstone	Calcareous	322	322	100	3,22	3,22	330	1000	940	965	35	1	109				
79	8_8	Sandstone	Calcareous	522	520	200	2,61	2,60	536	1000	910	935	65	1	125				
80	8_9	Sandstone	Slightly calcareous	756	754	320	2,36	2,36	784	1000	880	905	95	1	126				
81	8_10	Sandstone	Calcareous	482	482	200	2,41	2,41	490	1000	960	985	15	1	31				
82	8_11	Marl	Slightly calcareous	374	372	150	2,49	2,48	384	1000	920	945	55	2	148				
83	8_12	Conglomerattic sandstone	Slightly calcareous	874	870	360	2,43	2,42	892	1000	910	935	65	1	75				
84	8_13	Marly sandstone	Calcareous	382	380	150	2,55	2,53	396	1000	915	940	60	1	158				
85	8_14	Marly sandstone	Calcareous	374	372	100	3,74	3,72	390	1000	900	925	75	1	202				
86	8_14_1	Sandstone	Calcareous	426	426	180	2,37	2,37	440	1000	915	940	60	1	141				
87	8_15	Conglomerate	Calcareous	470	468	190	2,47	2,46	474	1000	930	955	45	1	96				
88	8_16	Sandy marl	Slightly calcareous	300	298	120	2,50	2,48	316	1000	900	925	75	1	252				

The PilotSTRATEGY project has received funding from the European Union's Horizon 2020 research and innovation programme under grant agreement No. 101022664

89	**8_17**	Sand	Slightly calcareous	696	690	380	1,83	1,82	766	1000	850	875	125	1	181					
90	**9_1**	Sandstone	Slightly calcareous	384	380	175	2,19	2,17	408	1000	924	949	51	1	134	**MIN**	**MAX**	**STDEV**	**AVG**	
91	**9_2**	Limestone conglomerate	Calcareous	448	446	160	2,80	2,79	450	1000	922	947	53	1	119	0	264	64	57	
92	**9_3**	Marly sandstone	Non calcareous	402	400	160	2,51	2,50	408	1000	960	985	15	1	38					
93	**9_4**	Sandstone	Calcareous	960	958	480	2,00	2,00	972	1000	970	995	5	1	5					
94	**9_5**	Sandstone	Calcareous	574	572	200	2,87	2,86	582	1000	925	950	50	1	87					
95	**9_6**	Sandstone	Calcareous	882	880	350	2,52	2,51	894	1000	925	950	50	1	57					
96	**9_7**	Sandstone	Slightly calcareous	448	446	180	2,49	2,48	458	1000	970	995	5	1	11					
97	**9_8**	Sandstone	Slightly calcareous	214	214	100	2,14	2,14	220	1000	970	995	5	1	23					
98	**9_9**	Sandstone	Slightly calcareous	490	490	175	2,80	2,80	506	1000	950	975	25	1	51					
99	**9_10**	Sandstone	Slightly calcareous	374	372	150	2,49	2,48	384	1000	940	965	35	1	94					
100	**9_11**	Sandstone	Sligthly calcareous	436	434	180	2,42	2,41	446	1000	960	985	15	1	35					
101	**9_12**	Marly sandstone	Calcareous	210	208	100	2,10	2,08	226	1000	920	945	55	2	264					
102	**9_13**	Ophiolitic breccia	Slightly calcareous	650	638	300	2,17	2,13	686	1000	875	900	100	1	157					
103	**9_14**	Serpentinized hurzburgite	Non calcareous	616	616	250	2,46	2,46	622	1000	960	985	15	1	24					
104	**9_15**	Ophiolitic conglomerate	Slightly calcareous	238	232	60	3,97	3,87	250	1000	927	952	48	1	207					
105	**9_16a**	Serpentinized	Non calcareous	542	542	200	2,71	2,71	550	1000	950	975	25	1	46					

The PilotSTRATEGY project has received funding from the European Union's Horizon 2020 research and innovation programme under grant agreement No. 101022664

		peridotite																	
106	**9_16b**	Serpentinized pyroxenite	Non calcareous	634	632	200	3,17	3,16	634	1000	975	1000	0	1	0				
107	**9_17a**	Pyroxenite	Non calcareous	126	124	50	2,52	2,48	128	1000	970	995	5	1	40				
108	**9_17b**	Norite gabbro	Non calcareous	1116	1116	370	3,02	3,02	1122	1000	965	990	10	1	9				
109	**9_18**	Norite gabbro	Non calcareous	432	432	70	6,17	6,17	434	1000	970	995	5	1	12				
110	**9_19**	Gabbro	Non calcareous	156	156	50	3,12	3,12	156	1000	975	1000	0	1	0				
111	**9_20i**	Diorite	Non calcareous	522	518	200	2,61	2,59	520	1000	975	1000	0	1	0				
112	**9_20ii**	Quartz diorite	Non calcareous	230	230	80	2,88	2,88	230	1000	975	1000	0	1	0				
113	**9_21**	Basalt	Non calcareous	680	680	225	3,02	3,02	682	1000	935	960	40	1	59				
114	**9_22**	Limestone	Highly calcareous	326	326	150	2,17	2,17	326	1000	975	1000	0	1	0				
115	**9_23**	Limestone	Highly calcareous	488	486	180	2,71	2,70	488	1000	975	1000	0	1	0				
116	**9_24**	Limestone	Highly calcareous	604	604	230	2,63	2,63	608	1000	960	985	15	1	25				
117	**9_25a**	Conglomerate	Highly calcareous	876	874	350	2,50	2,50	884	1000	935	960	40	1	46				
118	**9_25b**	Sandstone	Calcareous	378	376	130	2,91	2,89	394	1000	950	975	25	1	66				
119	**9_26**	Marly sandstone	Calcareous	268	266	120	2,23	2,22	270	1000	945	970	30	1	113				
120	**9_27**	Marly sandstone	Calcareous	488	484	200	2,44	2,42	510	1000	900	925	75	2	155				
121	**9_28**	Sand	Non calcareous	256	254	100	2,56	2,54	0	1000	975	1000	0	5	0				
122	**9_29**	Sandstone	Calcareous	308	308	125	2,46	2,46	312	1000	960	985	15	1	49				
123	**9_30**	Sandstone	Calcareous	622	622	250	2,49	2,49	632	1000	940	965	35	1	56				
124	**KIV01**	Limestone	Highly calcareous	152	152	75	2,03	2,03	152	1000	975	1000	0	1	0				

The PilotSTRATEGY project has received funding from the European Union's Horizon 2020 research and innovation programme under grant agreement No. 101022664

The PilotSTRATEGY project has received funding from the European Union's Horizon 2020 research and innovation programme under grant agreement No. 101022664